

Univerza
v Ljubljani
Fakulteta
*za gradbeništvo
in geodezijo*



Jamova cesta 2
1000 Ljubljana, Slovenija
<http://www3.fgg.uni-lj.si/>

DRUGG – Digitalni repozitorij UL FGG
<http://drugg.fgg.uni-lj.si/>

V zbirki je izvirna različica doktorske disertacije.

Prosimo, da se pri navajanju sklicujete na bibliografske podatke, kot je navedeno:

University
of Ljubljana
Faculty of
*Civil and Geodetic
Engineering*



Jamova cesta 2
SI – 1000 Ljubljana, Slovenia
<http://www3.fgg.uni-lj.si/en/>

DRUGG – The Digital Repository
<http://drugg.fgg.uni-lj.si/>

This is an original PDF file of doctoral thesis.

When citing, please refer as follows:

Čermelj, B. 2015. Potresna odpornost varjenih spojev prečka-steber v hibridnih pomičnih in zavetrovanih okvirih. = Seismic resistance of welded beam-to-column connections in hybrid moment and braced frames. Doctoral dissertation. Ljubljana, Univerza v Ljubljani, Fakulteta za gradbeništvo in geodezijo. (Mentor Beg, D.)

<http://drugg.fgg.uni-lj.si>

Univerza
v Ljubljani

Fakulteta za
*gradbeništvo in
geodezijo*



PODIPLOMSKI ŠTUDIJ
GRADBENIŠTVA

DOKTORSKI ŠTUDIJ

Kandidat:

BLAŽ ČERMELJ, univ. dipl. inž. grad.

**POTRESNA ODPORNOST VARJENIH SPOJEV
PREČKA-STEBER V HIBRIDNIH POMIČNIH IN
ZAVETROVANIH OKVIRIH**

Doktorska disertacija štev.: 244

**SEISMIC RESISTANCE OF WELDED BEAM-TO-COLUMN
CONNECTIONS IN HYBRID MOMENT AND BRACED
FRAMES**

Doctoral thesis No.: 244

Soglasje k temi doktorske disertacije je dala Komisija za doktorski študij Univerze v Ljubljani na 18. redni seji 8. junija 2011.

Za mentorja je bil imenovan prof. dr. Darko Beg.

Pisanje v angleškem jeziku je odobrila Komisija za doktorski študij Univerze v Ljubljani na 35. redni seji 16. januarja 2013.

Ljubljana, 22. januar 2015

Univerza
v Ljubljani

Fakulteta za
*gradbeništvo in
geodezijo*



Komisijo za oceno ustreznosti teme doktorske disertacije v sestavi:

- prof. dr. Darko Beg,
- akad. prof. dr. Peter Fajfar,
- prof. dr. Stojan Kravanja, UM FG,

je imenoval Senat Fakultete za gradbeništvo in geodezijo na 20. redni seji
20. aprila 2011.

Poročevalce za oceno doktorske disertacije v sestavi:

- izr. prof. dr. Sebastjan Bratina,
- prof. dr. Jože Korelc,
- prof. dr. Stojan Kravanja, UM FG,
- prof. dr. Raffaele Landolfo, Università degli Studi di Napoli Federico II,

je imenoval Senat Fakultete za gradbeništvo in geodezijo na 13. redni seji
24. septembra 2014.

Komisijo za zagovor doktorske disertacije v sestavi:

- prof. dr. Matjaž Mikoš, dekan UL FGG, predsednik,
- izr. prof. dr. Sebastjan Bratina,
- prof. dr. Jože Korelc,
- prof. dr. Stojan Kravanja, UM FG,
- prof. dr. Raffaele Landolfo, Università degli Studi di Napoli Federico II, Italy,
- doc. dr. Franc Sinur,

je imenoval Senat Fakultete za gradbeništvo in geodezijo na 6. dopisni seji,
ki je trajala od 8. do 12. januarja 2015.

Univerza
v Ljubljani

Fakulteta za
*gradbeništvo in
geodezijo*



IZJAVA O AVTORSTVU

Podpisani **BLAŽ ČERMELJ, univ. dipl. inž. grad.**, izjavljam, da sem avtor doktorske disertacije z naslovom **POTRESNA ODPORNOST VARJENIH SPOJEV PREČKASTEBER V HIBRIDNIH POMIČNIH IN ZAVETROVANIH OKVIRIH.**

Izjavljam, da je elektronska različica v vsem enaka tiskani različici.

Izjavljam, da dovoljujem objavo elektronske različice v repozitoriju UL FGG.

STATEMENT OF AUTHORSHIP

I, undersigned **BLAŽ ČERMELJ, Univ. B.C.E.**, hereby declare that I am the author of the doctoral thesis titled **SEISMIC RESISTANCE OF WELDED BEAM-TO-COLUMN CONNECTIONS IN HYBRID MOMENT AND BRACED FRAMES.**

Ljubljana, 22. januar 2015

.....
(podpis/signature)

ERRATA

Page	Line	Error	Correction
------	------	-------	------------

BIBLIOGRAPHIC-DOCUMENTALISTIC INFORMATION

UDC:	624.014.2: 624.21(043)
Author:	Blaž Čermelj
Supervisor:	prof. Darko Beg, Ph.D.
Title:	Seismic resistance of welded beam-to-column connections in hybrid moment and braced frames
Notes:	285 p., 44 tab., 252 fig., 72 eq., 1 app.
Keywords:	full strength beam-to-column joint, stiffened welded connection, composite column, low-cycle fatigue, plastic rotation, overstrength, ductility, EN 1998-1

Abstract

Cyclic tests with different loading protocols were carried out on full-strength welded rib-stiffened and cover-plate beam-to-column joints to study their seismic performance. Composite columns were used to increase the robustness of the applied strong column/weak beam design concept. Hybrid-steel approach for moment-resisting and braced frames was implemented with high strength steel used for columns as non-dissipative elastic members and mild carbon steel for beams acting as dissipative members. Additional parameter of the study was axial force of high level compression in the column. All rib-stiffened and cover-plate beam-to-column joints fulfilled the objective of the applied capacity design concept: the whole inelastic action was transferred away from the face of the beam-to-column connection into the beam section behind the stiffened region. All the joints subjected to variable amplitude loading met prequalification requirements from EN 1998-1 and ANSI/AISC 341-10. The test results with additional experimental data from literature were used to verify numerical model, which was employed for further parametric studies on both types of stiffened connection subjected to monotonic and cyclic loading. An important part of the study was also dedicated to the development of damage curve for low-cycle fatigue resistance evaluation of joints. Numerical parametric study was performed to support the proposed joint detailing and design guidelines for the two stiffened joint types against possibly adverse beam member size effects within the selected range of practically applicable I and H beam profiles typically used in Europe. All designed stiffened beam-to-column joints developed full plastic capacity of the connected beam under monotonic and cyclic loading. Parametric study confirmed the outcomes from experimental tests: cover-plate is superior to rib-stiffened connection; column axial compressive load up to 60 % of its capacity should not undermine welded beam-to-column connection; the applied joint design concept results in reasonable stiffening plate dimensions for the considered range of beam profiles. The study presents an important contribution also in terms of flexural ultimate behaviour of steel beams and confirms the need for a twofold classification of steel members according to their ductility and overstrength as the most appropriate approach for seismic design applications. Clear distinction is made between overstrength due to random material variability γ_{ov} and overstrength due to strain-hardening s , which is still not clearly addressed in the current European seismic design code. Maximum value of the complete overstrength factor $1.1 \times \gamma_{ov} = 1.375$ as exists in EN 1998-1 was shown to be too small to guarantee a sufficient overstrength of a connection in order to assure the development of the full plastic capacity of the connected beam. Proposed values for both $\gamma_{ov} = 1.25$ and $s = 1.2$ result in overall overstrength factor $\gamma_{ov}' = s \cdot \gamma_{ov} = 1.5$, which proved to be satisfactory.

BIBLIOGRAFSKO-DOKUMENTACIJSKA STRAN Z IZVLEČKOM

- UDK:** 624.014.2: 624.21(043)
- Avtor:** Blaž Čermelj, univ. dipl. inž. grad.
- Mentor:** prof. dr. Darko Beg, univ. dipl. inž. grad.
- Naslov:** Potresna odpornost varjenih spojev prečka-steber v hibridnih pomičnih in zavetrovanih okvirih
- Obseg in oprema:** 285 str., 44 pregl., 252 sl., 72 en., 1 pril.
- Ključne besede:** polnonosilni spoj prečka-steber, varjen ojačan spoj, sovprežen steber, nizekociklično utrujanje, plastična rotacija, dodatna nosilnost, duktilnost, EN 1998-1

Izvleček

V nalogi je bila, na osnovi eksperimentalnih cikličnih testov, opravljena študija potresne odpornosti varjenih polnonosilnih spojev prečka-steber ojačanih z rebroma in veznima pločevinama. Pri tem so bili uporabljeni različni protokoli obremenjevanja. Za dosego večje robustnosti koncepta močan steber/šibka prečka so bili uporabljeni sovprežni stebri. Upoštevana je hibridna zasnova momentnih okvirov, pri čemer je jeklo visoke trdnosti uporabljeno v stebrih, nedisipativnih elementih, mehko konstrukcijsko jeklo pa v disipativnih prečkah. Dodatni parameter študije je bil visok nivo osne sile v stebru. Vsi preizkušanci so izkazali obnašanje skladno s konceptom načrtovane nosilnosti: varovan neduktilen varjeni stik ob pasnici stebra je ostal nepoškodovan, vse plastične deformacije so bile skoncentrirane v prečki za ojačanim delom. Vsi spoji testirani s spremenljivo amplitudo rotacije so zadostili prekvalifikacijskim pogojem iz EN 1998-1 in ANSI/AISC 341-10. Rezultati testov skupaj z eksperimentalnimi podatki iz literature so služili za verifikacijo numeričnega modela, ki je bil uporabljen v nadaljni parametrični študiji obeh konfiguracij ojačanih spojev pri monotoni in ciklični obremenitvi. Pomemben del študije obsega razvoj krivulje poškodb za analizo nizekocikličnega utrujanja spojev. Namen numerične parametrične študije je podkrepitev predlaganih priporočil za detajliranje in dimenzioniranje obeh obravnavanih tipov ojačanih spojev; predvsem v smislu zajema morebitnih neugodnih vplivov iz naslova različnih velikosti in geometrije I in H prečnih prerezov prečk, ki se pogosto uporabljajo v Evropi. Vsi analizirani polnonosilni spoji izpostavljeni monotoni in ciklični obremenitvi so izkazali polno plastično kapaciteto priključene prečke. Parametrična študija je potrdila rezultate testov: spoj z veznima pločevinama se obnaša bolje kot spoj ojačan z rebroma; tlačna osna sila v stebru do vrednosti 60 % njegove tlačne nosilnosti ne vpliva na obnašanje varjenega stika prečka-steber; za analiziran nabor prerezov prečk predlagan koncept dimenzioniranja daje povsem sprejemljive dimenzije ojačilnih pločevin. Študija predstavlja pomemben doprinos tudi v smislu mejne upogibne nosilnosti jeklenih prečk in potrjuje potrebo po uporabi dvojne klasifikacije jeklenih elementov pri potresno odpornem projektiranju: glede na njihovo duktilnost in dodatno upogibno nosilnost. Pri tem je bila posebej obravnavana večja možna nosilnost prečke zaradi pričakovane vrednosti tečenja materiala γ_{ov} in dodatna nosilnost s zaradi plastičnega utrjevanja jekla, kar še vedno ostaja nejasno obravnavano v EN 1998-1. Največja vrednost skupnega faktorja dodatne nosilnosti v skladu z EN 1998-1 znaša $1.1 \times \gamma_{ov} = 1.375$. V študiji je jasno pokazano, da ta vrednost v določenih primerih ne zagotavlja dovolj velike dodatne nosilnosti spoja za razvoj polnplastične kapacitete priključene prečke. Predlagani vrednosti $\gamma_{ov} = 1.25$ in $s = 1.2$ dajeta vrednost skupnega faktorja dodatne nosilnosti $\gamma_{ov}' = s \cdot \gamma_{ov} = 1.5$, kar se je izkazalo zadovoljivo.

To my family and friends for their loving support.

ZAHVALE

Del predstavljenih rezultatov je bil dobljen v okviru evropskega projekta HSS-SERF “High Strength Steel in Seismic Resistant Building Frames”, RFSR-CT-2009-00024. Finančna pomoč je bila dobljena tudi s strani javne agencije za raziskovalno dejavnost Republike Slovenije v okviru programa mladih raziskovalcev, dokument št. 1000-08-310066. Omenjenima prispevkoma se lepo zahvaljujem.

Iskreno se zahvaljujem svojemu mentorju, sedaj žal že pokojnemu, prof. dr. Darku Begu. Hvala za podeljeno možnost, vaše mentorstvo in izkazano zaupanje v okviru doktorskega študija. Hvala za vse vaše nasvete, spodbude in vodstvo tekom raziskovalnega dela. Hvala za vaše zaupanje pri delu na evropskem projektu, s katerim ste mi odprli vrata tudi do novih poznanstev priznanih tujih strokovnjakov na tem področju.

Boštjan Jursinovič, Franci Čepon in Janez Zakotnik, hvala za vašo razpoložljivost in vso pomoč pri delu v laboratoriju. Boštjan, hvala za tvoje iskreno prijateljstvo.

Franci Sinur, na začetku mojega dela na katedri si mi bil najbližji sodelavec, vedno na razpolago za pogovor, nasvet in pomoč. Vedno si mi bil in si mi še vedno vzor pri raziskovalnem delu. Iskrena hvala za vso tvojo podporo, zaupanje, verodostojnost in poštenje, še posebej v zadnjem obdobju mojega študija, ko si mi bil tako rekoč za nadomestnega mentorja.

Primož Može, vedno si mi bil na razpolago za pomoč in podporo. Iskrena hvala.

Hvala tudi ostalim kolegom na Katedri za metalne konstrukcije: Blažu Hudobivniku, Barbari Gorenc, Urši Šolinc, Teji Melink, Luku Pavlovčiču in Petru Skubru.

Vesel sem, da me je pot zanesla tudi v tujino, kjer sem spoznal tebe prijatelj moj Andreas Kleiner.

Hvala prijateljem in vsej moji družini. Omogočili ste mi in me podpirali, da sem lahko stopal po tej poti.

Na koncu bi se rad zavalil tebi, Katarina, za tvojo ljubezen, vzpodbudo, pomoč in razumevanje. Hvala ti, da si kljub včasih težkim trenutkom vztrajala z menoj do konca.

TABLE OF CONTENTS

1	INTRODUCTION.....	1
1.1	FOREWORD.....	1
1.2	MOTIVATIONS, OBJECTIVES AND SCOPE OF THE STUDY	3
1.3	ORGANISATION OF THE THESIS	8
2	LITERATURE REVIEW	11
2.1	INTRODUCTION	11
2.2	PREVIOUS RESEARCH WORK ON STIFFENED MOMENT-RESISTING CONNECTIONS	12
2.2.1	<i>Welded cover-plate moment-resisting connections</i>	12
2.2.2	<i>Welded rib-stiffened moment-resisting connections</i>	15
2.2.3	<i>Conclusions</i>	16
2.3	PRINCIPLES OF PLASTIC AND SEISMIC DESIGN OF STEEL FRAMES	17
2.3.1	<i>On the ductility of steel beams</i>	17
2.3.2	<i>Beam flexural overstrength</i>	21
2.4	LOW-CYCLE FATIGUE IN STEEL ELEMENTS SUBJECTED TO SEISMIC LOADING	24
2.4.1	<i>The mechanism of low and extremely low cycle fatigue (LCF, ELCF)</i>	24
2.4.2	<i>Stress and strain indices</i>	25
2.4.3	<i>Prediction of local failure behaviour of steel members</i>	28
2.4.3.1	Effective damage concept for the prediction of ductile cracking of steel members under large-scale cyclic loading	29
2.4.3.2	Damage curves for structural steel S355.....	32
3	EXPERIMENTAL CYCLIC TESTS ON STIFFENED JOINTS.....	33
3.1	INTRODUCTION	33
3.2	DESIGN AND DETAILING OF THE STIFFENED CONNECTIONS SUPPORTED BY FEA	34
3.2.1	<i>Stiffened connection design concept</i>	34
3.2.2	<i>Rib-stiffened connection</i>	36
3.2.3	<i>Cover-plate connection</i>	37
3.3	EXPERIMENTAL PROGRAM.....	39
3.3.1	<i>Specimen description</i>	39
3.3.2	<i>Test setup</i>	44
3.3.3	<i>Instrumentation</i>	46
3.3.4	<i>Loading protocol</i>	47
3.4	TEST RESULTS	50
3.4.1	<i>Joint rotation analysis</i>	50
3.4.2	<i>Variable amplitude cyclic tests</i>	52
3.4.3	<i>Constant amplitude cyclic tests</i>	75
3.4.4	<i>Investigation of welded connections after the tests</i>	87
3.4.5	<i>Composite column behaviour</i>	90
3.4.6	<i>Evaluation of test results according to prequalification requirements</i>	91
3.4.7	<i>Energy dissipation capacity</i>	100
3.4.8	<i>Skeleton Curves: monotonic response characteristics obtained from variable amplitude cyclic tests</i> 102	
3.4.9	<i>Low-Cycle Fatigue Assessment</i>	105
3.4.10	<i>Conclusions to the cyclic test results</i>	106
4	NUMERICAL SIMULATIONS OF BEAM-TO-COLUMN JOINT BEHAVIOUR UNDER MONOTONIC AND CYCLIC LOADING.....	109
4.1	INTRODUCTION	109
4.2	FINITE ELEMENT MODEL DEVELOPMENT	110
4.2.1	<i>Selection of element types</i>	110
4.2.2	<i>Finite element meshes</i>	111

4.2.3	<i>Elastic and inelastic mesh convergence study</i>	113
4.2.3.1	Elastic mesh convergence study	113
4.2.3.2	Inelastic convergence study	119
4.2.4	<i>Material nonlinearity</i>	120
4.2.4.1	Monotonic loading	120
4.2.4.1.1	Structural steel material.....	120
4.2.4.1.2	Concrete material.....	122
4.2.4.2	Cyclic loading	124
4.2.4.2.1	Cyclic Material Hardening model	125
4.2.4.2.2	Calibration of cyclic material hardening model.....	126
4.2.5	<i>Geometric nonlinearity</i>	128
4.2.6	<i>Residual stresses</i>	130
4.2.7	<i>Solver procedures</i>	130
4.2.8	<i>Other basic modelling issues and assumptions</i>	131
4.2.8.1	FE modelling logic.....	131
4.2.8.2	Applied precision level.....	133
4.3	PERFORMANCE OF THE FINITE ELEMENT MODEL	134
4.3.1	<i>Introduction</i>	134
4.3.2	<i>Monotonic loading</i>	135
4.3.2.1	Cantilever beam subjected to non-uniform bending.....	135
4.3.2.2	Simulation of the skeleton curve response	139
4.3.3	<i>Cyclic loading</i>	145
4.3.3.1	Applied cyclic loading history	145
4.3.3.2	Constant amplitude cyclic loading tests	147
4.3.3.2.1	General findings from small and large constant amplitude loading.....	147
4.3.3.2.2	Constant displacement amplitude $\theta = 0.019$ rad	148
4.3.3.2.3	Constant displacement amplitude $\theta = 0.033$ rad	156
4.3.3.3	Variable amplitude cyclic loading tests.....	164
4.3.3.4	Local strain response	177
4.3.3.5	Evaluation of crack initiation based LCF failure in steel elements.....	184
4.3.3.5.1	Prediction of ductile cracking onset using effective damage concept – tests with increasing cyclic loading amplitude.....	184
4.3.3.5.2	Prediction of crack initiation based LCF failure – proposed unified LCF approach.....	187
4.4	SUMMARY AND CONCLUSIONS	193
5	PARAMETRIC NUMERICAL STUDY	195
5.1	INTRODUCTION	195
5.2	INFLUENCE OF COLUMN AXIAL COMPRESSIVE LOAD	196
5.3	BEHAVIOUR OF STIFFENED BEAM-TO-COLUMN JOINTS.....	200
5.3.1	<i>Complementary set of stiffened joints</i>	200
5.3.2	<i>Monotonic loading</i>	207
5.3.3	<i>Cyclic loading</i>	216
5.3.4	<i>Conclusions and discussion</i>	229
6	DESIGN GUIDELINES FOR PREQUALIFIED FULL-STRENGTH WELDED STIFFENED BEAM-TO-COLUMN JOINTS	231
6.1	INTRODUCTION	231
6.2	WELDED RIB-STIFFENED (RS) BEAM-TO-COLUMN JOINT	231
6.2.1	<i>Detailing guidelines</i>	231
6.2.2	<i>Design procedure</i>	232
6.2.2.1	Introduction.....	232
6.2.2.2	Local ductility requirements	233
6.2.2.3	Selection of the component size	234
6.2.2.4	Evaluation of plastic hinge location	234
6.2.2.5	Evaluation of nominal actions in the plastic hinge	234
6.2.2.6	Global ductility condition.....	235
6.2.2.7	Welded beam-to-column connection.....	235
6.2.2.8	Column design	237
6.2.2.8.1	Column web panel.....	237
6.2.2.8.2	Column web in transverse compression and tension.....	239

6.2.2.9	Summary	240
6.2.2.10	Design of rib-stiffened connection based on equivalent strut model	241
6.3	WELDED COVER-PLATE (CP) BEAM-TO-COLUMN JOINT	244
6.3.1	<i>Detailing guidelines</i>	244
6.3.2	<i>Design procedure</i>	245
6.3.2.1	Introduction	245
6.3.2.2	Local ductility requirements.....	246
6.3.2.3	Selection of the component size	246
6.3.2.4	Evaluation of plastic hinge location.....	247
6.3.2.5	Evaluation of nominal actions in the plastic hinge.....	247
6.3.2.6	Global ductility condition	247
6.3.2.7	Welded beam-to-column connection	247
6.3.2.8	Column design.....	248
6.3.2.9	Summary	249
7	CONCLUSIONS AND OUTCOMES	251
7.1	SUMMARY AND CONCLUSIONS	251
7.2	ORIGINAL CONTRIBUTIONS	255
7.3	SUGGESTIONS FOR FURTHER WORK	256
I	UVOD.....	257
II	EKSPERIMENTALNI TESTI	259
III	NUMERIČNI MODEL.....	278
IV	PARAMETRIČNA ŠTUDIJA	280
IV	ZAKLJUČEK.....	281
REFERENCES.....		283
APPENDIX A	GEOMETRIC DATA OF THE TEST SPECIMENS.....	289

TABLE OF FIGURES

Fig. 1:	Welded beam-to-column joint configurations	3
Fig. 2:	The process of seismic analysis of a steel frame	9
Fig. 3:	Cross-section classification criterion according to EN 1993-1-1	17
Fig. 4:	Definition of local ductility R and overstrength factor s from a moment-rotation curve	19
Fig. 5:	Classification of beam-to-column joint plastic behaviour, ECCS Manual on Design of Steel Structures in Seismic Zones (ECCS, 1994).....	21
Fig. 6:	Failure mechanisms in relation to the number of cycles to failure	25
Fig. 7:	Triaxiality versus equivalent plastic strain for reversed cyclic loading.....	27
Fig. 8:	Typical material damage curve.....	28
Fig. 9:	Criterion for ductile crack initiation as obtained by Ohata and Toyoda (2004) for SM490YB steel.....	30
Fig. 10:	Advanced two-parameter criterion for ductile cracking of structural members under cyclic loading based on effective damage concept: a) evolution of equivalent backstress with determination of effective plastic strain (schematic illustration), b) effective damage concept.....	31
Fig. 11:	Damage curves for structural steel S355J2 and S460M (Bleck et al., 2009. Feldmann et al., 2009).....	32
Fig. 12:	Design objective of the two solutions for enhanced beam-to-column joint performance: a) studied strengthened connection and b) alternative concept of weakened beam (RBS) ..	33
Fig. 13:	Single sided stiffened beam-to-column joint	36
Fig. 14:	Rib-stiffened and cover plate connection configurations studied.....	36
Fig. 15:	Distribution of MI for RS and CP joints at different values of joint rotation (beam flange in tension)	37
Fig. 16:	RI distribution for unstiffened (U) and stiffened (RS, CP) joints at story drift angle 0.035 rad (beam flange in tension)	38
Fig. 17:	Welded RS and CP beam-to-column joint details (concrete column encasement not illustrated).....	39
Fig. 18:	Constructional details of four designed stiffened joint specimens	40
Fig. 19:	N-M interaction curves for large (L) and small (S) composite column cross-section	41
Fig. 20:	Final preparation on the test specimens – composition of composite column.....	42
Fig. 21:	Check of specimen geometry: out-of-square shape of cover-plate (specimen CP2.3)	44
Fig. 22:	Static model of the specimen with boundary conditions and loads applied	44
Fig. 23:	Test setup with test specimen already fixed and during the test.....	45
Fig. 24:	Beam lateral bracing system	45
Fig. 25:	Instrumentation scheme for the measurement of local and global joint response	46
Fig. 26:	Strain gauge arrangements in case of RS and CP joint specimens	47
Fig. 27:	Comparison between ECCS N°45, the modified ECCS N°45 and AISC 341-10 cyclic loading protocols in terms of: a) loading amplitudes and b) accumulated plastic rotation. Loading sequences related to cyclic amplitudes in plastic range are only presented.	49
Fig. 28:	Beam-to-column joint kinematics.....	51
Fig. 29:	Comparison of cyclic response between the two equal joints tested with and without the presence of compressive column axial force	53
Fig. 30:	Specimen RS1.1 after the test.....	54
Fig. 31:	Specimen RS1.2 after the test.....	55
Fig. 32:	Specimen RS2.1 after the test.....	55
Fig. 33:	Specimen RS2.2 after the test.....	56
Fig. 34:	Specimen CP1.1 after the test.....	56
Fig. 35:	Specimen CP1.2 after the test.....	57
Fig. 36:	Specimen CP2.1 after the test.....	57
Fig. 37:	Specimen CP2.2 after the test.....	58

Fig. 38:	RS and CP joint response in terms of normalised moment M_h vs. total joint rotation θ with graphical representation of the three failure criteria	60
Fig. 39:	Normalised moment M_h at the subsequent joint rotation amplitudes: a) RS1.2 and RS2.2, b) CP1.2 and CP2.2	60
Fig. 40:	Normalised moment M_h at the subsequent joint rotation amplitudes as a function of the number of cycles: a) RS1.2 and RS2.2, b) CP1.2 and CP2.2.....	61
Fig. 41:	Principles of the applied evaluation criteria: a) strength criterion, b) stiffness criterion	62
Fig. 42:	Response of specimens RS1.1 and RS1.2: a) applied loading history, b) distribution of maximum moment per cycle, c) distribution of complete joint stiffness per cycle	68
Fig. 43:	Response of specimens CP1.1 and CP1.2: a) applied loading history, b) distribution of maximum moment per cycle, c) distribution of complete joint stiffness per cycle	69
Fig. 44:	Response of specimens RS2.1 and RS2.2: a) applied loading history, b) distribution of maximum moment per cycle, c) distribution of complete joint stiffness per cycle	70
Fig. 45:	Response of specimens CP2.1 and CP2.2: a) applied loading history, b) distribution of maximum moment per cycle, c) distribution of complete joint stiffness per cycle	71
Fig. 46:	Detail of top and bottom beam flange local buckling shape for specimens CP2: a) CP2.1 and b) CP2.2.....	72
Fig. 47:	Normalized moment M_h versus total joint rotation θ for constant amplitude cyclic tests, small amplitude.....	75
Fig. 48:	Normalized moment M_h versus total joint rotation θ for constant amplitude cyclic tests, large amplitude.....	76
Fig. 49:	Specimen RS1.3 after the test: a) local strained area of the beam just after the stiffened section, b) fracture of top beam flange, c) crack on top beam flange, side view, d) damaged bottom beam flange.....	77
Fig. 50:	Specimen RS2.3 after the test: a) local strained area of the beam just after the stiffened section, b) fracture of bottom beam flange, side view, c) crack on bottom beam flange, d) damaged top beam flange	77
Fig. 51:	Specimen CP1.3 after first 5 cycles: a) local strained area of the beam just after the stiffened section, b) detail of strain field on the beam lower flange	78
Fig. 52:	Specimen CP1.3 after the test: a) local strained area of the beam just after the stiffened section, b) top beam flange, c) crack on bottom beam flange, d) damaged edge of top beam flange.....	78
Fig. 53:	Specimen CP2.3 in 130 cycle: a) local strained area of the top beam just after the stiffened section, b) growth of cracks from the top flange free end just after the stiffened section ...	79
Fig. 54:	Specimen CP2.3 after the test: a) local strained area of the beam just after the stiffened section, b) fracture of top beam flange, c) crack on top beam flange, side view, d) damaged bottom beam flange.....	79
Fig. 55:	Specimen RS1.4 after the test	80
Fig. 56:	Specimen RS2.4 after the test	81
Fig. 57:	Specimen CP1.4 after the test	81
Fig. 58:	Specimen CP2.4 after the test	81
Fig. 59:	Normalised moment M_h at the subsequent joint rotation amplitudes as a function of number of cycles: a) RS1.3 and RS2.3, b) CP1.3 and CP2.3, c) RS1.4 and RS2.4, d) CP1.4 and CP2.4.....	82
Fig. 60:	Response of specimens RS1.3 and CP1.3: a) distribution of maximum moment per cycle, b) distribution of complete joint stiffness per cycle.....	85
Fig. 61:	Response of specimens RS2.3 and CP2.3: a) distribution of maximum moment per cycle, b) distribution of complete joint stiffness per cycle.....	85
Fig. 62:	Response of specimens RS1.4 and CP1.4: a) distribution of maximum moment per cycle, b) distribution of complete joint stiffness per cycle.....	86
Fig. 63:	Response of specimens RS2.4 and CP2.4: a) distribution of maximum moment per cycle, b) distribution of complete joint stiffness per cycle.....	86
Fig. 64:	a) Preparation of specimen for welded connection inspection, b) Magnetic particle testing (MT).....	87

Fig. 65:	a) Cracks at the end of the rib-stiffener fillet weld in specimen RS2.3, b) Practically undamaged transverse fillet weld, including its HAZ region, at the end of the cover plate in specimen CP1.4	88
Fig. 66:	Cracks at the edge of welded connection between the beam flange and the column flange a) specimen RS1.4, b) specimen CP1.3	88
Fig. 67:	Cross-section of welded connection details from specimen RS2.2: a) Fillet weld between beam flange and column flange b) Fillet weld at the end of the rib-stiffener	89
Fig. 68:	Cross-section of welded connection details from specimen CP1.4: a) Complete joint penetration single-bevel but weld used to connect the beam flange and the cover plate to the column flange, b) transverse fillet weld at the end of the cover-plate	89
Fig. 69:	Response of composite column: a) elastic column and elastic beam contribution to the total joint rotation for specimen CP1.2, b) recorded normal strains (compression) in encased steel sections	90
Fig. 70:	Composite column after the test: a) specimen RS1.4, b) specimen CP1.1	90
Fig. 71:	Envelope curve construction of joint RS1.1 with the identification of performance levels	95
Fig. 72:	State of joint RS1.1 corresponding to the three selected performance levels	95
Fig. 73:	Envelope curve construction of joint CP1.1 with the identification of performance levels	96
Fig. 74:	State of joint CP1.1 corresponding to the three selected performance levels	96
Fig. 75:	Envelope curve construction of joint RS2.1 with the identification of performance levels	97
Fig. 76:	State of joint RS2.1 corresponding to the three selected performance levels	97
Fig. 77:	Envelope curve construction of joint CP2.1 with the identification of performance levels	98
Fig. 78:	State of joint CP2.1 corresponding to the three selected performance levels	98
Fig. 79:	Envelope curves for all eight RS and CP joints subjected to variable amplitude cycling: a) moment to the plastic hinge centreline vs. total joint rotation, b) normalised moment to the plastic hinge centreline vs. total joint rotation	99
Fig. 80:	Definition of plastic rotation and cumulative plastic rotation according to Nakashima et al. (1998b)	100
Fig. 81:	Comparison of cumulative plastic rotations for all 16 specimens	100
Fig. 82:	Maximum plastic rotation amplitude vs. cumulative plastic rotation	101
Fig. 83:	Cumulative dissipated energy	101
Fig. 84:	Construction of a skeleton curve: a) response of specimen RS1.1, b) positive and negative skeleton curves with added descending part according to the modified procedure	102
Fig. 85:	Skeleton curves for specimens RS1 and RS2 subjected to variable cyclic loading	103
Fig. 86:	Skeleton curves for specimens CP1 and CP2 subjected to variable cyclic loading	104
Fig. 87:	Low-cycle fatigue assessment of the test results	105
Fig. 88:	Position of the sub-model in a beam-to-column joint; shell and solid sub-model geometry with the interface between beam flange and column flange marked as well as boundary conditions and load applied	113
Fig. 89:	Mesh densities for solid models used in the study: a) 4 element mesh, b) 8 element mesh, c) 16 element mesh, d) 20 element mesh and e) 32 element mesh	114
Fig. 90:	Deformed mesh of the sub-model using ordinary shell (left) and solid (right) elements ...	114
Fig. 91:	Stress distribution along the beam-column flange interface for meshes with shell elements S4R and SC8R. The number beside the element type defines the level of mesh refinement	115
Fig. 92:	Stress distribution along the interface for meshes with shell elements S4R and SC8R	116
Fig. 93:	Comparison of stress distribution along the interface for meshes with 20 and 32 elements using elements S4R and SC8R	116
Fig. 94:	Stress distribution along the interface for meshes with solid elements C3D8R and C3D8I	117
Fig. 95:	Stress distribution along the interface for meshes with solid elements C3D8R and C3D8RI	117
Fig. 96:	Comparison of stress distribution along the interface for meshes with 20 and 32 elements using elements C3D8R and C3D8RI	117
Fig. 97:	Comparison of stress distribution along the interface for meshes with 20 and 32 elements using shell elements S4R and SC8R and solid elements C3D8R and C3D8RI	118

Fig. 98:	Discretised material diagrams up to the point of the ultimate tensile strength from joint components of RS1 and CP1 specimens	121
Fig. 99:	Discretised material diagrams up to the point of the ultimate strength from joint components of RS2 and CP2 specimens	121
Fig. 100:	Comparison of experimental and simulated standard tensile test on the coupon from IPE270 beam	122
Fig. 101:	Concrete material behaviour used in the FE model for composite columns: a) compression, b) tension	123
Fig. 102:	Cyclic curve obtained from experimental tests with different strain amplitudes	127
Fig. 103:	Comparison between calibrated monotonic and cyclic stress-strain curve for steel S355. 127	
Fig. 104:	Static model of a joint with boundary conditions, loads applied and considered geometric imperfections	128
Fig. 105:	Tolerances on out-of-square of structural steel I and H sections according to EN 10034. 129	
Fig. 106:	Local beam geometric imperfection models	129
Fig. 107:	Beam-to column joint RS1 and CP1 finite element model	131
Fig. 108:	Details of steel joint components of RS and CP beam-to column joint finite element model	132
Fig. 109:	Stiffened cross-section detail for of RS and CP connection	132
Fig. 110:	Solid part of FE model for cantilever beam IPE300 and HEB240	135
Fig. 111:	Effect of the beam local imperfection amplitude on the simulated response of specimen IPE300 compared to the experimental curve from D'Aniello et al. (2012)	137
Fig. 112:	Experimental, D'Aniello et al. (2012), and simulated flexural performance of specimen IPE300	137
Fig. 113:	Effect of the beam local imperfection amplitude on the simulated response of HEB240 specimen compared to the experimental curve, D'Aniello et al. (2012)	137
Fig. 114:	Experimental, D'Aniello et al. (2012), and simulated flexural performance of HEB240 specimen	138
Fig. 115:	Deformed shape of cantilever beam IPE300 at rotation $\theta = 0.15$ rad: experiment - D'Aniello et al. (2012), and simulation	138
Fig. 116:	Deformed shape of HEB2400 cantilever beam at rotation $\theta = 0.50$ rad: experiment by D'Aniello et al. (2012), and simulation	139
Fig. 117:	Details of FE discretisation mesh over the beam flange and flange-web juncture region for model RS in case of three different meshes used for inelastic mesh convergence study ...	140
Fig. 118:	Inelastic convergence study for joint model RS1	141
Fig. 119:	Inelastic convergence study for CP1 joint model	141
Fig. 120:	Discretised S355 grade steel monotonic stress-strain diagrams up to the point of the ultimate strength	142
Fig. 121:	Simulated monotonic response for joints RS1 and RS2 and the corresponding skeleton curves	143
Fig. 122:	Simulated monotonic response for joints CP1 and CP2 and the corresponding skeleton curves	143
Fig. 123:	a) Comparison between the first hysteresis from simulation and the experimental response, b) experiment: first 30 cycles under AISC 341-10 loading protocol	146
Fig. 124:	Deformed shape of specimen RS1.3; comparison between the experiment and the simulation	148
Fig. 125:	Deformed shape of specimen RS2.3; comparison between the experiment and the simulation	148
Fig. 126:	Deformed shape of specimen CP1.3; comparison between the experiment and the simulation	148
Fig. 127:	Deformed shape of specimen CP2.3; comparison between the experiment and the simulation	149
Fig. 128:	Total beam rotation amplitudes; comparison between the experiment and the simulation	149
Fig. 129:	Moment M_c at rotation amplitudes; comparison between the experiment and the simulation	150

Fig. 130: Hysteretic response from the experiment and the simulation for complete loading history	151
Fig. 131: M_c vs. θ_b hysteresis for the experiment and the simulation: details at rotation amplitudes	151
Fig. 132: M_c vs. θ_b hysteresis for the experiment and the simulation: details at rotation amplitudes	152
Fig. 133: Comparison of hysteretic response in terms of moment M_c vs. total θ_b and plastic θ_{pl} beam rotation	152
Fig. 134: RS1.3 and CP1.3 experimental and simulated hysteretic response: 1 st cycle and the stabilised one	153
Fig. 135: RS2.3 and CP2.3 experimental and simulated hysteretic response: 1 st cycle and the stabilised one	153
Fig. 136: Specimens RS1.3 and CP1.3: dissipated energy per cycle and accumulated energy	155
Fig. 137: Specimens RS2.3 and CP2.3: dissipated energy per cycle and accumulated energy	155
Fig. 138: Deformed shape of specimen RS1.4; comparison between the experiment and the simulation	156
Fig. 139: Deformed shape of specimen RS2.4; comparison between the experiment and the simulation	156
Fig. 140: Deformed shape of specimen CP1.4; comparison between the experiment and the simulation	157
Fig. 141: Deformed shape of specimen CP2.4; comparison between the experiment and the simulation	157
Fig. 142: Total beam rotation amplitudes; comparison between the test and the simulation	158
Fig. 143: Moment M_c at rotation amplitudes; comparison between the test and the simulation	158
Fig. 144: Hysteretic response from the experiment and the simulation for complete loading history	159
Fig. 145: M_c vs. θ_b hysteresis for the experiment and the simulation: details at rotation amplitudes	159
Fig. 146: M_c vs. θ_b hysteresis for the experiment and the simulation: details at rotation amplitudes	160
Fig. 147: Comparison of hysteretic response in terms of moment M_c vs. total θ_b and plastic θ_{pl} beam rotation	160
Fig. 148: RS1.4 and CP1.4 experimental and simulated hysteretic response: 1 st cycle and the stabilised one	161
Fig. 149: RS2.4 and CP2.4 experimental and simulated hysteretic response: 1 st cycle and the stabilised one	162
Fig. 150: Specimens RS1.4 and CP1.4: dissipated energy per cycle and accumulated energy	163
Fig. 151: Specimens RS2.4 and CP2.4: dissipated energy per cycle and accumulated energy	163
Fig. 152: Deformed shape of specimen RS1.1; comparison between the experiment and the simulation	165
Fig. 153: Deformed shape of specimen RS1.2; comparison between the experiment and the simulation	165
Fig. 154: Deformed shape of specimen RS2.1; comparison between the experiment and the simulation	165
Fig. 155: Deformed shape of specimen RS2.2; comparison between the experiment and the simulation	166
Fig. 156: Deformed shape of specimen CP1.1; comparison between the experiment and the simulation	166
Fig. 157: Deformed shape of specimen CP1.2; comparison between the experiment and the simulation	166
Fig. 158: Deformed shape of specimen CP2.1; comparison between the experiment and the simulation	167
Fig. 159: Deformed shape of specimen CP2.2; comparison between the experiment and the simulation	167
Fig. 160: Experimental and simulated response for RS1.1: a) applied total beam plastic rotation amplitudes, b) hysteretic response, c) distribution of maximum values M_c , d) distribution of M_c at rotation amplitudes	168

Fig. 161:	Experimental and simulated response for RS1.2: a) applied total beam plastic rotation amplitudes, b) hysteretic response, c) distribution of maximum values M_c , d) distribution of M_c at rotation amplitudes	168
Fig. 162:	Experimental and simulated response for CP1.1: a) applied total beam plastic rotation amplitudes, b) hysteretic response, c) distribution of maximum values M_c , d) distribution of M_c at rotation amplitudes	169
Fig. 163:	Experimental and simulated response for CP1.2: a) applied total beam plastic rotation amplitudes, b) hysteretic response, c) distribution of maximum values M_c , d) distribution of M_c at rotation amplitudes	169
Fig. 164:	Experimental and simulated response for RS2.1: a) applied total beam plastic rotation amplitudes, b) hysteretic response, c) distribution of maximum values M_c , d) distribution of M_c at rotation amplitudes	170
Fig. 165:	Experimental and simulated response for RS2.2: a) applied total beam plastic rotation amplitudes, b) hysteretic response, c) distribution of maximum values M_c , d) distribution of M_c at rotation amplitudes	170
Fig. 166:	Experimental and simulated response for CP2.1: a) applied total beam plastic rotation amplitudes, b) hysteretic response, c) distribution of maximum values M_c , d) distribution of M_c at rotation amplitudes	171
Fig. 167:	Experimental and simulated response for CP2.2: a) applied total beam plastic rotation amplitudes, b) hysteretic response, c) distribution of maximum values M_c , d) distribution of M_c at rotation amplitudes	171
Fig. 168:	Comparison between experimental and simulated response for specimens RS1 and CP1: hysteresis curves from cyclic midlife of the specimens	172
Fig. 169:	Comparison between experimental and simulated response for specimens RS2 and CP2: hysteretic curves from cyclic midlife of specimens	173
Fig. 170:	Comparison between experimental and simulated response for RS1 and CP1 specimens: hysteretic curves from the cycle with predicted onset of ductile cracking	173
Fig. 171:	Comparison between experimental and simulated response for RS2 and CP2 specimens: hysteretic curves from the cycle with predicted onset of ductile cracking	174
Fig. 172:	Experimental and simulated response for specimens RS1 and CP1: distribution of energy per cycle	175
Fig. 173:	Experimental and simulated response for RS2 and CP2 specimens: distribution of energy per cycle	175
Fig. 174:	Experimental and simulated response for RS1 and CP1 specimens: distribution of accumulated energy	176
Fig. 175:	Experimental and simulated response for RS2 and CP2 specimens: distribution of accumulated energy	176
Fig. 176:	Comparison between experimental and simulated local strain response for joint RS1.3 ..	178
Fig. 177:	Experimental and simulated local strain response for joint RS1.3; S7 and S8, complete no. of cycles	178
Fig. 178:	Detailed comparison between experimental and simulated local strain response for RS1.3; S8	178
Fig. 179:	Comparison between experimental and simulated local strain response for joint RS2.3 ..	179
Fig. 180:	Experimental and simulated local strain response for joint RS2.3; S7 and S8, complete no. of cycles	179
Fig. 181:	Detailed comparison between experimental and simulated local strain response for joint RS2.3; S8	179
Fig. 182:	Comparison between experimental and simulated local strain response for joint CP1.3 ..	180
Fig. 183:	Experimental and simulated local strain response for joint CP1.3; S7 and S8, complete no. of cycles	180
Fig. 184:	Detailed comparison between experimental and simulated local strain response for joint CP1.3; S7	180
Fig. 185:	Comparison between experimental and simulated local strain response for joint CP2.3 ..	181
Fig. 186:	Experimental and simulated local strain response for joint CP2.3; S7 and S8, complete no. of cycles	181

Fig. 187:	Detailed comparison between experimental and simulated local strain response for joint CP2.3; S7	181
Fig. 188:	Deformed shape of beam top flange from specimen CP1.3 in 100 th cycle: comparison between a) experimental and b) simulated response (scale factor 1.0).....	183
Fig. 189:	Evaluation of ductile crack initiation based on the advanced 2-parameter criterion: a) evolution of equivalent backstress and estimation of effective damage strain, b) cumulative history of $(\bar{\epsilon}_{pl})_{eff}$ vs. $\sigma_m / \bar{\sigma}$	185
Fig. 190:	Location of crack initiation for specimen RS2.1: a) experiment (deformation after the test), b) simulation (state with prediction of ductile cracking onset).....	185
Fig. 191:	Location of crack initiation for specimen CP1.2: a) experiment (deformation after the test), b) simulation (state with prediction of ductile cracking onset).....	186
Fig. 192:	Specimen CP2.3: a) strain gauges placed in the vicinity of the beam flange final fracture, b) experimentally obtained strain-life diagram with the determination of estimated onset of crack growth	188
Fig. 193:	Proposed damage curve for LCF crack initiation	189
Fig. 194:	Location of crack initiation for specimen CP1.4: a) experiment (24 th cycle) and b) simulation (at the instance of LCF cracking criterion met in 19 th cycle)	190
Fig. 195:	Location of crack initiation for specimen CP2.4: a) experiment (55 th cycle) and b) simulation (at the instance of LCF cracking criterion met in 33 th cycle)	191
Fig. 196:	Evolution of combined stress-strain damage index from the end of the stiffened region of the beam against the proposed LCF crack initiation criterion for complete loading history of all eight joint specimens subjected to cyclic loading with increasing amplitude	192
Fig. 197:	Damage concentrations in the beam flange at the end of the stiffened region: a) RS1.1, b) CP2.2	192
Fig. 198:	Mises stress distribution in beam-column web-centre plane of joint RS1 for the considered three levels of column axial load: after the applied column axial load (left column), and at the maximum joint flexural resistance (right column).....	197
Fig. 199:	Hydrostatic pressure distribution in beam-column web-centre plane of joint RS1 at its maximum flexural resistance for the considered three levels of column axial load	198
Fig. 200:	Mises stress distribution in beam-column web-centre plane of joint CP1 for the considered three levels of column axial load: after the applied column axial load (left column), and at the maximum joint flexural resistance (right column).....	198
Fig. 201:	Hydrostatic pressure distribution in beam-column web-centre plane of joint CP1 at its maximum flexural resistance for the considered three levels of column axial load	199
Fig. 202:	Fracture indices for RS1 and CP1 beam flange in tension at the face of the column for the state at the maximum joint flexural resistance.....	199
Fig. 203:	I and H cross-sections used for the beams (actual relative geometric ratio preserved)	200
Fig. 204:	Static model and geometry of single-sided beam-to-column joint FE model.....	201
Fig. 205:	Typical mesh refinement on the HEB400 beam flange for RS and CP joints	202
Fig. 206:	Details of the stiffened beam-to-column connection models: a) RS joint in combination with beam IPE500, b) RS joint with beam HEB400, and c) CP joint in combination with beam HEB400.....	202
Fig. 207:	Flange and web width-to-thickness ratios for I and H beam cross-sections in bending	203
Fig. 208:	The method used for derivation of the steel material stress-strain curves to be applied in the complementary numerical analysis: a) for dissipative, and b) for non-dissipative components	205
Fig. 209:	a) Monotonic, and b) cyclic material curves for steel joint components used in the study	206
Fig. 210:	Rib-stiffener and cover-plate thicknesses obtained for complete range of I and H beam profiles according to the proposed design procedure	207
Fig. 211:	M_h vs. θ_b diagrams for all 16 beam-to-column stiffened joints.....	207
Fig. 212:	Normalised M_h vs. θ_b diagrams for all 16 beam-to-column stiffened joints	208
Fig. 213:	Overall beam overstrength γ_{ov}' due to the considered γ_{ov} and s	210
Fig. 214:	Beam rotation capacity: a) $R_{mon,1}$ and b) $R_{mon,2}$	210
Fig. 215:	RS and CP joints with IPE270 beam, instance of maximum flexural resistance, scale factor 1.0	212

Fig. 216:	RS and CP joint with IPE360 beam, instance of maximum strength, scale factor 1.0	212
Fig. 217:	RS and CP joint with IPE400 beam, instance of maximum strength, scale factor 1.0	212
Fig. 218:	RS and CP joint with IPE500 beam, instance of maximum strength, scale factor 1.0	212
Fig. 219:	RS and CP joint with HEA400 beam, instance of maximum strength, scale factor 1.0	213
Fig. 220:	RS and CP joint with HEB240 beam, instance of maximum strength, scale factor 1.0	213
Fig. 221:	RS and CP joint with HEB400 beam, instance of maximum strength, scale factor 1.0	213
Fig. 222:	RS and CP joint with HEB800 beam, instance of maximum strength, scale factor 1.0	213
Fig. 223:	Deformed shape of RS joints corresponding to 20 % fall of the maximum moment resistance: a) beam IPE400, b) beam HEA400, c) beam HEB400. Deformation scale factor 1.0.....	214
Fig. 224:	Deformed shape of CP joints corresponding to 20 % fall of the maximum moment resistance: a) beam IPE400, b) beam HEA400, c) beam HEB400. Deformation scale factor 1.0.....	214
Fig. 225:	RS and CP joints with beam IPE400: Mises stress and PEEQ strain state in the stiffened connection at the column flange at the instance of maximum joint flexural resistance.....	215
Fig. 226:	RS and CP joints with beam HEA400: Mises stress and PEEQ strain state in stiffened connection at the column flange at the instance of maximum joint flexural resistance.....	216
Fig. 227:	RS and CP joints with beam HEB400: Mises stress and PEEQ strain state in stiffened connection at the column flange at the instance of maximum joint flexural resistance.....	216
Fig. 228:	Cyclic response of RS and CP joints: a) beam IPE270 (15 cycles), b) beam IPE360 (15 cycles)	217
Fig. 229:	Cyclic response of RS and CP joints: a) beam IPE400 (14 cycles), b) beam IPE500 (14 cycles)	217
Fig. 230:	Cyclic response of RS and CP joints: a) beam HEA400 (16 cycles), b) beam HEB240 (18 cycles)	217
Fig. 231:	Cyclic response of RS and CP joints: a) beam HEB400 (16 cycles), b) beam HEB800 (15 cycles)	218
Fig. 232:	Deformed shape of RS and CP joints with beam IPE400. Predicted instance of LCF crack initiation according to the proposed criteria <i>crit.^a</i> . Deformation scale factor 1.0	220
Fig. 233:	Deformed shape of RS and CP joints with beam HEA400. Predicted instance of LCF crack initiation according to the proposed criteria <i>crit.^a</i> . Deformation scale factor 1.0	220
Fig. 234:	Deformed shape of RS and CP joints with beam HEB400. Predicted instance of LCF crack initiation according to the proposed criteria <i>crit.^a</i> . Deformation scale factor 1.0	220
Fig. 235:	Number of cycles to LCF crack initiation according to the proposed criterion <i>crit.^a</i> , see also Table 34	221
Fig. 236:	Plastic rotation $\theta_{pl,1}$ and the corresponding cumulative plastic rotation $\Sigma\theta_{pl,1}$ as a function of beam profile type and its depth	223
Fig. 237:	Plastic rotation $\theta_{pl,2}$ and the corresponding cumulative plastic rotation $\Sigma\theta_{pl,2}$ as a function of beam profile type and its depth	224
Fig. 238:	Plastic rotation $\theta_{pl,3}$ and the corresponding cumulative plastic rotation $\Sigma\theta_{pl,3}$ as a function of beam profile type and its depth	224
Fig. 239:	Cyclic rotation capacity $R_{cyc,1}$ and the corresponding ratio $R_{cyc,1} / R_{mon,1}$ as a function of beam profile type and its depth for all the joints.....	225
Fig. 240:	Cyclic rotation capacity $R_{cyc,2}$ and the corresponding ratio $R_{cyc,2} / R_{mon,2}$ as a function of beam profile type and its depth for all the joints.....	226
Fig. 241:	Effect of parameter γ_{ov} on the beam flexural ultimate response.....	228
Fig. 242:	Welded RS beam-to-column joint details (concrete column encasement not illustrated)..	232
Fig. 243:	Detail of composite column transverse reinforcement in the region of the beam-to-column connection	232
Fig. 244:	Sample frames with single-sided beam-to-column joint configuration	233
Fig. 245:	Typical beam span with stiffened joint, plastic hinge location and cross-sections used for design check.....	235
Fig. 246:	Maximal throat thickness of fillet weld in T-joint	237
Fig. 247:	Internal forces in the column panel zone for single-sided joint	238
Fig. 248:	Interaction model for deformation compatibility as defined in Lee (2002).....	241

Fig. 249: Definition of rib geometry with equivalent strut as defined in Lee (2002)	242
Fig. 250: Welded CP beam-to-column joint details (concrete column encasement not illustrated) ..	245
Fig. 251: Welding details of CP beam-to-column joint	245
Fig. 252: Three-sided fillet weld joining the cover-plate to the beam flange	248

LIST OF TABLES

Table 1:	Required cross-sectional class of dissipative elements in relation to ductility class and proper behaviour factor from EN 1998-1	18
Table 2:	Proposed s values by the classification of members in terms of ductility according to Mazzolani and Piluso (1993), in combination with factor γ_{ov} as suggested by OPCM 327422	
Table 3:	Parameters of the experimental study with the number of specimens	34
Table 4:	Typical column-beam moment ratio values for specimen with large and small column	41
Table 5:	Monotonic tensile steel material properties	43
Table 6:	Results of Charpy V-notch tests	43
Table 7:	Summary information on all 16 laboratory tests	48
Table 8:	Total number of completed inelastic cycles N_i according to the three failure criteria for all the specimens	62
Table 9:	Summary of experimental results for the RS group of specimens	63
Table 10:	Summary of experimental results for the CP group of specimens	63
Table 11:	Loading history details for specimen RS1.1 and RS1.2	64
Table 12:	Loading history details for specimen CP1.1 and CP1.2	65
Table 13:	Loading history details for specimen RS2.1 and RS2.2	65
Table 14:	Loading history details for specimen CP2.1 and CP2.2	66
Table 15:	Cyclic response details for RS group of specimens	74
Table 16:	Cyclic response details for CP group of specimens	74
Table 17:	Loading history details for specimens subjected to constant amplitude cycling	83
Table 18:	Onset of failure instance for selected specimens subjected to constant amplitude cycling ..	87
Table 19:	Complete beam and complete joint rotations for RS and CP joints	91
Table 20:	Complete joint rotations for RS and CP joints accounting for different flexural strength limits	92
Table 21:	Summary of the eight specimens tested using the variable amplitude cyclic loading	94
Table 22:	Cyclic performance of the investigated beam-to-column joints according to the acceptance criteria	99
Table 23:	Parameters of the nonlinear combined isotropic/kinematic hardening model for cyclic plasticity	127
Table 24:	Applied range of beam local imperfection amplitudes	136
Table 25:	Number of completed inelastic cycles for variable cyclic tests: experiment (nominally plastic range) and simulation	146
Table 26:	Comparison between experimental and simulated hysteretic energy response	154
Table 27:	Comparison between experimental and simulated response: hysteretic energy	162
Table 28:	Comparison of accumulated energy for cycles till the predicted ductile crack occurrence ..	174
Table 29:	Critical loading cycle for specimens tested with increasing cyclic loading amplitude: experiment vs. simulation prediction (effective damage concept by Ohata and Toyoda (2004))	186
Table 30:	RS and CP joints used for the complementary numerical study	201
Table 31:	S355 steel material monotonic stress-strain curve characteristics used in the parametric study	206
Table 32:	Distance between load insertion point and plastic hinge centreline on the beam L' with the corresponding b_f/L' ratio and beam yield rotation $\theta_{b,y}$ for all the analysed RS and CP joints	208
Table 33:	Summary on RS and CP joint responses under monotonic loading	209
Table 34:	Complete number of simulated cycles with LCF crack initiation onset identification (critical cycle)	219
Table 35:	Total number of completed inelastic cycles N_i according to the selected failure criteria ..	222
Table 36:	LCF response characteristics for RS joints	222
Table 37:	Response characteristics for CP joints	223
Table 38:	Cyclic rotation capacity and flexural overstrength for RS joints	225

Table 39: Cyclic rotation capacity and flexural overstrength for CP joints	225
Table 40: Rotation capacity and beam flexural overstrength for the eight RS and CP joint specimens subjected to variable cyclic loading, experimental test results	227
Table 41: Flexural performance of steel beams, experimental tests by D'Aniello et al. (2012).....	227
Table 42: Rotation capacities R_1 and R_2 , derived from experimental test results in D'Aniello et al. (2012).....	227
Table 43: Design capacity of basic RS joint components	240
Table 44: Design capacity of basic CP joint components	249

LIST OF ABBREVIATIONS

ELCF	Extremely low-cycle fatigue
FE	Finite element
FEA	Finite element analysis
FEM	Finite element method
HAZ	Heat-affected zone
HSS	High strength steel
HSS-SERF	High Strength Steel in Seismic Resistant Building Frames
LCF	Low-cycle fatigue
MCS	Mild carbon steel
RBS	Reduced beam section
RFCS	Research Fund for Coal and Steel

1 INTRODUCTION

1.1 Foreword

Steel moment-resisting frames and braced frames are nowadays commonly used structural systems. They are typically used for load-bearing systems of commercial, residential and industrial buildings. Structural system of frames consists of columns and beams interconnected with bolted or welded joints, and braces in case of braced frames. Due to their inherent ductility supply, steel frames represent one of the most widely used structural systems in seismic areas. However, their ductile behaviour results not only from the material properties of structural steel from which the structure is made, but depends largely also on adequate conception, design and construction of the earthquake-resistant structural system.

Compared to braced frames, moment resisting frames present more flexible solution under the effect of horizontal seismic action. For this reason, it may be difficult to meet damage limitation criteria using moment resisting frames compared to braced frames. Therefore, they are used primarily in low- and medium rise buildings. Seismic response of moment-resisting frames depends mainly on the rotation capacity and low-cycle fatigue (LCF) resistance of beam-to-column joints. It is a brace system that plays the key role in braced frames during the earthquake loading, where large axial forces are transmitted by columns as part of brace system, which may have an influence on the response of beam-to-column joints in the surrounding bays. In addition, moment resistant beam-to-column joints provide higher energy dissipation capacity under hysteresis loops (cycles of loading), which are more stable and greater than the hysteresis obtained from braces (Gioncu, Mazzolani, 2000).

In design practice it is generally accepted that steel is an excellent material for seismic-resistant structures because of its performance in terms of strength and ductility. In general it is true as it is capable of withstanding substantial inelastic deformation. In favour of this speaks also the fact that the percentage of failure of steel structures has always been very small compared to other structural materials (Gioncu, Mazzolani, 2000). However, in the recent past the popular myth of good ductility of steel structures has been found uncritical and in striking contrast to reality. Throughout the decade 1985 – 1995, strong earthquakes in Mexico City ($M_w = 8.1$) (1985), Loma Prieta ($M_w = 6.9$) (1989) and Northridge ($M_w = 6.7$) (1994) in California, and Hyogoken-Nanbu (Kobe) ($M_w = 6.9$) (1995) seriously compromised this ideal performance of steel structures. The performance of steel frames was in some cases very bad, and the same type of damage caused by different seismic events clearly showed that there are significant shortcomings in the current practice. In all the reported events, in buildings near the earthquake epicentre, unstiffened welded beam-to-column connections unexpectedly suffered large amount of damage (Miller, 1998. Nakashima et al., 1998a).

After these dramatic events extensive research was performed in the US and Japan, which confirmed that the seismic behaviour of steel frames depends largely on the approach of initial conception and design of the structural systems. By appropriate definition of location of plastic zones needed for the dissipation of input seismic energy, and by selection of adequate material characteristics as well as suitable geometric detailing for dissipative regions it is possible to assure adequate response of the structure under dynamic loading. Of the lessons to be learned from these events, improving the local ductility of structures under unfavourable conditions takes a leading place. Namely, adequate structural behaviour under seismic loading is characterized by sufficient deformation and energy dissipation capacity.

Steel beam-to-column connections present a very important detail of frames, connecting different structural components in an assembly, thus enabling integrity of complete structure during load events. Among different loads expected in the lifetime of a structure, taken into account during its design, earthquake is one of the most challenging. This is due to its unexpected and uncertain nature on one side as well as because the behaviour of the structural system is not completely known, on the other. Therefore, it is important to fully understand the behaviour of connections in order to predict the correct structural response.

Undoubtedly, welded beam-to-column joints in moment resisting frames, as connection between the dissipative beam and non-dissipative column, present important structural detail and as such deserve special design consideration. Numerous studies since 1994 have shown that the majority of brittle fractures in case of unstiffened connections, used to date, Fig. 1, occur in or around beam-to-column flange welded connections. During seismic events, excessive strength of beam material at yield (higher than the nominal yield strength), known as overstrength, imposes large force demands to the welded zone of the connection. Increased force demands along with uncertainty in workmanship as well as possible geometric and material defects made during fabrication may substantially reduce the seismic resistance of the welded connection between the beam and the column flange and thus may lead to complete beam-to-column joint brittle failure. At the same time, researchers have realized that the state of complicated and increased stress in welds leads to the initiation and progress of cracks in this region (FEMA, 1995b. 1999. Roeder, 2002).

Among many different connection typologies investigated in the literature, two types of connection designs are generally employed to enhance beam-to-column connection performance under severe seismic loading. The first one is reduced beam cross-section (RBS), also called “dog-bone” concept. Occurrence of plastic hinge is controlled by reducing beam flange width close to the connection, which prevents large flange forces and excessive straining to be transmitted to the beam-to-column connection (Iwankiw, Carter, 1996. Plumier, 1997). The other category is the stiffened connection solution, Fig. 1, in which flat plate or short haunch attached to beam flanges is used to strengthen beam-to-column connection (Engelhardt, Sabol, 1998. Chen et al., 2005). In both cases the design objective, based on the capacity design concept, is to transfer inelastic action away from the face of the beam-to-column connection, thus reducing the possibility for the appearance of brittle failure conditions.

The idea of seismic-resistant design incorporated in modern seismic codes is based on the capacity design concept. This means that structures exposed to seismic actions are designed in such way that they will respond in accordance with the planned (predicted) behaviour. According to this approach, the most advanced issue in the analysis of seismic-resistant structures nowadays is the assessment of structure ductility as the most efficient method of preparing the structure to resist unexpected strong seismic events. In other words, modern seismic design provisions require the design of structures and structural components that should be based on performance objectives: comparison between the required and the available ductility determined at the local and global level.

As such, this seismic design philosophy is forcing the designers to utilize advanced computational tools in an attempt to accurately predict structural behaviour.

Analysis tools based on finite element (FE) method are gaining popularity in practice and have become an indispensable tool, especially in applications involving large amplitude loading where the material is working well within the inelastic range. In such applications, accurate description of the material response is essential in order to arrive at an accurate and reliable prediction of the member or structural response. One of the non-negligible problems

that one has to keep in mind in relation with reliability of earthquake engineering is that high degree of exactness is not possible in seismic design because of uncertainties in input data on earthquake characteristics.

Good knowledge of the behaviour of beam-to-column joints is obviously essential for seismic design of steel moment-resisting frames and braced frames. However, vast amount of studies in the past decades have shown that just comprehensive analytical methodologies along with advanced numerical simulations are still not reliable enough, and despite high cost and the related time consuming activities, experiments are still an indispensable tool in seismic design and analysis on complex behaviour of steel welded moment-resisting joints and their components.

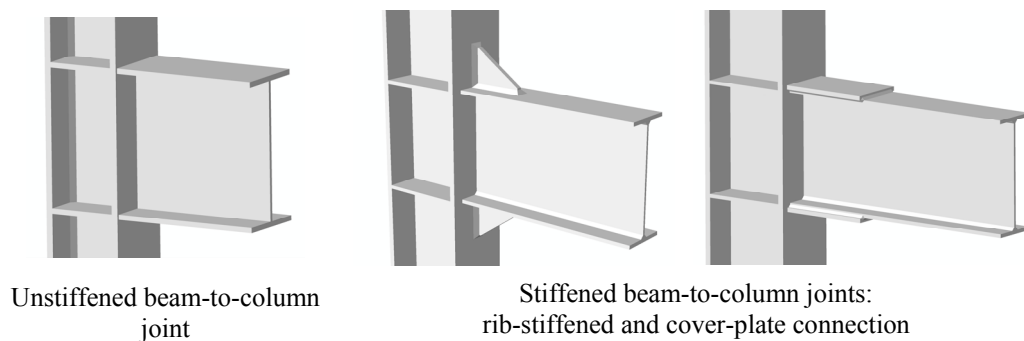


Fig. 1: Welded beam-to-column joint configurations
Slika 1: Konfiguracije varjenih spojev prečka-steber

1.2 Motivations, objectives and scope of the study

Lesson of The Oak and the Reeds story from Aesop's fables

A Giant Oak stood near a brook in which grew some slender Reeds. When the wind blew, the great Oak stood proudly upright with its hundred arms uplifted to the sky. But the Reeds bowed low in the wind and sang a sad and mournful song.

"You have reason to complain," said the Oak. "The slightest breeze that ruffles the surface of the water makes you bow your heads, while I, the mighty Oak, stand upright and firm before the howling tempest."

"Do not worry about us," replied the Reeds. "The winds do not harm us.

We bow before them and so we do not break. You, in all your pride and strength, have so far resisted their blows. But the end is coming."

As the Reeds spoke a great hurricane rushed out of the north. The Oak stood proudly and fought against the storm, while the yielding Reeds bowed low. The wind redoubled in fury, and all at once the great tree fell, torn up by the roots, and lay among the pitying Reeds.

Better to yield when it is folly to resist, than to resist stubbornly and be destroyed.



Aesop's Fables, by George Flyer Townsend, with illustrations by Harrison Weir, 1867.

In the circumstances of severe earthquake loading, questions have been raised as to whether the fractures occurred after the beams dissipated energy by their ductile response, expected in present seismic design, or whether they occurred prematurely.

After the devastating earthquake in Kobe, Japan, (Nakashima et al., 1998b).

Properly designed structure must preserve the general integrity, which is the quality of being able to sustain large damage, the structure as a whole remaining stable. This purpose can be achieved by an arrangement of structural elements that gives stability of the entire structural system. The local damaged portion must be able to dissipate a great part of seismic energy, being able to support important deformation in plastic range; the other parts remain in elastic range. The ability of a structure to undergo plastic deformations without any significant reduction of strength represents the structural ductility, being a measure of suitable structure behaviour during a severe earthquake. It is easy to understand that, in function of earthquake severity, there are different levels of ductility demands, and the ability to design a good structure is to supply it with sufficient available ductility.

On the ductility control, (Gioncu, Mazzolani, 2000).

In contrast with extensive research and detailed guidelines on enhanced connection performance in seismic design of moment-resisting frames in the US and Japan, in Europe lack of knowledge can still be found. One of significant and extensive researches in Europe, highlighting the influence of joints on the seismic behaviour of steel frames, was performed in the framework of the European research project “Reliability of Moment Resistant Connections of Steel Building Frames in Seismic Areas” (RECOs), launched in 1997 (Mazzolani, 2000). However, except for the influence of haunching on the beam-to-column joint response, no significant emphasis was put on stiffened joint solutions.

In the current practice, especially in the US, the RBS connection is a preferred solution among the enhanced beam-to-column joints, since strengthened connections have not consistently provided adequate performance in research projects. Nonetheless, it is recognised that beam-to-column joint behaviour depends largely on the size of the beam and the geometry of the plate elements constituting its cross-section. Therefore, by using different beam cross-section types from those typically used in the US and other non-European regions (as well as different design and manufacturing practices present between Europe and other countries), different stiffened joint response could be expected. In this aspect, by providing extensive data for evaluating stiffened beam-to-column joint performance under arbitrary loading conditions, in combination with the range of practically applicable I and H beam profiles typically used in Europe, this study brings forward some innovative results.

The present study derives its origin from the framework of a RFCS research project “High Strength Steel in Seismic Resistant Building Frames” (HSS-SERF) launched in 2009 (Dubina et al., 2014), which aimed at investigating and evaluating the seismic performance of dual-steel building frames made of two different steel grades, i.e. high strength steel (HSS) for non-dissipative elements and mild carbon steel (MCS) for elements in dissipative zones.

In addition to the foregoing discussion, the need and topicality of the research on strengthened connections addressed in this study can best be described from the outcomes of recent studies performed by other researchers. Statements listed below are presented in chronological order following the progress that has been achieved as well as to emphasise particular topics of research still needed.

Following observations of moment connection damage in earthquakes from the past decades, relating to seismic provisions, engineering society adopted the philosophy that the performance of beam-to-column connections should be verified by realistic-scale cyclic testing. This philosophy is based on the view that the behaviour of connections under severe cyclic loading, particularly in terms of the initiation and propagation of fracture, cannot be reliably predicted by analytical and numerical means alone. Consequently, satisfactory performance of connections must be confirmed by laboratory testing.

In their research El-Tawil et al. (1998) focused on unreinforced pre-Northridge type connections in which the beam plastic hinge is expected to form adjacent to the column. In their opinion it is important to extend analyses of this sort to other connection types such as dog-bones and strengthened connections in which plastic hinge is shifted away from the beam-column interface. Finally, the authors emphasise that much research is still needed to tie the results from local analyses to the global frame behaviour.

Research activity became topical again with the presence of the proposed new concepts and details of strengthened connections. The concept of welded steel moment-resisting connection reinforced with steel plates was popular in the design of improved connections, which means that welding technology still played an important role in connection detailing. In their conclusions to the report on experimental and numerical study of cover-plate and flange-plate moment-resisting connections Kim et al. (2000) explicitly emphasise that extrapolation of joint behaviour prediction to connections of a substantially different size should be undertaken with care.

According to ANSI/AISC 341-10 Seismic Provisions (ANSI/AISC, 2010b) the member sizes used in a test specimen should be as nearly as practical, with a full-scale representation of the member sizes used in the prototype. The purpose of this requirement is to ensure that any potentially adverse scale effect is adequately represented in the test specimen. As beams become deeper and heavier, their ability to develop inelastic rotation may be somewhat diminished. Arguments advanced from ANSI/AISC 341-10 may be used to explain such behaviour. Although such scale effects are not yet completely understood, at least two possible detrimental scale effects have been identified. First, as a beam gets deeper, larger inelastic strains are generally required in order to develop the same level of inelastic rotation. Second, the inherent restraint associated with joining thicker materials can affect joint and connection performance.

In his work Maranian (2010) summarises that the consideration of non-ductile modes of failure in steel framed buildings is not thoroughly addressed in the present standards of practice regarding building design. Of particular concern is the occurrence of short term cyclic loading, such as earthquakes, that may induce large plastic deformation in a building frame.

The primary aim of this study is to provide design guidelines for stiffened moment-resistant beam-to-column connections applied to hybrid-steel moment-resisting frames and dual braced frames utilising I and H beam profiles typically used in European design practice. Hybrid-steel approach represents an innovation in seismic design in Europe and actual seismic design rules do not cover this specific configuration. The idea is to use high strength steel (HSS) for columns as non-dissipative elastic members, whereas mild carbon steel (MCS) is utilised for the beams acting as dissipative members. Structures designed using the combination of HSS and MCS are also termed “dual-steel” structures.

Two different stiffened connection typologies are investigated: configuration with a single vertical rib plate and another one with cover plate attached to the beam flanges. Fully encased composite columns are used to increase the robustness of the applied strong column/weak

beam design concept. Other parameters of the study are: different cyclic loading and the level of axial force in the column, which may be important especially in braced frames.

On the basis of existing design recommendations for enhanced performance of both types of studied welded stiffened moment-resisting connections, sixteen large-scale single-sided beam-to-column joint specimens were designed for the experimental prequalification tests (Čermelj, Beg, 2014). Preliminary design of the test specimens was supported also by numerical simulations (Čermelj, Beg, 2011, 2012). Experimental cyclic tests were performed in order to demonstrate that joint detailing and welding technology for the tested joint configurations perform adequately under cyclic loading.

Another objective of this study is to develop a complete FE model that can be applied for a variety of geometries of stiffened beam-to-column joints, subjected to both monotonic and cyclic loading conditions, and to provide accurate simulations of behaviour without numerical difficulties well into the inelastic response (Čermelj et al., 2014). The performance of the applied numerical material models for monotonic and cyclic loading were calibrated against experimental test data found in literature. In addition, the accuracy of simulations was verified against self-experimental test data, by means of both global and local response characteristics.

An important part of the study is also dedicated to the development of damage curve for evaluating LCF failure of joint steel components subjected to plastic cyclic straining, which was used for the assessment of ductility and LCF resistance of stiffened joints. To manage this, in addition to the extensive experimental program, advanced nonlinear FE numerical models, using Abaqus v6.12-2 (SIMULIA, 2012), were developed to establish complementary parametric analysis based on models that had been validated against cyclic experimental test results.

Based on the experimental and numerical studies presented so far, an accurate numerical tool was developed, which enables comprehensive study and check of welded rib-stiffened and cover-plate beam-to-column connections performing under monotonic and cyclic loading. This enabled additional complementary numerical analysis to be done on both stiffened connections subjected to monotonic and cyclic loading. The primary objective is to support the proposed design guidelines for the two stiffened joints against possibly adverse beam member size effects within the range of practically applicable I and H beam profiles typically used in Europe.

The results of complementary numerical analysis also give important information on the ductility and overall overstrength of the beams in combination with specific configuration of stiffened connection. In this light the present research systematically complements the findings of the sort from past research activities.

The manners of addressing experimental results follow the concerns emphasized as crucial parameters of seismic response of moment-resistant connections after the past major earthquakes: evaluation of ductility, plastic rotation and energy dissipation capacity of beams with examination of the corresponding LCF resistance. In addition, the obtained response characteristics are checked against performance requirements from the present seismic design codes (EN 1998-1 (CEN, 2005c), ANSI/AISC 341-10).

The obtained experimental and numerical results were used to compare the response of both stiffened connections and to demonstrate that the applied joint detailing and the design concept for the joints result in reasonable stiffening plate dimensions as well as adequate joint response under monotonic and cyclic loading for the considered range of beam profiles.

The study intends to focus on plastic beam rotations in combination with the specific geometry configuration of stiffened connection. Therefore, plastic shear mechanism in the column panel zone and other column plastic deformations are prevented by suitable design.

Proposed design provisions concern avoidance of conditions that may lead to brittle failures and adoption of appropriate design strategies to allow for stable and reliable hysteretic energy-dissipation mechanisms. The design guidelines for both stiffened joint configurations make use of capacity design and elementary (elastic) beam theory. The author is very much aware that such simplified procedure will neither exclude possible moderate inelastic straining at the face of the column nor accurately predict the distribution of stress and strain over the length of the stiffened connection. Notwithstanding, if the applied beam size is modest and the stiffening plates are not overly thick, the use of design guidelines should produce connections capable of developing adequate plastic hinge rotations.

By systematically analysed and well documented experimental and numerical analysis results this work contributes to the increased knowledge of monotonic and cyclic behaviour of rib-stiffened and cover-plate beam-to-column joints in the field of European seismic design practice.

The outcomes of the study present an important contribution also in terms of ultimate behaviour of steel beams in combination with constraint details of the two typologies of stiffened connections, and confirm the need for a twofold classification of steel members according to their ductility and overstrength as the most appropriate approach for the seismic design applications (Piluso, Rizzano, 2007. D'Aniello et al., 2012. Güneyisi et al., 2013). According to this approach, clear distinction is made in this work between the overstrength due to random material yield stress variability and on the other side the overstrength due to the amount of post yield material strain-hardening, geometric characteristics of a beam cross-section and loading conditions. In this field the present work fills several gaps still not clearly addressed in the current European seismic design code.

1.3 Organisation of the thesis

The thesis consists of seven chapters. Chapter 1 introduces the type of beam-to-column connections studied herein and presents motivations, objectives and the scope of the research work.

Chapter 2 presents a short review on the literature related to the both stiffened moment-resisting connection types and explores in relative detail the experimental and numerical research works carried out on the both stiffened connections. An overview of the related design provisions included in the European seismic design code EN 1998-1, with their assessment and emphasises of the parts dealing with the topic addressed herein, that would need additional clarification and/or further development, are also presented in this chapter. The description of ductility and overstrength as two crucial parameters controlling the ultimate behaviour of steel beams (beam-to-column joints) in steel frames is further addressed in terms of the findings of recent research activities. In addition, the basis of the LCF phenomenon in relation to the seismic response of steel elements is presented. Short introduction to damage mechanics approaches for the definition of local failure of steel structural members subjected to arbitrary loading is provided, which had served as the basis of implemented method in this work for the prediction of crack initiation in steel parts of beam-to-column joints under the LCF loading.

The description of experimental cyclic tests on sixteen welded rib-stiffened and cover-plate beam-to-column joints, along with detailed report on the obtained results is given in Chapter 3. The design of the test specimens, which started from the point of the current foreign seismic design provisions and other related literature, and further on supported by FE numerical simulations, is presented. The final geometric and material properties of the test specimens, with experimental program description are gathered. The evaluation of experimental results is provided for global and local joint response by means of different response parameters: observations of plastic zone development and damage concentrations in the steel parts of the joint, damage in the column, joint ductility, amount of dissipated energy and the LCF resistance. In addition, the response of specimens was evaluated according to the prequalification criteria of applicable standards currently in use.

Chapter 4 presents the complete numerical study on the two types of welded stiffened beam-to-column joints. First, detailed description of the FE model development is given: from the selection of suitable finite element types, through the description of applied solver procedures, to material and geometric nonlinearities accounted in the model. The results of the numerical simulations of the test specimens used to validate the developed finite element model under monotonic and cyclic loading conditions are presented. Discussions on the comparison between the experimental and numerical response for monotonic (test results from literature) are included, as well as on cyclic loading with constant and variable loading amplitude for each of the tested specimen. Comparison of experimental and numerical local strain response is provided as well. On the basis of a highly consistent response found between the experiment and the numerical simulation, development of a damage curve for the prediction of crack initiation based LCF failure is demonstrated.

Complementary numerical study on both welded stiffened connections is presented in Chapter 5. Beside the effect of high level of column compressive axial force on the stress/strain transfer mechanism in the beam-to-column joint interface, the primary objective of this part of the work is to support the proposed design guidelines for the two stiffened joints against possibly adverse beam member type and size effects within the range of practically applicable I and H beam profiles typically used in Europe. Eight monotonic and eight cyclic simulations

were performed for each of the studied stiffened joint type in combination with a set of eight different beam profiles. The findings of the parametric study are demonstrated and discussed in terms of the obtained rotation capacities (monotonic and cyclic) and beam flexural overstrength, as the crucial parameters of the ultimate beam and also full-strength stiffened joint behaviour. In this aspect, first, comparison between responses of both the stiffened connection typologies is provided, and second, suppositions of the proposed design guidelines are checked.

On the basis of the findings from experimental and numerical studies in this research work, Chapter 6 presents design guidelines for the prequalified welded rib-stiffened and cover-plate connections, in terms of complete detailing rules and design procedure.

A summary and conclusions regarding the achievements of this research work are provided in Chapter 7, along with a list of contributions and recommendations for future research.

The idea of complete research work follows the process of seismic analysis of an arbitrary steel frame, and can be summarised as illustrated in Fig. 2.

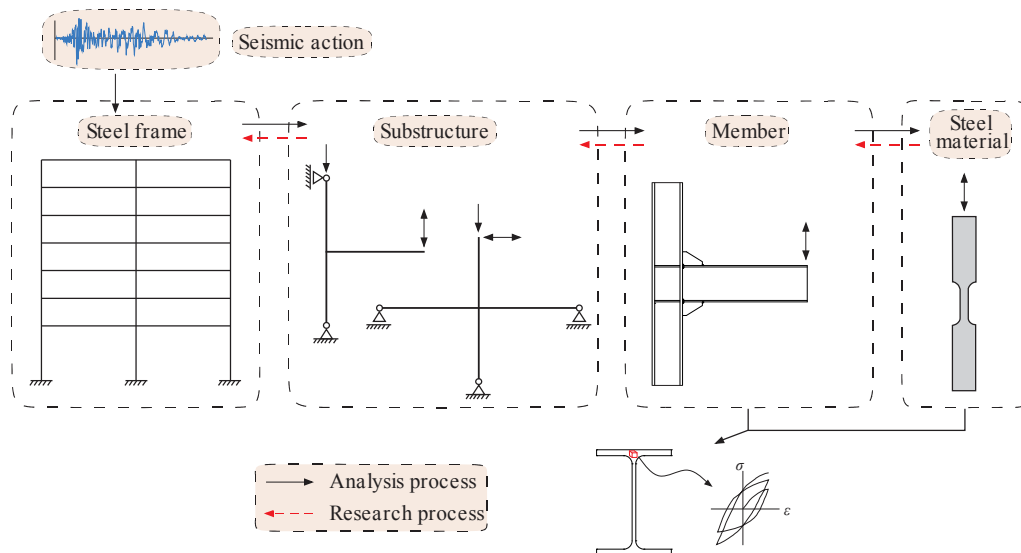


Fig. 2: The process of seismic analysis of a steel frame
Slika 2: Proces potresne analize jeklenega okvira

2 LITERATURE REVIEW

2.1 Introduction

The best way to look into the future is to understand the past.

To better understand the behaviour of the welded stiffened moment-resisting beam-to-column joints, which are the subject of the current study, a review of experimental and analytical investigations related to this type of connections is presented in this chapter. A brief review on the literature on unstiffened connections is also included to provide a complete picture of the works on moment-resisting joints.

From the engineering perspective, properly designed structure must preserve the general integrity by being able to sustain local damage during seismic event. However, after the devastating earthquakes in 1985 – 1995 the performance of unstiffened beam-to-column joints was found generally inadequate compared to the predicted one by design provisions of that time, thus invalidating the then existing design and constructional procedures for prequalified beam-to-column connections. The international scientific community agreed that numerous factors had contributed to the observed failures, found as obvious shortcomings in the current practice: poor welding practices with common use of low toughness weld metal and insufficient quality control, details that resulted in the development of excessive local ductility demands with large triaxial strain concentrations at the vulnerable welded beam-to-column interface. Design practices suspected to have contributed to poor performance include the use of significantly larger members and connections that had previously been tested as well as the use of design provisions that could result in excessively weak column panel zones.

To improve the overall design process (initial conception and design of the structural systems) and quality of buildings, the modern design guidelines are based on numerous research works, including new analytical, numerical and laboratory research on seismic demands, base material, welds, fracture mechanics, as well as on full-scale testing of connections.

In the USA, modern seismic design guidelines are provided by the FEMA P-750 provisions (FEMA, 2009), ANSI/AISC 341-10 seismic provisions (ANSI/AISC, 2010b), and in relation to prequalified connections for seismic applications by ANSI/AISC 358-10 (ANSI/AISC, 2010a).

The research work presented in this document follows the main outcomes of a large number of studies carried out mainly in the earthquake-prone parts of the world (USA, Japan) and continues research work in the field of earthquake engineering in Europe. For this reason, a brief overview of provisions for seismic design of steel structures contained in the present Eurocode EN 1998-1 (CEN, 2005c) is also presented in this chapter. Assessment of the current rules is made, along with emphasis on critical issues in relation with seismic design of moment-resisting beam-to-column joints, as found by research activities over the last years in the Europe, as well as worldwide research trends.

In order to provide complete state of the art on the topic, basic demands that moment-resisting beam-to-column joints designed for seismic zones have to satisfy, are covered:

- ductility (rotation capacity);
- overstrength;
- robustness (reliable detailing together with material behaviour).

In addition, the basis of low-cycle fatigue (LCF) phenomenon in relation to the seismic response of steel elements is addressed. Short introduction to damage mechanics approaches for definition of local failure of steel structural members subjected to cyclic loading conditions is provided as well.

2.2 Previous research work on stiffened moment-resisting connections

Information on the past research activities on welded stiffened beam-to-column joints is provided separately for cover-plate and rib-stiffened connections in the next two subsections. Conclusions to the complete research review are provided at the end of this section.

It should be noted that the review below is focused mainly on researches started after 1994, with the emphasis already put on the enhanced stiffened connection solutions.

2.2.1 Welded cover-plate moment-resisting connections

Shortly after the 1994 Northridge earthquake, Engelhardt and Sabol (1995) tested 12 single-sided steel moment-resisting connections strengthened with trapezoidal and rectangular cover plates. The typical beam size was W36x150 ($h = 911$ mm, $b_f = 304$ mm) of A36 steel. Beam flange yield strengths ranged between 292 and 340 MPa. Columns ranged in size from W14x257 ($h = 416$ mm, $b_f = 406$ mm) to W14x455 ($h = 483$ mm, $b_f = 428$ mm); Grade 50 (345 MPa) steel was used for all columns. Ten of the 12 test specimens developed large plastic rotations under cyclic loading with two of them performing poorly. In one of the two specimens, the groove weld joining the beam top flange and the cover plate fractured in a brittle manner, probably due to low toughness of the weld metal. In the other one, a brittle fracture occurred at the bottom flange, causing a complete separation of the beam bottom flange and cover plate from the column flange. Fractographic and metallographic examination by Engelhardt and Sabol suggested that higher yield strength, heavy and long cover plates, high heat input during welding, and the presence of an initial crack contributed to the observed failures. These two failures of cover-plate connections called into question the reliability of such connections, which led to further research program described below.

Popov et al. (1996) tested three identical beam-column connections that were reinforced with trapezoidal top cover plates and rectangular bottom cover plates. The specimens were constructed using a W36x245 A36 ($h = 916$ mm, $b_f = 419$ mm) beam and a W14x398 ($h = 465$ mm, $b_f = 421$ mm) Grade 50 (345 MPa) column. Transverse stiffeners were added to strengthen the beam-to-column panel zone. Two of the three specimens failed prematurely due to fracture of the column flange at the level of the underside of the beam flange. In the third case, the top (trapezoidal) cover plate, both column flanges, and the column web fractured. The maximum plastic rotation in this connection exceeded 0.04 radians. In case of the second specimen, the column flange and the column web inside the panel zone fractured at a lower maximum plastic rotation of 0.02 radians.

Whittaker et al. (1996) tested one single-sided cover-plate connection as part of the SAC Phase I project using the ATC-24 loading protocol (ATC, 1992). A trapezoidal top cover plate and a rectangular bottom cover plate were used. The top plate was narrower than the beam flange to permit down hand welding of the cover plate to the beam. The bottom plate was used as an erection seat and was groove welded to the column in the shop. This plate was wider than the beam flange to permit down hand fillet welding to the beam bottom flange. The connection of the beam web to the column flange utilized bolts and supplemental web tab welds. The connection represented the state-of-the-art in 1996 and was designed by industry representatives from the SAC Joint Venture and the research team. Two bolts were used at the

end of the bottom cover plate to delay separation of the beam bottom flange and the rectangular plate. No transverse stiffener was welded to the column web in this connection, even though the panel zone would not have met the requirements of the current AISC seismic provisions (ANSI/AISC, 1997). In this specimen, the panel zone yielded prior to the beam. Only after substantial strain hardening in the panel zone, the beam yielded beyond the nose of the cover plate. Yielding of the beam was followed by flange local buckling and web local buckling in the beam at the nose of the cover plate. Flange buckling at the nose of the bottom cover plate led to tearing of the longitudinal fillet weld joining the plate to the beam flange. The tear in the fillet weld propagated with repeated cycling of the test specimen back to the line of the two bolts. The bottom flange of the connection then suffered a net section fracture. The maximum beam plastic rotation was 0.023 radians.

Whittaker and Gilani (1996) tested a single-sided cover-plate specimen composed of a W36x359 ($h = 950$ mm, $b_f = 425$ mm) Grade 50 (345 MPa) beam and a BW36x670 ($h = 1043$ mm, $b_f = 450$ mm) column fabricated from Grade 50 (345 MPa) plate. A trapezoidal top cover plate and a rectangular bottom cover plate, both of Grade 50 steel plate were used. The beam web was groove welded to the column flange. Transverse stiffeners were welded to the column web to increase the strength of the panel zone and substantially eliminate plastic deformation in the panel zone. The beam fractured immediately beyond the nose of the top cover plate. The fracture propagated through the beam top flange, the beam web, and the beam bottom flange, and was stopped by the bottom cover plate. Fractographic analysis of the failure surface showed laminations and imperfections in the parent metal, and indicated that fracture initiated immediately below the end of the fillet weld joining the top trapezoidal cover plate and the beam top flange. Subsequent finite element analysis of this connection showed high triaxial stresses at the fracture initiation site.

Bjorhovde et al. (1999) tested 17 full-scale, beam-column connections strengthened with cover plates. All specimens were constructed with W14x176 ($h = 387$ mm, $b_f = 398$ mm) columns and W21x122 ($h = 550$ mm, $b_f = 315$ mm) beams of ASTM A572 Grade 50 (345 MPa) steel. The variables considered by the authors included cover-plate thickness, column-straightening protocol, strain rate, transverse stiffeners location and weld details, and cover plate-column flange weld geometry. Thirteen of the 17 specimens achieved a maximum plastic rotation of 0.025 radians or greater. The authors concluded that there was no significant difference in response between assemblies using strengthened and un-straightened columns and that the loading protocol was unimportant, although dynamic testing appeared to be a more severe loading condition than static testing.

It has to be noted that most of the experimental studies described above included no pre-test numerical FE analysis. This also applies to the research work of the SAC Phase I project. The SAC project was formed in 1994 by Federal Emergency Management Office (FEMA) and California Office of Emergency Services (OES), as a joint venture of three different structural engineering research associations from California (SEAOC, ATC, CUREe), with a specific aim to investigate the damage to welded steel moment-resisting frame buildings after the Northridge earthquake and to develop repair techniques and new design approaches to minimize damage to steel moment-frame buildings in future earthquakes. The SAC Phase I lasted for one year, and focused on the development of interim solutions for the identification, evaluation, repair, and modification of damaged welded steel moment-resisting frame buildings. Some effort was also devoted to new approaches to the design and construction of steel moment-resisting frames. The results of the SAC Phase I project were published as FEMA 267 (FEMA, 1995b), and in numerous other technical reports.

After the completion of the SAC Phase I project, FEMA funded the SAC Phase II project that focused on new steel moment-resisting frame construction. Among six topical areas covered by the complete research work, Connection Performance work package (analytical studies and large-scale testing) involved a series of testing programs on: reduced beam sections, welded cover plates and flange plates, alternative weld details, bolted connections, retrofit strategies, strain-rate effects, and load-history effects. Each of the programs included ten large-scale beam-to-column connection tests.

The SAC Phase II project enabled the first systematically covered research program focused on the response of steel moment-resisting connections strengthened with flat steel plates that served to relocate the plastic hinge away from the face of the column.

First, the key design variables for cover-plate moment-resisting connections (geometry of the cover plate and effect of its thickness, arrangement of the welds between the plate and the beam flange, welding details at the column face, etc.) were identified. An experimental program was developed in order to study such variables. For the purpose of quasi-static cyclic testing, design, detailing, and construction of ten full-size single-sided specimens was done using the procedures of FEMA 267A (FEMA, 1995a). The SAC cyclic protocol and near-field displacement history were used for the testing program (Krawinkler, 1998). The same beam-column profiles were used as in SAC Phase I project: all the specimens were fabricated from W14x176 ($h = 387$ mm, $b_f = 398$ mm) Grade 50 (345 MPa) columns and W30x99 ($h = 753$ mm, $b_f = 265$ mm) Grade 50 (345 MPa) beams. Prior to the testing of the specimens, nonlinear FE analysis models of all specimens were developed to study the effect of weld and plate geometry on important elastic stress, plastic strain, and fracture-mechanics parameters. The main outcome of the study was the interpretation of the analytical and experimental data for the purposes of developing prequalified cover-plate moment-resisting connections and preparing guidelines for the design, detailing, and construction of cover-plate moment-resisting connections (Kim et al., 2000).

Important conclusions of the aforementioned study on cover-plate moment-resisting connections can be summarized as follows:

- none of the ten experimentally tested cover plate connections failed prematurely in a brittle manner;
- the applied design procedures from FEMA 267A assured robust stiffened connections;
- maximum obtained beam plastic rotations at the end of the test ranged between 0.041 and 0.052 rad, with the corresponding values of the beam plastic rotations at which the maximum beam resistance dropped below 80 % of the peak resistance between 0.016 and 0.019 rad; as defined by the Joint Venture, the beam plastic rotations were computed by dividing the plastic component of the beam displacement (computed by subtracting the rigid displacement, and contributions from the column and panel zone deformation from the measured beam tip displacement) by the distance between the centreline of the column and centreline of the actuator.
- cover-plate connections perform substantially better than unstiffened connections and are technically viable alternatives to moment-resisting connections reinforced with haunches or connections utilizing reduced beam sections;
- experimental tests on large-scale specimens is recommended, with member sizes as a full-scale representation of the member sizes used in practice. Extrapolation of the reported results to stiffened connections of a substantially different size or configuration should be undertaken with care.

2.2.2 Welded rib-stiffened moment-resisting connections

In comparison with cover-plate connections, only very limited test data are available concerning the welded moment-resisting connections stiffened by vertical rib-plates. Specimens and their behaviour are briefly described below. In addition, outcomes of numerical study on the rib-stiffened connection are presented.

Engelhardt et al. (1995) tested two full-scale moment connections stiffened by vertical ribs. Two specimens were fabricated using a W14x426 ($h = 474$ mm, $b_f = 424$ mm) of A572 Grade 50 (345 MPa) column and a W36x150 ($h = 911$ mm, $b_f = 304$ mm) beam made of A36. Two tapered ribs were welded to the top and bottom beam flanges to reduce the stress on the beam flange groove welds and to move the location of the beam plastic hinge away from the face of the column. The backup bar on the bottom flange of the beam was removed. Test results revealed that both specimens performed very well with maximum beam plastic rotation of 0.025 and 0.03 radians, and exhibited the same ductile behaviour and failure modes. Failure occurred by gradual tearing of the beam bottom flange at the tips of the ribs. Notably, failure did not occur in the column flange near the welded ribs, since the columns used in the test were very heavy.

In their study Zekioglu et al. (Zekioglu et al., 1997) utilised combination of dual rib-stiffened moment-resisting connection and reduced beam section at the end of the stiffened region of the beam. Two triangular rib plates (dual rib configuration) were welded to each beam flange. The experimental study comprised three single-sided test specimens with three different beam profiles: W27x178 ($h = 706$ mm, $b_f = 358$ mm), W33x152 ($h = 851$ mm, $b_f = 294$ mm), and W36x150 ($h = 911$ mm, $b_f = 304$ mm), all made of Grade 50 (345 MPa) steel. Brittle failure of welded connections did not occur. Stress concentration caused significant yielding of the beam at the narrowest beam section, where final fracture of the beam flange, identical for all three specimens, occurred. The effect of the ribs was positive, since they appeared to assist in reducing stresses of groove welds between the beam and the column flange. No damage was observed in the vertical rib plates. High beam plastic rotation capacities with considerable flexural strength were obtained. The maximum beam plastic rotations for the three specimens ranged from 3.5 to 6.4 % radians, based on a span from the beam tip to the midpoint of the reduced beam section. Other important conclusions of the study were: lateral bracing at or near the plastic hinge zone is very important to avoid rapid strength degradation; beams with high yield and ultimate strengths appear to have achieved smaller plastic rotations – the authors expressed the need for an upper limit on material strengths of the beam.

Anderson and Duan (1998) tested three specimens with a vertical triangular rib-plate welded to the top and bottom flanges of the beam, built from W21x68 ($h = 537$ mm, $b_f = 210$ mm) cross-section. Test results showed that the specimens developed capacities for plastic rotation in the range of 2.5–3.0% radians. The specimen with a welded solid rib failed due to the pull-out of the top rib from the weld at the face of the column. One of two specimens with a welded perforated rib (a hole in the centre of the rib with a diameter of 38 mm) exhibited severe local buckling of the beam flange and web, and minor cracking in the weld at the toe of the rib. The other specimen with perforated rib failed suddenly because of cracking in the weld between the rib and the column flange, by pulling out the beam bottom flange from the column flange, with the penetration of crack into the column flange and its propagation into the column web.

In 2002, Cheol-Ho Lee (Lee, 2002) presented a seismic design procedure for rib-stiffened steel moment-resisting connections based on an equivalent strut model. Based on results from numerical finite element analyses it was shown that the classical beam theory cannot provide reliable force transfer predictions in the rib-stiffened moment connection. In addition, it was

noted that an inclined strip in the rib-stiffener acted as a strut rather than following the beam theory. According to this approach, an equivalent strut model, which considers the strut action in the rib, is proposed for practical design purposes. Based on the proposed model, a step-by-step design procedure, calibrated against the results from FE analyses, is recommended.

2.2.3 Conclusions

In moment resisting frames energy dissipation during seismic action is achieved by the formation of plastic hinges in the beam sections near the beam-to-column connection. Brittle type failures in the vicinity of the welded beam-to-column connection can lead to sudden loss of the structure's load bearing capacity and its structural integrity. On the basis of previous research works, rib-stiffened and cover-plate connections perform substantially better than the unstiffened connections, and present good alternatives to moment-resisting connections reinforced with haunches or connections utilizing reduced beam sections. Although the studies did not provide consistent joint response in all the reported cases, the aim of the stiffened connections, based on the capacity design concept, to shift the plastic hinging away from the beam-column welded section at the face of the column, was successfully achieved.

The reported inconsistency in the cyclic response of both rib-stiffened and cover-plate connections can be attributed to the fact that despite the relatively large number of tests performed on the stiffened connections, in most cases the key design variables for such connections were not systematically identified and evaluated. A prime example of a thorough and comprehensive study with a high consistency of result was done by Kim et al. (2000), which certainly speaks in favour of the stiffened connection solutions.

Most of the studies described above were experimental, while FE analysis was rarely undertaken as part of the research program. On the contrary, if experimental research works were supported by numerical analysis, simulations of monotonic loading only were used to foresee the effects of the cyclic loading conditions on the response of analysed connections (study on cover-plate connections in SAC Phase II project (Kim et al., 2000), rib-stiffened connection behaviour (Lee, 2002)).

Another consideration of great importance for the interpretation of beam-to-column joint response is a beam member size effect. In relation to reported research works on the stiffened connections, one can observe that the beam height used in the studies ranged from about 500 mm to about 950 mm. Sections commonly used in the US for modern steel moment-resisting frames are greater than 21 in \approx 533 mm.

In contrast to lack of research activities directly addressing the seismic behaviour of welded stiffened moment-resistant beam-to-column joints, a great number of recent research works in Europe is dedicated to the understanding of the ultimate flexural behaviour of steel beams. As the main response parameters, rotation capacity and flexural ultimate resistance are identified. The two parameters have a direct influence also on the overall beam-to-column joint performance. In this light some general considerations, with reference to the provisions of present design codes and outcomes from the recent research works, are outlined in the following section.

2.3 Principles of plastic and seismic design of steel frames

2.3.1 On the ductility of steel beams

A structure is said to behave in a ductile manner if it is capable of withstanding large inelastic deformations without significant degradation in strength, and without the development of instability and collapse. The design forces specified by building codes for particular structural systems are related to the amount of ductility the system is deemed to possess. Generally, the building codes allow structural systems with more ductility to be designed for lower forces than less ductile systems, as ductile systems are deemed capable of resisting demands that are significantly greater than their elastic strength limit.

In case of moment-resisting frames and also dual system frames, the ultimate behaviour of steel beams deeply influences the overall performance of steel frames. The development of adequate level of beam plastic rotation capacity represents the basis for plastic design as well as seismic design of steel building structures. According to this approach, members should be able to develop plastic hinge rotations to such extent that anticipated collapse mechanism is completely developed, without dropping their moment capacity, thus providing the required redistribution of bending moments. Rotations of plastic hinges required to achieve the needed displacement levels as well as to fully develop the collapse mechanism are provided by the plastic rotation demands, varying for different structural configurations, loading arrangements, geometry, material strengths and the level of the seismic intensity. It has been widely investigated in the literature, especially for continuous beams and frames (Driscoll, 1957. ASCE, 1971).

Nowadays safety requirements along with even more important economic aspect of construction require the need to know more about the behaviour of steel construction members under cyclic loading conditions characterized by seismic events. To achieve this, attention has to be paid to the cross-section geometrical limitations of components and to the laterally unrestrained lengths of members, since the flexural behaviour of steel beams is highly susceptible to plastic local buckling of compressed cross-section elements and inelastic flexural-torsional buckling of the member.

According to the European design codes, both plastic and seismic designs of structures are based on the slenderness classification of steel sections, thus emphasizing local buckling phenomenon as the limiting condition. EN 1993-1-1 (CEN, 2005a) provides basic classification of cross-sections, subdividing them into four classes, depending on the geometric properties of compression elements and strain distribution, Fig. 3. For plastic global analysis, it is required that all members with plastic hinges should belong to Class 1, i.e. to be made of ductile sections.

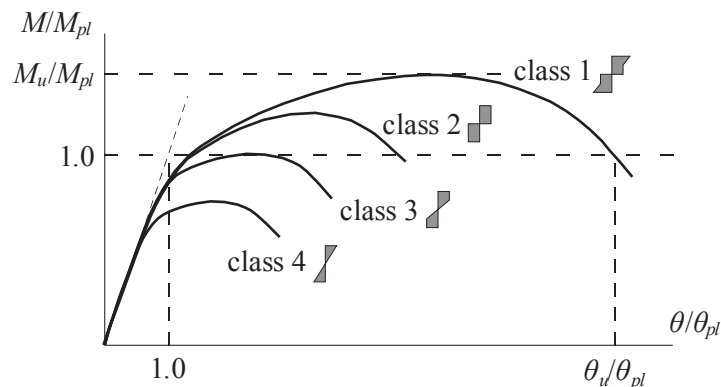


Fig. 3: Cross-section classification criterion according to EN 1993-1-1
Slika 3: Kriterij klasifikacije prečnih prerezov po EN 1993-1-1

According to EN 1998-1 (CEN, 2005c), the cross-section classes defined in EN 1993-1-1 provide a limitation for the selection of appropriate behaviour factor q , see Table 1; e.g. ductility class DCH with $q > 4$ requires Class 1 cross-sections for dissipative zones.

Preglednica 1: Zahtevan razred prečnega prereza za disipativne elemente v povezavi z razredom duktilnosti in pripadajočim faktorjem obnašanja po EN 1998-1

Table 1: Required cross-sectional class of dissipative elements in relation to ductility class and proper behaviour factor from EN 1998-1

Ductility class	Behaviour factor q	Required cross-sectional class
DCM	$1.5 < q \leq 2$	Class 1, 2 or 3
	$2 < q \leq 4$	Class 1, 2
DCH	$q > 4$	Class 1

This means that in EN 1998-1 beam performance, i.e. member rotation capacity, is simply referenced directly to the cross-section classification criteria provided in EN1993-1-1, relating it to material and cross-section factors only, at the same time neglecting other behavioural issues important for seismic or dynamic loading, such as beam flange-web interaction (relative restraint between the web and the flange), overall member slenderness, moment gradient along the member, lateral restraints, and cyclic loading conditions. In contrast with Eurocode provisions, ANSI/AISC 341-10 seismic provisions and ANSI/AISC 360-10 specification for structural steel buildings (ANSI/AISC, 2010c) comprise more severe member cross-section classification for seismic loading, i.e. cyclic loading conditions.

In the light of the aforementioned discussion, researchers have pointed out the need to conduct further assessment of the adequacy of Class 1 cross-sections from EN 1993-1-1 to satisfy the cyclic demands imposed during seismic loading conditions (ECCS, 2013). Namely, the ductility and susceptibility of fracture are directly related to the occurrence of local buckling.

In their research D'Aniello et al. (2012) clearly pointed out the need for a twofold classification of steel members according to their ductility and overstrength as the most appropriate approach for seismic design applications. Accordingly, there are two main response parameters for steel beams: rotation capacity and flexural ultimate resistance. While beam rotation capacity is the source of the local ductility supply needed to achieve a global dissipative behaviour of structures under seismic actions, beam flexural ultimate resistance governs the flexural overstrength. The latter gives important information for an appropriate application of capacity seismic design approach of structures, where element distribution among elastic, for non-dissipative, and plastic behaviour, for dissipative members, creates important hierarchy criteria.

At the beginning of this research work it is also worth pointing out the meaning of local ductility or rotation capacity of a typical steel member. A wide range of literature can be found discussing about the concept of local ductility. Here, part of a survey on the topic from D'Aniello et al. (2012) is summarized, reproducing from there much of the text together with the stated literature review. As the authors found out, it is the moment-curvature approach that has been widely used in literature to study cold-formed steel sections (Hasan, Hancock, 1989). According to this approach, the cross-section local ductility is defined in terms of curvature ductility as follows:

$$\mu_{\chi} = \frac{\chi_u}{\chi_{pl}} - 1, \quad (1)$$

where χ_{pl} is evaluated as M_{pl}/EI , M_{pl} being the beam plastic bending moment, and χ_u the ultimate limiting curvature at which the moment resistance drops below M_{pl} .

Following the above definition, rotation capacity R is the measure of local ductility at the member level. Therefore, rotation ductility is evaluated from moment-rotation relationship (Rondal et al., 1995) as follows:

$$R = \mu_\theta = \frac{\theta_u}{\theta_{pl}} - 1, \quad (2)$$

where θ_{pl} is the rotation corresponding to the flexural yielding and θ_u the ultimate beam rotation. Rotation capacity can be divided into two parts: the stable part of rotation capacity developed up to the occurrence of local buckling, and the unstable part due to the post-buckling resistance (Mazzolani, Piluso, 1996).

Both presented approaches define local ductility as a non-dimensional parameter. The meaning of the definition of local ductility is depicted in Fig. 4, by means of the generalized force-displacement curve of a member capable of withstanding plastic deformations.

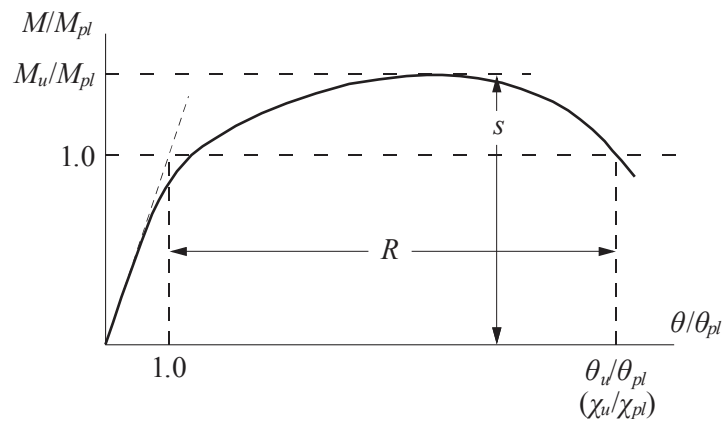


Fig. 4: Definition of local ductility R and overstrength factor s from a moment-rotation curve
Slika 4: Definicija lokalne duktilnosti R in dodatne nosilnosti s na podlagi krivulje moment-rotacija

In contrast to the definition of the ultimate beam rotation, as depicted in Fig. 4, there exist several other definitions for θ_u in the literature: failure defined at the instance when the resistance is reduced to less than 90% (FEMA, 2011) or less than 80% (Nakashima et al., 1998b) of the maximum resistance.

In general, the experimental results in case of I and H beam sections indicate that the loading condition has a significant influence on rotation capacity which is reduced (by about 70%) under cyclic loading conditions, when compared with monotonic loading conditions, due to the more prominent beam web and flange local buckling, and low-cycle fatigue effects (D'Aniello et al., 2012).

Further on, based on the experimental data presented and those already available from the existing literature, empirical equations for predicting the rotation capacity R under monotonic loading were derived in (D'Aniello et al., 2012) by means of multiple linear regression analyses. From multiple regressions analysing the experimental data considered for this purpose it was observed that R is influenced mostly by the following parameters: the aspect ratio of the cross-section, the ratio between flange area on total gross section area, and the length of plastic hinge.

As has already been emphasised, according to EN 1993-1-1, verification of required against available rotation capacity is simply satisfied by limiting the cross-sectional dimensions in accordance with appropriate behavioural classes. On the other side, the term rotation capacity

method, i.e. direct comparison between the plastic rotation demand and the corresponding plastic rotation capacity, implies that local ductility demands are explicitly carried out. In this case existing theoretical/empirical relations for the determination of the available plastic rotation of steel beams under monotonic loading can be used and then directly compared to the plastic rotation demand of the corresponding plastic hinge in the analysed structural model. However, for structural members subjected to cyclic loading conditions such theoretical relations do not exist and additional rules are required in this case to account for the effect of the LCF on rotation capacity.

A great number of researches have been carried out to determine the minimum beam plastic rotation demand in order to achieve a plastic mechanism under monotonic loading. In the absence of an accurate plastic analysis, plastic rotation capacity of 0.03 rad may be considered as adequate. This value is confirmed also by the ANSI/AISC 360-10, which states that compact sections are those that possess at least a rotation capacity of approximately 0.03 rad.

For seismic design application, the evaluation of the minimum required rotation capacity is even more complex, because it is also strictly related to the design value of the behaviour factor, the intensity of the seismic event and its frequency content. Some indications can be found in the related literature and current codes as described below.

Nakashima et al. (1998b), commenting experimentally obtained results of cyclically loaded beam-to-column joints, express that in a typical moment frame in which points of contraflexure of beams and columns are located near their mid-lengths, a beam rotation of 0.04 rad leads to a story drift angle of 0.04 rad even if the column is assumed to behave rigidly, and to a larger drift angle if column flexibility is included. In Japanese seismic design, a limit to a maximum story drift angle of 0.01 rad is implicitly assumed for large earthquakes (equivalent to 1.0·g for the maximum elastic response acceleration). Although various structural irregularities and other uncertainties may result in larger beam rotation demands in many cases, a rotation capacity of 0.04 rad (or plastic rotation capacity of 0.03 rad) is deemed sufficient in most cases.

Recently, Lignos and Krawinkler analysed the NEES database (available from <https://nees.org/warehouse/project/84>), which includes comprehensive data of more than 300 experiments on steel wide flange beams and beam-to-column joints. In line with the study presented in this paper, they highlighted that rotation capacity is strongly dependent on the beam depth, the shear span-to-depth ratio (L/h_b), the lateral braces, the flange and web slenderness. In addition, they pointed out that a description of the beam deformation capacity in terms of absolute rotation is misleading since by increasing L the yield rotation increases as well. Hence, it is more effective to define the rotation capacity in terms of plastic deformation only.

According to the prequalification criteria, the required rotation capacity of the plastic hinge region from EN 1998-1 is 0.035 rad for structures of ductility class DCH and 0.025 rad for structures of ductility class DCM, Table 1. In both cases the rotation capacity should be ensured under cyclic loading without degradation of maximal strength and initial stiffness larger than 20 %. For beam-to-column connections used in the seismic force resisting system the ANSI/AISC 341-10 provides the following two requirements: the connection shall be capable of accommodating a total joint rotation of at least 0.04 and 0.02 rad, for special moment frames (SMF) and intermediate moment frames (IMF), respectively; the measured flexural resistance of the connection, determined at the column face, shall equal at least 0.80 M_{pl} of the connected beam at the aforementioned story drift angles for SMF and IMF, where M_{pl} is nominal plastic beam moment.

It should be noted that the AISC acceptance criterion is based on joint rotation, which includes elastic and inelastic rotations from beam and column, while the criterion from Eurocode takes into account total beam rotation and column web panel shear deformation without column elastic deformation. Beside the complete lack of information on the protocol of cyclic loading to be used, in Eurocode it is also not clearly stated whether the rotation limits should account for the rotation capacity of the plastic hinge region or the whole beam.

FEMA 356 (FEMA, 2000a) and EN 1998-3 provide the minimum required rotation capacity for each performance level. In particular, for compact beams a rotation capacity equal to 6 for life safety (LS) state, and equal to 8 for collapse prevention (CP) limit state is expected.

2.3.2 Beam flexural overstrength

In moment-resisting frames, the properties of beam-to-column joints significantly influence the structural global characteristics, i.e. resistance, stiffness and ductility. In addition, the degree of moment resistance of beam-to-column joints in relation with the moment resistance of the connected members (beams) is of primary importance in the seismic design of moment resisting steel frames, because it directly affects the location of dissipative zones. Under severe ground motions, the dissipation of the earthquake input energy at the beam ends is expected. In case of partial-strength beam-to-column joints, this is obtained through the yielding of the connecting elements. Even though a ductile behaviour can be obtained when designing the fastening elements, i.e. welds and/or bolts, so that they remain in the elastic range, it is generally recognised that full-strength joints are able to assure the best behaviour from the dissipative point of view (Gioncu, Mazzolani, 2000. Piluso, Rizzano, 2007). For this reason full-strength beam-to-column joints have to possess sufficient overstrength with respect to the connected beam, in order to allow for the complete development of the plastic deformation capacity of the connected beam, Fig. 5.

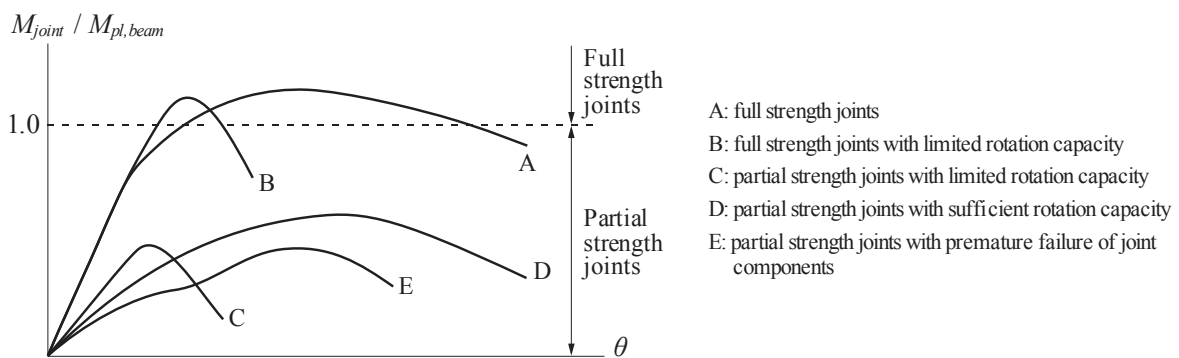


Fig. 5: Classification of beam-to-column joint plastic behaviour, ECCS Manual on Design of Steel Structures in Seismic Zones (ECCS, 1994)

Slika 5: Klasifikacija obnašanja spojev prečka-steber po priročniku ECCS za dimenzioniranje jeklenih konstrukcij na potresnih območjih (ECCS, 1994)

In the same way as the evaluation of rotation capacity, presented in the foregoing chapter, also flexural overstrength s can be defined as the non-dimensional measure of the ultimate bending capacity of steel beams, due to the amount of strain-hardening, which can be exhibited before the complete development of local buckling, Fig. 4. In general, s may be defined in terms of bending moments by means of the following expression:

$$s = \frac{M_{LB}}{M_{pl}}, \quad (3)$$

Where $M_{LB} = M_u$ is the peak bending moment produced by the beam and corresponds to the complete development of the beam local buckling, and M_{pl} is the beam plastic bending moment. This definition is presented in Fig. 4. The methods for predicting the non-

dimensional ultimate bending capacity of steel members are essentially the same as those adopted for predicting the rotation capacity.

The stress corresponding to the complete development of local buckling is influenced by the relative restraint between the web and the flange and also by the stress distribution across the section depth. These effects were early underlined by tests performed by Kuhlmann (1989), which showed that for I and H beams the buckling length of the flange is approximately 1.20 - times larger than flange width b_f . In addition, Mazzolani and Piluso (1992) showed that the influence of the longitudinal stress gradient on the ultimate stress depends on ratio b_f/L' , L' being the distance between the point of zero moment and the plastic hinge.

The estimation of flexural overstrength factor s was provided by means of theoretical formulation already by Mazzolani and Piluso (1993), which was included in the former Italian code OPCM 3274, nowadays no longer in use. Note that the estimation of factor s is based on ductility classification criteria for members accounting for both cross-section slenderness and member slenderness. According to this formulation, s can be estimated for I and H cross-sections subjected to axial and/or flexural loads, considering usual steel grades (S235, S275 and S 355), see Table 2.

Taking into account all the considerations mentioned in the previous chapter on ductility, it is clear that, in seismic applications, a twofold classification of steel beams accounting for ductility and overstrength factor classes is needed. For sure, the subdivision of beams into ductility classes remains of primary concern, because the rotation capacity directly governs the global ductility of structures. However, additional classification of members into overstrength classes is also necessary in order to properly apply capacity design criteria both at local level, i.e. to design connections between dissipative and non-dissipative zones, and at global level, i.e. to provide adequate overstrength for the design of non-dissipative members.

Dissipative zone taken to occur in the beam, with the well-known fact that beam ends are actually able to transmit their ultimate resistance, beam-to-column joints are designed according to the following capacity design principle:

$$M_{j,Rd} \geq s \cdot \gamma_{ov} \cdot M_{b,Rd}, \quad (4)$$

where factor γ_{ov} accounts for random material variability and factor s for the strain-hardening exhibited before the complete development of the beam local buckling. The values of factors s and γ_{ov} suggested by OPCM 3274 for different member categories and steel grades are presented in Table 2.

Preglednica 2: Priporočene vrednosti faktorja s in γ_{ov} iz OPCM 3274, določenih glede na klasifikacijo elementov po duktilnosti, privzeto po Mazzolani in Piluso (1993)

Table 2: Proposed s values by the classification of members in terms of ductility according to Mazzolani and Piluso (1993), in combination with factor γ_{ov} as suggested by OPCM 3274

Member category	s	Steel	γ_{ov}
Ductile	$s \geq 1.2$	S235	1.2
Plastic	$1 \leq s < 1.2$	S275	1.15
Slender	$s < 1.2$	S355	1.1

As opposed to the exhibited amount of rotation capacity, the flexural overstrength of I and H beam profiles under cyclic loading tends to be dependent more or less on the shape of the cross-section. In particular, in experiments performed by D'Aniello et al. (2012) the flexural overstrength exhibited by H and I profiles under cyclic loading conditions was similar to that occurring under monotonic loading. The flexural overstrength of I and H beam profiles under

cyclic conditions compared to that obtained from monotonic loading, was found almost the same for sections classified as Class 1 according to EN1993-1-1, while it was slightly less than monotonic for Class 2 sections, owing to the occurrence of some degradation phenomena. This aspect implies that the monotonic flexural overstrength factor can be reasonably utilised for seismic capacity design under dissipative structural behaviour concept, where only sections of Classes 1 and 2 can be adopted according to EN 1998-1. In all other cases, the monotonic overstrength should be considered as the upper bound.

On the basis of the experimental data presented and those already available from the existing literature, empirical equations for predicting flexural overstrength s under monotonic loading were derived in D'Aniello et al. (2012), by means of multiple linear regression analyses. Analysing the experimental data considered for this purpose, it was observed that s is influenced by less parameters than R . In particular, the flange and web slenderness, the shear length (i.e. the distance between the plastic hinge and the point of zero moment, which accounts for the influence of the stress gradient along the member axis) and the steel post-yield hardening properties are the most representative for s .

The way flexural overstrength is covered in current codes deserves special discussion, since the value of flexural overstrength is needed to allow for an appropriate application of hierarchy criteria in capacity design concept. The need to provide moment resisting connections with sufficient overstrength is recognized by modern seismic codes, but different design criteria are suggested to assure this design goal.

According to ANSI/AISC 341-10 the beam flexural overstrength is equal to $1.1 \cdot R_y$, where factor 1.1 accounts for strain-hardening, as well as other possible sources of overstrength, whereas R_y represents ratio between the expected yield stress and the specified minimum yield stress (R_y varies in the range between 1.1 and 1.5, depending on steel grade), so that it accounts for the influence of random material variability. Factor 1.1 was obtained from the wide experimental research aimed at providing qualified moment-resisting connections during the SAC project (FEMA, 2000b).

For the design of full-strength welded moment-resisting beam-to-column joints EN 1998-1 considers a similar overall overstrength factor, expressed as $1.1 \gamma_{ov}$:

$$M_{j,Rd} \geq 1.1 \cdot \gamma_{ov} \cdot M_{b,Rd} . \quad (5)$$

According to EN 1998-1, γ_{ov} is an overstrength factor accounting for the random variability of the steel yield stress, while coefficient 1.1 stands for s , i.e. to allow for the effects of material strain hardening.

According to the code, factor γ_{ov} can be assumed equal to 1.0 when the maximum value of the yield stress of dissipative zones is evaluated by means of specific experimental tests or in the case of dissipative zones belonging to a steel grade the maximum yield stress of which is lower than the nominal value of the yield stress of non-dissipative zones. In other cases, the value of γ_{ov} greater than 1.0 has to be adopted. As already emphasized by European engineering society (Piluso, Rizzano, 2007. D'Aniello et al., 2012. ECCS, 2013), EN 1998-1 does not provide a criterion for an appropriate evaluation of γ_{ov} , but recommends the use of $\gamma_{ov} = 1.25$.

This assumption leads to an overall overstrength factor equal to $1.1 \cdot \gamma_{ov} = 1.1 \cdot 1.25 = 1.375$, having an important role in the practical application of hierarchy criteria in capacity design.

In addition, according to D'Aniello et al. (2012), all current codes do not consider that the amount of strain-hardening, which can be exhibited before the complete development of local

buckling, is related to the width-to-thickness ratios of the plate elements constituting the cross-section.

Last but not least, an important issue that needs to be adequately covered in the hierarchy criteria principle of seismic design is also structural robustness. In order to prevent progressive collapse of moment-resisting frame under severe seismic loading, the surrounding members (connections, columns) should be appropriately designed to resist ultimate bending resistance coming from dissipative zones in the beams.

2.4 Low-cycle fatigue in steel elements subjected to seismic loading

The consideration of non-ductile modes of failure in steel building frames is not thoroughly addressed in the present standards for seismic design. Of particular concern is the occurrence of short term cyclic loading during seismic event that may induce large plastic deformations in building frames. The discussion in the following subsections is intended to provide a general overview of the principles describing LCF phenomena themselves as well as the LCF induced failures in steel structural elements.

2.4.1 The mechanism of low and extremely low cycle fatigue (LCF, ELCF)

In order to interpret correctly the LCF behaviour of steel components, the current state of understanding the phenomenon should be reviewed. Firstly, the phenomenological explanation and comparison of material damage under monotonic and cyclic loading regime are given. Afterwards, the principle of low-cycle fatigue of steel material is presented in order to characterise effects of seismic loading on steel components.

It is well established that under tension monotonic loading, void growth and coalescence lead to ductile crack initiation. The increasing void size intensifies the situation of stress and strain between adjacent voids until critical cleavage stress causes the necked material to fracture. For cyclic loading, the situation is similar but for two key differences (Kanvinde, Deierlein, 2004). Firstly, the voids encounter alternating excursions of positive and negative mean stress, which causes alternate expansion and shrinkage or squeezing of the voids that have already nucleated. Secondly, due to the cyclicity of loading, damage accumulates differently in the necked material. This damage is defined by assuming that the loading cyclicity affects the unique correspondence between the void volume fraction and the stress/strain condition that triggers void coalescence. In other words, a smaller void volume fraction (as compared to the monotonic case) is assumed to trigger coalescence due to damage accumulation.

Testing regimes in which the elastic strain amplitude is higher than the plastic strain amplitude are generally referred to as high cycle fatigue (HCF); such tests are usually stress-controlled and typically involve more than 10^6 cycles to cause failure. Conversely, traditional low-cycle fatigue (LCF) is applied when plastic strain dominates, and the number of cycles to failure generally ranges from 10^2 to 10^4 . While high cycle fatigue test is stress controlled, low cycle fatigue testing is generally strain-controlled (either by total or plastic strain).

The failure of the structures subjected to cyclic loading resulting from seismic events occurs usually after less than ten cycles. These fatigue conditions, characterized by a few reverse (in general less than 20) loading cycles with large amplitude scale straining are termed as extremely low cycle fatigue (ELCF). The damage mechanism during ELCF, where large plastic strain concentrations occur in material, is a combination of fracture process and fatigue mechanism. The fracture process during monotonic loading is governed by nucleation, growth and coalescence of micro-voids and thus depends strongly on microstructure. The slip and decohesion mechanism behind low cycle fatigue results from blunting and re-sharpening of the

crack tip. This means that during ELCF cyclicality is not required for crack propagation, though fracture occurs at seemingly less severe stress and strain states due to accumulated damage effects from cycling under LCF. Fig. 6 summarises the leading damage mechanisms in dependence on the type of loading.

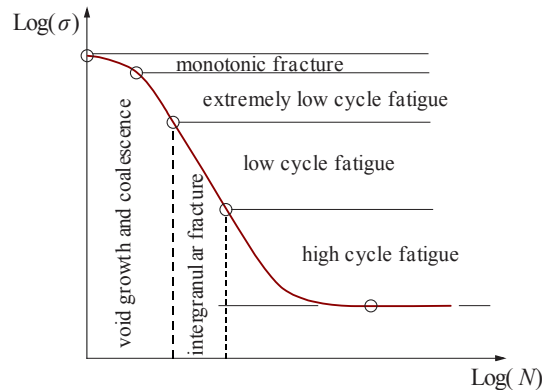


Fig. 6: Failure mechanisms in relation to the number of cycles to failure
Slika 6: Mehanizmi porušitve glede na število opravljenih ciklov do porušitve

Phenomena under ELCF have been investigated in far less detail than the traditional low-cycle fatigue process, primarily because of their lack of significance to the mechanical engineering, aerospace and material science communities (Kanvinde, Deierlein, 2004). Two of the recent researches dealing with structural carbon steel that make reference to this issue were done by Nip et al. (2010) and Jesus et al. (2012), who also note the lack of research in characterizing this type of low-cycle fatigue behaviour on structural materials.

The primary objective in the seismic design of steel structures is that brittle fracture of steel structural components should be prevented even under large-scale seismic loading. Especially, large-scale straining at the stress/strain concentration regions in structural components frequently lowers both the ductility and the fracture toughness of structural steel, thereby facilitating the initiation of local ductile cracking and subsequent crack extension by cyclic loading, which can lead to brittle fracture. An important step in preventing brittle fracture of steel structure is critical design for preventing the initiation of ductile cracking under large-scale cyclic loading.

2.4.2 Stress and strain indices

To compare the local behaviour of different configurations analysed and to assess the effect of the parameters of interest, a number of different stress, strain, and combined stress/strain indices were computed. The stress and strain values are normalised by their corresponding yield stress or strain in order to enable comparison between materials with different yield strengths; the beam yield strength is used for normalisation when points at the interface between the beam and column flange are considered. Definitions of the indices employed in the study were adopted from literature (Lemaitre, Chaboche, 1990. Lemaitre, 1992. El-Tawil et al., 1998. Barsom, Rolfe, 1999), and are described below.

Pressure index

Pressure index PI is defined as hydrostatic stress (mean normal stress) σ_m divided by yield stress σ_y .

$$PI = \frac{\sigma_m}{\sigma_y} \quad (6)$$

The pressure index is a negative number for tensile hydrostatic stresses. The hydrostatic stress is defined as the negative of one-third of the first invariant (trace) of the stress tensor σ_{ij} :

$$\sigma_m = -1/3 \text{trace}(\sigma_{ij}) = -1/3 \sigma_{ii} = -1/3 \sum_{i=1}^3 \sigma_{ii}, \quad (7)$$

where i and j represent the global directions, i.e. $i = 1, 2, 3$ and $j = 1, 2, 3$. A large tensile (negative) hydrostatic stress is often accompanied by large principal stresses and generally implies a greater potential for either brittle or ductile fracture. In the presence of a crack or defect, large tensile hydrostatic stress can produce large stress intensity factors at the tip of the crack or defect, and increase the likelihood of brittle fracture. On the other hand, a large tensile hydrostatic stress can lead to rapid damage accumulation in metals due to microvoid nucleation, growth, and coalescence under high tensile triaxial stresses and a substantial reduction in component ductility. Such a process is known as ductile fracture initiation, and is usually accompanied by plastic deformations prior to fracture. In either case, the presence of high tensile hydrostatic pressure implies a greater potential for fracture (Lemaitre, 1992). The index is also used to complement other indices described below.

In Abaqus invariant of hydrostatic stress is represented with equivalent pressure stress p output variable (negative for tensile stresses).

Mises index

The Mises index MI is defined as Mises stress $\bar{\sigma}$ divided by yield stress σ_y , where the Mises stress is defined as the second invariant of the deviatoric stress tensor

$$\bar{\sigma} = \sqrt{\frac{3}{2} S_{ij} S_{ij}}, \quad (8)$$

where S_{ij} is the deviatoric stress component, which is calculated as $S_{ij} = \sigma_{ij} + \sigma_m \delta_{ij}$. The index is used also to complement other indices described below.

PEEQ index

Equivalent plastic strain index PEEQI is defined as equivalent plastic strain (PEEQ in Abaqus) divided by yield strain. Equivalent plastic strain is the second invariant of the plastic strain tensor and is calculated as

$$PEEQ = \sqrt{\frac{3}{2} \varepsilon_{ij}^{pl} \varepsilon_{ij}^{pl}}, \quad (9)$$

where ε_{ij}^{pl} is the plastic strain component. The index is a measure of ductility at the local level (El-Tawil et al., 1998).

Triaxiality index

Triaxiality index TI is defined as hydrostatic stress σ_m (mean normal stress) divided by the Mises stress $\bar{\sigma}$ (equivalent flow stress):

$$TI = \frac{-\sigma_m}{\bar{\sigma}} = \frac{-PI}{MI}. \quad (10)$$

Since the study deals not only with monotonic but also cyclic loading, a more generalized loading history needs to be considered, which includes the possibilities of negative as well as positive triaxialities. This is accounted for in the above equation with a negative sign added to the mean normal stress σ_m . Mathematically, it is the magnitude of the triaxiality that is

important for the void growth, rather than its sign. However, such a sign convention for the triaxiality index TI is applied in the study to correlate it with physical material observations: the void will grow under plastic straining if the triaxiality is positive or the mean stress is tensile ($\sigma_m < 0$), and the void will shrink under plastic straining if the triaxiality is negative and the mean stress is compressive ($\sigma_m > 0$) in nature.

In Abaqus TRIAX (stress triaxiality) as output variable is directly available in Abaqus/Explicit only (not in Abaqus/Standard) and is positive for tension stresses.

Researchers Becker et al. (1989) identified that a weak triaxial stress (triaxiality less than 1) would cause the voids to grow asymmetrically into a prolapse shape such that the major axis is aligned along the direction of remote plastic strain. On the other hand, situations with large triaxiality (triaxiality greater than 3) would cause the void to grow into an oblate shape with the larger dimension normal to the axis of straining. Furthermore, El Tawil et al. (1998) state that high triaxiality ($0.75 < TI < 1.5$) can cause large reduction in the rupture strain of metals. Very high triaxiality ($TI > 1.5$) can result in brittle behaviour (Lemaitre, 1992. Barsom, Rolfe, 1999).

Fig. 7 shows a schematic plot of the triaxiality versus the equivalent plastic strain at the critical location in the plastic hinge zone on the beam in a typical beam-to-column specimen during reversed cyclic loading. The figure indicates the regions with positive triaxiality index, where the voids are assumed to grow, and the regions with negative triaxiality, where they are assumed to shrink.

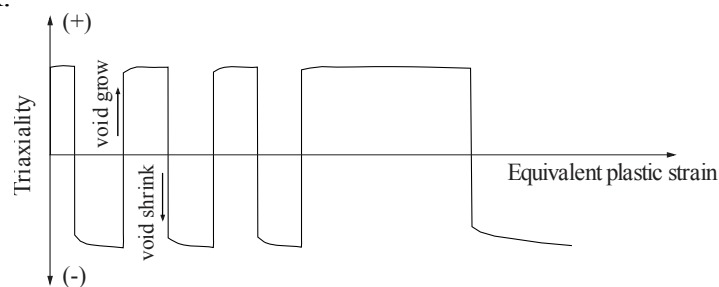


Fig. 7: Triaxiality versus equivalent plastic strain for reversed cyclic loading

Slika 7: Indeks triosnega napetostnega stanja in ekvivalentne plastične deformacije za ciklično obremenjevanje

Rupture index

The definition of the rupture index RI used in this study is adopted by El-Tawil et al. (El-Tawil et al., 1998), namely

$$RI = a \frac{PEEQ}{\varepsilon_r} = \frac{PEEQ}{\exp\left(1.5 \frac{\sigma_m}{\bar{\sigma}}\right)}, \quad (11)$$

where a is a material constant, ε_r is the rupture strain defined from uniaxial tension test, with other terms already defined above. Hydrostatic compression (positive value) increases the rupture strain, while hydrostatic tension (negative value) decreases the rupture strain. The rupture index is used to compare the likelihood of fracture at critical regions as well as between the two connection types.

2.4.3 Prediction of local failure behaviour of steel members

In general, there are two mechanics approaches to define the limit state for structural members subjected to arbitrary (monotonic and cyclic) loading: fracture (FMA) and damage (DMA) mechanics approaches. Both damage mechanics approaches allow for the prediction of ductile crack initiation and propagation under monotonic and cyclic loading. Both approaches require to be calibrated utilizing small scale tests performed to obtain the basic characteristics of the analysed material and to determine fracture and damage mechanics values. While for the fracture mechanics approach the assumption of a crack-like defect is necessary, damage mechanics can be applied with or without integration of an initial flaw. Generally, for both approaches the failure criterion “crack initiation” is used, either via J -integral or ultimate strain ε_u , for fracture and damage mechanics approach, respectively, e.g. (Bleck et al., 2009).

Fracture mechanics approach, given either in terms of the J -integral or transferred into a limit state of plastic strain, applies the action effect (termed as crack driving forces (CDF)), which appears at the crack tip of the assumed crack which is integrated at the hot-spot (critical region in the structure, e.g. weld toe) of a typical component. On the other side, the material resistance, defined either by physical crack initiation value, technical initiation value or crack resistance curve, is determined experimentally in small scale tests. The first of the three possible material fracture resistance definitions is the only one that shows no dependency on geometry and can therefore be transferred from small scale test result to a structural detail. However, it provides very conservative value, since no crack growth and constraint effects are utilized. The technical initiation value and crack resistance curve are less conservative as they consider crack growth, but both show a dependency on many parameters (e.g. crack length, specimen geometry, loading, etc.) and therefore cannot be easily transferred to the structural component.

A widespread constitutive model for damage evolution is the GTN (Gurson–Tvergaard–Needleman) model. In this model the damage effects are taken into account by a softening term in the plastic potential, which is usually related to volume fraction of voids in the material. This internal variable induces a progressive shrinkage of the yield surface until failure occurs due to loss of stress carrying capability. In this case yield condition is extended with material damage parameters and needs to be included as a routine in a finite element code program.

In addition to both presented mechanics approaches the prediction of local failure behaviour of a member can also be given by damage curves, which present a quantitative relation between equivalent plastic strain and stress triaxiality, Fig. 8. The main difference between this approach and the damage mechanics approach model lies in avoidance of defining a “microscopical” damage parameter and exclusive application of continuum mechanics or “macroscopic” values.

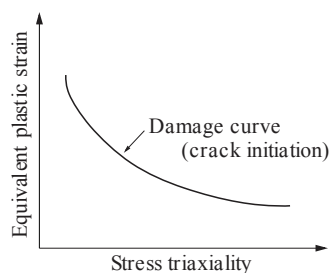


Fig. 8: Typical material damage curve
Slika 8: Tipična krivulja poškodb v materialu

According to this approach, effective damage concept with the “advanced two-parameter” criterion was proposed by Ohata and Toyoda (2004). It is based on the idea that material

damage is only controlled by the effective plastic strain. The crack initiation occurs when the cumulative effective plastic strain depending on the stress triaxiality reaches the two-parameter critical condition, which is defined as a damage curve presented in Fig. 8. The “advanced two-parameter criterion” is proposed for the evaluation of ductile crack initiation in steel structures under cyclic loading.

In (Bleck et al., 2009) this approach was examined with respect to accurate damage prediction due to cyclic plastic loading under different stress triaxiality levels. Based on this study, it can be concluded that the effective damage concept with the advanced two-parameter criterion gives reasonable results compared with the experiments and is able to capture some qualitative features of deformation. Its use was recommended by the authors also for cases when implemented constitutive model for damage evolution failed due to convergence issues.

The effective damage concept, with the advanced two-parameter criterion, was applied also in the present study for damage analysis. It is presented in detail in the following section.

2.4.3.1 Effective damage concept for the prediction of ductile cracking of steel members under large-scale cyclic loading

Evaluation of ductile crack initiation in steel welded structures subjected to seismic loading is crucial for structural design or safety assessment to prevent brittle fracture induced by ductile cracking. A new material damage concept under reverse loading, which correlates the material damage from micro-void nucleation to macro-scale mechanical parameters, was proposed by Ohata and Toyoda (2004). The proposed damage concept for evaluating ductile cracking of steel structures subjected to large-scale cyclic straining was adopted in the current work as a method that links the beam-to-column joint behaviour to a material model in order to allow the prediction of the onset of cracking in the steel components of beam-to-column joints. Accordingly, to understand better the applied damage concept, its theoretic background is introduced in detail below, reproducing much of the text of Ohata and Toyoda (2004).

The general behaviour of ductile failure usually involves the formation of voids around large inclusions or second-phase particles and the subsequent growth of the voids to final coalescence. In an effort to develop a comprehensive criterion for ductile failure, several theoretical models of void growth have been proposed in the past, including Thomason’s model (Thomason, 1968), McClintok’s model (McClintock, 1968. 1996) and Rice’s and Tracey’s model (Rice, Tracey, 1969), for the case where void growth is the dominant mechanism for ductile fracture in materials of interest. Since the growth stage of voids would be affected by the hydrostatic component of stress conditions, in McClintock’s model ductile failure initiation strain was first related to stress triaxiality. On the basis of these models, the dependence of stress triaxiality on ductility for various metals has been considered by researchers through employment of small-scale tensile specimens with circumferential notches tested under single tension. As established by Ohata and Toyoda (2004), only a few studies have attempted to quantitatively assess critical ductile crack initiation for steel structures subjected to large-scale cyclic loading. According to the authors this might be due to a low level of understanding of material damage for ductile cracking of structural steels under large-scale straining as well as under monotonic straining.

The authors propose a damage concept for ductile crack initiation of structural steel on the basis of experimental clarification of a mechanism for ductile cracking. Ductile cracking behaviour of structural (Ferrite-Pearlite) steel was investigated on small-scale specimens, Fig. 9, subjected to axial tension tests at room temperature. The damage evolution which controls the ductile cracking was observed in detail, with focus placed on void nucleation until ductile cracking.

Numerous micro voids were found to nucleate in the soft Ferrite phase near the Ferrite-Pearlite interface. The authors suggest this nucleation behaviour of micro-voids could be due to the highly condensed pile-up of dislocations near the interface of microstructures with mismatch in strength. Moreover, almost no such micro-voids or other larger voids were observed before about 100% plastic straining. This indicates that ductile cracking can be controlled by nucleation of micro-voids in the employed steel, not by the growth of larger voids, which is the conventionally interpreted mechanism of ductile cracking.

The mechanical conditions for ductile crack initiation were examined by using the experimental results for small-scale tensile specimens, Fig. 9, on the basis of two-parameter criterion in which plastic strain and stress triaxiality were adopted as mechanical parameters that control ductile cracking (McClintock, 1968. Thomason, 1968). All tensile tests were additionally simulated by FE-analysis in Abaqus. On the basis of stress and strain fields in the specimens as obtained by FE-analysis, the mechanical conditions under which the crack initiation mechanisms would operate were considered. In all specimens under tensile loading until ductile cracking, the equivalent plastic strain $\bar{\epsilon}_{pl}$ at the crack initiation point observed from the experimental tests was related to the stress triaxiality $\sigma_m / \bar{\sigma}$. In this way the diagram of critical local equivalent plastic strain, required to initiate ductile cracking, plotted over stress triaxiality for the applied structural steel, was obtained and is presented in Fig. 9.

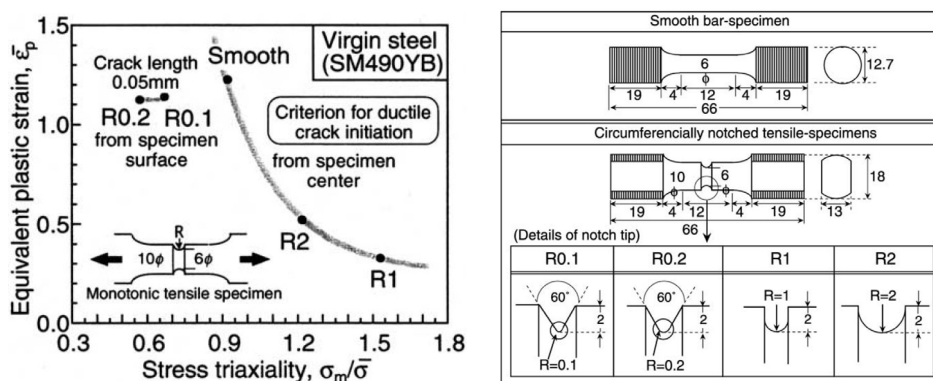


Fig. 9: Criterion for ductile crack initiation as obtained by Ohata and Toyoda (2004) for SM490YB steel
 Slika 9: Kriterij za nastanek duktilne razpoke po Ohata and Toyoda (2004) za jeklo SM490YB

The critical condition for ductile cracking (damage curve) presented in Fig. 9 can be used for the estimation of ductile cracking load of specimen of any other geometry subjected to monotonic loading. Namely, ductile cracking for any structural member can be predicted with high accuracy by estimating the stress/strain field using FE-analysis.

Damage curve presented above is based on monotonic loaded small-scale tensile specimens. If the accumulation of equivalent plastic strains for specimen subjected to cyclic loading is computed as is for monotonic loading, then by using damage curves conservative results would be obtained. In order to use damage curves for the case of cyclically loaded members, the effective damage concept proposed by the authors has to be used. Explanation of the effective damage concept is summarized below.

In the case where the applied stress is reversed under cyclic loading, the influence of the Bauschinger effect should be taken into account in relation not only to the stress/strain field, but also to the material damage related to ductile cracking. As suggested from the observation of micro-voids, the material damage related to ductile cracking should be correlated to the material behaviour up to micro-void nucleation: the material damage is assumed to correspond to the evolution of dislocation density near the Ferrite-Pearlite interface. On the other hand, the Bauschinger effect of materials had been recognized to be caused mainly by

the accumulation of long-range internal stress due to pile-up of dislocations around obstacles, which is in the steel of interest the Ferrite-Pearlite interface. In the case where the applied stress is reversed, some of the pile-up reversely mobile dislocations move in the opposite direction, and after certain straining form dislocation structures equivalent to those before reverse loading; i.e. the same dislocation density. Thus, in addition to plastic strain induced by reversely mobile dislocations at the early stage of reverse loading, subsequent plastic straining up to the same dislocation density as reached previously would presumably not aggravate the material damage for ductile cracking.

In order to estimate the evolution of material damage on the basis of the assumed effective damage concept, the evolution of long-range internal stress (or backstress) should be quantitatively modelled in the FE-method. Considering the mechanical aspect of the Bauschinger effect, a nonlinear combined isotropic/kinematic hardening material model implemented in Abaqus was employed by the authors. In this nonlinear material FE-model the material damage for ductile cracking under cyclic loading can be assumed to be controlled by evolution of long-range internal stress expressed as backstress. The effective damage concept serves as the basis for proposing the advanced two-parameter criterion for the evaluation of ductile crack initiation for cyclically strained steel structures on the basis of the criterion for ductile crack initiation from the results of the small-scale specimens. The method includes the following main ideas as shown in Fig. 10:

- applied plastic strain, where the backstress exceeds the maximum backstress under the preceding loading cycle; it does not affect the material damage – only the effective plastic strain $\bar{\epsilon}_{pl,eff}$ at each cycle contributes to the damage, see Fig. 10a);
- ductile cracking occurs when the accumulation of $\bar{\epsilon}_{pl,eff}$ as a function of $\sigma_m / \bar{\sigma}$ during cyclic loading reaches the two-parameter critical condition obtained from monotonic loading tests and FE-analysis for the steel of interest, see Fig. 10b).

About the diagram in part b) of Fig. 10, it should be pointed out that damage histories presented, all accumulation and corresponding effective accumulation, were obtained for a particular studied case in this work. Corresponding damage curve is derived from a combined experimental and FE-analysis study on small-scale single tension specimens from S355 structural steel material, adopted from literature and presented in Chapter 2.4.3.2.

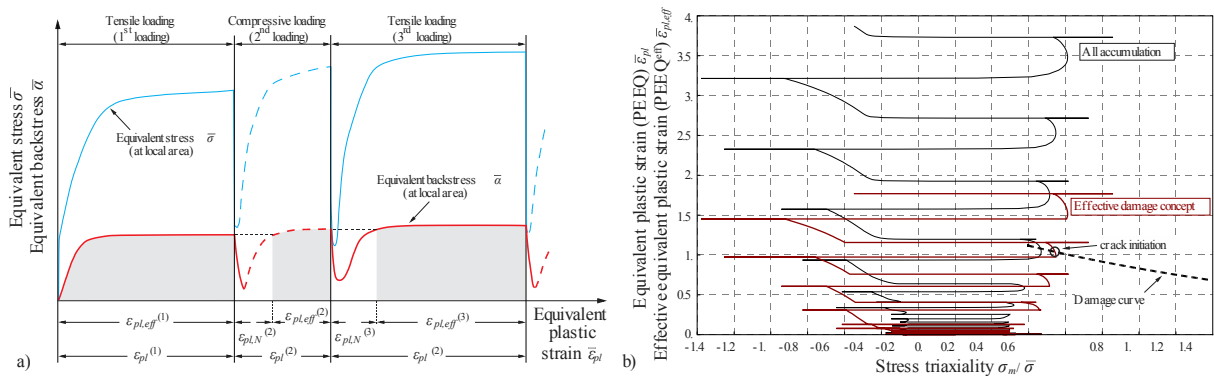


Fig. 10: Advanced two-parameter criterion for ductile cracking of structural members under cyclic loading based on effective damage concept: a) evolution of equivalent backstress with determination of effective plastic strain (schematic illustration), b) effective damage concept

Slika 10: Napreden dvoparametrični kriterij na podlagi učinkovitega principa akumulacije poškodb za nastop duktilne razpoke jeklenih konstrukcijskih elementov izpostavljenih ciklični obremenitvi: a) razvoj napetosti z določitvijo učinkovnih plastičnih deformacij (shematski prikaz), b) učinkoviti princip akumulacije poškodb

Presented advanced two-parameter criterion associated with the proposed effective damage concept would be applicable for ductile cracking estimation of structural members if the

dominant mechanism for ductile cracking is nucleation of micro-voids after large-scale plastic straining.

2.4.3.2 Damage curves for structural steel S355

Damage curve provides the mechanical conditions for the ductile crack initiation in terms of a quantitative relationship between the equivalent plastic strain values and stress triaxiality at the moment in which the crack initiation mechanisms would operate. It is derived from a combination of experimental results and additional FE-analysis on small-scale tensile specimens of different geometry (smooth-bars and notched specimens), see Fig. 9, in order to capture the onset of ductile cracking at different locations, from the specimen surface and from its centre, for the smooth- and notched specimens, respectively. For a detailed description see Chapter 2.4.3.1.

According to this approach, damage curves depend on the type of the steel used, the temperature and the strain rate. Since the definition of damage curve for exactly the same type of structural steel as used for dissipative beam members in the present study (S355 JR) is far beyond the scope of this work, suitable curves were adopted from the literature. For this purpose damage curve was adopted from Feldmann et al. (2009) and Bleck et al. (2009). Fig. 11 shows damage curves for steel S355 J2 and S460 M adopted from the literature. In our case damage curve of steel grade S355 J2 was used in cyclic simulations to imitate damage mechanical characteristics of actually used S355 JR steel for the beams.

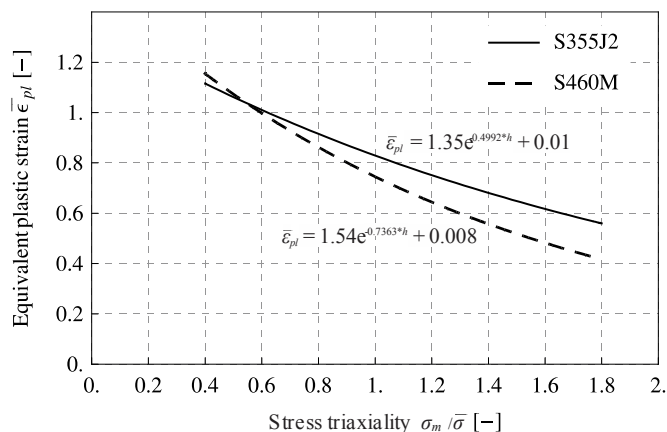


Fig. 11: Damage curves for structural steel S355J2 and S460M (Bleck et al., 2009. Feldmann et al., 2009)
 Slika 11: Materialni porušni krivulji za jeklo S355J2 in S460M (Bleck et al., 2009. Feldmann et al., 2009)

It is to be noted once again that damage curves presented in Fig. 11 are derived from monotonic tensile tests on small-scale test specimens. The critical condition for ductile cracking presented by the damage curves can be directly employed for critical assessment of steel structures of any other geometry and subjected to monotonic loading. Nevertheless, by applying damage concept for ductile crack initiation proposed by Ohata and Toyoda (2004), the damage curves can also be used for the evaluation of critical loading cycle of structural members subjected to large-scale cyclic straining.

3 EXPERIMENTAL CYCLIC TESTS ON STIFFENED JOINTS

3.1 Introduction

This chapter presents experimental investigation of cyclic behaviour of full-strength welded stiffened beam-to-column joints performed in the framework of this research work. Two different types of stiffened connections applied to hybrid-steel moment resisting frames and dual braced frames were investigated: configuration with a single vertical rib plate and another one with cover plate attached to the beam flanges. The design objective of both strengthened beam-to-column connections, based on the capacity design concept, is to transfer inelastic action away from the column face, thus avoiding the problem of poor ductile behaviour and potential fragility of the beam-to-column welded region, Fig. 12a.

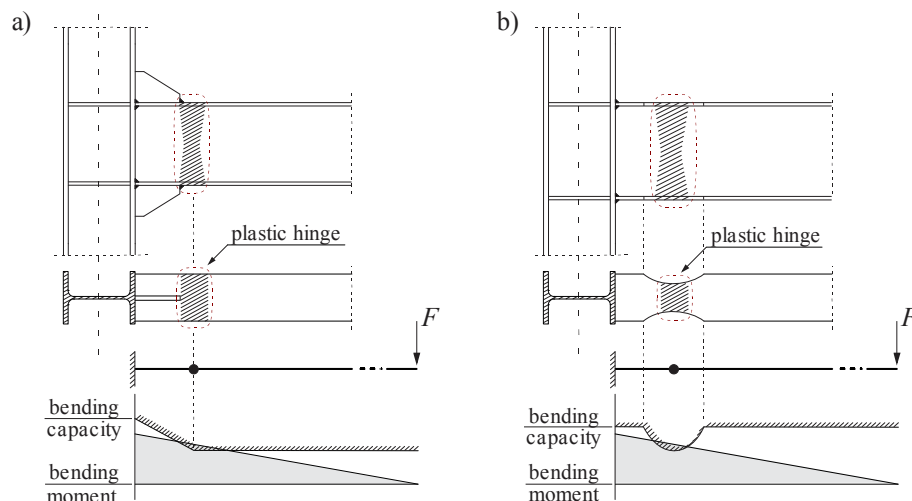


Fig. 12: Design objective of the two solutions for enhanced beam-to-column joint performance: a) studied strengthened connection and b) alternative concept of weakened beam (RBS)

Slika 12: Osnovni koncept izboljšane zasnove momentnega spoja prečka-steber: a) obravnavan koncept ojačanega spoja, b) alternativna rešitev z oslavljenim prerezom prečke (RBS)

Sixteen cyclic tests on full-scale beam-to-column joint specimens were carried out to study their seismic performance. High strength steel (HSS) was used for columns as non-dissipative elastic members, while mild carbon steel (MCS) for the beams acting as dissipative members. Hybrid-steel approach presents an innovation in seismic design practice in Europe and the actual seismic design rules do not cover this specific configuration. To take advantage of the additional fire resistance, structural stiffness and strength, fully encased composite columns were used. Beside two different stiffened joint typologies and two different column-beam material combinations, S460/S690 grade steel column and S355 grade steel beam, further parameters of the study were: different cyclic loading histories (with constant and variable amplitude) and high level of compressive axial force in the column, which may be important especially in braced frames. The last parameter is still not well investigated in the literature. The main parameters of the study with the number of joint specimens are summarized in Table 3.

Sixteen tests on large scale specimens were performed to demonstrate that both stiffened joints, with connection detailing and welding technology applied, perform adequately under cyclic loading. At the beginning, the description of the specimen design is presented,

emphasizing the selection of suitable detailing of both studied welded stiffened beam-to-column connections. The key aspects and variables of the pre-test preliminary finite element (FE) analysis utilised to support the design of stiffened connections is provided as well. Evaluation of experimental results is provided by means of different response parameters, such as strength, stiffness, ductility and energy dissipation, along with damage observations, in order to compare systematically the behaviour of each type of stiffened connection. With the aim of the joint prequalification, the experimentally obtained cyclic joint responses were compared to the prequalification requirements from the current seismic design codes. Low-cycle fatigue assessment of the test results is described and discussed.

Throughout the chapter, presentation of results is organized in such way that direct comparison between both studied stiffened connection typologies is feasible, enabling better understanding of the response of strengthened connections under cyclic loading. Complete and systematically evaluated test results were used later to support stiffened joint design recommendations.

Preglednica 3: Parametri eksperimentalne študije s številom preizkušancev
Table 3: Parameters of the experimental study with the number of specimens

PARAMETER	VARIABLE	No. of VARIATIONS	No. of SPECIMENS
Joint type	rib-stiffened (RS) & cover-plate (CP)	2	
HSS grade	S460 (RS1, CP1) and S690 (RS2, CP2)	2	16
Cyclic loading	variable (.1, .2) & constant (.3, .4)	2	
Level of axial force	low (.1) and high (.2, .3, .4)	2	

3.2 Design and detailing of the stiffened connections supported by FEA

Prior to the testing program, the study was focused on the selection of suitable design and geometrical detailing of both rib-stiffened and cover-plate connections. For this purpose recommendations from related standards as well as findings from technical reports and recent research works stated in Chapter 2 and hereinafter were taken into account. The results of the literature review guided the development of the testing program and the selection of the design variables for stiffened connections.

Additionally, preliminary nonlinear FE analysis (FEA) was used to investigate the performance of the designed joint specimens prior to testing, in order to collect all the relevant technical information needed to design testing setup, as well as to verify joint design procedure and connection detailing used to construct the specimens.

Preliminary study on the welded stiffened joints led to the conclusions presented below.

3.2.1 Stiffened connection design concept

Only a brief overview of welded stiffened beam-to-column connection design procedure is presented below for convenience. For a detailed description of the design procedure proposed for full-strength welded stiffened beam-to-column joints the reader is referred to Chapter 6.

The overall criterion used to design full-strength welded stiffened joint is that the region of welded connection at the face of the column remains nominally elastic under maximum bending moment on the order $\gamma_{ov}' M_{pl,b}$ and the corresponding shear force, developed by the fully yielded and strain hardened beam. According to this approach, overall overstrength factor $\gamma_{ov}' = 1.5$ was used, taking into account the random variability of the material yield

stress γ_{ov} and additional strain hardening factor s of the steel in dissipative zone of the beam. Commentary on the selected value γ_{ov}' is provided in the text below.

For the most common design situation, where the actual maximum yield strength $f_y^{act,max}$ of the steel of dissipative zones should satisfy requirement $f_y^{act,max} \leq 1.1 \cdot \gamma_{ov} \cdot f_y^{nom}$, a unique value of the material overstrength factor $\gamma_{ov} = 1.25$ is recommended by EN 1998-1 code. However, as observed from experimental data, the actual yield strength f_y^{act} of steel products can have a large variation depending on several parameters, such as steel grade and type of product. In particular, lower grade steel is characterised by larger values of the actual yield strength and consequently larger material overstrength factors (ECCS, 2013).

In the research work mild carbon steel grade S355 is considered for a beam, acting as dissipative member in a full-strength beam-to-column joint. To this aim, the results of tensile tests on specimens from hot-rolled sections performed within the experimental program on beam-to-column connections reported in Dubina et al. (2008) were considered to support the estimation of level γ_{ov} . In case of steel grade S355 J0 + M the average value of γ_{ov} was 1.26 for beam flanges and 1.31 for beam webs. In addition, in case of our own material test results performed as part of the experimental study on stiffened beam-to-column joints, maximum factor γ_{ov} obtained for beams was 1.25.

Based on the above discussion, possible overstrength due to the random variability of the actual steel grade S355 yield stress was accounted by the same value as proposed in EN 1998-1, i.e. $\gamma_{ov} = 1.25$.

To account for the amount of strain hardening, which can be exhibited before the complete development of the beam local buckling, factor 1.1 is considered in EN 1998-1. However, the degree of additional flexural resistance developed by the beam due to the post yield strain-hardening depends not only on the material stress-strain curve characteristics but also on the beam cross-sectional geometry (cross-section class), and other geometric boundary and loading conditions (Mazzolani, Piluso, 1993. Piluso, Rizzano, 2007. D'Aniello et al., 2012. Güneyisi et al., 2013). To account for this, larger value of the coefficient accounting for the effects of material strain hardening was chosen, i.e. $s = 1.2$.

According to this approach, the proposed design criterion for full-strength welded stiffened beam-to-column joint, accounting for capacity design principle and simple elementary (elastic) beam theory is as follows:

$$M_j \geq s \cdot \gamma_{ov} \cdot M_{pl,b} = \gamma_{ov}' \cdot M_{pl,b},$$

where:

$$\left. \begin{array}{l} s = 1.2 \\ \gamma_{ov} = 1.25 \end{array} \right\} \rightarrow \gamma_{ov}' = 1.5. \quad (12)$$

It is to be noted that the proposed values for both, $\gamma_{ov} = 1.25$ and $s = 1.2$, may be estimated as a rational compromise between safety and economy, rather than statistically obtained maximum values. On the other hand, the design procedure neglects positive effect coming from the fact that part of the stiffened connection is also comprised of a beam section that is made of the same material as that in the plastic hinge zone. Due to this fact, along with the yield strength of non-dissipative stiffened connection components is less likely to be less than the nominal value, the overall overstrength factor $\gamma_{ov}' = s \cdot \gamma_{ov} = 1.5$ used in the design procedure may be treated as even more conservative.

Corresponding moment at the centreline of the column M_c as well moment at the column face M_{cf} are defined taking into account single-sided beam-to-column joint sub-assembly from a

moment-resisting frame, i.e. assuming static model of a cantilever beam attached to the column. Assuming linear distribution of moment along the beam, the moments are calculated as follows (see also Fig. 13):

$$M_c \geq M_{pl,b} \cdot \left(\frac{L}{L - d_h} \right), \quad M_{cf} \geq M_{pl,b} \cdot \left(\frac{L - h_c / 2}{L - d_h} \right), \quad (13)$$

where:

- L is the distance between the centreline of the column and the application of transverse load at the beam tip,
- d_h is the distance between column centreline and assumed location of the centre of plastic hinge,
- h_c is the height of the steel cross-section of the column.

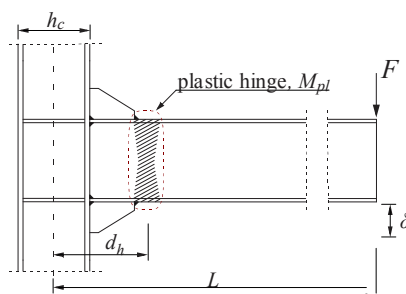


Fig. 13: Single sided stiffened beam-to-column joint
Slika 13: Enostranski ojačan spoj prečka-steber

The latter one, M_{cf} , provides the value of the moment under which the reinforced connection is to remain essentially elastic. Following this approach, the size of the stiffening plates was designed taking into account the moment at the face of the column M_{cf} and using the elastic section modulus of the complete stiffened section for the moment resistance.

3.2.2 Rib-stiffened connection

Two types of rib-stiffened moment connection typologies were observed: with single and dual tapered rib plates welded to the top and bottom beam flanges, Fig. 14a, b. For both stiffened solutions results from FEA evidenced that the beam flanges and welds at the beam-column interface should remain mainly in elastic state. Comparison of local response showed that dual rib configuration is more efficient to prevent penetration of yielding and flange local buckling beyond the tip of the ribs. However, ribs are not so effectively mobilized as in the case of single rib type, where vertical rib plate is placed in the plane of the beam and column web, enabling direct transmission of forces between the beam and the column. In the case of single rib configuration, joint stiffness is larger, resulting in higher concentration of strains in tension beam flange at the tip of the rib, Fig. 15a. As no substantial advantage was gained with dual rib configuration in comparison with the single rib type, bearing in mind also the practical aspect that the first one is labour intensive and costly, the single rib type configuration was chosen, hereinafter referred to as rib-stiffened (RS) joint.

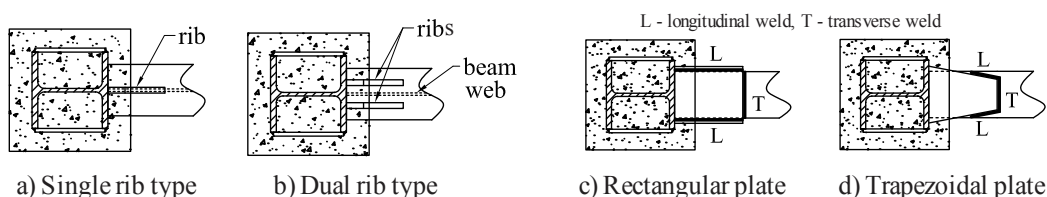
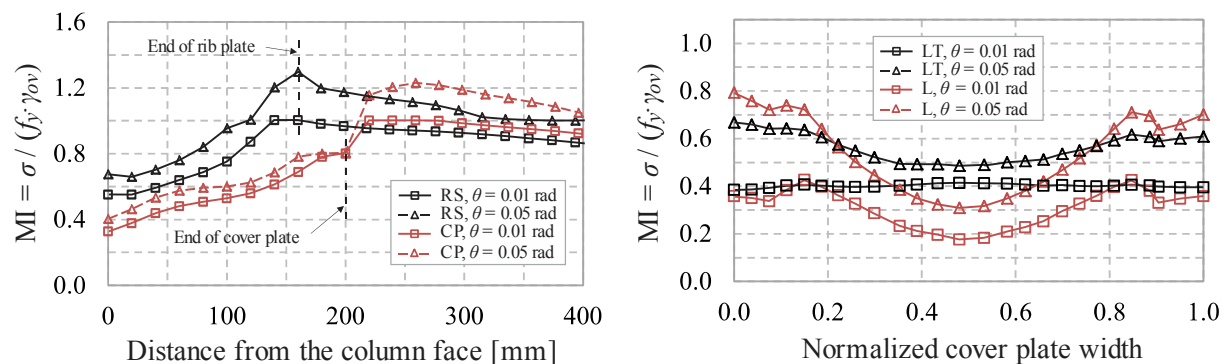


Fig. 14: Rib-stiffened and cover plate connection configurations studied
Slika 14: Obravnavane zasnove ojačanega spoja z rebri in veznima pločevinama

Typical distribution of normalised Mises stress (Mises stress divided with yield stress, also called Mises index MI) along the beam flange in tension obtained from FEA for RS joint is presented in Fig. 15a. Distributions obtained for two different values of joint rotation (displacement of the beam tip divided by the distance from the beam tip to the column centreline $\theta = \delta/L$, see Fig. 13) 0.01 and 0.05 rad are shown. Substantial reduction of stresses at the column face as well as formation of plastic hinge at the end of the rib stiffener can be observed.



a) along the beam flange close to beam web
a) vzdolž prečke v bližini stojine

b) in transverse direction at the end of cover plate:
LT – longitudinal and transverse welds,
L – longitudinal welds only
b) v prečni smeri na koncu vezne pločevine
LT – vzdolžna in prečni zvar,
L – samo vzdolžna zvara

Fig. 15: Distribution of MI for RS and CP joints at different values of joint rotation (beam flange in tension)
Slika 15: Razpored indeksa MI za spoj RS in CP pri različnih vrednostih rotacije spoja (pasnica prečke v nategu)

The geometry of the rib stiffener was determined taking into account the approach of seismic design of rib-reinforced moment connections according to Lee (2002). In our case the following assumptions for preliminary rib sizing were used: rib height $b \approx h_b/3$; rib diagonal angle $\theta \approx 35^\circ$; rib length $a = b/\tan(\theta)$, and trimmed lengths $c = 25$ mm, see Fig. 17. Rib thickness was determined by applying the design criterion that stiffened connection at the column face remains nominally elastic under maximum moment developed by the connected beam. Rib thickness $t = 15$ mm met the applied design requirement for both designed RS joint specimens presented hereinafter. Fillet welds were used to join all the components together, including complete beam-column connection at the column face. In this case full-strength peripheral fillet weld was made all around the beam cross-section before attaching both rib plates. Throat thickness of fillet welds joining rib to the beam and the column flange were designed to develop at least the yield strength of the rib plate.

3.2.3 Cover-plate connection

Two reinforcing plate geometries, rectangular and trapezoidal, and two fillet weld arrangements, two-sided and three-sided, adopted from Kim et al. (Kim et al., 2000. 2002a. 2002b), were studied, Fig. 14c, d. There was almost no difference in the global response of the joint using different stiffening plates and weld geometries. However, comparison of local responses showed that the rectangular plate and the use of three-sided fillet weld arrangement are superior to both the trapezoidal plate and the use of only two longitudinal fillet welds, without transverse weld at the end of the cover plate. The use of three-sided weld arrangement prevents the penetration of excessive deformations beyond the end of the cover-plate toward the column, and normal stress distribution in reinforcing plate is more evenly distributed when using both longitudinal and transverse welds, Fig. 15b. The rectangular plate shape in combination with three-sided fillet weld profile enables greater length for the placement of the

longitudinal and transverse fillet welds, thus reducing the size of fillet welds. Therefore, configuration with rectangular plate and three-sided fillet weld arrangement was chosen, hereinafter referred to as cover plate (CP) joint. In comparison with the rib-stiffened configuration, cover plate solution provides larger reduction of stresses in beam flange at the column face as well as along the stiffened part of the beam, with concentration of longitudinal stresses transferred far beyond the end of the reinforcing plate, Fig. 15.

To evaluate and compare the response of each stiffened joint configuration, several response indices adopted from literature (Lemaitre, 1992. El-Tawil et al., 1998) were used. Rupture index (RI) is used to compare the likelihood of fracture at critical regions as well as between the two connection types. Distribution of RI in beam-to-column connection at the column face for both stiffened and unstiffened joint solutions is presented in Fig. 16a. For all three joints the values of RI were extracted from beam flange in tension at the same joint rotation of 35 mrad.

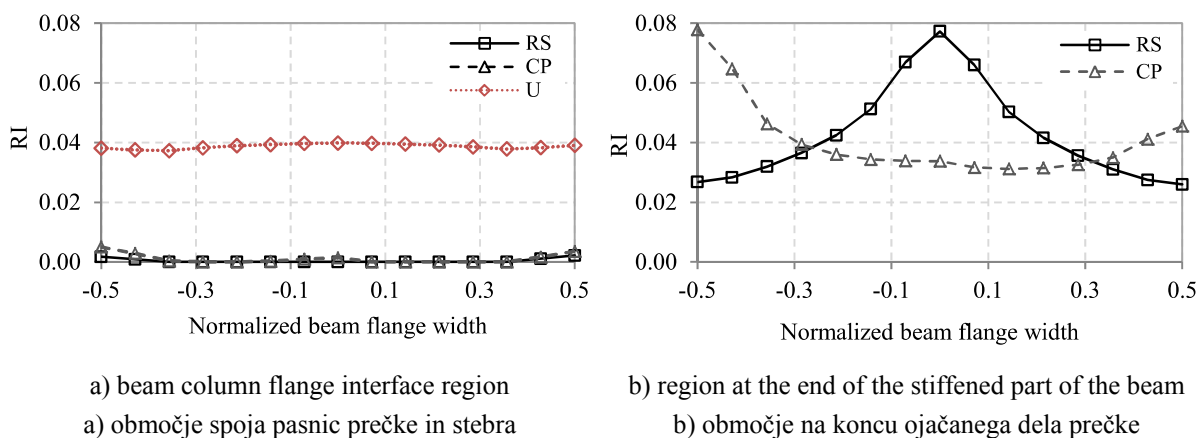


Fig. 16: RI distribution for unstiffened (U) and stiffened (RS, CP) joints at story drift angle 0.035 rad (beam flange in tension)

Slika 16: Razpored indeksa RI za neojačan spoj (U) in za ojačana spoja (RS in CP) pri rotaciji spoja 0.035 rad (pasnica prečke v nategu)

Values of RI at the column face obtained for unstiffened joint are approximately ten times larger in comparison with both stiffened joints, indicating high potential for brittle failure conditions for unstiffened connection in the welded beam-column interface region. Higher values of RI at the same plastic joint rotation can be observed at the end of the stiffened part of the beam in both cases of stiffened joints, Fig. 16b. Asymmetry in the distribution of RI across beam flange resulted from buckled flange shape. Flange mid width region and flange edge at the end of the stiffened part of the beam are potential sites of rupture for RS and CP joints, respectively.

Design recommendations for enhanced performance of the cover-plate connection were adopted from (FEMA, 2000c. 2000d. 2000b. Kim et al., 2002a). Rectangular cover plates of a width greater than that of the beam flange were used to provide the required space for longitudinal fillet welds as well as to reduce the thickness of the plates. The latter was taken to be the same as the thickness of beam flange, which resulted in a cross-sectional area of the cover plate near 120 % of the beam flange area.

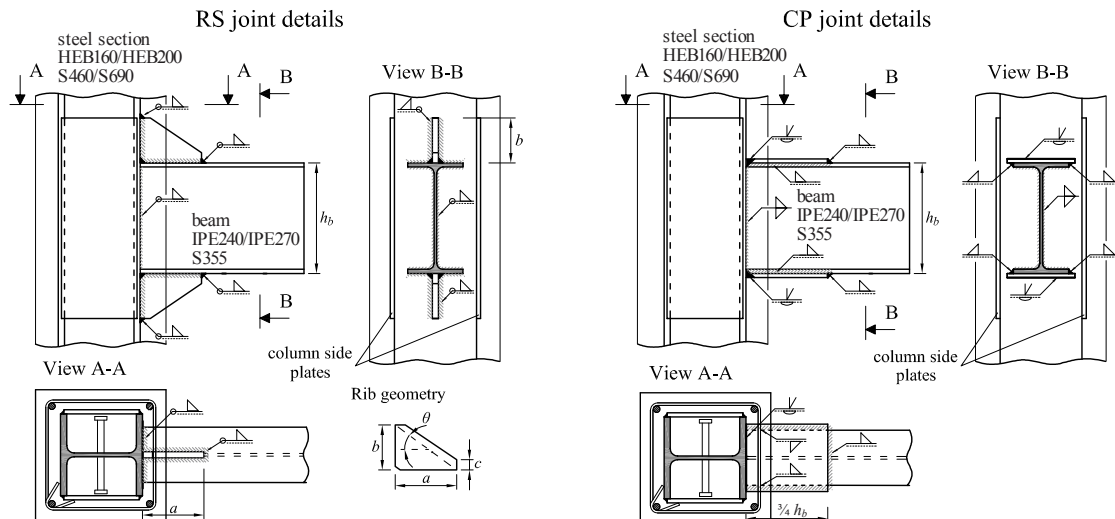


Fig. 17: Welded RS and CP beam-to-column joint details (concrete column encasement not illustrated)
Slika 17: Detajli ojačanih spojev RS in CP (betonski ovoj sovprežnih stebrov ni prikazan)

The length of the cover plate was chosen to permit the placement of sufficiently long fillet welds to develop at least the yield strength of the cover plate. The final length of reinforcing plates was chosen to be three quarters of the beam height. Complete joint penetration single-bevel butt weld was used to join the combined thickness of a cover plate and beam flange to the column flange, Fig. 17. No permanent backing bar was used, since its presence may be undesirable under fatigue conditions (Engelhardt, Sabol, 1998). Butt weld was completed by depositing a sealing run on the back of the joint using fillet weld, which continued over the root radius of a the beam section to the web connection. The complete solution, taking into account the robustness of elastic design, does not require the use of weld access holes.

3.3 Experimental program

3.3.1 Specimen description

The main purpose that guided the design of the experimental part of the study was to investigate and evaluate the seismic performance of hybrid-steel building frames made of two different steel grades, taking into account both RS and CP stiffened connections. To address different MCS (S355) beam – HSS (S460/S490) column material combinations, each of the two stiffened joint configurations is represented by two different joints, resulting in four different single-sided beam-to-column joint specimens designed for the tests. Fully encased H-profile steel composite columns were used and no concrete slab was considered on the beam. Constructional details with member sizes, steel beam-column material combinations as well as composite column cross-section characteristics for all four different specimens are presented in Table 3 and Figs 17 and 18.

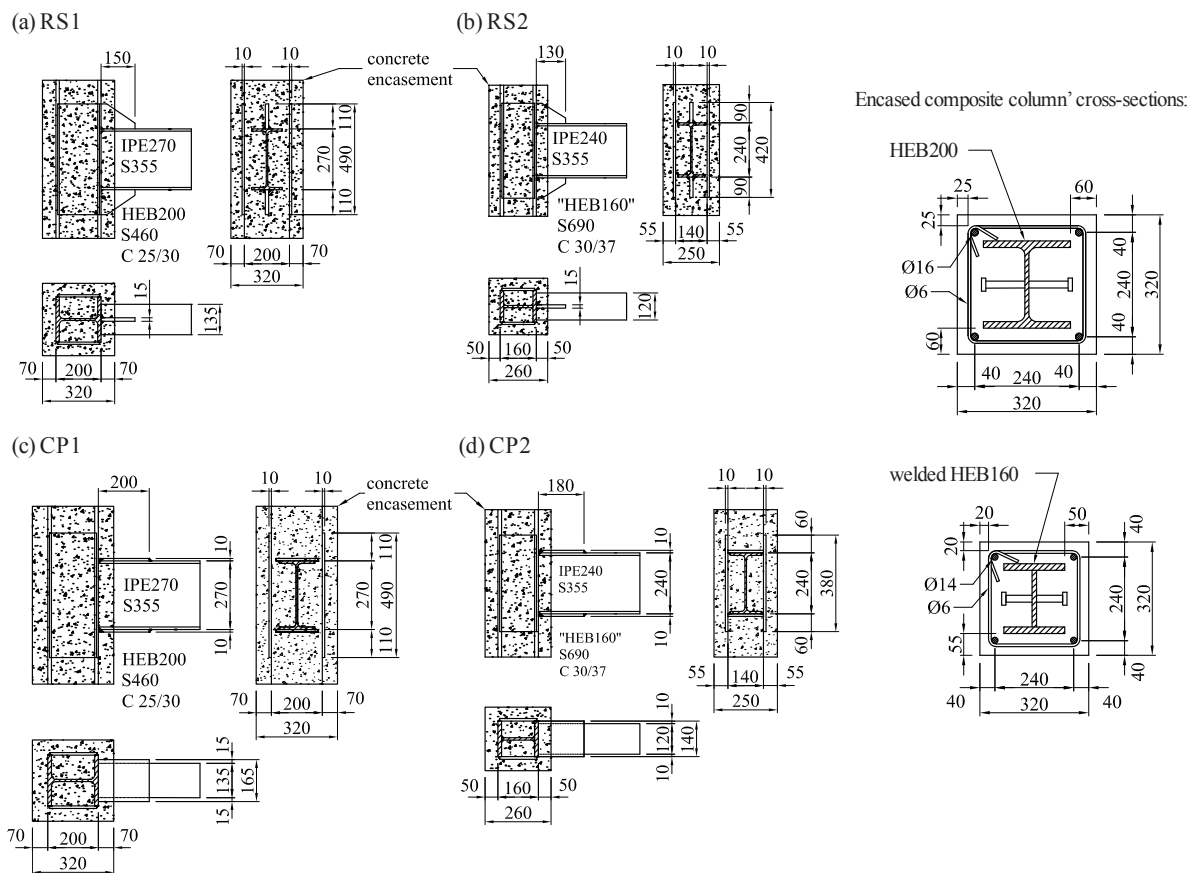


Fig. 18: Constructional details of four designed stiffened joint specimens
Slika 18: Konstruktivski detajli zasovanih štirih različnih ojačanih spojev

All the joints were designed as full-strength connections where plastic hinge is expected to occur in the beam section, which is referred to as dissipative region. Design approach with the intended plastic mechanism in case of all four different RS and CP beam-to-column-joints fulfils the criterion that the region of the stiffened connection at the column face remains essentially elastic under the maximum loads transmitted from the connected beam during cyclic loading.

Specimens RS1 and CP1 comprise beam profile IPE270 in steel grade S355 and steel column profile HEB200 in steel grade S460, hereafter referred to as large column. Specimens RS2 and CP2 are made of beam profile IPE240 in steel grade S355 and steel column profile HEB160 in steel grade S690, hereinafter referred to as small column. Steel profile of the small composite column was welded because hot-rolled profile in steel grade S690 was not available. Beside strong column/weak beam requirement from EN 1998-1 that was fulfilled for all the joints, columns were designed to provide strong column panel zone taking into account additional contribution of concrete in compression and side plates welded to the steel column, see Figs 17 and 18.

Typical values of the resulting column-beam moment ratios for specimens with large and small columns in case of cover-plate connections CP1 and CP2 are presented in Table 4. Actual material characteristics measured from the specimens are taken into account. Values of the ratio are quite large in comparison to the required minimal value 1.3 from EN1998-1, see Fig. 19.

Preglednica 4: Razmerja momentne odpornosti steber-prečka za preizkušanca z velikim in malim stebrom
Table 4: Typical column-beam moment ratio values for specimen with large and small column

Steel column characteristics		Composite column characteristics			
Column	Material	$\Sigma M_{Rc} / \Sigma M_{Rb}$		$\Sigma M_{Rc} / \Sigma M_{Rb}$	
		designed	actual	designed	actual
HEB200	S460	2.74	1.97	3.61	2.73
HEB160	S690	3.02	2.48	4.17	3.61

Reliable inelastic deformation capacity for highly ductile members requires that width-to-thickness ratios of the cross-section parts subject to compression should be limited to a range that provides cross-section resistance to local buckling well into the inelastic range. Both selected beam cross-sections IPE 240 and IPE 270 meet compactness limits for Class 1 cross-sections in bending according to EN 1993-1, as well as from ANSI/AISC 341-10 seismic provisions.

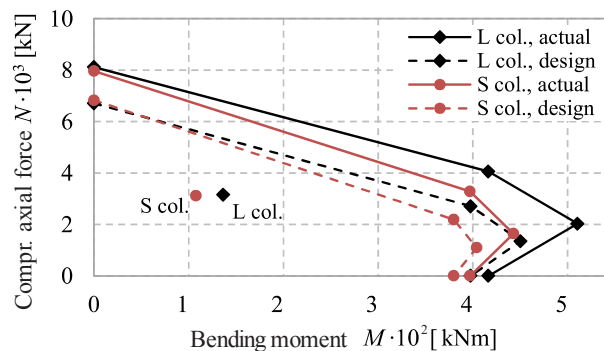


Fig. 19: N-M interaction curves for large (L) and small (S) composite column cross-section
Slika 19: Interakcijski krivulji N-M za velik (L) in mali (S) sovprežni prežez stebra

The overall beam-to-column joint member size selection was dictated by the composite column bearing capacity, designed in such way that relatively high level of compression axial load-to-design plastic resistance ratio was achieved within maximum available actuator load capacity equal to 3000 kN. Longitudinal and transverse reinforcements were defined according to recommendations from EN 1994-1-1 (CEN, 2004) and EN 1998-1. Additional shear studs were applied in the region of both column ends to achieve appropriate load introduction during the test, Fig. 20.

Normal strength concrete of grades C25/30 and C30/37 was considered for large and small columns, respectively. However, to facilitate easier casting and for the sake of good quality of cast concrete, additives were applied to the concrete mixture, which resulted in somewhat greater concrete compressive strengths ranging between 51 and 66 MPa. All the specimens were naturally cured in the indoor climate of the factory of concrete producer. Three concrete cubes were taken for each specimen at the same time as particular column was cast. Concrete cube strength for all three samples of the same series was then defined a day before each test was done. All the concrete cubes were tested at the age between 51 and 93 days. The above reported compressive strength of the concrete was taken as a mean value obtained on the three samples.



Fig. 20: Final preparation on the test specimens – composition of composite column
 Slika 20: Zadnja faza priprave preizkušancev – izdelava sovprežnih stebrov

Concrete initial modulus of elasticity was not measured from material tests. The elastic deformations of concrete largely depend on its composition, especially the aggregates. In our case local limestone from Slovenia was used. Detailed study on the type of aggregate used in our case were recently done by Bokan Bosiljkov et al. (2010). Therefore, on the basis of pre-knowledge, the estimated value of concrete modulus of elasticity was taken equal to 40 GPa.

Resistance of both composite column cross-sections to combined compression and bending, represented by simplified interaction curve, is shown in Fig. 19, where interaction curves for the design and the actual material characteristics are plotted. Characteristic and design values of composite column plastic resistances to compression were 8115 and 6710 kN for the large column and 7962 and 6829 kN for the small column. Taking into account the maximal actuator force of 3000 kN, used to apply the constant column compressive axial force as well as additional axial force in the column because of the transverse force applied at the tip of the beam, the axial load-to-actual composite column plastic resistance ratio ranged between 0.37 and 0.39 in case of the large column and between 0.39 and 0.41 in case of the small column. The same ratio, taking into account the design resistance, ranged between 0.45 and 0.47 and between 0.41 and 0.48 for the large and the small columns, respectively.

All the steel parts of the specimens were fabricated and assembled using standard workmanship quality typically applied in the European practice.

Two tensile coupons were taken from particular steel component of specimens: from each different plate used to cut out cover plates, ribs and lateral plates of columns and separately from flange and web parts of beam and column profiles. The average results from the tensile tests on the steel coupons are presented in Table 5.

Preglednica 5: Mehanske lastnosti vzorcev jekla iz enoosnih nateznih preizkusov
Table 5: Monotonic tensile steel material properties

Sample type	Steel material	Yield strength, f_y (N/mm ²)	Ultimate tensile strength, f_u (N/mm ²)	f_u/f_y	Percentage elongation at fracture, A (%)
IPE 240, web	S355	435	516	1.19	32
IPE 240, flange	S355	385	486	1.26	31
IPE 270, web	S355	444	514	1.16	33
IPE 270, flange	S355	385	498	1.29	32
“HEB 160” web	S690	808	864	1.07	18
“HEB 160” flange	S690	783	818	1.04	18
HEB 200	S460	468	576	1.23	28
Rib stiffener	S355	450	491	1.09	33
Cover plate	S355	424	501	1.18	34

Since cyclic behaviour is undergone in the study, the steel material of the joint components was tested also on toughness. The toughness of all the steel joint components was determined by standard Charpy V-notch tests at a temperature of -20 °C, including three specimens for each component. Values of absorbed energy for steel material grade S355 ranged between 108 and 226 J, for grade S460 between 151 and 185 J, and for grade S690 between 91 and 185 J, which is satisfactory.

Preglednica 6: Rezultati Charpy-V testov
Table 6: Results of Charpy V-notch tests

Sample type	Test temperature (°C)	Absorbed Energy (J)		
IPE 240, web	-20	144	126	132
IPE 240, flange		184	174	177
IPE 270, web		107	107	111
IPE 270, flange		154	174	140
“HEB 160” web		174	198	182
“HEB 160” flange		96	83	94
HEB 200, flange		185	151	152
Rib stiffener		209	222	246
Cover plate	208	212	206	

Prior to testing, geometrical measurements were done on all the joint specimens. No extra discrepancies in the geometry of joint specimens were observed, with the exception of some minor defects regarding out-of-square shapes of cover-plates, Fig. 21. In addition, check of possible global beam/column and local beam imperfections was also performed and no substantial irregularities were observed.

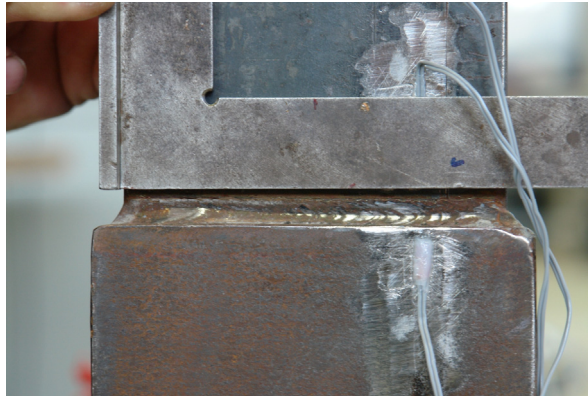


Fig. 21: Check of specimen geometry: out-of-square shape of cover-plate (specimen CP2.3)
 Slika 21: Kontrola geometrije preizkušanca – nepravokotna oblika vezne pločevine (preizkušanec CP2.3)

The geometrical characteristics of all four different beam-to-column joint configurations are presented in Appendix A to this document.

3.3.2 Test setup

The complete test was designed to simulate the boundary conditions of a beam-to-column exterior connection in a moment-resisting frame or inner connection in a braced frame under typical lateral loading, Fig. 22. The composite slab that is most common in the field was not included in the experiments. As reported from past research works, absence of the composite slab accelerates the formation of flange and web local buckles and permits the consequent shortening of the beam during laboratory experiment that is not physically possible in the field (Kim et al., 2000).

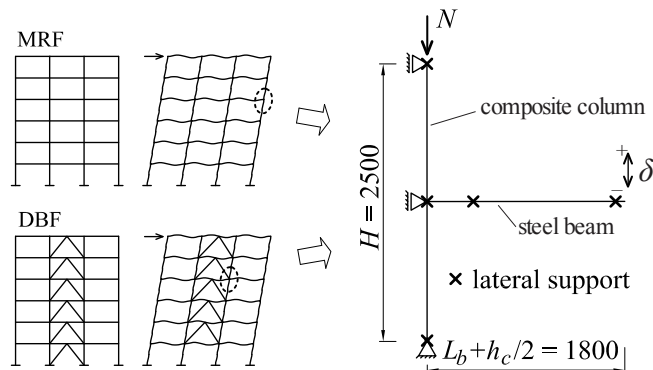


Fig. 22: Static model of the specimen with boundary conditions and loads applied
 Slika 22: Statični model preizkušanca z robnimi pogoji in obtežbo

The effect of column axial force may have influence on the welded connection performance, and its inclusion in the test program was considered as means to obtain more realistic test conditions. The column was assumed to be pin-supported at its both ends. Additional support in loading plane was provided at column mid-height constraining the horizontal displacement at the building's floor level. In addition, the column was laterally supported at the bottom, top and mid-height location in order to prevent any horizontal displacements in case of large column axial force.

Since plastic behaviour analysis is undertaken in the study, lateral braces were provided to the beam near the location of plastic hinge ($1.5 \cdot h_b$ from estimated centreline of the plastic hinge). In addition, lateral brace was provided also near the actuator (315 mm from insertion point of transverse force at the free end of the beam) to protect the actuator from damage due to horizontal translation and rotation of the beam as a result of lateral-torsional buckling, Figs 22 and 23.



Fig. 23: Test setup with test specimen already fixed and during the test
Slika 23: Postavitev eksperimenta s prikazom preizkušanca med testom

Special care was taken to design a beam lateral bracing system, which was provided to both beam flanges and from both beam sides by means of vertical beam HEB140. Additional sliding plates made from *Novilon Oilon* were attached between the beam and the vertical brace in order to provide no clear space and minimal friction between the beam flanges and the supporting system. Sliding panels were additionally greased to provide even less friction between the contact surfaces, Fig. 24. Verification of stable length of beam segment between restraints was performed according to EN 1993-1-1 design provisions.



Fig. 24: Beam lateral bracing system
Slika 24: Sistem bočnega podpiranja prečke

3.3.3 Instrumentation

The instrumentation scheme in all the tests allowed for the measurement and subsequent calculation (elastic and plastic components of displacement and rotations) of specimen global and local response quantities.

Global response quantities with the corresponding measuring devices applied were as follows:

- force; a load cell in-line with the actuator measuring axial forces for both actuators;
- displacements; displacement transducers (LVDT) and digital displacement indicators (DDI) placed on the actuators centreline and other locations on the specimen measuring the imposed displacements of joint as well as displacements of supports;
- rotations; inclinometers placed at strategic locations measuring local beam and column rotations.

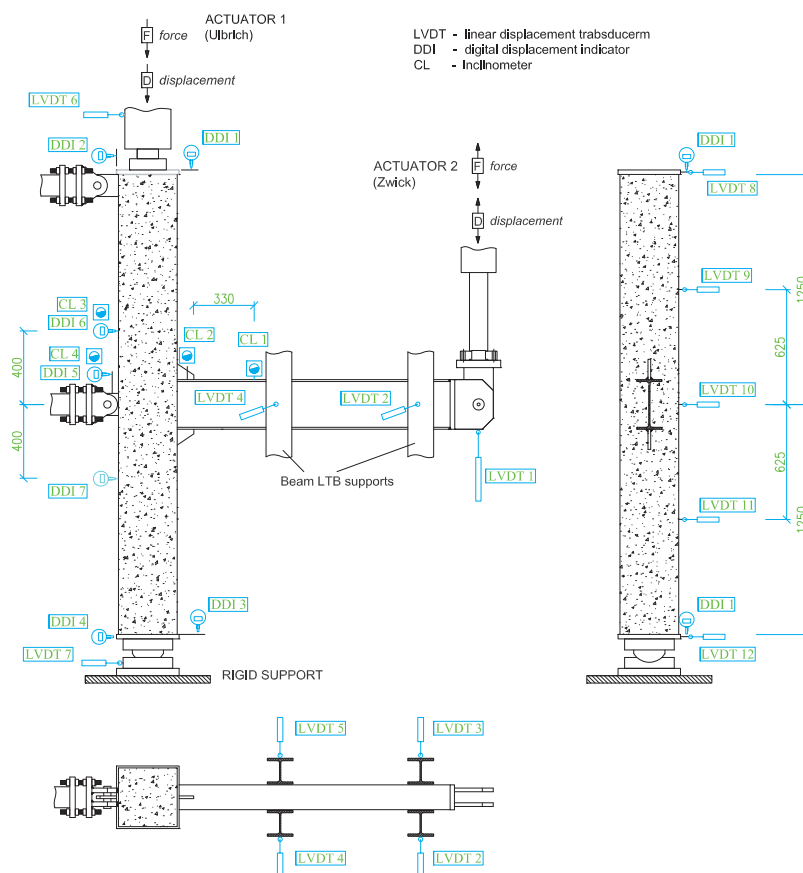


Fig. 25: Instrumentation scheme for the measurement of local and global joint response
 Slika 25: Shema merilnega sistema za zajem lokalnega in globalnega odziva spoja

In addition, uniaxial strain gauges were used to capture local strain response on the beam in and around the yielding zone and at the beam-column interface. Additional strain gauges were placed on the column steel section near beam-to-column connection, Figs 20 and 26.

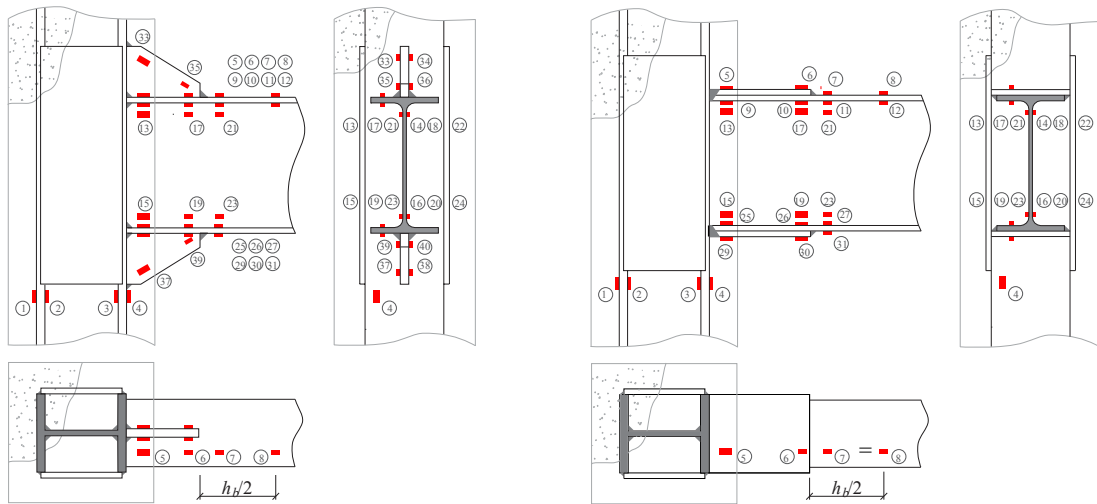


Fig. 26: Strain gauge arrangements in case of RS and CP joint specimens
 Slika 26: Postavitev lističev za merjenje deformacij posebej v primeru spoja RS in CP

3.3.4 Loading protocol

A quasi-static cyclic loading was used in all the tests, with applied loading rate small enough so that strain rate effects of viscoplastic behaviour of constructional steel material did not affect the response of the specimens. Force control loading was used for the first several elastic cycles with displacement control loading applied in the subsequent cycles with amplitude in plastic range, measured directly in terms of total displacement δ at the free end of the beam.

No specific guidance on loading rate to be used in the beam-to-column joint tests was found in related codes. Therefore, the following limit values for tensile tests from EN ISO 6892-1 (2009) were taken into account: in elastic range 6-60 MPa/s, when stress control is used; in plastic region $\dot{\varepsilon} = 0.00025 - 0.0025 \text{ s}^{-1}$, when strain control is used.

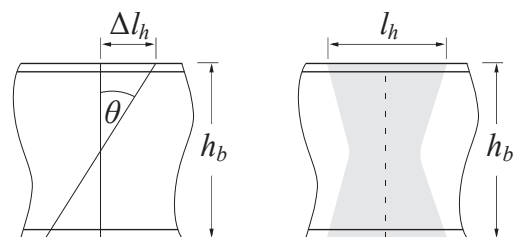
For elastic cycles the value of loading rate equal to 2.5 kN/s applied in terms of force at the beam tip was considered. By using simplified calculation, the stress rate in the extreme fibre of the beam flange, obtained for the IPE 240 and IPE270 beam profiles, would be of the order 10 MPa/s, which was considered satisfactory.

According to the same standard, taking into account the recommended range for plastic strain rate between $0.00025 - 0.0025 \text{ s}^{-1}$, the loading rate of 80 mm/min (1.33 mm/s) in terms of total displacement δ applied at the beam tip was considered. The adequacy of the selected loading rate in plastic region, assuming a plastic hinge length l_h equal to half the beam depth h_b , can be checked by using simplified relations as follows:

$$\left. \begin{aligned} \theta &= \frac{\Delta l_h}{h_b / 2} = \frac{\varepsilon \cdot l_h}{h_b / 2} \\ l_h &\approx h_b / 2 \end{aligned} \right\} \rightarrow \theta \approx \varepsilon,$$

$$\delta \approx L \cdot \theta \approx L \cdot \varepsilon \rightarrow \dot{\delta} = L \cdot \dot{\varepsilon},$$

$$\delta_{pl} \approx L \cdot \theta_{pl} \approx L \cdot \varepsilon_{pl} \rightarrow \dot{\delta}_{pl} = L \cdot \dot{\varepsilon}_{pl},$$

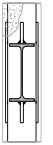
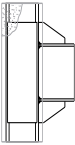
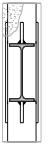
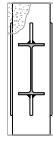
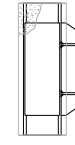
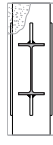
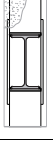
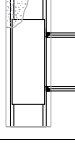
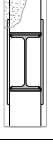





where L (1800 mm) is the distance from the assumed centreline of the plastic hinge to the location of the application of transverse force at the tip of the beam.

Following the above approach for the calculation of maximum plastic strain rate $\dot{\epsilon}_{pl}$ in the beam section, values between 0.0008 and 0.0009 were obtained for both beam profiles used for the specimens. Indeed, the maximum measured strain rate in the beam of about 0.0009/s during the tests confirmed the values obtained from preliminary simple calculation.

For the first two tests, specimens RS1.1 and RS1.2 (complete nomenclature of the test specimens is provided in the text below), Tables 3 and 7, modified protocol from ECCS N°45 recommendations (ECCS, 1986), as proposed by Calado (2000), was used. Namely, according to the pre-test finite element simulations on the specimens, the original ECCS N°45 loading history was called into question, due to too large plastic increments inherent. By applying the original loading protocol, the joints would sustain too few (≈ 4) cyclic loading amplitude levels before the complete failure, and thus typical LCF behaviour of the specimens would not be possible, see Fig. 27.

Preglednica 7: Pregled po vseh 16 laboratorijskih testih
 Table 7: Summary information on all 16 laboratory tests

Specimen	Specimen's column/beam characteristics		Loading protocol	Column axial force
	Steel section	Material combination		
RS1.1	IPE270/HEB200	S355/S460	variable, ECCS*	0
RS1.2			variable, AISC	3000 kN
RS1.3			constant, small	3000 kN
RS1.4			constant, large	3000 kN
RS2.1	IPE240/HEB160	S355/S690	variable, AISC	0
RS2.2			variable, AISC	3000 kN
RS2.3			constant, small	3000 kN
RS2.4			constant, large	3000 kN
CP1.1	IPE270/HEB200	S355/S460	variable, AISC	0
CP1.2			variable, AISC	3000 kN
CP1.3			constant, small	3000 kN
CP1.4			constant, large	3000 kN
CP2.1	IPE240/HEB160	S355/S690	variable, AISC	0
CP2.2			variable, AISC	3000 kN
CP2.3			constant, small	3000 kN
CP2.4			constant, large	3000 kN

*) modified ECCS N°45 loading protocol

In favour of the above finding speaks also recently published assessment of the current Eurocode seismic design provisions (ECCS, 2013), which clearly states that the ECCS (1986) loading procedure is probably the most used in Europe, but it is outdated and it does not give any qualification criteria. Therefore, a major revision of this document is proposed.

According to the modified loading protocol proposed by Calado, the following cyclic sequence was applied: (1) three cycles in elastic range with a semi-amplitude equal to $\frac{1}{4}$, $\frac{1}{2}$,

$\frac{3}{4}$, 1 of δ_y , where δ_y is the yield displacement obtained from preliminary non-linear FEA; (2) three cycles at each amplitude $i \cdot \delta_y$, with $i = 2, 3, 4, \dots$, up to the complete failure of the specimen.

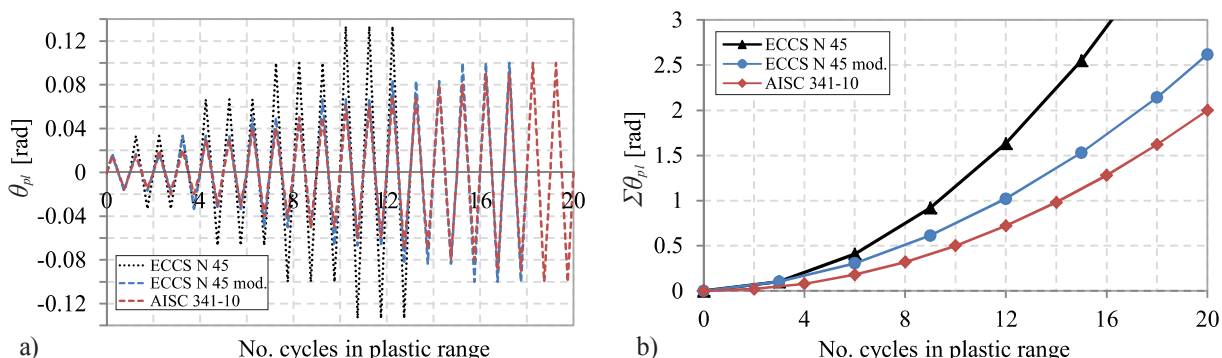


Fig. 27: Comparison between ECCS N°45, the modified ECCS N°45 and AISC 341-10 cyclic loading protocols in terms of: a) loading amplitudes and b) accumulated plastic rotation. Loading sequences related to cyclic amplitudes in plastic range are only presented.

Slika 27: Primerjava med protokolom obremenjevanja ECCS N°45, modificiranim ECCS N°45 in protokolom AISC 341-10: a) amplitude pomikov in b) akumulirana plastična deformacija. Prikazani so le cikli z amplitudami v plastičnem območju.

On the basis of the results obtained from the first two tests, displacement increment between the two successive amplitudes was considered to be still somewhat too large. Therefore, for the other six specimens subject to cyclic loading with stepwise increasing amplitude, Tables Table 3 and Table 7, loading procedure according to ANSI/AISC 341-10 (ANSI/AISC, 2010b) was used. Another noteworthy reason for applying the latter loading protocol is also to obtain specimen cyclic response comparable to the vast amount of test results in literature that were produced using the same loading history. Comparison of all three considered loading protocols, taking into account joint yield displacement 0.017 rad as obtained from the specimens, is given in Fig. 27.

Variable amplitude cyclic loading according to the aforementioned description was adopted for the first eight tests: each of the four different joints (RS1, RS2, CP1 and CP2) was tested with full level of column compressive axial force and without it (two tests (specimens) on the same joint), hereinafter designated with suffixes 1 and 2 to the corresponding name of joint specimen, RS1.1 and RS1.2, RS2.1 and RS2.2, CP1.1 and CP1.2, CP2.1 and CP2.2, respectively, Tables 3, 7.

Since the study is focused on beam-to-column joint response under arbitrary cyclic loading histories, in addition to the variable loading, two different inelastic constant displacement amplitude levels were considered. From the examination of the beam local inelastic strain response of specimens previously tested under variable amplitude loading, two constant amplitudes were chosen: 35 mm and 60 mm, hereinafter referred to as small and large constant amplitudes, respectively. Both values of constant amplitudes were chosen to capture two distinct responses of the beam in plastic hinge region: with and without the presence of local buckling for large and small amplitudes, respectively. At the same time, the amplitudes had to be different enough in order to produce different fatigue endurance on the same type of specimen. This allowed damage phenomena due low-cycle fatigue (LCF) to be properly evaluated.

Both constant cyclic amplitudes were applied on each of the four different designed joint configurations, in combination with full level of column axial force, hereinafter designated with suffixes 3 and 4 to the joint name for small and large constant amplitudes, respectively, Tables 3 and 7.

Each test was run until the failure of specimen, characterized by complete fracture of the beam flange followed by apparent loss of load resistance.

3.4 Test results

The evaluation of results obtained from experimental cyclic tests on sixteen welded rib-stiffened and cover-plate beam-to-column joints is presented hereinafter. Description of global joint response, separately for variable and constant amplitude cyclic tests, is provided in the first two subsections. In the subsequent sections response evaluation of all the joints is provided by means of different response parameters: observations of plastic zone development and damage concentrations in the steel parts of the joint, damage in the column, joint ductility, amount of dissipated energy and LCF resistance. In addition, the response of specimens is evaluated according to the acceptance and prequalification-type criteria from the current seismic design codes.

The obtained experimental results were used to compare the response of both types of stiffened connection and to demonstrate that the applied joint detailing and the design concept for the stiffened connections result in adequate joint response under cyclic loading conditions.

All the experimental data presented hereinafter, including graphic representations as well as all other reported information on specimen response characteristics, are related to the fully completed loading cycles only.

Wolfram *Mathematica* v 9.0.1 (Wolfram Research, 2012) was used to process the experimental data. The data were filtered appropriately to eliminate noise and then zero corrected. *Mathematica* was also used to encode all algorithms and routines developed for the purpose of complete processing and evaluation of cyclic experimental data as well as all results from FE analyses that are presented in the subsequent chapters of this document.

3.4.1 Joint rotation analysis

In order to provide clear and systematic overview of experimental beam-to-column joint response, first the description of local joint kinematics is presented. Note that joint rotation components described below were identified as the most contributing for the tested stiffened beam-to-column joints, with the strong column/weak beam design principle used.

Systematic treatment of the following global and local joint kinematics was enabled by the instrumentation scheme presented in Chapter 3.3.3. The following rotations of single-sided beam-to-column joint under the applied transverse force at the free end of the beam were defined:

- total joint rotation;
- elastic joint rotation (contributions from the beam and the column);
- plastic joint rotation (contributions from the beam and the column);
- rotations at the column panel zone and its boundary;

Total joint rotation

Total displacement at the beam tip δ is composed from elastic δ_{el} and plastic δ_{pl} deformation of the whole beam-to-column joint assemblage. Contributing elastic and plastic parts of joint displacement (rotation) are illustrated in Fig. 28.

Together with applied vertical displacement at the beam tip, the corresponding rotations with respect to the column centreline can be defined as follows:

$$\delta = \delta_{el} + \delta_{pl},$$

$$\theta = \frac{\delta}{(L_b + h_c / 2)} = \theta_{el} + \theta_{pl}. \quad (14)$$

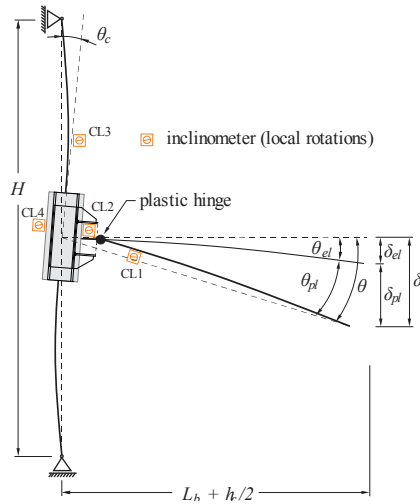


Fig. 28: Beam-to-column joint kinematics
Slika 28: Kinematika spoja prečka-steber

Elastic joint rotation

The total elastic displacement at the beam tip δ_{el} representing elastic global rotation is composed of the displacement due to the elastic deformation of the column $\delta_{el,c}$, and the displacement resulting from the elastic deflection of the steel beam $\delta_{el,b}$.

$$\delta_{el} = \delta_{el,c} + \delta_{el,b}, \quad (15)$$

$$\theta_{el} = \theta_{el,c} + \theta_{el,b}. \quad (16)$$

Rotations of the column panel zone and its boundary

During the analysis of experimental results, presented in the subsequent chapters, complete column rotation, measured by inclinometer CL4, fixed at the column mid-height, was found elastic in case of all sixteen test specimens, with contribution to the total joint rotation between 5.8 and 9.3 %.

$$\theta_c = \theta_{el,c}. \quad (17)$$

In addition, from comparison between measured complete column rotation by inclinometer CL3 and column bending rotation captured by inclinometer CL4, it was found that rotations of the column panel zone were very small and are therefore neglected in the analysis. Accordingly, column panel zone is considered as infinitely rigid in case of all sixteen specimens.

Since total column rotation was measured by inclinometer CL4, total beam rotation can be defined as follows

$$\theta_b = \theta - \theta_c. \quad (18)$$

Plastic joint rotation - beam plastic hinge rotation

Following the outcomes of the foregoing discussion on joint rotation measurements, all the plastic deformation (rotation) occurred in the steel beam. Indeed, in case of all the sixteen joint specimens plastic deformations were bounded in the region of unstiffened beam section just behind the stiffened part of the beam, hereinafter referred to as plastic hinge. The plastic beam rotation was obtained by subtracting elastic bending and shear deformation from the beam:

$$\begin{aligned}\theta_{pl} &= \theta_{pl,b}, \\ \theta_{pl,b} &= \theta_b - \theta_{el,b}.\end{aligned}\tag{19}$$

All the above defined rotations are computed with respect to the column centreline (displacement at the free end of the beam divided by the distance between the loading point and the centreline of the column), including beam plastic rotation, see Fig. 28.

In addition, from the applied instrumentation scheme, presented in Fig. 25, local plastic hinge rotation can be determined directly from measurements by inclinometer CL1 and inclinometer CL2:

$$\theta_{pl,h} = \theta_{CL1} - \theta_{CL2}.\tag{20}$$

The above value of local plastic hinge rotation also includes elastic deformations in the portion of the beam between inclinometers.

To conclude, a summary on the principles of joint rotation issue used in this study is given below. For a complete description of single-sided beam-to-column joint response under the applied displacement at the beam tip, contributing rotations (elastic and plastic) from each joint component were identified following the procedure described below. Joint rotations presented in this work are calculated as the corresponding beam tip displacement, divided by the distance between the loading point and the centreline of the column (1800 mm). To be consistent with the loading directions applied in the tests, positive rotation is supposed to be in counter clock direction, Fig. 22. The plastic joint rotation θ_{pl} is obtained by subtracting elastic bending and shear deformation from the beam as well as complete contribution from the column: elastic column bending and panel zone deformations. Although the column web panel contribution is generally considered as plastic deformation, it was not included in θ_{pl} . Since all the specimens were designed taking into account strong column/weak beam design concept, and due to additional strength and stiffness resulting from column side plates and concrete encasement, Figs 17 and 18, very small elastic deformation of the column panel zone was observed in all the specimens. Accordingly, θ_{pl} is attributed to the plastic hinge rotation in the beam, and is referred to also as plastic beam rotation $\theta_{pl,b}$.

3.4.2 Variable amplitude cyclic tests

The response of all eight RS and CP joint specimens tested under cyclic loading with stepwisely increasing amplitude (ANSI/AISC 341-10 loading protocol) revealed stable hysteretic response capable of developing large plastic rotations without premature brittle failure. Each joint from the group of specimens RS1.2, RS2.2, CP1.2 and CP2.2 tested with the presence of column compressive axial force showed very similar response to the same joint from the group of the other four specimens RS1.1, RS2.1, CP1.1, and CP2.1 tested without column axial force. The irrelevance in difference in global cyclic response between the two equal stiffened joints tested with and without the presence of compressive column axial force can be observed from diagrams in Fig. 29, where moment M_c versus total joint rotation θ , both computed with respect to the column centreline, is presented. Except for minor deviations resulting from different onsets of strength degradation as a result of the

beam local buckling, and differences in the onset of final specimen failure (up to ± 1 cycle, see also Table 8), the corresponding two responses for all the four joint configurations RS1, RS2, CP1 and CP2 are basically very similar. Also macro examination of welded beam-to-column interface at the face of the column performed after the tests did not reveal any detrimental cracks that could be directly related to the applied level of compressive column axial force (40 % of actual composite column plastic resistances to compression), see Chapter 3.4.4.

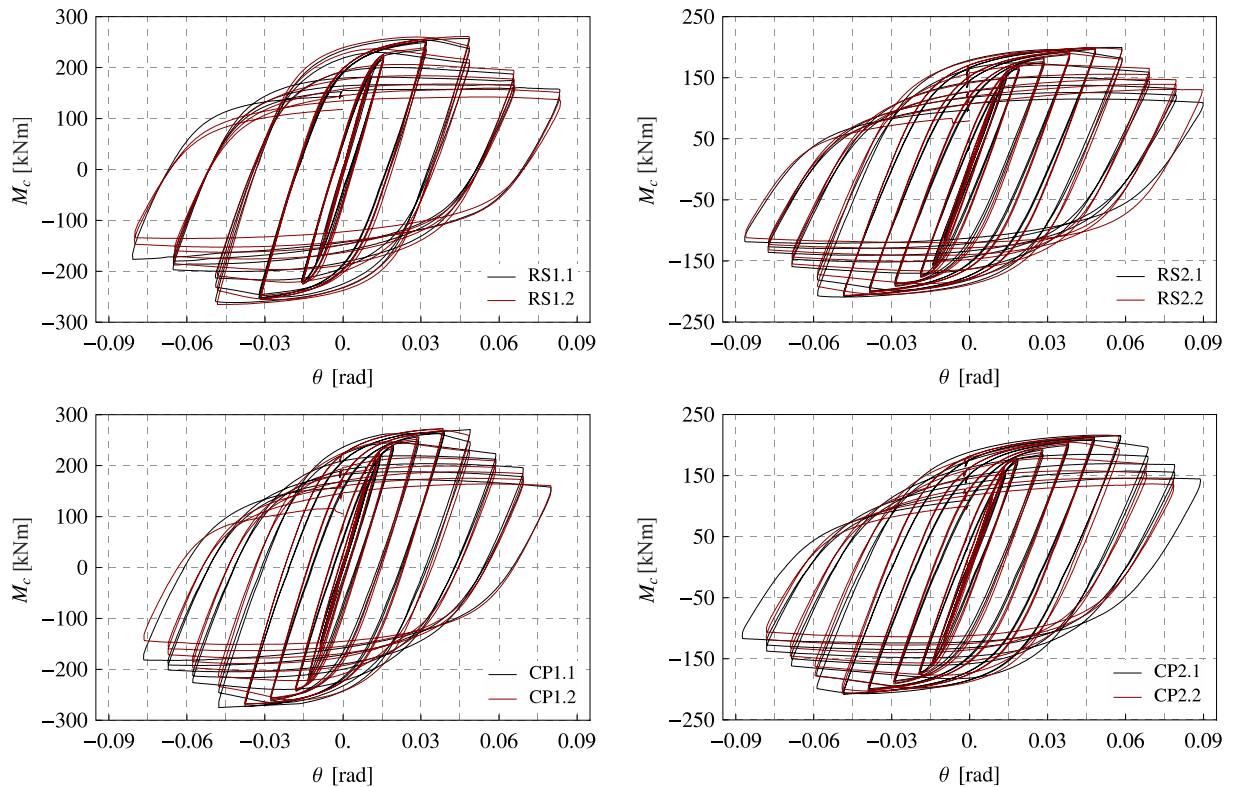


Fig. 29: Comparison of cyclic response between the two equal joints tested with and without the presence of compressive column axial force

Slika 29: Primerjava cikličnega odziva dveh enakih spojev testiranih z in brez tlačne osne sile v stebru

Based on the above observations the following two conclusions can be made:

- the applied level of the column compressive axial force did not cause any apparent detrimental effect on the beam-to-column welded connection that would undermine the cyclic behaviour of the joints;
- results obtained are repeatable.

Overview of deformed shape of all the eight specimens subjected to variable cyclic loading with stepwisely increasing amplitude is presented in Figs 30 to 37. Each photograph was taken after the failure of the specimen and illustrates the key failure characteristics of a particular beam-to-column joint: overall view on the plastic hinge zone in the beam with the spread of plastic deformations (seen as a darker region as a result of limewash coat peeling during the test), beam flange and web local buckling with beam cross-section distortion, and detail of fracture in the beam flange.

In all the eight tests, plastic local buckling of compressed flange and flexural-torsional buckling of a beam section in the plastic hinge region led to excessive out-of-plane inelastic displacements of the IPE-beam sections, Figs 30 to 37. This happened even though lateral braces were provided close to the plastic hinge region, Figs 22 to 25, and no substantial lateral movement at the location of the lateral supports was measured during the tests. The same

observation for unstiffened beam-to-column joints with IPE-beam sections subjected to large inelastic rotations was reported by other researchers (Schafer et al., 2005 - 2008).

The resemblance between the same two joints from the group of four different beam-to-column joints designed for the tests, RS1: RS1.1 and RS1.2, RS2: RS2.1 and RS2.2, CP1: CP1.1 and CP1.2, CP2: CP2.1 and CP2.2, can also be observed from the consistent deformed shape and failure mechanism presented in Figs 30 to 37.



Fig. 30: Specimen RS1.1 after the test
Slika 30: Preizkušane RS1.1 po končanem testu

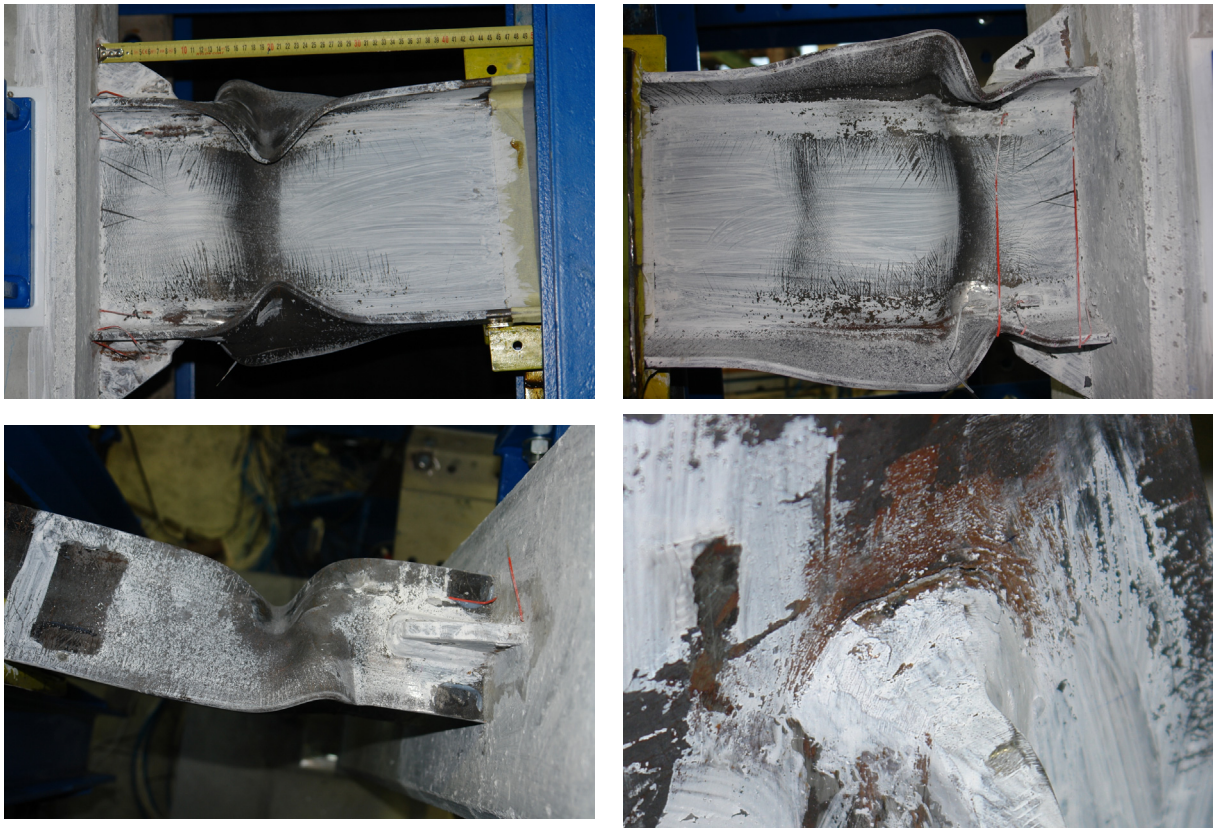


Fig. 31: Specimen RS1.2 after the test
Slika 31: Preizkušanec RS1.2 po končanem testu

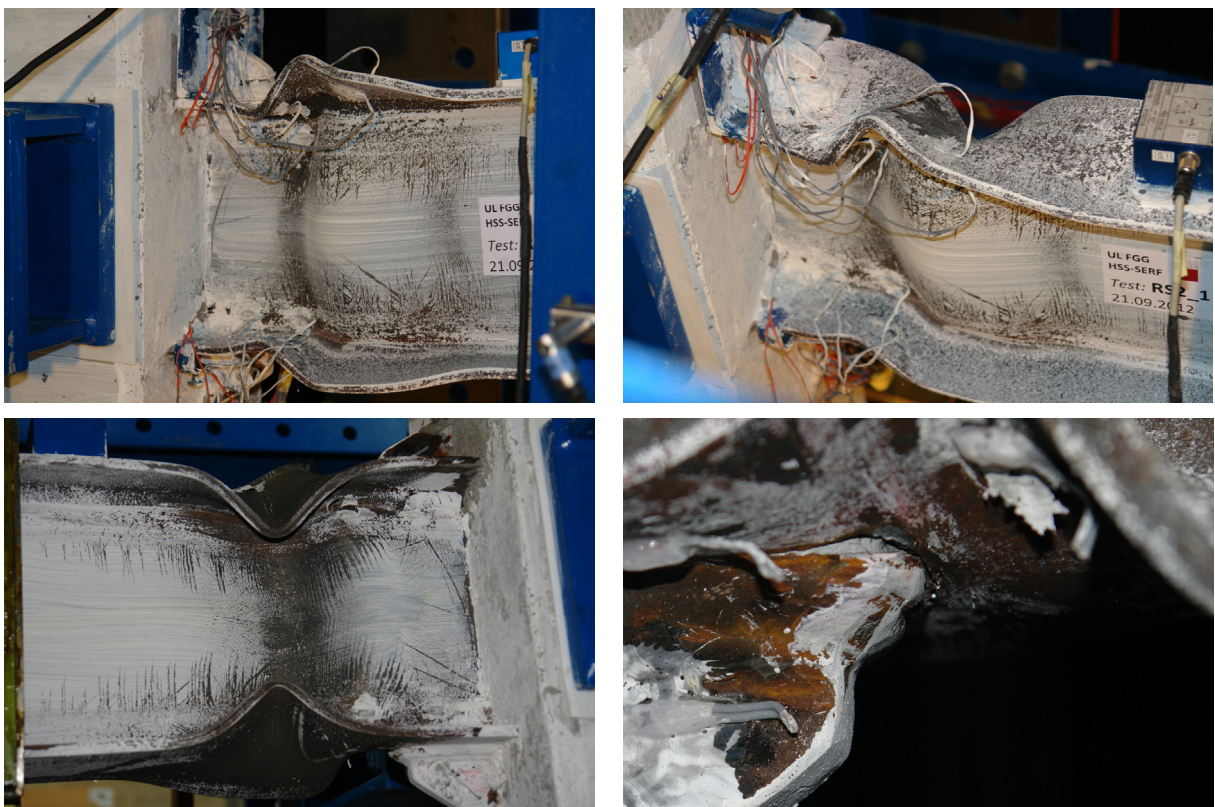


Fig. 32: Specimen RS2.1 after the test
Slika 32: Preizkušanec RS2.1 po končanem testu

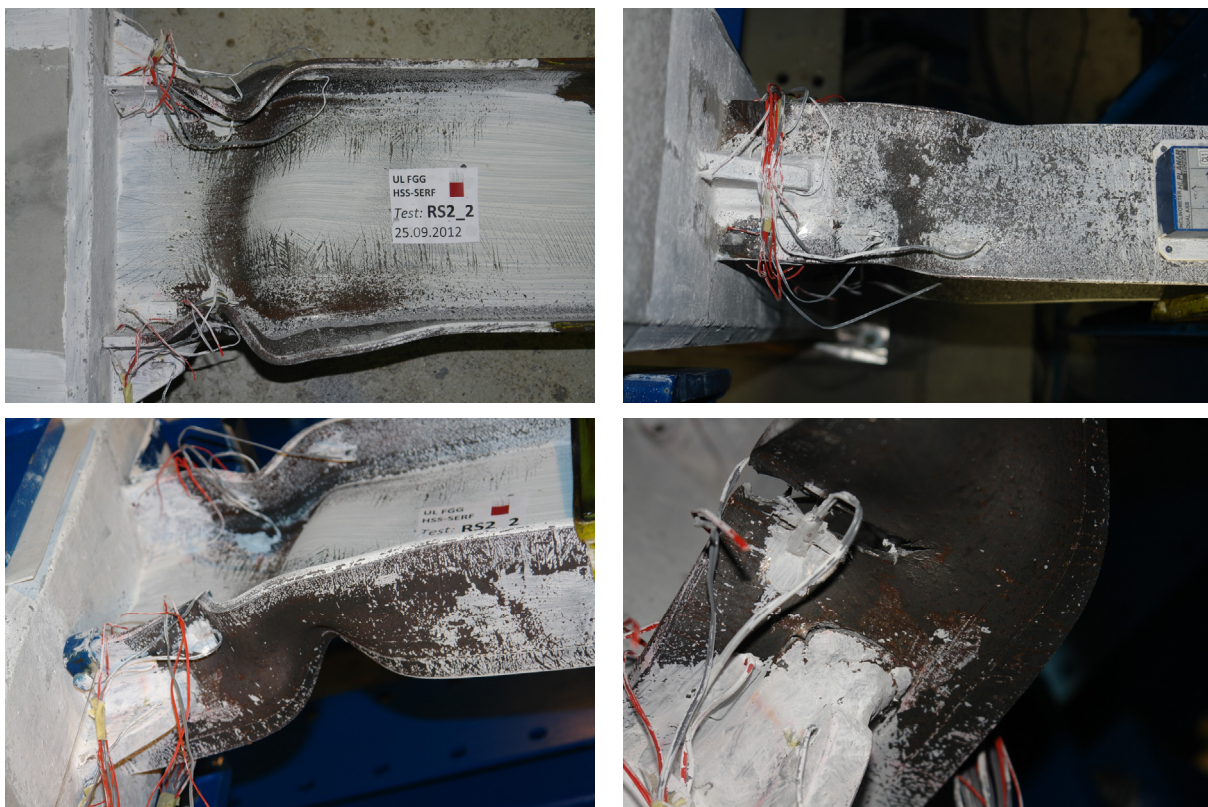


Fig. 33: Specimen RS2.2 after the test
Slika 33: Preizkušavec RS2.2 po končanem testu



Fig. 34: Specimen CP1.1 after the test
Slika 34: Preizkušavec CP1.1 po končanem testu

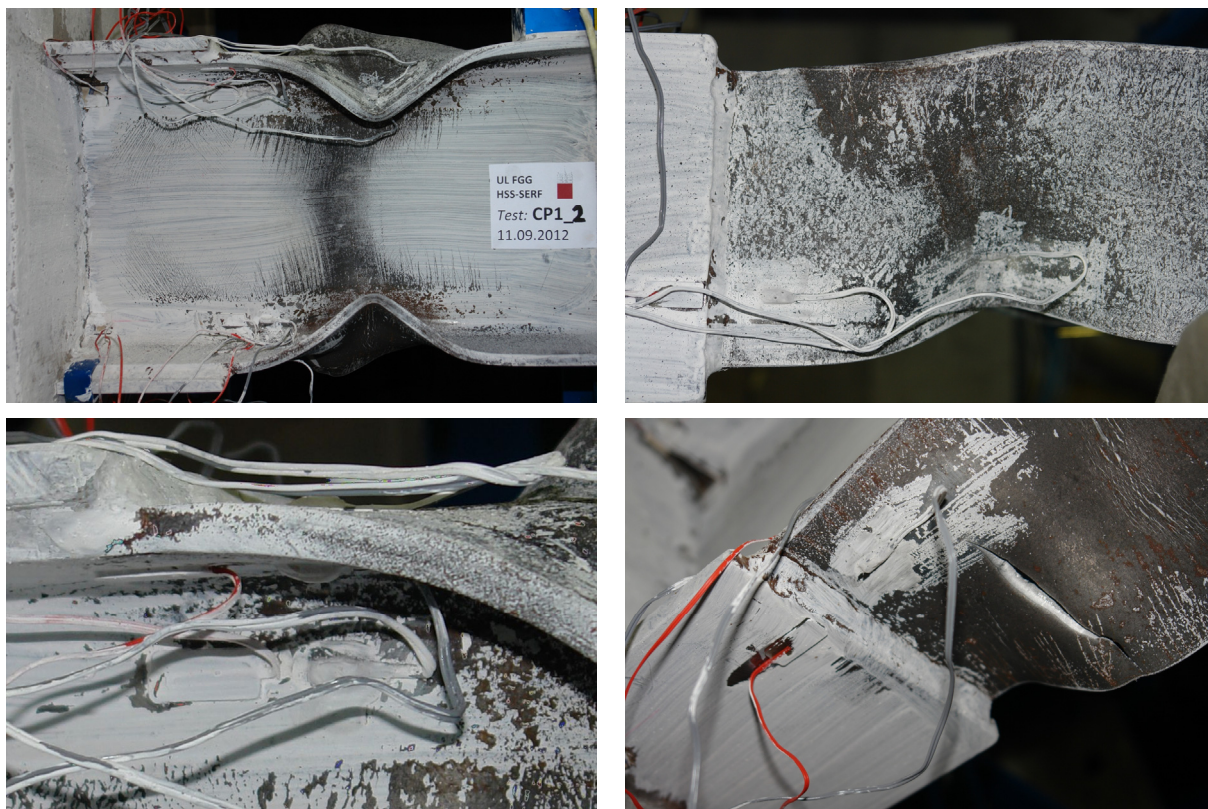


Fig. 35: Specimen CP1.2 after the test
Slika 35: Preizkušavec CP1.2 po končanem testu



Fig. 36: Specimen CP2.1 after the test
Slika 36: Preizkušavec CP2.1 po končanem testu



Fig. 37: Specimen CP2.2 after the test
 Slika 37: Preizkušaneec CP2.2 po končanem testu

Based on the response observations during the tests and close inspection of beam-to-column joint components after each test, also provided by the above photographs, it can be concluded that the objective of the applied design concept of the rib-stiffened and cover-plate connection was fulfilled for all the eight tests: no yielding of the reinforcing plates either for RS or CP connection was observed, with the whole inelastic action transferred away from the vulnerable (non-ductile) welded beam-to-column connection into the un-stiffened beam section behind the stiffened region.

No damage of welds, either in the beam-column connection at the column face or around the reinforcing plates, was observed from macro examination after the tests, see Chapter 3.4.4.

In case of RS joints, the first cracks were always observed in the heat-affected zone (HAZ) around fillet weld at the end of the rib-stiffener, Figs 30 to 33. However, these cracks did not have any detrimental effect on the response of the specimens, since failure always occurred as a result of fracture initiated in the largest buckle of the beam flange due to the LCF effects.

To conclude, none of the specimens failed due to the failure of stiffened beam-to-column connection or connection detail in the local vicinity of the column. Plastic hinge mechanism of the beam formed away from the face of the column and it moved behind the stiffened region.

Due to the large amplitude cycling, with stepwisely progressing rotation amplitude throughout the applied loading protocols (modified ECCS N°45, ANSI/AISC 341-10, see Table 7), beam local buckling occurred in the plastic hinge zone beyond the end of the stiffened region of the beam. In all eight tests flanges buckled prior to webs. Before the onset of large flange and web local buckling, modest flange buckling occurred, with amplitudes around beam flange thickness. At this state local buckling did not lead to the strength degradation, although increased reduction in the rate of developed strength could already be observed. In the

following cycle buckled flanges in tension were straightened again, which was not the case when larger buckling of flanges and flange induced web buckling (beam local buckling) had occurred. As a consequence, the degradation of overall joint strength and stiffness took place simultaneously, as can be observed in Fig. 29, Table 8 and in all the related hysteretic response curves presented beforehand. Finally, failure occurred in the buckled zone of the beam with the ultimate fracture initiated in the beam flange as a result of the LCF effects. Despite distorted and partly fractured beam cross-section due to pronounced beam local buckling in the dissipative zone, the resistance of all the eight joints just before the failure ranged between 51 and 63 % of their maximum strength.

In relation to the beam local buckling it was observed that local buckling of the beam flange and web indirectly protected the welding zone at the end of the stiffened region from higher strength demands, by means of reduced flexural resistance of the buckled beam. The same observation in case of unstrengthen moment connections was reported from the past experimental research activities (Bernuzzi et al., 1999). On the other hand, flange local buckling also directly led to the increase of local strain demand due to the local flange curvature close to the stiffener end, resulting in tearing of the base material in the weld HAZ at the end of the stiffener, which somewhat diminished the positive effect of the beam local buckling in terms of reduced strength demand, Figs 30 to 33.

In contrast to large amplitude cycling, cyclic loading with smaller amplitudes, where the beam local buckling is not reveal to such extend or it does not occur at all, LCF fracture at the end of the rib stiffener in the welded region can trigger complete fracture of the beam flange, see Chapter 3.4.3.

Except for minor cracks at the very local region around beam-to-column connection that had no detrimental effect on joint behaviour, concrete encasement remained undamaged in all the tests, see Figs 30 to 33.

Cyclic response of the specimens was further on investigated by means of different strength, stiffness and global deformation (rotation, plastic rotation) response indices, among which the exhibited joint strength (overstrength) and stiffness are addressed first.

To this end, the response of four RS and CP beam-to-column joint specimens, RS1.2, RS2.2, CP1.2 and CP2.2, tested with the presence of full level of column compressive axial load is shown in Figs 38 to 40. In Fig. 38 moment M_h determined at the centreline of the plastic hinge and normalized by the nominal value of the beam plastic moment $M_{pl,b}^{nom}$ is plotted against total joint rotation θ . Plastic hinge centreline was assumed to be located at a distance of one quarter of the beam height ($1/4h_b$) from the end of the stiffener for both RS and CP stiffened joint configurations.

For the same four joint specimens, the distribution of moments at the subsequently applied joint rotation amplitudes as a function of the corresponding joint rotation amplitude and number of cycles is presented in Figs 39 and 40. Moment amplitudes corresponding to both positive and negative loading directions for complete loading history applied are presented. Limits associated with 20 % fall of the ultimate flexural resistance M_h^{max} and actual beam plastic moment $M_{pl,b}^{act}$, calculated with actual geometric and material beam characteristics, are included in all the diagrams. In addition, labels associated with the last cycle without stiffness degradation of more than 20 % of its initial value, are marked in Figs 39 and 40 as well.

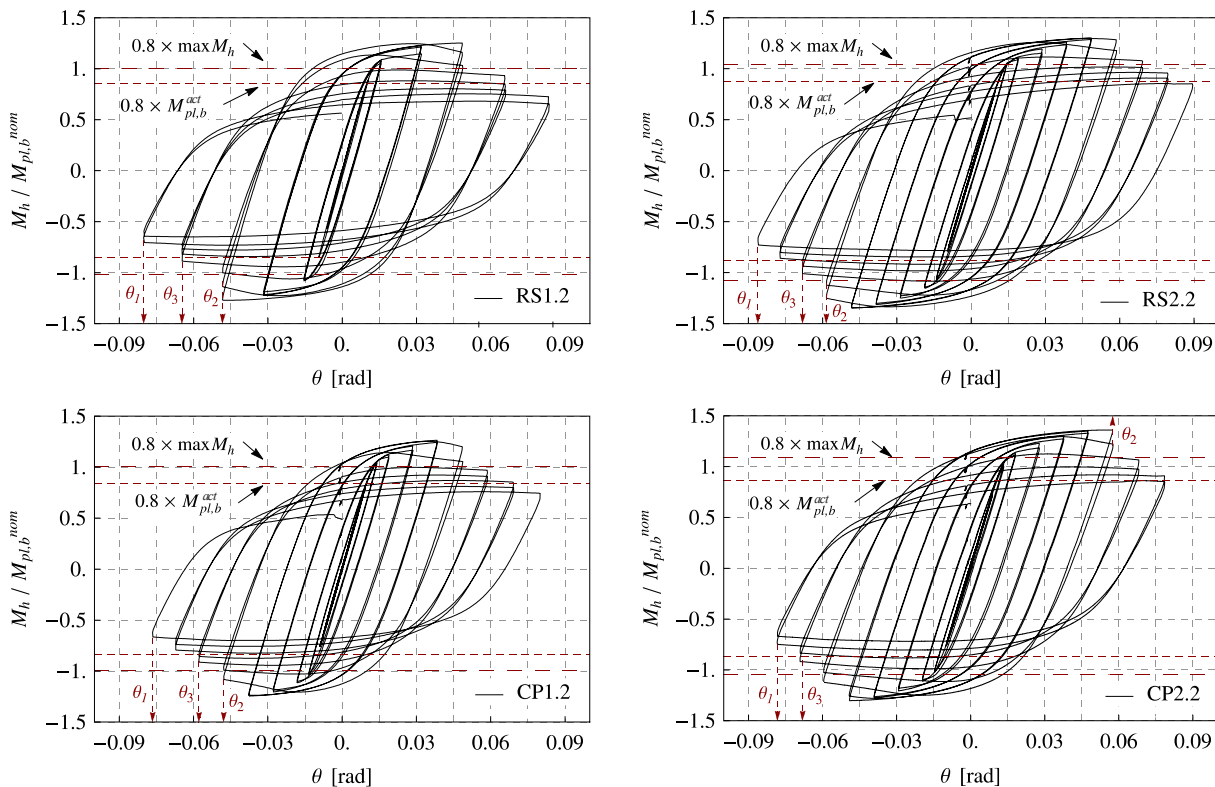


Fig. 38: RS and CP joint response in terms of normalised moment M_h vs. total joint rotation θ with graphical representation of the three failure criteria

Slika 38: Odziv preizkušancev RS in CP v smislu normiranega momenta M_h in celotne rotacije spoja θ s prikazom treh uporabljenih mejnih kriterijev

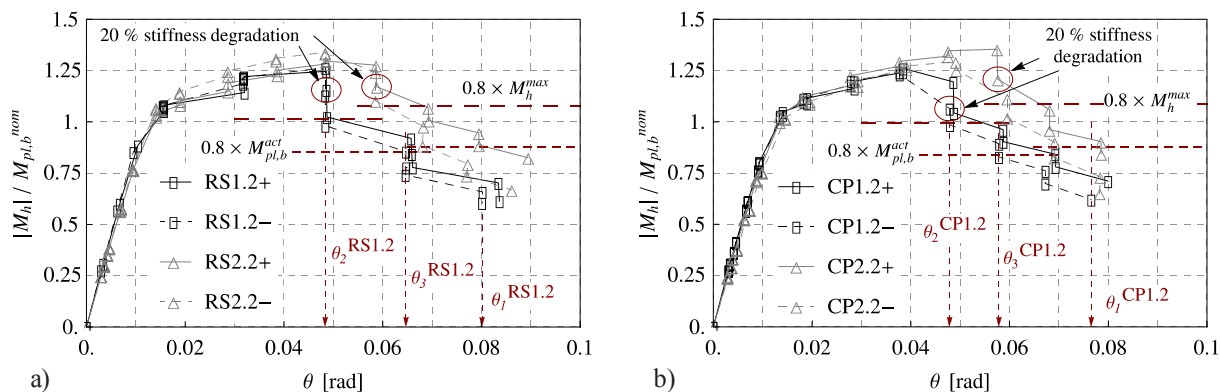


Fig. 39: Normalised moment M_h at the subsequent joint rotation amplitudes: a) RS1.2 and RS2.2, b) CP1.2 and CP2.2

Slika 39: Normiran moment M_h v zaporednih amplitudah vsiljene rotacije: a) RS1.2 in RS2.2, b) CP1.2 in CP2.2

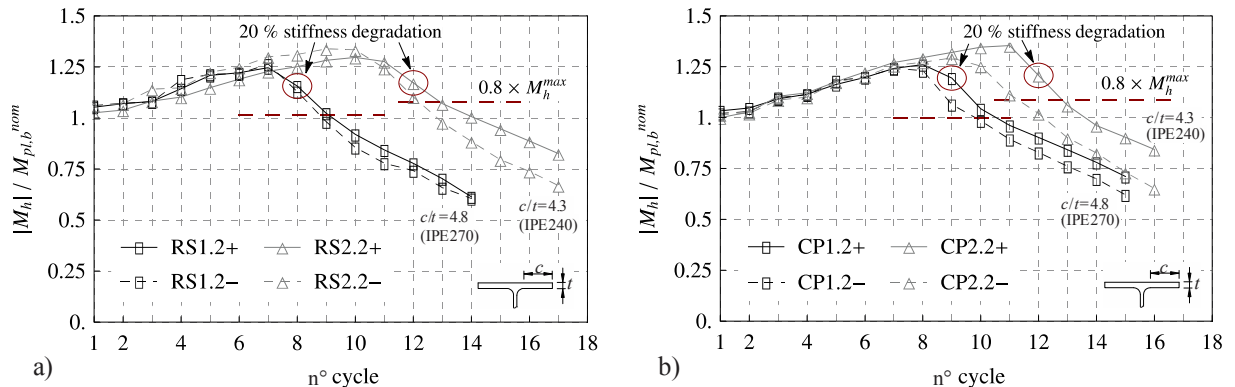


Fig. 40: Normalised moment M_h at the subsequent joint rotation amplitudes as a function of the number of cycles: a) RS1.2 and RS2.2, b) CP1.2 and CP2.2

Slika 40: Normiran moment M_h v zaporednih amplitudah vsiljene rotacije v odvisnosti od števila ciklov: a) RS1.2 in RS2.2, b) CP1.2 in CP2.2

The maximum strength developed by the two equal specimens, RS1.1, RS1.2 (IPE270 beam), and RS2.1, RS2.2 (IPE240 beam), for RS joint, and CP1.1, CP1.2 (IPE270 beam), and CP2.1, CP2.2 (IPE240 beam), for CP joint, observed from Fig. 29, is practically the same because the specimens' resistance was controlled by the flexural ultimate strength of the beam, being theoretically the same for each of the four pairs. However, by comparing the values of the ultimate resistance between the specimens comprising the same beam but different type of stiffened connection, M_c^{max} values belonging to the CP joints are somewhat (about 3.5 % for both beams) larger in comparison to those obtained from the RS joints. The reason for this is inherent in geometric characteristics of both designed joint configurations: the cover plates are longer than the ribs, forcing plastic hinge to occur far away from the column face, thus producing shorter distance to the load insertion point at the free end of the beam.

Consistent assessment of developed joint overstrength, in relation to the nominal beam material strength characteristics (calculated by using nominal material yield strength 355 MPa), can be provided by taking into account joint moment resistance at the assumed plastic hinge centreline. Values of the beam flexural overstrength $M_h^{max}/M_{pl,b}^{nom}$ obtained for all test specimens are provided in Tables 9 and 10. In case of the eight specimens subjected to variable cyclic loading, highly consistent flexural overstrength values can be observed for large IPE 270 (between 1.25 and 1.27) and small IPE240 (between 1.35 and 1.37) beam profile, regardless of the stiffened joint type, which shows the correctness of the defined plastic hinge centreline along the beam. Larger values of overstrength factor produced by specimens with smaller, more compact beam cross-section IPE240, can also be observed.

To evaluate and compare the response of each joint specimen, three failure criteria, graphically presented in Figs 38 to 40, were applied. The first criterion (N_1, θ_1) represents the state with the onset of complete joint failure (the last fully completed cycle). The second criterion (N_2, θ_2) relates to 20 % fall of the maximum beam-to-column joint strength and the initial stiffness, which corresponds to the acceptance criterion from EN 1998-1, and the third one (N_3, θ_3) describes the instance with 20 % fall of the actual beam plastic moment $M_{pl,b}^{act}$.

Reduction of joint strength and stiffness for the second and the third failure criteria was checked separately for both positive and negative directions in relation to the corresponding maximum joint strength and initial stiffness from both loading directions. The basic philosophy encoded in the algorithm, used to process response data, follows the idea that both the stiffness and the strength requirements should be ensured throughout complete hysteresis loop, see Fig. 41.

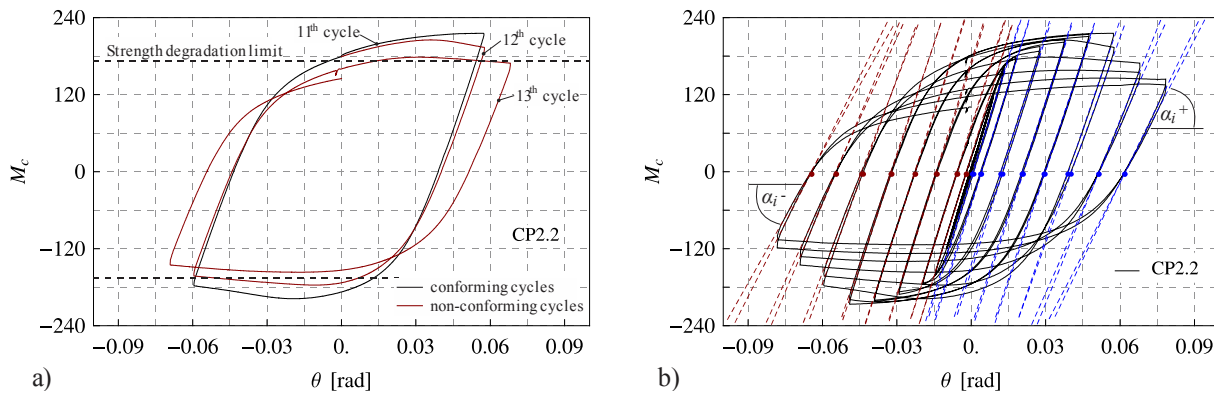


Fig. 41: Principles of the applied evaluation criteria: a) strength criterion, b) stiffness criterion
 Slika 41: Principi uporabljenih kriterijev analize odziva: a) kriterij nosilnosti, b) kriterij togosti

The total number of completed inelastic cycles N_i according to the three failure criteria for all the test specimens is gathered in Table 8.

Preglednica 8: Celotno število polnih neelastičnih ciklov N_i v skladu s tremi mejnimi kriteriji za vse teste

Table 8: Total number of completed inelastic cycles N_i according to the three failure criteria for all the specimens

Specimen	Load case	N_1	N_2	N_3	Specimen	N_1	N_2	N_3
RS1.1	variable	13 ^{LB}	9 ^{a,b}	10	CP1.1	15 ^{LB}	11 ^a , 10 ^b	13
RS1.2	variable	14 ^{LB}	8 ^{a,b}	10	CP1.2	15 ^{LB}	9 ^{a,b}	12
RS1.3	const. ^{small}	76 ^{FR}	73 ^a , 76 ^b	73	CP1.3	126 ^{FR}	124 ^a , 125 ^b	125
RS1.4	const. ^{large}	29 ^{FR}	13 ^a , 23 ^b	26	CP1.4	40 ^{LB}	12 ^a , 38 ^b	36
RS2.1	variable	17 ^{LB}	12 ^{a,b}	14	CP2.1	17 ^{LB}	12 ^{a,b}	15
RS2.2	variable	17 ^{LB}	12 ^{a,b}	14	CP2.2	16 ^{LB}	11 ^a , 12 ^b	15
RS2.3	const. ^{small}	138 ^{FR}	133 ^a , 138 ^b	134	CP2.3	155 ^{FR}	153 ^a , 154 ^b	153
RS2.4	const. ^{large}	32 ^{FR}	31 ^{a,b}	31	CP2.4	62 ^{LB}	41 ^a , 61 ^b	61

Failure mode: LB - beam local buckling, FR – beam flange fracture.

Second failure criterion (N_2): ^a 20 % strength degradation, ^b 20 % stiffness degradation.

As can be observed from Table 8 and Figs 39 and 40, for all specimens tested under the variable cyclic loading, 20 % strength and stiffness degradation observed in the second criterion were both met in the same cycle and thus proved to be more or less equally stringent. Two exceptions can be observed, i.e. CP1.1 and CP2.2. However, in both cases the strength and the stiffness degradation limit were reached in the two consecutive cycles (this might result from differences in the applied rotation amplitudes between both loading directions, see Fig. 39), and the two criteria still represent more or less equal limit. As already stated, the degradation of strength and stiffness evident from Fig. 29 and Figs 38 to 41 were a consequence of the beam local buckling in the plastic hinge zone immediately beyond the end of the strengthened connection.

Tables 9 and 10 present a summary of experimental response characteristics of all the test specimens. Beside information on the beam flexural overstrength $M_h^{max}/M_{pl,b}^{nom}$, the tables include values of maximum beam plastic rotations θ_{pl} ($\theta_{pl,1}$, $\theta_{pl,2}$, $\theta_{pl,3}$) and the corresponding cumulative beam plastic rotations $\Sigma\theta_{pl}$ ($\Sigma\theta_{pl,1}$, $\Sigma\theta_{pl,2}$, $\Sigma\theta_{pl,3}$) evaluated for the three selected failure criteria. Reported plastic joint rotations are evaluated with respect to the column centreline and represent the smaller absolute value obtained from positive and negative loading directions.

Preglednica 9: Povzetek eksperimentalnih rezultatov za skupino preizkušancev RS
 Table 9: Summary of experimental results for the RS group of specimens

Specimen group: RS1&RS2	Response characteristic							
	M_h^{max} (kNm)	$M_h^{max}/M_{pl,b}^{nom}$	θ_{pl} (rad)			$\Sigma\theta_{pl}$ (rad)		
			$\theta_{pl,1}$	$\theta_{pl,2}$	$\theta_{pl,3}$	$\Sigma\theta_{pl,1}$	$\Sigma\theta_{pl,2}$	$\Sigma\theta_{pl,3}$
RS1.1	215.2	1.25	0.071	0.036	0.054	1.505	0.626	0.829
RS1.2	218.3	1.27	0.074	0.036	0.055	1.832	0.531	0.877
RS1.3	192.8	1.12		0.006		1.728	1.640	1.640
RS1.4	210.2	1.22		0.021		2.167	0.930	1.930
RS2.1	177.7	1.36	0.076	0.041	0.055	2.044	0.852	1.264
RS2.2	175.7	1.35	0.078	0.044	0.056	2.138	0.921	1.344
RS2.3	149.5	1.15		0.006		2.305	2.191	2.212
RS2.4	165.1	1.27		0.017		2.018	1.942	1.942

Preglednica 10: Povzetek eksperimentalnih rezultatov za skupino preizkušancev CP
 Table 10: Summary of experimental results for the CP group of specimens

Specimen group: CP1&CP2	Response characteristic							
	M_h^{max} (kNm)	$M_h^{max}/M_{pl,b}^{nom}$	θ_{pl} (rad)			$\Sigma\theta_{pl}$ (rad)		
			$\theta_{pl,1}$	$\theta_{pl,2}$	$\theta_{pl,3}$	$\Sigma\theta_{pl,1}$	$\Sigma\theta_{pl,2}$	$\Sigma\theta_{pl,3}$
CP1.1	218.8	1.27	0.062	0.030	0.051	1.547	0.546	1.088
CP1.2	217.3	1.26	0.071	0.037	0.061	1.658	0.480	0.967
CP1.3	198.2	1.15		0.005		2.316	2.272	2.293
CP1.4	220.5	1.28		0.021		2.920	0.809	2.609
CP2.1	177.9	1.37	0.076	0.039	0.064	1.981	0.815	1.458
CP2.2	177.2	1.36	0.068	0.040	0.054	1.815	0.726	1.103
CP2.3	148.7	1.14		0.004		2.302	2.260	2.260
CP2.4	166.8	1.28		0.019		3.960	2.526	3.887

For all the eight specimens subjected to variable cyclic loading with stepwisely increasing loading amplitude plastic rotations $\theta_{pl,1}$ range between 0.062 and 0.078 rad without any significant difference between the two stiffened joint types, although the RS joints provided more uniform values than the CP joints. All $\theta_{pl,1}$ values obtained by a more compact small beam section IPE240 are larger than those obtained by large beam section IPE270.

Values of $\theta_{pl,2}$ vary from 0.48 to 0.59 of the corresponding plastic rotation at failure $\theta_{pl,1}$, with the values ($\theta_{pl,2}$) obtained by large beam profile being 10 % smaller compared to those obtained by small beam section, for both stiffened joint types.

Ratio $\theta_{pl,3}/\theta_{pl,1}$ varies between 0.72 and 0.86, with values obtained for the CP joints by about 12 % larger compared to values obtained by the RS joints, regardless of the beam profile.

Values of cumulative plastic rotations $\Sigma\theta_{pl,1}$ obtained from small beam profile vary between 1.815 and 2.138 rad and are significantly larger compared to those obtained by large beam section, which range from 1.505 to 1.832, for both RS and CP joints. Again, the reason for larger values of reported cumulative plastic rotations in case of small beam profile IPE240

compared to those obtained by large beam profile IPE270, can be attributed to larger LCF resistance of the more compact smaller beam cross-section of IPE240, which directly resulted in larger number of cycles to failure compared to beam profile IPE270, Fig. 40 and Table 8. The effect of the beam local buckling can also be observed in considerably reduced values of $\Sigma\theta_{pl,2}$ and $\Sigma\theta_{pl,3}$.

For a more detailed discussion on evaluation of accumulated plastic rotations in terms of LCF effects, emphasising the effect of both stiffened joint types in combination with both beam profiles, with different beam cross-section geometric characteristics, the reader may refer to Chapter 3.4.7.

Review on the applied loading histories for all eight specimens subjected to variable cyclic loading is presented in Tables 11 to 14 by means of measured total joint θ and total beam θ_b rotation amplitudes. In addition, corresponding relative values according to total joint θ_y and beam $\theta_{b,y}$ yield rotation are added.

The average value for all reported cycles of the same incremental step, for positive and negative loading direction, is provided. Reference to the applied nominal cyclic loading protocol is provided as well, with rotation amplitudes normalised according to the corresponding yield rotations. This enables an overview on the actual applied plastic loading histories in order to facilitate consistent comparison between the responses of the specimens. The reported cyclic loading amplitudes for a number of cycles in plastic range, see also Table 8, were used later on for a definition of loading history in numerical simulations, see Chapter 4.3.

The yield displacement of each specimen used in the report of actual loading histories, Tables 11 to 14, was determined according to one of the procedures provided in ECCS N°45 (ECCS, 1986). In addition, results from monotonic numerical FE simulations on the test specimens were used for higher accuracy, see Chapter 4.3.2.2.

Preglednica 11: Popis zgodovine obremenjevanja preizkušancev RS1.1 in RS1.2
Table 11: Loading history details for specimen RS1.1 and RS1.2

Loading protocol		Rotation amplitudes measured on specimen*							
mod. ECCS N°45 1986 [§]		RS1.1				RS1.2			
n° cycles	θ	θ [rad]	θ/θ_y	θ_b [rad]	$\theta_b/\theta_{b,y}$	θ [rad]	θ/θ_y	θ_b [rad]	$\theta_b/\theta_{b,y}$
1	$\frac{1}{4} \theta_y$	0.0033	0.26	0.0023	0.26	0.0032	0.27	0.0025	0.28
1	$\frac{1}{2} \theta_y$	0.0068	0.54	0.0046	0.51	0.0065	0.55	0.0050	0.55
1	$\frac{3}{4} \theta_y$	0.0106	0.85	0.0070	0.78	0.0099	0.85	0.0076	0.85
3	θ_y	0.016	1.27	0.011	1.25	0.016	1.33	0.013	1.44
3	$2 \theta_y$	0.032	2.60	0.027	2.96	0.032	2.72	0.029	3.20
3	$3 \theta_y$	0.049	3.94	0.043	4.83	0.049	4.15	0.045	5.08
3	$4 \theta_y$	0.065	5.28	0.061	6.84	0.065	5.59	0.063	7.05
3^(1,2) ◊	$5 \theta_y$	0.082 ⁽¹⁾	6.63	0.078 ⁽¹⁾	8.77	0.082 ⁽²⁾	7.00	0.080 ⁽²⁾	8.96

[§]) For the definition of the applied loading protocol, see Chapter 3.3.4.

^{*}) Average rotation amplitude value from positive and negative loading directions of all cycles from the same loading step is reported.

[◊]) Consecutive cycle of particular loading amplitude level with the onset of failure for both specimens.

Preglednica 12: Popis zgodovine obremenjevanja preizkušancev CP1.1 in CP1.2
 Table 12: Loading history details for specimen CP1.1 and CP1.2

Loading protocol		Rotation amplitudes measured on specimen*							
ANSI/AISC 341-10 [§]		CP1.1				CP1.2			
n° cycles	θ [rad]	θ [rad]	θ/θ_y	θ_b [rad]	$\theta_b/\theta_{b,y}$	θ [rad]	θ/θ_y	θ_b [rad]	$\theta_b/\theta_{b,y}$
6	0.00375	0.0033	0.23	0.0023	0.26	0.032	0.24	0.0026	0.29
6	0.005	0.0044	0.31	0.0027	0.31	0.0044	0.32	0.0034	0.39
6	0.0075	0.0067	0.47	0.0039	0.45	0.0068	0.50	0.0052	0.59
4	0.01	0.0091	0.64	0.0049	0.56	0.0091	0.67	0.0070	0.80
2	0.015	0.013	0.98	0.007	0.84	0.014	1.01	0.011	1.21
2	0.02	0.019	1.32	0.011	1.27	0.019	1.36	0.015	1.73
2	0.03	0.029	2.00	0.020	2.29	0.028	2.07	0.024	2.80
2	0.04	0.038	2.70	0.029	3.34	0.038	2.79	0.034	3.90
2	0.05	0.048	3.40	0.039	4.49	0.048	3.54	0.045	5.13
2	0.06	0.058	4.09	0.050	5.78	0.058	4.27	0.055	6.36
2	0.07	0.068	4.80	0.062	7.06	0.068	5.00	0.066	7.55
2 ^(1,1) ◊	0.08	0.078 ⁽¹⁾	5.50	0.072 ⁽¹⁾	8.29	0.078 ⁽¹⁾	5.73	0.076 ⁽¹⁾	8.73

[§]) For the definition of the applied loading protocol, see Chapter 3.3.4.

^{*)} Average rotation amplitude value from positive and negative loading directions of all cycles from the same loading step is reported.

[◊]) Consecutive cycle of particular loading amplitude level with the onset of failure for both specimens.

Preglednica 13: Popis zgodovine obremenjevanja preizkušancev RS2.1 in RS2.2
 Table 13: Loading history details for specimen RS2.1 and RS2.2

Loading protocol		Rotation amplitudes measured on specimen*							
ANSI/AISC 341-10		RS2.1				RS2.2			
n° cycles	θ [rad]	θ [rad]	θ/θ_y	θ_b [rad]	$\theta_b/\theta_{b,y}$	θ [rad]	θ/θ_y	θ_b [rad]	$\theta_b/\theta_{b,y}$
6	0.00375	0.0034	0.23	0.0023	0.22	0.0033	0.24	0.0023	0.22
6	0.005	0.0046	0.31	0.0029	0.28	0.0044	0.33	0.0030	0.29
6	0.0075	0.0071	0.48	0.0043	0.42	0.0069	0.51	0.0047	0.46
4	0.01	0.0095	0.65	0.0054	0.52	0.0094	0.69	0.0064	0.62
2	0.015	0.014	0.97	0.008	0.75	0.014	1.04	0.010	0.95
2	0.02	0.019	1.30	0.012	1.11	0.019	1.40	0.014	1.38
2	0.03	0.029	1.97	0.021	1.99	0.029	2.12	0.024	2.28
2	0.04	0.039	2.65	0.030	2.88	0.039	2.85	0.033	3.20
2	0.05	0.048	3.33	0.039	3.80	0.048	3.58	0.043	4.14
2	0.06	0.059	4.03	0.050	4.81	0.059	4.33	0.054	5.17
2	0.07	0.069	4.72	0.062	5.95	0.069	5.08	0.065	6.23
2	0.08	0.079	5.39	0.072	6.99	0.078	5.79	0.075	7.22
2 ^(1,1) ◊	0.09	0.088 ⁽¹⁾	6.05	0.083 ⁽¹⁾	7.99	0.088 ⁽¹⁾	6.49	0.085 ⁽¹⁾	8.18

^{*)} Average rotation amplitude value from positive and negative loading directions of all cycles from the same loading step is reported.

[◊]) Consecutive cycle of particular loading amplitude level with the onset of failure for both specimens.

Preglednica 14: Popis zgodovine obremenjevanja preizkušancev CP2.1 in CP2.2
Table 14: Loading history details for specimen CP2.1 and CP2.2

Loading protocol		Rotation amplitudes measured on specimen*							
ANSI/AISC 341-10		CP2.1				CP2.2			
n° cycles	θ [rad]	θ [rad]	θ/θ_y	θ_b [rad]	$\theta_b/\theta_{b,y}$	θ [rad]	θ/θ_y	θ_b [rad]	$\theta_b/\theta_{b,y}$
6	0.00375	0.0031	0.21	0.0017	0.17	0.0033	0.23	0.0023	0.22
6	0.005	0.0043	0.29	0.0024	0.23	0.0043	0.31	0.0029	0.29
6	0.0075	0.0068	0.45	0.0035	0.35	0.0068	0.49	0.0046	0.44
4	0.01	0.0092	0.62	0.0045	0.44	0.0092	0.66	0.0062	0.60
2	0.015	0.014	0.93	0.007	0.69	0.014	1.00	0.009	0.93
2	0.02	0.019	1.25	0.011	1.06	0.019	1.34	0.014	1.34
2	0.03	0.029	1.90	0.020	1.94	0.029	2.04	0.023	2.25
2	0.04	0.038	2.56	0.029	2.85	0.038	2.74	0.032	3.17
2	0.05	0.048	3.22	0.039	3.77	0.048	3.45	0.042	4.12
2	0.06	0.058	3.90	0.049	4.79	0.059	4.18	0.053	5.18
2	0.07	0.069	4.58	0.061	5.91	0.069	4.90	0.064	6.27
2	0.08	0.079	5.24	0.072	7.00	0.078⁽²⁾	5.60	0.075⁽²⁾	7.31
2^(1,0)◇	0.09	0.088⁽¹⁾	5.88	0.082⁽¹⁾	8.01				

*) Average rotation amplitude value from positive and negative loading directions of all cycles from the same loading step is reported.

◇) Consecutive cycle of particular loading amplitude level with the onset of failure for both specimens.

The response of all the eight specimens tested with variable cyclic loading is described in detail below in terms of joint strength and stiffness variation throughout the actual applied loading history, Figs 42 to 45. Observations during particular test, giving information on cyclic behaviour details, such as the instance and location of crack and the beam local buckling onset, are reported as well and are gathered below to manage the final comparison between the responses of the specimens, Tables 15 and 16.

In general, cyclic plasticity of steel material in the subsequent cycles depends upon the strain history already applied in the previous cycles (strain memory effect). Indeed, plastic cyclic response of steel members may strongly be affected by the local buckling effects in the plastic hinge zone, the onset of which depends on the loading history applied. Since two different loading protocols were used (and not both on the same specimens), see Table 7, the detailed description of cyclic response of tests is presented to highlight the relation between the actual load applied and the cyclic results obtained.

The response of the same two joints, of four different designed test specimens RS1, RS2, CP1 and CP2, tested with nominally the same, either modified ECCS or ANSI/AISC loading protocol, is presented in the same figure to allow direct comparison between the same test repetitions.

To this end, analysis of each of the eight specimen responses is presented in Figs 42 to 45. Completed cycles in the plastic range are presented. First, information is provided on actual applied loading protocol in terms of total beam rotation normalised according to the beam yield rotation $\theta_b/\theta_{b,y}$. The second and the third parts of each figure present distribution of maximum moment M_c , and tangent modulus α of the unloading phase of a hysteresis curve, Fig. 41b, determined for the subsequent loading cycles. Both parameters are evaluated for

positive and negative loading directions. In addition, relative change of M_c and α between the two consecutive cycles is presented:

$$\begin{aligned}\Delta |M_c^{\max}|^{(i,i-1)} &= |M_c^{\max}|^{(i)} - |M_c^{\max}|^{(i-1)}, \\ \Delta |\alpha|^{(i,i-1)} &= |\alpha|^{(i)} - |\alpha|^{(i-1)}.\end{aligned}\tag{21}$$

The twofold representation of M_c and α distributions allows a better insight into the history of parameter variation and the best way to instance the failure events. For that purpose combined plot of the two curves with the same domain but different ranges was applied, where different scales on the primary and secondary ordinate axes are used so that their ranges appear to be the same.

Before going into a detailed report, it should be mentioned that in general, somewhat smaller realized total beam rotation θ_b (and consequently smaller $\theta_b/\theta_{b,y}$ ratio) and joint stiffness α can be observed for all four specimens tested without the presence of the column compressive axial load (RS1.1, RS2.1, CP1.1 and CP2.1) compared with other four tests (RS1.2, RS2.2, CP1.2 and CP2.2), where full level of column axial force was applied, Tables 11 to 14 and Figs 42 to 45. Apparently, vertical column compressive load resulted also in stabilisation of column lateral displacements, which further resulted in somewhat larger portion of applied absolute displacement at the beam tip that was induced to the specimen.

Loading histories for particular specimens presented in Figs 42 to 45 comprise rotation of the beam normalised with its yield value in order to emphasise the dependence of the beam local buckling evolution upon the beam (plastic) rotations.

In case of RS1.1 and RS1.2 specimens, the first flange local buckling was observed during the first cycle of 4.8 and 5.1 $\theta_b/\theta_{b,y}$ amplitude (7th cycle). Through the next cycle flange local buckling amplitudes progressed with the onset of clearly seen combined flange and flange induced web local buckling in the second cycle of 4.8 and 5.1 $\theta_b/\theta_{b,y}$ amplitude (8th cycle). The strength degradation from this cycle on is clearly seen from Fig. 42 for both specimens. Although the stiffness degradation is present from the early start of the plastic range history, increased stiffness softening can be noticed after the onset of the beam local buckling in the 8th cycle.

During the first cycle of 4.8 and 5.1 $\theta_b/\theta_{b,y}$ amplitude (7th cycle), crack was detected at fillet weld HAZ at the end of the rib-stiffener in the beam flange mid width in case of both specimens. With the progress in stepwise incrementally increasing cyclic loading the appeared crack widen and progressed around the periphery of the rib tip fillet weld. Additional bending tension strains resulting from locally buckled beam flange caused even more increased intensity of ductile crack propagation. However, this crack was not detrimental for the joint response in case of both specimens, since the most strained plastic zone moved away due to the progress of the beam local buckling. Ductile cracks in the most buckled part of the beam flange were observed in the first cycle of 6.8 and 7.1 $\theta_b/\theta_{b,y}$ amplitude (10th cycle), and they progressed across the upper beam flange till the specimen's ultimate failure: during the second (loading phase in the negative excursion – second half of the cycle) and the third cycle (unloading phase in the positive excursion – first half of the cycle) of 8.8 and 9.0 $\theta_b/\theta_{b,y}$ amplitude (14th and 15th cycle) for RS1.1 and RS1.2, respectively, see Figs 30 and 31.

Under large plastic rotations ($\theta_b/\theta_{b,y} > 6$) flexural resistance of the beams decreased as a consequence of increase of beam local buckling effects, and it progressively intensified even due to ductile cracking of steel material at locally most buckled part on the beam flange. Due to the simultaneous increase of local buckling and ductile cracking of the beam flanges, it was

difficult to recognise the undermining effect of solely flange ductile cracking on the strength and stiffness degradation. Nevertheless, the effect of ultimate crack propagation on somewhat increased strength and stiffness degradation in the last reported cycle can be seen from Fig. 42b and c.

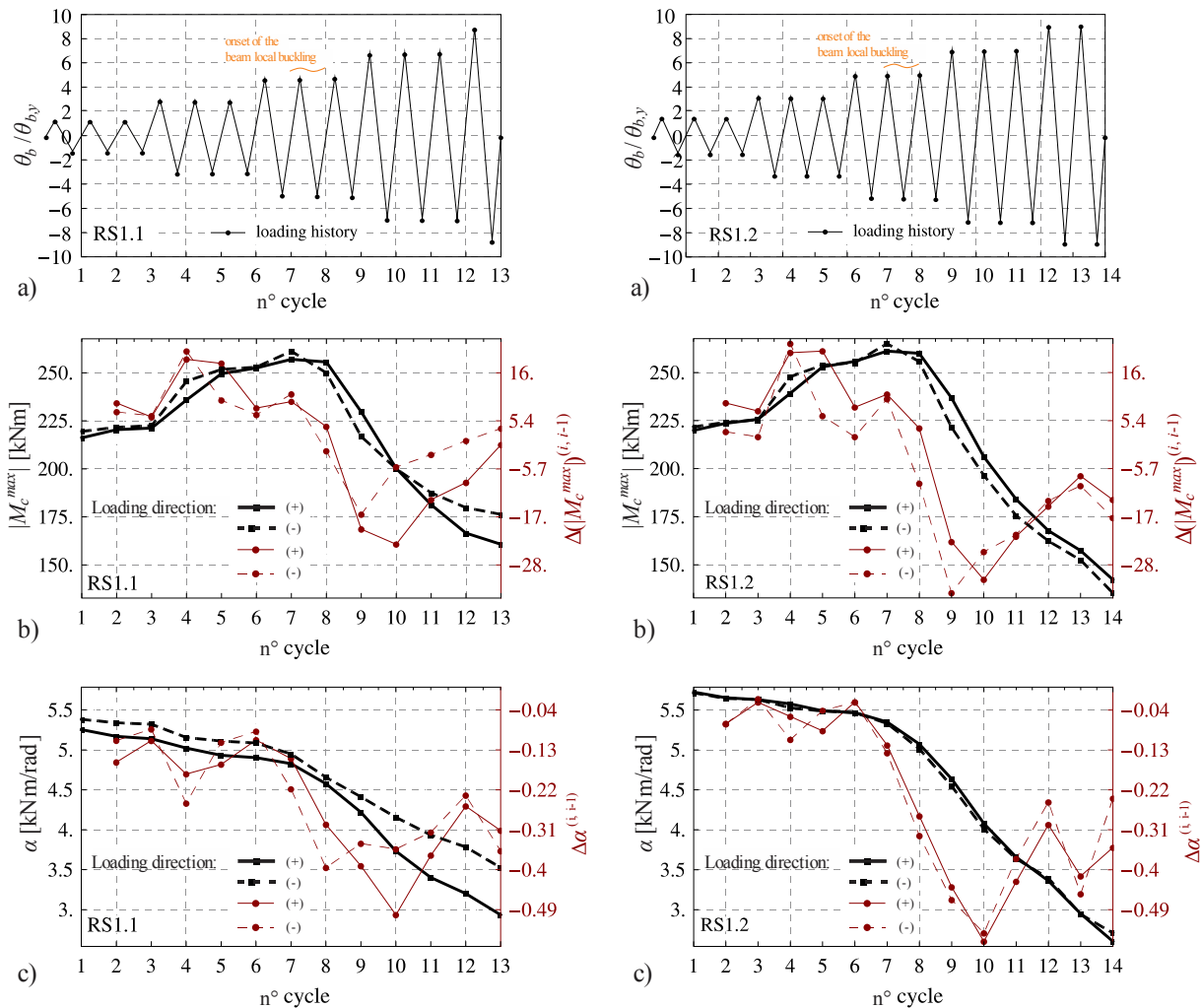


Fig. 42: Response of specimens RS1.1 and RS1.2: a) applied loading history, b) distribution of maximum moment per cycle, c) distribution of complete joint stiffness per cycle

Slika 42: Odziv preizkušancev RS1.1 in RS1.2: a) dejanska zgodovina obremenjevanja, b) potek največjih momentov v posameznih ciklih, c) potek togosti celotnega spoja v posameznih ciklih

In case of specimens CP1.1 and CP1.2, the first flange local buckling was observed during the first cycle of 4.5 and 3.9 $\theta_b/\theta_{b,y}$ amplitude (9th and 7th cycles for CP1.1 and CP1.2, respectively). Through the next cycle flange local buckling amplitudes progressed with the onset of clearly seen combined flange and flange induced web local buckling in the second cycle of 4.5 and 3.9 $\theta_b/\theta_{b,y}$ amplitude (10th and 8th cycles for CP1.1 and CP1.2, respectively). The strength degradation from this cycle on is clearly seen from Fig. 43 for both specimens. Although the stiffness degradation is present from the early start of the plastic range history, increased stiffness softening can be noticed after the onset of the beam local buckling in the reported cycles for specimens CP1.1 and CP1.2.

During loading till the onset of the beam local buckling, where plastic strain concentration moved in the locally most buckled region of the plastic hinge zone, strain concentrations were observed in the beam flange region just behind the transverse fillet weld at the end of the cover plates. However, no cracks at all were observed in this region in either of the specimens. Ductile cracks on the most buckled part of the beam flange were observed in the

first cycle of 5.8 and 6.4 $\theta_b/\theta_{b,y}$ amplitude (11th cycle), and they progressed width-wise the upper and bottom beam flange, respectively for CP1.1 and CP1.2, till the specimen ultimate failure during the second cycle (negative excursion – second half of the cycle, positive excursion – first half of the cycle) of 8.3 and 8.7 $\theta_b/\theta_{b,y}$ amplitude (16th cycle) for specimens CP1.1 and CP1.2, respectively, see Figs 34 and 35.

Under large plastic rotations ($\theta_b/\theta_{b,y} > 5$) flexural resistance of the beams decreased as a consequence of progress of the beam local buckling, and it progressively intensified even due to ductile cracking of steel material at locally most buckled part on the beam flange. Due to the simultaneous increase of local buckling and ductile cracking of the beam flanges, it is difficult to recognise the undermining effect of solely flange ductile cracking on the strength and stiffness degradation, Fig. 43.

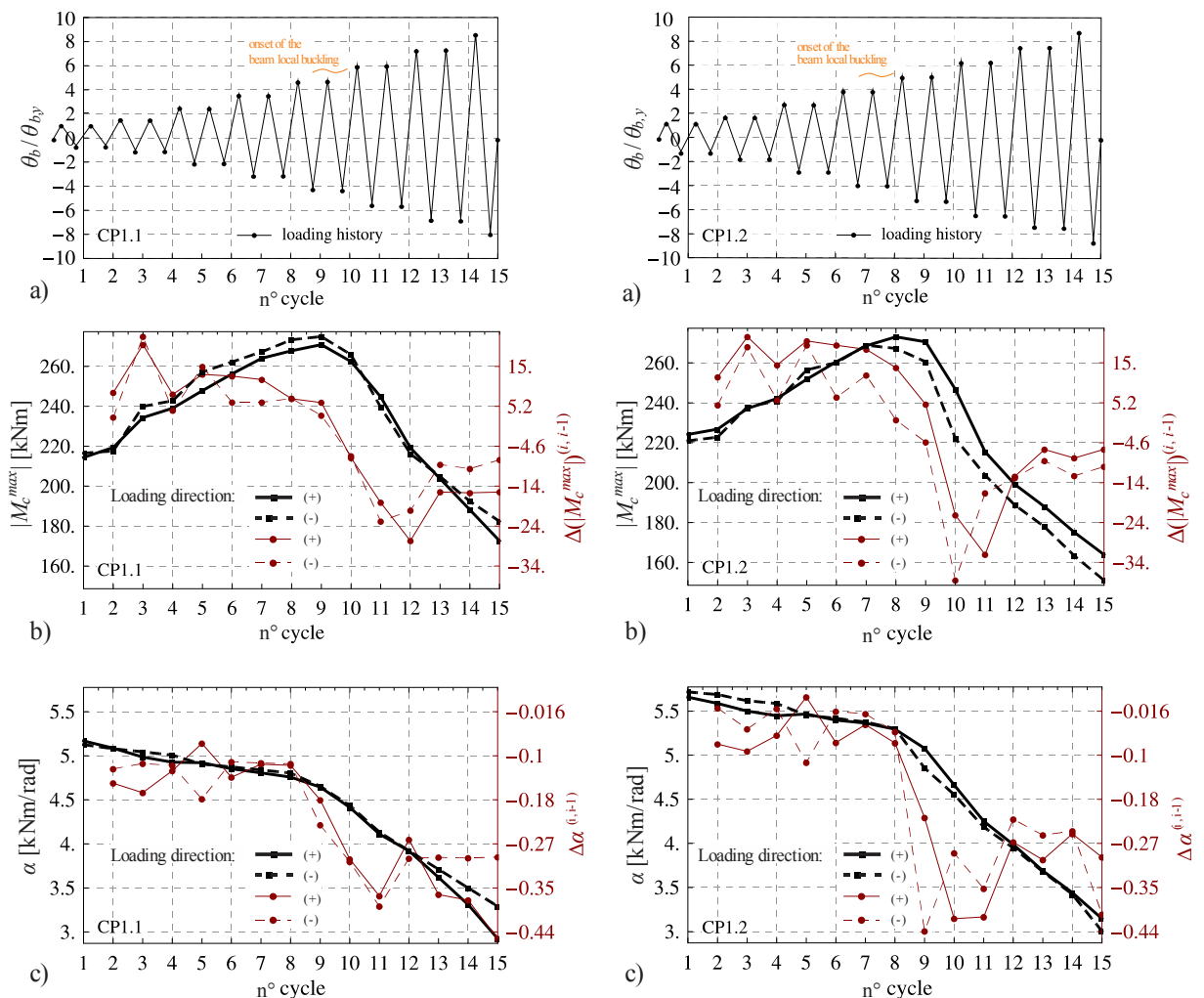


Fig. 43: Response of specimens CP1.1 and CP1.2: a) applied loading history, b) distribution of maximum moment per cycle, c) distribution of complete joint stiffness per cycle

Slika 43: Odziv preizkušancev CP1.1 in CP1.2: a) dejanska zgodovina obremenjevanja, b) potek največjih momentov v posameznih ciklih, c) potek togosti celotnega spoja v posameznih ciklih

In case of specimens RS2.1 and RS2.2, the first flange local buckling was observed during the first cycle of 3.8 and 4.1 $\theta_b/\theta_{b,y}$ amplitude (9th cycle). Through the next cycle flange local buckling amplitudes progressed with the onset of clearly seen combined flange and flange induced web local buckling in the first cycle of 4.8 $\theta_b/\theta_{b,y}$ amplitude (11th cycle) for RS2.1 and in the second cycle of 4.1 $\theta_b/\theta_{b,y}$ amplitude (10th cycle) for RS2.2. The strength degradation from this cycle on is clearly seen from Fig. 44 for both specimens. Although the stiffness degradation is present from the early start of the plastic range history, increased

stiffness softening can be noticed after the onset of the beam local buckling in the 11th and 10th cycles, for RS2.1 and RS2.2, respectively.

During the first cycle of 4.8 and 5.2 $\theta_b/\theta_{b,y}$ amplitude (11th cycle), crack was detected at weld HAZ at the end of the rib-stiffener fillet weld in the beam flange mid width in case of both specimens. With the progress in stepwise increasing cyclic loading the appeared crack widened and progressed around periphery of the rib tip fillet weld. Additional bending tension strains resulting from locally buckled beam flange caused even more increased intensity of ductile crack propagation. However, this crack was not detrimental for the joint response in case of both specimens, since the most strained plastic zone moved away due to the progress of the beam local buckling. Ductile cracks on the most buckled part of the beam flange were observed in the first cycle of 6.0 and 6.2 $\theta_b/\theta_{b,y}$ amplitude (13th cycle), and they progressed across the upper/bottom beam flange till the specimen ultimate failure during the second cycle (positive excursion – first half of the cycle) of 8.0 and 8.2 $\theta_b/\theta_{b,y}$ amplitude (18th cycle) for specimens RS2.1 and RS2.2, respectively, see Figs 32 and 33.

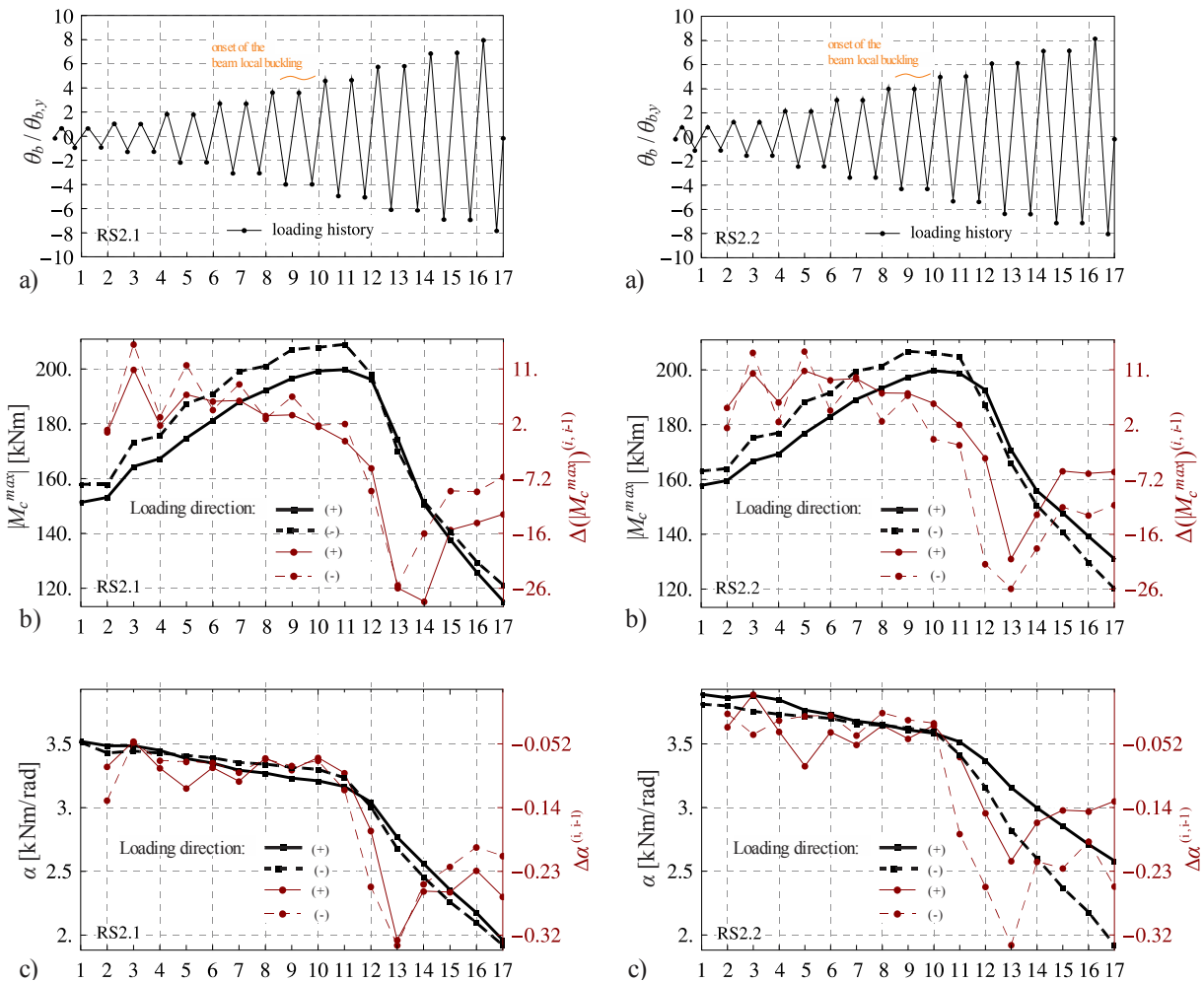


Fig. 44: Response of specimens RS2.1 and RS2.2: a) applied loading history, b) distribution of maximum moment per cycle, c) distribution of complete joint stiffness per cycle

Slika 44: Odziv preizkušancev RS2.1 in RS2.2: a) dejanska zgodovina obremenjevanja, b) potek največjih momentov v posameznih ciklih, c) potek togosti celotnega spoja v posameznih ciklih

Under large plastic rotations ($\theta_b/\theta_{b,y} > 6$) flexural resistance of the beams decreased as a consequence of increase in beam local buckling, and it progressively intensified even due to ductile cracking of steel material at locally most buckled part on the beam flange. Due to the simultaneous increase of local buckling and ductile cracking of the beam flanges, it is difficult

to recognise the undermining effect of solely flange ductile cracking on the strength and stiffness degradation, Fig. 44.

In case of specimens CP2.1 and CP2.2, the first flange local buckling was observed during the first cycle of 4.8 and 4.1 $\theta_b/\theta_{b,y}$ amplitude (11th and 9th cycles), respectively. Through the next cycle flange local buckling amplitudes progressed with the onset of clearly seen combined flange and flange induced web local buckling in the second cycle of 4.8 and 4.1 $\theta_b/\theta_{b,y}$ amplitude (12th and 10th cycles) for CP1.1 and CP1.2, respectively. The strength degradation from this cycle on is clearly seen from Fig. 45 for both specimens. Although the stiffness degradation was present from the early start of the plastic range history, increased stiffness softening can be seen after the onset of the beam local buckling in the reported cycles for specimens CP1.1 and CP1.2.

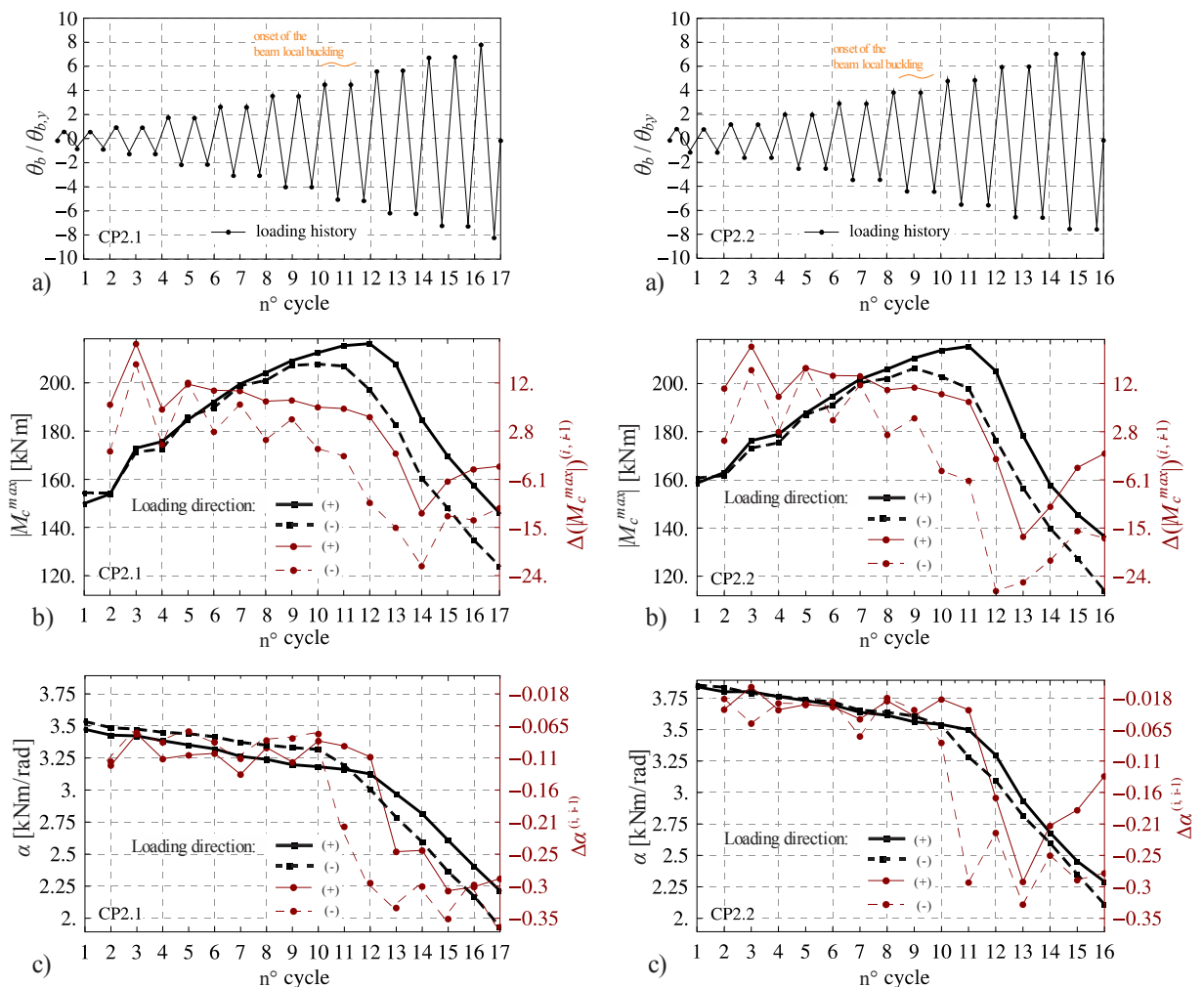


Fig. 45: Response of specimens CP2.1 and CP2.2: a) applied loading history, b) distribution of maximum moment per cycle, c) distribution of complete joint stiffness per cycle

Slika 45: Odziv preizkušancev CP2.1 in CP2.2: a) dejanska zgodovina obremenjevanja, b) potek največjih momentov v posameznih ciklih, c) potek togosti celotnega spoja v posameznih ciklih

From the distribution of maximum moment per cycle presented in Fig. 45b, considerable difference between moment values from positive and negative loading directions can be observed in case of both specimens. The difference starts to grow just before the strength degradation caused by the beam local buckling. Not so large deviation in resistance between positive and negative loading directions from other test results, either from RS and CP specimens, can be observed (with the exception of both RS2 specimens, where the difference originates already in the first cycles due to the asymmetry in loading amplitudes).

The reason for the deviation in case of specimens CP2.1 and CP2.2 comes from unique buckled shape of the top beam flange. Namely, the top beam flange, which was exposed first in compression, buckled in a way to produce higher mode double wave buckling shape just behind the tip of the cover plate, thus producing larger moment resistance for positive (upwards) load excursions. In both specimens lower flange buckled in a typical single wave shape and at larger distance from the end of strengthened part of the beam, Figs 36, 37 and 46.

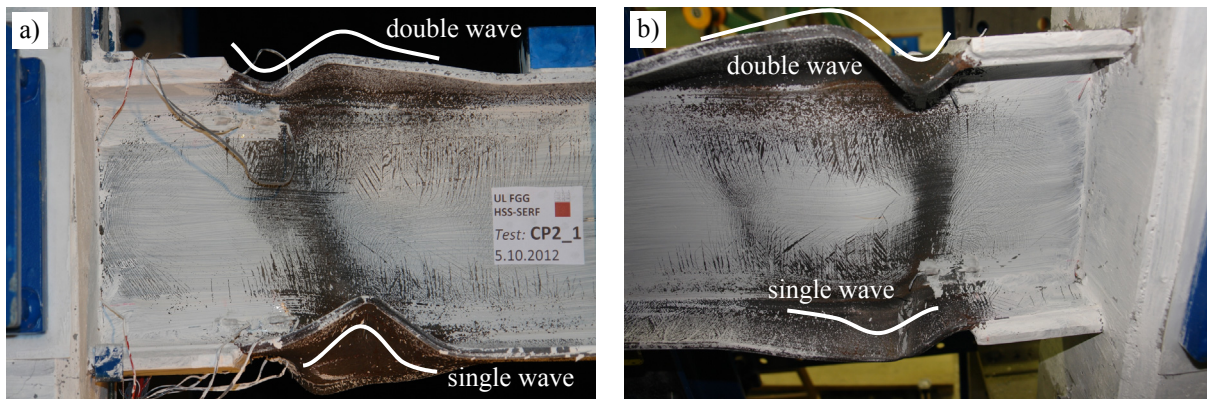


Fig. 46: Detail of top and bottom beam flange local buckling shape for specimens CP2: a) CP2.1 and b) CP2.2
 Slika 46: Detajl lokalnega izbočenja zgornje in spodnje pasnice prečke spojev CP2: a) CP2.1 in b) CP2.2

Possible explanation for this is twofold and is discussed below. In the first cycle of plastic range, compression force in the top beam flange, of previously strain unhardened steel material, produced plastic deformations in the region just behind the end of the cover-plate. In the subsequent compression loadings of the flange, plastic strain zone was propagating (due to the strain hardening of steel material) along the beam away from the end of strengthened region. Strain hardened material pushed plastic deformations into the region of unstrengthened material just behind the end of the plastic strain zone from the previous cycle. However, at certain extent ($\approx 1.5 h_b$, as observed from the tests) the spreading of plastic zone on the beam stopped, and due to the moment gradient as a result of non-uniform beam bending, plastic straining moved again toward the flange region just behind the end of the cover-plate.

Similar phenomenon occurs for the lower beam flange with a distinction that in the first plastic cycle the flange is hardened in tension, which results in subsequent compression plastic straining to be more distant from the end of the cover-plate than in case of the upper flange.

For a complete explanation of the phenomenon observed, consideration has to be paid also to material and beam flange geometric imperfections, which affect the occurrence of the beam local buckling, as discussed in the text below.

After the spread of plastic strains lengthwise the beam plastic hinge zone in cycles with moderate rotation amplitudes ($\theta_b/\theta_{b,y} < 3$), flange local buckling occurred in the subsequent cycles with larger rotation amplitudes. At the stage of moderate loading amplitudes, plastic deformations on the flange, in combination with initial imperfections, act as imperfection mode for compression loadings in the subsequent cycles. In case of both CP1 specimens (CP1.1 and CP1.2) the top beam flange buckled in a typical single-wave shape, while slightly smaller width-to-thickness flange ratio ($c/t = 4.8$ for IPE270 compared to $c/t = 4.3$ for IPE240) of a more compact beam flange in case of both CP2 specimens (CP2.1 and CP2.2) resulted in double-wave-mode buckling, producing larger moment resistance at positive load excursions.

For complete information of the phenomenon the reader may refer also to Chapter 4.3.3.4, where additional discussion on local strain response in the plastic hinge region of the beam is given.

No such phenomenon was observed in any case of specimens RS2, since flanges are not constrained across their full width as in case of CP joint configuration.

During loading till the onset of the beam local buckling, where plastic strain concentration moved in the locally most buckled region of the plastic hinge zone in the beam, strain concentrations were observed in the beam flange region just behind the transverse fillet weld at the end of the cover plates. In spite of increased local plastic strain demand on the transverse fillet weld at the end of the cover plate, due to the increased local flange bending, Fig. 46, no obvious cracks were observed in this region in case of both specimens CP2.1 and CP2.2. Ductile cracks on the most buckled part of the beam flange were observed in the first cycle of 5.9 and 6.3 $\theta_b/\theta_{b,y}$ amplitude (13th cycle) for CP2.1 and CP2.2, respectively, and they progressed across the bottom beam flange, till the specimen ultimate failure during the second and the first cycles of 8.0 and 7.3 $\theta_b/\theta_{b,y}$ amplitude (18th and 17th cycle), for specimens CP1.1 and CP1.2, see Figs 36 and 37.

Under large plastic rotations ($\theta_b/\theta_{b,y} > 5$) flexural resistance of the beams decreased as a consequence of increase in beam local buckling, and it progressively intensified even due to ductile cracking of steel material at locally most buckled part on the beam flange. Due to the simultaneous increase of local buckling and ductile cracking of the beam flanges, it is difficult to recognise the undermining effect of solely flange ductile cracking on the strength and stiffness degradation, Fig. 45.

Reported response of all the eight specimens tested under variable cyclic loading with stepwisely increasing loading protocol is summarized in Tables 15 and 16.

The instance and location of the onset of the beam local buckling, first crack initiation and the ultimate failure are reported. The instance of particular event is described, e.g. as 4.8(+) $\theta_b/\theta_{b,y}$, 2, 8, which indicates that an event occurred in the positive excursion of 4.8 $\theta_b/\theta_{b,y}$ amplitude, during the second cycle of the current amplitude, in 8th cycle of complete inelastic loading history. Location of the first crack initiation is stated, no matter if it ultimately caused specimen's failure or not.

The potential primary cause of failure is considered to be either fracture as a result of the extension of ductile cracks initiated at the end of the stiffened region, or ductile fracture due to the progress of flange and web local buckling.

Preglednica 15: Popis cikličnega odziva skupine preizkušancev RS
 Table 15: Cyclic response details for RS group of specimens

Specimen	Instance ^{*)} and location of described event			Failure mode
	beam local buckling	first crack initiation	ultimate failure	
RS1.1	$4.8 \cdot \theta_b / \theta_{b,y}$, 2, 8	<ul style="list-style-type: none"> ▪ $4.8 \cdot \theta_b / \theta_{b,y}$, 1, 7; weld HAZ at the end of rib stiffener (not detrimental) ▪ $6.8 \cdot \theta_b / \theta_{b,y}$, 1, 10; locally most buckled part of the bottom and top beam flange 	$8.8^{(-)} \cdot \theta_b / \theta_{b,y}$, 2, 14; beam top flange	Beam local buckling followed by the beam upper flange ductile fracture
RS1.2	$5.1 \cdot \theta_b / \theta_{b,y}$, 2, 8	<ul style="list-style-type: none"> ▪ $5.1 \cdot \theta_b / \theta_{b,y}$, 1, 7; weld HAZ at the end of rib stiffener (not detrimental) ▪ $7.1 \cdot \theta_b / \theta_{b,y}$, 1, 10; locally most buckled part of the bottom and top beam flange 	$9.0^{(+)} \cdot \theta_b / \theta_{b,y}$, 3, 15; beam top flange	Beam local buckling followed by the beam upper flange ductile fracture
RS2.1	$4.8 \cdot \theta_b / \theta_{b,y}$, 1, 11	<ul style="list-style-type: none"> ▪ $4.8 \cdot \theta_b / \theta_{b,y}$, 1, 11; weld HAZ at the end of rib stiffener (not detrimental) ▪ $6.0 \cdot \theta_b / \theta_{b,y}$, 1, 13; locally most buckled part of the bottom and top beam flange 	$8.0^{(-)} \cdot \theta_b / \theta_{b,y}$, 2, 18; beam top flange	Beam local buckling followed by the beam upper flange ductile fracture
RS2.2	$4.1 \cdot \theta_b / \theta_{b,y}$, 2, 10	<ul style="list-style-type: none"> ▪ $5.2 \cdot \theta_b / \theta_{b,y}$, 1, 11; weld HAZ at the end of rib stiffener (not detrimental) ▪ $6.2 \cdot \theta_b / \theta_{b,y}$, 1, 13; locally most buckled part of the bottom and top beam flange 	$8.2^{(+)} \cdot \theta_b / \theta_{b,y}$, 2, 18; beam bottom flange	Beam local buckling followed by the beam upper flange ductile fracture

^{*)} Instance of reported event described with: rotation amplitude ($\theta_b / \theta_{b,y}$), consecutive cycle at the current plastic rotation amplitude, consecutive cycle in complete plastic loading range.

Preglednica 16: Popis cikličnega odziva skupine preizkušancev CP
 Table 16: Cyclic response details for CP group of specimens

Specimen	Instance ^{*)} and location of described event			Failure mode
	beam local buckling	first crack initiation	ultimate failure	
CP1.1	$4.5 \cdot \theta_b / \theta_{b,y}$, 2, 10	$5.8 \cdot \theta_b / \theta_{b,y}$, 1, 11; locally most buckled part of the bottom and top beam flange	$8.3^{(-)} \cdot \theta_b / \theta_{b,y}$, 2, 16; beam top flange	Beam local buckling followed by the beam upper flange ductile fracture
CP1.2	$3.9 \cdot \theta_b / \theta_{b,y}$, 2, 8	$6.4 \cdot \theta_b / \theta_{b,y}$, 1, 11; locally most buckled part of the bottom and top beam flange	$8.7^{(+)} \cdot \theta_b / \theta_{b,y}$, 2, 16; beam bottom flange	Beam local buckling followed by the beam upper flange ductile fracture
CP2.1	$4.8 \cdot \theta_b / \theta_{b,y}$, 2, 12	$5.9 \cdot \theta_b / \theta_{b,y}$, 1, 13; locally most buckled part of the bottom and top beam flange	$8.0^{(+)} \cdot \theta_b / \theta_{b,y}$, 2, 18; beam top flange	Beam local buckling followed by the beam upper flange ductile fracture
CP2.2	$4.1 \cdot \theta_b / \theta_{b,y}$, 2, 10	$6.3 \cdot \theta_b / \theta_{b,y}$, 1, 13; locally most buckled part of the bottom and top beam flange	$7.3^{(+)} \cdot \theta_b / \theta_{b,y}$, 1, 17; beam bottom flange	Beam local buckling followed by the beam upper flange ductile fracture

^{*)} Instance of reported event described with: rotation amplitude ($\theta_b / \theta_{b,y}$), consecutive cycle at the current plastic rotation amplitude, consecutive cycle in complete plastic loading range.

3.4.3 Constant amplitude cyclic tests

The response of the other eight specimens tested under constant amplitude cyclic loading in combination with the full level of compressive column axial force is shown in Fig. 47 for the small joint rotation amplitude of $\theta = 0.019$ rad (35 mm) and in Fig. 48 for the large joint rotation amplitude of $\theta = 0.033$ rad (60 mm).

All the eight specimens tested under constant amplitude cyclic loading revealed good and stable hysteretic response.

With systematically chosen test parameters, taking into account the two different values of constant amplitude loading (small and large) in combination with the two different beam cross-sections (IPE240 and IPE270) for each joint type (RS and CP), two distinct types of LCF response, discussed below, were obtained.

As it was planned by the selection of amplitude for constant loading protocol, none of the four specimens tested with the small constant amplitude, RS1.3, RS2.3, CP1.3, CP2.3, revealed any beam local buckling prior to the final LCF failure.

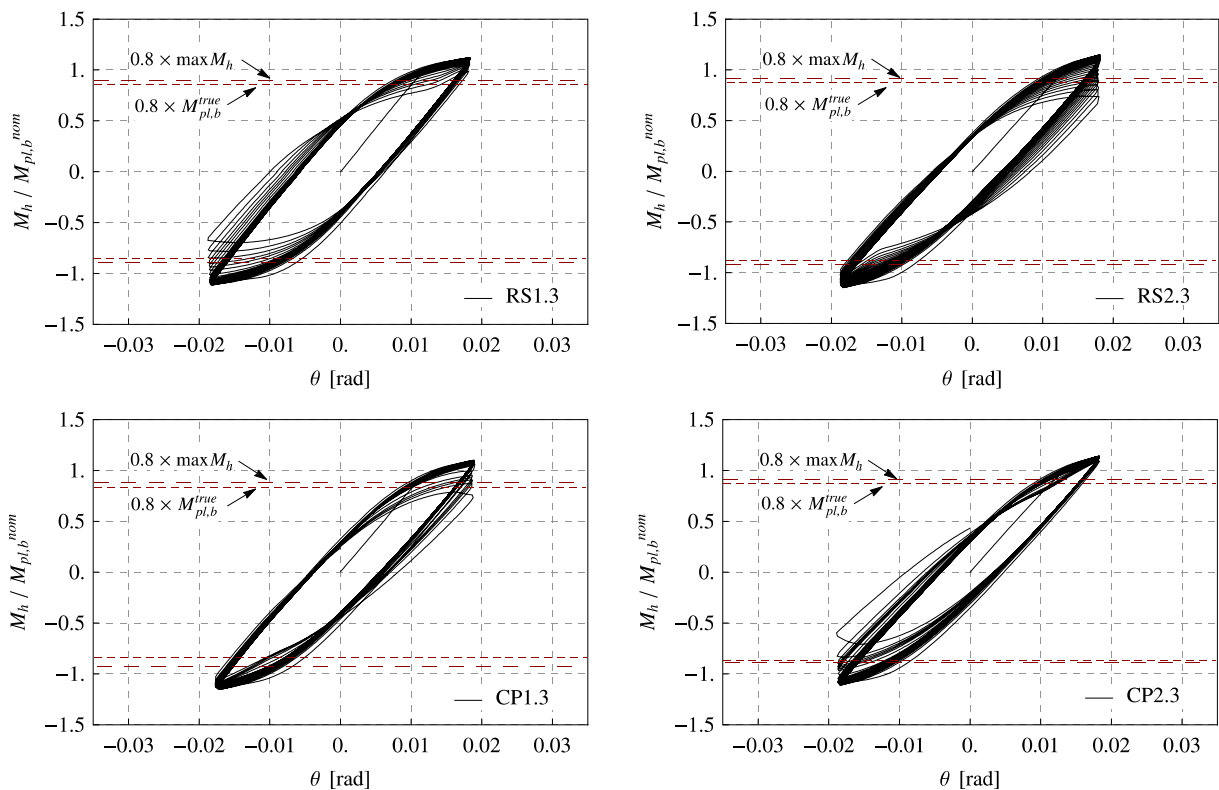


Fig. 47: Normalized moment M_h versus total joint rotation θ for constant amplitude cyclic tests, small amplitude
Slika 47: Normiran moment M_h v odvisnosti od celotne rotacije spoja θ za teste z malo konstantno amplitudo

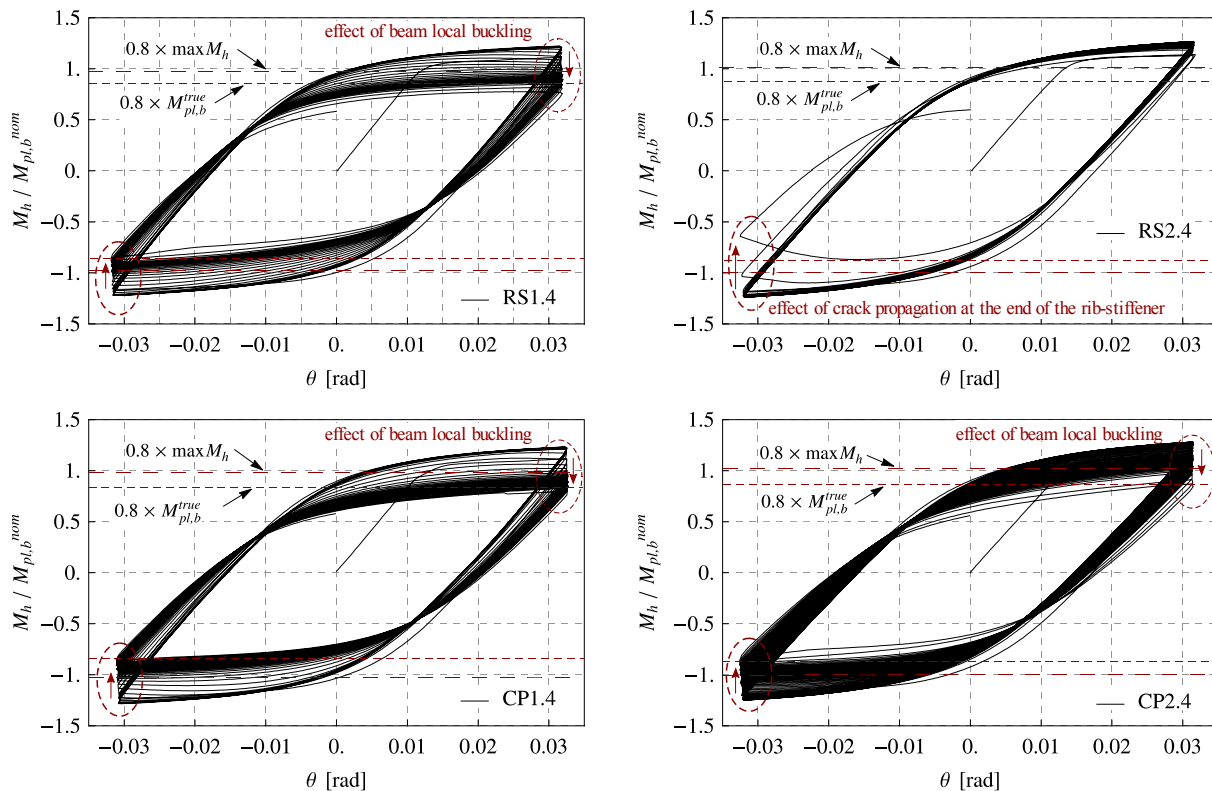


Fig. 48: Normalized moment M_h versus total joint rotation θ for constant amplitude cyclic tests, large amplitude
 Slika 48: Normirani moment M_h v odvisnosti od celotne rotacije spoja θ za teste z veliko konstantno amplitudo

After each test, maximum residual local deformations due to buckling of the beam flanges were measured. In case of specimens CP1.3 and CP2.3 practically no beam flange out-of-plane deformation was noticed. Almost the same applies for specimens RS1.3 and RS2.3. Maximum residual amplitude for RS1.3 and RS2.3 was 1.3 and 0.8 mm, respectively. In none of the four cases any buckling of the beam web was observed.

The primary cause of failure in case of both stiffened RS and CP joints was fracture as a result of the propagation of ductile cracks initiated at the end of the stiffened region with stable crack propagation until complete fracture of beam flange. In case of the RS joints the first crack initiation was always located in the beam flange at the tip of the rib (fillet weld HAZ), Figs 49, 50, while in case of the CP joints the first crack was always observed on the beam flange edge in the HAZ of transverse fillet weld, Figs 51 to 54. No yielding or damage of stiffened region of the beam, including welds, was observed.

A brief overview on deformed shape of the four RS and CP specimens tested under small constant amplitude cyclic loading is given in Figs 49 to 54. Strain concentrations located in the very local region just after the stiffened region of the beam could be observed already a few cycles after the beginning of each test: at the flange mid width for RS connections and at both flange edges in case of CP connections. During particular test, initiation of crack was observed in these regions, with progressive and stable crack propagation width-wise the beam flange, until well formatted cracks in the beam flange led to complete joint failure. Comparison between the beam local response at the early stage of the test and the deformed state of the beam after the failure does not reveal much difference, except for additional cracks at the bottom/top half of the beam web toward the column face, which appeared instantaneously with the final crack propagation through the beam flange thickness into the root radius of a beam section.

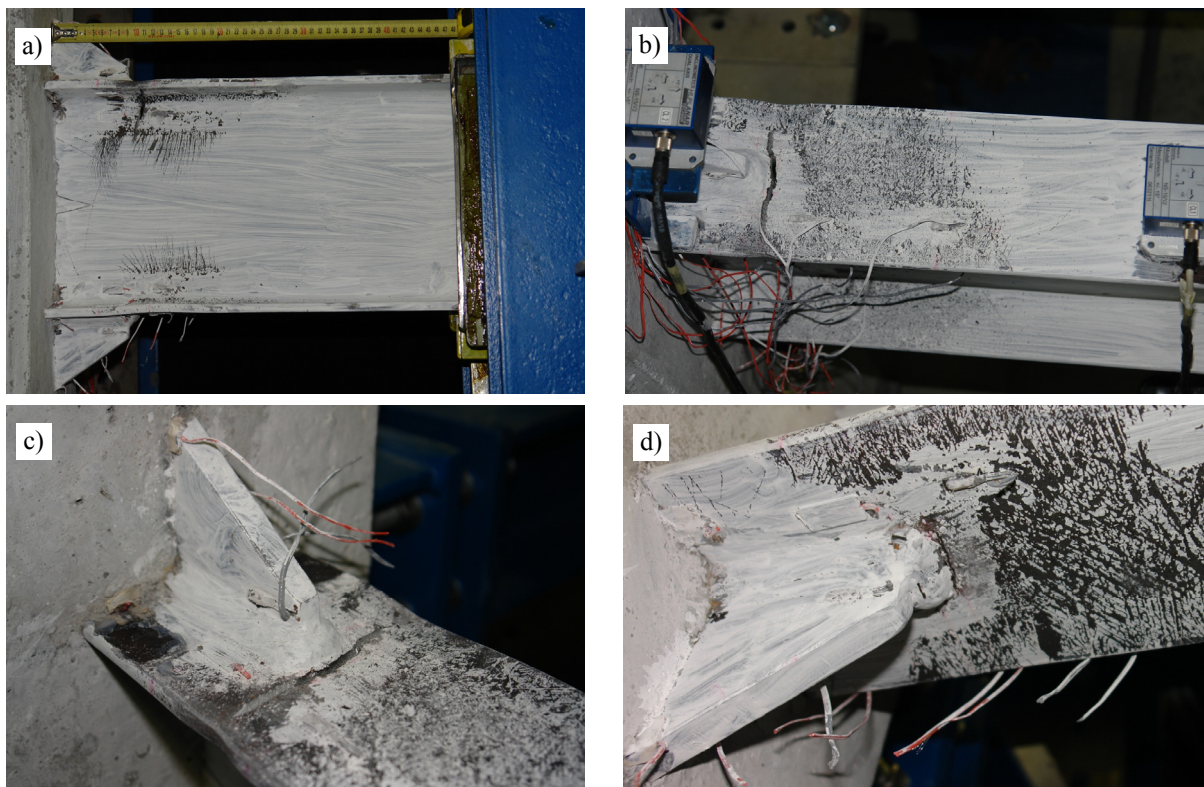


Fig. 49: Specimen RS1.3 after the test: a) local strained area of the beam just after the stiffened section, b) fracture of top beam flange, c) crack on top beam flange, side view, d) damaged bottom beam flange
Slika 49: Preizkušane RS1.3 po testu: a) lokalno deformirano območje prečke tika za ojačanim delom, b) pretrg zgornje pasnice, c) razpoka na zgornji pasnici, d) poškodbe na spodnji pasnici prečke

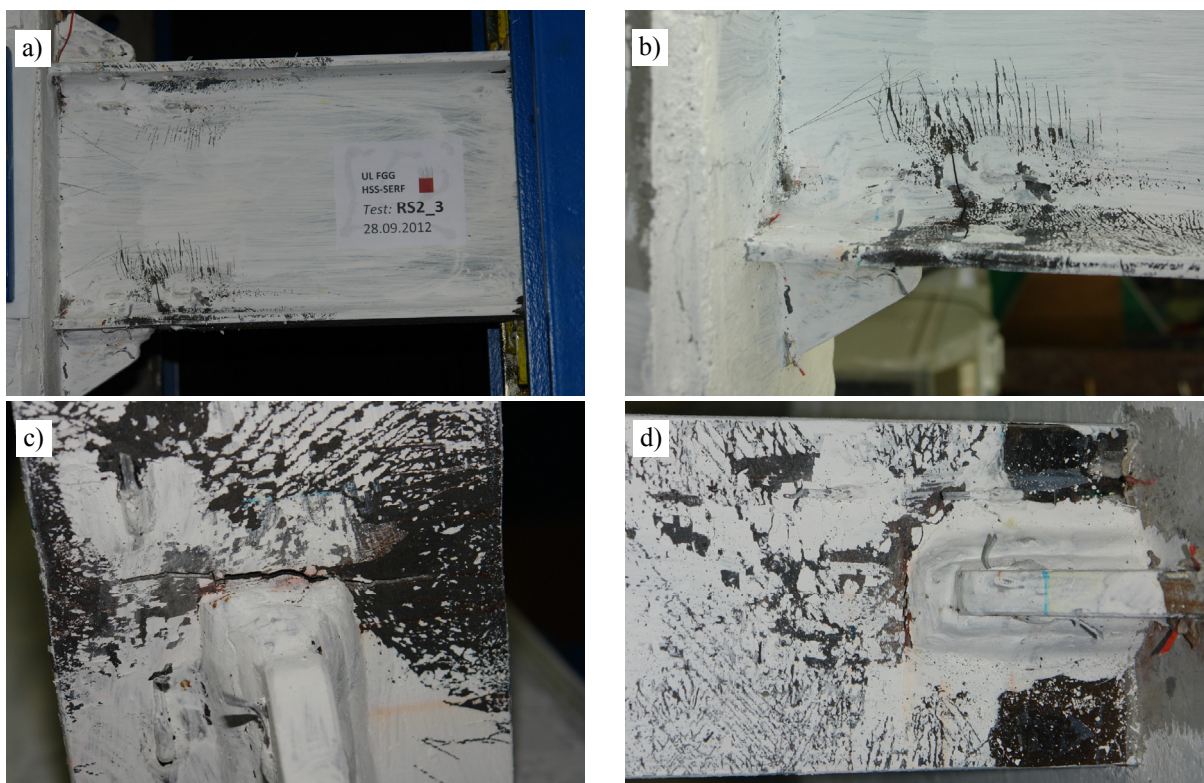


Fig. 50: Specimen RS2.3 after the test: a) local strained area of the beam just after the stiffened section, b) fracture of bottom beam flange, side view, c) crack on bottom beam flange, d) damaged top beam flange
Slika 50: Preizkušane RS2.3 po testu: a) lokalno deformirano območje prečke tika za ojačanim delom, b) pretrg spodnje pasnice, c) razpoka na spodnji pasnici, d) poškodbe na zgornji pasnici prečke

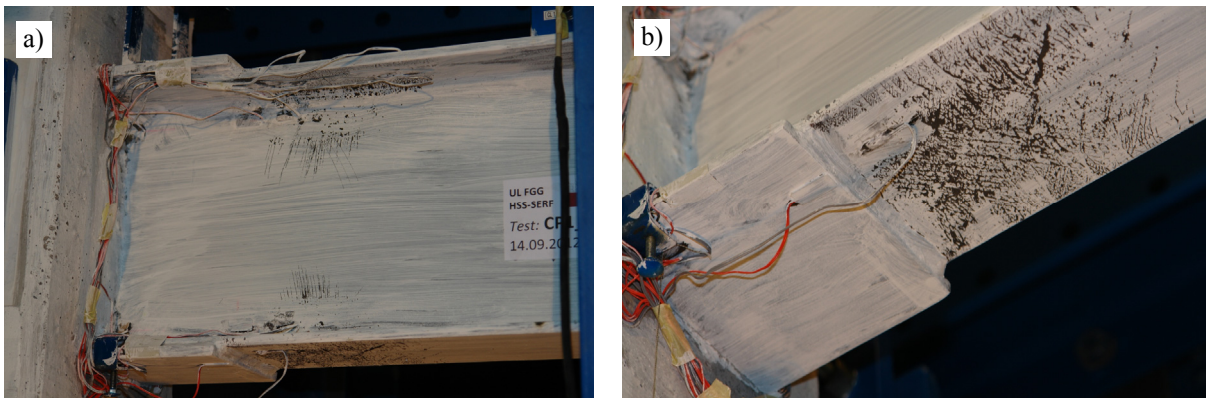


Fig. 51: Specimen CP1.3 after first 5 cycles: a) local strained area of the beam just after the stiffened section, b) detail of strain field on the beam lower flange
 Slika 51: Preizkušavec CP1.3 po prvih 5 ciklih: a) lokalno deformirano območje prečke tika za ojačanim delom, b) detajl deformacijskega polja na spodnji pasnici prečke

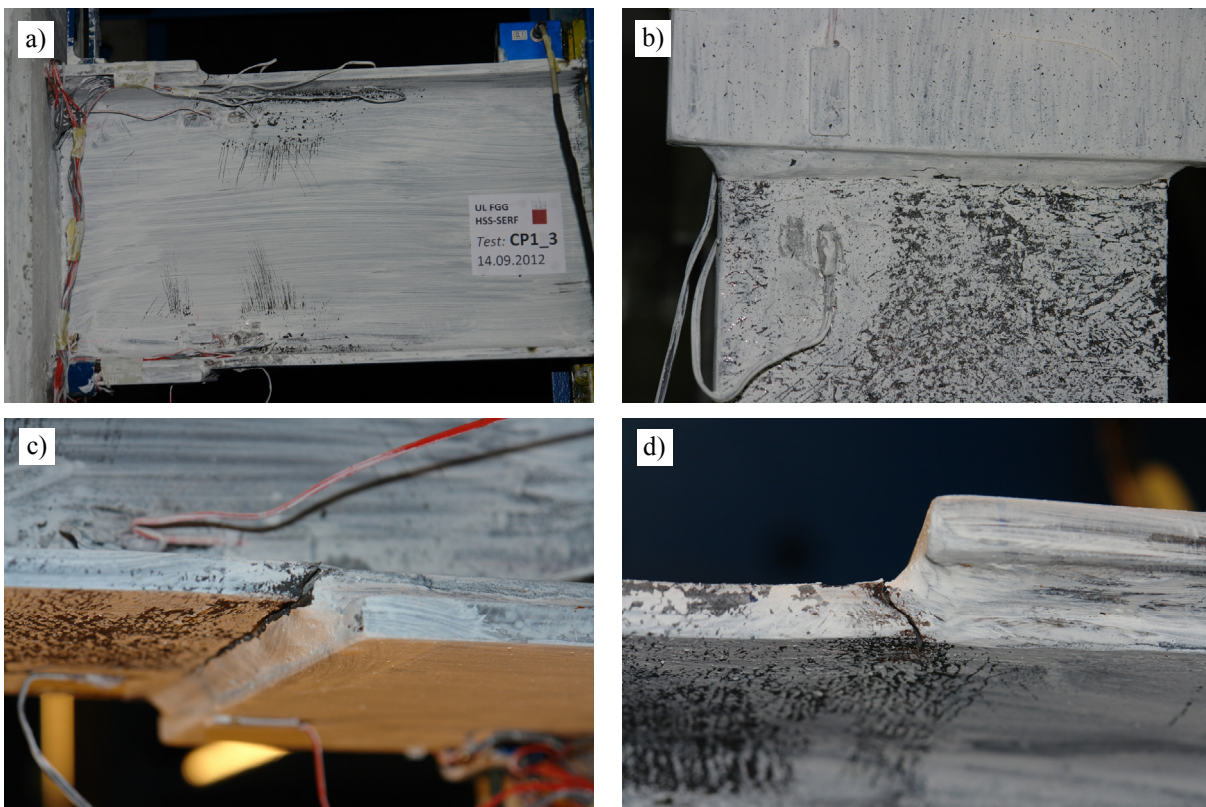


Fig. 52: Specimen CP1.3 after the test: a) local strained area of the beam just after the stiffened section, b) top beam flange, c) crack on bottom beam flange, d) damaged edge of top beam flange
 Slika 52: Preizkušavec CP1.3 po testu: a) lokalno deformirano območje prečke tika za ojačanim delom, b) zgornja pasnica c) razpoka na spodnji pasnici, d) poškodbe na robu zgornje pasnice prečke

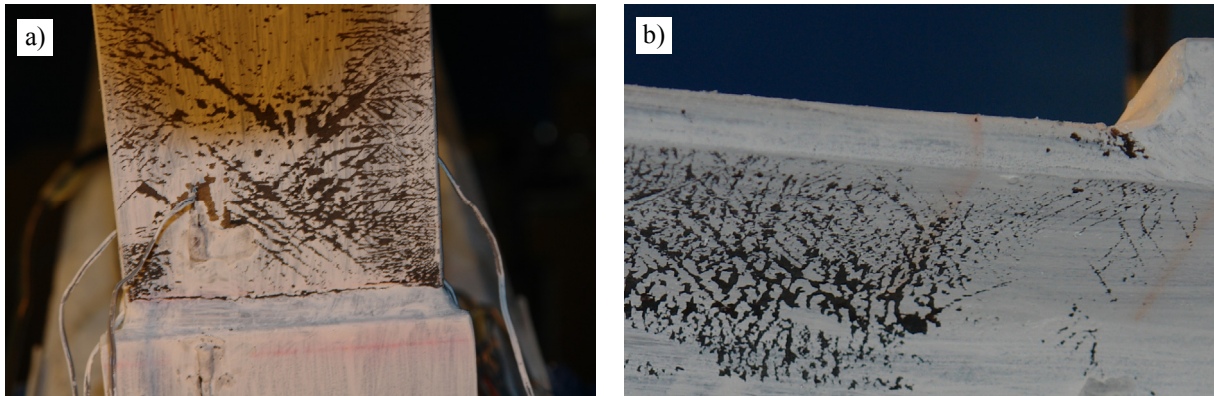


Fig. 53: Specimen CP2.3 in 130 cycle: a) local strained area of the top beam just after the stiffened section, b) growth of cracks from the top flange free end just after the stiffened section
Slika 53: Preizkušane CP2.3 v 130 ciklu: a) lokalno deformirana zgornja pasnica prečke tik za ojačanim delom, b) širjenje razpok iz prostega roba zgornje pasnice tik za ojačanim delom

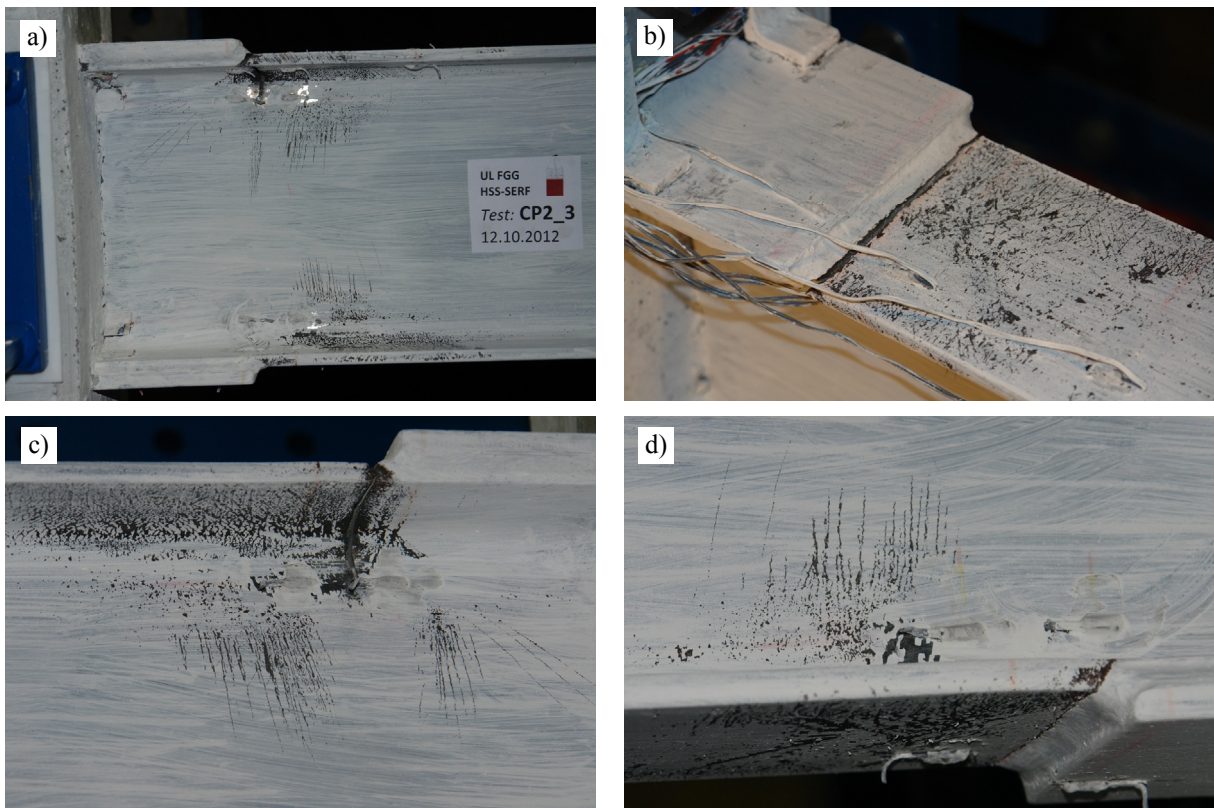


Fig. 54: Specimen CP2.3 after the test: a) local strained area of the beam just after the stiffened section, b) fracture of top beam flange, c) crack on top beam flange, side view, d) damaged bottom beam flange
Slika 54: Preizkušane CP2.3 po testu: a) lokalno deformirano območje prečke tik za ojačanim delom, b) pretrg zgornje pasnice c) pogled na razpoko na zgornji pasnici, d) poškodbe na spodnji pasnici prečke

Cyclic response of the remaining four specimens tested under large constant amplitude cycling, RS1.4, RS2.4, CP1.4 and CP2.4, was governed by the beam local buckling in the plastic hinge zone behind the stiffened region of the beam, Fig. 48 and Figs 55 to 58.

Failure of both CP specimens was the same as in case of all eight specimens tested under variable cyclic loading: deterioration of resistance due to the progress of the beam flange and flange induced web local buckling with cross-section distortion, followed by ductile LCF fracture in the locally most deformed part of the beam flange, Figs 57 and 58. The beam local

buckling in the plastic hinge region in the unstiffened beam section took place progressively with the increased number of cycles, leading to gradual degradation of strength, Fig. 59c, d.

However, in case of both RS specimens, RS1.4 and RS2.4, crack propagation at the end of the rib stiffener in the fillet weld HAZ led to the complete fracture of the beam flange, similar to the failure of RS1.3 and RS2.3 subjected to small constant amplitude cycling, Figs 55 and 56.

In contrast to the well-developed beam local buckling in all three test specimens, CP1.4, CP2.4 and RS1.4, in case of specimen RS2.4 only limited extend of the beam local buckling revealed before the final failure: maximum residual deformation amplitude on the upper flange was 14.6 mm, whilst the lower flange remained practically straight, Fig. 56. As a matter of the fact, no strength reduction due to the flange local buckling in the bottom beam flange was present, which consequently led to even more prominent crack initiation, its propagation and final fracture of the top beam flange at the end of the rib-stiffener. An in-depth discussion on the RS1.4 and RS2.4 joint response, compared to the cyclic response of the other six specimens subject to constant amplitude cycling, in terms of the LCF endurance is provided in the text below.

According to the aforementioned observations, the responses of both RS joints subjected to large constant amplitude cycling clearly showed the shortcoming of the rib-stiffened beam-to-column connection, as it was not able to force the final failure to occur in the parent beam section away from the welded detail (weld HAZ) at the end of the rib-stiffener. In this aspect the CP connection proved to be superior to the RS connection.

As in case of variable amplitude and small constant amplitude cyclic tests, also in case of the four specimens subjected to large constant amplitude cycling, no yielding of the reinforcing plates or damage of welds in case of both stiffened connections was observed during the tests.

A brief overview on deformed shape of the four RS and CP specimens tested under large constant amplitude cyclic loading is given in Figs 55 to 58.

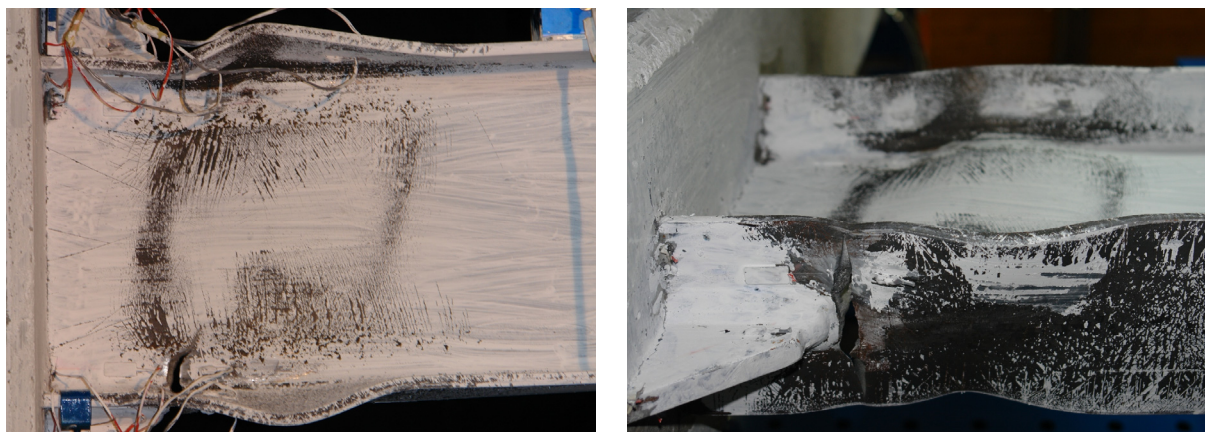


Fig. 55: Specimen RS1.4 after the test
Slika 55: Preizkušane RS1.4 po končanem testu

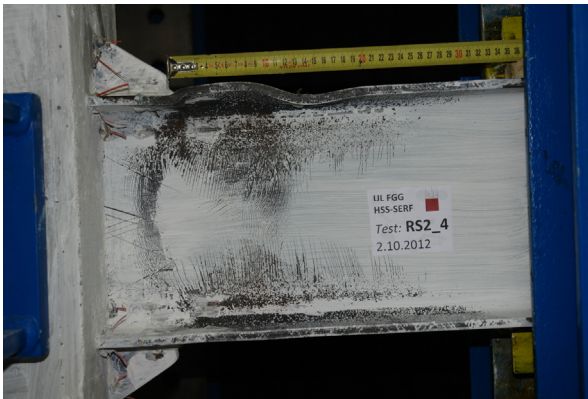


Fig. 56: Specimen RS2.4 after the test
Slika 56: Preizkušane RS2.4 po končanem testu

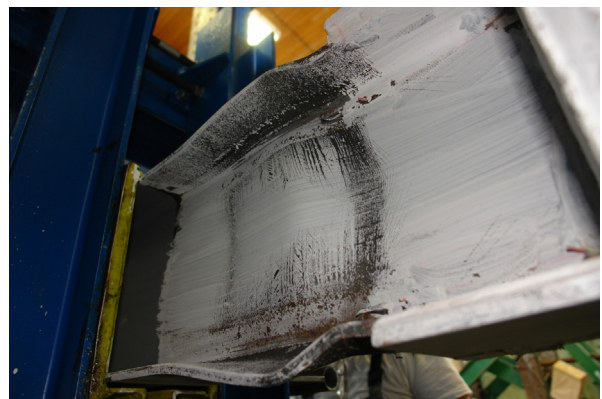
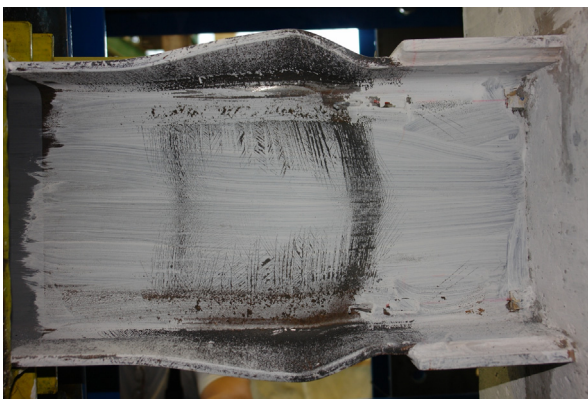


Fig. 57: Specimen CP1.4 after the test
Slika 57: Preizkušane CP1.4 po končanem testu

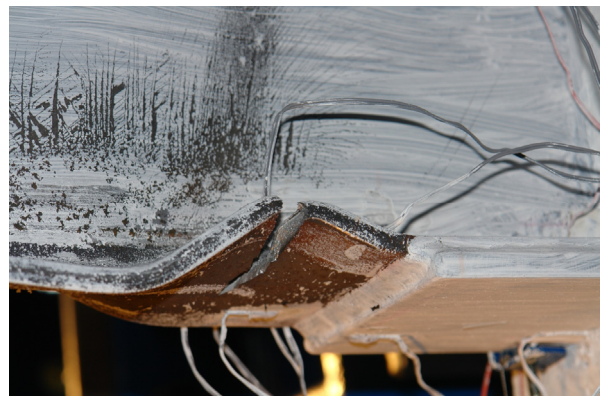


Fig. 58: Specimen CP2.4 after the test
Slika 58: Preizkušane CP2.4 po končanem testu

Practically constant value of moment amplitudes throughout the test is characteristic for the specimens subjected to small constant amplitude cycling. Their strength was abruptly reduced only in the last few cycles, when fracture of the beam flange just behind the stiffened region led to the complete joint failure, Fig. 47 and Fig. 59a, b. On the other hand, in case of joints subjected to large constant amplitude cycling, the beam local buckling in the plastic hinge region of unstiffened beam section took place progressively with the increased number of cycles, leading to gradual degradation of strength, Fig. 59b, c.

An important difference in the response of specimens tested under small and large constant amplitude is also in the experimental life, addressed by the number of complete cycles before

the failure of specimen. Summary of the test results in terms of the number of completed inelastic cycles N_i according to the three failure criteria presented in Chapter 3.4.2 is gathered in Table 8.

All four specimens tested under small constant amplitude revealed considerable number of cycles to failure N_1 compared to those subjected to large constant amplitude cycling. In case of the small constant amplitude, the number of cycles to failure for both RS and CP joints varies between 76 and 155, while for the large amplitude it is between 29 and 62. In the latter case, the increase of local plastic deformations in the plastic hinge zone beyond the stiffened beam region due to the flange local buckling caused more pronounced LCF effect, which clearly resulted in substantial reduction of the fatigue resistance.

In all four tests with small amplitude, RS1.3, RS2.3, CP1.3, CP2.3, and in case of one test with large amplitude, RS2.4, where the beam local buckling did not substantially affect the response of the specimens, the total number of cycles according to the second failure criteria N_2 , accounting for 20 % fall of the maximum strength and initial stiffness, is very close to the number of cycles to complete failure, N_1 , Table 8 and Fig. 59a, b. However, in case of the other three specimens subjected to large amplitude cycling, RS1.4, CP1.4 and CP2.4, the beam local buckling caused significant reduction of N_2 , with the values of N_2/N_1 ratio for the three specimens being 0.45, 0.30 and 0.66, respectively, Table 8 and Fig. 59c, d.

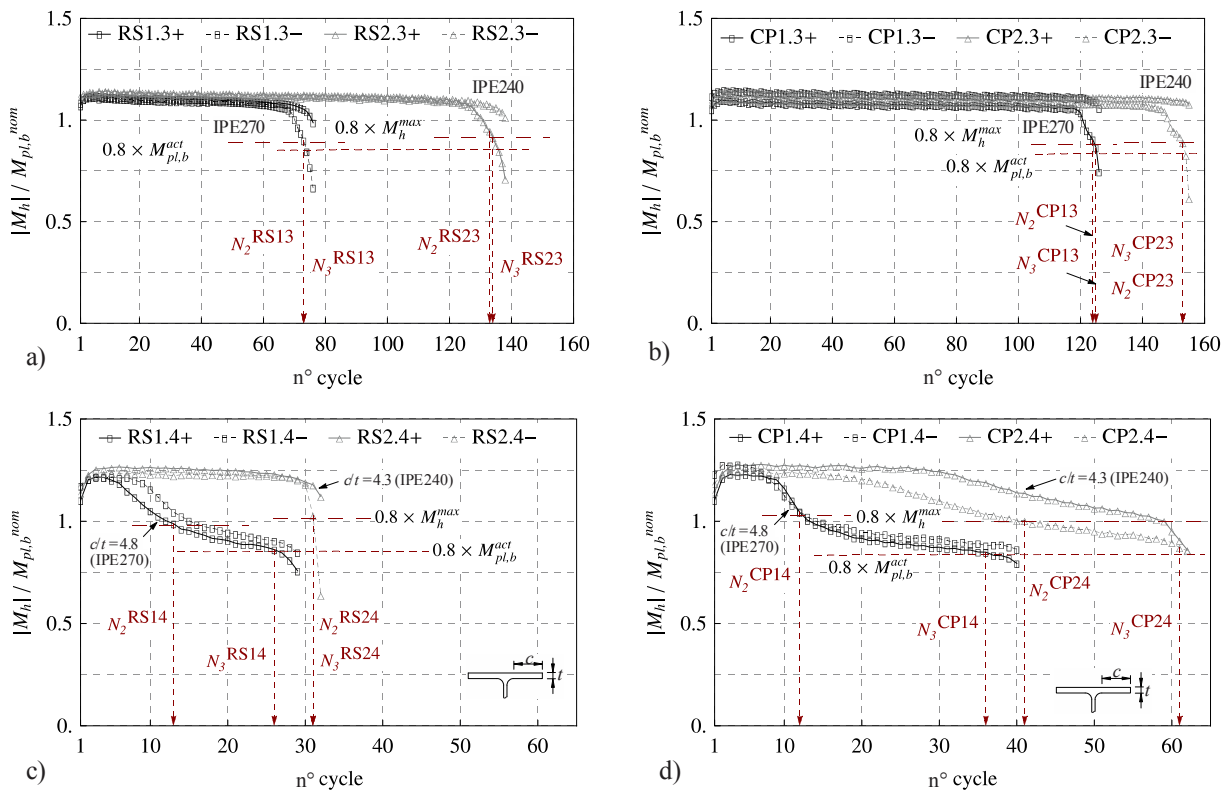


Fig. 59: Normalised moment M_h at the subsequent joint rotation amplitudes as a function of number of cycles:
 a) RS1.3 and RS2.3, b) CP1.3 and CP2.3, c) RS1.4 and RS2.4, d) CP1.4 and CP2.4

Slika 59: Normiran moment M_h v zaporednih amplitudah rotacije spoja v odvisnosti od števila ciklov: a) RS1.3 in RS2.3, b) CP1.3 in CP2.3, c) RS1.4 in RS2.4, d) CP1.4 in CP2.4

The effect of the beam local buckling on the strength and the stiffness degradation was more pronounced in joints with the large beam cross-section IPE270, as they are more prone to local buckling in comparison to IPE240 beam profile, due to larger flange and web plate width-to-thickness ratios, Fig. 59c, d. In addition, all specimens with the small beam profile revealed significantly larger experimental life N_1 in comparison to those designed with large

beam section. However, exception with no significant difference in complete number of cycles to failure N_1 was observed in the case of rib-stiffened joints RS1.4 and RS2.4, Fig. 59c (compared to Fig. 59d), see also Figs 62 and 63. As already noted, in these two cases it is the stiffened connection detail at the end of the rib-stiffener that the overall joint LCF resistance was found to be dependent on.

Contrary to the specimens tested under variable cyclic loading, in case of specimens subjected to constant amplitude cycling, the strength criterion proved to be equally stringent as or even more stringent than the stiffness degradation criterion, Table 8.

For a detailed discussion on the evaluation of accumulated plastic rotations in terms of LCF effect, emphasising the effect of both stiffened joint types in combination with both beam profiles and different cyclic loadings applied, the reader may refer to Chapter 3.4.7.

Detailed review of the applied loading histories for all eight specimens subjected to constant cyclic loading is presented in Table 17 by means of measured total joint θ and total beam θ_b rotation amplitudes. In addition, corresponding relative values to the total joint $\theta_{pl,j}$ and beam $\theta_{pl,b}$ yield rotation are added.

Average value for complete number of cycles, for positive and negative loading directions, is presented. Reference to the applied nominal rotation amplitude is provided as well, with values of rotation amplitudes normalised with the corresponding yield rotations. This enables on overview of actual applied plastic loading histories in order to facilitate consistent comparison between the responses of the specimen. Reported cyclic loading amplitudes for a number of cycles in plastic range, see also Table 8, were used later for the definition of loading history in numerical simulations of the specimens, see Chapter 4.3.3.2.

The yield displacements of each specimen used for the report of loading histories in Table 17 was determined according to one of the procedures provided in ECCS N°45 (ECCS, 1986). In addition, results from monotonic numerical FE simulations on the test specimens were used for higher accuracy, see Chapter 4.3.2.2.

Preglednica 17: Zgodovina obremenjevanja za preizkušance obremenjene s konstantno amplitudo rotacije
 Table 17: Loading history details for specimens subjected to constant amplitude cycling

Specimen	Rotation amplitude	Rotation amplitudes measured on specimen *			
	θ [rad]	θ [rad]	$\theta/\theta_{pl,j}$	θ_b [rad]	$\theta_b/\theta_{pl,b}$
RS1.3	0.019	0.018	1.55	0.015	1.73
RS2.3		0.018	1.33	0.013	1.30
CP1.3		0.018	1.45	0.014	1.64
CP2.3		0.018	1.39	0.013	1.29
RS1.4	0.033	0.032	2.62	0.029	3.21
RS2.4		0.032	2.32	0.027	2.56
CP1.4		0.032	2.50	0.029	3.29
CP2.4		0.032	2.26	0.026	2.58

*) Average rotation amplitude value from positive and negative loading directions for all performed cycles is reported.

The response of all the eight specimens tested with small and large constant cyclic loading is described in detail below in terms of strength and stiffness variation through the entire applied plastic loading history, Figs 60 to 63.

Distribution of maximum moment M_c and tangent modulus α of the unloading phase of a hysteresis curve, Fig. 41b, determined for the subsequent loading cycles in plastic range is presented. Both parameters are evaluated for positive and negative loading directions. In addition, relative change of M_c and α between the two consecutive cycles is presented in accordance with Eq. (21).

The twofold representation of M_c and α distribution provides a better insight into the history of parameter variation and the best way to instance the failure events. For that purpose combined plot of the two curves with the same domain but different ranges was applied, where different scales on the primary and secondary ordinate axes are used so that their ranges appear to be the same.

In addition, information on the locally observed crack initiation and the onset of overall joint strength degradation is provided on the diagrams of particular specimen. Onset of crack initiation was estimated from observations of experimentally obtained strain history data measured by uniaxial strain gauges oriented along the longitudinal axis of the beam, Fig. 26, and placed in closed vicinity of location on specimen, where crack growth on the beam flange took place during the experiments. It was performed only for six specimens, where the final crack occurred in the beam flange close to the end of the stiffener: for all small constant amplitude cyclic tests, RS1.3, RS2.3, CP1.3 and CP2.3, as well as in case of specimens RS1.4 and RS2.4.

Estimation of the crack initiation according to the described methodology was not possible for specimens CP1.4 and CP2.4, where LCF failure occurred due to the progress of the beam local buckling in the middle of the plastic hinge zone. Namely, due to the extremely high plastic straining in this buckled region, all strain gauges in experiments soon became overloaded (strain limit 5 %) and it was practically impossible to measure the strain.

The information on the estimated onset of crack initiation was utilized later to provide crack initiation based LCF failure criterion for structural steel components subjected to large-scale cyclic straining typical for LCF loading conditions of beam-to-column joints under seismic loading, see Chapter 4.3.3.5.

The response of the RS and CP joints, comprising the same beam-column cross-section characteristics and subjected to the same constant amplitude loading history (RS1.3 and CP1.3, RS2.3 and CP2.3, RS1.4 and CP1.4, RS2.4 and CP2.4), is presented in the same figure to manage direct comparison between the response of both stiffened joint configurations.

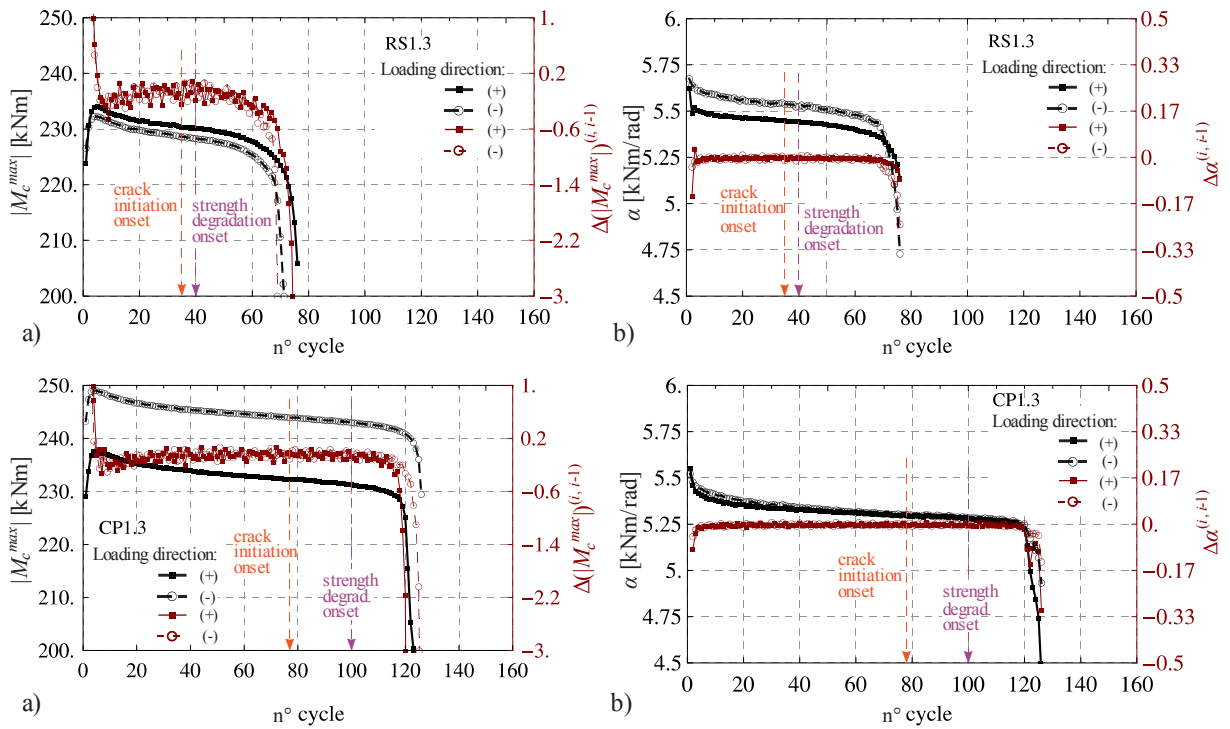


Fig. 60: Response of specimens RS1.3 and CP1.3: a) distribution of maximum moment per cycle, b) distribution of complete joint stiffness per cycle

Slika 60: Odziv preizkušancev RS1.3 in CP1.3: a) potek največjih momentov po ciklih, b) potek togosti celotnega spoja po ciklih

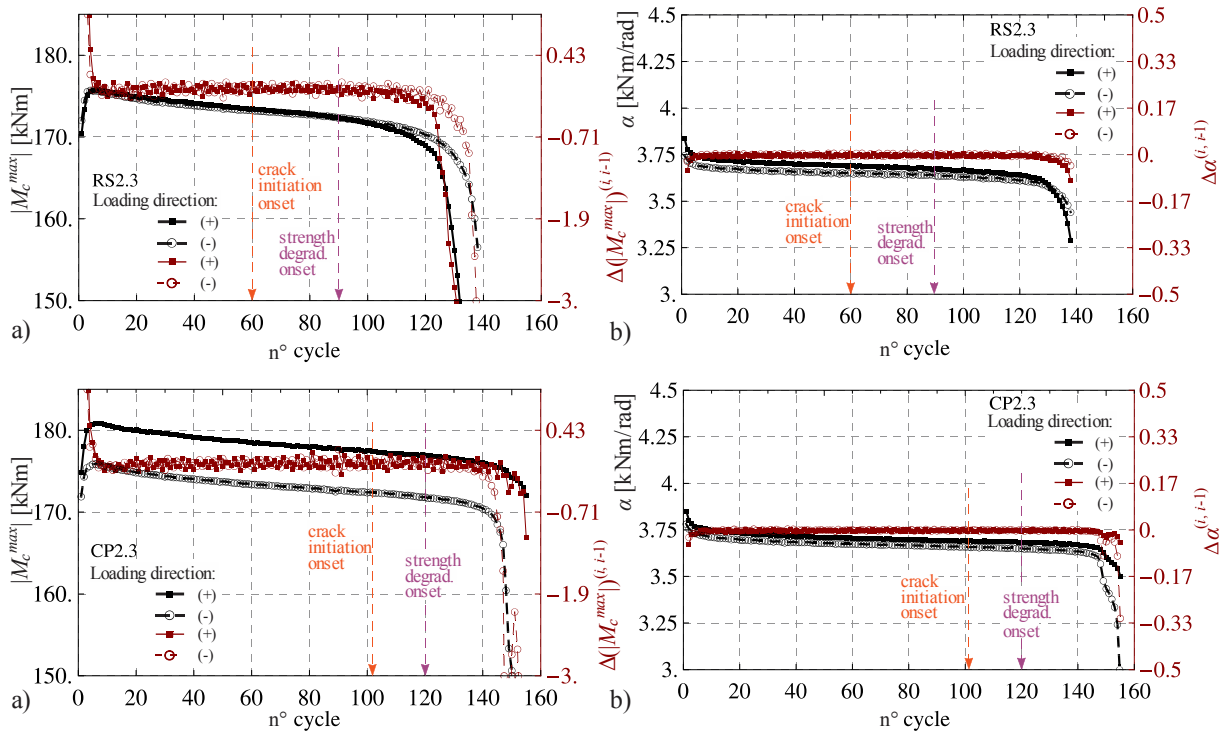


Fig. 61: Response of specimens RS2.3 and CP2.3: a) distribution of maximum moment per cycle, b) distribution of complete joint stiffness per cycle

Slika 61: Odziv preizkušancev RS2.3 in CP2.3: a) potek največjih momentov po ciklih, b) potek togosti celotnega spoja po ciklih

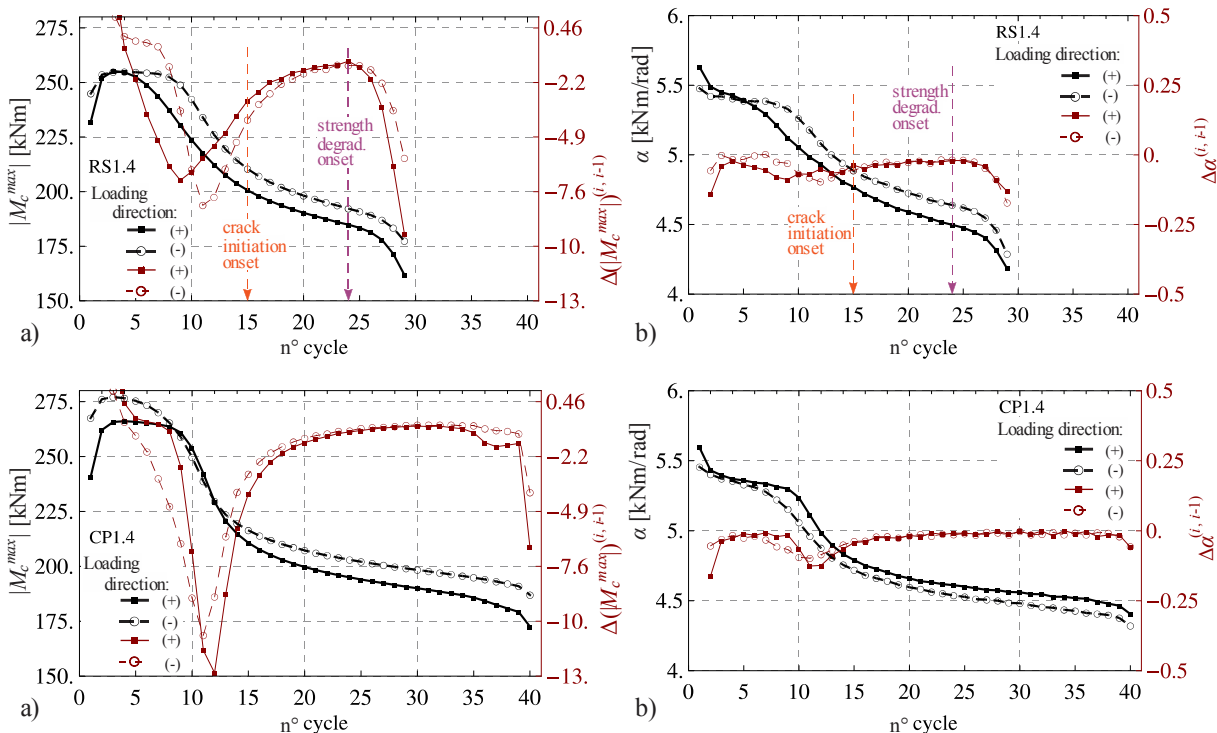


Fig. 62: Response of specimens RS1.4 and CP1.4: a) distribution of maximum moment per cycle, b) distribution of complete joint stiffness per cycle

Slika 62: Odziv preizkušancev RS1.4 in CP1.4: a) potek največjih momentov po ciklih, b) potek togosti celotnega spoja po ciklih

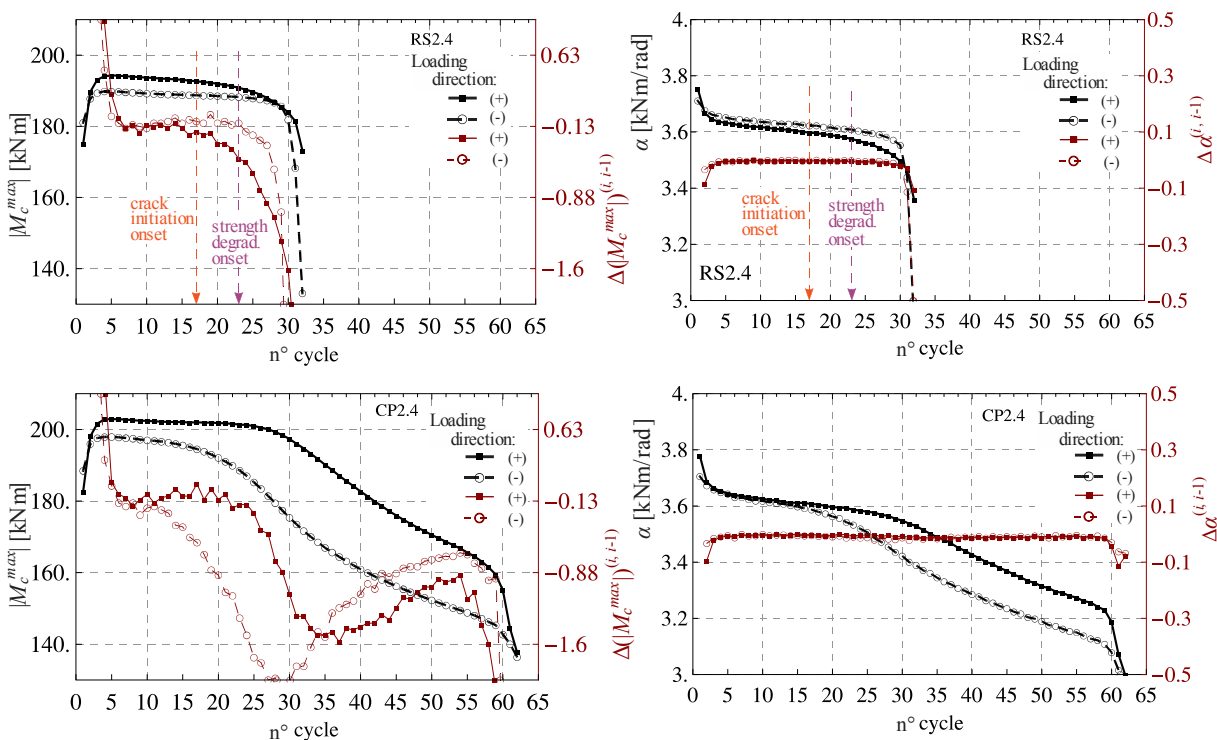


Fig. 63: Response of specimens RS2.4 and CP2.4: a) distribution of maximum moment per cycle, b) distribution of complete joint stiffness per cycle

Slika 63: Odziv preizkušancev RS2.4 in CP2.4: a) potek največjih momentov po ciklih, b) potek togosti celotnega spoja po ciklih

Information on cycles with the estimated crack initiation and the onset of joint strength degradation is presented in Table 18.

Preglednica 18: Nastop opazovanega porušnega fenomena za izbrane preizkušance testirane s konstantno amplitudo rotacije spoja

Table 18: Onset of failure instance for selected specimens subjected to constant amplitude cycling

Specimen	Actual measured rotation amplitude	tot No. of cycles	Failure instance	
	$\theta_b/\theta_{pl,b}$		Onset of strength degradation	Estimated onset of crack growth
RS1.3	1.73	76	40	35
RS2.3	1.30	138	90	60
CP1.3	1.64	126	100	77
CP2.3	1.29	155	120	102
RS1.4	3.21	29	24	15
RS2.4	2.56	32	23	17

3.4.4 Investigation of welded connections after the tests

After the tests, investigation was started with the aim to determine the condition of welded connections in the joints. In order to assess the extent of damage of welds in the stiffened connections, non-destructive testing with magnetic particle inspection (MT) was applied first.

Column concrete encasement in the region around beam-to-column welded connection was removed prior to the inspection, Fig. 64.

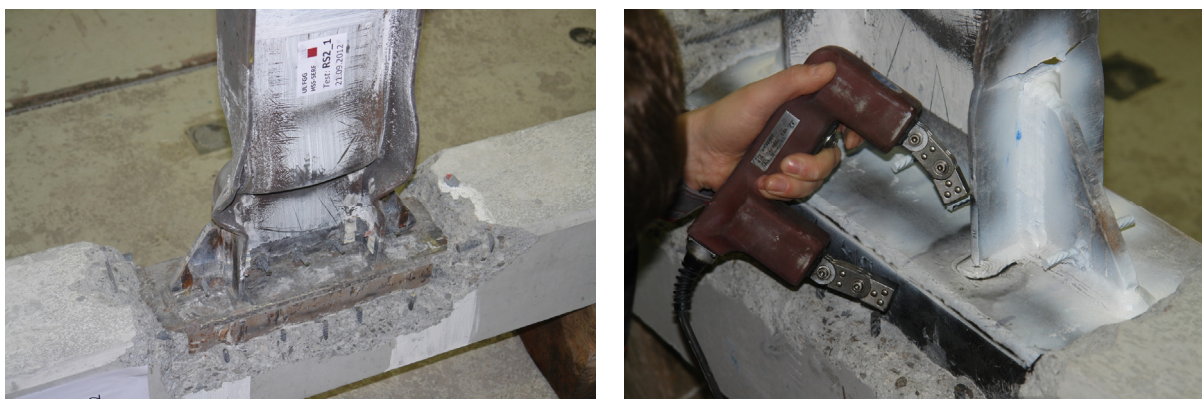


Fig. 64: a) Preparation of specimen for welded connection inspection, b) Magnetic particle testing (MT)
Slika 64: a) priprava preizkušanca za pregled varjenih spojev, b) preiskava varjenih spojev z magnetnimi delci

No apparent cracks, as a result of damage during the tests, were found by visual inspection in any of the welds along the stiffening plates and at their ends. Fig. 65 presents the typical observed difference between the local response of RS and CP joint configuration at the end of the stiffener.

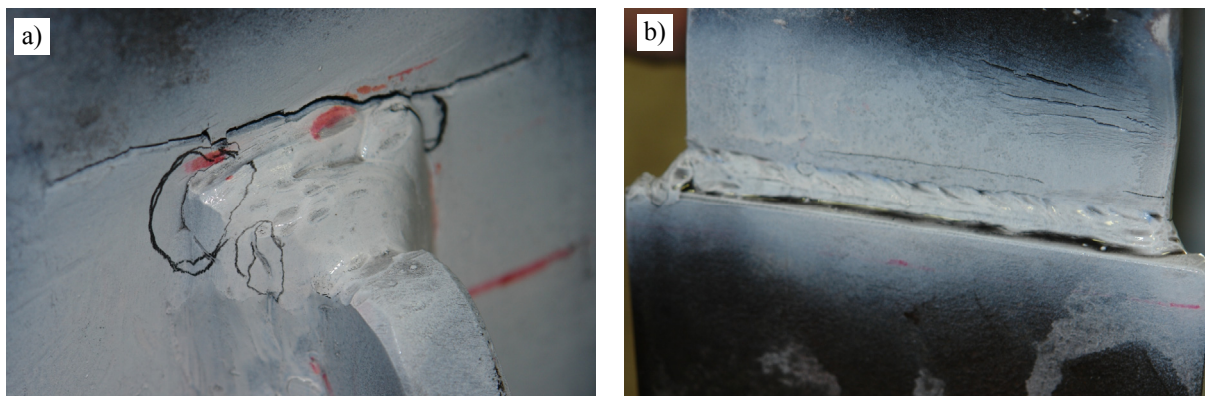


Fig. 65: a) Cracks at the end of the rib-stiffener fillet weld in specimen RS2.3, b) Practically undamaged transverse fillet weld, including its HAZ region, at the end of the cover plate in specimen CP1.4
Slika 65: a) razpoke po koncu kotnega zvara ojačilnega rebra na preizkušancu RS2.3, b) praktično nepoškodovan prečni kotni zvar, vključno z območjem HAZ, na koncu vezne pločevine na preizkušancu CP1.4

While cracks appeared in the HAZ at the end of the rib-stiffener fillet weld in all of RS joints, CP joints succeeded in moving the plastic strain concentration away from the welded region at the end of the cover plate.

The only damage of welds in the deformed specimens was observed in front cracks at the edge of welded connection between the beam flange and the column flange, see Fig. 66. Observed cracks were small and localised. While they were observed only in two cases of RS joints, they were typical for all CP joints. The reason can be found in the fabrication detail: the end of the weld between beam and column flange was not ground smoothly, but cut sharply, which resulted in undesired stress/strain notch effect. Although the observed cracks were not detrimental in either case, such a fabrication detail should not be allowed.

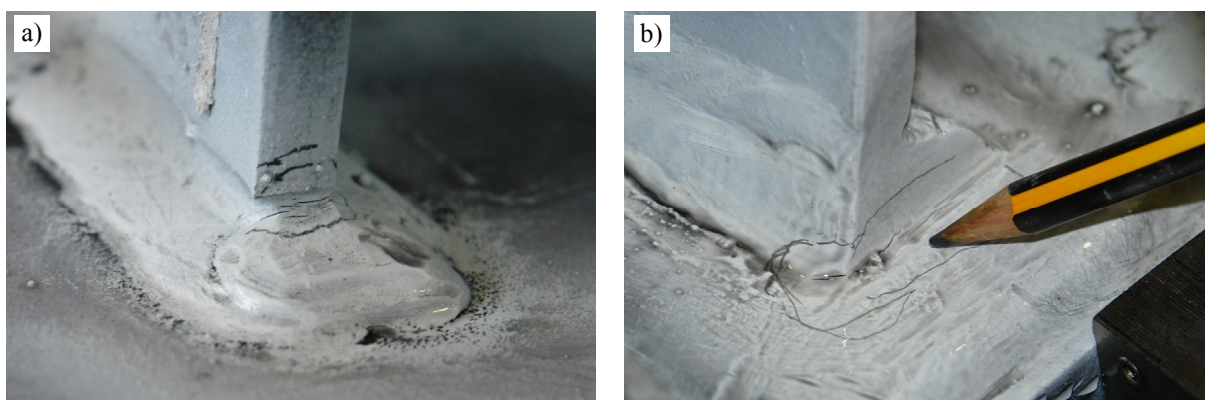


Fig. 66: Cracks at the edge of welded connection between the beam flange and the column flange a) specimen RS1.4, b) specimen CP1.3

Slika 66: Razpoke na robu varjenega stika med pasnico prečke in pasnico stebra: a) preizkušavec RS1.4, b) preizkušavec CP1.3

Additionally, two specimens were selected, i.e. RS2.2 and CP1.4, to perform macro examination of welds from two regions of the stiffened connection: from welded connection at the column flange, and fillet weld at the end of the stiffener.

From all the examined cross-sections no damage of welds was observed. The state of the examined welded connections can be observed from selected samples presented in Figs 67 and 68.

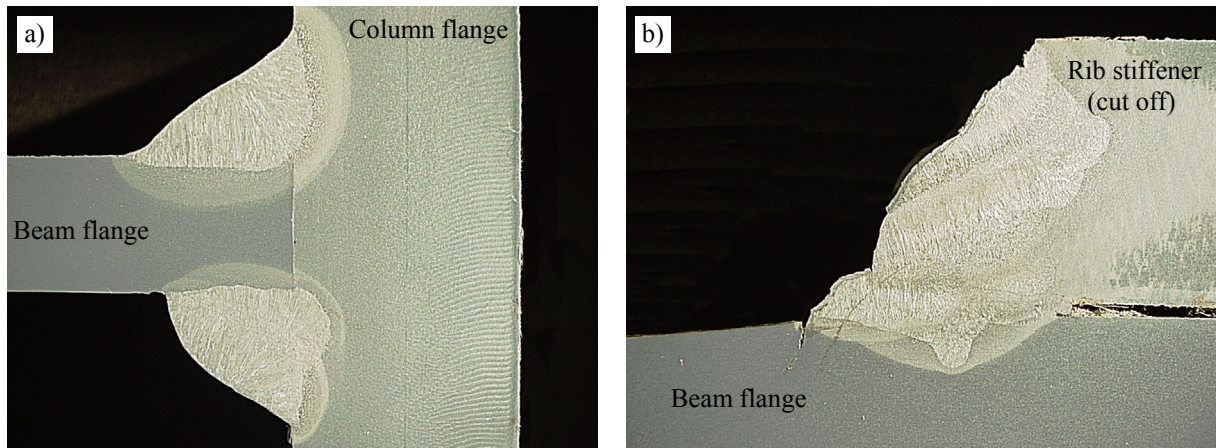


Fig. 67: Cross-section of welded connection details from specimen RS2.2: a) Fillet weld between beam flange and column flange b) Fillet weld at the end of the rib-stiffener

Slika 67: Obrus prečnega prereza varjenih stikov iz preizkušanca RS2.2: a) kotni zvar med pasnico prečke in pasnico stebra, b) kotni zvar na koncu rebra

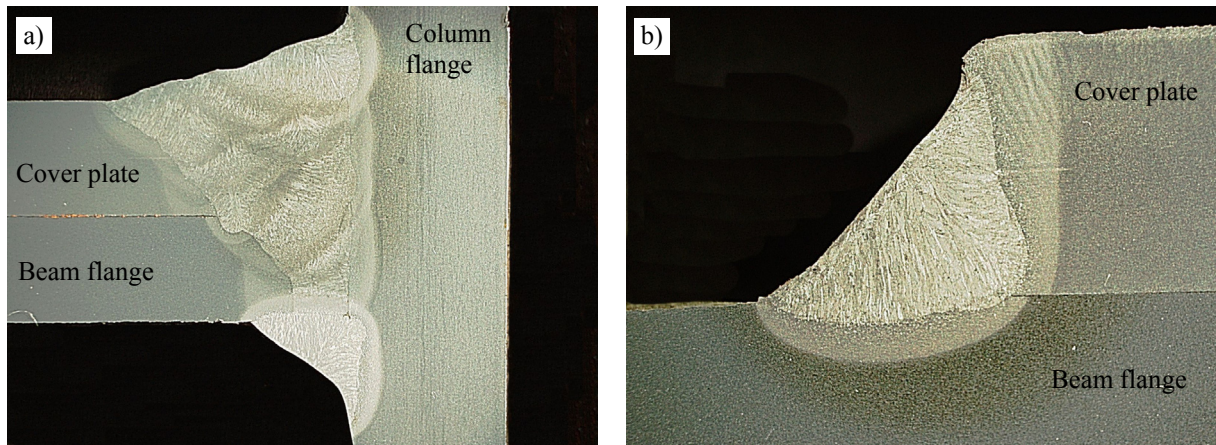


Fig. 68: Cross-section of welded connection details from specimen CP1.4: a) Complete joint penetration single-bevel but weld used to connect the beam flange and the cover plate to the column flange, b) transverse fillet weld at the end of the cover-plate

Slika 68: Obrus prečnega prereza varjenih stikov iz preizkušanca CP1.4: a) polnopenetriran čelni V-zvar med pasnico prečke in vezno pločevino ter pasnico stebra, b) prečni kotni zvar na koncu vezne pločevine

3.4.5 Composite column behaviour

The whole inelastic action in all 16 beam-to-column joints was forced into the beam beyond the stiffened connection. Measured typical rotation contributions from column and beam are shown in Fig. 69(a).

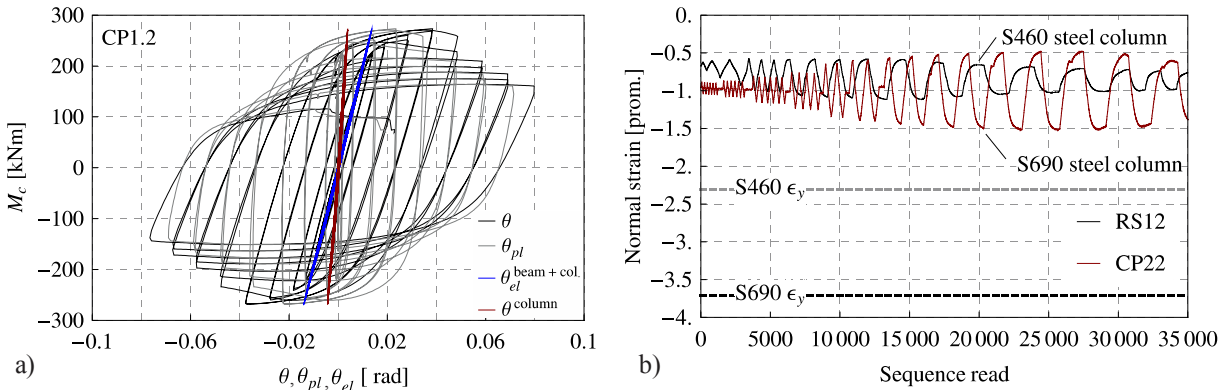


Fig. 69: Response of composite column: a) elastic column and elastic beam contribution to the total joint rotation for specimen CP1.2, b) recorded normal strains (compression) in encased steel sections

Slika 69: Odziv sovpreznega stebra: a) elastični prispevek stebra in prečke k celotni rotaciji spoja CP1.2, b) izmerjene normalne napetosti (tlačne) jeklenega profila stebra

For the group of specimens tested under cyclic loading with stepwisely increasing amplitude, complete column contribution to the total joint rotation, when maximum strength was recorded, ranged between 5.8 and 9.3 % in case of large column and between 5.4 and 8.1 % in case of small column. Encased steel section remained in elastic state in all the tests. Except for minor cracks at the very local region around beam-column connection that had no detrimental effect on joint behaviour, concrete encasement remained undamaged in all the tests, Fig. 70.

As was already presented in the previous Chapters, 3.4.2 and 3.4.3, no difference was observed in the failure mode for specimens tested with and without the presence of the compressive column axial force. Fig. 69(b) shows the level of normal strains measured on flanges of encased column steel profile. In spite of considerably strained steel column flange during the test, no damage of welds from column-beam flange interface was observed from examination of welded connections performed after the tests.

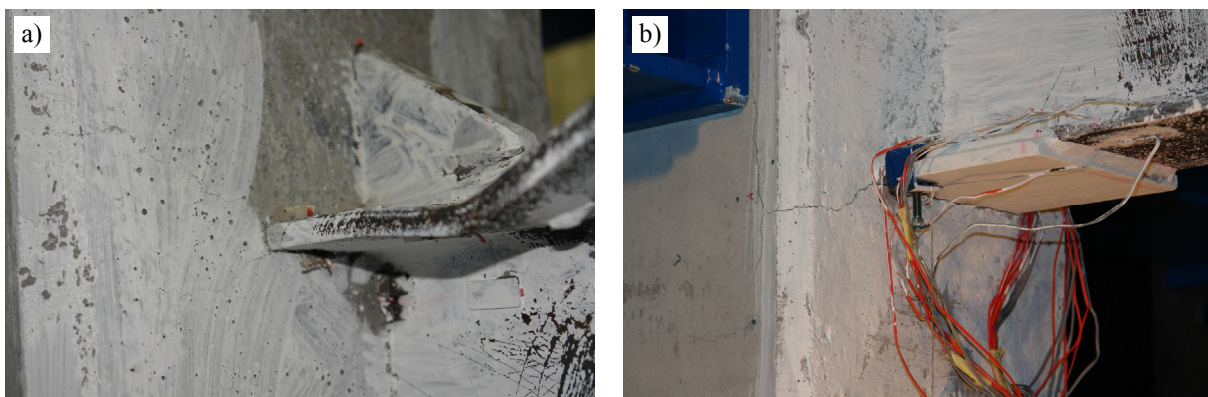


Fig. 70: Composite column after the test: a) specimen RS1.4, b) specimen CP1.1
 Slika 70: Stanje sovpreznega stebra po koncu testa: a) preizkušane RS1.4, b) preizkušane CP1.1

It has to be noted that the inclusion of the column axial force in the tests represented a real loading conditions present in building. Although the deformation of the column was limited to elastic response, in case of possible poorly designed and/or fabricated beam-column welded interface, axially unloaded column might not give realistic beam-to-column joint behaviour.

3.4.6 Evaluation of test results according to prequalification requirements

The response of eight specimens tested under cyclic loading with stepwisely increasing amplitude was evaluated according to the acceptance criteria of applicable standards currently in use.

The required rotation capacity of the plastic hinge region from EN 1998-1 (CEN, 2005c) is 0.035 rad for structures of ductility class DCH and 0.025 rad for structures of ductility class DCM. In both cases the rotation capacity should be ensured under cyclic loading without degradation of maximum strength and initial stiffness larger than 20 %.

For beam-to-column connections used in the seismic force resisting system ANSI/AISC 341-10 (ANSI/AISC, 2010b) provides the following two requirements: the connection shall be capable of accommodating a total joint rotation of at least 0.04 and 0.02 rad, for special moment frames (SMF) and intermediate moment frames (IMF), respectively; the measured flexural resistance of the connection, determined at the column face, shall equal at least 0.80 M_p of the connected beam at the aforementioned story drift angles for SMF and IMF, where M_p is nominal beam plastic moment.

It should be noted that the AISC acceptance criterion is based on joint rotation, which includes elastic and inelastic rotations from beam and column, while the criterion from Eurocode takes into account the total beam rotation and the column web panel shear deformation (if its contribution is less than 30 % of the total plastic rotation capability) without the column elastic deformation.

In EN 1998-1 it is also not clearly stated whether the rotation limits should account for the rotation capacity of the plastic hinge region or the whole beam. However, in our case, also when the rotational capacity of the plastic hinge region is used, all the eight specimens fulfil the required limit 0.035 rad, see Tables 9 and 10.

Values of rotations obtained from all the eight specimens to be compared with the required limits from both considered recommendations are gathered in Table 19. Minimal rotations from both loading directions are collected. For all eight joints the value of the total beam rotation θ_b , without degradation of maximal strength and initial stiffness greater than 20 %, is larger than the more stringent limit value of 0.035 rad from Eurocode standard.

Similarly, the value of total joint rotation θ is larger than the required value of 0.04 rad for structures classified as SMF for all tested joints. The later requirement is obviously less stringent and large reserve can be noticed for all the specimens, although complete joint rotation in Table 19 presents minimal joint rotation at 20 % fall of the actual beam plastic moment $M_{pl,b}^{act}$, and not the nominal one $M_{pl,b}^{nom}$ as stated in the AISC seismic provisions.

Preglednica 19: Celotna rotacija prečke in celotna rotacija spoja za preizkušance RS in CP
 Table 19: Complete beam and complete joint rotations for RS and CP joints

Specimen	θ_b (rad)	θ (rad)	Specimen	θ_b (rad)	θ (rad)
RS1.1	0.043	0.065	CP1.1	0.037	0.067
RS1.2	0.045	0.065	CP1.2	0.044	0.058
RS2.1	0.050	0.068	CP2.1	0.048	0.078
RS2.2	0.054	0.068	CP2.2	0.050	0.068
Rotation limit	> 0.035^a	> 0.04^b		> 0.035^a	> 0.04^b
Required rotation capacity according to: ^a EN 1998-1, ^b AISC 341-10					

Except for two specimens, RS2.1 and RS2.2, for all other six specimens values of complete joint rotation were found the same regardless of whether using $M_{pl,b}^{act}$ or $M_{pl,b}^{nom}$ for the strength limit, Table 20.

Preglednica 20: Celotna rotacija spoja za preizkušance RS in CP glede na različna nivoja upošteevane upogibne nosilnosti

Table 20: Complete joint rotations for RS and CP joints accounting for different flexural strength limits

Specimen	θ (rad)		Specimen	θ (rad)	
	strength limit			strength limit	
	$M_{pl,b}^{act}$	$M_{pl,b}^{nom}$		$M_{pl,b}^{act}$	$M_{pl,b}^{nom}$
RS1.1	0.065	0.065	CP1.1	0.067	0.067
RS1.2	0.065	0.065	CP1.2	0.058	0.058
RS2.1	0.068	0.078	CP2.1	0.078	0.078
RS2.2	0.068	0.077	CP2.2	0.068	0.068

In addition to the comparison between the values of achieved joint rotations and required values from related prequalification requirements from the codes, presented in Table 19, evaluation of seismic performance of the investigated stiffened beam-to-column joints in terms of envelope curves is presented hereinafter.

Envelope curve plot is a possible way commonly adopted when comparing and characterizing the deformation capacity of beam-to column joints subjected to cyclic loading. Envelope curves constructed from moment versus rotation hysteresis loops are presented herein. In addition, typical performance levels were identified for cyclic response envelope curve of particular specimen in order to facilitate comparison between the RS and CP stiffened joints.

Definition of the acceptance criteria and procedure for the evaluation of the seismic performance of joints were adopted from (FEMA, 2011. Dubina et al., 2014) and can be summarized as follows:

- the cyclic moment-rotation curve is computed for each joint assembly considering the column centreline as a reference point;
- an envelope curve is constructed for both positive and negative loading directions; from the two obtained envelope curves, the more detrimental one should be further considered;
- the following performance levels are identified:

DL – Damage Limitation

Description of the performance level:

Light damage, with the component retaining the initial strength and stiffness.

Criteria for identifying the performance level:

Deformation at which permanent, visible damage occurred in the experiments (yielding attained in the component) but not greater than 0.67 times the deformation at significant damage (SD) performance level. For the evaluation of the yield point, any other rational method can be used, i.e.:

- compute the plastic bending moment of the beam using the measured material properties and project it at the column centreline;
- compute the yield displacement from the experimental curve using the ECCS (1986) recommendations.

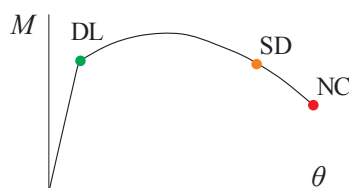
SD – Significant Damage

Description of the performance level:

Significant damage, with some margin against total collapse of the component.

Criteria for identifying the performance level:

Deformation corresponding to the intersection between the envelope curve and the $0.8 \cdot M^{max}$ strength limit, but not more than 0.75 times the deformation at Near Collapse (NC) performance level.



NC – Near Collapse

Description of the performance level:

Heavy damage, with low residual strength and stiffness of the component.

Criteria for identifying the performance level:

Deformation corresponding to the instance in which the flexural moment resistance drops to $0.2 \cdot M^{max}$, but not more than the maximum deformation attained during the test.

- the three identified performance levels (DL, SD, NC) are marked on each envelope curve;
- an illustration with the deformed state of the joint assembly is plotted corresponding to each of the three performance levels;
- the seismic performance of the joints is considered as acceptable if the rotation corresponding to the Significant Damage performance level is larger than 0.04 rad.

In addition to the last clause of the above procedure it has to be noted that, according to EN 1998-1, the column elastic deformation should not be included in the evaluation of the rotation capacity of the plastic hinge region θ_{pl} , and for structures of ductility class DCH the rotation capacity should be not less than 35 mrad. To provide consistent results in terms of complete joint response it was decided that the column elastic rotation should be accounted for. Consequently, the required minimum rotation capacity of the joint assembly should consistently be higher than 35 mrad. Assuming that the elastic rotation of the column is 5 mrad (maximum values between 0.002 and 0.0035 were measured in the experimental tests), then the 35 mrad rotation criterion from EN 1998-1 is substituted to 40 mrad of total joint rotation used hereinafter.

As guidance for the construction of the cyclic envelope curve, the provisions from FEMA P-795 (FEMA, 2011) were adopted. The following requirements should be used:

- the envelope curve should be constructed separately for positive and negative directions of loading;
- at each deformation level, up to the peak load experienced in the test, the load value of the cyclic envelope curve should be taken as the greater of: (1) the maximum value of

load for all cycles at that level of deformation; or (2) the value of load described by a series of straight lines that connect points of peak load at subsequent deformation amplitudes;

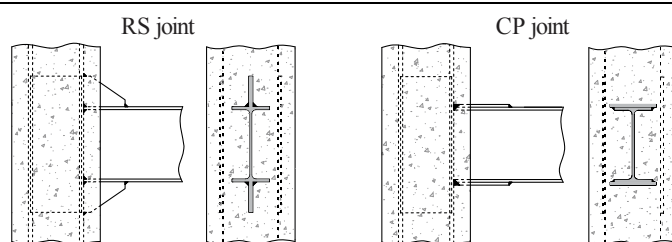
- after the peak load has been reached, the envelope curve should be defined using only (1) above for the following two cases:
 - if there is more than 20 % difference in peak loads at subsequent deformation amplitudes;
 - if the cyclic response curve has a negative stiffness (i.e., strength is lost in a single cycle of loading);
- the value of the cyclic envelope curve should drop to zero load at the maximum deformation executed in the test.

Summary of the eight stiffened beam-to-column joints subjected to variable amplitude cyclic loading is presented in Table 21. Each of the four different joints, RS1, RS2, CP1 and CP2, was tested with and without the column axial force. Corresponding cyclic response of all the eight specimens is presented in Fig. 29.

Preglednica 21: Povzetek osmih testov z uporabljeno spremenljivo korakoma naraščajočo amplitudo rotacije
 Table 21: Summary of the eight specimens tested using the variable amplitude cyclic loading

Specimen	Column	Beam	Loading protocol	Column axial force
RS1.1	HEB200, S460	IPE270, S355	ECCS N°45 1986 modified	/
RS1.2				38 % $N_{pl,act}$ *)
RS2.2	HEB160, S690	IPE240, S355	ANSI/AISC 341-10	/
RS2.2				40 % $N_{pl,act}$
CP1.1	HEB200, S460	IPE240, S355	ANSI/AISC 341-10	/
CP1.2				38 % $N_{pl,act}$
CP2.2	HEB160, S690	IPE270, S355	ANSI/AISC 341-10	/
CP2.2				40 % $N_{pl,act}$

*) Compression axial load to actual compression composite column plastic resistance ratio according to measured column characteristics



Since the cyclic response of the same two RS and CP joints was found very similar, see Chapter 3.4.2, only one of the two repeated tests for each different joint is used to present in detail the evaluation of the seismic performance according to the above procedure. Final results and comparison between all the eight specimens are gathered at the end of this chapter.

Specimen RS1.1

Fig. 71a illustrates the cyclic response of joint RS1.1 and the corresponding envelope curve for both positive and negative loading directions. The envelope curve from the negative loading was found to be more detrimental, Fig. 71b, and was further considered for the performance evaluation. Fig. 71c shows the computed yield rotation ($\theta_{pl,j} = 0.012$ rad), and the 80% strength degradation limit ($0.8 \cdot M_{max} = 206.9$ kNm) corresponding to $M^{max} = 258.6$ kNm. The deformations corresponding to the three performance levels presented in Fig. 71d are:

- DL: 0.012 rad
- SD: $0.75 \cdot 0.081 = 0.061$ rad > **0.04 rad**
- NC: 0.081 rad

The rotation capacity at significant damage (SD) is larger than the 0.04 rad limit. The state of the joint corresponding to the three performance levels is illustrated in Fig. 72.

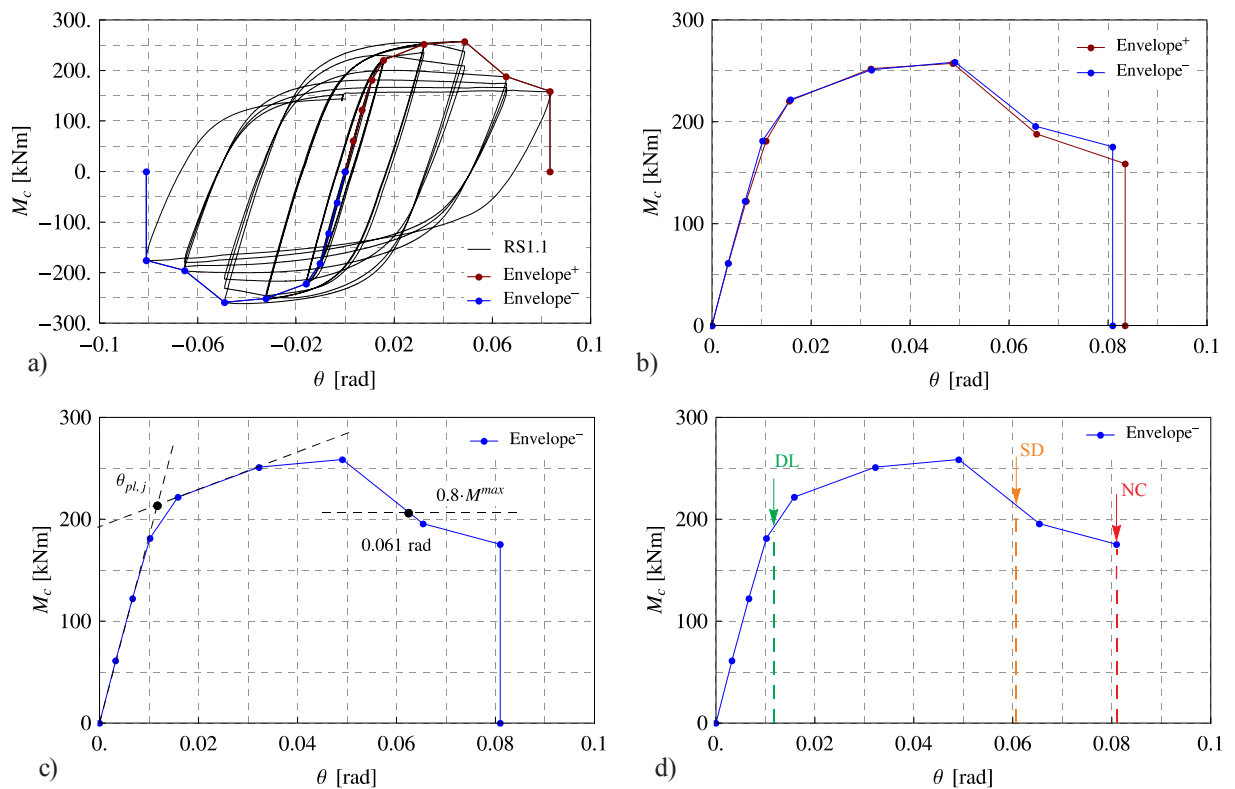
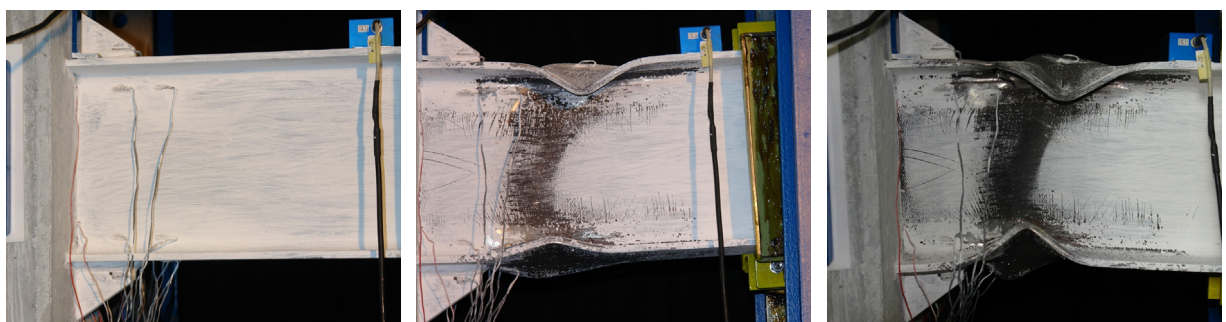


Fig. 71: Envelope curve construction of joint RS1.1 with the identification of performance levels
Slika 71: Konstrukcija ovojnice nizkocikličnega odziva spoja RS1.1 z določitvijo deformacijskih stanj



a) Damage limitation (DL) b) Significant damage (SD) c) Near collapse (NC)

Fig. 72: State of joint RS1.1 corresponding to the three selected performance levels
Slika 72: Odziv spoja RS1.1 glede na obravnavana tri deformacijska stanja

Specimen CP1.1

Fig. 73a illustrates the cyclic response of joint CP1.1 and the corresponding envelope curve for both positive and negative loading directions. The envelope curve from the negative loading was found to be more detrimental, Fig. 73b, and was further considered for the performance evaluation. Fig. 73c shows the computed yield rotation ($\theta_{pl,j}=0.013$ rad), and the 80% strength degradation limit ($0.8 \cdot M^{max} = 220.0$ kNm) corresponding to $M^{max} = 274.9$ kNm. The deformations corresponding to the three performance levels presented in Fig. 73d are:

- DL: 0.013 rad
- SD: $0.75 \cdot 0.077 = 0.058$ rad > **0.04 rad**
- NC: 0.077 rad

The rotation capacity at significant damage (SD) is larger than the 0.04 rad limit. The state of the joint corresponding to the three performance levels is illustrated in Fig. 74.

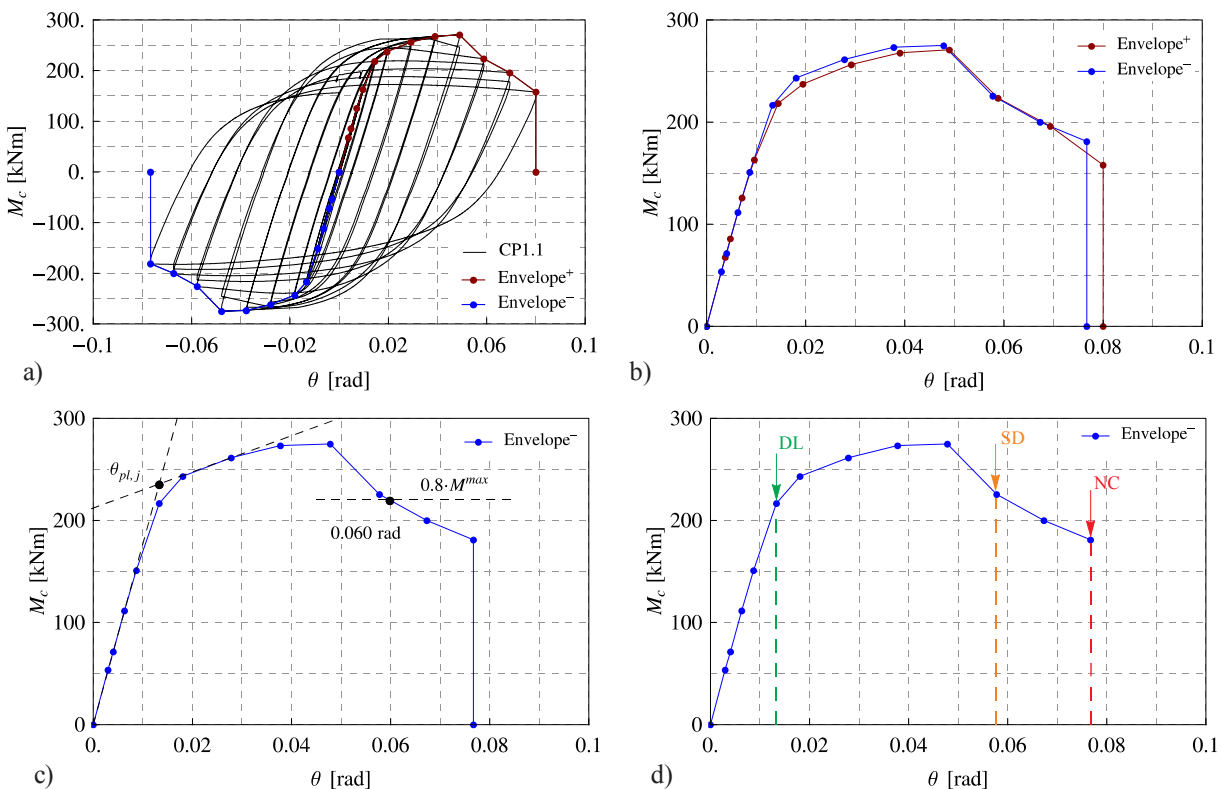
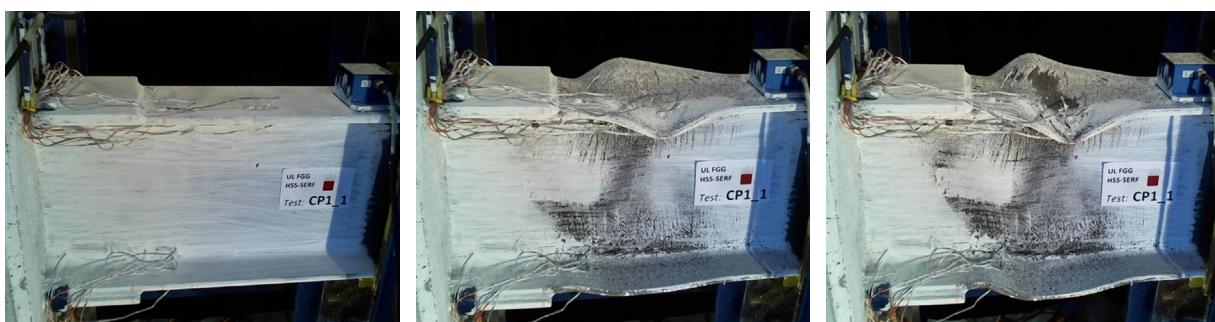


Fig. 73: Envelope curve construction of joint CP1.1 with the identification of performance levels
Slika 73: Konstrukcija ovojnice nizkocikličnega odziva spoja CP1.1 z določitvijo deformacijskih stanj



a) Damage limitation (DL)

b) Significant damage (SD)

c) Near collapse (NC)

Fig. 74: State of joint CP1.1 corresponding to the three selected performance levels
Slika 74: Odziv spoja CP1.1 glede na obravnavana tri deformacijska stanja

Specimen RS2.1

Fig. 75a illustrates the cyclic response of joint RS2.1 and the corresponding envelope curve for both positive and negative loading directions. The envelope curve from the negative loading was found to be more detrimental, Fig. 75b, and was further considered for the performance evaluation. Fig. 75c shows the computed yield rotation ($\theta_{pl,j} = 0.014$ rad), and the 80% strength degradation limit ($0.8 \cdot M^{max} = 165.5$ kNm) corresponding to $M^{max} = 206.8$ kNm. The deformations corresponding to the three performance levels presented in Fig. 75d are:

- DL: 0.014 rad
- SD: $0.75 \cdot 0.086 = 0.065$ rad > **0.04 rad**
- NC: 0.086 rad

The rotation capacity at significant damage (SD) is larger than the 0.04 rad limit. The state of the joint corresponding to the three performance levels is illustrated in Fig. 76.

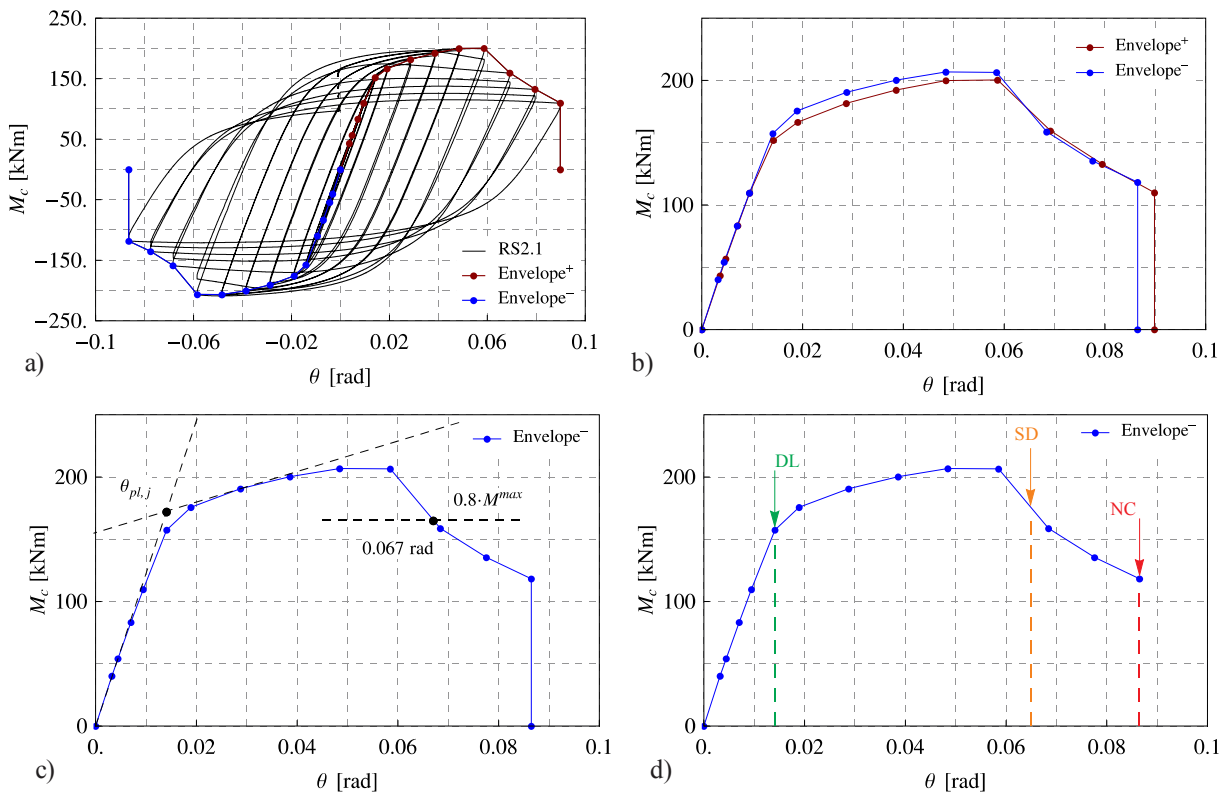
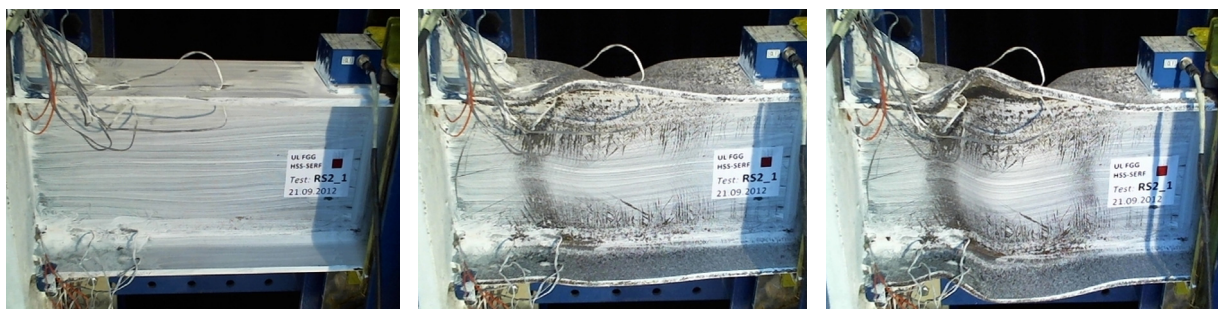


Fig. 75: Envelope curve construction of joint RS2.1 with the identification of performance levels
Slika 75: Konstrukcija ovojnice nizkocikličnega odziva spoja RS2.1 z določitvijo deformacijskih stanj



a) Damage limitation (DL) b) Significant damage (SD) c) Near collapse (NC)

Fig. 76: State of joint RS2.1 corresponding to the three selected performance levels
Slika 76: Odziv spoja RS2.1 glede na obravnavana tri deformacijska stanja

Specimen CP2.1

Fig. 77a illustrates the cyclic response of joint CP2.1 and the corresponding envelope curve for both positive and negative loading. The envelope curve from the negative loading was more detrimental, Fig. 77b, and was further considered for the performance evaluation. Fig. 77c shows the computed yield rotation ($\theta_{pl,j} = 0.014$ rad), and the 80% strength degradation limit ($0.8 \cdot M^{max} = 165.6$ kNm) corresponding to $M^{max} = 206.9$ kNm. The deformations corresponding to the three performance levels presented in Fig. 77d are:

- DL: 0.014 rad
- SD: $0.75 \cdot 0.088 = 0.066$ rad > **0.04 rad**
- NC: 0.088 rad

The rotation capacity at significant damage (SD) is larger than the 0.04 rad limit. The state of the joint corresponding to the three performance levels is illustrated in Fig. 78.

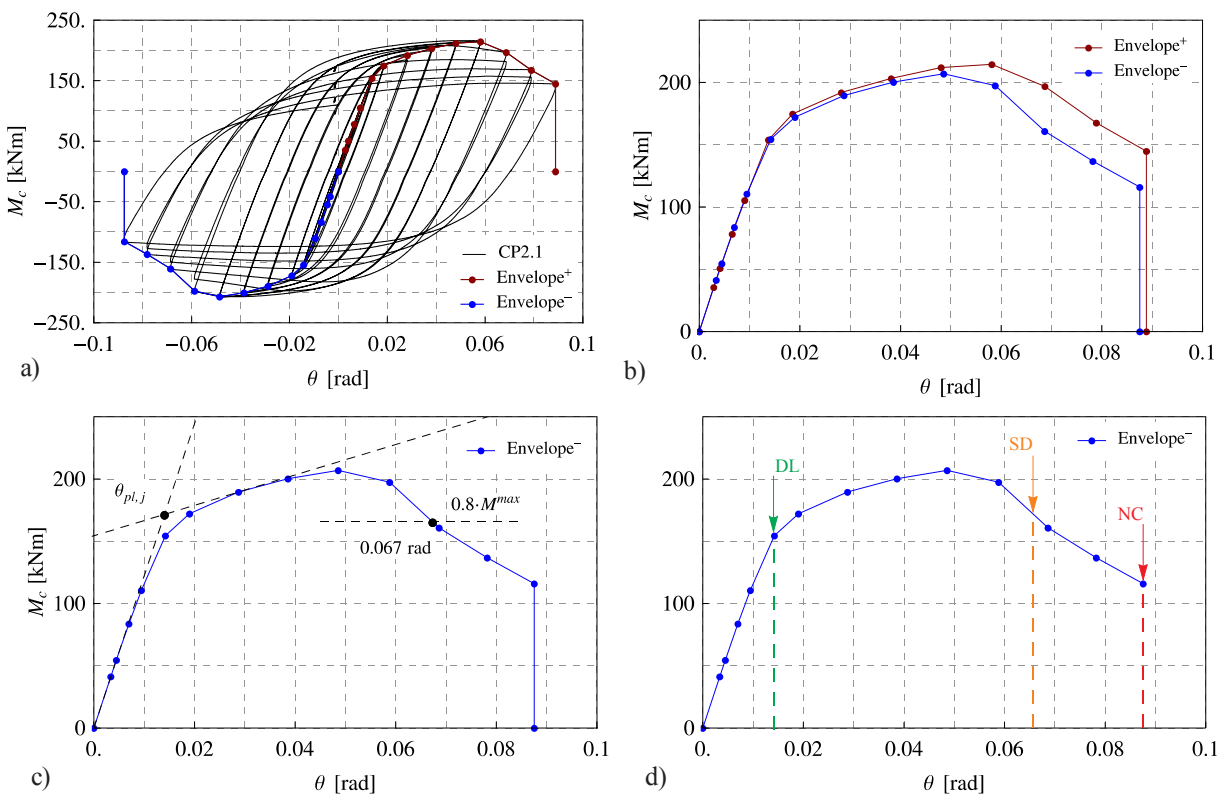
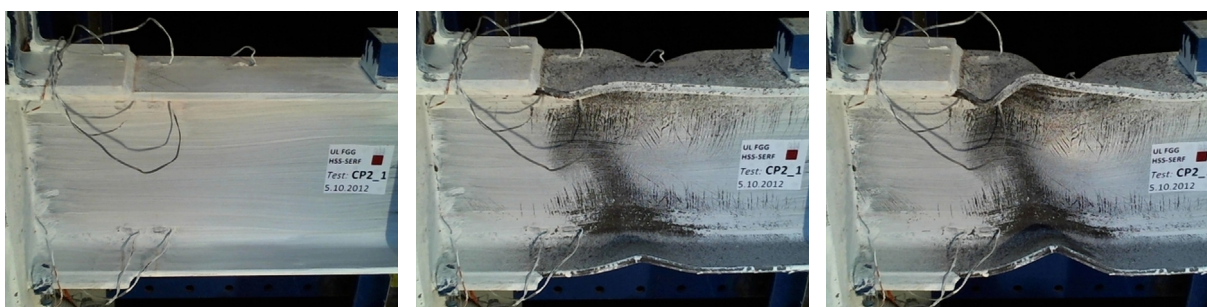


Fig. 77: Envelope curve construction of joint CP2.1 with the identification of performance levels
 Slika 77: Konstrukcija ovojnice nizkocikličnega odziva spoja CP2.1 z določitvijo deformacijskih stanj



a) Damage limitation (DL) b) Significant damage (SD) c) Near collapse (NC)

Fig. 78: State of joint CP2.1 corresponding to the three selected performance levels
 Slika 78: Odziv spoja CP2.1 glede na obravnavana tri deformacijska stanja

Overview of seismic performance of all eight welded rib-stiffened (RS) and cover-plate (CP) beam-to-column joints comprising fully encased composite column is presented in Table 22 and Fig. 79.

Preglednica 22: Ciklični odziv testiranih spojev glede na izbrane kriterije obnašanja
Table 22: Cyclic performance of the investigated beam-to-column joints according to the acceptance criteria

RS joint	Achieved joint rotation for performance level [rad]			CP joint	Achieved joint rotation for performance level [rad]		
	DL	SD	NC		DL	SD	NC
RS1.1	0.012	0.061	0.081	CP1.1	0.013	0.058	0.077
RS1.2	0.011	0.059	0.080	CP1.2	0.012	0.053	0.077
RS2.1	0.014	0.065	0.086	CP2.1	0.014	0.066	0.088
RS2.2	0.013	0.065	0.086	CP2.2	0.014	0.059	0.078

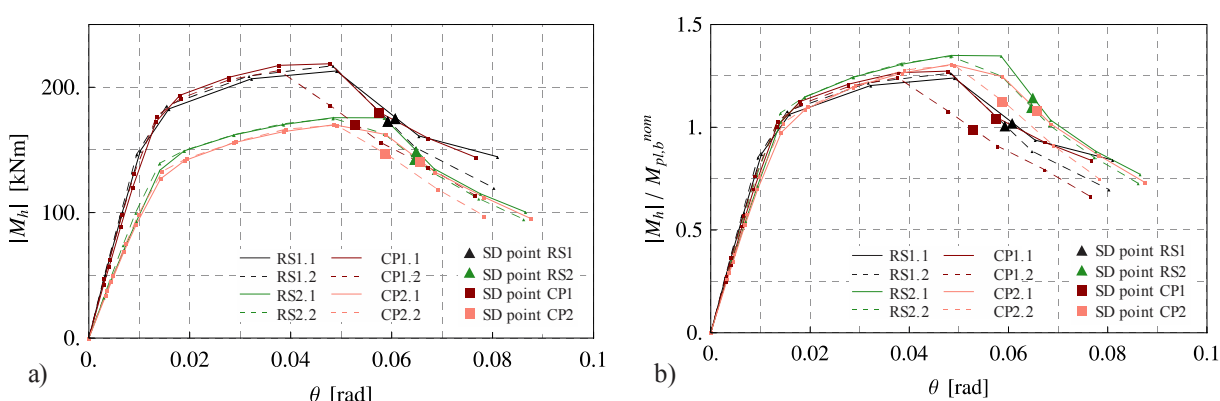


Fig. 79: Envelope curves for all eight RS and CP joints subjected to variable amplitude cycling: a) moment to the plastic hinge centreline vs. total joint rotation, b) normalised moment to the plastic hinge centreline vs. total joint rotation

Slika 79: Ovojnice cikličnega odziva vseh osem spojev RS in CP testiranih s spremenljivo korakoma naraščajočo amplitudo rotacije: a) moment na center plastičnega v odvisnosti od celotne rotacije spoja, b) normiran moment na center plastičnega v odvisnosti od celotne rotacije spoja

All four joint configurations, RS1, RS2, CP1 and CP2, evidenced a stable hysteretic response with rotation capacities larger than 0.040 rad limit that corresponds to the significant damage (SD) performance level. Values of joint rotation at SD limit state observed from Fig. 79a are fully comparable for all eight analysed specimens, although performance of joints CP1 and CP2 shows somewhat less consistency compared to the result obtained from joints RS1 and RS2: rotations at SD limit state produced by specimens CP1.2 and CP2.2 are somewhat smaller and clearly deviate from values obtained by all other specimens.

The observation given above can even better be seen in Fig. 79b, where envelope curves with normalised moment M_h according to the nominal plastic beam moment $M_{pl,b}^{nom}$ are presented. In addition, larger values of SD limit state joint rotation can be observed for all the specimens comprising small beam profile IPE240, RS2 and CP2, compared to the corresponding joints with IPE270 beam profile, RS1 and CP1.

Following the foregoing discussion, it should be clearly noted that the reason for poorer response of specimens CP1.2 and CP2.2 was certainly not the effect of the high level of compression column axial force, which was present also in both the tests. Complete response of all the eight joints was governed exclusively by the plastic behaviour of the beam in the

plastic hinge zone beyond the stiffened region, and the beam-column welded interface that might be affected by the stress field of the compressed column remained intact in all the tests.

Further observations of the joint performance presented in Figs 71 to 79 evidenced a very good correlation with the proposed definitions for the other two performance levels, i.e. for damage limitation (DL) representing the state with the onset of permanent plastic deformations, and for ultimate near collapse (NC) state with large reduction of strength and stiffness before the low-cycle fatigue failure of the joint.

3.4.7 Energy dissipation capacity

Cumulative plastic rotation $\Sigma\theta_{pl}$, presented in Tables 9 and 10, is considered as the primary indicator to evaluate the energy dissipation capacity of the specimens and was computed as in Nakashima et al. (1998b), Fig. 80.

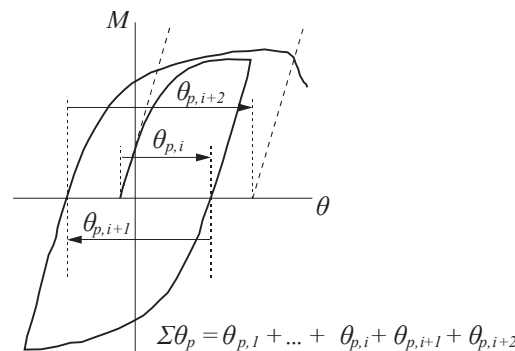


Fig. 80: Definition of plastic rotation and cumulative plastic rotation according to Nakashima et al. (1998b)

Slika 80: Definicija plastične rotacije in kumulativne plastične rotacije, privzeto po Nakashima et al. (1998b)

The response of all 16 specimens is graphically presented in Fig. 81 by comparing of $\Sigma\theta_{pl,1}$ and $\Sigma\theta_{pl,2}$.

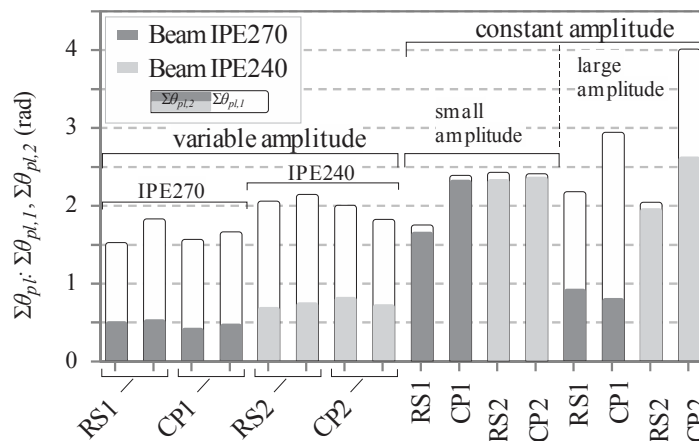


Fig. 81: Comparison of cumulative plastic rotations for all 16 specimens

Slika 81: Primerjava doseženih kumulativnih plastičnih rotacij za vseh 16 preizkušancev

In case of all eight specimens tested under variable cyclic loading, significant reduction in $\Sigma\theta_{pl,2}$ can be observed, with $\Sigma\theta_{pl,2}/\Sigma\theta_{pl,1}$ ratios between 0.28 and 0.41. Larger values of both cumulative plastic rotations can be observed for specimens with the small beam section.

Cumulative plastic rotations for constant amplitude tests are considerably larger due to increased number of cycles, which is a consequence of smaller applied amplitude, except for specimens tested with large constant amplitude in combination with large beam section IPE270, where the beam local buckling occurred.

Comparing the response of RS and CP joints, deviation can be observed for RS configuration in terms of lower values of cumulative plastic rotations obtained from both constant small and large amplitude tests, see Figs 81 and 82. It seems the reason for this can be attributed to the more pronounced strain concentrations at the end of the rib-stiffener, see also Figs 30 to 33. No such obvious differences between the RS and the CP joint in the response of eight specimens tested under variable cyclic loading can be noticed.

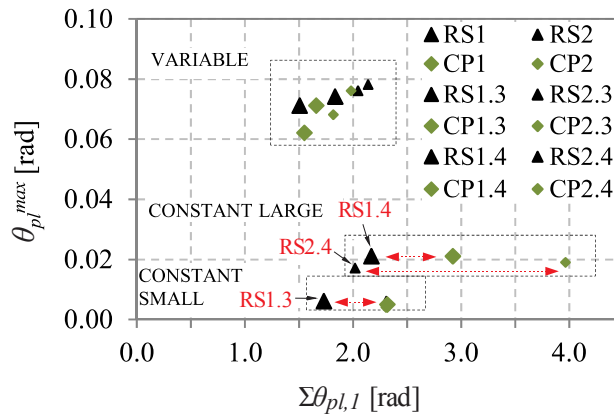


Fig. 82: Maximum plastic rotation amplitude vs. cumulative plastic rotation
Slika 82: Največja dosežena plastična rotacija v odvisnosti od akumulirane plastične rotacije

The above findings show that:

- (1) during large amplitude cyclic loading beam local buckling occurred, which led to pronounced LCF failure in the buckled zone of the beam irrespective of the joint configuration (applies to variable cyclic loading as well),
- (2) small amplitude loading resulted in LCF failure of the material without the occurrence of beam local buckling. In the latter case the RS joint configuration proved to be more critical under LCF effects, due to unfavourable higher strain concentrations together with weld residual stress and HAZ at the end of the rib-stiffener.

Comparison of cumulative dissipated energy for all test specimens is presented in Fig. 83. In addition to the total dissipated energy up to the complete failure of the specimen, the portion of dissipated energy, corresponding to the failure criterion related to 20 % fall of maximum strength and initial stiffness, is illustrated. In cases with no buckling the reduction is small, whilst for cases with beam local buckling the reduced portion is not negligible and ranges between 30 and 68 %.

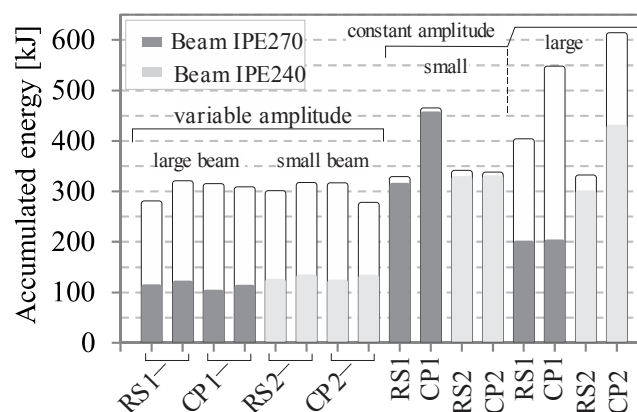


Fig. 83: Cumulative dissipated energy
Slika 83: Kumulativna disipirana energija

3.4.8 Skeleton Curves: monotonic response characteristics obtained from variable amplitude cyclic tests

Another index, characterizing the deformation and energy dissipation capacity of steel members subjected to load reversals, is the concept of skeleton curve that has been commonly used by Japanese researchers (Kato, Akiyama, 1968. Nakashima et al., 1998a. Suita et al., 1998). The skeleton curve principle is also useful to compare the ductility and energy dissipation capacity of hysteresis curves obtained from different loading histories.

Since monotonic tests were not performed in the framework of the study, skeleton curves were employed to deduce the monotonic response of the joints. The curves were later useful also for the calibration of numerical model simulating monotonic response, see Chapter 4.3.2.2.

The following procedure, adopted from the paper by Suita et al. (1998), was used to construct skeleton curves from force versus deformation hysteretic curves obtained from the cyclic loading tests.

The portion of a force deformation curve that exceeds the maximum force achieved in the previous loading cycles is defined as a new skeleton portion. This portion is added to the skeleton curve already constructed, with the horizontal (deformation) origin of the new skeleton portion translated to the end of the already built skeleton curve. This procedure is repeated, and the maximum deformation obtained is considered as the skeleton deformation capacity.

A skeleton curve is constructed for each of the positive and negative loading directions. Fig. 84 shows skeleton curves obtained by using the above procedure for the case of specimen RS1.1.

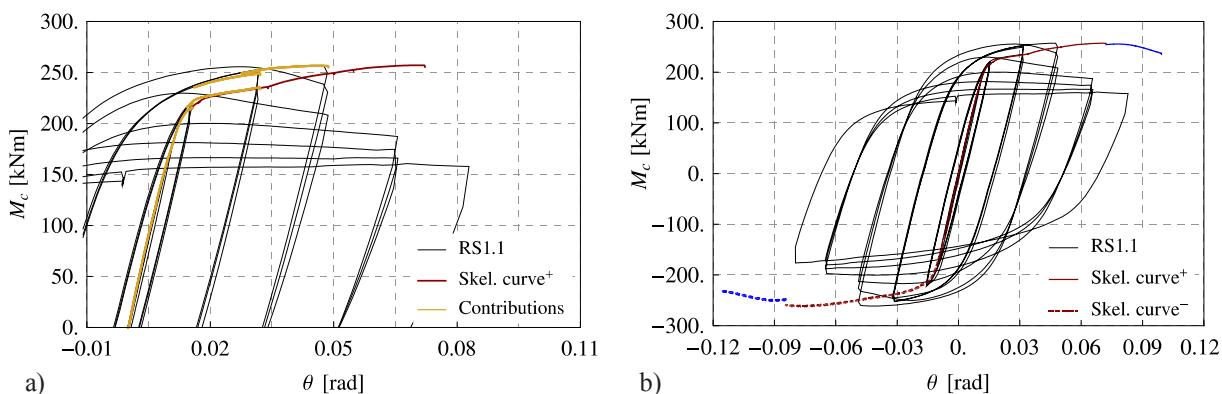


Fig. 84: Construction of a skeleton curve: a) response of specimen RS1.1, b) positive and negative skeleton curves with added descending part according to the modified procedure

Slika 84: Določitev skeleton krivulje: a) odziv preizkušanca RS1.1, b) skeleton krivulja za pozitivno in negativno smer obremenjevanja z dodanim končnim padajočim delom po modificirani metodi

The basic hypothesis of the skeleton curve principle is that small loading cycles experienced after a large loading cycle do not contribute to damage and that the obtained skeleton curve for a cyclic loading test is the same as the curve obtained from a monotonic loading test. This hypothesis is not necessarily valid for a fatigue type loading. However, for earthquake loading, where the number of large deformation cycles is normally rather small, this hypothesis should be correct when estimating the ductility capacity of structural steel members.

In addition to the original skeleton curve procedure adopted from Suita et al. (1998), which yields ascending format of skeleton curves, Fig. 84a, algorithm to detect also descending part

of the curve was implemented, hereinafter referred to as modified procedure, Fig. 84b (curve part coloured in blue).

Skeleton curves defined according to the modified procedure were used to calibrate numerical model for the simulation of a monotonic beam-to-column response, see Chapter 4.3.2.2.

Skeleton curves (for positive and negative loading directions) constructed for each of the four RS and CP joint specimens subjected to the variable cyclic loading protocol are presented in Fig. 85 and Fig. 86. For each specimen three different curves are presented in terms of total joint rotation, total beam rotation (without contribution from the column), and plastic joint rotation.

Curves representing total joint rotation and plastic rotation are very similar for each of the four different specimens (RS1, RS2, CP1 and CP2). Contribution from column rotation is smaller in all the cases where full level of column axial force was applied. Increased ductility of all the joints with the small beam profile IPE240 (RS2.1, RS2.2, CP2.1, CP2.2) compared to the other four joints with larger IPE270 beam (RS1.1, RS1.2, CP1.1, CP1.2) can also be observed.

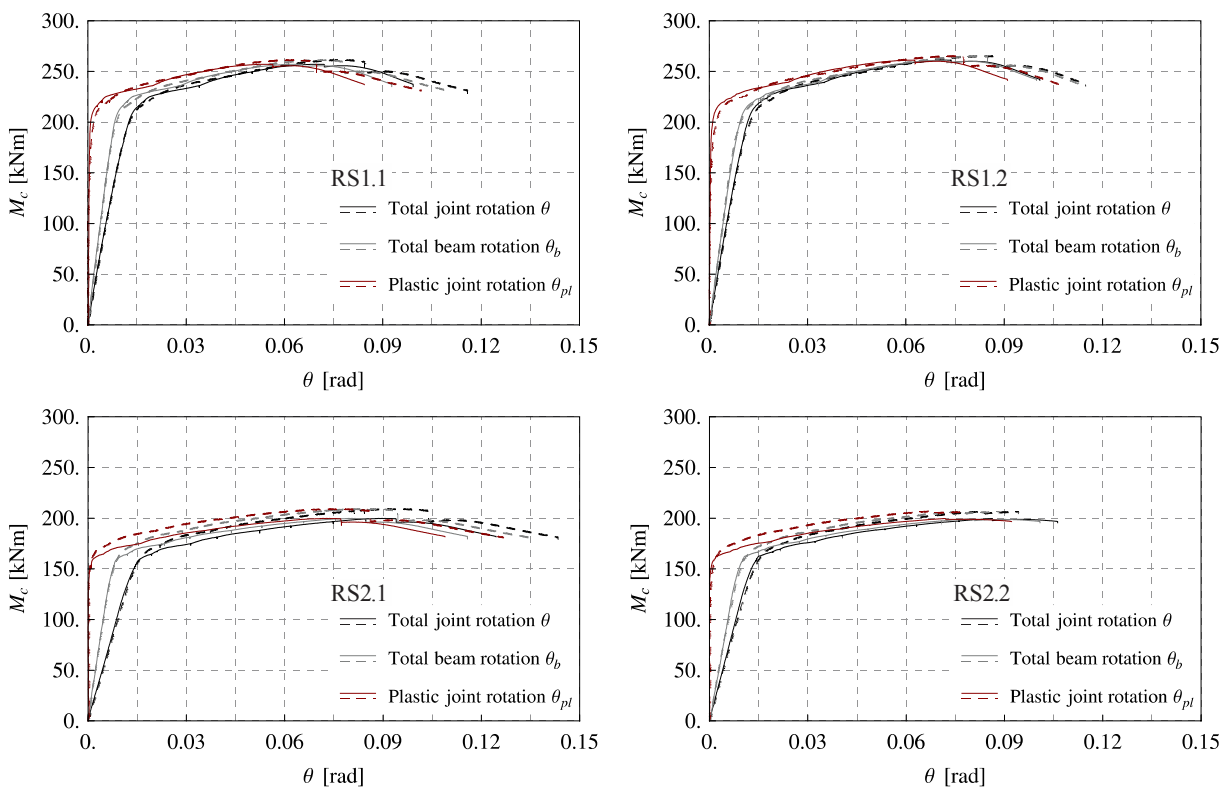


Fig. 85: Skeleton curves for specimens RS1 and RS2 subjected to variable cyclic loading
Slika 85: Skeleton krivulje za preizkušance RS1 in RS2 testirane s spremenljivo amplitudo ciklične obremenitve

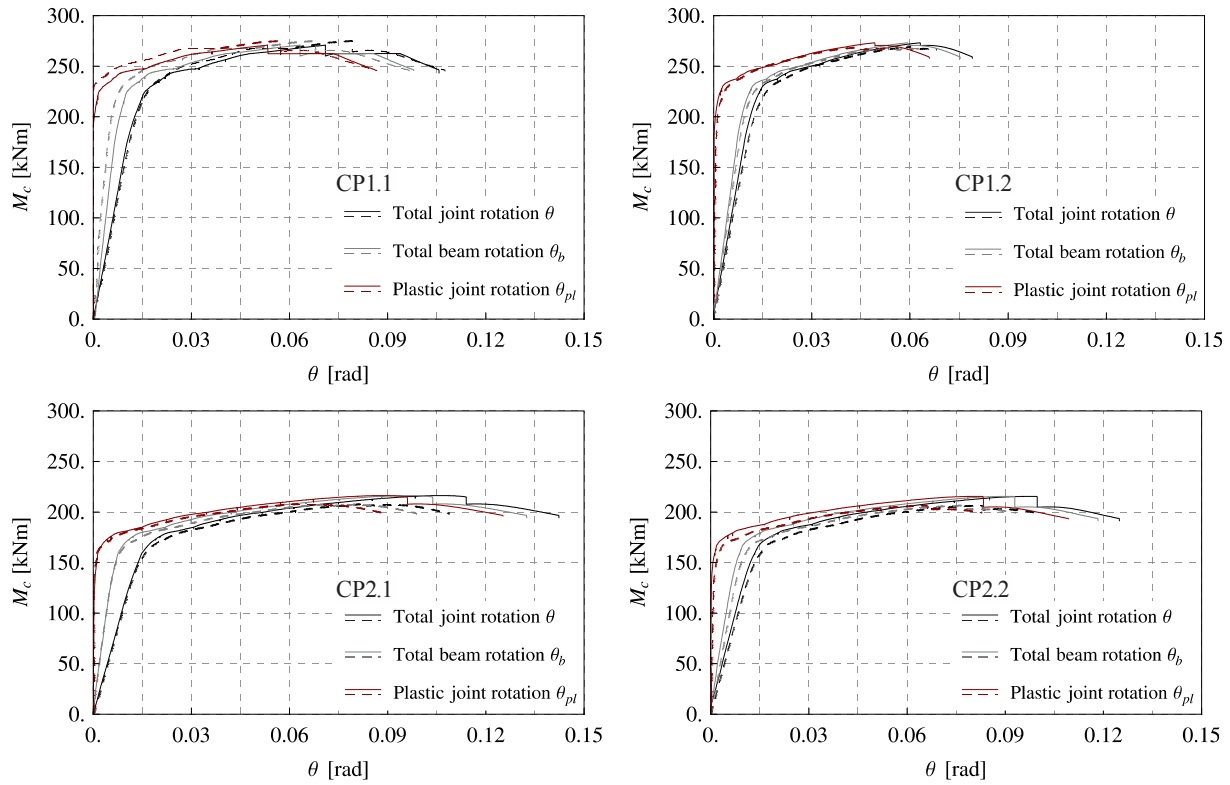


Fig. 86: Skeleton curves for specimens CP1 and CP2 subjected to variable cyclic loading

Slika 86: Skeleton krivulje za preizkušance CP1 in CP2 testirane s spremenljivo amplitudo ciklične obremenitve

3.4.9 Low-Cycle Fatigue Assessment

For the prediction of the low-cycle fatigue resistance of the joints, a standard $S-N$ curve approach was selected:

$$N \cdot S^m = K. \quad (22)$$

For the deformation parameter range S , global structural ductility parameter $\Delta\theta_{pl}$ was taken, originally proposed by Krawinkler & Zohrei (Krawinkler, Zohrei, 1983):

$$N \cdot (\Delta\theta_{pl})^m = K, \quad (23)$$

where $\Delta\theta_{pl}$ is a plastic rotation amplitude in constant amplitude test. The number of complete cycles to failure is plotted against plastic joint rotation on a log-log scale for all the 16 specimens and shown in Fig. 87.

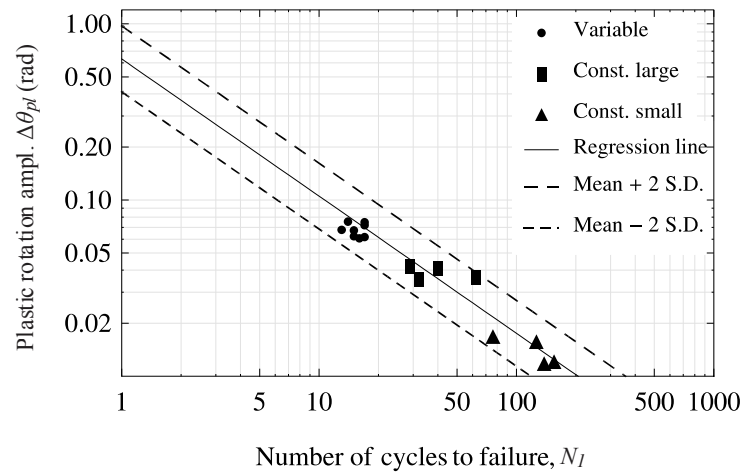


Fig. 87: Low-cycle fatigue assessment of the test results
Slika 87: Analiza nizkocikličnega utrujanja experimentalnih rezultatov

Linear regression line was obtained by fitting the data obtained from eight constant amplitude cyclic tests and is presented as solid line. The obtained value of parameter m , identifying the slope of the $S-N$ line, is 1.28, which is significantly lower compared to the value of 2 proposed by Krawinkler & Zohrei (Krawinkler, Zohrei, 1983), while the value of $\text{Log } K$, representing the intersection of the line with horizontal ($\text{Log } N$) axis, is 5.33. Scatter bands at \pm two times the standard deviation are shown as dashed lines. Data from the eight variable amplitude cyclic tests are plotted as well. In order to use Eq. (22), the points are represented by equivalent plastic rotation range $\Delta\theta_{pl,eq}$. Using Miner's rule the following relation can be defined:

$$\Delta\theta_{pl,eq} = \left(\sum_{i=1}^k (N_i \cdot \Delta\theta_{pl,i}^m) / N_{tot} \right)^{\frac{1}{m}}, \quad (24)$$

where N_{tot} is the total number of cycles in the loading history, N_i is the number of cycles at the same range of $\Delta\theta_{pl,i}$, and k is the number of different ranges of $\Delta\theta_{pl,i}$.

The latter data may be considered as very well predicted by the regression line obtained from constant amplitude tests.

3.4.10 Conclusions to the cyclic test results

Cyclic tests on full-strength welded stiffened beam-to-column joints were carried out to study their seismic performance. Two different typologies of stiffened connections were studied: rib stiffened (RS) and cover plate (CP) connection. A hybrid-steel approach was implemented with high strength steel used for the columns as non-dissipative elastic members and mild carbon steel for the beams acting as dissipative members. Additional parameter of the study was axial force of a high level compression in the column. A total of 16 cyclic tests were carried out: eight tests using variable loading with stepwisely increasing amplitude and additional eight tests at two different inelastic constant displacement levels.

Detailed description of experimental test results on 16 beam-to-column RS and CP moment-resisting connections is presented. Systematically addressed results provide valuable database on the behaviour of the stiffened beam-to-column joints and thus fill the gap of knowledge in this field, especially in combination with the type of steel profiles used in the European design practice.

All 16 welded rib-stiffened and cover-plate beam-to-column joints subjected to variable and constant cyclic loading amplitude fulfilled the objective of the applied design concept: the whole inelastic action was transferred away from the face of the beam-to-column connection into the beam section behind the stiffened region. Unlike the events from the past major earthquakes, where premature brittle failures without prior signs of plastic deformation were observed at the unstiffened beam-column welded connections of moment-resisting frames, complete stiffened beam-to-column connection remained undamaged in all the 16 joint specimens; i.e. no damage of welds, either in beam-column connection or around reinforcing plates, was observed from macro examination after the tests. In this aspect both designed stiffened beam-to-column connections would behave substantially better under seismic loading than the unstiffened ones.

Since cyclic response was governed solely by the behaviour of unstiffened beams, possessing reliable inelastic deformation capacity as compact sections, all the joints tested with stepwisely increasing amplitude meet the pre-qualification requirements according to the EN 1998-1 and ANSI/AISC 341-10 seismic provisions. Maximum plastic rotations of eight specimens subjected to variable amplitude loading, at 20 % degradation of maximum strength and initial stiffness, were between 0.030 and 0.044 rad with the corresponding cumulative plastic rotations between 0.480 and 0.921 rad.

The total number of completed cycles to failure obtained from constant amplitude cyclic tests varied between 76 and 155 for small ($\theta = 0.019$ rad) and from 29 to 62 for large ($\theta = 0.033$ rad) amplitude tests, with corresponding total cumulative plastic rotations between 1.728 and 3.960 rad.

During large constant amplitude loading beam local buckling occurred. This led to the reduction of strength and stiffness, and finally to LCF failure in the buckled zone of the beam in case of both CP joints. However, both RS joints subjected to large constant amplitude cycling failed due to the beam flange fracture in the HAZ of the fillet weld at the end of the rib-stiffener. Accordingly, both RS joints sustained considerably less cycles to failure compared to the corresponding CP beam-to-column joints.

Beam local buckling was not observed under small amplitude loading and the degradation of joint resistance took place only during the last few cycles when LCF fracture of the flange just behind the stiffened region led to complete joint failure. Also in this case, the CP joint displayed better fatigue performance, attributed to the increased level of unfavourable strain

concentrations, larger weld residual stress and HAZ at the end of the rib-stiffener in the RS joint.

Both column-beam HSS/MCS material combinations evidenced a good performance without any noticeable effect of the applied level of column compressive axial force, being around 40 % of the actual composite column plastic resistance to compression, on the cyclic response of the specimens.

Tests clearly evidenced that the proposed concept of both full-strength beam-to-column joints provides a good solution in all aspects. Beside an excellent performance, an important advantage is simple design and fabrication of these connections. During seismic action the vulnerable welded connection at the face of the column remains nominally elastic under maximal forces from the connected beam, reducing the possibility for the appearance of brittle failure conditions at the beam-column interface, and thus no additional requirements for welds are needed, while a compact beam section can easily provide adequate ductility. The application of full-strength stiffened connections, especially rib-stiffened solution, can be extended to the end plate moment resisting connections.

It is to be noted that beam-to-column member sizes used in the test specimens were limited by composite column bearing capacity, designed in such way that relatively high level of compressive axial load-to-plastic resistance ratio was achieved with laboratory equipment capacities. Extrapolation of joint behaviour prediction to connections of a substantially different type and size should be undertaken with care. Namely, the observed trend from the experimental test results clearly shows that as beams become deeper and heavier, their ability to develop inelastic rotation may be somewhat diminished.

In order to provide reliable and comprehensive design guidelines for both stiffened beam-to-column connections in combination with hot rolled I and H steel beam profiles commonly used in the European design practice, additional research is still needed.

To this aim, the research work at this stage was continued with the numerical study utilising finite element method in order to perform advanced numerical simulations of the cyclic response of the stiffened beam-to-column joints.

Complete development and performance of the developed numerical finite element models against experimental test results is presented in the following Chapter 4, which is followed by additional complementary numerical study on both welded stiffened connections in Chapter 5.

4 NUMERICAL SIMULATIONS OF BEAM-TO-COLUMN JOINT BEHAVIOUR UNDER MONOTONIC AND CYCLIC LOADING

4.1 Introduction

The idea of the work is to be able to simulate with high accuracy the behaviour of steel structures under monotonic and cyclic loading. The use of FEM software tools gives us the opportunity of doing sophisticated simulations of the problem addressed.

Nonlinear finite-element analysis (FEA) of rib-stiffened (RS) and cover plate (CP) moment-resisting connections was undertaken with two specific aims: as part of advanced preliminary numerical simulations in order to support the design of the test specimens (shortly discussed in Chapter 3.2) and to establish complementary parametric analysis based on models validated against the experimental tests results. Abaqus v6.12-2 (SIMULIA, 2012) FEM tool was used for all the numerical simulations presented in this work.

Specific goals of the numerical part of the study are as follows:

- to gain better understanding of the inelastic behaviour of beam-to-column connections;
- to investigate the effect of the two stiffened connection types in the force (load) transfer mechanism in local stiffened region as well as in the plastic hinge zone;
- to assess the deformation capacity of both RS and CP joints;
- to support design recommendations for RS and CP stiffened connections.

Finite element beam-to-column joint model development was guided on the basis of pre-knowledge on beam-to-column joint response obtained from experimental test results performed in the framework of this study as well as from the related literature summarised in Chapter 2.

Among others, the most crucial aspects that should be considered for proper numerical simulation of joints are comprised in a twofold phenomenon that affects the monotonic as well as cyclic response of full-strength joints, i.e. beam local buckling as a result of large plastic rotations (plastic strains) concentrated in plastic hinge region on the beam and material LCF endurance, both inherently connected and inevitably important to understand properly beam-to-column joint behaviour under arbitrary loading with large plastic joint load excursions.

Beside introductory part, the present chapter consists of two major subdivisions, i.e. description of finite element model development, and the subsequent presentation of the developed finite element model performance against experimental test results. Although the subdivisions follow the logical chronological sequence of the study, the reader should be aware of iterative development of both parts during the whole research work.

Nonlinear material behaviour employed for concrete and steel, complex geometry of the stiffened beam-to-column joints, heavy models with considerable number of FEs along with large number of applied loading cycles led to time consuming work that took a great portion of time spent in the study. The foregoing remarks along with high consistency achieved

between the simulated and the experimental results for both monotonic and cyclic joint behaviour gives even greater weight to the work presented hereinafter.

The effect of structural steel material low-cycle fatigue on the response of the stiffened joints is analysed in the last part of the finite element model calibration phase, Chapter 4.3.3.5. Accordingly, in combination with a detailed results report, the study provides reliable information on the ductility of the stiffened joints influenced by fatigue that may lead to failure of individual member of the structure during earthquake event.

Nonlinear finite element analysis can provide deeper insight into the likely behaviour of complex welded connections such as those analysed in this work. However, due to actual material as well as geometric imperfections, residual stresses and strains, and flaws or defects that can be present in real structure and cannot be modelled a priori, such analysis has significant limitations too, and the author is certainly aware of that. These limitations may substantially impact the local and consequently global behaviour of a stiffened connection.

However, limitations aside, nonlinear finite element analysis can be used for both better understanding of states of stress and strain in stiffened connections and to compare the effectiveness of different stiffened typologies (RS and CP in this case), alternate reinforcement plate geometries, weld profile geometries, column resistance along with the panel zone strengths, and other geometric details of a beam-to-column stiffened connection. At the same time FEM technique offers a complementary advantage to gain considerable insight in the state of localised response indices that govern the response of the structural element. Such information cannot be cost-effectively obtained from full-scale laboratory testing.

First, the accuracy of FEM predictions has to be checked at the local level, since response indices, used to characterize the behaviour of the structure subassemblies, are sensitive to the type of finite element and mesh density, solver procedure, applied material formulations and geometry imperfections. Before going into details of interpretation of simulated structure response, all these factors must be carefully considered by addressing a number of modelling issues presented in the following chapter.

4.2 Finite element model development

4.2.1 Selection of element types

It is necessary at this stage to explain certain terms in relation to the finite element types supported by Abaqus that are discussed in the following sections of this chapter. Abaqus/Standard element library offers both second-order (quadratic interpolation) and first-order (linear interpolation) elements. It is generally known that the second-order elements provide higher accuracy than the first-order elements for »smooth« problems that do not involve complex contact conditions or severe element distortions. They capture stress concentrations more effectively and are better for modelling geometric features.

However, there are two main reasons why the first order (shell and solid) elements should be used in this study: in comparison with the second-order elements they are computationally more economic and secondly, they perform better in analyses where there are large element distortions or large strain gradients. They are therefore more appropriate for the purpose of the research because of the large plastic deformations and strain gradients expected in the connection region on the beam.

Reduced integration was used for all shell and solid elements for computational efficiency – reduces running time, especially in three dimensions. Reduced integration uses a lower-order

integration to form the element stiffness, whereas the mass matrix and the distributed loadings use full integration.

Second-order reduced-integration elements in Abaqus/Standard generally yield more accurate results than the corresponding fully integrated elements. However, for first-order elements the accuracy achieved with full versus reduced integration depends on the nature of the problem. Therefore, reduced-integration elements are not necessarily less accurate than fully integrated elements.

For the solid elements employed in the study, reduced integration implies the use of one integration point to represent the element. The number of integration points through the thickness of shell elements was taken as 5. Namely, work by Huang (1994) indicated that while 3 integration points gave slightly inaccurate results, 7 integration points provided no real advantage.

Hourglassing can be a problem with first-order, reduced-integration elements in stress/displacement analyses. Since the elements have only one integration point, they may distort in such way to produce spurious zero energy deformation modes, which, in turn, leads to uncontrolled distortion of the mesh. First-order, reduced-integration elements in Abaqus include hourglass control (if a reduced-integration element is chosen, the enhanced hourglass formulation is applied automatically), but they should be used with reasonably fine meshes. Hourglassing can also be minimized by distributing point loads and boundary conditions over a number of adjacent nodes.

4.2.2 Finite element meshes

Before detailed simulation of the connections, a convergence study was performed in order to select the most accurate finite element formulation as well as to determine the appropriate level of mesh refinement. The topic is addressed as a compromise between reasonable computational time on one hand and accuracy of results achieved on the other.

Regarding steel parts of analysed structures, two types of finite element are utilized in this research, resulting in all-shell, all-solid and hybrid shell/solid models. However, concrete encasement is modelled using solid elements in all cases. At the first step shell-element models were prepared to study the global response of the joints. Such models are computationally more effective for this purpose than solid-element models. Two types of shell elements were included:

- conventional 4-node quadrilateral general-purpose, stress/displacement shell element with reduced integration (Abaqus library: S4R) is used. The element has 6 unknowns - 3 displacements and 3 rotations - per node. The shell element is based on large-strain formulation; accounts for finite (also called large) membrane strains and arbitrarily large rotations. Therefore, it is suitable for large-strain analysis. It allows transverse shear deformation (uses thick shell theory as the shell thickness increases and becomes discrete Kirchhoff thin shell elements as the thickness decreases; the transverse shear deformation becomes very small as the shell thickness decreases).
- continuum shell elements (Abaqus library: SC8R), which are used to model shell-like solids with greater accuracy than conventional shell elements, as described in (SIMULIA, 2012). In this case, the thickness of elements is defined from the geometry of the part. Although a model consists of 3D hexahedral- or wedge-shaped elements, its kinematic and constitutive behaviour is similar to conventional shell elements and at the same time is still more computationally efficient than solid continuum elements.

Hybrid shell/solid models were used to study in detail the stress and strain distributions as well as to evaluate selected response indices in the connections at different levels of load applied. For this purpose different solid element formulations were employed in the convergence study in order to select the most suitable one for the problem addressed.

- a first order 8-node brick element with reduced integration with one integration point per element (Abaqus library: C3D8R). The element has 3 unknowns (3 displacements) per node. The solid element allows for finite strains and finite rotations.
- incompatible mode element (Abaqus library: C3D8I) is a first order element that is enhanced by incompatible modes to improve its bending behaviour. Because of the added internal degrees of freedom due to the incompatible modes (13 for C3D8I), these elements are somewhat more expensive than the regular first-order displacement elements; however, they are significantly more economical than the second-order elements. The incompatible mode elements use full integration. However, some hourglassing issues may also be encountered.
- a second order 20-node brick element with reduced integration and eight integration points per element (Abaqus library: C3D20R).

In both types of FE models, shell and shell/solid, a relatively fine mesh was used near the connection of the beam to the column, comprising part of column below and above the connection as well as part of the beam near the reinforcing plates, where plastic hinging is expected to occur. Steel parts of the joints in the shell/solid models were modelled with solid elements in aforementioned regions only. For parts outside these regions shell elements are used.

With the same purpose as hybrid shell/solid model, also hybrid beam/solid FE model was used in the study in order to achieve even greater computational efficiency. In this case beam finite elements were used for parts of column and beam, which remain in elastic state throughout the analysis.

A typical hybrid shell/solid or beam/solid model is constructed initially in several parts. The parts are then assembled to produce the complete model using the “part”, “instance” and “assembly” modules in Abaqus. At the common interfaces between the two adjacent parts in the model, the corresponding degrees of freedom are linked using multi-point constraints to ensure compatibility within the model.

4.2.3 Elastic and inelastic mesh convergence study

4.2.3.1 Elastic mesh convergence study

Elastic convergence study was conducted on the sub-model of a typical unstiffened beam-to-column joint, considering typical beam and column member profiles used for the test specimens (steel column profile HEB200 and steel beam profile IPE270), Fig. 88.

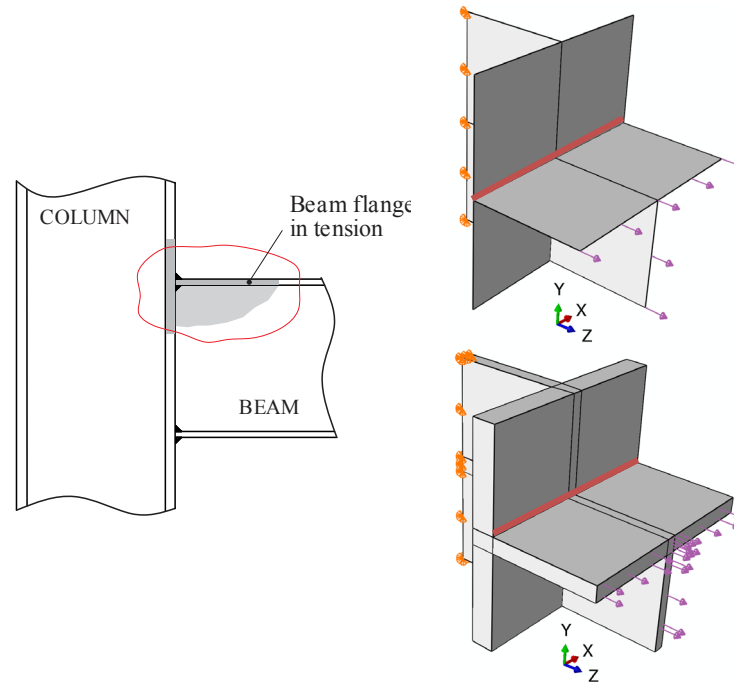


Fig. 88: Position of the sub-model in a beam-to-column joint; shell and solid sub-model geometry with the interface between beam flange and column flange marked as well as boundary conditions and load applied
Slika 88: Pozicija pod-modela v spoju prečka-steber; pod-model zgrajen iz lupinastih in prostorskih končnih elementov z označeno linijo med pasnico prečke in pasnico stebra ter označenimi podporami in obtežbo

The sub-model represents the connection between the flange and the web of the beam and the flange of the column with a portion of column web in tension. However, complete beam flange width is included. No reinforcing plate on the beam flange, side plates or transverse stiffeners on column as well as no concrete encasement are considered to be part of the sub-model. Dimensions in millimetres of the sub model are: beam flange: 135/70/10.2, beam web: 70/64.9/6.6, column flange: 140/135/15, column web: 140/70/9. A uniformly distributed surface load of 15 kN/cm^2 is applied in Abaqus at the right end with surface pressure function. The model is supported along the left vertical edge. Elastic definition for steel material is used.

Meshes comprised of 4 node reduced integration shell elements (S4R element), continuum shell elements (SC8R element), reduced integration 8 node brick elements (C3D8R element), and 8 node brick elements with incompatible modes (C3D8I elements) were used in the study. Different mesh densities for solid models used in the study are shown in Fig. 89. Several levels of mesh refinement are considered regarding the number of elements used across the beam flange width. For example, an 8 element mesh has 8 elements along the width of the beam. Solid model meshes with 4 and 8 elements across the beam flange include 2 elements through the thickness of all the plates. However, in all three finer meshes 2 elements through the thickness of webs and 4 elements through the thickness of flanges are used, according to Mikesell (1997) and El-Tawil et al. (1998). In case of ordinary shell elements (S4R elements),

where thickness is defined from section properties assigned, 5 integration points are used for cross section integration.

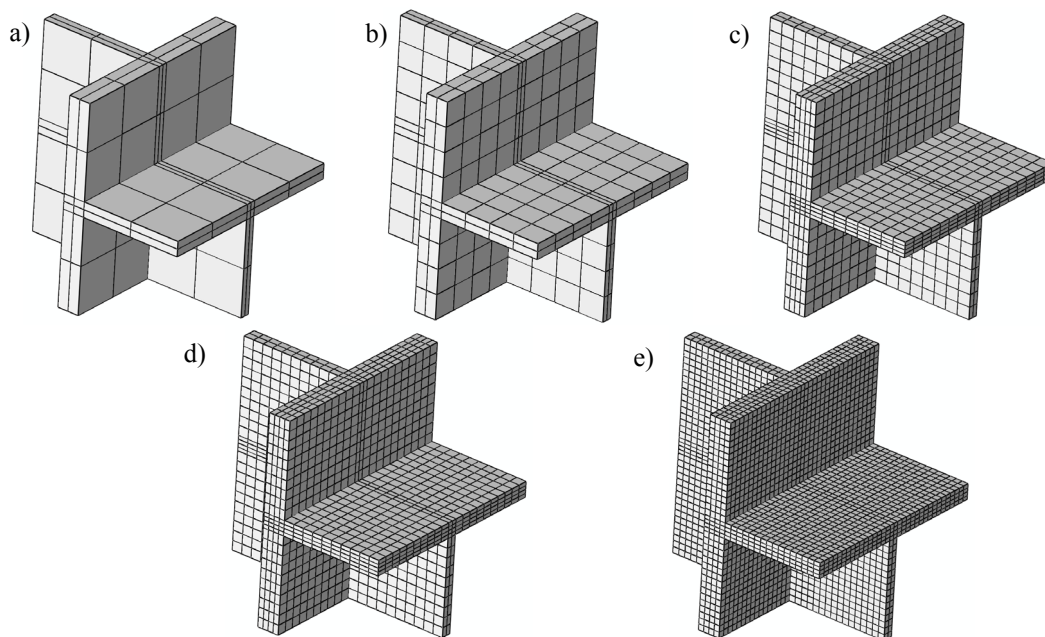


Fig. 89: Mesh densities for solid models used in the study: a) 4 element mesh, b) 8 element mesh, c) 16 element mesh, d) 20 element mesh and e) 32 element mesh

Slika 89: Gostota mreže modelov iz prostorskih končnih elementov: a) mreža s 4 elementi, b) mreža z 8 elementi, c) mreža s 16 elementi, d) mreža z 20 elementi in e) mreža z 32 elementi

Convergence is studied by examining the stress distribution at the interface between horizontal beam flange and vertical column flange on the top size, Fig. 88. The horizontal component of the stress is presented as a function of location along the interface line across the beam flange width. Typical deformed meshes of the sub-models are shown in Fig. 90.

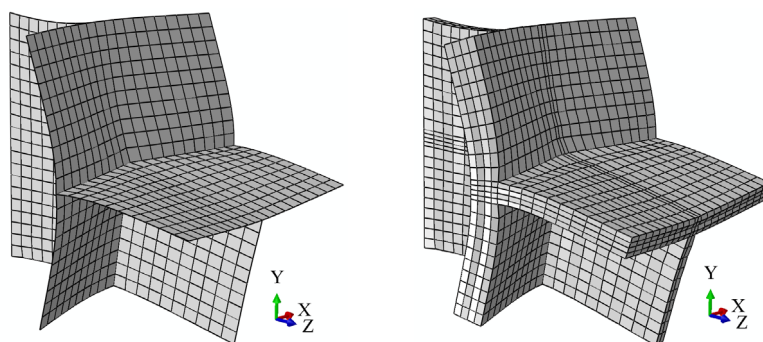


Fig. 90: Deformed mesh of the sub-model using ordinary shell (left) and solid (right) elements

Slika 90: Deformirana oblika mreže pod-modela iz lupinastih (levo) in prostorskih (desno) končnih elementov

Abaqus calculates values for a given variable at a variety of positions. The possible report positions are: integration point, centroid, element nodal and unique nodal. Element nodal and unique nodal positions both involve reporting results at the nodes of the model; however, reporting of unique nodal values produces only a single value at each node, whereas reporting of element nodal values produces one value for each element that has a contribution at that node. Only unique nodal values are provided in the case of node-based variables such as displacement. For element-based variables such as stress, extrapolation and averaging must be carried out to obtain unique nodal values. The shape functions of the element are used for purposes of extrapolation and interpolation of output variables.

Extrapolated values are generally not as accurate as the values calculated at the integration points in the areas of high stress gradients. The use of averaging threshold values and the control of averaging across regional and material boundaries affects the element nodal values reported for element based results. No averaging was used in this case. In addition, reporting of element nodal values contributed only from elements of beam flange along the interface was taken into account.

From the stress distributions shown in Fig. 91 through Fig. 97 it can be seen that stress concentration exists at the centre of the flange. The same distribution shape was observed in all other studies of stress distribution at this local region of the joint.

First, meshes with the general purpose shell element S4R were done. The meshes with 4 and 8 elements do not provide good results. As can be seen from Fig. 91, the mesh with 16 elements produces almost converged results. The difference in comparison with the other finer meshes occurs at both edges and at the centre of the beam flange, where the peak value of stress is growing with the larger number of elements used. However, for the most part of the flange width, distributions of stresses for meshes with 16 elements and more are practically the same.

The reason for non-convergence of central stress is the geometry of configuration. As can be seen from Fig. 88, the beam flange is supported along its width by column flange and at the centre with beam and column web. Because both webs are much stiffer than the flange of the column, they attract considerable portion of the applied load. What is more, this high stiffness is concentrated at a single point; thickness of plates is represented by a single element. Therefore, unrealistically high stress may develop at the centre of the flange. It is therefore not advantageous to refine meshes in this case of shell elements in the central region of the flange, since this would result in unrealistically high elastic stress concentrations. This can be seen from Fig. 91, where distribution, for additional mesh with 70 elements across the beam flange width is depicted.

The right diagram in Fig. 91 presents the results for meshes with continuum shell elements SC8R. Similar conclusions as in the previous case with elements S4R can be drawn. However, it can be seen from comparison between both that in the last case meshes with 16 elements and more give not so converged values of stresses across the beam flange.

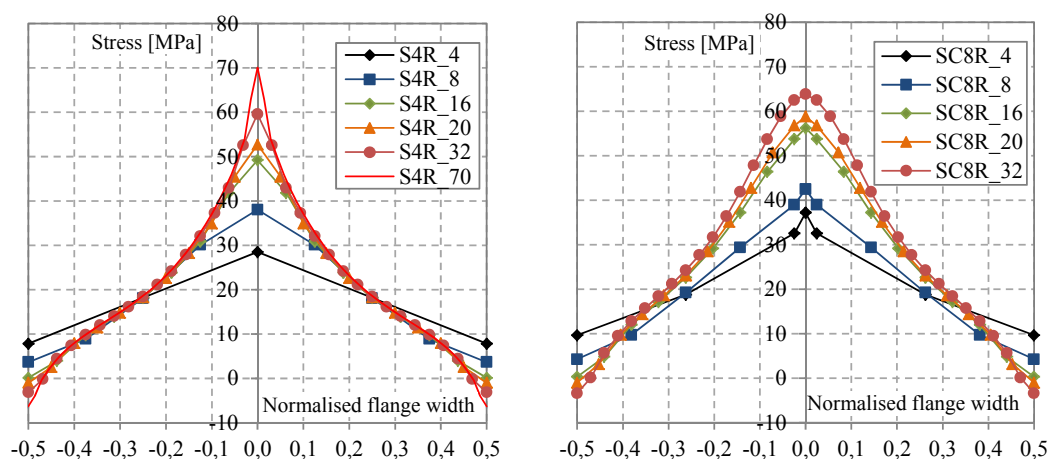


Fig. 91: Stress distribution along the beam-column flange interface for meshes with shell elements S4R and SC8R. The number beside the element type defines the level of mesh refinement

Slika 91: Potek napetosti vzdolž izbrane linije med pasnico prečke in stebra za mreže z lupinastima elementoma S4R in SC8R. Številka dodana k tipu končnega elementa označuje gostoto mreže

Closer inspection by comparing results from both used shell elements reveals that continuum shell element gives larger stresses for more or less complete length of the interface, Fig. 92.

The differences grow as we approach the centre of the flange as well as with the larger number of elements used. Measured at relative position of 0.1 from the centre of the beam flange, element SC8R gives 32 % and 39 % larger value, for meshes with 20 and 32 elements, respectively, along the flange width according to the results of S4R, Fig. 93.

Results obtained using solid C3D8R and C3D8I are presented in Fig. 94. Like in the case of shell elements, the meshes with 4 and 8 solid elements do not provide good results. However, for the most part of the flange width, distributions of stresses for meshes with 16 elements and more give more or less the same stress distribution.

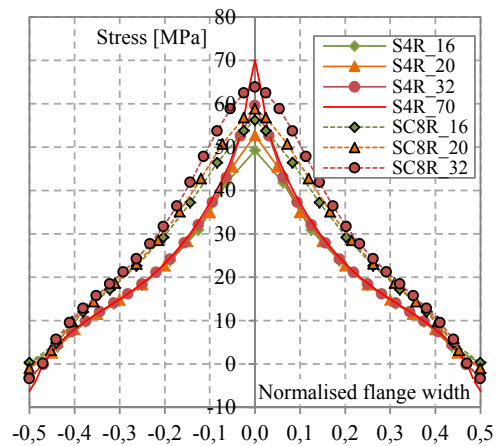


Fig. 92: Stress distribution along the interface for meshes with shell elements S4R and SC8R
Slika 92: Potek napetosti vzdolž izbrane linije za mreže z elementoma S4R in SC8R

As in case of shell elements the differences occur particularly around the centre of the flange, where the peak value of stress grows with larger number of elements used. In case of solid elements with incompatible modes these differences are even more emphasised. From the comparison of stress distribution along the interface between both used solid elements, Fig. 95, one can observe higher values of stresses in case of using C3D8RI elements. The differences increase as we approach the centre of the flange as well as with larger number of elements used.

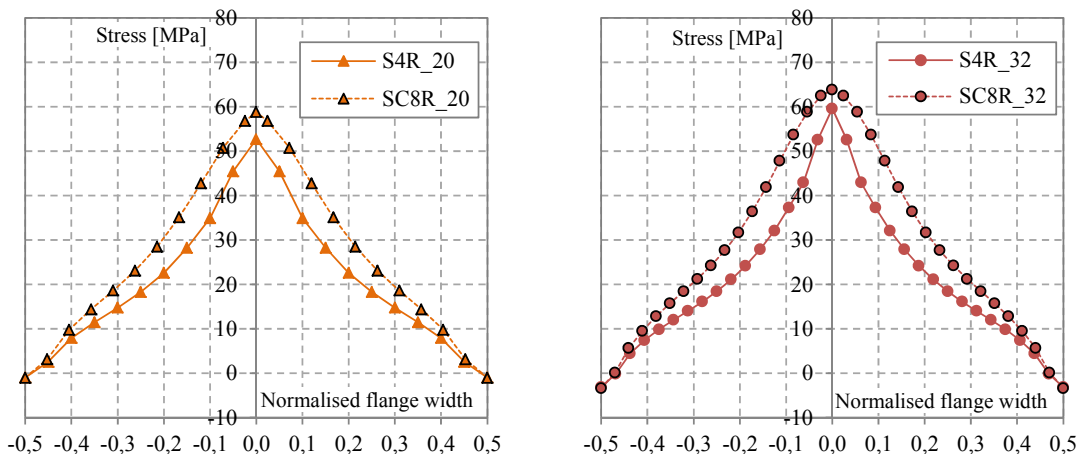


Fig. 93: Comparison of stress distribution along the interface for meshes with 20 and 32 elements using elements S4R and SC8R

Slika 93: Primerjava poteka napetosti vzdolž izbrane linije med pasnico prečke in pasnico stebra za mreži z 20 in 32 elementi po širini pasnice za elementa S4R in SC8R

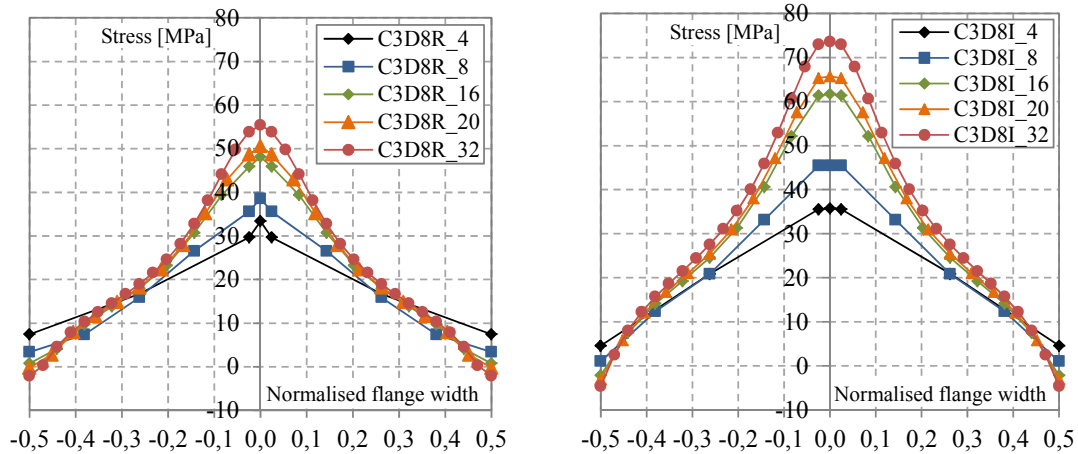


Fig. 94: Stress distribution along the interface for meshes with solid elements C3D8R and C3D8I
Slika 94: Potek napetosti vzdolž izbrane linije za mreže z elementoma C3D8R in C3D8I

According to (SIMULIA, 2012) the most accurate among solid elements addressed in this study are the brick elements with incompatible modes. Because of their enhanced formulation, these elements are particularly well suited for cases involving bending. From deformed shape of the sub-model, Fig. 90, it can be seen that bending is actually present in both column and beam flange. We cannot claim the results using solid elements with incompatible modes to be the most accurate in this case, but we can state that the behaviour is for sure dependent on bending as well. Measured at relative position of 0.1 from the centre of the beam flange, in comparison with element C3D8R, element C3D8RI gives 34 % and 38 % greater value for meshes with 20 and 32 elements, respectively, along beam width, Fig. 96.

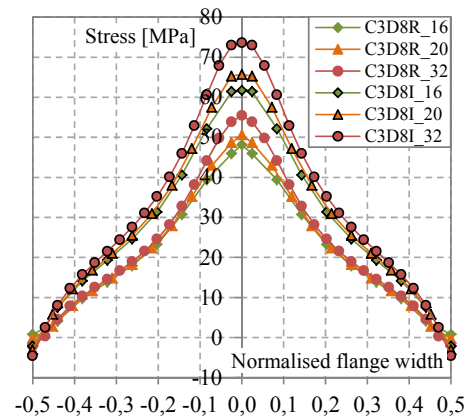


Fig. 95: Stress distribution along the interface for meshes with solid elements C3D8R and C3D8RI

Slika 95: Potek napetosti vzdolž izbrane linije za mreže z elementoma C3D8R in C3D8RI

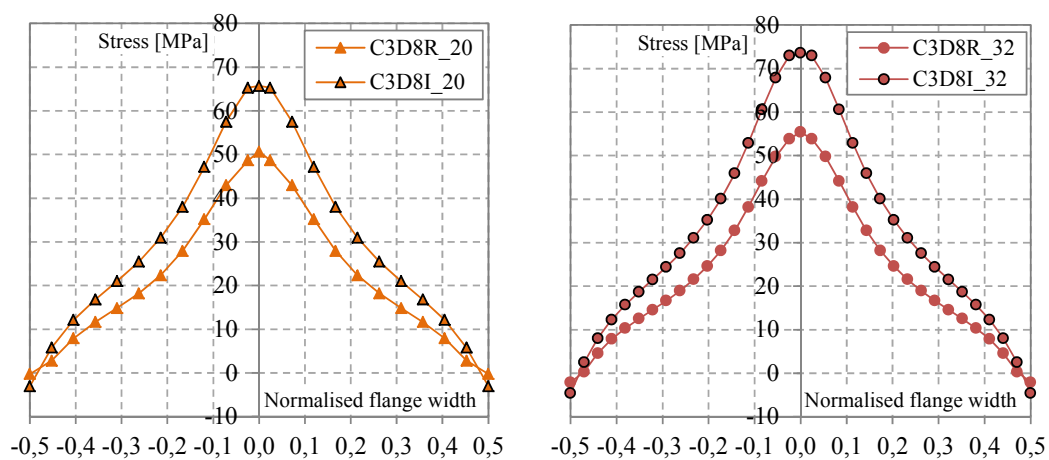


Fig. 96: Comparison of stress distribution along the interface for meshes with 20 and 32 elements using elements C3D8R and C3D8RI

Slika 96: Primerjava poteka napetosti vzdolž izbrane linije za mreži z 20 in 32 elementi po širini pasnice za elementa C3D8R and C3D8RI

Fig. 97 presents diagrams where stress distributions along the interface for cases of shell and solid elements involving meshes with 20 and 32 elements across the beam flange are plotted for final comparison. In both cases one can observe that the distributions of stresses for elements S4R and C3D8R are very close, while on the other hand the distributions for elements SC8R and C3D8I give in both cases greater values and they are also more close to each other compared with the first two elements.

To be more precise, measured at relative position of 0.1 from the centre of the beam flange, compared with element S4R, element C3D8R gives 10 % and 13 % greater value and compared with element SC8R, element C3D8I gives 12 % and 13 % greater value, for meshes with 20 and 32 elements, respectively.

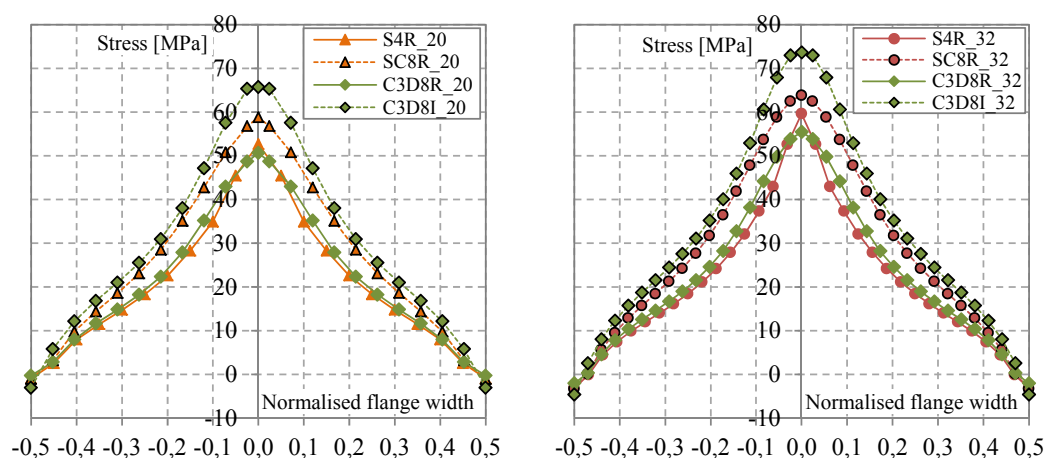


Fig. 97: Comparison of stress distribution along the interface for meshes with 20 and 32 elements using shell elements S4R and SC8R and solid elements C3D8R and C3D8I

Slika 97: Primerjava poteka napetosti vzdolž izbrane linije za mreži z 20 in 32 elementi po širini pasnice za lupinasta elementa S4R in SC8R ter za prostorska elementa C3D8R in C3D8I

Conclusions and implications for further work

From the results of elastic convergence tests on the sub-model it is clear that longitudinal stress distribution along the beam-to-column flange interface is sensitive to both the type of finite element and the mesh density used. As a consequence, these factors must be carefully considered when comparing and evaluating the stress distributions and concentrations published in the literature. Since the study of the local behaviour of steel components of designed connection details is of prime importance of this research work, the conducted simulations have to imitate the real situation well enough. This is even more important for reliability of results from additional parametric study presented later in this document, see Chapter 5.

For this reason the developed numerical model was finally calibrated against experimental test results on beam-to-column joint specimens in terms of global and additionally local strain response. Additional information on the topic is provided in the subsequent section 4.2.3.2 discussing inelastic convergence study.

Based on the results of the foregoing elastic convergence study the decision on the finite element size to be used in the most strained regions on the beam and column was taken for further simulations including the final calibration of the models against the test results. Mesh characterized with element in-plane dimensions corresponding to the mesh with 20 elements used across the beam flange was selected. This means that for the elements used near the connection of the beam to the column, the largest element in plane dimension is $b/20$. Meshes comprising 2 solid elements through the thickness of webs and 4 elements through the

thickness of flanges should be used. In case of ordinary shell elements 5 integration points are used for cross section integration. Models made of solid elements C3D8R and C3D8I are used in all further analyses.

4.2.3.2 Inelastic convergence study

In addition to elastic mesh convergence study on the sub-models, final developed solid FE model was checked in order to study the sensitivity of the inelastic solution to mesh refinement. Performance of developed finite element models was checked against experimental test results.

Complete beam-to-column joint model performance was examined by means of global strength-displacement response under monotonic and cyclic loading. Since no experimental monotonic test on beam-to-column joint was performed in the scope of this study, well documented experimental monotonic test results from literature were used for this purpose. Global performance of the developed beam-to-column joint numerical model is presented in detail in Chapter 4.3.

In addition, local strain field obtained from the simulated cyclic response of the stiffened joints was compared with strain measurements captured during the cyclic experimental tests by means of strain gauges placed on strategic positions on the beam. For a detail discussion on comparison of simulated and experimental strain response, the reader may refer to Chapter 4.3.3.4.

Conclusions from complete inelastic convergence study may be summarised in advance for convenience as follows:

- ultimate flexural behaviour of the beam, characterised by the occurrence of the beam local buckling in the beam plastic hinge zone, was found strongly dependent on the number of C3D8R finite elements used across the beam flange width: too little finite elements across the free-length of the beam flange, generally resulted in too stiff response;
- mesh utilising C3D8I elements for discretisation of the stiffened region including plastic hinge zone of the beam with the element in-plane dimensions and the number of elements through the flanges and the web of the beam according to the conclusions from elastic convergence study result in enough accurate simulated response and was used for further complementary study;
- the rest of steel and concrete solid parts of a beam-to-column joint that remain in elastic state are modelled using computationally more efficient C3D8R elements.

Before proceeding with the final results of the performance of the developed finite element model, presented in Chapter 4.3, the bases of the applied constitutive material model (for concrete and steel) as well as geometric nonlinearity issues are presented in the following sections.

4.2.4 Material nonlinearity

The basic aim of the employed design procedure for stiffened moment resisting beam-to-column connections is to constrain inelastic deformations to ductile dissipative member of a beam and, therefore, to prevent inelastic deformations in brittle non-dissipative beam-to-column welded connection. In order to accomplish the design objective, stiffened beam-to-column connection as well as column, both designed as non-dissipative members, should resist maximum forces corresponding to the fully yielded and strain hardened beam.

It is well known that plastic strength developed by the dissipative steel beam member can be substantially larger than the nominal yield stress limit, due to the aforementioned strain hardening effect. Namely, the stress corresponding to the ultimate behaviour of the beam, i.e. complete development of the beam local buckling, is not influenced only by the beam cross-sectional geometric characteristics and other loading conditions (stress distribution across the section depth), but also largely depends on the stress-strain characteristics of the material from which the structure is made.

When using simplified elastic-perfectly plastic material, unrealistically short plastic hinge zones may develop during bending, which cause excessive localised strains in the beam. On the other hand, by properly accounted stress-strain relation characteristic for mild carbon structural steel, strain hardening elongates the plastic zones, producing a more favourable strain distribution along the length of the beam than would exist without it (Radomski, White, 1968. White, Radomski, 1968).

To account for a nonlinear material behaviour, nonlinear stress-strain relations were accounted for structural steel as well as for concrete material subjected to monotonic loading. In addition, special attention was paid to the calibration of a nonlinear cyclic constitutive model for the steel material used for the beam and other components of the strengthened connection.

4.2.4.1 Monotonic loading

4.2.4.1.1 Structural steel material

Uniaxial stress-strain material relationship for all the steel joint components was defined according to the results of tensile tests on the steel coupons taken from particular joint component (flanges and webs of beam and column profiles, stiffening plates), see also Chapter 3.3.1.

Material diagrams of joint components in terms of nominal stress-strain relationship for all four different RS and CP joints, used in the simulations, are presented in Fig. 98 and Fig. 99. Average results from the tensile tests on the steel coupons from each joint component were taken into account. For simplicity reasons, only ascending part of the nominal curves till the point representing ultimate steel tensile strength is presented.

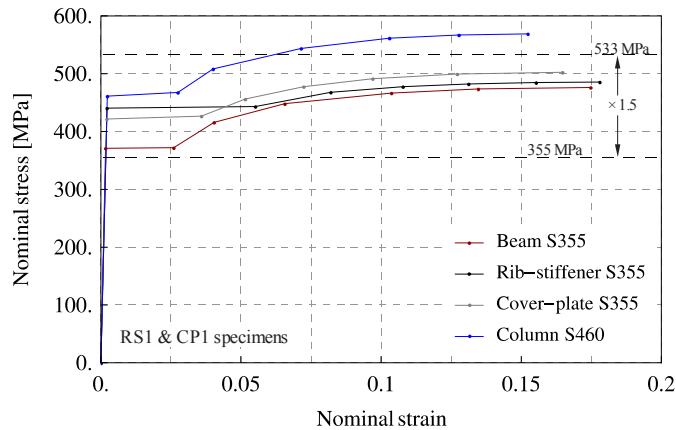


Fig. 98: Discretised material diagrams up to the point of the ultimate tensile strength from joint components of RS1 and CP1 specimens

Slika 98: Diskretizirani materialni diagrami do točke natezne trdnosti dobljeni iz komponent spojev RS1 in CP1

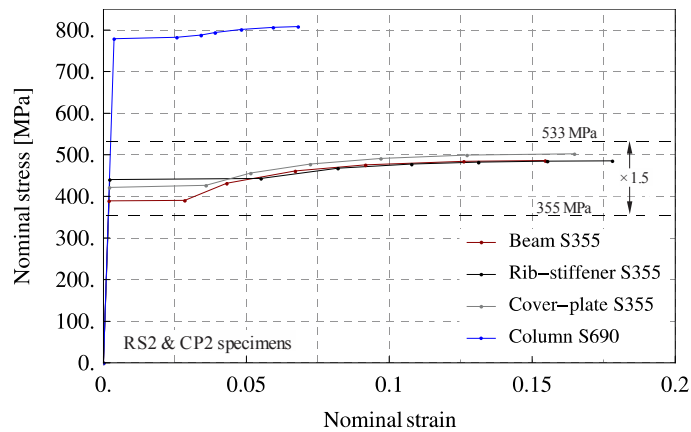


Fig. 99: Discretised material diagrams up to the point of the ultimate strength from joint components of RS2 and CP2 specimens

Slika 99: Diskretizirani materialni diagrami do točke natezne trdnosti dobljeni iz komponent spojev RS2 in CP2

For the interpretation of results obtained from the simulated response of all the sixteen test specimens, presented in the following Chapter 4.3, it is necessary to review the actual material resistance of each particular beam-to-column joint component in relation to material characteristics of other components.

In relation to the presented material diagrams of the steel joint components, it is interesting to note that the measured yield strength of all the stiffening plates is greater than the measured beam flange yield strength in case of all the sixteen test specimens.

Material overstrength γ_{ov} , taking into account the actual yield values, range from 1.08 to 1.25 and 1.19 to 1.27 for beam and stiffening plates material, respectively. The value of ultimate-to-nominal yield stress ratio f_u/f_y^{nom} , representing theoretical upper limit of complete beam overstrength γ_{ov} 's, ranges between 1.37 and 1.45 for all the beams.

Behaviour of the structural steel material subjected to monotonic loading was modelled using classical metal plasticity model in Abaqus, which accounts for the isotropic hardening rule with the Von Mises yield criterion.

Constructional steel material exhibits ductile behaviour as it is capable of developing large inelastic strains. Since large (in mechanics expressed also finite) strain plasticity is undertaken in the analysis, material properties for finite-strain calculations are used: “stress” means “true” (Cauchy) stress and “strain” means logarithmic strain.

Material data for all steel definitions were, therefore, given in the true stress-logarithmic plastic strain relationship, as it is required by Abaqus. From nominal stress-strain data obtained from a uniaxial test of isotropic steel material, a simple conversion to true stress and logarithmic plastic strain is done considering the two equations below:

$$\sigma_{true} = \sigma_{nom} (1 + \varepsilon_{nom}), \quad (25)$$

$$\varepsilon_{ln}^{pl} = \ln(1 + \varepsilon_{nom}) - \frac{\sigma_{true}}{E}, \quad (26)$$

where E is the Young's modulus.

Comparison between the results of experimental and simulated standard tensile test on the coupon from IPE beam flange performed in order to check the suitability of the applied material model is presented in Fig. 100.

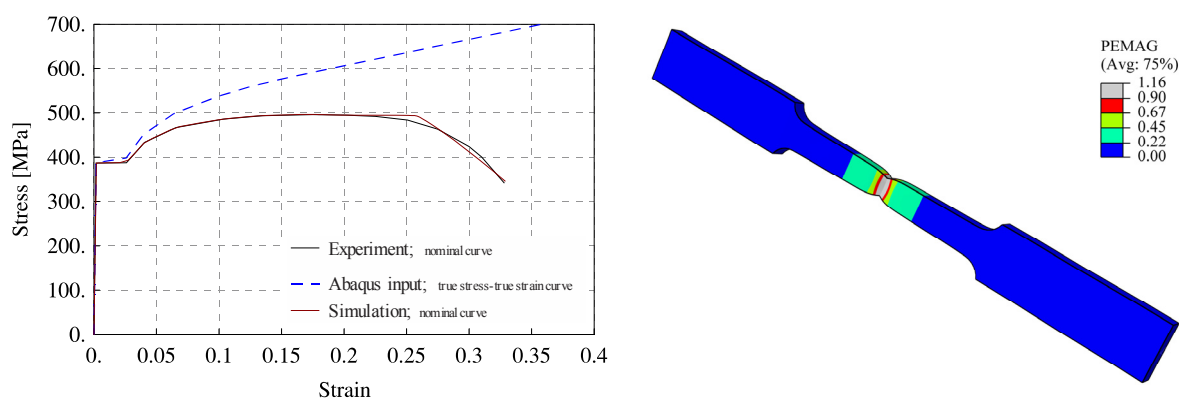


Fig. 100: Comparison of experimental and simulated standard tensile test on the coupon from IPE270 beam
Slika 100: Primerjava eksperimentalnega in simuliranega odziva standardnega nateznega preizkusa na jeklu iz prečke IPE270

Similarly as shown in Fig. 100, a good agreement was found between the experimental and simulated response of the standard tensile tests of all the steel joint components. However, in spite of successfully performed material model calibration on the local material response from uniaxial tension tests, it was the case of simulating complete joint response, see Chapter 4.3.2.2, where a good match between experimental and simulated complete global elastic-plastic response of the beam-to-column joint was found very difficult to obtain.

The reason for this can be related to the fact that not complete hot-rolled I beam cross-section consists from material with unique mechanical characteristics. Especially in case of the yield strength and the subsequent strain hardening rate and range, non-negligible differences were found in the material samples taken from flanges and web of particular hot-rolled beam profile used for test specimens.

4.2.4.1.2 Concrete material

Concrete plasticity model available in Abaqus material library was used to simulate the concrete material behaviour in the composite columns of the test specimens. The model is part of *concrete damaged plasticity* constitutive model, which provides a general capability for modelling concrete and other quasi-brittle materials in all types of structures. However, with damage parameters omitted, the model behaves as a plasticity model. The applied model uses concepts of isotropic elasticity in combination with isotropic tensile (cracking) and compressive (crushing) plasticity to represent the inelastic behaviour of concrete.

The uniaxial compressive stress-strain response of concrete was assumed to be linear up to 30 % of its compressive strength. In the plastic regime, the complete stress-plastic strain relationship, see Fig. 101a, is described through a simple stress-strain function in uniaxial compression proposed by Carreira and Chu (Carreira, Chu, 1985):

$$f_c = f_{cu} \left[\frac{\beta \left(\frac{\varepsilon}{\varepsilon_u} \right)}{\beta - 1 + \left(\frac{\varepsilon}{\varepsilon_u} \right)^\beta} \right] \quad (27)$$

According to the authors, the proposed formulation is particularly suitable for concrete with its compressive strength ranging from 50 to 120 MPa, and therefore was used for both the ascending and the post-peak descending branch of the uniaxial compressive response.

According to the research work performed by Bokan Bosiljkov et al. (2010) elastic modulus of concrete $E = 40$ was used with strain at ultimate strength $\varepsilon_{cu} = 0.00245$. Mean value of concrete compressive strength, obtained from concrete cubes as part of the experimental study performed in this research work, and converted to the compressive strength of standard cylindrical test specimens, $f_{cu} = 50.3$ MPa was used.

Simplified expression for β as a function of f_{cu} as proposed by Popovics (1973) was used:

$$\beta = 0.058 \cdot f_{cu} + 1.0 \quad (f_{cu} \text{ in MPa}), \quad (28)$$

with the final value obtained $\beta = 3.92$.

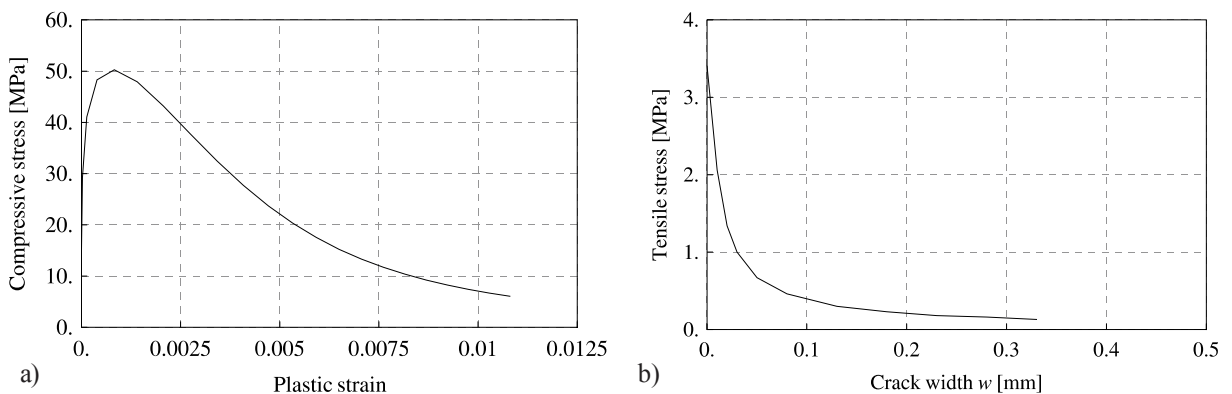


Fig. 101: Concrete material behaviour used in the FE model for composite columns: a) compression, b) tension
Slika 101: Upošteevano obnašanje betona v računskem modelu za sovprežne stebre: a) tlak, b) nateg

For an accurate nonlinear finite element analysis, the stress-displacement relationship for concrete in cracked state under uniaxial tension is required. In uncracked state, the stress-strain relationship under uniaxial tension can be expressed with a linear function. Therefore, in the study the stress-strain response under uniaxial tension follows a linear elastic relationship until the tensile strength is reached. After cracking, the stress versus crack width response is more appropriate for representing the material behaviour under uniaxial tension, since no unique stress-strain relationship exists in the post-peak softening region.

Numerous expressions are available in the literature to represent the stress versus crack width relationship of concrete in uniaxial tension. These expressions vary from simple linear functions to sophisticated exponential functions to represent the post-cracking behaviour of concrete.

To avoid unreasonable mesh-sensitive results due to the lack of reinforcement in the structure (reinforcement present in the column of the test specimens was not explicitly modelled), the

tensile post failure behaviour is given in terms of a fracture energy cracking criterion by specifying a stress-displacement curve, following the relationship proposed by Li and Ansari (2000). According to the approach, post tension stiffening is included as an effect of reinforcement present in the real structure. In the applied model the post-peak response is represented as an exponential function of the ratio of crack width w to final crack width w_f , see Fig. 101b:

$$f_t = f_{tu} \left[1 - \exp \left[- \left(\frac{0.03}{w/w_f} \right)^{0.9} \right] \right]. \quad (29)$$

In relation with the adopted formulation, the ultimate tension strength f_{tu} was taken to be 3.4 MPa according to Duh (2008), as this value is largely dependent on the type of aggregate used in the concrete, in this case limestone. Crack width $w_f = 0.3$ mm as adopted from Begum et al. (2007) was used.

4.2.4.2 Cyclic loading

In order to describe how a material behaves under cyclic loading with different stress or strain amplitudes before reaching stabilised state, a constitutive model of a cyclic plasticity is needed. The theory of cyclic plasticity provides a mathematical description of a material stress-strain response in plastically deformed (time-independent plasticity) solids under cyclic loading.

The study deals with a time-independent constitutive model for cyclic plasticity of metals implemented in the nonlinear finite element software Abaqus, which is based on the work of Lemaitre and Chaboche (1990). In this model, the von Mises yield criterion and associative flow rule are assumed. The evolution law in the model consists of a kinematic hardening component which describes the translation of the yield surface in the stress space. An isotropic component, which describes the change of the elastic range, is added for the nonlinear isotropic/kinematic hardening model.

The same finite elements as for monotonic simulations, eight noded, solid elements type C3D8R as well as enhanced elements C3D8I were used for the cyclic analysis.

The modelling of fatigue induced initiation and growth of cracks was not considered in the study. Instead of this, stress and strain response indices were used, as described in Chapters 2.4.2 and 4.3.3.5, in order to evaluate the LCF response of the analysed stiffened beam-to-column joints.

A brief description of the constitutive model, which is capable of capturing the main features of response of the steel material for proportional and non-proportional cyclic loading paths in engineering sense, are given.

The performance of the applied constitutive model was first calibrated and verified at the level of small steel specimens subjected to low-cycle fatigue loading. To this aim, experimental test data obtained from literature were used.

In addition, validation of the developed constitutive cyclic material model was performed by means of simulation of all the sixteen cyclic experimental tests (with variable and constant cyclic loading amplitude) on the stiffened beam-to-column joints performed in the framework of this research work.

4.2.4.2.1 Cyclic Material Hardening model

Nonlinear isotropic/kinematic hardening model with multiple backstresses in combination with the Mises yield surface (isotropic yield plasticity) was used as Abaqus integrated material model for metals subjected to cyclic loading. The assumption of associated plastic flow is acceptable for metals subjected to cyclic loading as long as microscopic details, such as localization of plastic flow occurring as a metal component ruptures due to cyclic fatigue loads, are not of interest (SIMULIA, 2012).

The nonlinear isotropic/kinematic hardening model has both nonlinear kinematic and nonlinear isotropic hardening components. The evolution law of this model consists of two components: a nonlinear kinematic hardening component, which describes the translation of the yield surface in stress space through the backstress α , and an isotropic hardening component, which describes the change of the equivalent stress defining the size of the yield surface σ^0 as a function of plastic deformation.

The kinematic hardening component is defined to be an additive combination of a purely kinematic term (linear Ziegler hardening law) and a relaxation term, which introduces the nonlinearity. In addition, several kinematic hardening components (backstresses) can be superposed, which may considerably improve results in some cases. When temperature and field variable dependencies are omitted, the hardening laws for each backstress are:

$$\dot{\alpha}_k = C_k \frac{1}{\sigma_0} (\sigma - \alpha) \dot{\bar{\varepsilon}}^{pl} - \gamma_k \alpha_k \dot{\bar{\varepsilon}}^{pl} \quad (30)$$

and the overall stress is defined as

$$\alpha = \sum_{k=1}^N \alpha_k, \quad (31)$$

where N is the number of backstresses, and C_k and γ_k are material parameters that must be calibrated from cyclic test data. C_k are the initial kinematic hardening moduli, and γ_k determines the rate at which the kinematic hardening moduli decrease with increasing plastic deformation.

Integration of the backstress evolution laws over uniaxial strain cycle provides the following expression:

$$\alpha_k = \frac{C_k}{\gamma_k} (1 - e^{-\gamma_k \cdot \varepsilon_{pl}}) + \alpha_{k,1} \cdot e^{-\gamma_k \cdot \varepsilon_{pl}} \quad (32)$$

The above equation enables calibration of parameters C_k and γ_k .

The isotropic hardening behaviour of the model defines the evolution of the yield surface size (i.e. describes the progression of the elastic range) σ^0 as a function of the equivalent plastic strain $\bar{\varepsilon}^{pl}$ (i.e. cumulative plastic strain). This evolution can be introduced by specifying σ^0 directly as a function of $\bar{\varepsilon}^{pl}$ in tabular form or by using the simple exponential law:

$$\sigma^0 = \sigma|_0 + Q_\infty (1 - e^{-b \bar{\varepsilon}^{pl}}), \quad (33)$$

where $\sigma|_0$ is the yield stress at zero plastic strain and Q_∞ and b are material parameters. Q_∞ is the maximum change in the size of the yield surface (i.e. between the first cycle and the stabilized cycle), and b defines the rate at which the size of the yield surface changes as plastic straining develops.

The model considers the same isotropic hardening at all strain ranges, without loading history effect included. However, physical observations indicate that the amount of isotropic

hardening depends on the magnitude of the strain range. Furthermore, if the specimen is cycled at two different strain ranges, one followed by the other, the deformation in the first cycle affects the isotropic hardening in the second cycle. Thus, the applied model provides only a coarse approximation of actual cyclic behaviour.

4.2.4.2.2 Calibration of cyclic material hardening model

In the current study, cyclic stress-strain data needed for calibration of cyclic material hardening model were collected from experimental results from fatigue tests on small smooth specimens that were performed in the framework of other research works (Skuber, 2003. Nip et al., 2010. Jesus et al., 2012).

Considered experimental tests include specimens from mild steel S275 and S355, subjected to uniaxial symmetric strain-controlled cycles with different strain amplitude levels. In particular, results from tests carried out at $\pm 0.25\%$, $\pm 0.5\%$, $\pm 1\%$, $\pm 3\%$, $\pm 5\%$ and $\pm 7\%$ total strain amplitude were taken into account in order to cover both the LCF and ELCF regimes.

Choosing an appropriate material hardening model is indispensable to proper numerical simulation of the cyclic loading of steel components. To obtain accurate cyclic hardening data needed for low-cycle fatigue calculations, the calibration experiment should be performed at a strain range that corresponds to the strain range anticipated in the analysis. This is due to the limitation of the applied cyclic material model in terms of the same isotropic hardening considered at all strain ranges.

On the other hand, this is due to inherent LCF behaviour of the material. Namely, general applicability of the applied cyclic material hardening model is suitable for materials that show stabilised cyclic response as well as Masing behaviour. The Masing behaviour is observed if the upper branches of the hysteresis loops are all coincident. For a material obeying the Masing behaviour, the relationship between the cyclic stress and elastoplastic strain ranges and the shape of the hysteresis loops may be both described by the cyclic curve of the material.

In case of the considered cyclic tests results, cyclic elastoplastic behaviour of mild steel S355 was found to be non-Masing, with some tests that also did not show clear stabilisation (Nip et al., 2010. Jesus et al., 2012).

During the calibration phase, a number of simulations of fatigue tests were done. The best accuracy was reached by using parameters generated from tests with the same strain amplitude as in the analysis. However, it was found that kinematic hardening defined from large strain amplitude can be used for lower strain amplitudes, without losing much accuracy. On the other side, cyclic hardening was found to be strongly dependent on particular strain amplitude level.

In case of particular strain amplitude cyclic test, parameters defining the kinematic and the isotropic hardening were obtained by fitting Eqs. (32) and (33) to the corresponding data pairs obtained from the cyclic tests response. In case of kinematic hardening component, parameters were defined by using test data from a stabilised cycle defined at specimen's half-life.

To cover the complete strain amplitude range available from the cyclic test data (up to $\pm 7\%$ total strain amplitude) cyclic curve obtained from all considered cyclic tests was used for the definition of the kinematic hardening, Fig. 102.

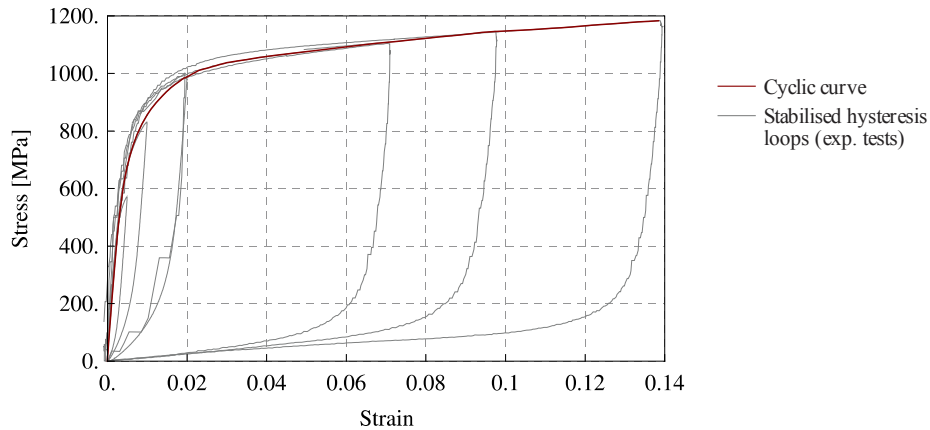


Fig. 102: Cyclic curve obtained from experimental tests with different strain amplitudes

Slika 102: Ciklična krivulja dobljena na podlagi eksperimentalnih testov z različnimi amplitudami deformacije

Final calibrated parameters for the isotropic and kinematic hardening of mild steel S355, to be applied in the cyclic simulations of beam-to-column joints, are presented in Table 23.

Preglednica 23: Parametri kinematično/izotropnega utrjevanja nelinearnega modela za ciklično obnašanje
Table 23: Parameters of the nonlinear combined isotropic/kinematic hardening model for cyclic plasticity

Isotropic hardening		Kinematic hardening			
σ_0 [MPa]	304	backstress			
Q_∞ [MPa]	16	α_1	α_2	α_3	
b	15	C [MPa]	848	6862	48844
		γ	17	128	682

Comparison between monotonic and cyclic stress-strain curve for mild steel S355 is presented in Fig. 103. Depicted monotonic curve is already the calibrated one, see chapter 4.3.2.2.

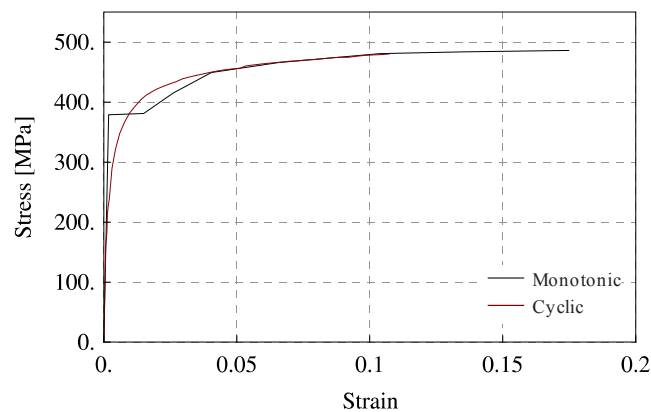


Fig. 103: Comparison between calibrated monotonic and cyclic stress-strain curve for steel S355

Slika 103: Primerjava med kalibrirano monotono in ciklično krivuljo napetost-deformacija za jeklo S355

4.2.5 Geometric nonlinearity

Geometric nonlinearity may substantially affect inelastic behaviour of connection components near location of plastic hinge where excessive straining is expected. The material nonlinearity was combined with geometric nonlinearity in order to capture effects of the beam local buckling and the subsequent beam flexural strength degradation.

Imperfections are usually introduced by geometric perturbations as deviations from perfect shape. Abaqus offers three ways to define an imperfection: as a linear superposition of buckling eigenmodes, from displacements of a static analysis, or by specifying the node number and imperfection values directly.

At the beginning of the study, beside the beam local imperfection in the plastic hinge region, initial global imperfections were considered also in the column. However, since the strong column design concept is used in the study, negligible effect from global imperfection was observed in case of column response, even in the presence of the applied high level of column compressive axial load. Beside the beam local imperfections in the plastic hinge region, no global imperfection was considered on the beam, since the beam is always fully laterally supported.

For the purpose of this study additional eigenvalue analysis, prior to the main analysis step with monotonic or cyclic loading, was used to compute the buckling mode shapes of each specimens beam. In case of analysis with additional axial force in the composite column, where imperfections were introduced in both, beam and column, combination of additional eigenvalue analysis with displacement analysis was used. This approach requires two analysis runs with the same model definition; nodal information from previous auxiliary (buckling or static) analysis is written to the results file, which is afterward imported to the input file of the main static analysis. For complete definition of imperfect geometry two assumptions described below were made.

According to standard EN 1993-1-5 (CEN, 2007), local geometric imperfections on the beam may base on the shape of the critical element buckling modes. Therefore, the initial imperfections in a beam-to-column joint base on a proportion of the amplitude of the first elastic buckling mode of the model, loaded with transverse concentrated load at the free end of the beam. In case of introducing imperfections on both beam flanges (cyclic loading), also mode with the same, but negative, eigenvalue is considered. Imperfection on the composite column was defined with the combination of global and local bow imperfection with combination factor 1.0 for the leading global and 0.7 for local imperfection as accompanying imperfection, according to EN 1994-1-1, see Fig. 104.

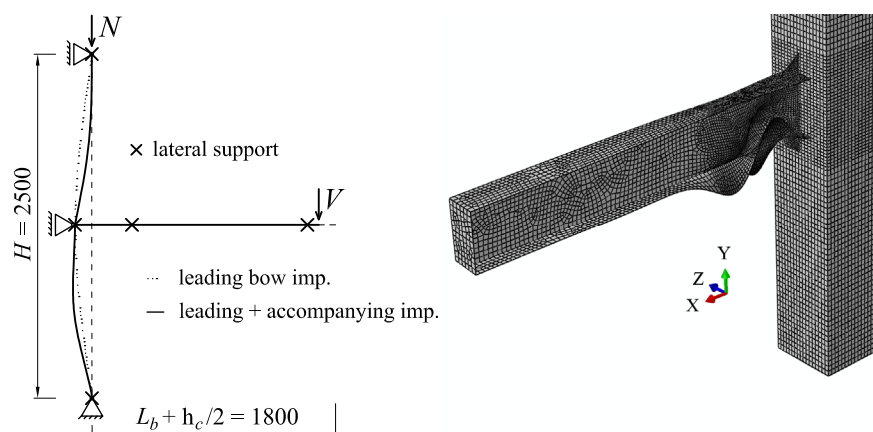


Fig. 104: Static model of a joint with boundary conditions, loads applied and considered geometric imperfections
Slika 104: Statični model spoja z robnimi pogoji, obtežbo in upoštevanimi geometrijskimi nepopolnostmi

The maximum value of geometric imperfection on the beam was taken to be measured in a per cents of a relative structural dimension. However, in order to use reasonable values for the resulting imperfection amplitudes, tolerances from related standard for hot rolled steel profiles type I and H were examined. According to standard EN 10034 (CEN, 1993), tolerances on out-of-square of structural steel I and H sections are expressed relative to the flange width, Fig. 105.

According to the same standard, the total out-of-square tolerance for a cross-section, with a flange width b more than 110 mm, is 2 % of b . Assuming that this value is evenly distributed between the four flange projections, Fig. 105, the permissible imperfection is approximately 0.5 % of b ($\frac{1}{4} \times 2\%$ of b). For instance, in case of beam IPE300, the amplitude on one side of the beam is 0.75 mm. It was observed from the results of buckling analyses, that the point with the largest eigenvector component (value 1.0, which is scaled to prescribed amplitude) does not exist always on the beam flange, but may correspond to a location on the beam web. In such case, in order to prescribe the proper value of imperfection amplitude on the beam flange, the amplitude value has to be divided with the largest eigenvector component on the beam flange.

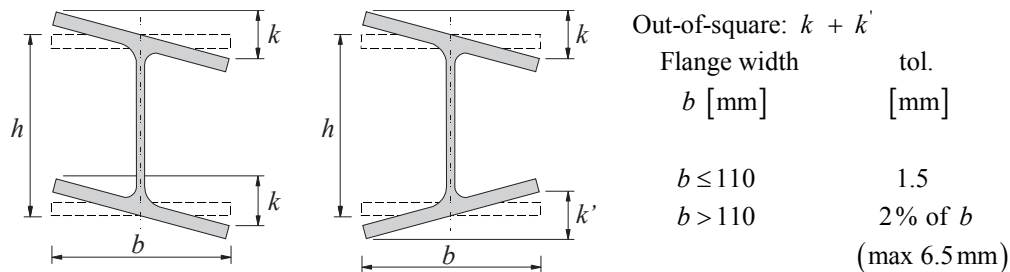


Fig. 105: Tolerances on out-of-square of structural steel I and H sections according to EN 10034
Slika 105: Tolerance za geometrijsko nepopolnost jeklenih I in H prerezov po standardu EN 10034

In case of the beam local imperfection applied in the unstiffened region of the beam just behind the stiffened region, three different imperfection models were considered, Fig. 106.

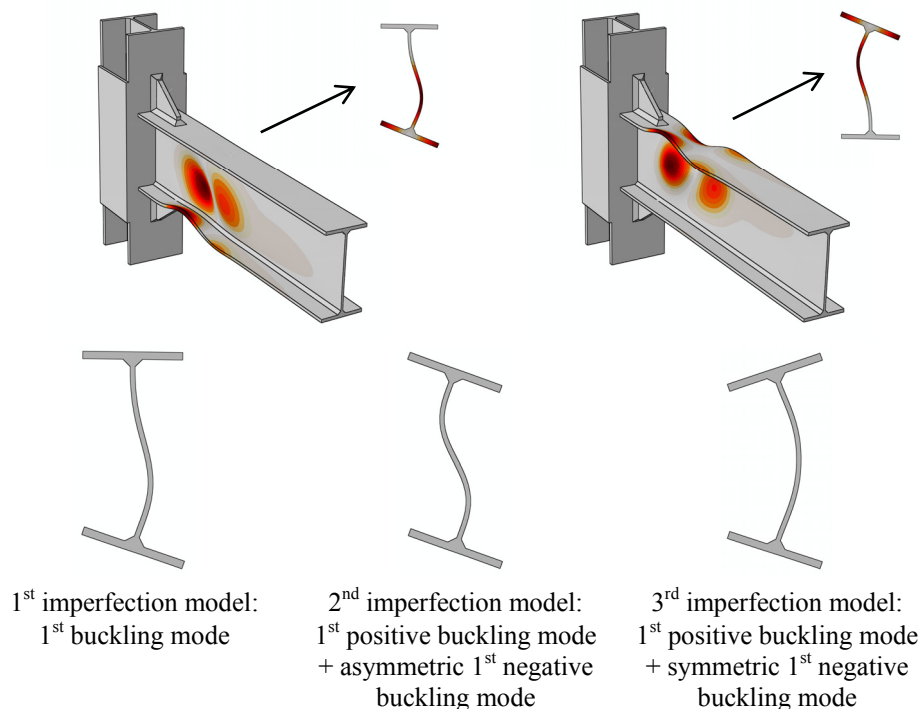


Fig. 106: Local beam geometric imperfection models
Slika 106: Upoštevani modeli za lokalno geometrijsko nepopolnost prečke

With exception of the first imperfection model, where geometric imperfection is applied only in the compressed flange, see Fig. 106, simulations with the third imperfection model produced the best agreement against experimentally obtained beam response and therefore was used for all the subsequent simulations.

4.2.6 Residual stresses

Residual stresses in steel members occur mainly because of rolling steel plates to form the steel sections or due to welding of plates during erection phase. Since these stresses might have effect in reducing the buckling capacity of the plates constituting cross-section of the beam, they were included in the numerical model in the early phase of the numerical study.

In the FE model, residual stresses in the flange and web plates of beam profile were modelled as initial stresses introduced in the preliminary step before the main loading step. The residual stress distribution across the beam cross-section was not directly measured on the test specimens. Instead of this, the stress distribution across the beam profile was adopted from related document (ECCS, 1976) and it was assumed to be constant along the beam length. Introduced initial stressed state in Abaqus was analysed in the preliminary step in order to restore equilibrium state. After its completion, FE model including residual stresses in the beam, defined as initial conditions, is subjected to mechanical loading in the subsequent step of analysis.

It should be noted that no additional higher values of residual stresses in the location of heat affected zones of the welds in the strengthened part of the beam were accounted for.

Results from preliminary calibration of numerical model had shown that the presence of the applied level of residual stresses will accelerate some buckling modes in the beam under monotonic loading, but have limited effect on the overall hysteretic response of the beam.

On the basis of the above considerations it was concluded that residual stresses do not need to be included in the numerical FE model with the aim to obtain more accurate response. Therefore, residual stresses were not included in the subsequent analyses of beam-to-column joints.

4.2.7 Solver procedures

Before continuing with a detailed description of other modelling issues applied, the solver procedures used in Abaqus to run the simulations, may first be introduced. Namely, to better understand some decisions made during the development process of numerical models, the information of this sort is indispensable.

Commercial finite element software Abaqus offers two analysis modules Abaqus/Standard and Abaqus/Explicit that use different solution strategies for solving nonlinear quasi-static and dynamic problems. The Abaqus/Standard uses an implicit strategy and must iterate to establish equilibrium for a nonlinear problem, whereas the Abaqus/Explicit determines the solution without iterations by explicitly advancing the kinematic state over small time increments (SIMULIA, 2012). Each iteration in an implicit analysis requires solving a large system of linear equations and requires considerable computational effort.

In the study Abaqus/Explicit was used for all the simulations where convergence was not possible by using the implicit method. These were all the cases where nonlinear material model for concrete was included. Namely, in spite of elastic global behaviour of composite column, concrete crushing and cracking were always present in the very local region around beam-to-column connection.

The other source of convergence discontinuity in Abaqus/Standard was in some cases related to the state of the beam-to-column joint just before the onset of the beam local buckling. Under monotonic loading, analyses with the more compact beams in combination with the smaller beam local imperfection amplitude were found difficult to be solved in Abaqus/Standard. Again, Abaqus/Explicit solution method was used for the sort of cases.

Although originally developed for dynamic problems, explicit method can be applied to quasi-static problems with some special considerations in the applied loading history. A quasi-static analysis should be performed with moderate loading rates in order to ensure that the ratio of kinetic energy to internal energy does not get too large – typically it is about a few per cents (< 10 %). As a consequence of small loading rates, large running times can be faced.

To reduce the computational cost, *mass scaling* was used in the study. The duration of the applied displacement and the value of the *mass scaling* factor for the numerical models were chosen through an iterative process to obtain a quasi-static response, as well as an economic solution time. Typical loading rates for transverse displacement applied at the free end of the beam were around 30 mm/s.

In addition, an accurate and efficient quasi-static analysis requires the loading to be as smooth as possible. For this purpose, displacement was prescribed by using *smooth step* function in Abaqus. Namely, when the displacement time history is defined using a *smooth step* amplitude curve, the velocity and acceleration are zero at every data point specified, although the average velocity and acceleration are nonzero, (SIMULIA, 2012).

4.2.8 Other basic modelling issues and assumptions

4.2.8.1 FE modelling logic

To reduce the computational cost of FE models, a decision was made to use simple beam finite elements (a 2-node linear beam in space, element B31 from Abaqus Element library) to model parts of the beam and the column that remains elastic throughout the entire analysis, Fig. 107. However, parts of the beam and the column near the beam-to-column connection were modelled with 3D solid elements.

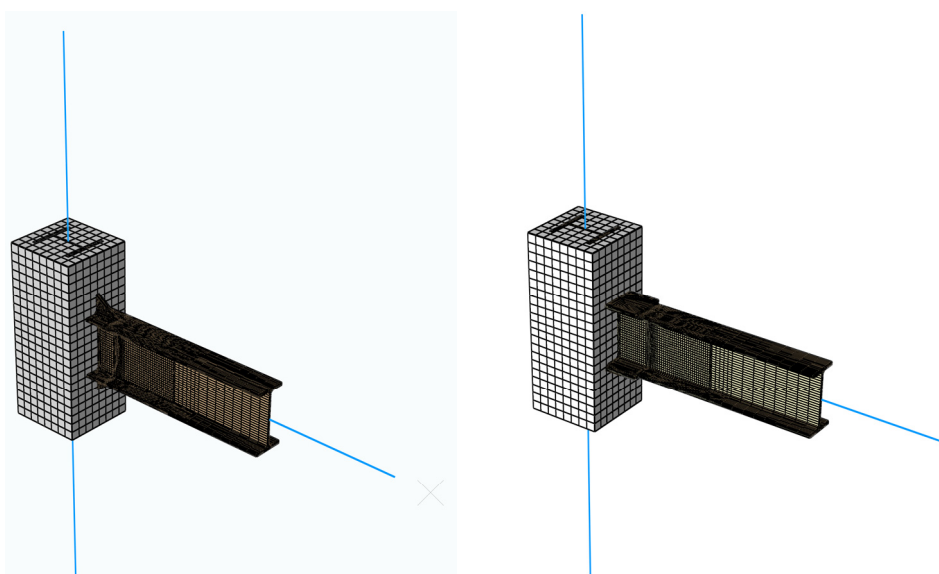


Fig. 107: Beam-to column joint RS1 and CP1 finite element model
Slika 107: Računski model na osnovi končnih elementov za spoj prečka-steber RS1 in CP1

Typical lengths of members discretised by solid elements, used for all models, followed the following scheme: $3.0 \cdot h_b$ from the end of the stiffener and $1.5 \cdot h_c$ above and below the complete stiffened connection for beam and column, respectively, where h_b and h_c are the beam and the column cross-section height. In this way, the whole plastic deformation on the beam, including the beam local buckling deformation, as well as deformed shape of complete beam-to-column connection was still enough accurately modelled, Fig. 108.

The whole solid part of particular beam-to-column joint model is made in a single part, thus no further use of constraints to tie different solid parts together in the assembly module is needed. Parts comprising beam type finite elements are constructed in the separate parts. The parts are then assembled to produce the complete model using the “part”, “instance” and “assembly” modules in Abaqus. At the common interfaces between the two adjacent parts in the model, the corresponding degrees of freedom are linked using multi-point constraints to ensure compatibility within the model.

But welds joining the combined thickness of the beam flange and cover plate to column flange were not modelled explicitly. Similarly, complete beam-column welded connection was not included explicitly in the FE model. On the contrary, all fillet welds between rib-stiffener and beam and column flange were included. Similarly, both longitudinal and transverse fillet weld between cover-plate and beam flange were modelled as well. Material for the welds was used the same as for the beam, Fig. 108.

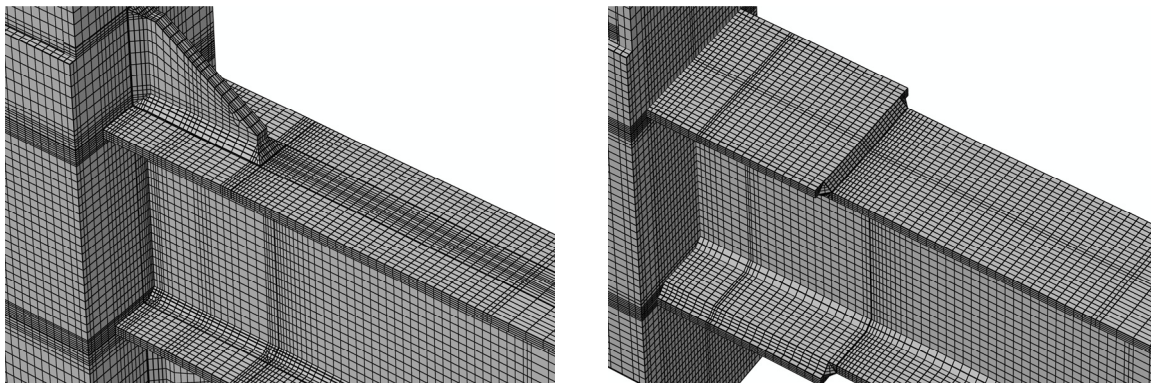


Fig. 108: Details of steel joint components of RS and CP beam-to column joint finite element model
Slika 108: Detajli računskega modela za jeklene komponente spoja prečka-steber RS in CP

Rib-stiffener and cover-plate are connected with the beam/column flange by fillet welds only. There is a gap of 1 mm modelled between the surface of the beam and the attached surface of the stiffener, see Fig. 109.

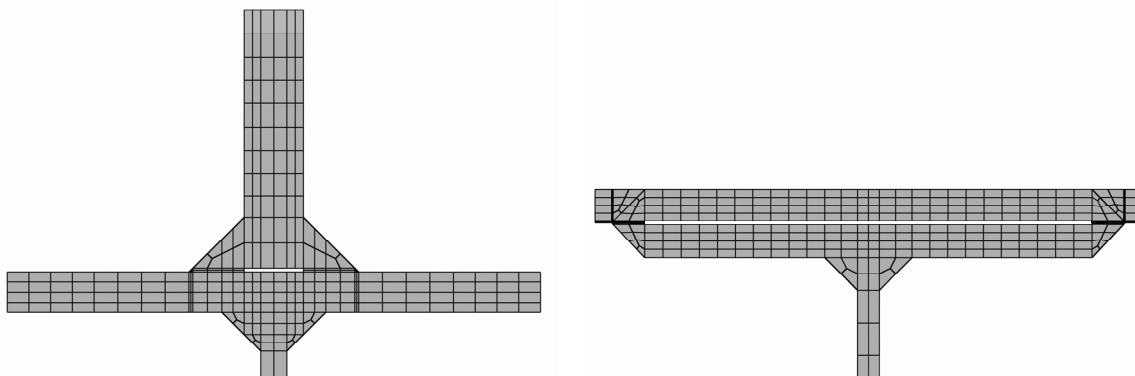


Fig. 109: Stiffened cross-section detail for of RS and CP connection
Slika 109: Detajl ojačanega prereza prečke za spoj RS in CP

Surface contact between the beam flange and the cover-plate was ignored in the study to substantially improve the computational efficiency of the analysis.

4.2.8.2 Applied precision level

An important job parameter used to control adequate precision level of the Abaqus/Explicit analysis is a double-precision executable (with 64-bit word lengths). While the single-precision executable, which typically results in a CPU savings of 20 % to 30 % compared to the double-precision executable, provided enough accurate results in case of using Abaqus/Standard, it proved to be inadequate for analyses in Abaqus/Explicit, where considerably larger number of required increments were needed (more than 300 000).

Further on, running in double precision is more suitable for this kind of deformable part analysis because of the high number of reversals of the joint throughout the entire cyclic loading history.

Due to the facts, the double-precision executable was used for Abaqus/Explicit analyses (both the Abaqus/Explicit packager and analysis run in double precision) in order to follow properly the prescribed displacement loading history and to assure the best accuracy of the results. Without the option used, discrepancies in the response were noticed at higher (> 50) cycle numbers.

4.3 Performance of the finite element model

4.3.1 Introduction

In order to establish reliable and optimised FE numerical model capable of predicting beam-to-column joint response under arbitrary loading, FE models were calibrated against experimental monotonic and cyclic test results. This chapter presents description of developed FE model performance based on comparison between simulated and experimental test results.

First, simulated monotonic behaviour is checked against global load-deformation cantilever beam response found in literature as well as against the reproduced monotonic behaviour (use of the skeleton curve principle) of cyclic tests performed in the scope of this research work.

After successfully calibrated simulated monotonic response, outcomes of the first calibration phase were implemented in the second step, where calibration of simulated joint response subjected to cyclic loading was done. This chapter provides a comprehensive description on cyclic performance of the developed cyclic plasticity based numerical model in Abaqus. Once again it should be noted that material model used to simulate monotonic and cyclic responses of steel members is not the same, since material model for cyclic loading in Abaqus is the so called phenomenological model, intended to simulate strictly cyclic metal plasticity.

Determination of cyclic loading protocol used in the simulations is addressed. After that, comparison between simulated and experimental constant and variable cyclic behaviour of the tested joints is brought forward. First, simulated response of specimens subjected to constant amplitude cyclic loading is presented. Experimental results from constant cyclic tests offered a great opportunity to check the capability of the numerical model: on one hand, in terms of pure material low-cycle fatigue (LCF) without the presence of the beam local buckling, and on the other, combined effect of the beam local buckling followed by the subsequent LCF failure. The acquired knowledge was then used for the simulation of specimens' experimental response under stepwise increasing cyclic loading amplitude.

The validation of the numerical models against the experimental results involves comparison of force displacement diagrams, beam local buckling geometry, local strains captured in the vicinity of stiffened joint region and several stress/strain response indices.

Performance of the numerical model for cyclic loading was also checked with respect to the prediction of ductile crack initiation. Results from these simulations were used to demonstrate the transferability of the applied damage parameter characteristic values determined by small scale tests from literature. Furthermore, each cyclic test was simulated by FEM analysis in order to explore inelastic behaviour with distribution of accumulated damage indices.

Based on highly consistent results obtained from both experimental and simulated joint responses, the idea is to use the obtained pattern and values of response indices at the onset of local failure (reported from the experiments) to propose new failure criterion for steel elements subjected to LCF loading. The established LCF failure criterion was later applied in complementary analysis for the systematic response evaluation criteria of different beam-to-column joints subjected to cyclic loading.

First, Abaqus/Explicit solver was used for analysis of all the test specimens to facilitate stable convergence due to locally nonlinear behaviour of concrete. In this way, response of all the steel components encased in concrete was accurately simulated. After that, Abaqus/Standard was also used with linear material definition for concrete to check the Abaqus/Explicit response and to gain some response variables that are not available in Abaqus/Explicit solver (e.g. ALPHA variable).

The chapter is concluded with applicability assessment of developed FE models for simulation of monotonic and cyclic response of stiffened beam-to-column joints.

4.3.2 Monotonic loading

4.3.2.1 Cantilever beam subjected to non-uniform bending

In addition to the calibration of simulated monotonic response against the skeleton curves, which were obtained from the cyclic experimental test results, see Chapter 3.4.8, additional two experimental monotonic tests on steel cantilever beam from literature were chosen for this purpose. Namely, simulated beam monotonic behaviour was evaluated against complete experimentally obtained response curve of a beam subjected to non-uniform bending, including the stable part of rotation capacity developed up to the occurrence of the beam local buckling in the plastic hinge zone and the subsequent unstable part due to post-buckling behaviour. Especially the latter part of monotonic response curve, describing the post buckling behaviour, cannot be well represented by the skeleton curve principle.

Results from two experimental tests on steel cantilever beams under non-uniform bending from research study performed by D'Aniello et al. (2012) were selected for this purpose. Two different types of beam cross-section made of mild carbon steel were chosen: hot rolled I and H sections, with IPE300 and HEB240 beam profiles, respectively.

The net length of the tested cantilever (distance from the transverse load insertion point to the stiffened part of the beam) is equal to 1875 mm. In order to reduce computational weight of each FE model, not complete cantilever beam was modelled with 3D solid finite elements. Only the first part of the beam length, $3.0 h_b$ from the end of the stiffened part, was discretised with solid elements, while for the rest part of the beam, where elastic response is expected, a 2-node linear beam in space elements were applied, see Fig. 110.

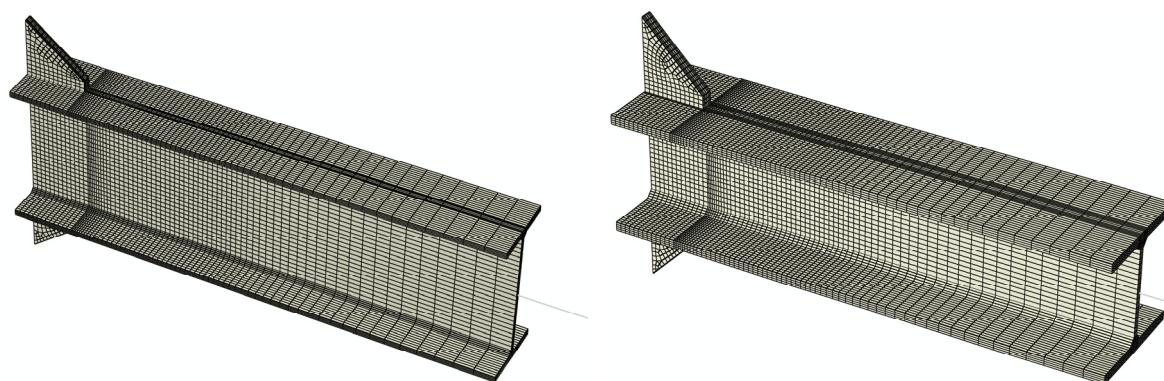


Fig. 110: Solid part of FE model for cantilever beam IPE300 and HEB240

Slika 110: Del modela konzolno vpete prečke IPE300 in HEB240 modeliran s prostorskimi končnimi elementi

Complete FE mesh of the solid part of each model was created according to the outcomes of the elastic mesh convergence study presented in Chapter 4.2.3.1. Finer mesh was also used in the region behind the stiffened part of the beam, where concentration of plastic deformations is expected. Each simulation was run till the maximum value of beam rotation used in the experiment as reported in the literature. Transverse force applied at the free end of the beam, as used in the tests, without additional beam axial load was considered in the study.

Corresponding steel material stress-strain curves for both specimens' model were defined on the basis of material test results as reported by D'Aniello et al. (2012).

For each case of cantilever beam IPE300 and HEB240 a set of seven analyses was performed, accounting for different value of the beam local imperfection amplitude. As already described in Chapter 4.2.5, applied beam local imperfection amplitude value was expressed relative to the beam flange width b_f .

The reference value of imperfection amplitude was selected according to the standard EN 10034 (CEN, 1993). Accordingly, total out-of-square tolerance for a cross-section, see Fig. 105, with a flange width more than 110 mm, in terms of k is $\frac{1}{2} \times 2\%$ of b_f . Beside the case with no imperfection applied on the beam, five additional values of imperfection amplitude, relative to the reference value of 1.0% of b_f , were included in the study to explore the one, which gives the best match with the experimentally obtained result in terms of complete global elastic-plastic beam response. The selection of applied imperfection amplitudes for both cantilever beams is reported in Table 24.

In addition, two different types of 3D solid finite elements were applied, namely C3D8R and C3D8I, in order to check their performance for the problem of this sort. In total, fourteen simulations for each case of cantilever beam were performed.

Beside different imperfection amplitudes and both considered types of finite elements, all other parameters of the two finite element models remained the same, including parameters of constitutive material model as well as other geometric issues including finite element discretisation mesh.

Preglednica 24: Upoštevan nabor vrednosti amplitud lokalne geometrijske nepopolnosti prečke
Table 24: Applied range of beam local imperfection amplitudes

Imperfection amplitude $k + k'$	IPE300, $b_f = 150$ mm		HEB240, $b_f = 240$ mm	
	$k / 2$ [mm]			
No imperf.	/	/	/	/
ref. value	2.0 % b_f	0.75		1.2
ref.·0.5	1.0 % b_f	0.375		0.6
ref.·0.4	0.8 % b_f	0.3		0.48
ref.·0.3	0.6 % b_f	0.225		0.36
ref.·0.2	0.4 % b_f	0.15		0.24
ref.·0.1	0.2 % b_f	0.075		0.12

Comparison between response curves obtained from the experiment and the simulation are presented in Figs 111, 112 and in Figs 113, 114, for IPE300 and HEB240 beams, respectively.

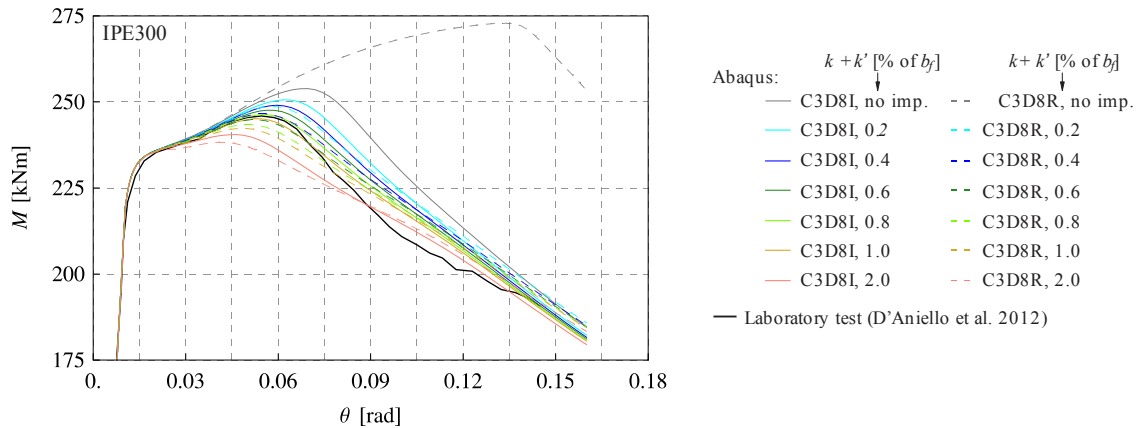


Fig. 111: Effect of the beam local imperfection amplitude on the simulated response of specimen IPE300 compared to the experimental curve from D'Aniello et al. (2012)

Slika 111: Vpliv velikosti upoštevane amplitude lokalne nepopolnosti prečke IPE300 na rezultat simulacije in primerjava z eksperimentalnim odzivom iz D'Aniello in drugi (2012)

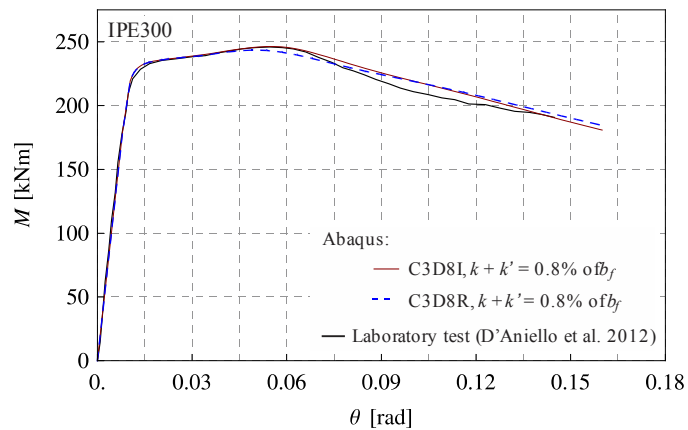


Fig. 112: Experimental, D'Aniello et al. (2012), and simulated flexural performance of specimen IPE300
Slika 112: Primerjava med eksperimentalnim odzivom, D'Aniello in drugi (2012), in simulacijo testa IPE300

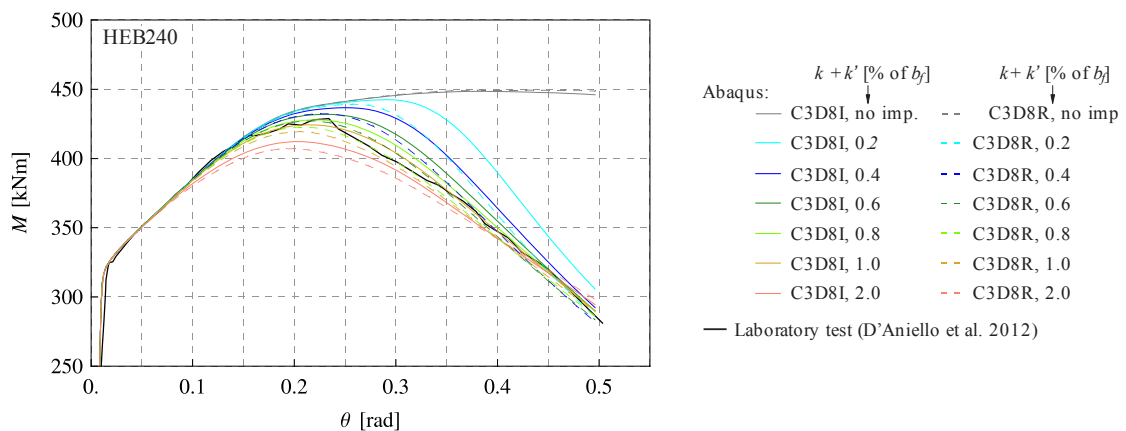


Fig. 113: Effect of the beam local imperfection amplitude on the simulated response of HEB240 specimen compared to the experimental curve, D'Aniello et al. (2012)

Slika 113: Vpliv velikosti upoštevane amplitude lokalne nepopolnosti prečke HEB240 na rezultat simulacije in primerjava z eksperimentalnim odzivom iz D'Aniello in drugi (2012)

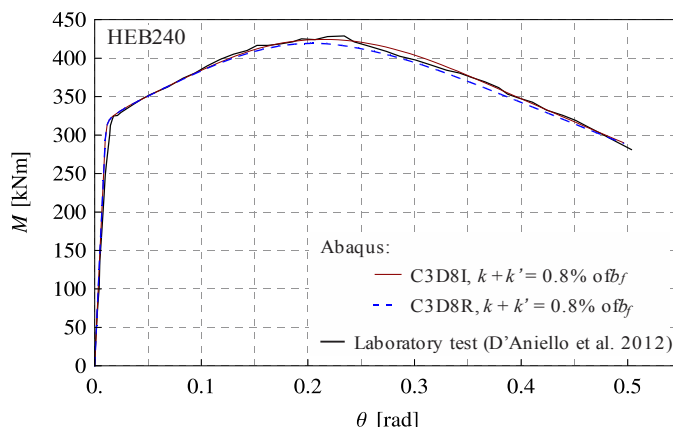


Fig. 114: Experimental, D'Aniello et al. (2012), and simulated flexural performance of HEB240 specimen
 Slika 114: Primerjava med eksperimentalnim odzivom, D'Aniello in drugi (2012), in simulacijo testa HEB240

In case of both specimens IPE300 and HEB240 non-negligible sensitivity level of the beam buckling strength to the applied initial beam local imperfection amplitude level can be observed from Figs 111 and 113. By using beam imperfection amplitude value for $k + k'$ arbitrarily selected in the range of 0. – 2 % of the beam flange width b_f , simulation may lead to substantially different results.

As can be observed from Figs 111 and 113, value of applied imperfection amplitude affects beam flexural overstrength s and consequently also its rotation capacity R . Both ultimate flexural response parameters are decreasing with increasing value of imperfection amplitude.

For specimen IPE300, the use of imperfection amplitude on the order of $k + k' = 0.8\%$ of the beam flange width b_f leads to the best agreement with the corresponding experimental result, see Fig. 112. However, for specimen HEB240 a bit larger value of imperfection amplitude, i.e. $k + k' = 1.0\%$ of b_f , provides the highest consistency with experimentally obtained response, Fig. 114.

Comparison of deformed shape between the experiment and the simulation is presented in Fig. 115 and Fig. 116, for cantilever beams IPE300 and HEB240, respectively. The variant with imperfection amplitude that provides the best agreement with experimental result is shown for both specimens. Also from comparison of the deformed shapes a high consistency between the experiment and the simulation for both IPE300 and HEB240 specimens can be observed.

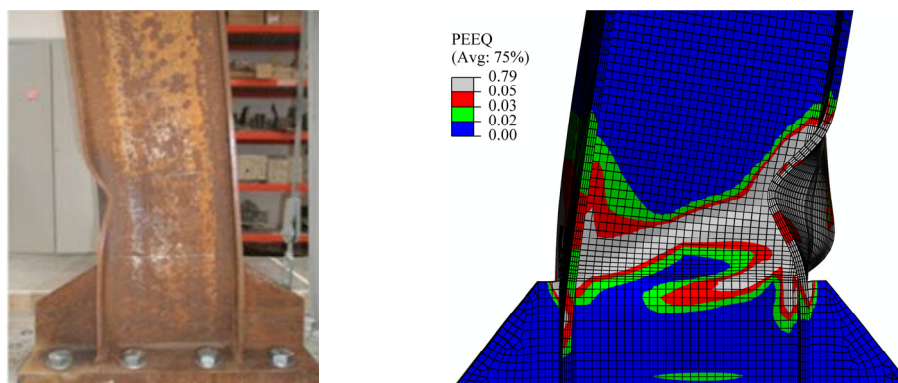


Fig. 115: Deformed shape of cantilever beam IPE300 at rotation $\theta = 0.15$ rad: experiment - D'Aniello et al. (2012), and simulation

Slika 115: Deformacijska oblika konzolno vpete prečke IPE300 pri rotaciji $\theta = 0.15$ rad: eksperiment - D'Aniello et al. (2012) in simulacija

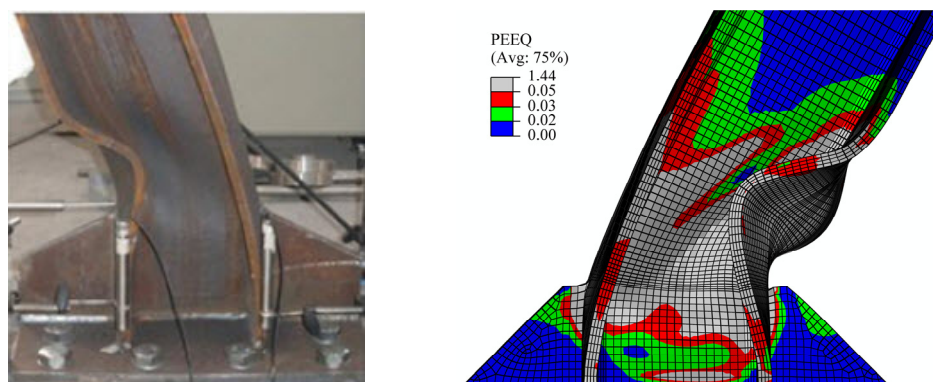


Fig. 116: Deformed shape of HEB2400 cantilever beam at rotation $\theta = 0.50$ rad: experiment by D'Aniello et al. (2012), and simulation

Slika 116: Deformacijska oblika konzolno vpete prečke HEB240 pri rotaciji $\theta = 0.50$ rad: eksperiment - D'Aniello et al. (2012) in simulacija

From Figs 111 to 114, almost insignificant difference can be observed between the simulated response obtained by using solid elements C3D8R and the enhanced ones C3D8I. In this case it must have been due to coincidence in the applied mesh refinement level (i.e. enough refined mesh), that no obvious difference in the response between both the applied finite elements was revealed. However, in the next chapter it is clearly shown that generally C3D8R elements may perform poorly in bending compared to the enhanced C3D8I ones.

On the basis of this calibration study it was shown that the developed finite element model is capable of simulating response of a beam subjected to monotonic non-uniform bending with high accuracy regardless of the beam cross-section geometry. Even both the specimens possess different cross-sectional shapes, highly consistent local imperfection amplitude values for $k + k'$ were obtained, namely for IPE300 0.8 % b_f , while for HEB240 1.0 % b_f .

For all the subsequent analyses decision was taken to use $k + k' = 0.8$ % b_f , no matter for the I and H beam cross-section dimensions.

4.3.2.2 Simulation of the skeleton curve response

Skeleton curve response defined for the eight experimental cyclic tests with variable stepwisely increasing loading amplitude according to ANSI/AISC 341-10 protocol and ECCS N°45 modified loading protocol, presented in Chapter 3.4.8, were simulated in order to confirm the adequacy of the beam local imperfection amplitude level selected in the previous Chapter 4.3.2.1.

Four stiffened beam-to-column joint finite element models were built in order to represent the four different joint specimens designed for the experimental cyclic tests, see Chapter 3.3.1. Specimens RS1 and RS2 represent rib-stiffened beam-to-column joint with IPE270 and IPE240 beam sections, respectively. Similarly, specimens CP1 and CP2 represent cover-plate beam-to-column joint with IPE270 and IPE240 beam sections, respectively. As no extra discrepancies in geometry of the joint specimens were observed prior to the experimental testing, nominal geometry (as designed) was used for all the numerical models, the reader may also refer to Chapter 4.2.8.

At the beginning, numerical models of all the joints were developed following the outcomes of previously performed elastic mesh convergence study on beam-to-column joint sub-models. Mesh characterized with element in-plane dimensions around $b_f/20$ was decided to be applied in the region of the stiffened beam section and around location where plastic hinge is supposed to occur. Four elements through the thickness of the beam flanges and column

flanges were used, with 2 solid elements through the thickness of webs for the whole part of the finite element model of joint discretised with 3D solid elements.

However, additional remeshing was needed in the region of the strengthened beam section in order to make feasible that complete steel beam-to-column joint was made in a single part, see Figs 108 and 109. It should be noted that for each stiffened joint configuration mesh strongly depends on its local geometry in the vicinity of the stiffened part of the beam. Especially in case of both RS models this resulted in a larger number of solid finite elements across the beam flange width, with considerably smaller element dimensions at the centre region of the flange, see Fig. 117.

During the numeric model calibration phase, the ultimate flexural response of beam, governed by the beam local buckling, was found strongly dependent on the number of finite elements used across the beam flange. Namely, using solid elements C3D8R, too little finite elements across the free-length of the beam flange, generally resulted in too stiff response. The latter phenomenon contributed also to the use of unrealistically large values of initial beam local imperfections in order to match laboratory tests results.

Before continuing with the performance check of the FE model configuration, additional finite element model calibration performed during the phase of model development is discussed below.

In relation to the performance of different applied solid finite elements C3D8R and elements with enhanced flexural performance C3D8I, comparison based on different mesh refinements was performed and is presented hereinafter.

To this end, three different meshes were utilized on RS1 and CP1 models that differ in the number of elements across the free length of flange in the beam transverse direction. In case of model RS1, see Fig. 117, 4 elements across the considered width of the beam flange means element in plane dimension 11×10 mm, for 8 elements 5.5×10 mm, for 12 elements 3.7×10 mm and for 12 elements with additional reduction of element dimension along beam centreline 3.7×5 mm. In case of model CP1 the same level of mesh refinements was used, with typical element in plane dimensions in the observed location being slightly different due to different geometry of the stiffened connection: 4 elements across the considered width of the beam flange means element in plane dimension 13.6×10 mm, for 8 elements 6.8×10 mm, for 12 elements 4.5×10 mm and for 12 elements with additional reduction of element dimension along beam centreline 4.5×5 mm.

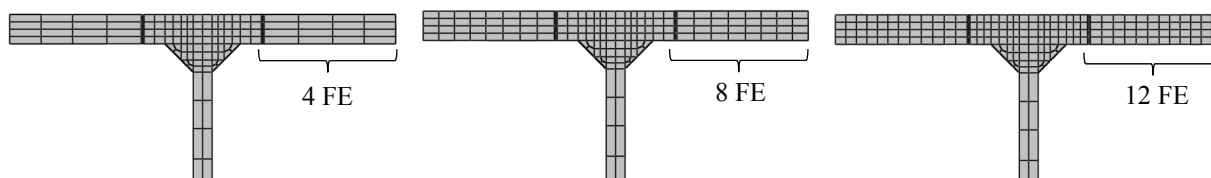


Fig. 117: Details of FE discretisation mesh over the beam flange and flange-web juncture region for model RS in case of three different meshes used for inelastic mesh convergence study

Slika 117: Detajli mreže končnih elementov po pasnici prečke in stičišču pasnice in stojine prečke za tri različne gostote mreže uporabljene v neelastični konvergenčni študiji

Beside different imperfection amplitude values and both considered types of finite elements C3D8R and C3D8I along with four different discretisation mesh levels presented above, all other parameters of the two finite element models remained the same, including parameters of constitutive material model as well as other geometric issues.

Results of inelastic convergence study for both RS1 and CP1 models are presented in Figs 118 and 119. Additional curve obtained by using more accurate C3D20 finite elements is

depicted in each diagram in order to confirm the response to which all the models should converge.

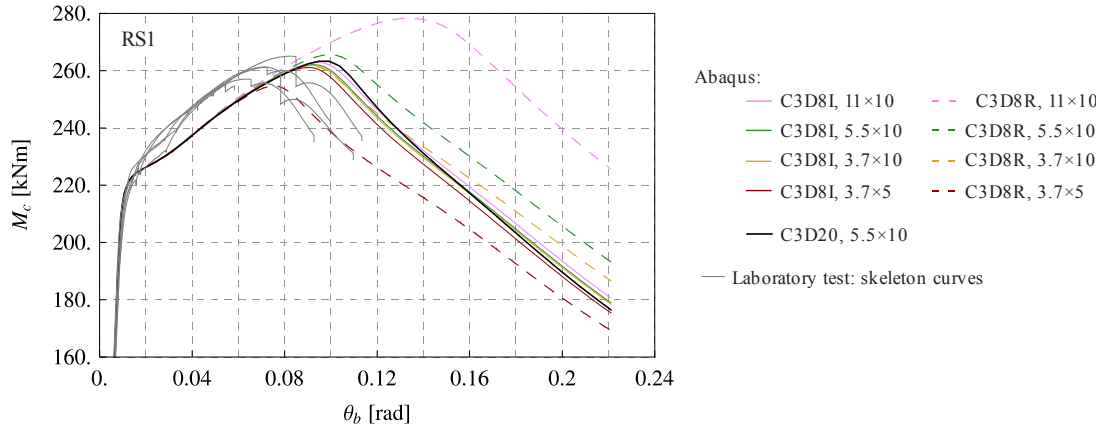


Fig. 118: Inelastic convergence study for joint model RS1
Slika 118: Neelastična konvergenčna študija za model spoja RS1

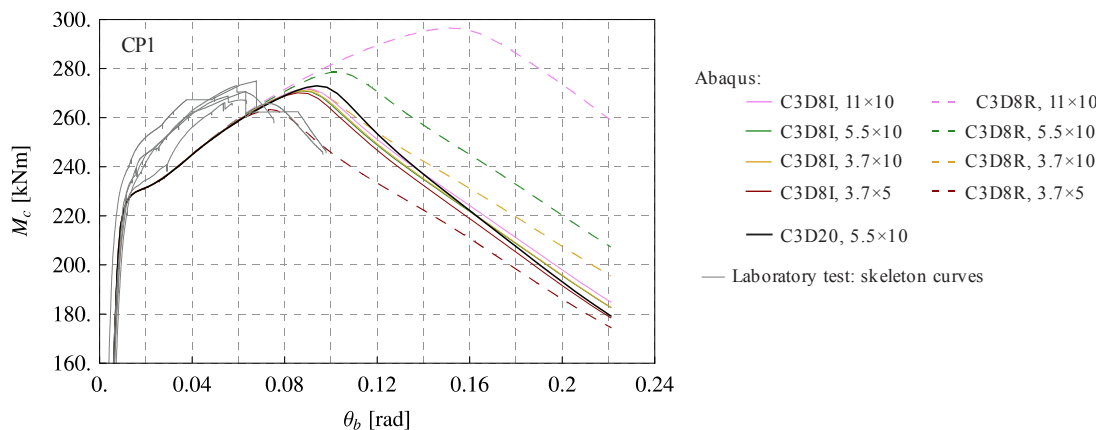


Fig. 119: Inelastic convergence study for CP1 joint model
Slika 119: Neelastična konvergenčna študija za model spoja CP1

The presented results of inelastic convergence study clearly show high dependence of inelastic joint response on discretisation mesh density in case of the use of C3D8R finite elements for both RS1 and CP1 models. On the contrary, performance of the numerical models proved to be almost independent on the finite element discretisation mesh issue in case of using incompatible mode elements C3D8I.

The comparison of results certainly speaks in favour of using enhanced C3D8I elements for all the subsequent models in order to provide accurate as well as consistent results, i.e. not being dependent on the finite element discretisation mesh issues that may be governed also by geometry details of the stiffened connection.

Although full integration elements C3D8I are somewhat more expensive than the regular first-order displacement elements, because of the added internal degrees of freedom due to the incompatible modes (13 for C3D8I), which result in improved bending performance, their use is indispensable for the proper results obtained in the subsequent complementary study, see Chapter 5, where beam cross-sections of different types and sizes are analysed. It should also be noted that elements C3D8I are significantly more economical than the second-order elements, e.g. C3D20. Another advantage is also the fact that geometric order is the same for both C3D8R and C3D8I (8-node brick element), which allows their combination in the model without introducing an incompatibility between the regions containing particular solid element type.

In combination with elements C3D8I, discretisation mesh level with element dimensions according to the stated conclusions from elastic mesh convergence study, see Chapter 4.2.3.1, is reasonable and was used for all further numerical models.

It should be remarked, that simulated monotonic responses of both RS1 and CP1 specimens presented in Figs 118 and 119 were obtained on the basis of steel stress-strain material curves directly obtained by material tests. In this case, not so good agreement with the corresponding skeleton curves, in terms of plastic response, can be observed for both RS1 and CP1 joints. In particular, material strain hardening rate obtained from the simulations underestimates the corresponding one obtained from the tests. However, after the calibration process, more consistent results compared to the experimental ones were obtained and are presented hereinafter.

The reason for discrepancies between the simulated and the experimental response can be justified by the fact that not complete hot-rolled I beam cross-section is consisted from material with unique mechanical characteristics. Especially in case of the yield strength and the subsequent strain hardening rate and range, non-negligible differences were found in the material samples taken from flanges and web of particular hot-rolled beam profile used for test specimens, see also Chapter 4.2.4.1.1.

Due to the simplicity, unique stress-strain material curve was used in the subsequent finite element models for particular joint component (beam and column member, stiffening plates, welds). Particular curve was defined as an average from all the stress-strain curves obtained for particular joint member or plate, see Chapter 4.2.4.1.1. Accordingly, as it follows from the above discussion, the applied steel stress-strain curve had to be modified in order to imitate the global experimentally obtained response.

In particular, no substantial changes were applied to the corresponding average value of the yield stress and the ultimate strength obtained from the material tests on beams. Modification of calibrated curve consists of reduction of strain corresponding to the beginning of hardening, and an increase of the initial hardening modulus in the post-yield region. As already mentioned, no substantial change was applied to the complete material strain hardening range measured by ultimate-to-yield stress ratio f_u / f_y , Fig. 120. Eventually, the calibrated material curve was used to simulate monotonic response of all the four specimens, RS1, RS2, CP1 and CP2.

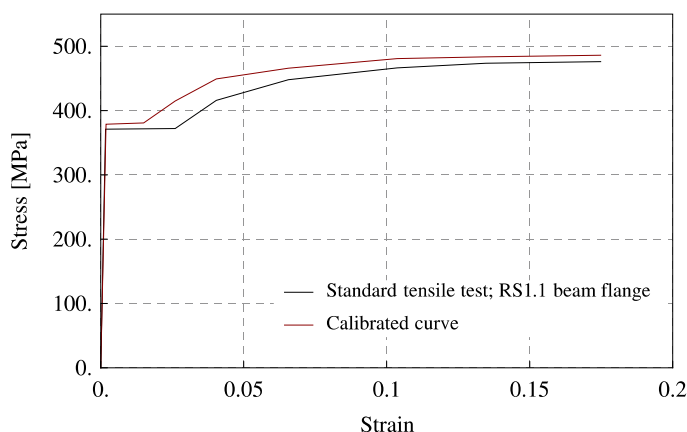


Fig. 120: Discretised S355 grade steel monotonic stress-strain diagrams up to the point of the ultimate strength
 Slika 120: Diskretizirani materialni krivulji napetost-deformacija za jeklo S355 do točke natezne trdnosti

It is interesting to note that the calibrated material stress-strain curve also shows high consistency in terms of the initial strain hardening rate with material curves used for simulations of cantilever beams presented in the previous Chapter 4.3.2.1.

Simulations of the beam-to-column joints' monotonic responses were performed in terms of displacement load at the free end of the beam, with all boundary conditions resembling laboratory test conditions.

Total joint displacement of 300 mm was used for joints RS1 and CP1 with large beam section IPE270 and 350 mm for joints RS2 and CP2 with small beam section IPE240, which results in total joint rotation $\theta = 300/1800 = 0.17$ rad and $\theta = 350/1800 = 0.19$ rad, for joints with large and small beam sections, respectively.

After first several trials, the complete joint response was found somewhat difficult to be accurately simulated, due to highly nonlinear response of the concrete column of all 16 specimens (anisotropy in behaviour of concrete encasement observed as localized cracks, see Chapter 3.4.5). At the same time, the contribution of the column was small in all the tests. For this reason decision was made to present moment-rotation curves not for total joint rotation, but total beam rotation in order to emphasize the consistency between the responses of joint steel components. However, nonlinear material model for concrete was still included in the models, to simulate its actual contribution to the joint response (column web panel with other steel components encased in concrete), see Chapter 4.2.8.

According to the adopted procedure for construction of a skeleton curves, the modified principle was used herein to include also part of the unstable range due to the beam post buckling behaviour captured during the cyclic tests. For a detailed discussion of the skeleton curve principle and its modified variant, the reader may refer to Chapter 3.4.8.

Final comparison between the experimental and the simulated monotonic responses for all the four different beam-to-column joint specimens is presented in Figs 121 and 122.

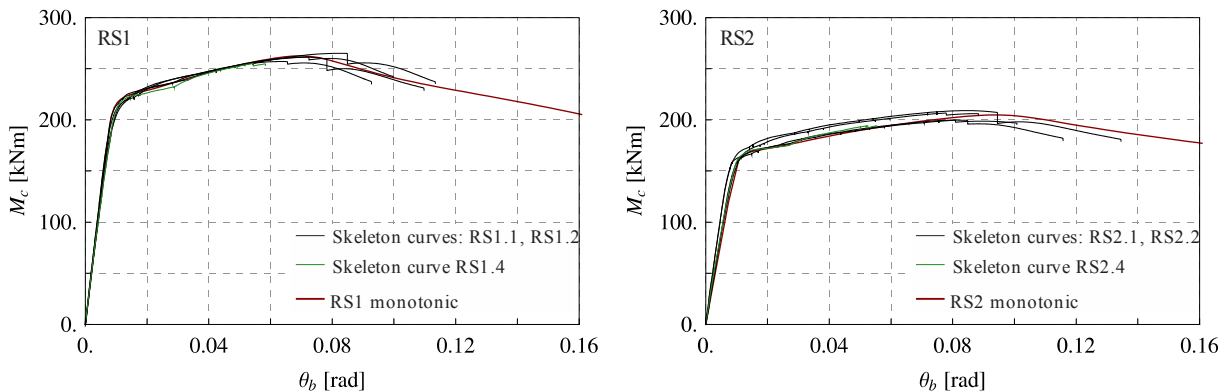


Fig. 121: Simulated monotonic response for joints RS1 and RS2 and the corresponding skeleton curves
Slika 121: Simuliran monotoni odziv spojev RS1 in RS2 in pripadajoče skeleton krivulje

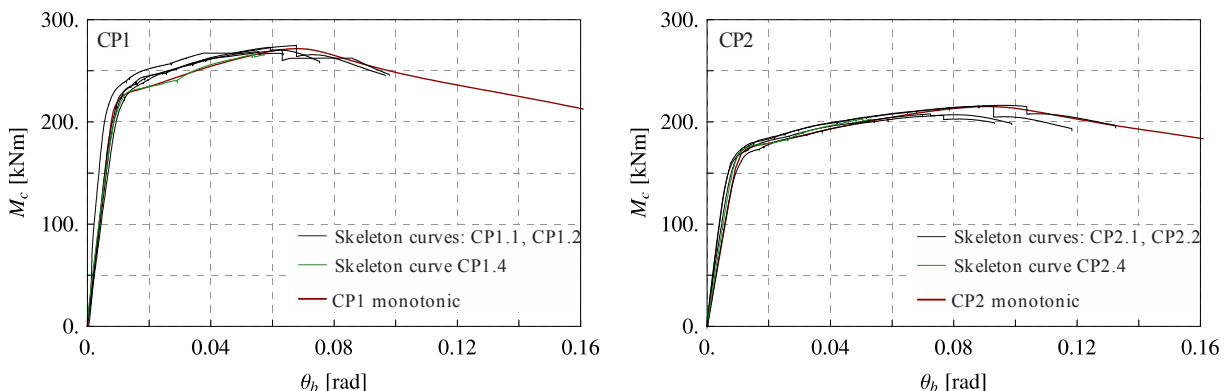


Fig. 122: Simulated monotonic response for joints CP1 and CP2 and the corresponding skeleton curves
Slika 122: Simuliran monotoni odziv spojev CP1 in CP2 in pripadajoče skeleton krivulje

As observed from the above figures, simulated response for all the four joint specimens RS1, RS2, CP1 and CP2 is in a very good agreement with the corresponding experimental results.

The last part of the experimentally obtained curves show somewhat larger rate in drop of flexural resistance, which can be attributed to the LCF effects in terms of accumulated plastic deformation throughout the previous cycles.

4.3.3 Cyclic loading

4.3.3.1 Applied cyclic loading history

First important step toward an accurate simulation of experimental cyclic tests is a definition of proper loading history to be used in the finite element model job definition. In particular, cyclic loading history was defined for each of 16 tests separately, to resemble actually applied displacement/rotation amplitudes based on measurements during the laboratory tests, following an idea and procedure described below.

As already presented in Chapter 3.3.4, displacement load at the free end of the beam in the tests was applied in terms of total joint rotation θ . In the early stage of the calibration phase, composite column behaviour, although contributing rotations less than 0.005 rad, was found difficult to simulate. Therefore, decision was made to use total beam rotation as a basis of loading protocol definition used in the finite element models. The instrumentation scheme presented in Chapter 3.3.3 allowed for removal of complete column rotation as well as deformations of the supports. Thereby, complete cyclic loading history used in the simulations, characterised by positive and negative amplitudes for each loading cycle, was defined using the following two equalities:

$$\begin{aligned}\theta_b^{SIM.} &= \theta_b^{EXPER.}, \\ \theta^{SIM.} &= \theta_b^{SIM.} + \theta_c^{SIM.} = \theta_b^{EXPER.} + \theta_c^{SIM.},\end{aligned}\tag{34}$$

where $\theta_b^{SIM.}$, $\theta_b^{EXPER.}$ is a total beam rotation obtained from simulation and experiment, respectively, and $\theta_c^{SIM.}$ is a total column rotation from simulation, including elastic bending and column panel zone rotation. Values of $\theta_c^{SIM.}$ were obtained from previously performed monotonic simulations on the joint specimens RS1, RS2, CP1 and CP2, see Chapter 4.3.2.2, and is expressed as a function of transverse force applied at the beam tip for each of the four specimens.

Prescribed boundary condition for complete cyclic loading history in case of a particular joint model was defined in Abaqus within a single *General Step* after the *Initial* one. A simple built-in type of amplitude, called *Smooth Step*, which automatically creates the smoothest possible loading path between the two consecutive amplitude points, for a deeper description see Chapter 4.2.8, was used in case of both Abaqus/Standard and Abaqus/Explicit solver types.

All the analyses in Abaqus/Explicit were performed using a double precision floating point accuracy, since the number of time increments to complete the simulation for duration of applied cyclic loading histories was very large (larger than 300 000), see Chapter 4.2.8 for a detailed description.

First trial elastic cycles performed in each experiment prior to the applied cyclic loading protocol, variable and constant, were not included in the simulations. Also first elastic cycles of the applied ECCS N°45 modified protocol and AISC 341-10 loading procedure were not tried to simulate. The decision was made by taking into account the limitation of the applied cyclic material model, which do not account for yield plateau phenomenon. Namely, response in the upper elastic region, where specimen's resistance is close to the proportional limit, is not accurate, in terms of somewhat greater deformation, compared to the actual one, Fig. 123a.

Taking into account all the above considerations, cycles with loading amplitudes well into the plastic range only were simulated in case of variable amplitude cyclic tests, Fig. 123b and Tables 11 to 14.

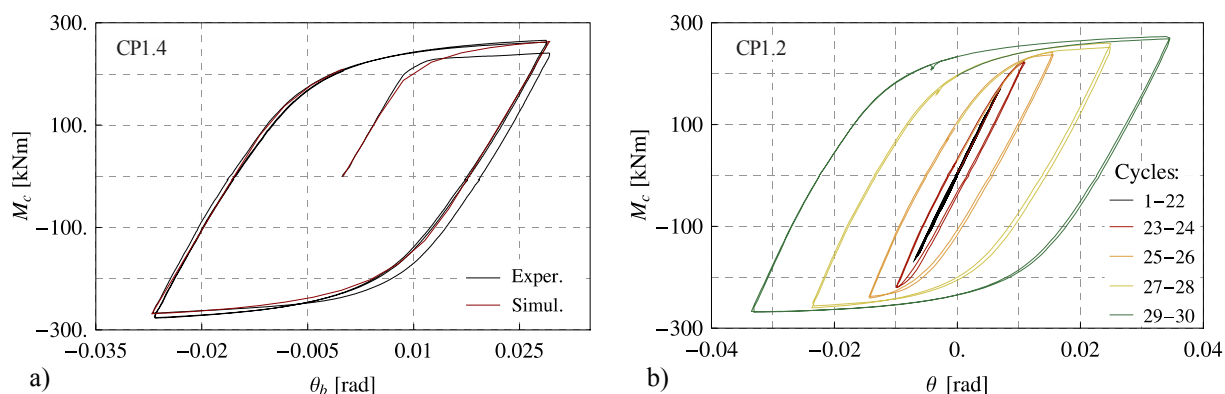


Fig. 123: a) Comparison between the first hysteresis from simulation and the experimental response, b) experiment: first 30 cycles under AISC 341-10 loading protocol

Slika 123: a) Primerjava prve histerezne zanke med simulacijo in eksperimentom, b) eksperiment: prvih 30 ciklov v primeru protokola AISC 341-10

Table 25 provides information on complete number of cycles performed by the simulations, compared to complete number of nominally plastic cycles according to the experimentally applied loading protocols. In case where the number of simulated cycles is smaller than the number of nominally plastic cycles performed in the experiment, simulated cycles represent all cycles in plastic range, but without few cycles (the exact number depends on particular case) at the beginning of experimentally applied loading protocol, which turned out to be in elastic range, see also Fig. 123b (first 22 cycles in elastic range).

Preglednica 25: Število polnih neelastičnih ciklov za teste z variabilno amplitudo: eksperiment (nominalno plastični cikli) in simulacija

Table 25: Number of completed inelastic cycles for variable cyclic tests: experiment (nominally plastic range) and simulation

Specimen RS	completed cycles in plastic range		Specimen CP	completed cycles in plastic range	
	experiment	simulation		experiment	simulation
RS1.1	13	13	CP1.1	15	13
RS1.2	14	14	CP1.2	15	15
RS2.1	17	15	CP2.1	17	15
RS2.2	17	17	CP2.2	16	16

According to the above approach, in case of both tests with modified ECCS N°45 loading protocol (RS1.1 and RS1.2), first three nominally elastic cycles were excluded in the simulations. As it was already mentioned, displacement load at the free end of the beam in the tests was applied in terms of total joint rotation θ , which included additional displacements coming from the supports and deformations of the loading frame. Due to the fact, as well as a result of smaller increments in stepwise increasing AISC 341-10 loading protocol, two sceneries, depending on the presence or absence of high level of column axial force, which provided additional stabilization of the specimen column, can be observed from Table 25 and Fig. 123b. It is 23th and 25th consecutive cycle used as the first cycle of the simulated loading protocol, for specimens with and without the presence of column axial force, respectively, see also Tables 11 to 14.

In case of all eight specimens subjected to both levels of constant amplitude cyclic loading, simulations were done for complete number of cycles performed in the experiment, see Table 8.

At this point a general comment should a priori be given about the degree of agreement between the experimental and the simulated beam-to-column joint cyclic response presented in the following sections.

From the following chapters one may observe somewhat better agreement between the experimental and simulated cyclic response in case of the test specimens with the presence of column compression axial force rather than those without the column axial force. This was the case for all four different joints, RS1, RS2, CP1 and CP2, where the column axial force provided additional stabilisation of the specimens. Even though parasitic movements of all supports were measured and included in the response data processing, some discrepancies in experimental response obviously still remain.

4.3.3.2 Constant amplitude cyclic loading tests

4.3.3.2.1 General findings from small and large constant amplitude loading

Beam local imperfection was accounted for in all the numerical finite element models. At the beginning of the calibration phase, the value of the beam local imperfection amplitude was chosen according to the outcomes of the previous finite element model calibration phase for monotonic loading, see Chapter 4.3.2.1. According to the monotonic response calibration, beam local imperfection amplitude, in terms of complete out-of-square measure $k + k' = 0.8 \% b_f$ was observed to produce accurate results.

However, during the simulations of large constant amplitude tests, RS1.4, RS2.4, CP1.4 and CP2.4, the adopted value of the beam local imperfection was found to be too large. Namely, buckling effects were triggered earlier and with larger intensity, resulting in substantially underestimated flexural strength during cyclic loading. The onset of the beam local buckling and its extent was found strongly dependent on the beam imperfection amplitude value. The more compact the beam, the greater sensitivity to the applied geometric imperfection amplitude was observed. After reducing the imperfection amplitudes, improved consistency with experimentally obtained results was found.

Finally, a very small values of the beam local imperfection amplitudes, ranging between 10^{-5} to 10^{-2} mm ($\approx 10^{-7}$ to $10^{-4} b_f$), were used for the simulations. The same value of imperfection amplitude was considered for both top and bottom beam flanges in case of all the simulations.

It is necessary at this stage to explain that the same value of beam local imperfection was used also for all I beam profiles (IPE sections) in the subsequent complementary numerical study, Chapter 5. However, for all other H beam profiles (HEA and HEB sections), imperfection amplitude value of this level was too small and eventually the same value as defined in the monotonic calibration phase $k + k' = 0.8 \% b_f$ was found to give the most consistent results for these type of beam cross-sections.

In case of the specimens subjected to small constant amplitude cycling, where beam local buckling in the experiments did not occur at all, RS1.3, RS2.3, CP1.3 and CP2.3, applied imperfection amplitude did not have effect on the performance of finite element models. Nevertheless, it was also applied to provide consistency of the work.

4.3.3.2.2 Constant displacement amplitude $\theta = 0.019$ rad

Comparison of deformed shape obtained from experiment and simulation for all four specimens RS1.3, RS2.3, CP1.3 and CP2.3 is presented in Figs 124 to 127. Despite locally slightly buckled beam flanges in the region just beyond the stiffened beam section, which can be observed also in the experiment, no beam buckling occurred at the applied level of joint rotation, which is in a good agreement with the experimental results. The extent of plastic deformations obtained from simulation also shows close agreement with the plastic strain field from experiment for all four specimens.

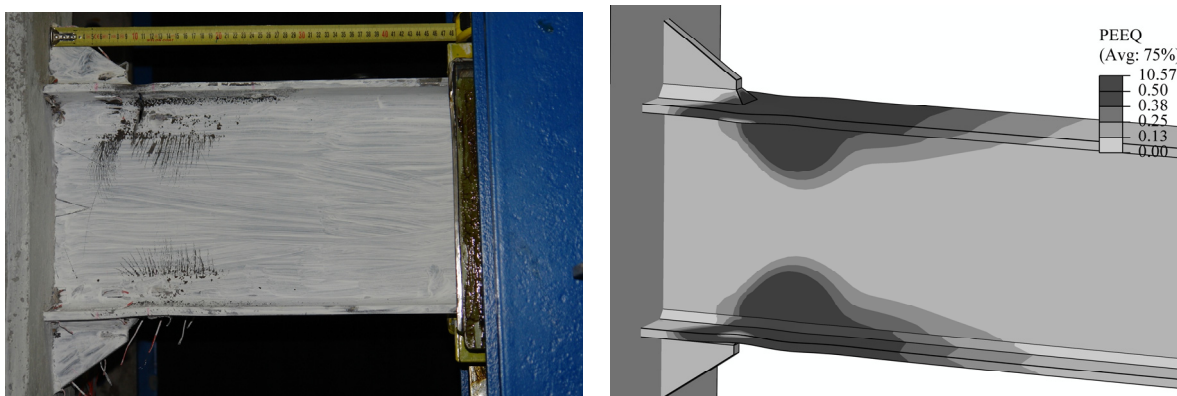


Fig. 124: Deformed shape of specimen RS1.3; comparison between the experiment and the simulation
 Slika 124: Deformacijska oblika preizkušanca RS1.3; primerjava med eksperimentom in simulacijo

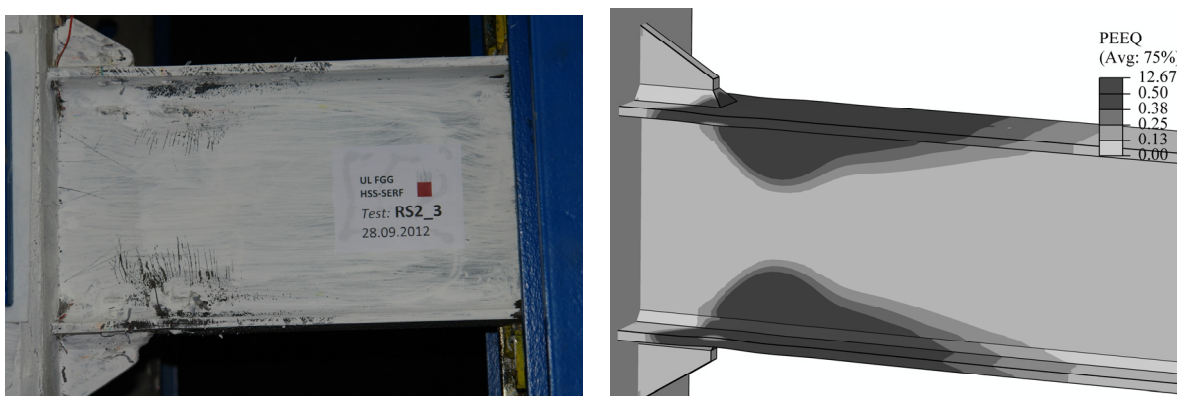


Fig. 125: Deformed shape of specimen RS2.3; comparison between the experiment and the simulation
 Slika 125: Deformacijska oblika preizkušanca RS2.3; primerjava med eksperimentom in simulacijo

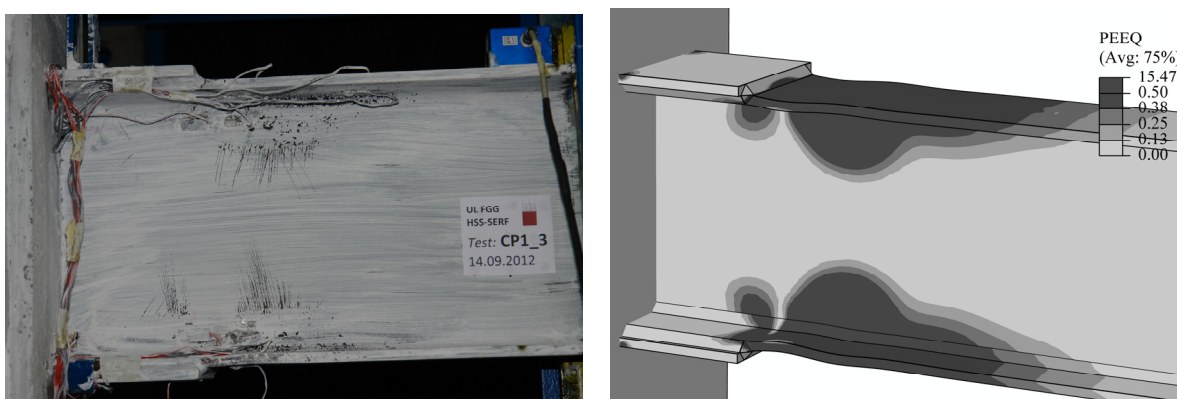


Fig. 126: Deformed shape of specimen CP1.3; comparison between the experiment and the simulation
 Slika 126: Deformacijska oblika preizkušanca CP1.3; primerjava med eksperimentom in simulacijo



Fig. 127: Deformed shape of specimen CP2.3; comparison between the experiment and the simulation
Slika 127: Deformacijska oblika preizkušanca CP2.3; primerjava med eksperimentom in simulacijo

Displacement protocol used in the simulations accurately followed the monitored displacement history from the laboratory tests for all four specimens, Fig. 128.

In addition, comparison of flexural resistance M_c (moment calculated to the column centreline) obtained in the consecutive rotation amplitudes for experimental and simulated responses is presented in Fig. 129 for all four specimens RS1.3, RS2.3, CP1.3 and CP2.3.

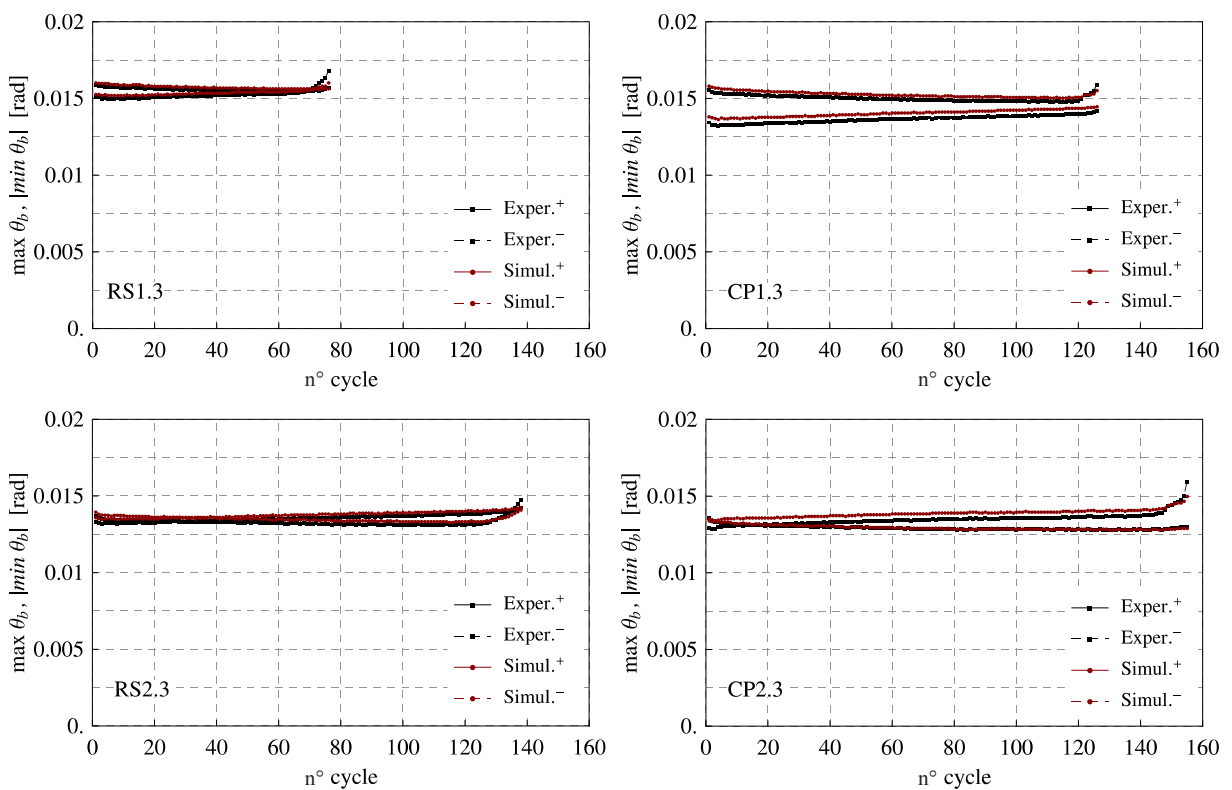


Fig. 128: Total beam rotation amplitudes; comparison between the experiment and the simulation
Slika 128: Amplitude za celotno rotacijo prečke; primerjava med eksperimentom in simulacijo

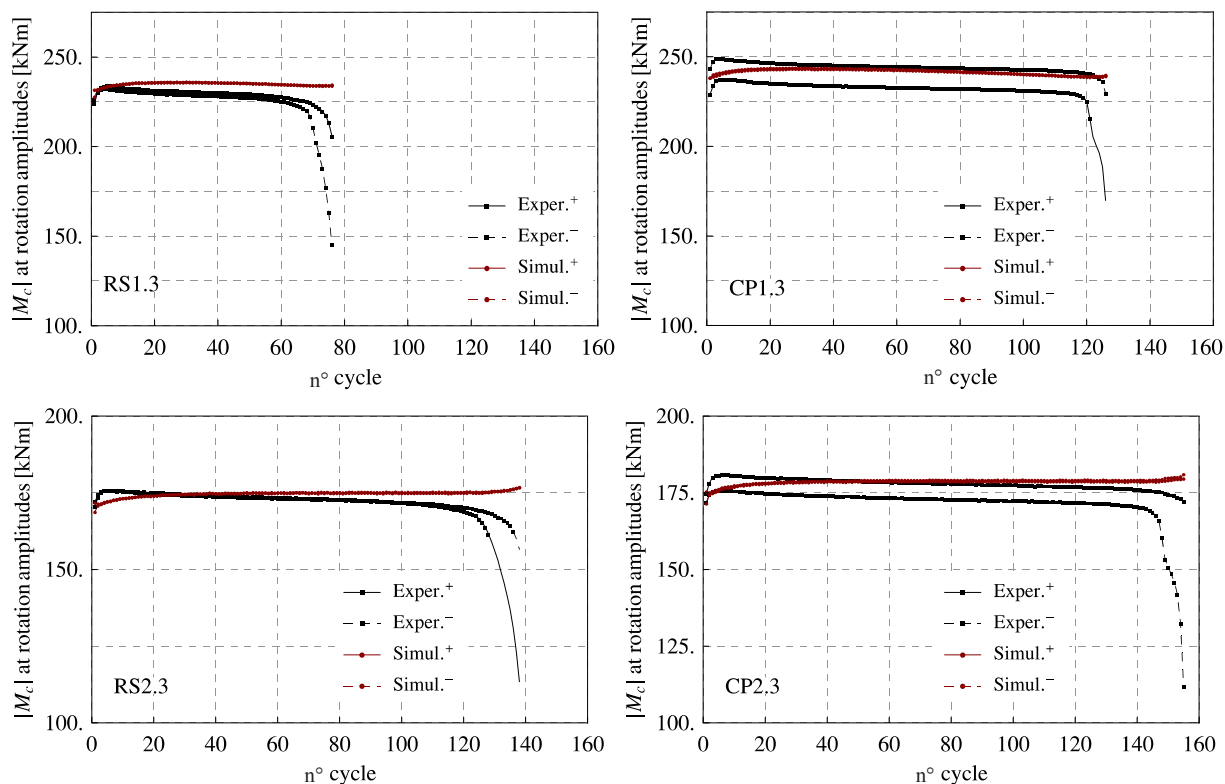


Fig. 129: Moment M_c at rotation amplitudes; comparison between the experiment and the simulation
 Slika 129: Moment M_c v amplitudah rotacije; primerjava med eksperimentom in simulacijo

The largest difference between the simulated and the experimental result can be observed for specimens RS. Experimental response of both RS specimens reveals softening of material from the flange zone at the end of the stiffened beam section. As already documented in Chapter 3.4, large strain concentrations in case of RS joints are concentrated in the flange mid-width local region at the end of the fillet weld at the tip of the rib-stiffener.

Initially hardened material in the fillet weld HAZ at this local region caused material softening soon after a few first cycles (initially hardened materials tends to soften under cyclic loading). No such observation was noticed in the response of both CP specimens.

However, simulated response of RS joints showed stable response, since no LCF damage effects are accounted for in the applied material model.

Additional comparison between experiment and simulation in terms of hysteretic curve shapes is presented in Figs 130 to 133.

In general, a high consistency can be observed between the experimental and simulated response of the joints.

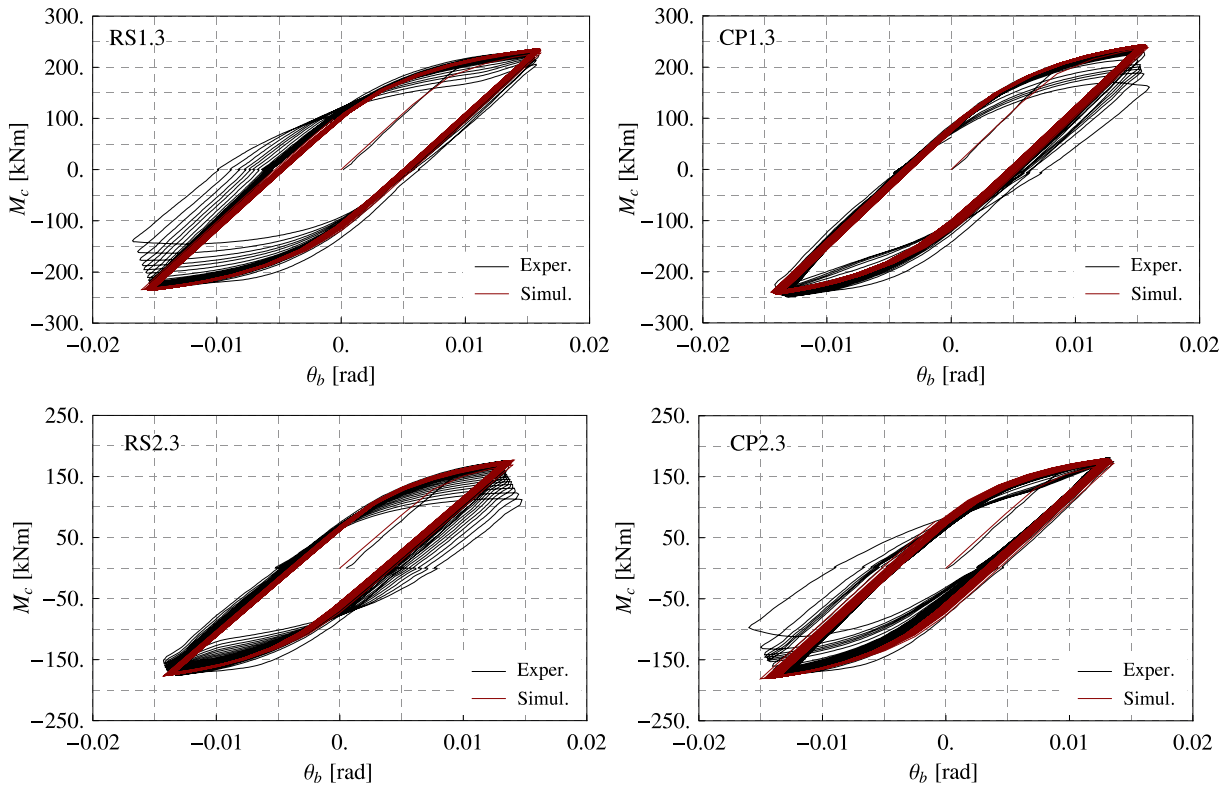


Fig. 130: Hysteretic response from the experiment and the simulation for complete loading history
Slika 130: Primerjava histereznega odziva med eksperimentom in simulacijo za celotno zgodovino obremenjevanja

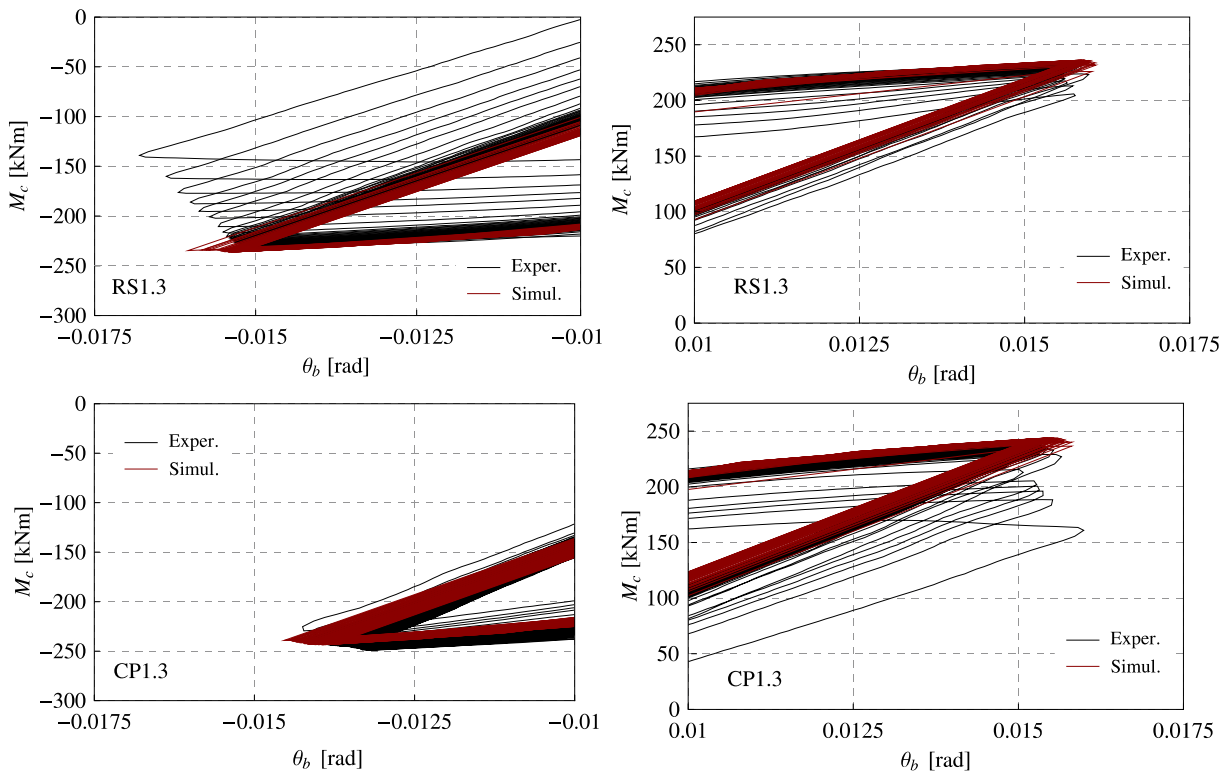


Fig. 131: M_c vs. θ_b hysteresis for the experiment and the simulation: details at rotation amplitudes
Slika 131: Histereze $M_c - \theta_b$ za eksperiment in simulacijo: prikaz v amplitudah rotacije

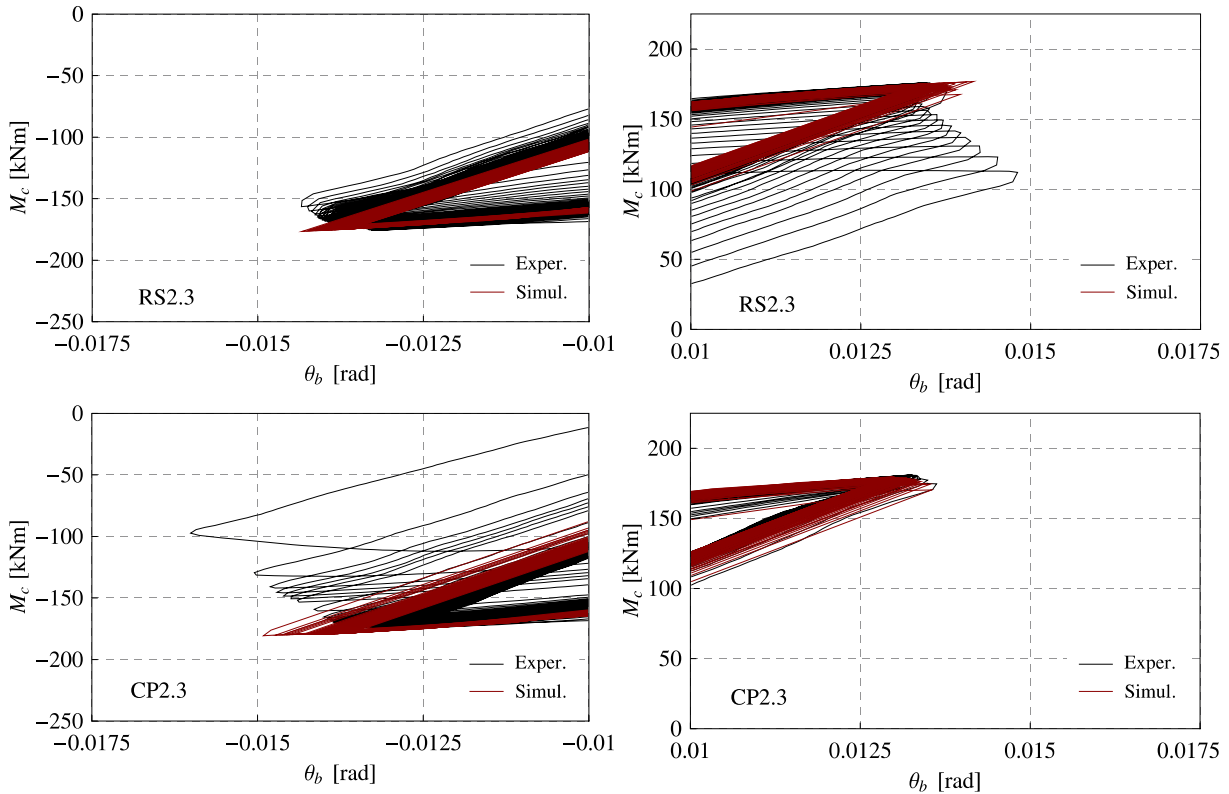


Fig. 132: M_c vs. θ_b hysteresis for the experiment and the simulation: details at rotation amplitudes
 Slika 132: Histereze $M_c - \theta_b$ za eksperiment in simulacijo: prikaz v amplitudah rotacije

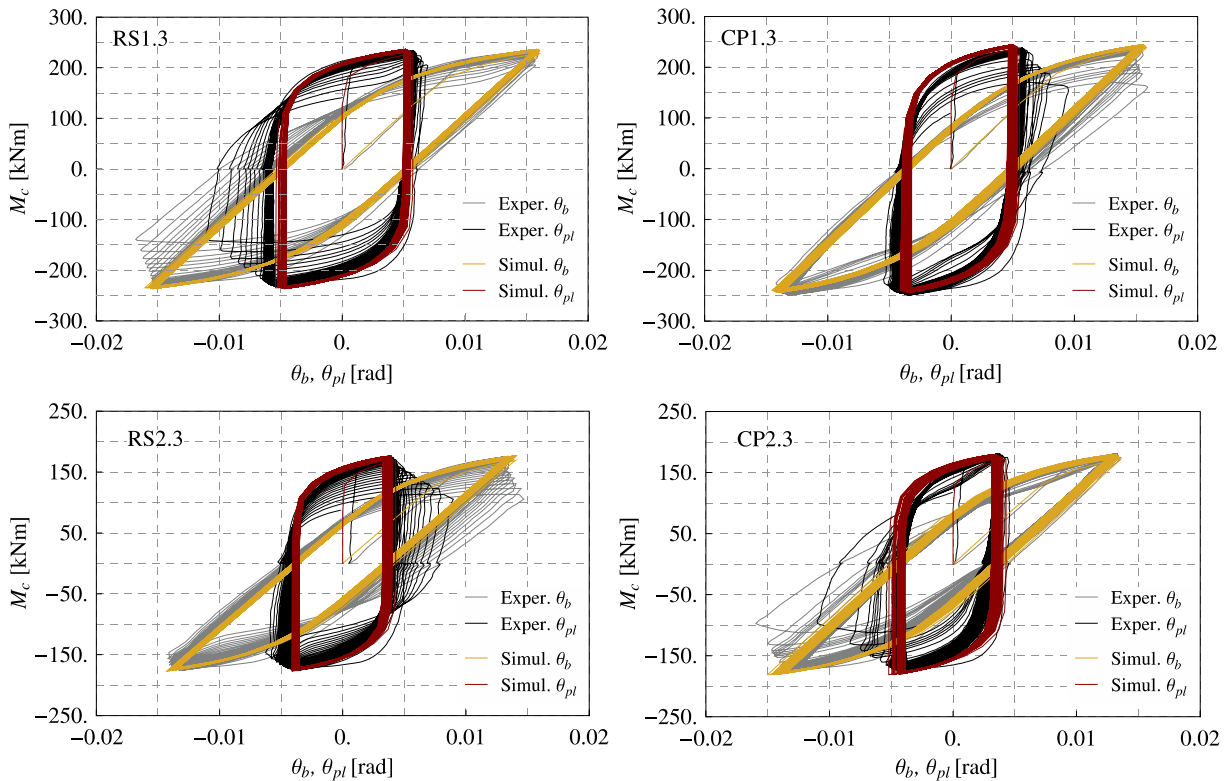


Fig. 133: Comparison of hysteretic response in terms of moment M_c vs. total θ_b and plastic θ_{pl} beam rotation
 Slika 133: Primerjava histerez $M_c - \theta_b$ oziroma $M_c - \theta_{pl}$

In Figs 134 and 135, comparison of hysteresis loop shapes is presented for selected two cycles for all the four specimens: for the first cycle and for cycle with the estimated crack occurrence, hereinafter referred to as stabilised cycle. In the latter case, total number of cycles

according to the criterion for the estimated first crack occurrence, as described in Chapter 4.3.3.5.2, was used. In addition, summary on the obtained cycles with the estimated crack initiation and the onset of overall joint strength degradation is presented in Table 18. The reader may also refer to graphic representation presented in Figs 60 and 61.

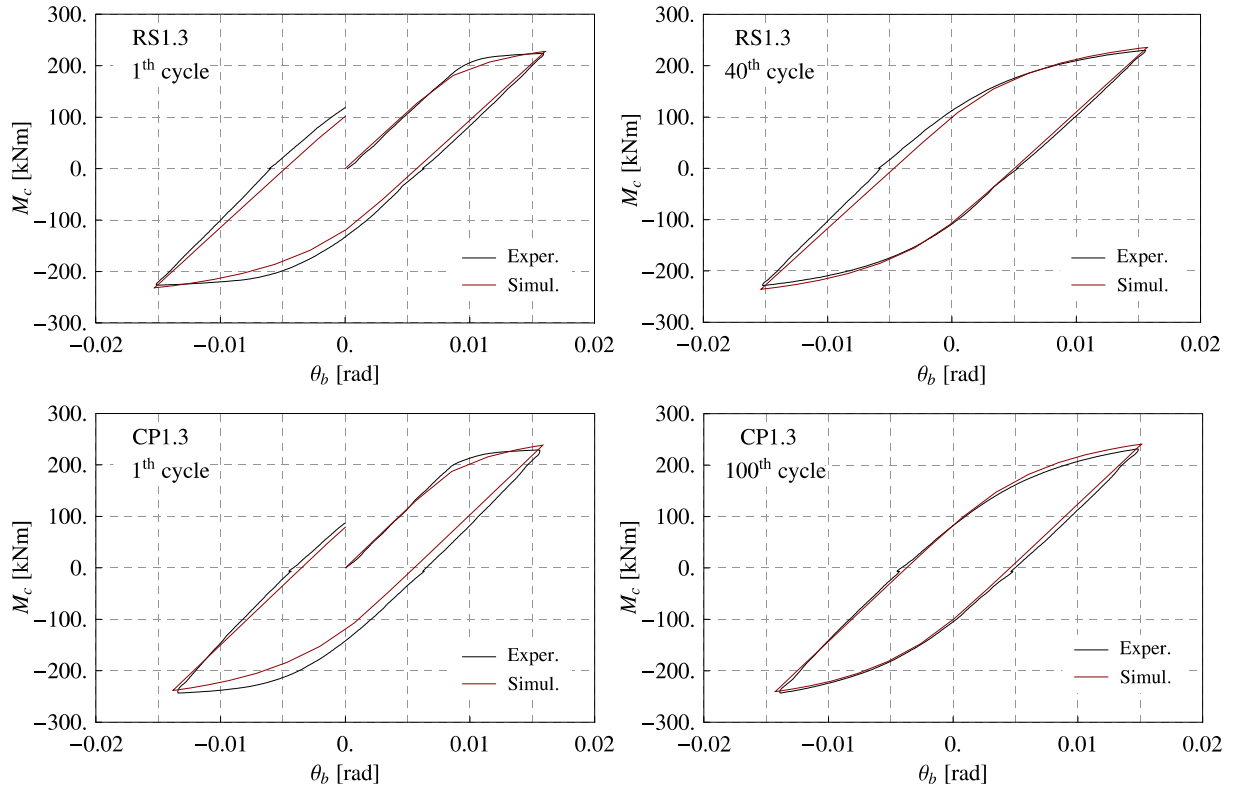


Fig. 134: RS1.3 and CP1.3 experimental and simulated hysteretic response: 1st cycle and the stabilised one
Slika 134: Eksperimentalni in simuliran odziv spojev RS1.3 in CP1.3: primerjava za prvi in stabiliziran cikel

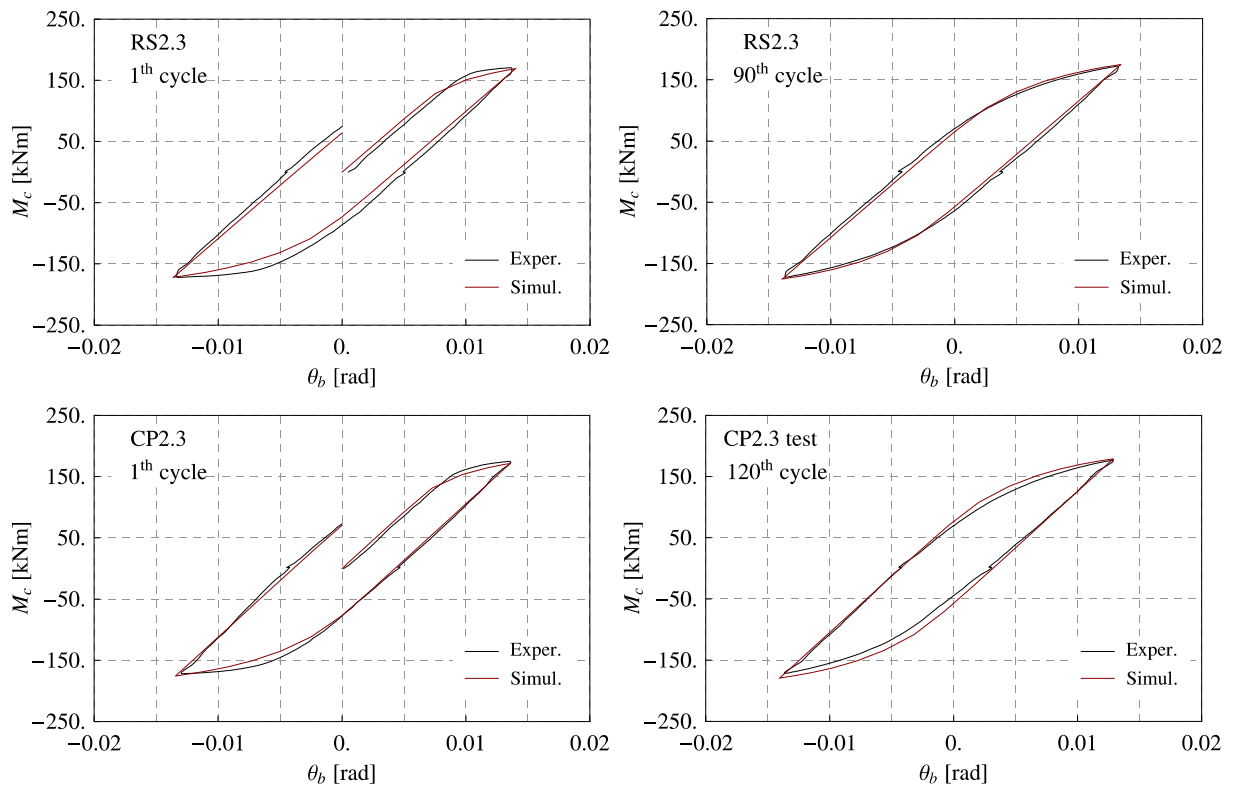


Fig. 135: RS2.3 and CP2.3 experimental and simulated hysteretic response: 1st cycle and the stabilised one
Slika 135: Eksperimentalni in simuliran odziv spojev RS2.3 in CP2.3: primerjava za prvi in stabiliziran cikel

In the engineering sense, a good match of hysteretic curve shapes between the test and the simulation can be observed from Fig. 134 and Fig. 135. The largest deviation in hysteresis shapes between experiment and simulation is recognized for the first cycle, whereas high consistency between both results can be observed for the cycle considered as the stabilised one. The mismatch occurred in the first hysteresis is a consequence of a supposition of the applied cyclic material model, which do not accurately capture the yield-point phenomenon (yield point followed by a stress plateau in the first tension loading).

However, by comparing hysteresis loop areas, which present direct estimation of the amount of dissipated energy, more precise quantitative estimation of the accuracy of simulated response can be obtained.

Comparison of hysteretic energy obtained from experiment and simulation for both selected cycles, namely the first and the stabilised one, is given in Table 26. Deviation of simulated according to the experimentally obtained values is presented in per cents for all the four specimens. Except for specimen CP2.3, deviation of the first loading cycle ranges between 16 and 29 %, while increased consistency can be observed for the stabilised cycle with deviations up to 7 %.

Preglednica 26: Primerjava energije pod histerezami dobljenimi iz eksperimenta in simulacije
Table 26: Comparison between experimental and simulated hysteretic energy response

Specimen	Cycle energy deviation [%]		Accumulated energy till the crack occurrence		
	First cycle	Stabilised cycle	Test [kNm]	Simulation [kNm]	Deviation [%]
RS1.3	14.7	7.0	167.7	156.3	6.8
RS2.3	16.1	5.5	206.2	192.2	6.8
CP1.3	18.5	2.9	353.1	335.8	4.9
CP2.3	5.8	16.2	240.4	270.3	12.4

Energy dissipated through simulated and experimental hysteretic response is also provided in Table 26. Since numerical model does not account for material LCF degradation effects as well as crack growth throughout the process of low-cyclic fatigue, it was decided not to take into account the last cycles from the test just before the complete failure of specimen, where deviation from stabilised specimen response is increased.

Absolute and relative values for total accumulated hysteretic energy obtained from all cycles till the estimated crack occurrence are presented. Again, differences are computed relative to the experimental results.

Comparison of dissipated energy per cycle and cumulative energy throughout the complete loading protocol for all the four specimens is presented in Figs 136 and 137.

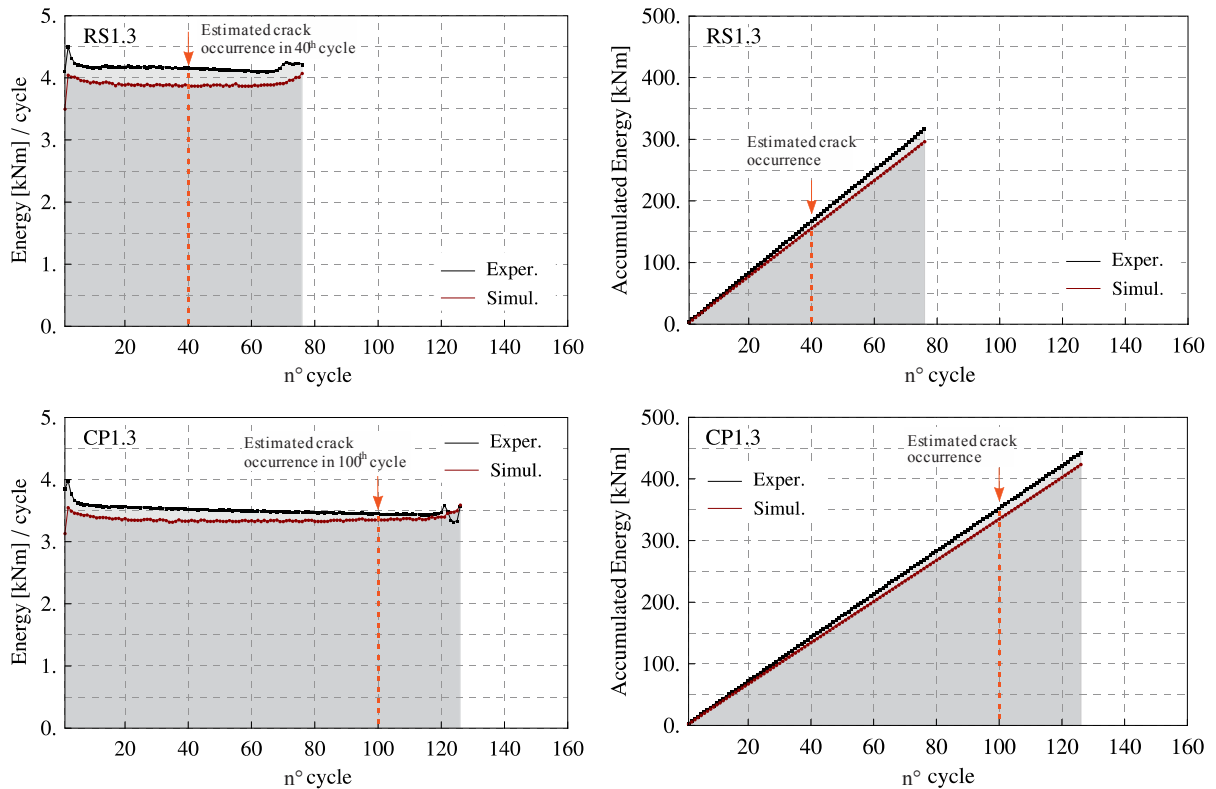


Fig. 136: Specimens RS1.3 and CP1.3: dissipated energy per cycle and accumulated energy
Slika 136: Preizkušanca RS1.3 in CP1.3: dissipirana energija po ciklih in akumulirana energija

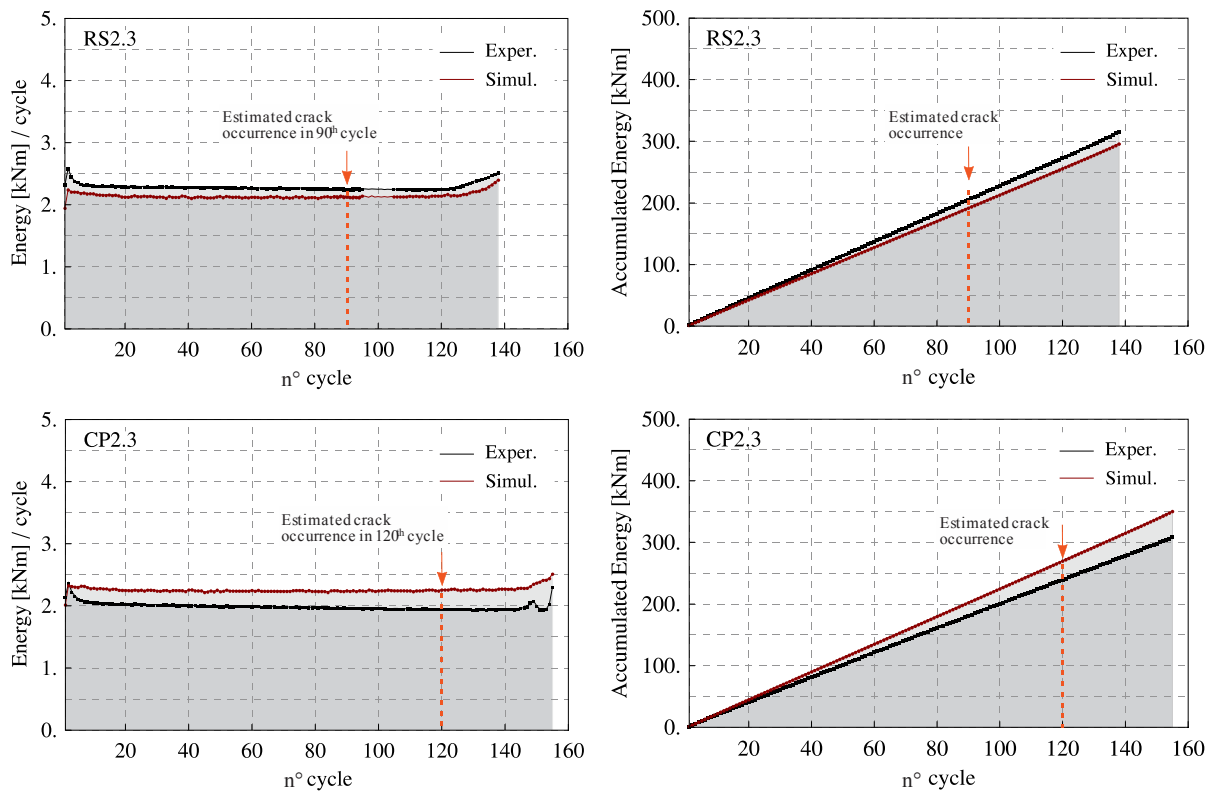


Fig. 137: Specimens RS2.3 and CP2.3: dissipated energy per cycle and accumulated energy
Slika 137: Preizkušanca RS2.3 in CP2.3: dissipirana energija po ciklih in akumulirana energija

4.3.3.2.3 Constant displacement amplitude $\theta = 0.033$ rad

Comparison of deformed shape obtained from experiment and simulation for all four specimens RS1.4, RS2.4, CP1.4 and CP2.4 is presented in Figs 138 to 141.

As a result of material softening response under LCF effects, beam flange buckles tended to grow throughout the experimental tests. Unlike the latter observation from the experiments beam flange buckle wave amplitudes were not so pronounced and remained at limited level in simulations. Nonetheless, the onset of degradation in flexural resistance of a beam observed in the simulation is highly consistent with the experimental response, as can be observed from diagrams presented below.

The extent of plastic deformations obtained from simulation also shows close agreement with the plastic strain field from experiment in case of all the four specimens, Figs 138 to 141.

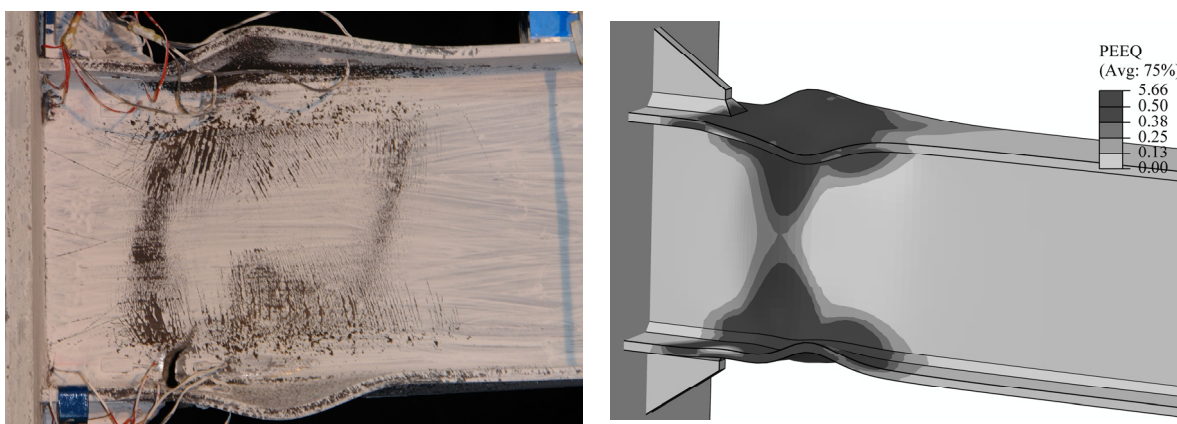


Fig. 138: Deformed shape of specimen RS1.4; comparison between the experiment and the simulation
 Slika 138: Deformacijska oblika preizkušanca RS1.4; primerjava med eksperimentom in simulacijo

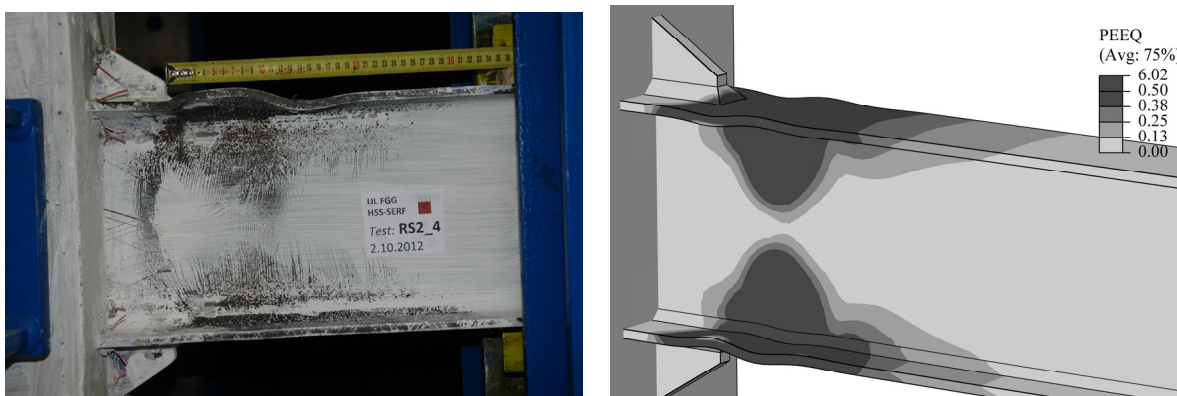


Fig. 139: Deformed shape of specimen RS2.4; comparison between the experiment and the simulation
 Slika 139: Deformacijska oblika preizkušanca RS2.4; primerjava med eksperimentom in simulacijo

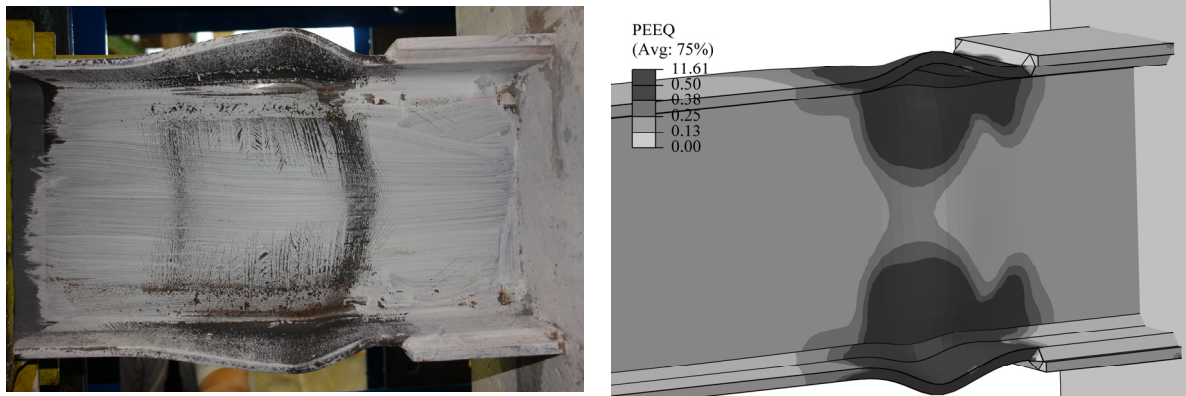


Fig. 140: Deformed shape of specimen CP1.4; comparison between the experiment and the simulation
Slika 140: Deformacijska oblika preizkušanca CP1.4; primerjava med eksperimentom in simulacijo

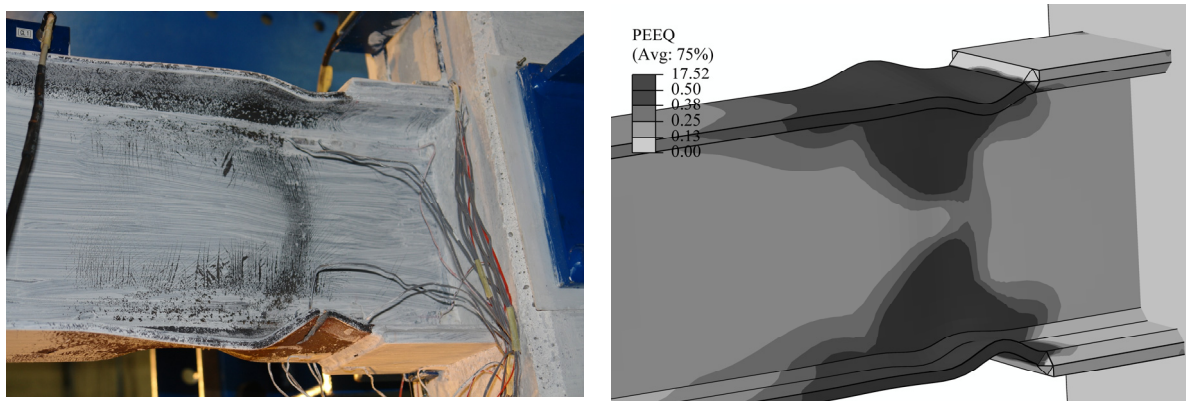


Fig. 141: Deformed shape of specimen CP2.4; comparison between the experiment and the simulation
Slika 141: Deformacijska oblika preizkušanca CP2.4; primerjava med eksperimentom in simulacijo

Displacement protocol used in the simulations accurately followed the monitored displacement history from the laboratory tests for all four specimens, Fig. 142.

In addition, comparison of flexural resistance M_c (moment calculated to the column centreline) obtained in the consecutive rotation amplitudes for experimental and simulated responses is presented in Fig. 143 for all four specimens RS1.4, RS2.4, CP1.4 and CP2.4

Additional comparison between experiment and simulation in terms of hysteretic curve shapes is presented in Figs 144 to 147.

In general, a high consistency can be observed between the experimental and simulated response of the joints.

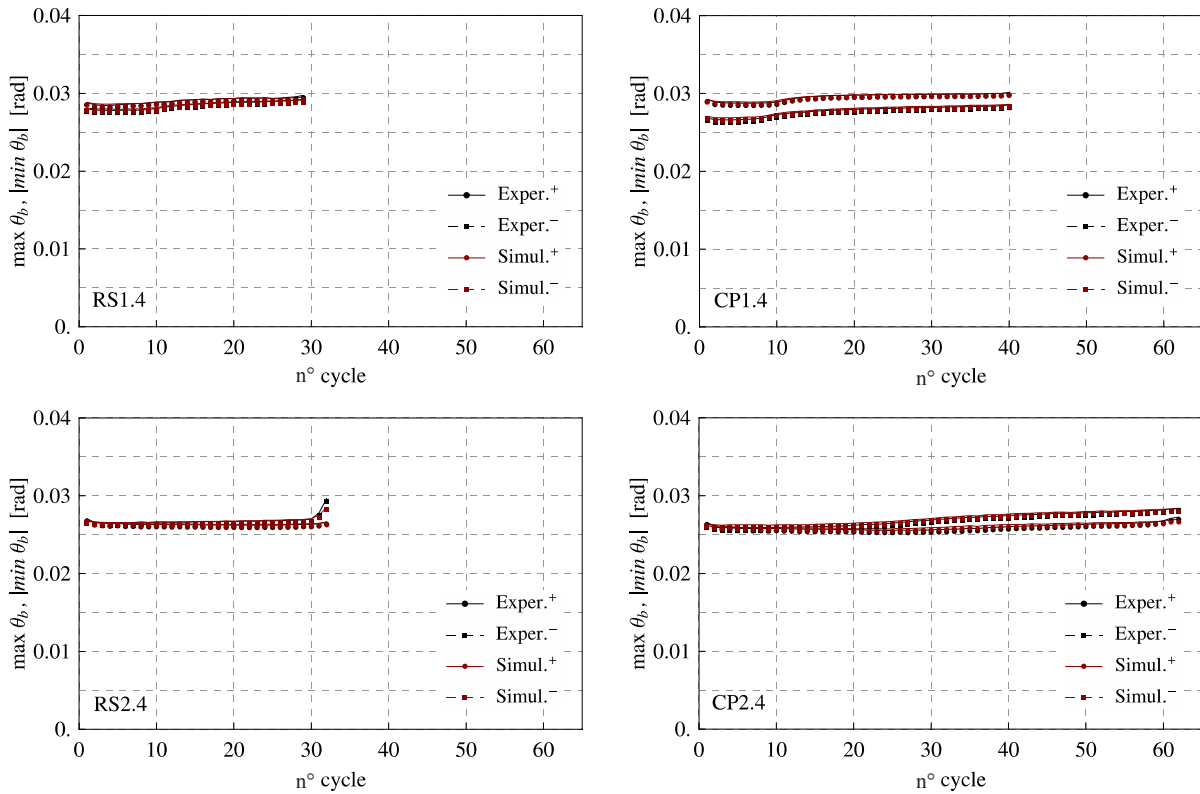


Fig. 142: Total beam rotation amplitudes; comparison between the test and the simulation
 Slika 142: Amplitude za celotno rotacijo prečke; primerjava med eksperimentom in simulacijo

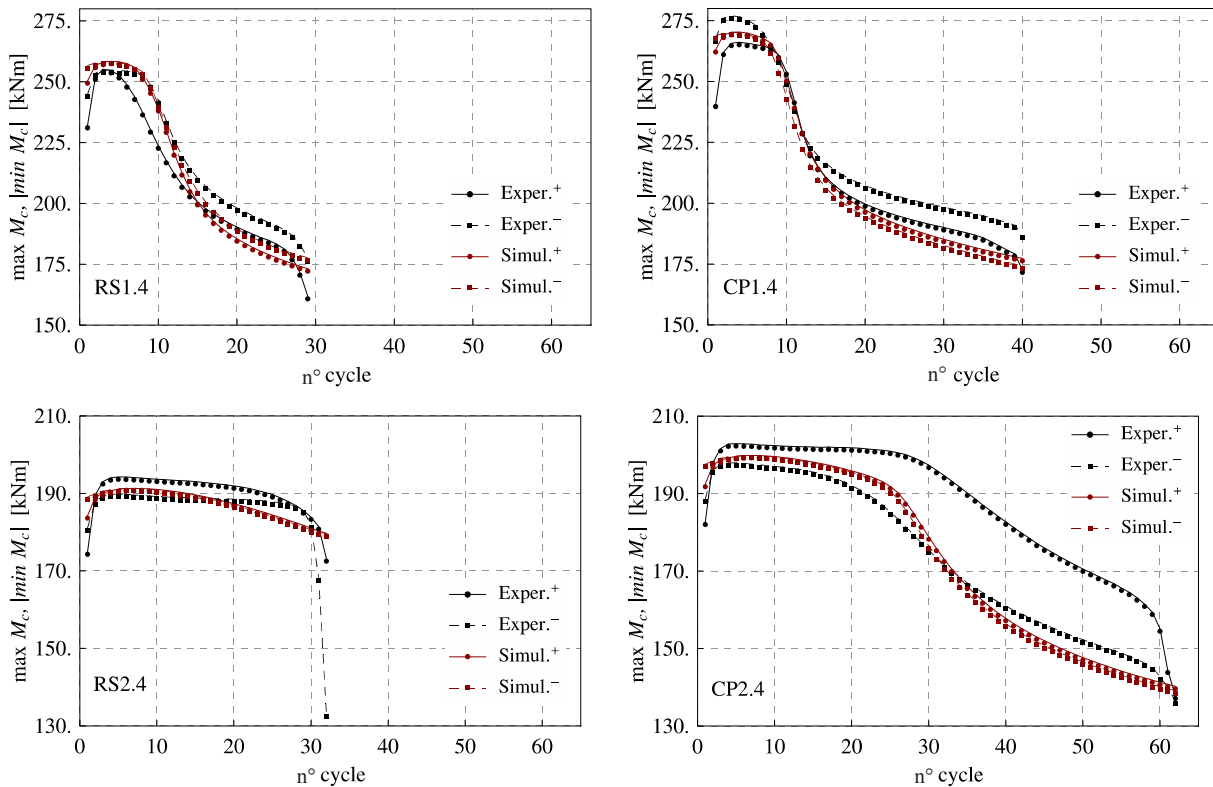


Fig. 143: Moment M_c at rotation amplitudes; comparison between the test and the simulation
 Slika 143: Moment M_c v amplitudah rotacije; primerjava med eksperimentom in simulacijo

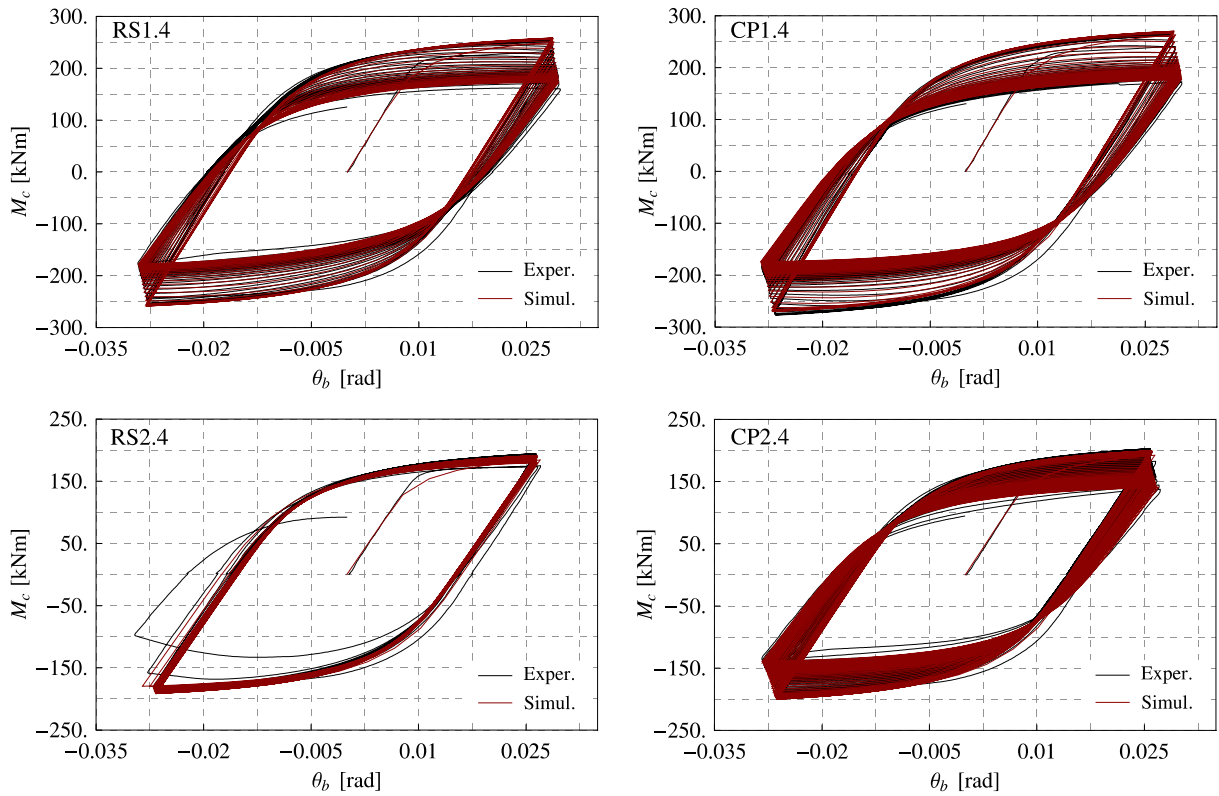


Fig. 144: Hysteretic response from the experiment and the simulation for complete loading history
Slika 144: Primerjava histereznega odziva med eksperimentom in simulacijo za celotno zgodovino obremenjevanja

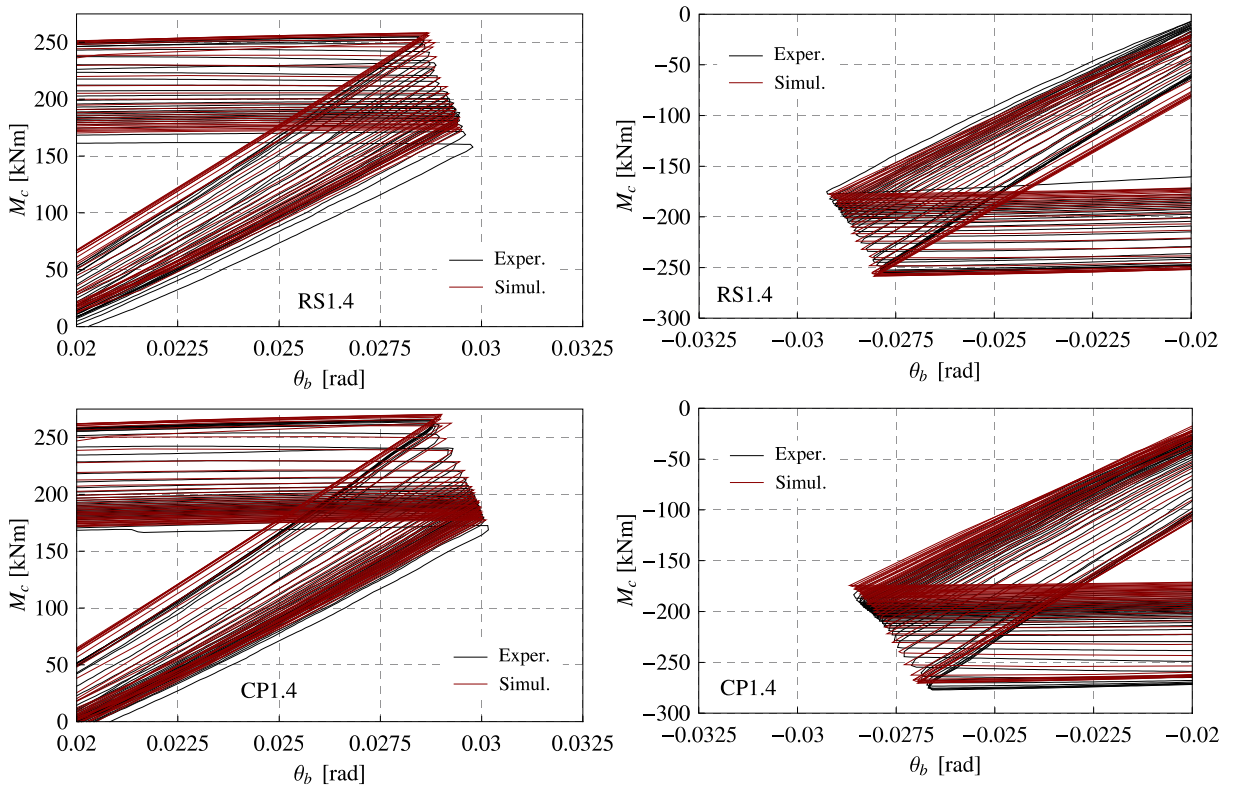


Fig. 145: M_c vs. θ_b hysteresis for the experiment and the simulation: details at rotation amplitudes
Slika 145: Histereze $M_c - \theta_b$ za eksperiment in simulacijo: prikaz v amplitudah rotacije

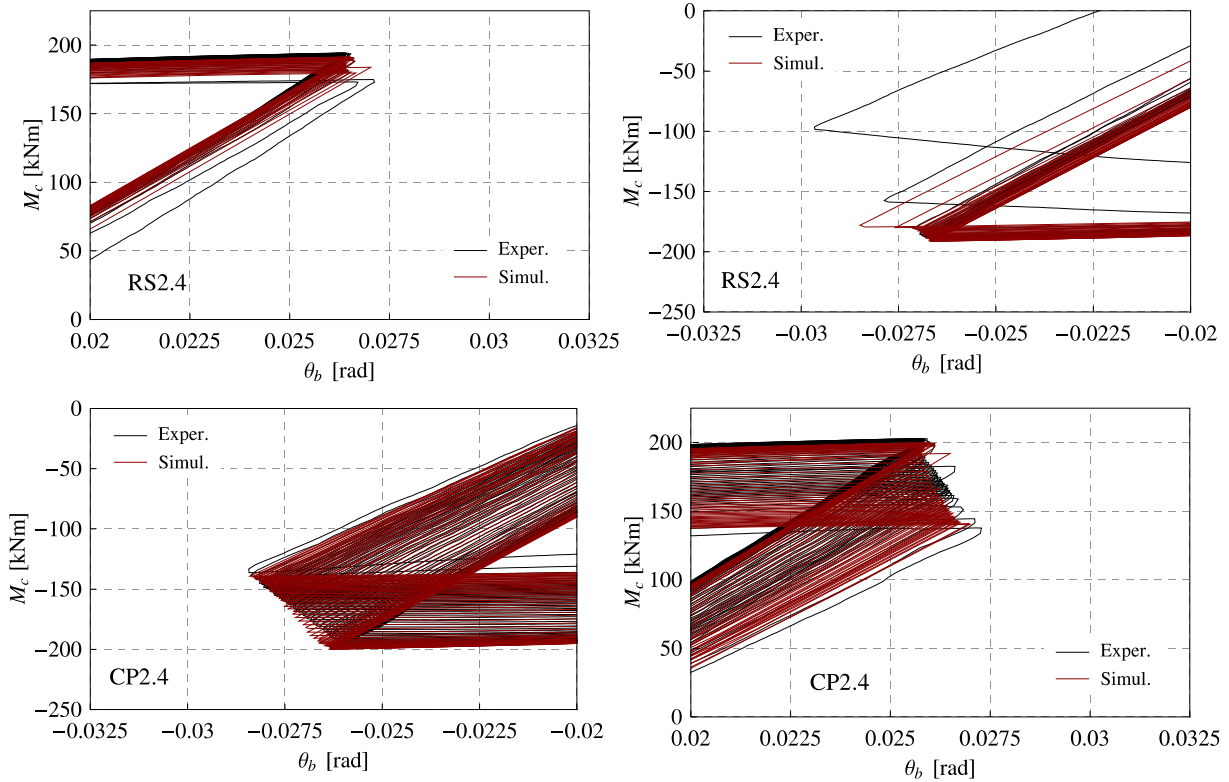


Fig. 146: M_c vs. θ_b hysteresis for the experiment and the simulation: details at rotation amplitudes
 Slika 146: Histereze $M_c - \theta_b$ za eksperiment in simulacijo: prikaz v amplitudah rotacije

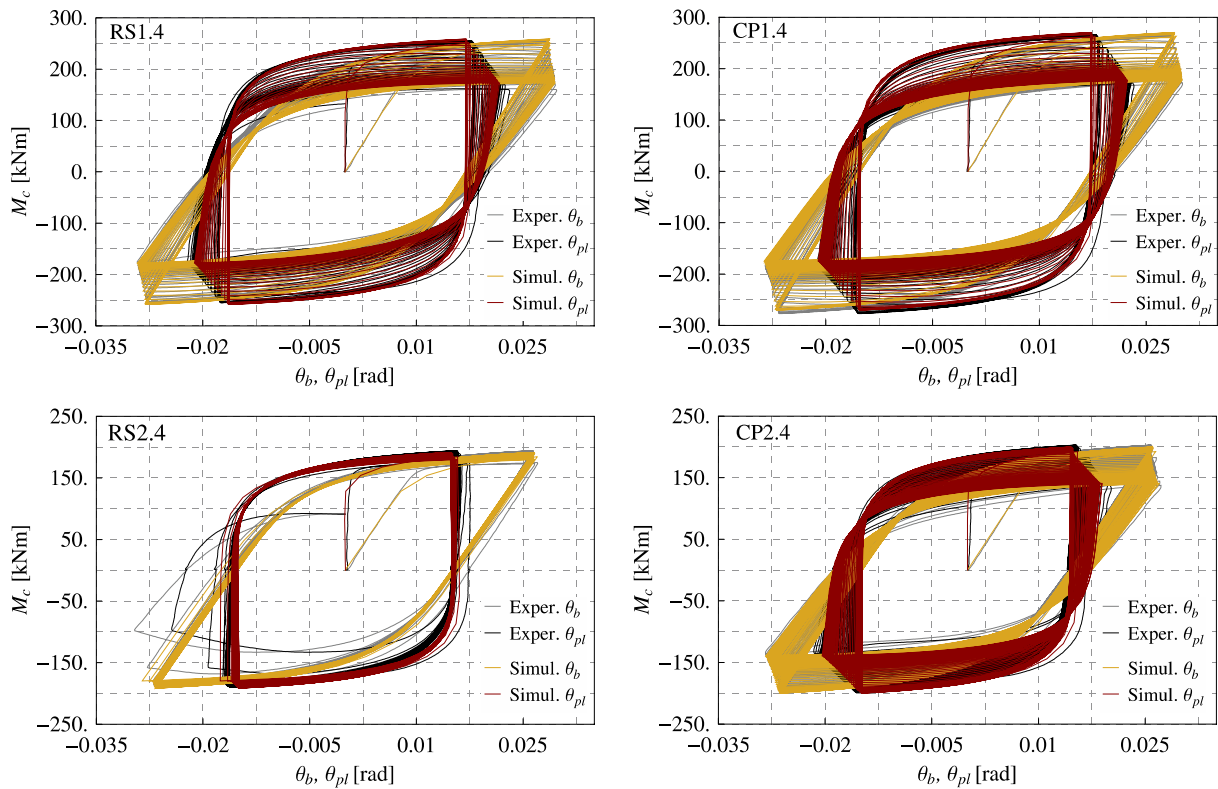


Fig. 147: Comparison of hysteretic response in terms of moment M_c vs. total θ_b and plastic θ_{pl} beam rotation
 Slika 147: Primerjava histerez $M_c - \theta_b$ oziroma $M_c - \theta_{pl}$

In Figs 148 and 149, comparison of hysteresis loop shapes is presented for selected two cycles for all the four test specimens: for the first cycle and for cycle with the estimated crack occurrence, hereinafter referred to as stabilised cycle. In the latter case, total number of cycles according to the criterion for the estimated first crack occurrence, as described in Chapter 4.3.3.5.2, was used.

In addition, summary on the obtained cycles with the estimated crack initiation and the onset of overall joint strength degradation is presented in Table 18. The reader may also refer to graphic representation presented in Figs 62 and 63.

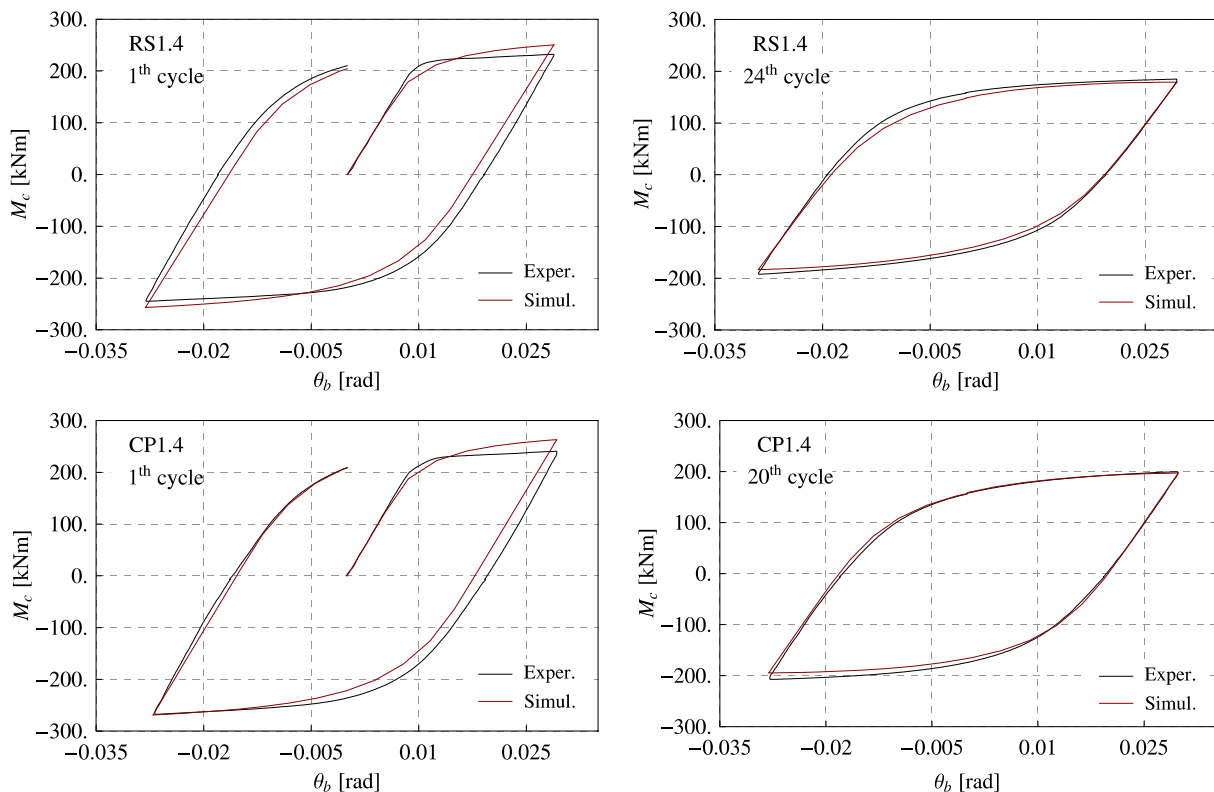


Fig. 148: RS1.4 and CP1.4 experimental and simulated hysteretic response: 1st cycle and the stabilised one
Slika 148: Eksperimentalni in simuliran odziv spojev RS1.4 in CP1.4: primerjava za prvi in stabiliziran cikel

In case of specimens CP1.4 and CP2.4, where the onset of LCF crack was not able to define according to the methodology applied, see Chapter 4.3.3.5.2, cycle from experimentally obtained midlife was taken as stabilized cycle: 20th cycle for CP1.4 and 31st cycle in case of CP2.4 specimen, see Table 8.

In the engineering sense, a good match of hysteretic curve shapes between the test and simulation can be observed from Fig. 148 and Fig. 149. The largest deviation in hysteresis shapes between experiment and simulation is recognized for the first cycle, whereas high consistency between both results can be observed for the stabilised cycle.

The mismatch from the first hysteresis is a consequence of a supposition of the applied cyclic material model, which do not accurately capture the yield-point phenomenon (yield point followed by a stress plateau in the first tension loading).

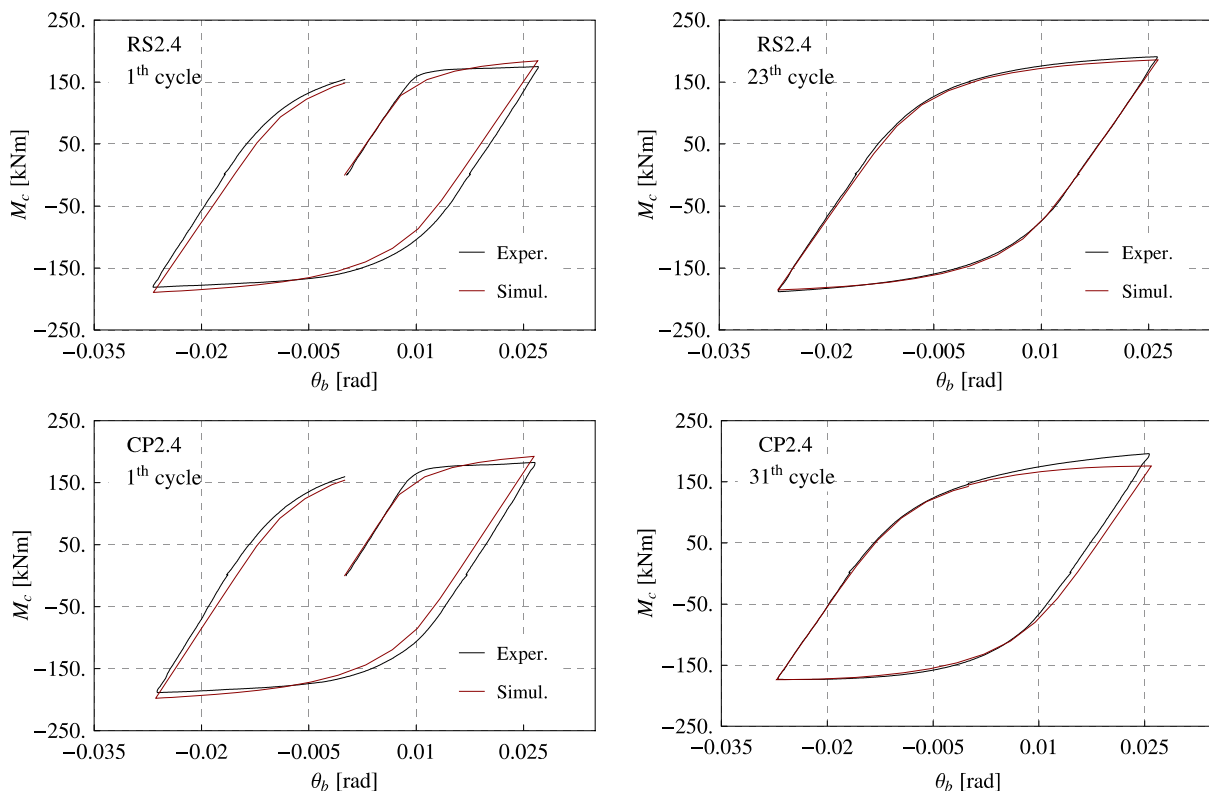


Fig. 149: RS2.4 and CP2.4 experimental and simulated hysteretic response: 1st cycle and the stabilised one
 Slika 149: Eksperimentalni in simulirani odziv spojev RS2.4 in CP2.4: primerjava za prvi in stabiliziran cikel

However, by comparing hysteresis loop areas, which presents direct estimation of the amount of dissipated energy, more precise quantitative estimation of the accuracy of simulated response can be obtained.

Comparison of hysteretic energy obtained from experiment and simulation for both selected cycles, namely the first and the stabilised one, is given in Table 27. Deviation of simulated according to the experimentally obtained values is presented in per cents for all the four specimens. In all the cases, very consistent results were obtained from the simulations. Deviation of the first loading cycle ranges between 6.5 and 7.6 %, while increased consistency can be observed for all the stabilised cycles with deviations up to 6.3 %.

Preglednica 27: Primerjava energije pod histerezami dobljenimi iz eksperimenta in simulacije
 Table 27: Comparison between experimental and simulated response: hysteretic energy

Specimen	Cycle energy deviation [%]		Accumulated energy till the crack occurrence		
	First cycle	Stabilised cycle	Test [kNm]	Simulation [kNm]	Deviation [%]
RS1.4	7.1	6.3	336.9	324.2	3.8
RS2.4	7.6	1.7	233.9	229.4	1.9
CP1.4	6.5	1.2	290.1	286.0	1.4
CP2.4	7.6	1.0	314.5	311.9	0.8

Absolute and relative values for total accumulated hysteretic energy obtained from all cycles till the estimated crack occurrence are presented in Table 27. Again, differences are computed relative to the experimental results.

Comparison of dissipated energy per cycle and cumulative energy throughout the complete loading protocol for all the four specimens is presented in Figs 150 and 151.

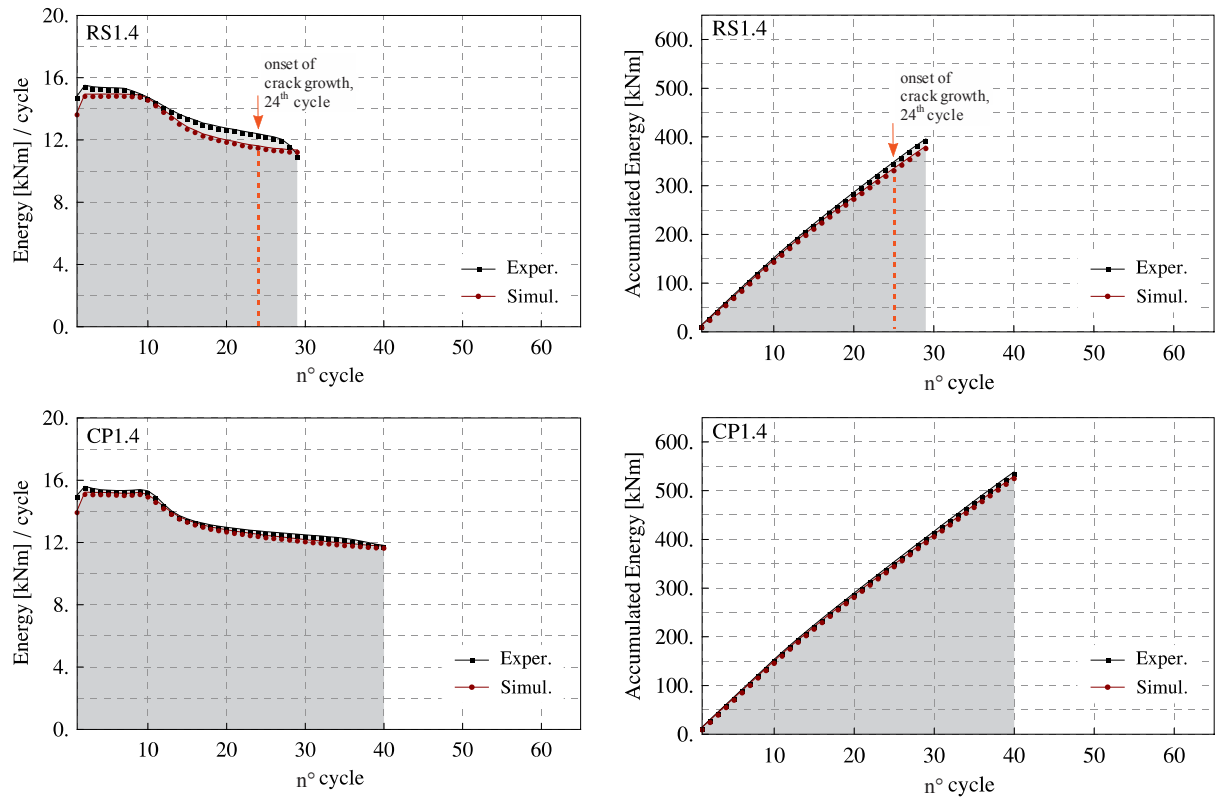


Fig. 150: Specimens RS1.4 and CP1.4: dissipated energy per cycle and accumulated energy
Slika 150: Preizkušanca RS1.4 in CP1.4: dissipirana energija po ciklih in akumulirana energija

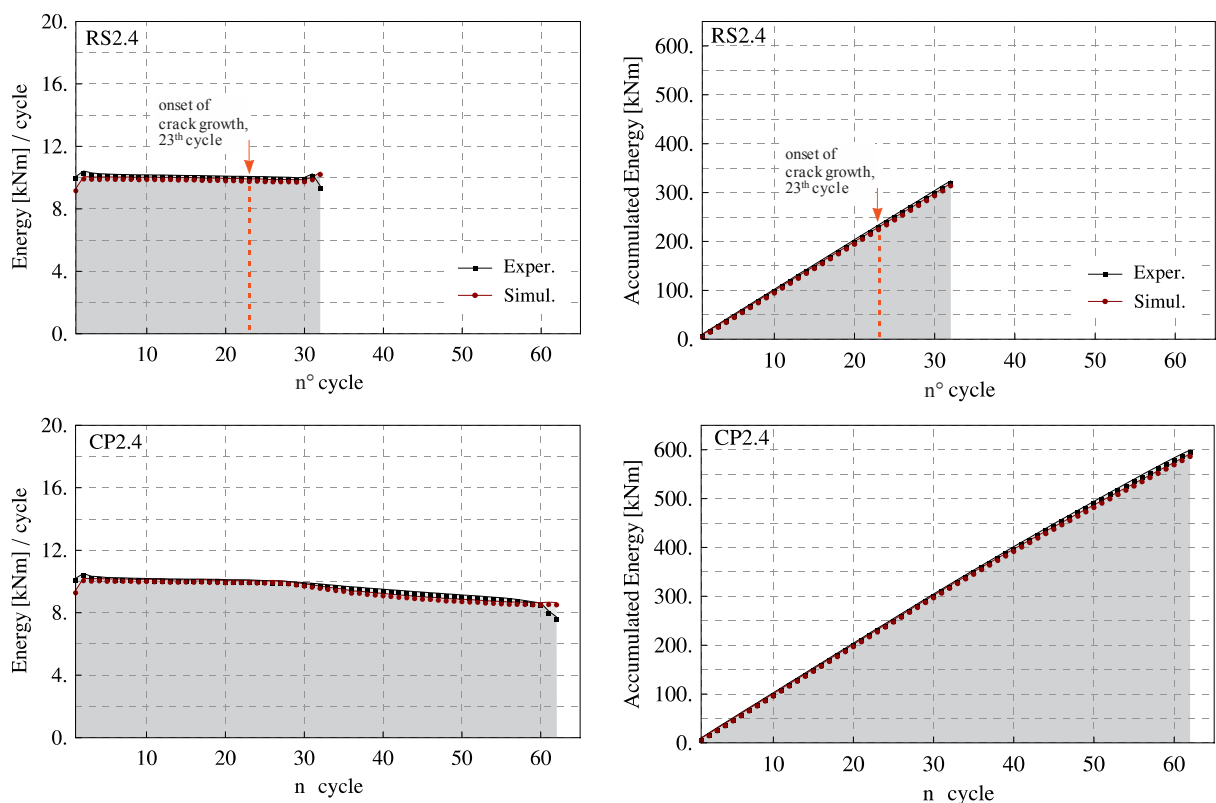


Fig. 151: Specimens RS2.4 and CP2.4: dissipated energy per cycle and accumulated energy
Slika 151: Preizkušanca RS2.4 in CP2.4: dissipirana energija po ciklih in akumulirana energija

4.3.3.3 Variable amplitude cyclic loading tests

Comparison between simulated and experimental response for all eight specimens RS and CP subjected to variable cyclic loading with stepwisely increasing displacement/rotation is presented in detail hereinafter. Cycles in plastic range were simulated only – without cycles in elastic range, see Chapter 4.3.3.1 and Table 25 for an in-depth discussion.

The first step in the validation of the simulated response against the test results involves comparison of the beam deformed shape in the plastic hinge region just after the stiffened part of the beam. Comparison of deformed shape between experimental and simulated response after complete loading history applied is presented in Figs 152 to 159.

Equivalent plastic strain $PEEQ$ variable is plotted on deformed shape of a particular finite element model, where contour colours are selected in order to imitate limewash coat peeling as a result of the spread of plastic deformations in the plastic hinge zone in the beam (marked as darker region) from the corresponding experiment: from white colour for elastic regions toward dark grey colour for the most plastified regions.

As it is demonstrated in the figures, all the key features, e.g. the beam local buckling shape and the beam out of plane displacements, are captured with satisfactory accuracy, although beam flange and web local buckles do not necessarily take exactly the same direction and position as in experiment.

Despite close agreement of simulated joint response with experimental results, two major differences in comparison with laboratory test results were found and are discussed below.

In simulations, buckle waves appeared a bit closer to the end of the stiffened region. Even though several combinations of initial imperfection shapes on the beam were tried, no major difference in the beam buckled shape was gained.

The second major difference that can be observed from the figures is the magnitude of buckle amplitudes. Smaller buckles and consequently not so pronounced inelastic flexural-torsional buckling of the beam section were produced by the simulation.

The latter observation can be justified with the fact that the applied cyclic material model do not account for the low-cycle fatigue damage of the steel material. Namely, buckle amplitudes in the experiments grew intensively especially in a few last cycles before the final failure of specimen. Cracks on the tensioned part of the beam flanges contributed to the degradation of local resistance and stiffness, which resulted in larger beam flange buckles.

Increased degradation of steel material in the last cycles of experimental response compared to the results from simulations can be seen from response curves presented in Figs 160 to 167.

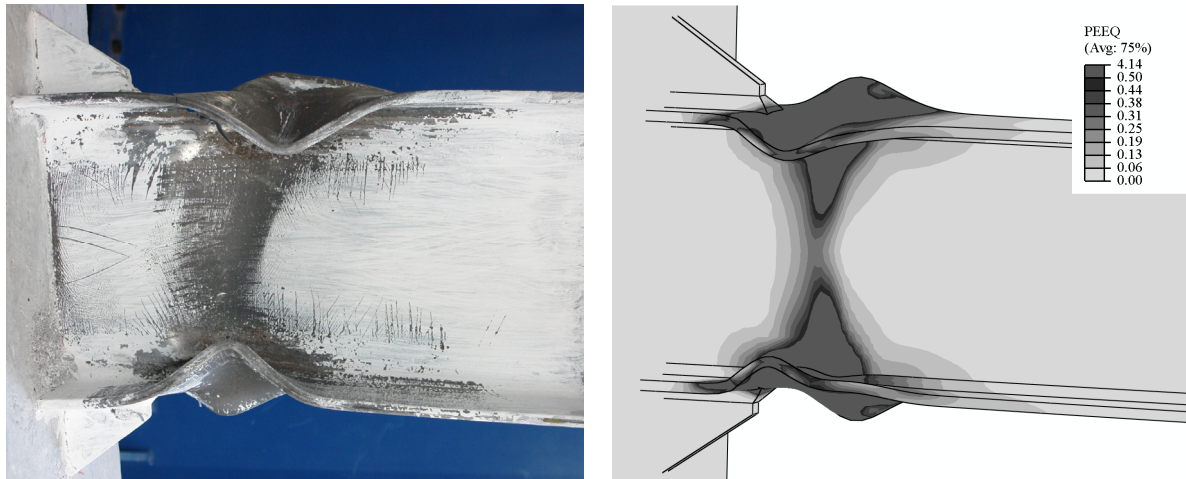


Fig. 152: Deformed shape of specimen RS1.1; comparison between the experiment and the simulation
Slika 152: Deformacijska oblika preizkušanca RS1.1; primerjava med eksperimentom in simulacijo

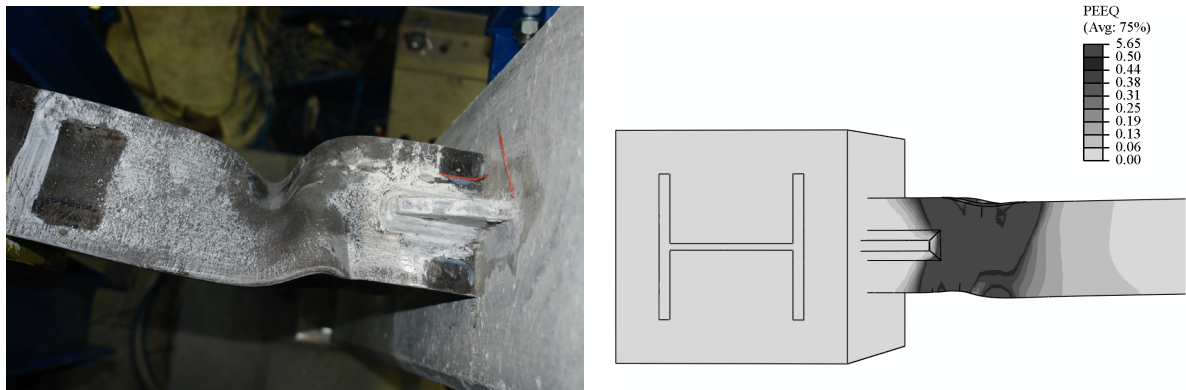


Fig. 153: Deformed shape of specimen RS1.2; comparison between the experiment and the simulation
Slika 153: Deformacijska oblika preizkušanca RS1.2; primerjava med eksperimentom in simulacijo

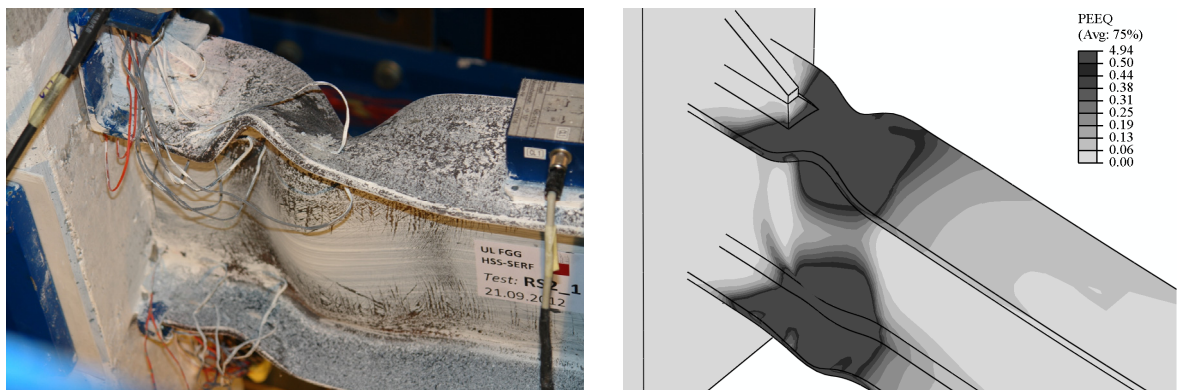


Fig. 154: Deformed shape of specimen RS2.1; comparison between the experiment and the simulation
Slika 154: Deformacijska oblika preizkušanca RS2.1; primerjava med eksperimentom in simulacijo

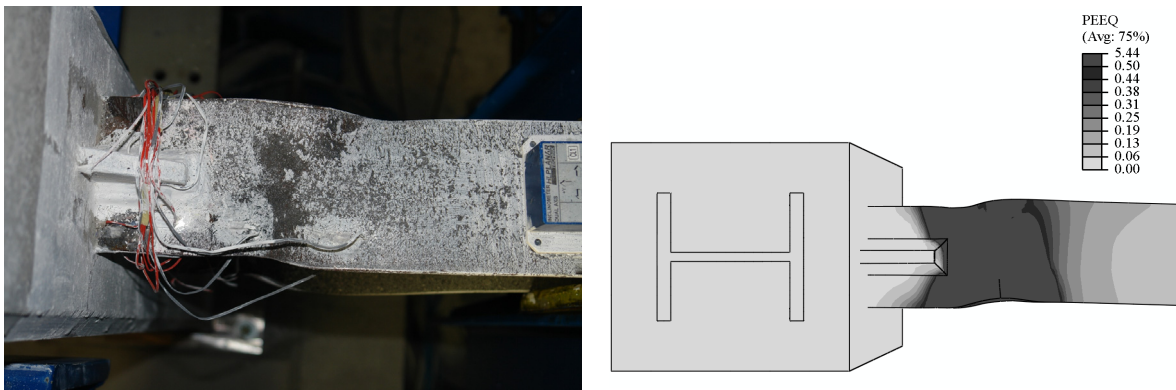


Fig. 155: Deformed shape of specimen RS2.2; comparison between the experiment and the simulation
 Slika 155: Deformacijska oblika preizkušanca RS2.2; primerjava med eksperimentom in simulacijo

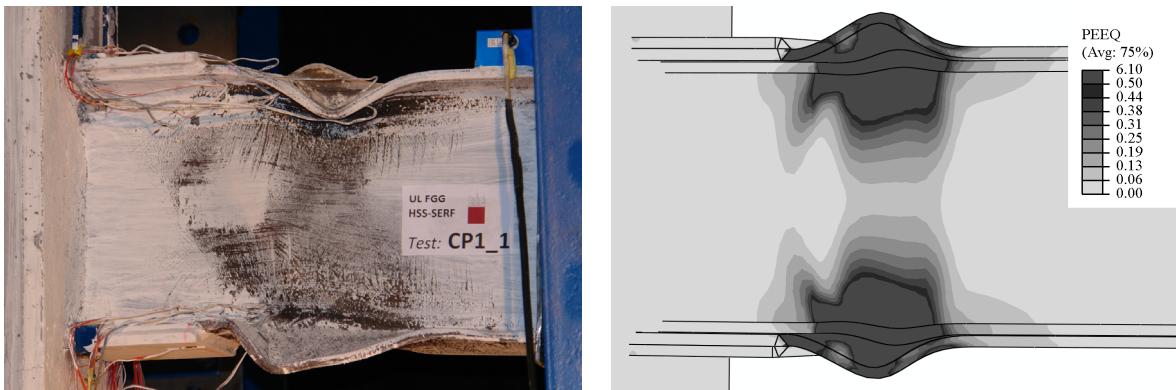


Fig. 156: Deformed shape of specimen CP1.1; comparison between the experiment and the simulation
 Slika 156: Deformacijska oblika preizkušanca CP1.1; primerjava med eksperimentom in simulacijo

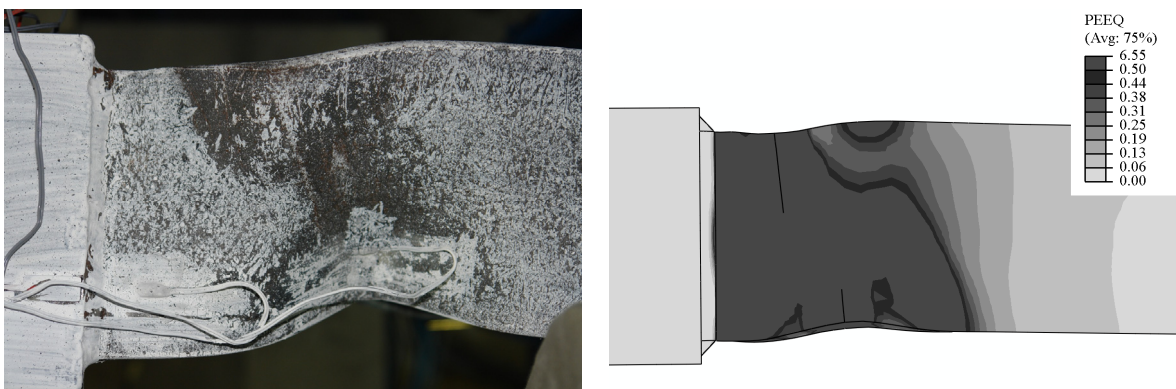


Fig. 157: Deformed shape of specimen CP1.2; comparison between the experiment and the simulation
 Slika 157: Deformacijska oblika preizkušanca CP1.2; primerjava med eksperimentom in simulacijo

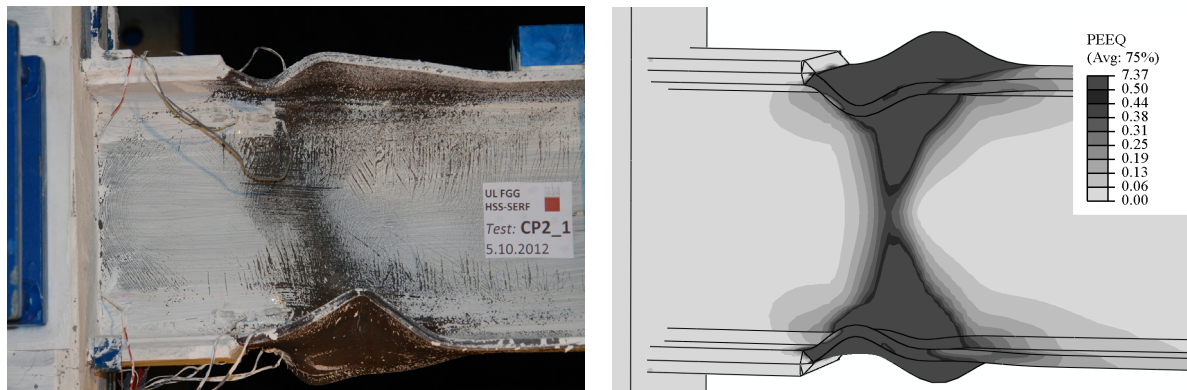


Fig. 158: Deformed shape of specimen CP2.1; comparison between the experiment and the simulation
Slika 158: Deformacijska oblika preizkušanca CP2.1; primerjava med eksperimentom in simulacijo

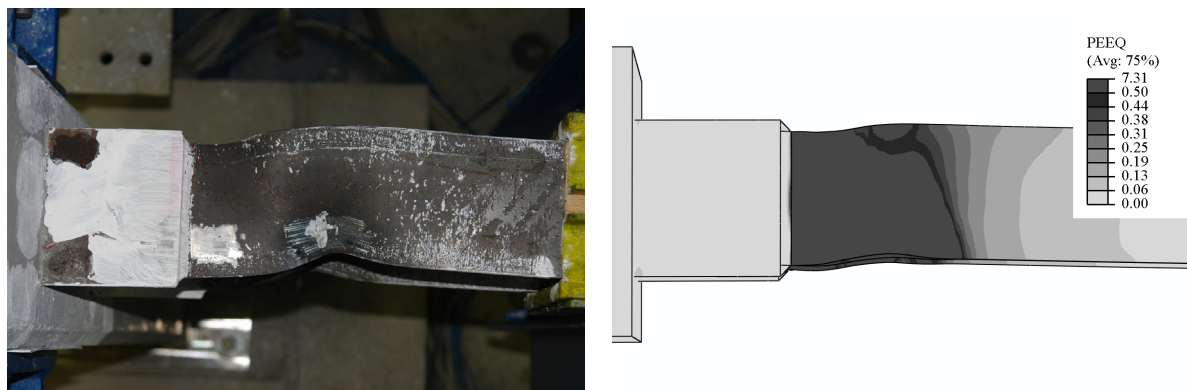


Fig. 159: Deformed shape of specimen CP2.2; comparison between the experiment and the simulation
Slika 159: Deformacijska oblika preizkušanca CP2.2; primerjava med eksperimentom in simulacijo

Further comparison between simulated and experimental response for all the eight specimens RS and CP is presented on diagrams in Figs 160 to 167.

In the figures comparison between experimental and simulated response is made in terms of four different representations.

First, applied cyclic loading history of a total beam rotation, rather than complete joint rotation, since composite column experimental behaviour was difficult to simulate, is presented in part a) of the figures. Comparison between experimental and simulated hysteretic response of particular specimen is presented in part b) of each figure.

To gain better insight into comparison of the simulated and the experimental cyclic response, value of maximum moment resistance M_c (moment to the column centreline) per cycle is presented in part c), and moment M_c at rotation amplitudes is presented in part d). All the quantities are provided for positive and negative loading directions.

On the last two diagrams (diagrams c and d) in each figure the predicted LCF crack onset, obtained according to the effective damage concept proposed by Ohata and Toyoda (2004), see Chapters 2.4.3 and 4.3.3.5.1, is also depicted.

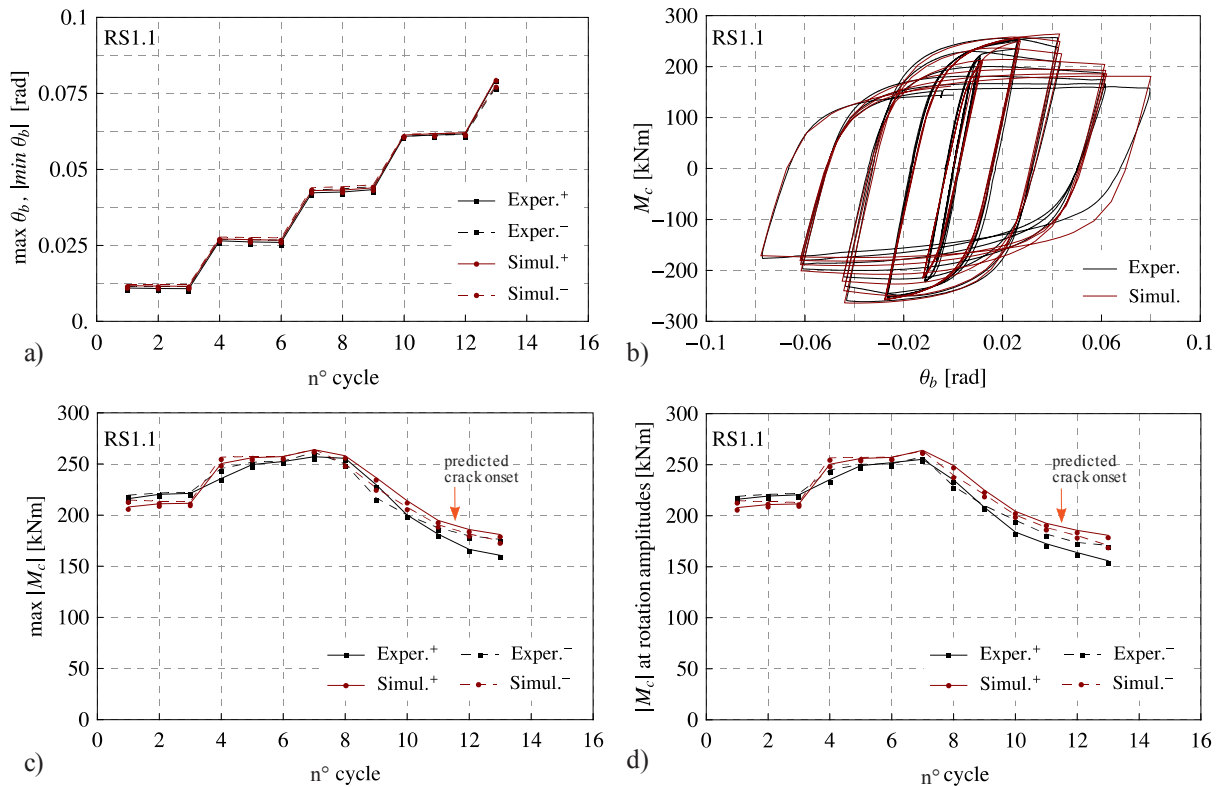


Fig. 160: Experimental and simulated response for RS1.1: a) applied total beam plastic rotation amplitudes, b) hysteretic response, c) distribution of maximum values M_c , d) distribution of M_c at rotation amplitudes
Slika 160: Eksperimentalni in simulirani odziv RS1.1: a) amplitude vsiljene celotne rotacije prečke, b) histerezni odziv, c) potek največjih vrednosti M_c , d) potek vrednosti M_c v amplitudah rotacije

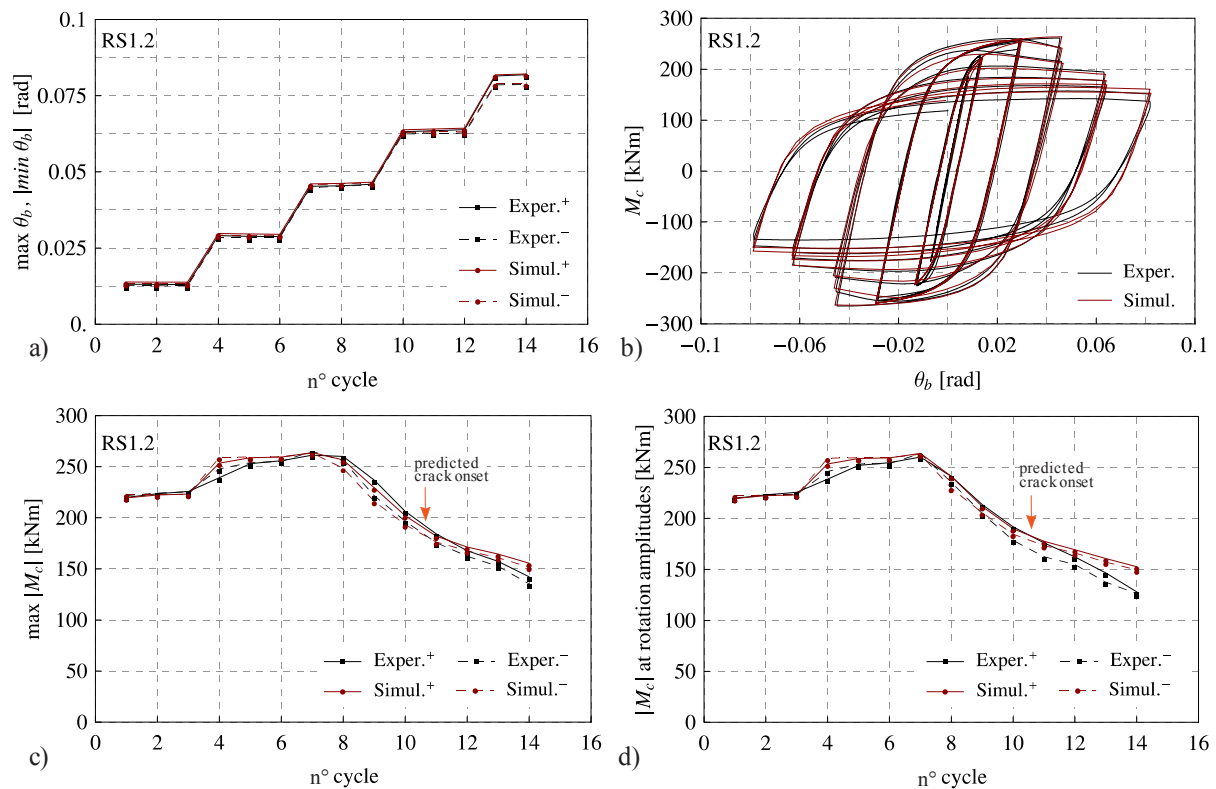


Fig. 161: Experimental and simulated response for RS1.2: a) applied total beam plastic rotation amplitudes, b) hysteretic response, c) distribution of maximum values M_c , d) distribution of M_c at rotation amplitudes
Slika 161: Eksperimentalni in simulirani odziv RS1.2: a) amplitude vsiljene celotne rotacije prečke, b) histerezni odziv, c) potek največjih vrednosti M_c , d) potek vrednosti M_c v amplitudah rotacije

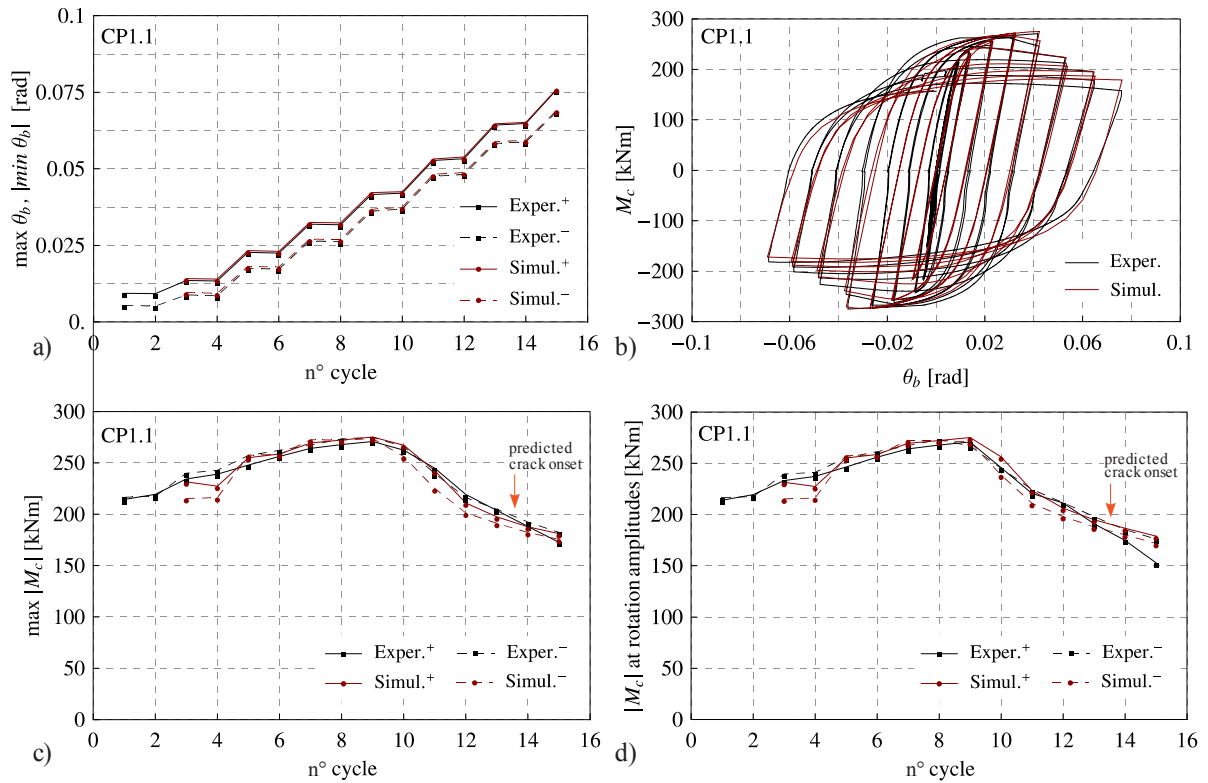


Fig. 162: Experimental and simulated response for CP1.1: a) applied total beam plastic rotation amplitudes, b) hysteretic response, c) distribution of maximum values M_c , d) distribution of M_c at rotation amplitudes
 Slika 162: Eksperimentalni in simulirani odziv CP1.1: a) amplitude vsiljene celotne rotacije prečke, b) histerezni odziv, c) potek največjih vrednosti M_c , d) potek vrednosti M_c v amplitudah rotacije

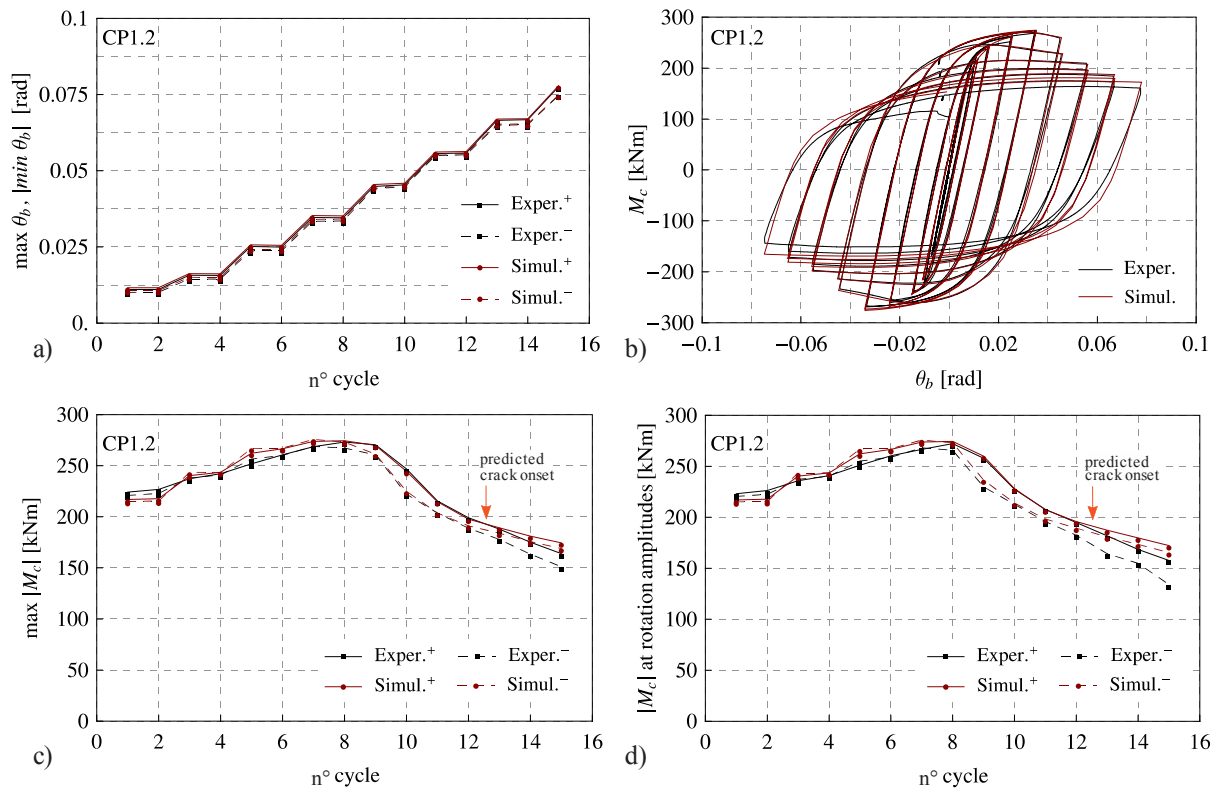


Fig. 163: Experimental and simulated response for CP1.2: a) applied total beam plastic rotation amplitudes, b) hysteretic response, c) distribution of maximum values M_c , d) distribution of M_c at rotation amplitudes
 Slika 163: Eksperimentalni in simulirani odziv CP1.2: a) amplitude vsiljene celotne rotacije prečke, b) histerezni odziv, c) potek največjih vrednosti M_c , d) potek vrednosti M_c v amplitudah rotacije

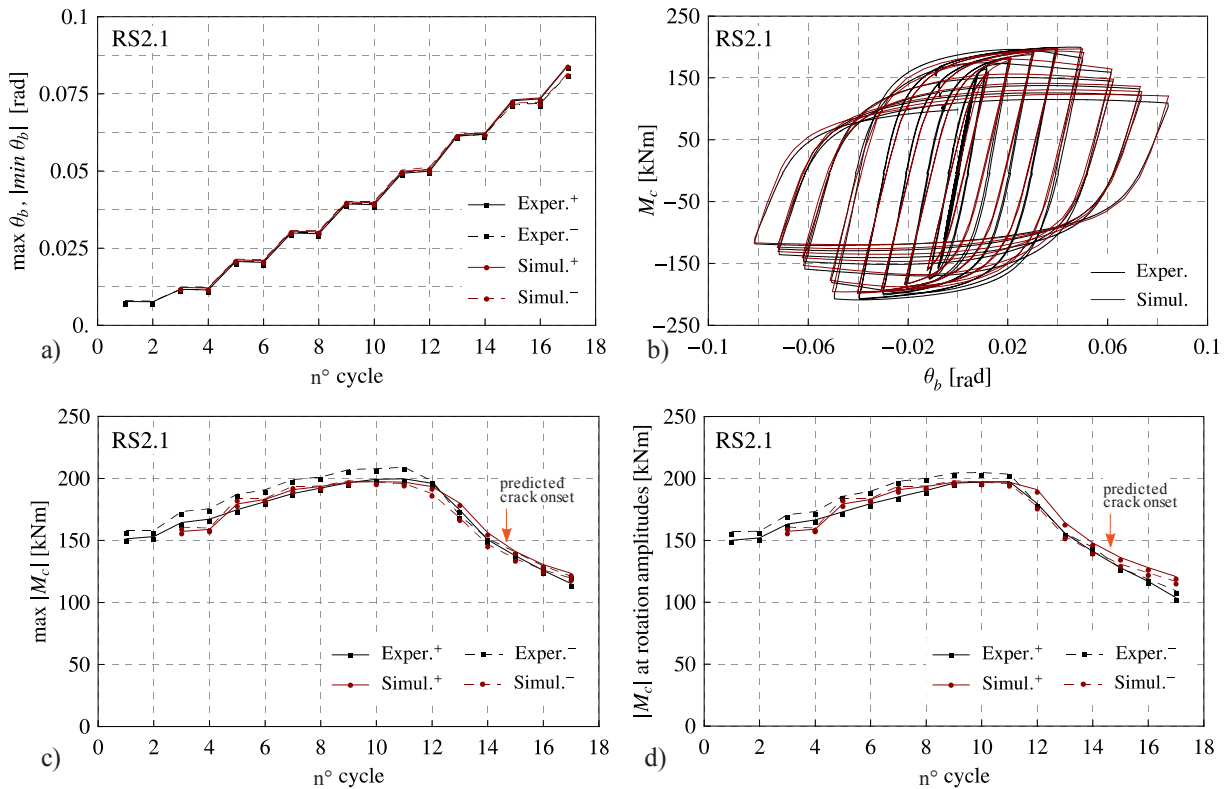


Fig. 164: Experimental and simulated response for RS2.1: a) applied total beam plastic rotation amplitudes, b) hysteretic response, c) distribution of maximum values M_c , d) distribution of M_c at rotation amplitudes
Slika 164: Eksperimentalni in simulirani odziv RS2.1: a) amplitude vsiljene celotne rotacije prečke, b) histerezni odziv, c) potek največjih vrednosti M_c , d) potek vrednosti M_c v amplitudah rotacije

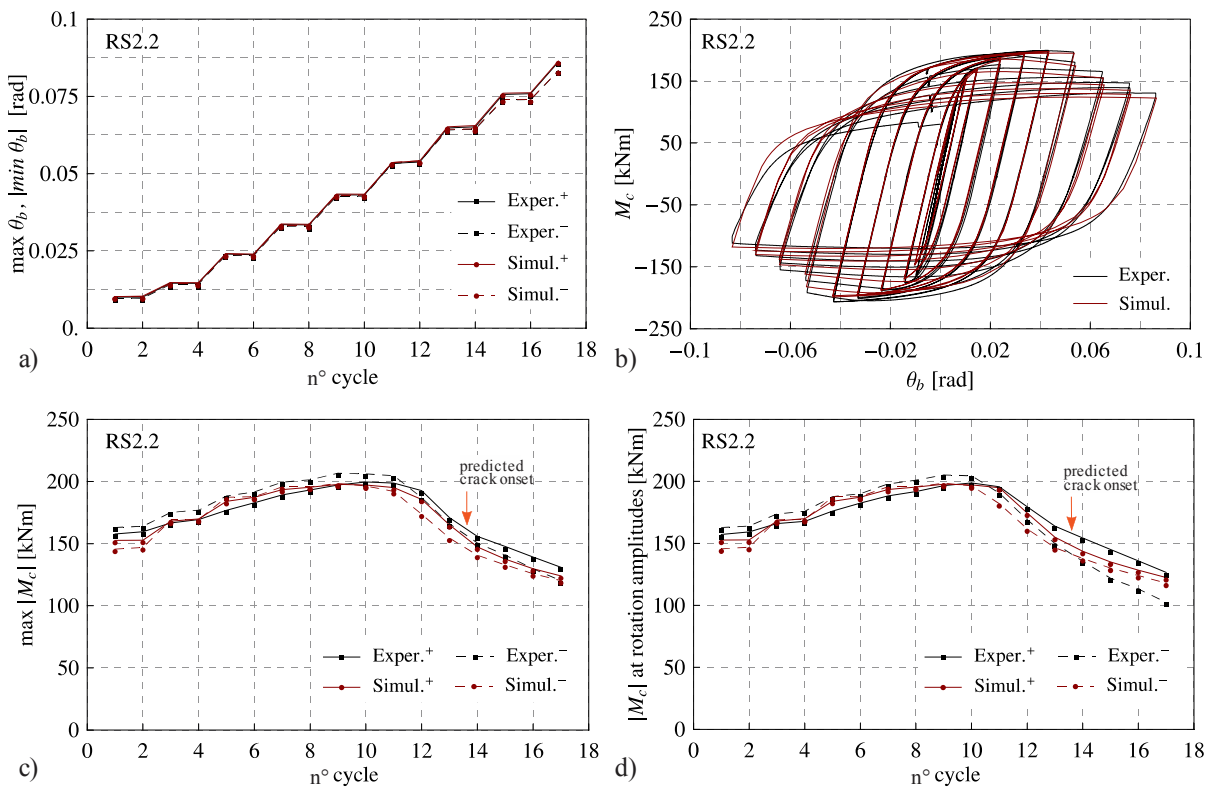


Fig. 165: Experimental and simulated response for RS2.2: a) applied total beam plastic rotation amplitudes, b) hysteretic response, c) distribution of maximum values M_c , d) distribution of M_c at rotation amplitudes
Slika 165: Eksperimentalni in simulirani odziv RS2.2: a) amplitude vsiljene celotne rotacije prečke, b) histerezni odziv, c) potek največjih vrednosti M_c , d) potek vrednosti M_c v amplitudah rotacije

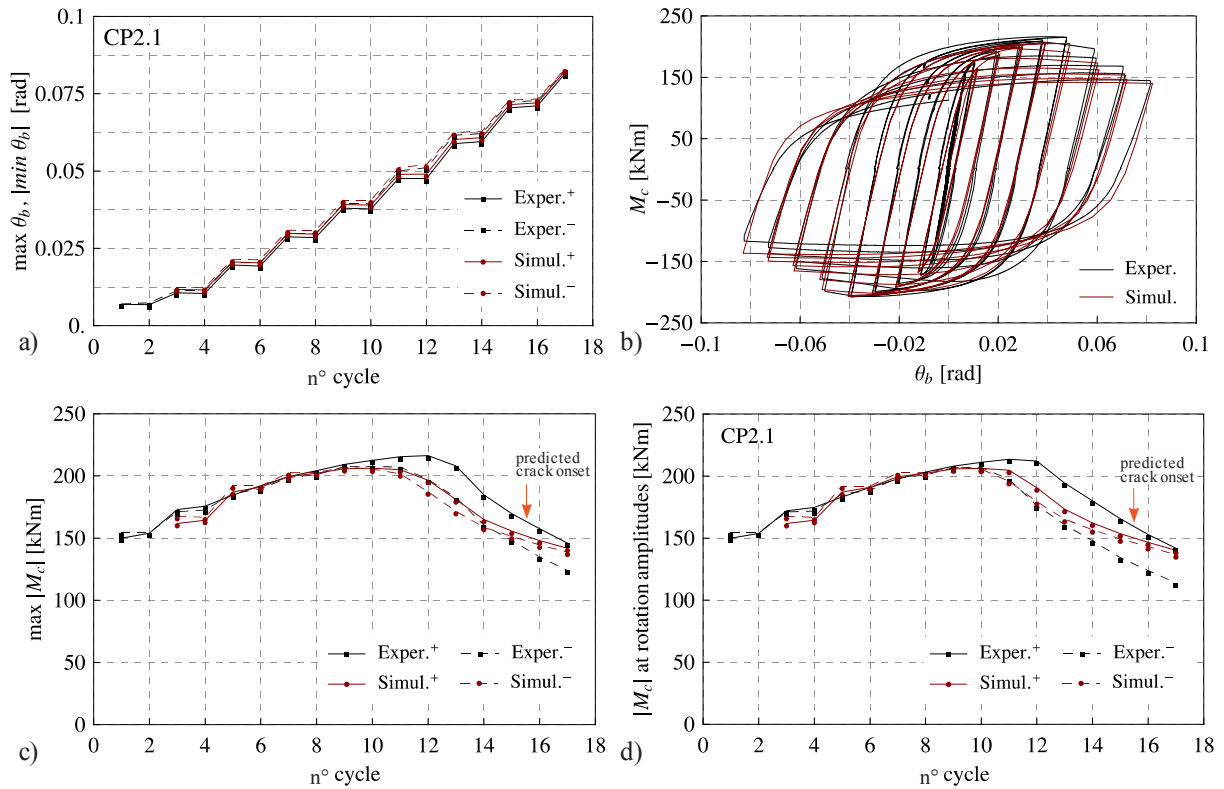


Fig. 166: Experimental and simulated response for CP2.1: a) applied total beam plastic rotation amplitudes, b) hysteretic response, c) distribution of maximum values M_c , d) distribution of M_c at rotation amplitudes
Slika 166: Eksperimentalni in simulirani odziv CP2.1: a) amplitude vsiljene celotne rotacije prečke, b) histerezni odziv, c) potek največjih vrednosti M_c , d) potek vrednosti M_c v amplitudah rotacije

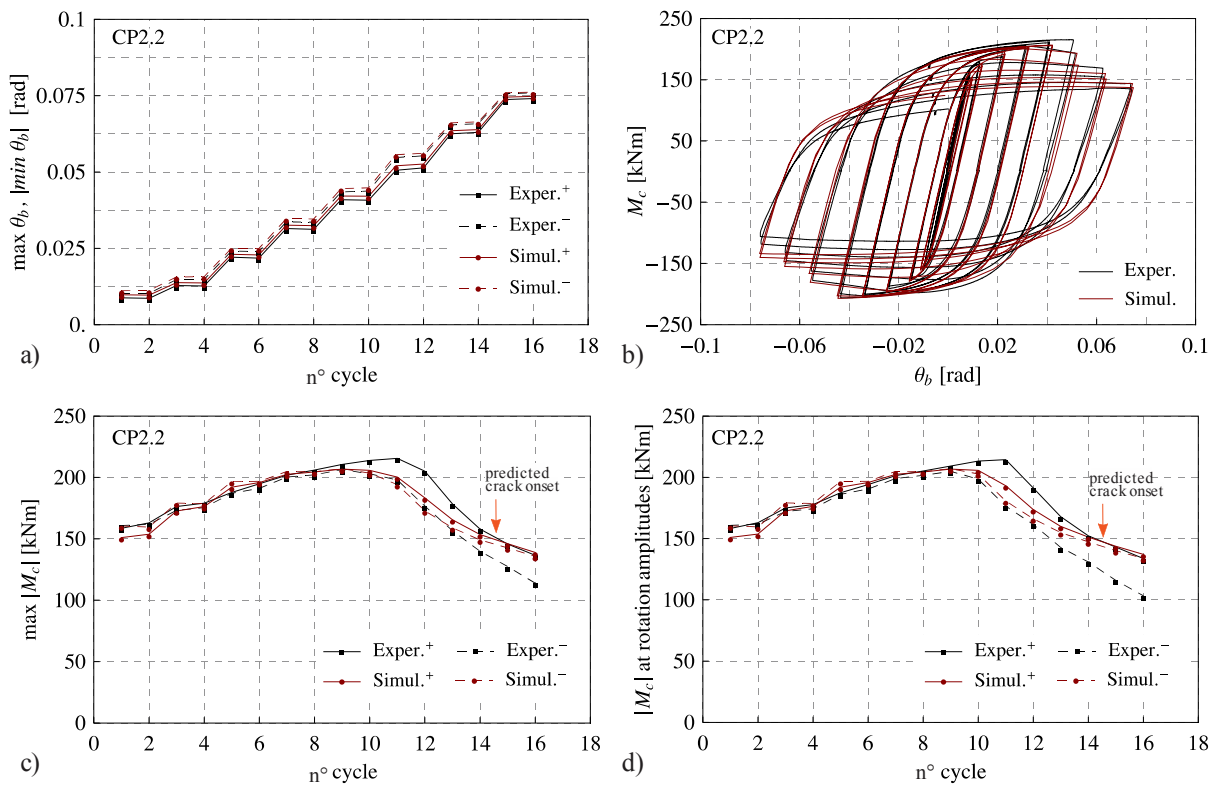


Fig. 167: Experimental and simulated response for CP2.2: a) applied total beam plastic rotation amplitudes, b) hysteretic response, c) distribution of maximum values M_c , d) distribution of M_c at rotation amplitudes
Slika 167: Eksperimentalni in simulirani odziv CP2.2: a) amplitude vsiljene celotne rotacije prečke, b) histerezni odziv, c) potek največjih vrednosti M_c , d) potek vrednosti M_c v amplitudah rotacije

In general, very close agreement between the experimental and the simulated cyclic response can be noticed in case of all the eight specimens. Somewhat larger mismatch occurs in case of both specimens CP2, CP2.1 and CP2.2, particularly in the reported distribution of moment M_c .

Explanation of the possible reason for higher moment resistance measured during experimental tests for positive loading direction compared to the resistance from negative loading direction is provided in detail in Chapter 3.4.2. No such discrepancy was measured from all the other six tests. For the reported two cases closer matching with the experimental results was not tried to simulate, since it largely depends upon the initial geometric imperfections on the beam in the local region just behind the strengthened part of the beam.

Increasing trend of difference between the experimental and simulated responses can be noticed from a few last cycles in case of all the eight specimens. Namely, from a certain cycle on, clearly seen negative trend in joint resistance, was not able to be simulated with applied material cyclic model that do not account for material low-cycle fatigue damage.

Diagrams presented in Figs 168 to 171 show comparison between simulated and experimental hysteresis loop shapes from midlife as well as from the last cycle with predicted occurrence of ductile cracking, according to the effective damage concept proposed by Ohata and Toyoda (2004). Hysteresis curves from two different stiffened joint configurations (RS1 and CP1, RS2 and CP2) with the same beam cross-section are presented in the same figure to facilitate direct comparison between the simulated performance of RS and CP joint behaviour.

It should be noted that the experimentally obtained hysteresis shapes from the response of specimen CP1.1, presented in Fig. 168, contain a defect that must had been occurred during measurement in the test.

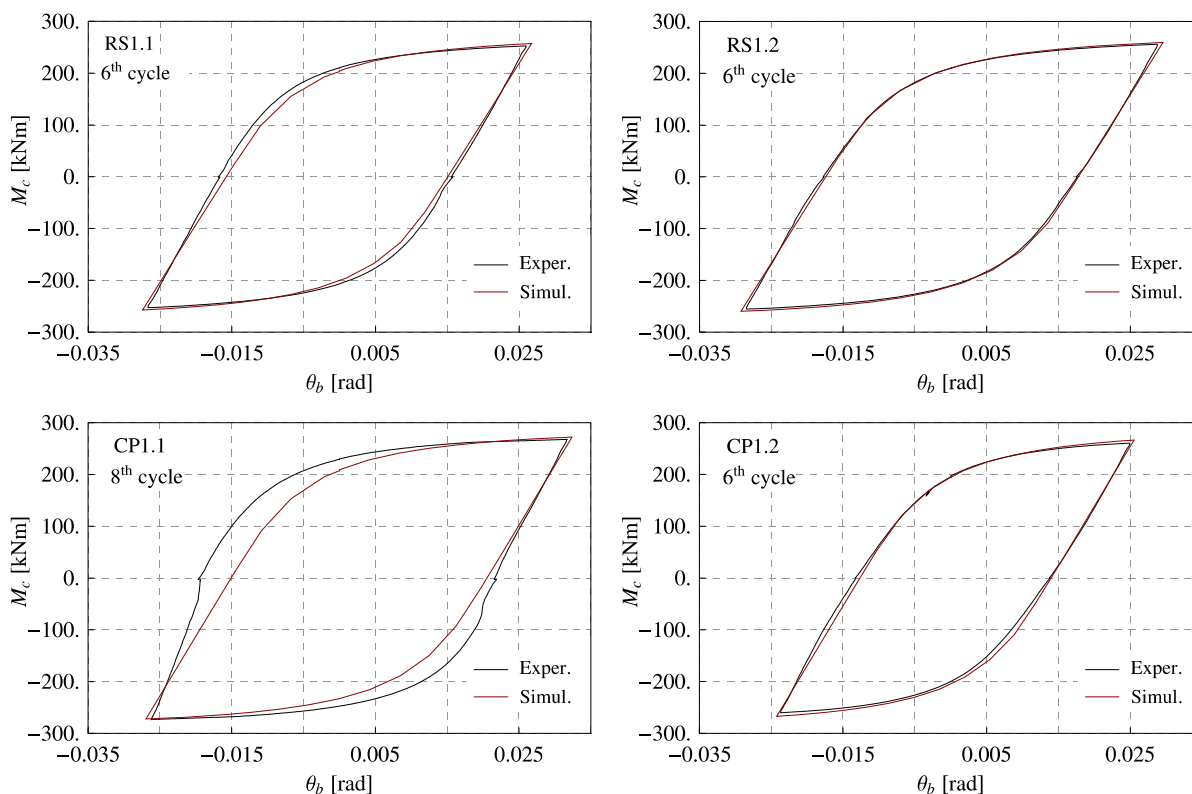


Fig. 168: Comparison between experimental and simulated response for specimens RS1 and CP1: hysteresis curves from cyclic midlife of the specimens

Slika 168: Primerjava med eksperimentalnim in simuliranim odzivom preizkušancev RS1 in CP1: histerezni krivulji iz sredine nizkociklične življenjske dobe spoja

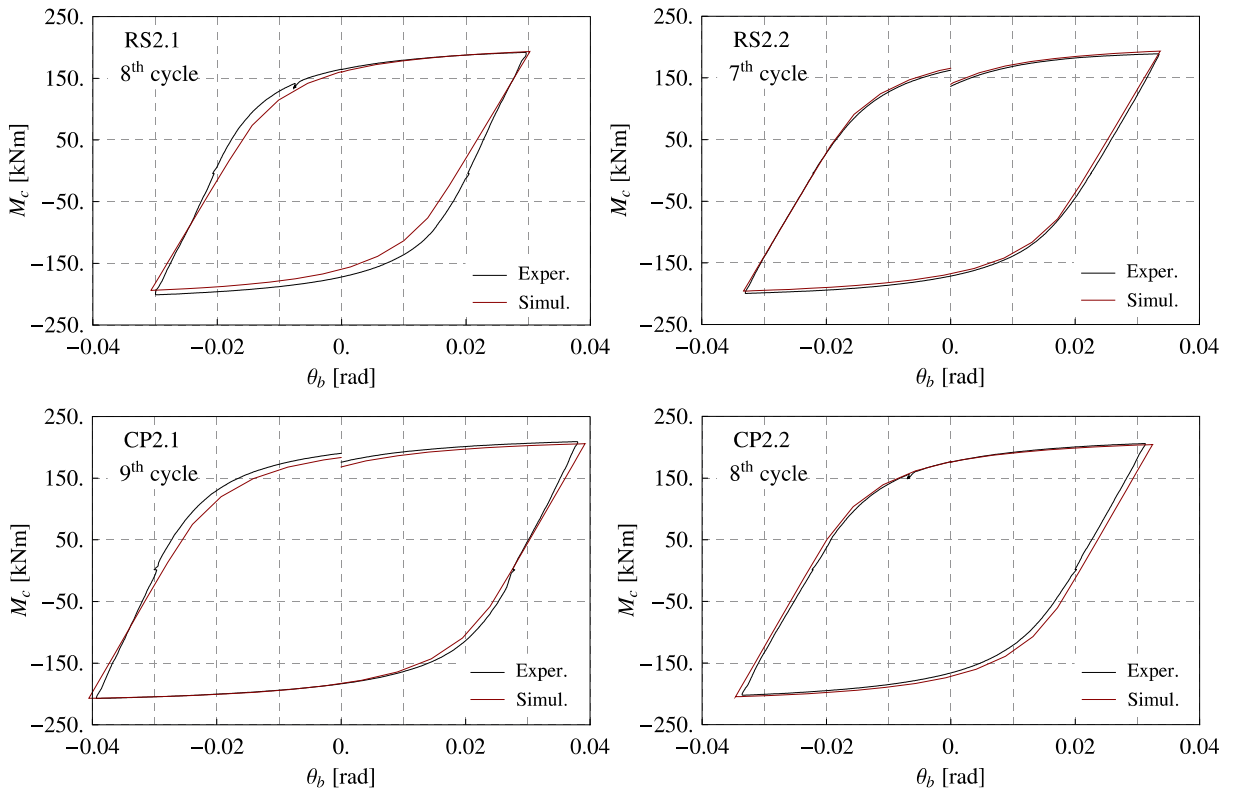


Fig. 169: Comparison between experimental and simulated response for specimens RS2 and CP2: hysteretic curves from cyclic midlife of specimens

Slika 169: Primerjava med eksperimentalnim in simuliranim odzivom preizkušancev RS2 in CP2: histerezni krivulji iz sredine nizkociklične življenjske dobe spoja

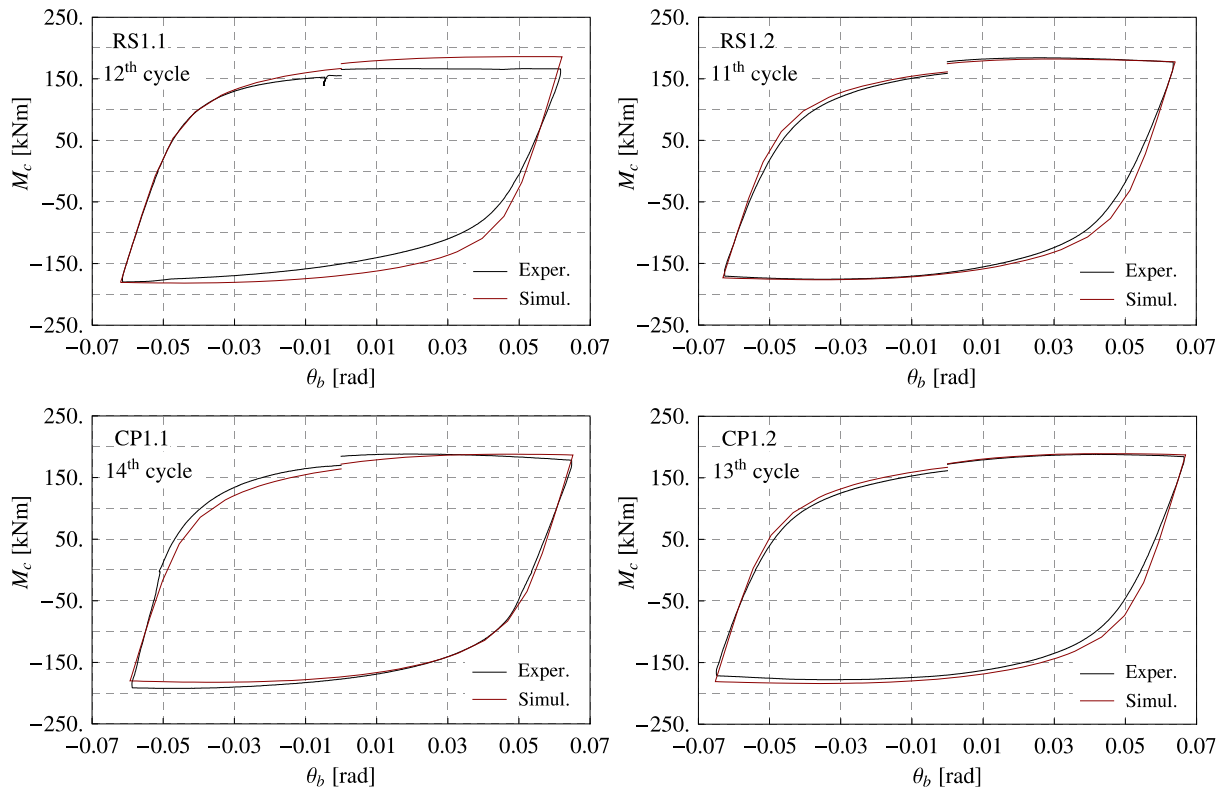


Fig. 170: Comparison between experimental and simulated response for RS1 and CP1 specimens: hysteretic curves from the cycle with predicted onset of ductile cracking

Slika 170: Primerjava med eksperimentalnim in simuliranim odzivom preizkušancev RS1 in CP1: histerezni krivulji iz cikla z napovedanim nastopom duktilne razpoke

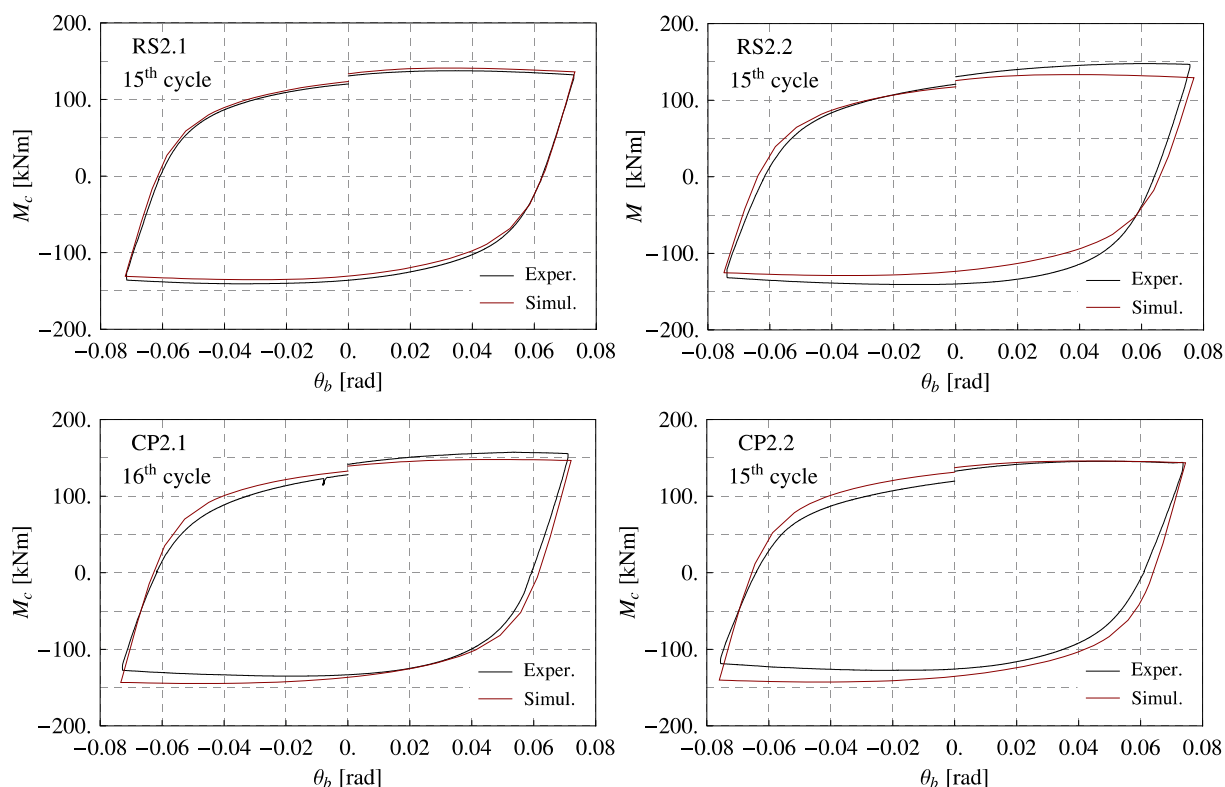


Fig. 171: Comparison between experimental and simulated response for RS2 and CP2 specimens: hysteretic curves from the cycle with predicted onset of ductile cracking

Slika 171: Primerjava med eksperimentalnim in simuliranim odzivom preizkušancev RS2 in CP2: histerezni krivulji iz cikla z napovedanim nastopom duktilne razpoke

Final correlation between the results from laboratory tests and simulations is assessed by comparison of dissipated hysteretic energy, see Table 28 and Figs 172 to 175. This is important for proper evaluation of accuracy, since nonlinear finite element model does not account for LCF material damage.

Preglednica 28: Primerjava akumulirane energije za cikle do predvidenega nastopa prve duktilne razpoke
 Table 28: Comparison of accumulated energy for cycles till the predicted ductile crack occurrence

Specimen	$N_{crack}^{predicted}$	Accumulated energy till the crack occurrence		
		Test [kNm]	Simulation [kNm]	Deviation [%]
RS1.1	12	234.5	239.1	2.0
RS1.2	11	216.3	216.4	0.01
RS2.1	15	237.8	223.4	6.1
RS2.2	15	250.4	243.3	2.8
CP1.1	14	268.7	237.7	11.6
CP1.2	13	235.4	239.9	1.9
CP2.1	16	277.4	264.5	4.6
CP2.2	15	244.7	252.6	3.2

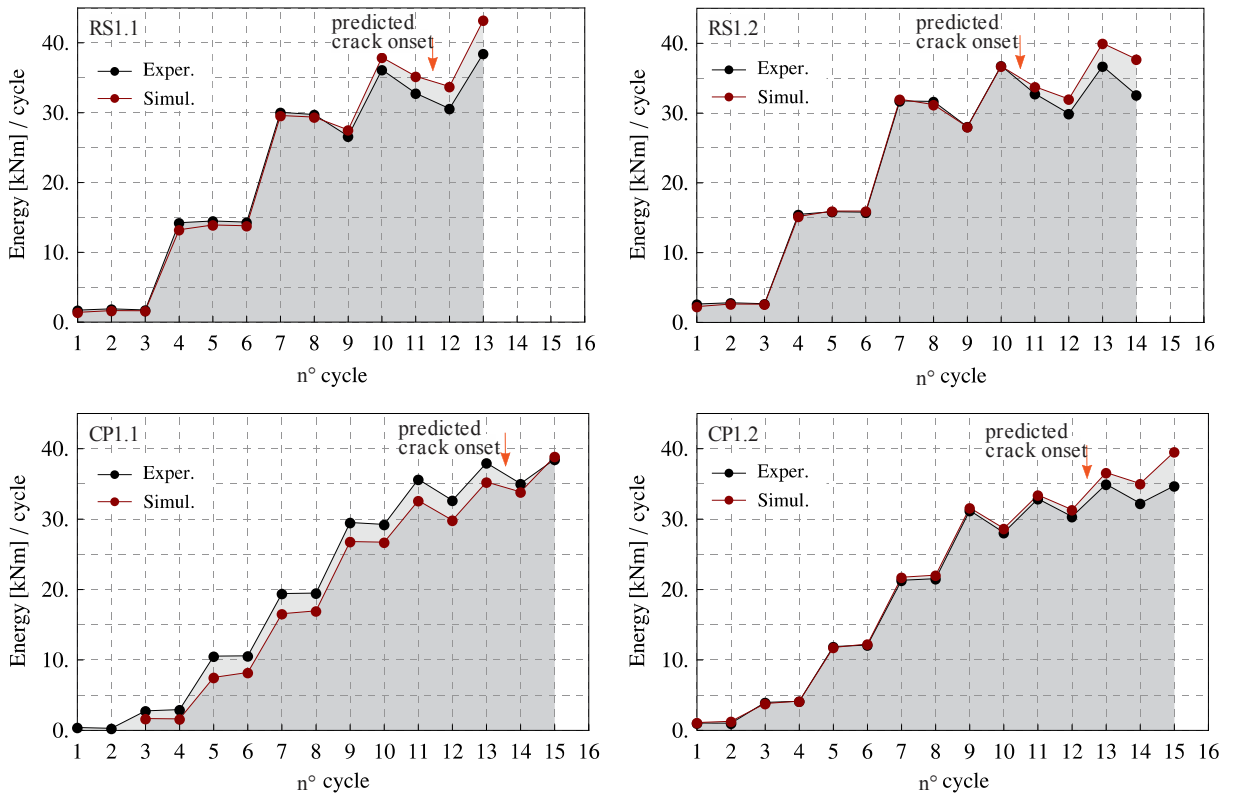


Fig. 172: Experimental and simulated response for specimens RS1 and CP1: distribution of energy per cycle
Slika 172: Eksperimentalni in simulirani odziv preizkušancev RS1 and CP1: potek energije po ciklih

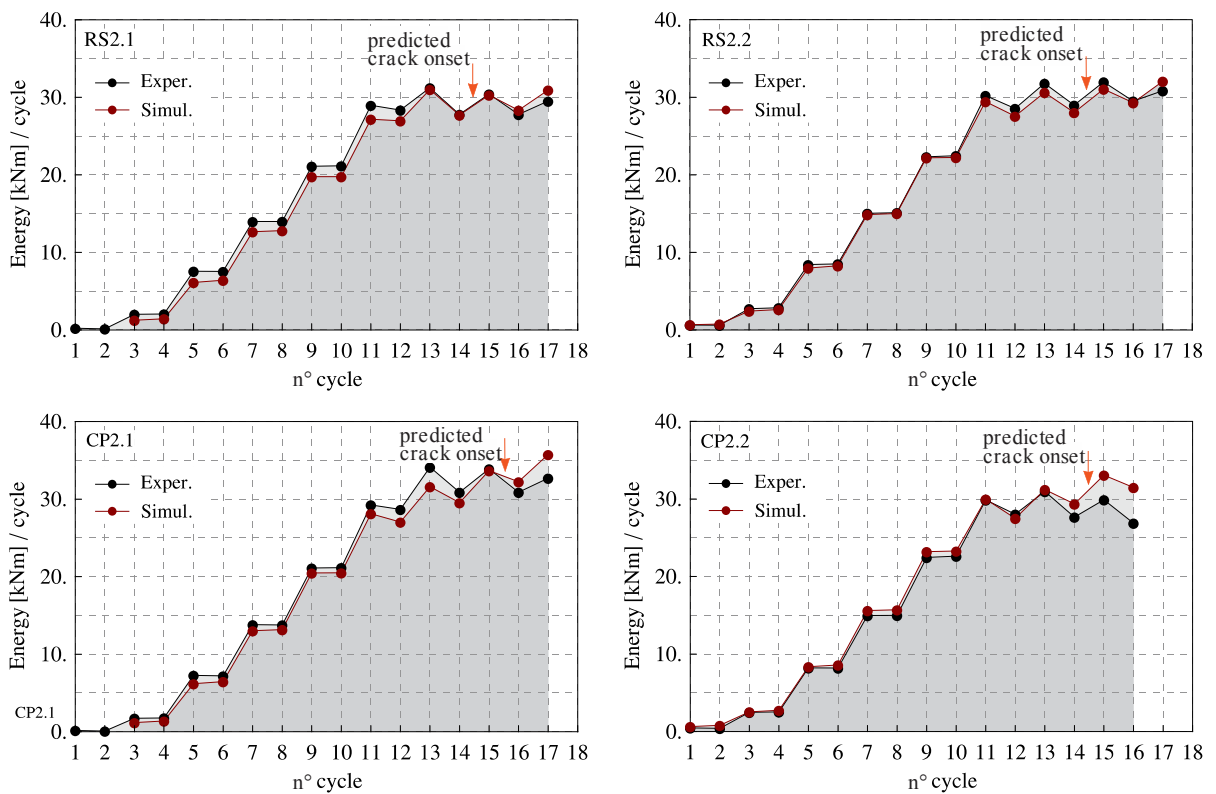


Fig. 173: Experimental and simulated response for RS2 and CP2 specimens: distribution of energy per cycle
Slika 173: Eksperimentalni in simulirani odziv preizkušancev RS2 and CP2: potek energije po ciklih

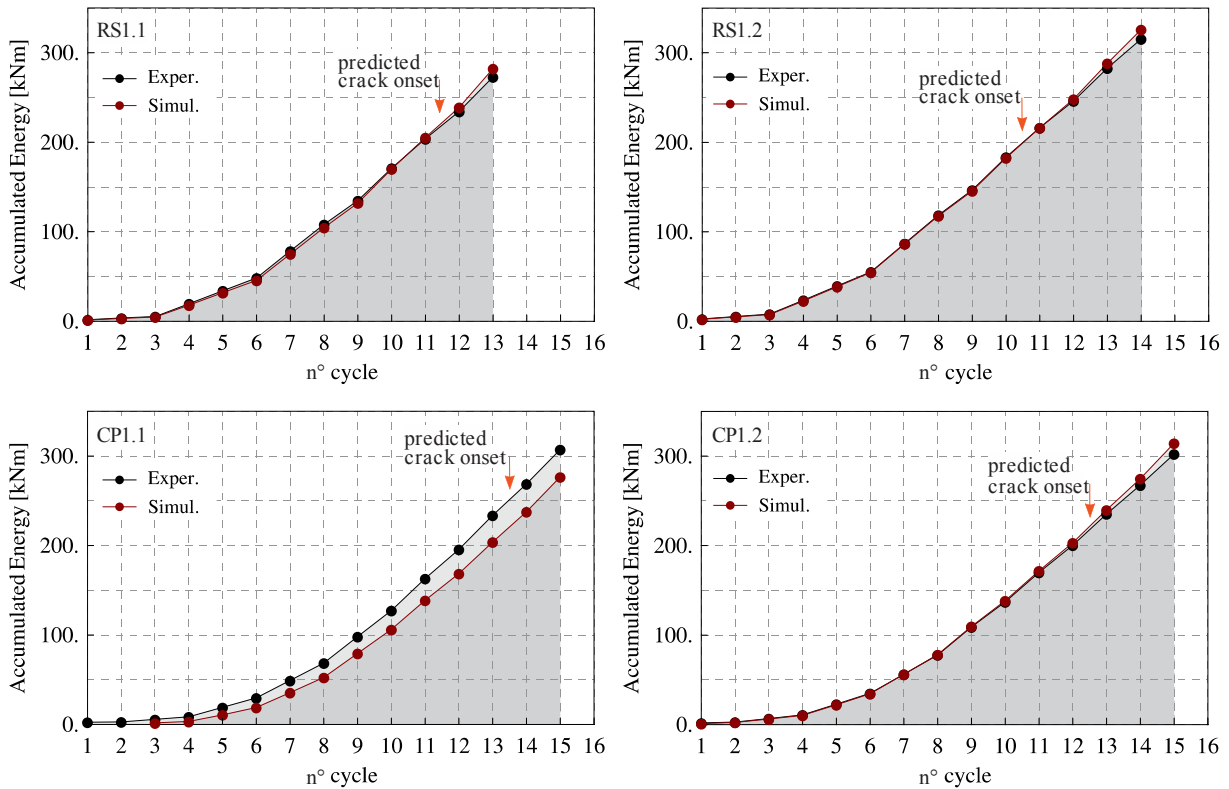


Fig. 174: Experimental and simulated response for RS1 and CP1 specimens: distribution of accumulated energy
Slika 174: Eksperimentalni in simulirani odziv preizkušancev RS1 and CP1: potek akumulirane energije

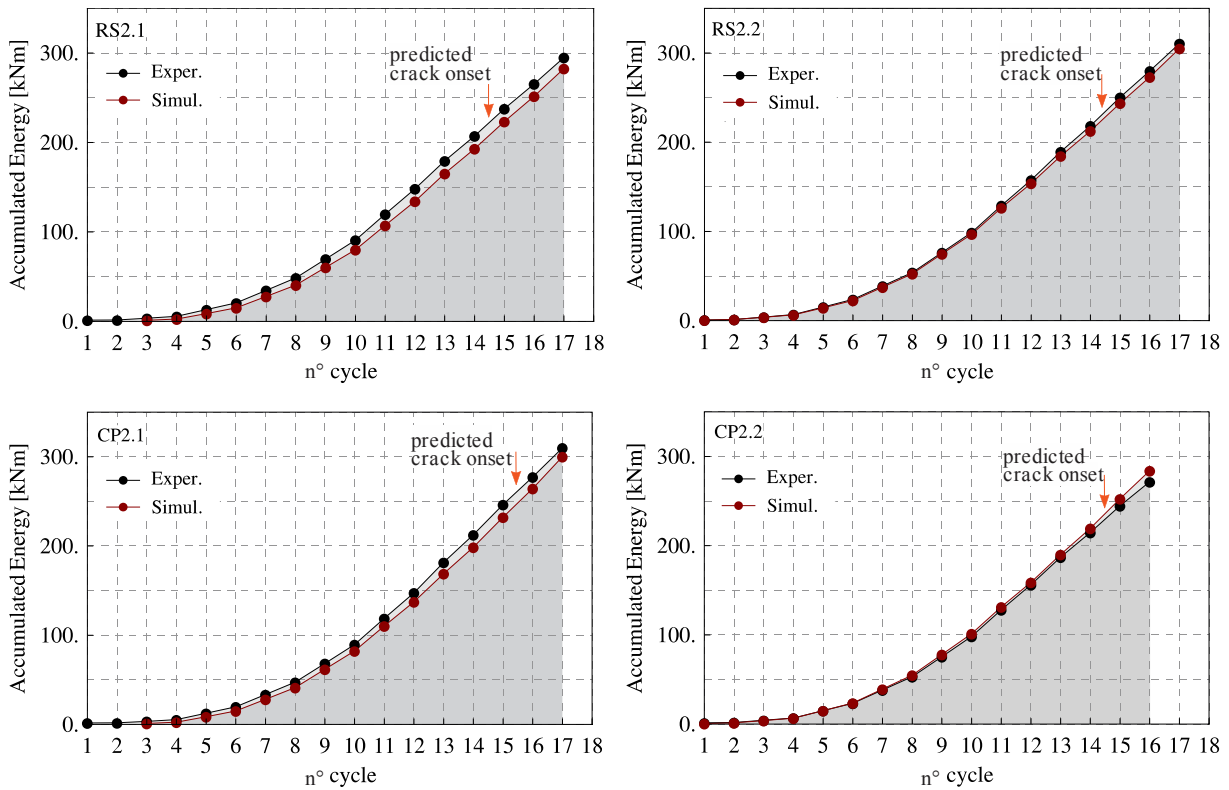


Fig. 175: Experimental and simulated response for RS2 and CP2 specimens: distribution of accumulated energy
Slika 175: Eksperimentalni in simulirani odziv preizkušancev RS2 and CP2: potek akumulirane energije

Also from the distribution of accumulated energy a very good agreement between experiment and simulation can be observed for all the eight joint specimens subjected to variable cyclic loading.

4.3.3.4 *Local strain response*

In this chapter local strain distribution along stiffened part of the beam including plastic hinge region is presented. Strain data measured by the uniaxial strain gauges during experiments and those obtained from FE simulations are presented and compared in order to:

- (i) validate local response of the FE-model against experimental results;
- (ii) confirm the applied design concept for RS and CP stiffened beam-to-column joints in terms of transfer of inelastic action away from the face of the beam-to-column connection in the unstiffened beam section.

For this purpose, experimental and simulated results from four different RS and CP joint specimens subjected to small constant amplitude cyclic loading, RS1.3, RS2.3, CP1.3 and CP2.3, were selected for the presentation.

In case of all the rest twelve tests, including four joints subjected to large constant amplitude cycling and eight joints subjected to cyclic loading with stepwisely increasing loading amplitude, extremely high plastic straining in the plastic hinge region of the beam led to the overload of all the strain gauges (with strain limit 50 %) in this zone. Although measured strains in the stiffened region of the beam remained moderate and in elastic state, complete experimental strain distribution, with strain gauges placed also at the end of the stiffened region, for these cases was not obtained.

For each of the selected four joint specimens, measured experimental strain data are presented for the top beam flange in accordance with the applied strain gauge scheme presented in Fig. 26. In order to exclude possible spurious experimental strain data, distribution of longitudinal strains for top and bottom side of the beam flange of the same specimen is provided.

Strain distributions are obtained at negative amplitude of applied joint rotation, when the observed top beam flange is in tension.

Reported strain data from FE simulations (total logarithmic strain component in longitudinal beam direction) were adopted from elements on the top and bottom surface of the beam flange along the straight line connecting positions of the selected strain gauges from experiment.

Values from integration points are reported, since extrapolated values in element are generally not as accurate as the values calculated at the integration points for the areas of high stress/strain gradients.

Local strain distributions along the stiffened part of the beam, including plastic hinge region, are not reported for complete number of cycles performed in experiments, but only for cycles till the onset of clear strength degradation of the joints, see Table 18.

In addition to the reported local strain distributions, comparison between experimental and simulated strain life response is presented for selected positions on the beam flange in terms of hysteresis presenting measured strain vs. moment to the column centreline M_c .

For RS1.3 specimen the strain data are presented in Figs 176 to 178, for RS2.3 specimen in Figs 179 to 181, for CP1.3 specimen in Figs 182 to 184 and for CP2.3 specimen in Figs 185 to 187.

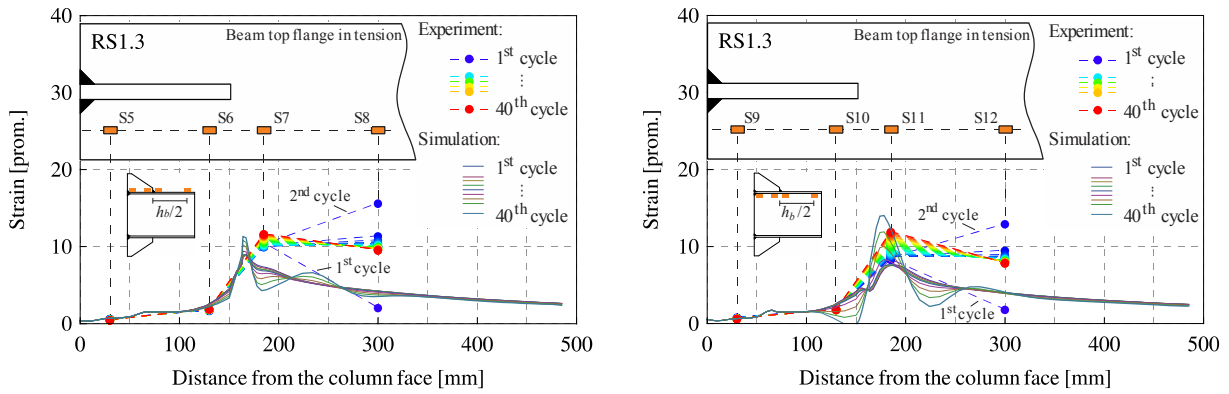


Fig. 176: Comparison between experimental and simulated local strain response for joint RS1.3
 Slika 176: Primerjava med lokalnimi deformacijami iz eksperimenta in simulacije za spoj RS1.3

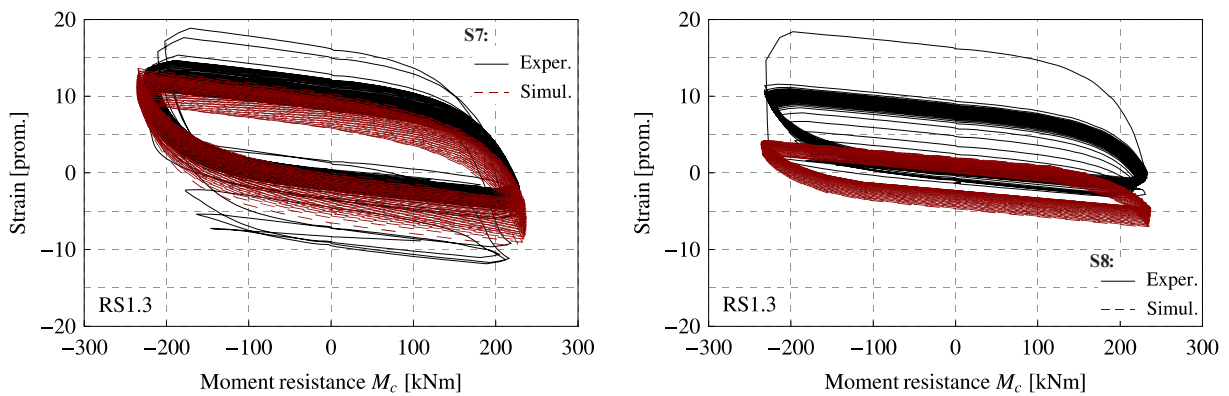


Fig. 177: Experimental and simulated local strain response for joint RS1.3; S7 and S8, complete no. of cycles
 Slika 177: Lokalne deformacije iz eksperimenta in simulacije za spoj RS1.3; S7 in S8, celotno število ciklov

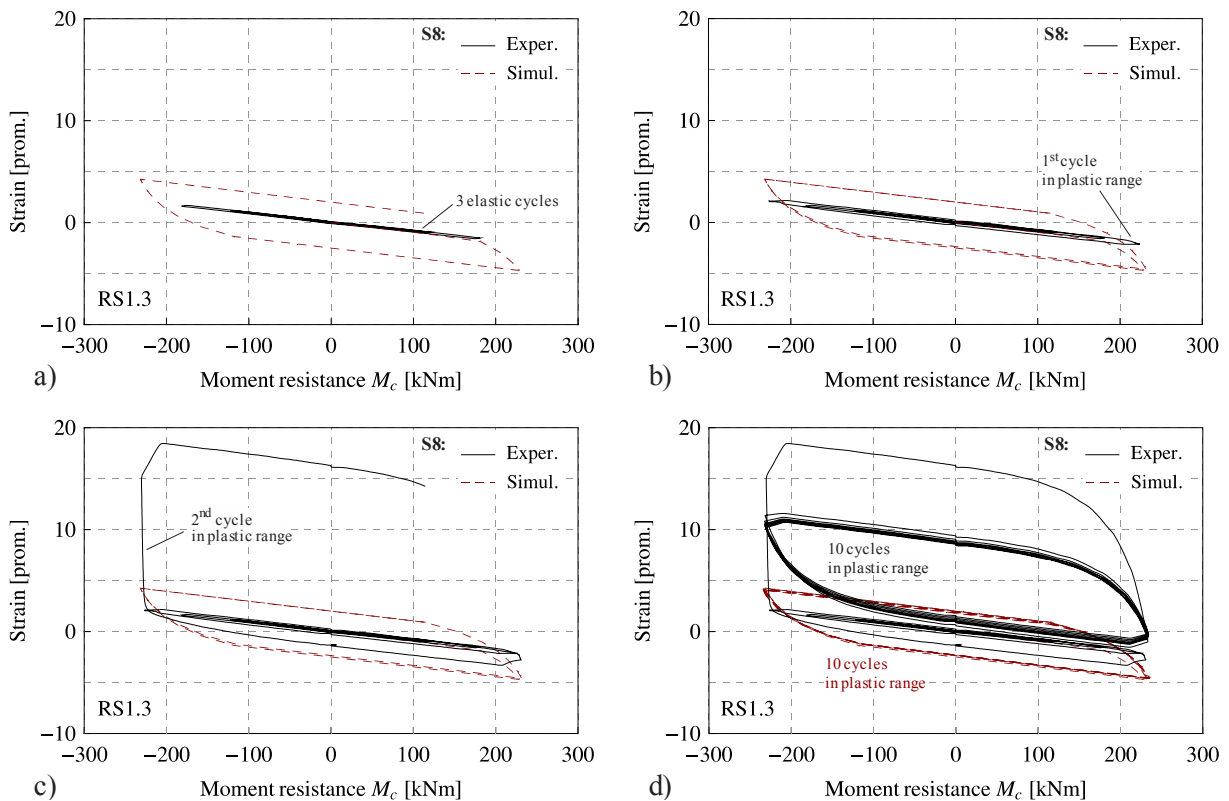


Fig. 178: Detailed comparison between experimental and simulated local strain response for RS1.3; S8
 Slika 178: Natančna primerjava lokalnih deformacij iz eksperimenta in simulacije za spoj RS1.3; S8

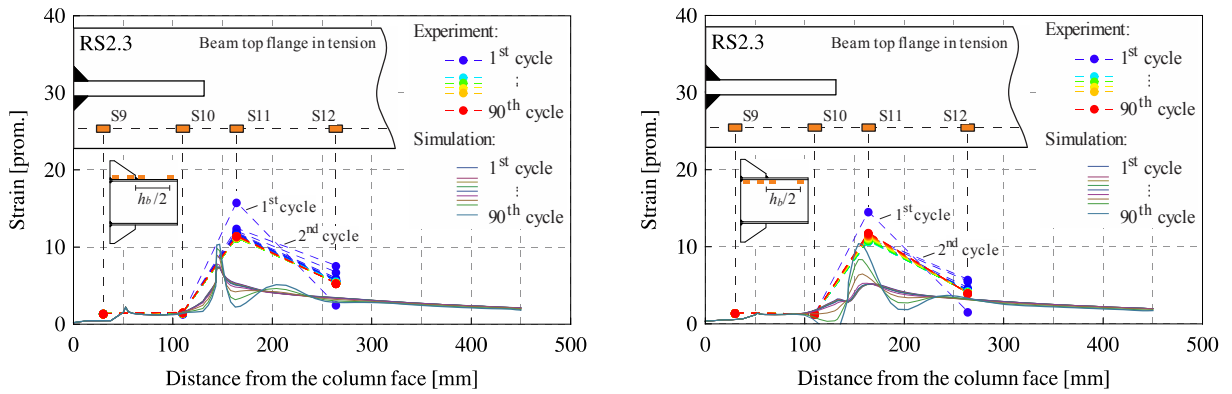


Fig. 179: Comparison between experimental and simulated local strain response for joint RS2.3
Slika 179: Primerjava med lokalnimi deformacijami iz eksperimenta in simulacije za spoj RS2.3

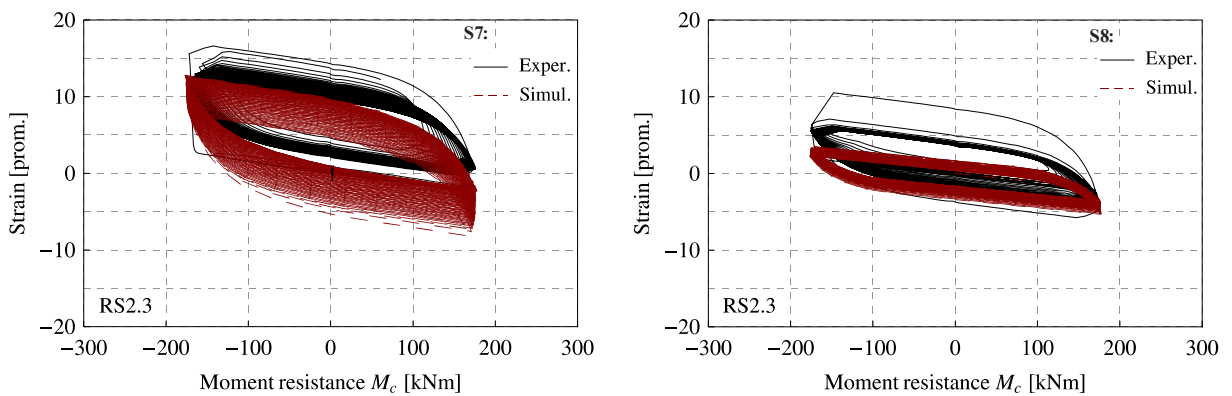


Fig. 180: Experimental and simulated local strain response for joint RS2.3; S7 and S8, complete no. of cycles
Slika 180: Lokalne deformacije iz eksperimenta in simulacije za spoj RS2.3; S7 in S8, celotno število ciklov

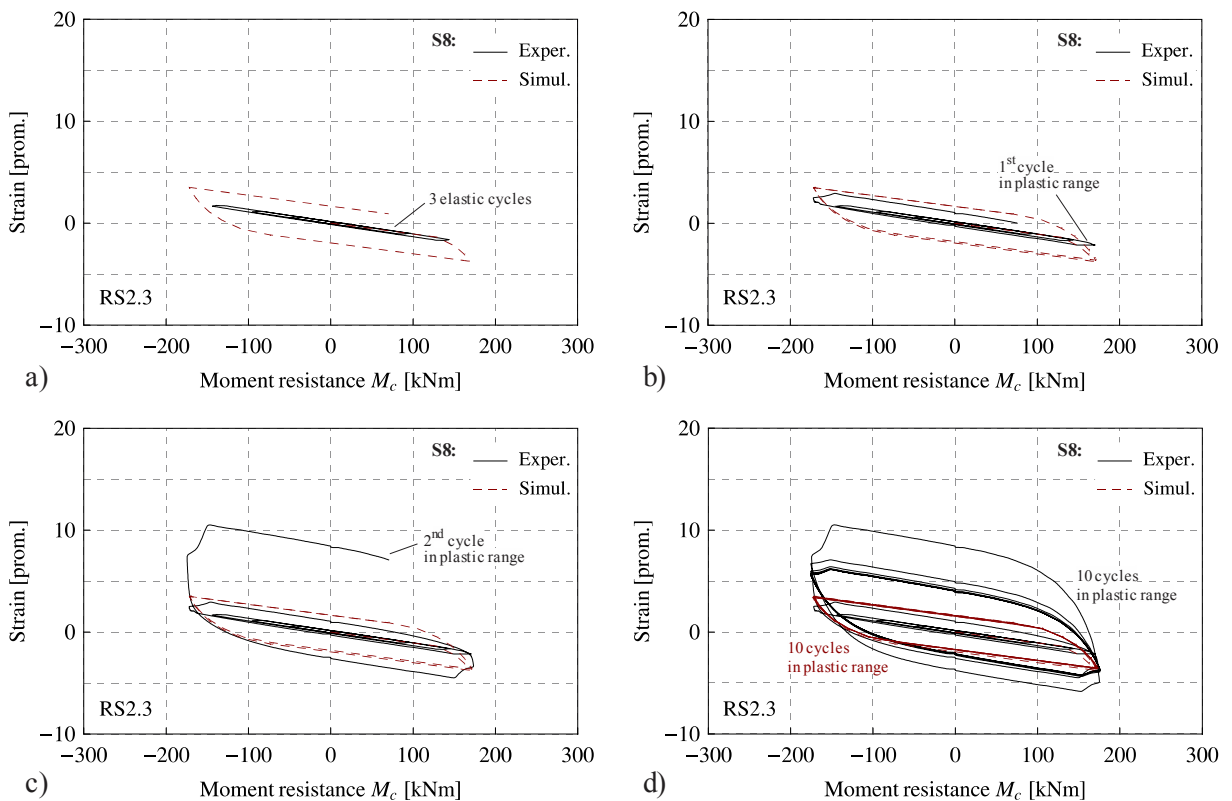


Fig. 181: Detailed comparison between experimental and simulated local strain response for joint RS2.3; S8
Slika 181: Natančna primerjava lokalnih deformacij iz eksperimenta in simulacije za spoj RS2.3; S8

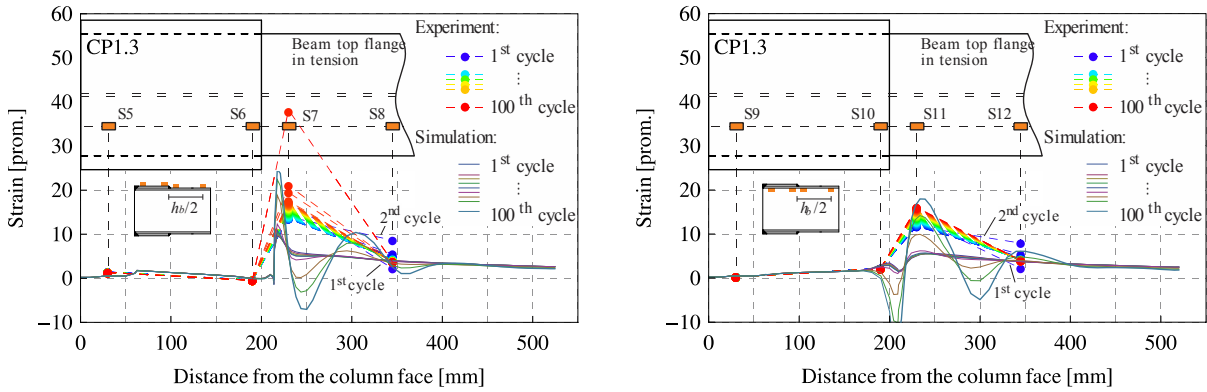


Fig. 182: Comparison between experimental and simulated local strain response for joint CP1.3
Slika 182: Primerjava med lokalnimi deformacijami iz eksperimenta in simulacije za spoj CP1.3

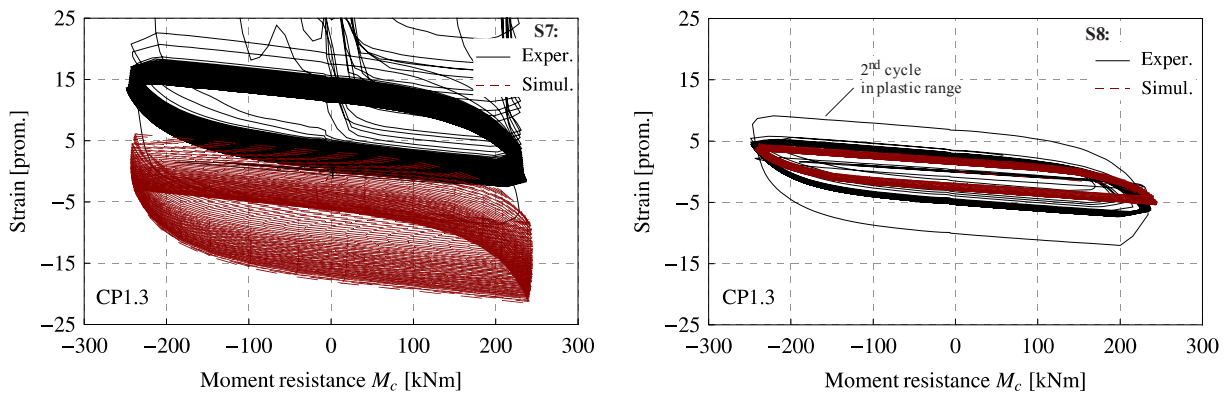


Fig. 183: Experimental and simulated local strain response for joint CP1.3; S7 and S8, complete no. of cycles
Slika 183: Lokalne deformacije iz eksperimenta in simulacije za spoj CP1.3; S7 in S8, celotno število ciklov

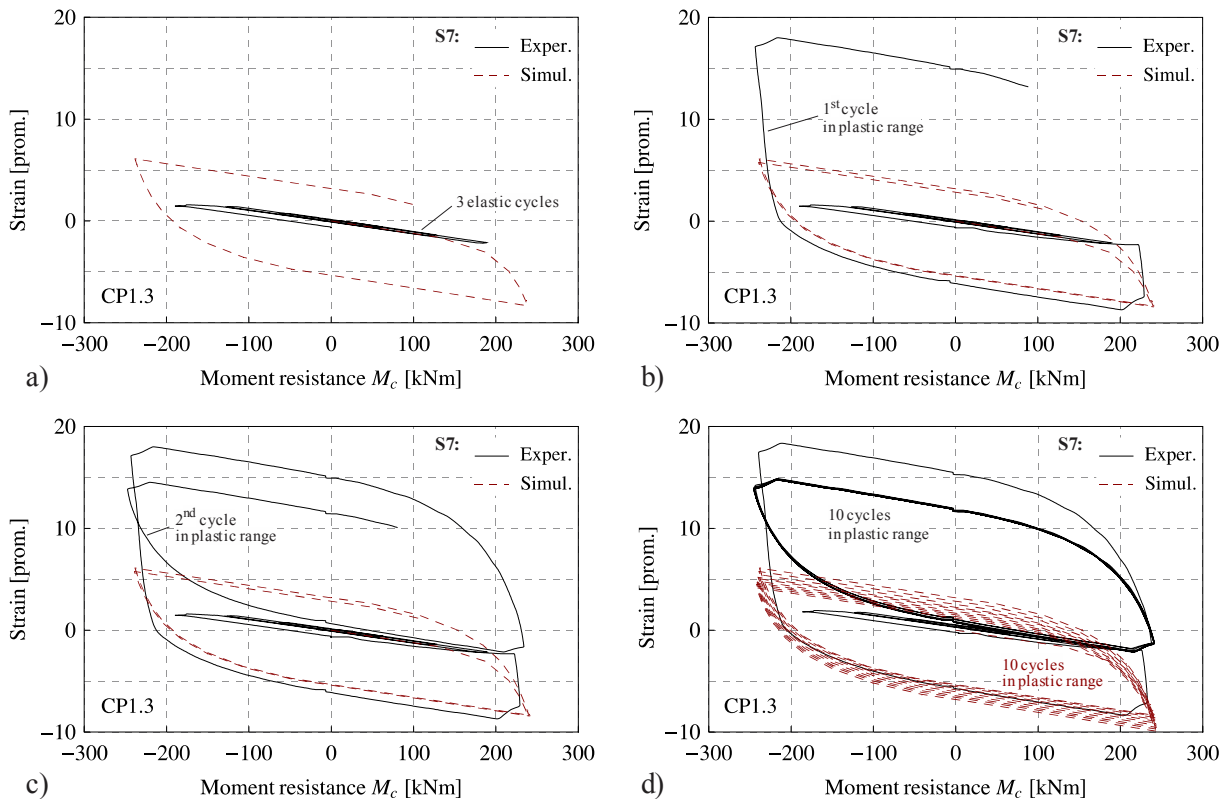


Fig. 184: Detailed comparison between experimental and simulated local strain response for joint CP1.3; S7
Slika 184: Natančna primerjava lokalnih deformacij iz eksperimenta in simulacije za spoj CP1.3; S7

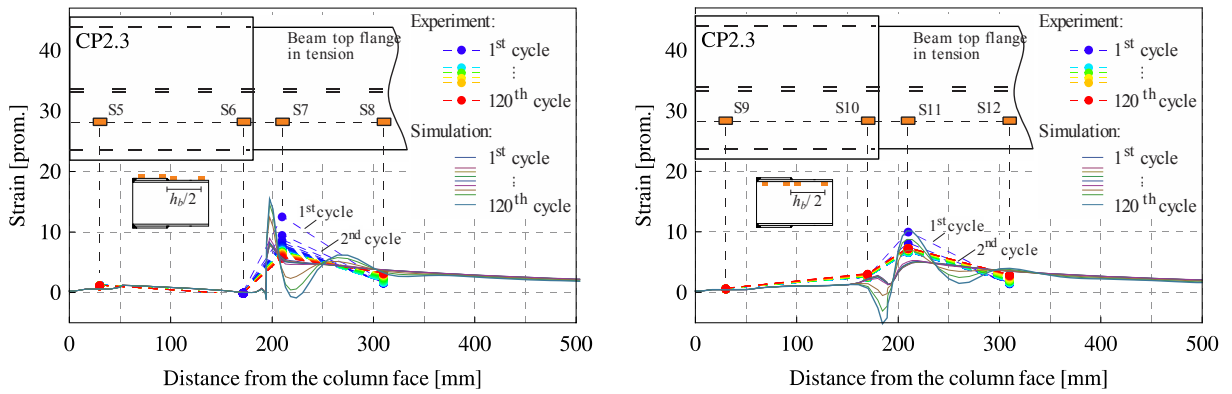


Fig. 185: Comparison between experimental and simulated local strain response for joint CP2.3
Slika 185: Primerjava med lokalnimi deformacijami iz eksperimenta in simulacije za spoj CP2.3

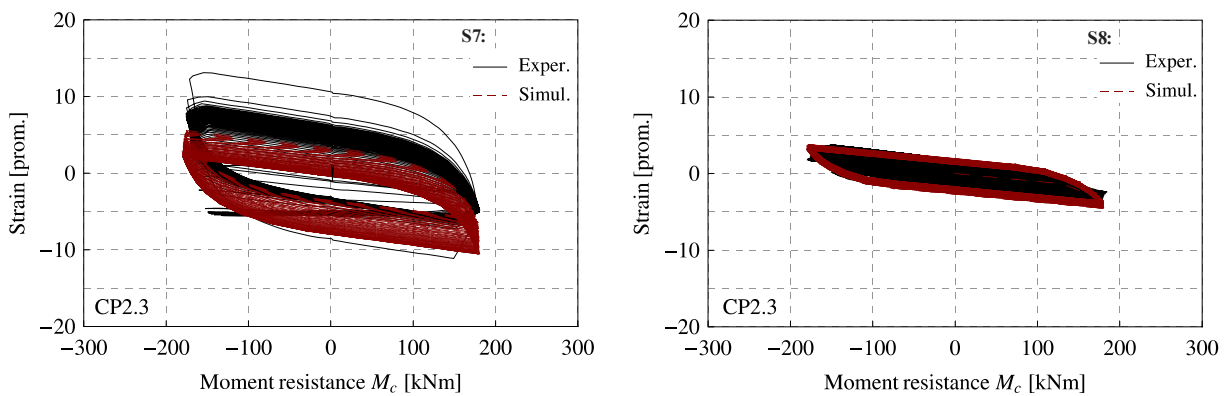


Fig. 186: Experimental and simulated local strain response for joint CP2.3; S7 and S8, complete no. of cycles
Slika 186: Lokalne deformacije iz eksperimenta in simulacije za spoj CP2.3; S7 in S8, celotno število ciklov

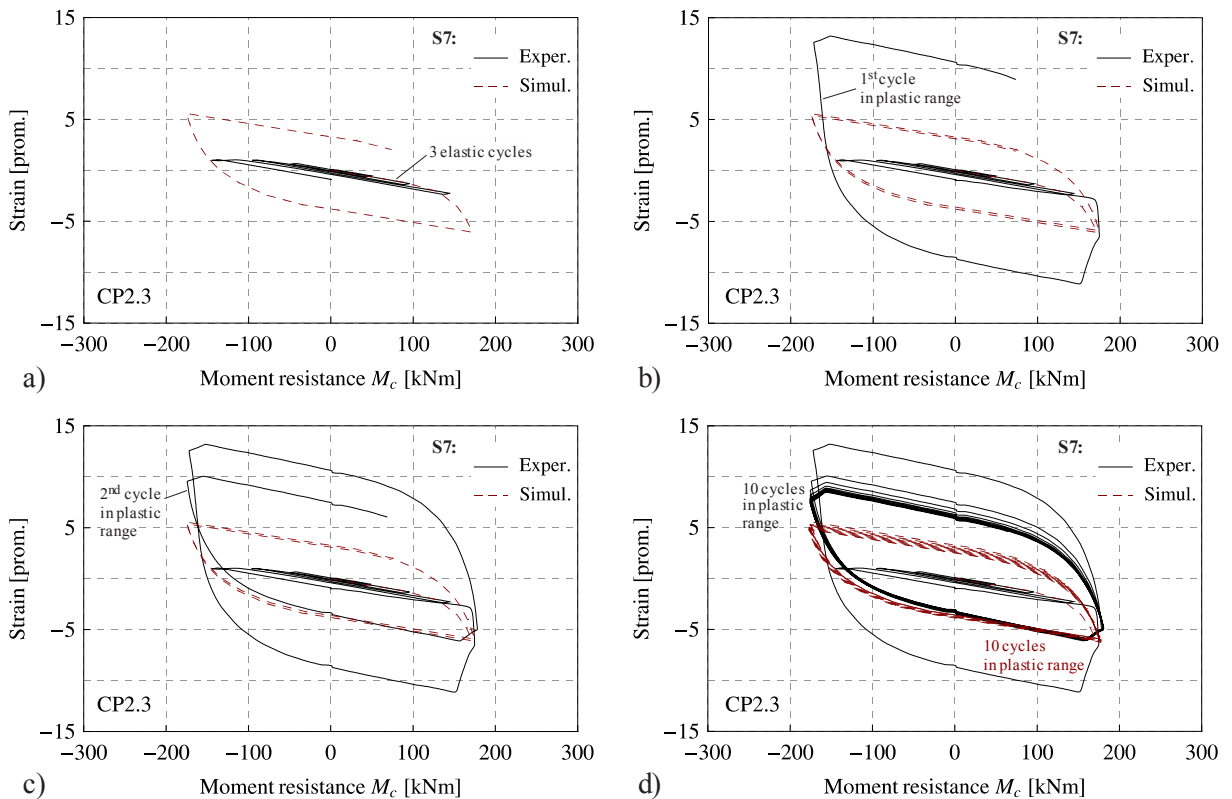


Fig. 187: Detailed comparison between experimental and simulated local strain response for joint CP2.3; S7
Slika 187: Natančna primerjava lokalnih deformacij iz eksperimenta in simulacije za spoj CP2.3; S7

In what concerns the presented local strain data from experiments, the reader should be aware of the fact that values are captured at limited number of positions (marked points linked with dotted lines on diagrams). This means that presented experimental strain distributions may not capture maximum or minimum values in the observed strain field on the beam flange.

For all the four joint specimens presented strain distributions on both sides (top and bottom) of the top beam flange are highly consistent.

For all the presented joint strain distributions, the stiffened beam region remains essentially elastic. The applied design criterion for both RS and CP stiffened joints to limit the strains in the stiffened region of the beam, i.e. to keep them elastic, was confirmed by all 16 experimental tests as well as by the corresponding FE simulations.

Simulated strain response in the stiffened region of the beam shows perfect match with experimentally obtained values (positions S5/S9 and S6/S10).

Maximal strain concentrations at the end of the stiffened region from simulations are also in a good agreement with the measured strain levels from experiments (position S7/S11).

For both specimens CP1.3 and CP2.3 high consistency between experimental and simulated local strain response was found also for the plastic hinge region beyond the end of the cover plate (position S8/S12). However, in case of both specimens RS1.3 and RS2.3 non-negligible underestimation of the strain level from FE simulation compared to experimental one can be observed in this region.

Major differences observed between simulated and experimental local strain response were investigated by detailed report of strain life for selected positions on the beam flange: position S8 for specimens RS1.3 and RS2.3, Fig. 178 and Fig. 181, and position S7 for specimens CP1.3 and CP2.3, Fig. 184 and Fig. 187. For all the reported positions, areas of hysteresis loops from experiment and simulation are fully comparable. The major difference is in somewhat shifted position of hysteresis loops obtained from the experiment, as a result of suddenly increased tension strains. An in-depth explanation of the phenomenon is described below.

In the experimentally obtained strain life from the point S7 of specimens CP1.3 and CP2.3, considerable increase of tension strain can be observed during the first loading cycle in plastic range, while such increase in tension strain in the point S8 of RS1.3 and RS2.3 specimens is observed during the second cycle. The reason for sudden increase of tension strain can be attributed to the false measurement of the strain gauges.

However, the observed phenomenon might be a consequence of changing position of strain concentrations along the beam flange during the first few loading cycles in plastic range. During the experiments the phenomenon was observed like spreading/moving of plastic zone in longitudinal beam direction away and again close to the end of the stiffened region. Possible explanation for this phenomenon was already given by Radomski and White (1968) and White and Radomski (1968).

In the first paper authors give some theoretical background relating to the strain concentration in elastic-plastic bending of simple beams. Consideration is given to different factors that the strain concentration in the yielded region is dependent on: geometry, mode of loading, and the stress-strain characteristics of the material from which the structure is made. The points were highlighted by analytical and, where it was not possible, by numerical solutions. In order to investigate the effect of stress-strain relation, both elastic-perfectly plastic and real stress-strain curves characteristic for different metals (mild steel, stainless steel and aluminium) were considered.

The calculations performed by the authors show that in elastic-perfectly plastic material short plastic zones may develop, which cause large localised strains in the beam, even though global behaviour (the deflection) of the beam corresponding to first yield is not greatly exceeded.

On the other hand, strain hardening elongates the plastic zones, producing a more favourable strain distribution along the length of the beam than would exist without it. The more pronounced the strain-hardening characteristic, i.e. the greater the rate of increase of stress with strain, the less concentrated will be the plastic strains.

The mode of loading was found important in that the higher the rate of change of bending moment, in the region of the maximum bending moment, the greater is the rate of increase of the plastic strain and the shorter is the plastic hinge zone (the more concentrated the local strains).

The study also brings forward peculiarity in local strain response in case of mild steel material. Namely, except for the mild steel, all results (elastic-perfectly plastic as well as stress-strain curves from stainless steel and aluminium) show a continuous increase in strain concentration with deflection. For mild steel the curve of strain concentration vs. deflection showed a peak in strain concentration followed by a continuous decrease with increasing deflection.

Authors explained this by the particular characteristics of the stress-strain curve for mild carbon steel. The stress-strain curve in this case has a flat portion at transition from the elastic into the plastic region (also called plateau after the onset of first yield) and then begins to display strain hardening behaviour – in case of our own material measurements - at about 2.5 per cent strain. When this strain is reached at the critical section, with further deflection there will be little increase in strain at that location and yielding will extend along the length of the beam. Thus the increased deflection causes the increase in strain to take place mainly away from the position of greatest strain.

For comprehensive description of observations during the tests the reader may also refer to Chapter 3.4.2 (commentary to Fig. 46).

Undulations in all the presented strain distributions from FE simulations were the consequence of small local crimping of the beam flange in the plastic hinge region, which were observed also in experiments, Fig. 188.

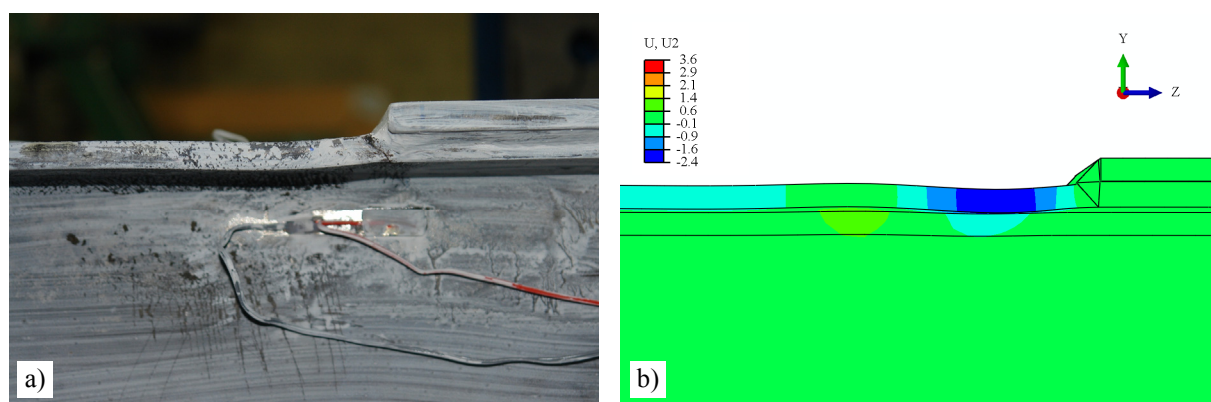


Fig. 188: Deformed shape of beam top flange from specimen CP1.3 in 100th cycle: comparison between a) experimental and b) simulated response (scale factor 1.0)

Slika 188: Deformirana oblika zgornje pasnice prečke preizkušanca CP1.3 v 100. ciklu: primerjava med a) eksperimentom in b) simulacijo (faktor povečave deformacij 1.0)

4.3.3.5 Evaluation of crack initiation based LCF failure in steel elements

This chapter is dedicated to the prediction of crack initiation based failure in steel elements of the analysed joints under cyclic loading. At least as far as the kind of failure observed in all the experimental tests is concerned (failure in the beam section beyond the stiffened region), this type of failure may not be followed by immediate brittle fracture of steel joint components (e.g. beam-to-column welded connection, stiffener or beam flange and consequently complete beam failure). This is substantial improvement in relation with unstiffened beam-to-column joints from the past major earthquakes, where unexpected brittle fractures of welded beam-to-column connection details revealed in steel structures (Miller, 1998. Nakashima et al., 1998a).

Evaluation of LCF crack initiation in steel welded structures subjected to seismic loading is crucial for structural design or safety assessment to prevent brittle fracture induced failures. To this aim, damage concept for evaluation of ductile cracking of structural steel components subjected to large-scale cyclic straining as proposed by Ohata and Toyoda (2004) was used in case of all eight specimens tested under cyclic loading with stepwisely increasing loading amplitude.

However, the criterion for ductile cracking is proposed on the basis of the effective damage concept and the two-parameter criterion, which can be applied only to the steel structures under increasing loading amplitude. For more information see Chapter 2.4.3.1.

To overcome the above limitation, unified approach for the evaluation of LCF induced cracking was proposed in this work on the basis of experimental results from all the 16 constant and variable cyclic loading experimental tests on stiffened beam-to-column joints. The approach allows for the identification of crack initiation due to accumulated damage effects under LCF loading with arbitrary loading amplitude history.

The proposed concept was used for improved assessment of ductility and LCF resistance of simulated joints' response in complementary parametric numerical analysis, as presented in Chapter 5.

Since no damage evolution law under LCF is accounted for in the applied cyclic material model in Abaqus, further softening behaviour of steel components after the predicted occurrence of cracking was not simulated. In fact, the identification of locations with the most severe plastic strain concentrations till the predicted onset of cracking, gives important information on ductility and the start of failure mechanism of the joint under applied cyclic loading history.

4.3.3.5.1 Prediction of ductile cracking onset using effective damage concept – tests with increasing cyclic loading amplitude

At the current stage of the work, after reliable FE-model for monotonic and cyclic loading was established, next objective of the study is to compare each beam-to-column joint local response with the simulated stress/strain field from FE-model. The prediction of ductile cracking initiation for all eight joints tested under increasing cyclic loading amplitude was performed based on the effective damage curve for the S355 J2 structural steel adopted from the literature (Bleck et al., 2009. Feldmann et al., 2009), see Chapter 2.4.3.2. Evaluation of critical loading cycle was performed in conjunction with the material damage concept proposed by Ohata and Toyoda (2004), which correlates the material damage for micro void nucleation to macro-scale mechanical parameters.

For this purpose, the stress and strain fields in the specimens, as obtained by FE-analysis, were used to identify the mechanical conditions under which the crack initiation mechanism would operate. For each of the eight specimens (RS1.1, RS1.2, RS2.1, RS2.2, CP1.1, CP1.2, CP2.1 and CP2.2) FE simulation was done for a complete number of inelastic cycles as presented in Table 25.

The equivalent plastic strain $\bar{\epsilon}_{pl}$ for the critical region in the specimen was related with the stress triaxiality $\sigma_m / \bar{\sigma}$ (σ_m is mean stress and $\bar{\sigma}$ is von Mises equivalent stress). The estimated parameters were adopted from integration points of elements close to the top or bottom beam flange surface in the plastic hinge zone. Actually, these locations correspond to the ductile crack initiation area observed in the tests. For each simulated case the location with the most severe history of effective plastic strain accumulation with stress triaxiality was chosen.

Fig. 189 presents the case of RS2.1 specimen as an example for the estimation of effective plastic strain $(\bar{\epsilon}_{pl})_{eff}$ obtained from the analysed evolution of effective backstress $\bar{\alpha}$, and cumulative history of $(\bar{\epsilon}_{pl})_{eff}$ as a function of $\sigma_m / \bar{\sigma}$ until ductile cracking.

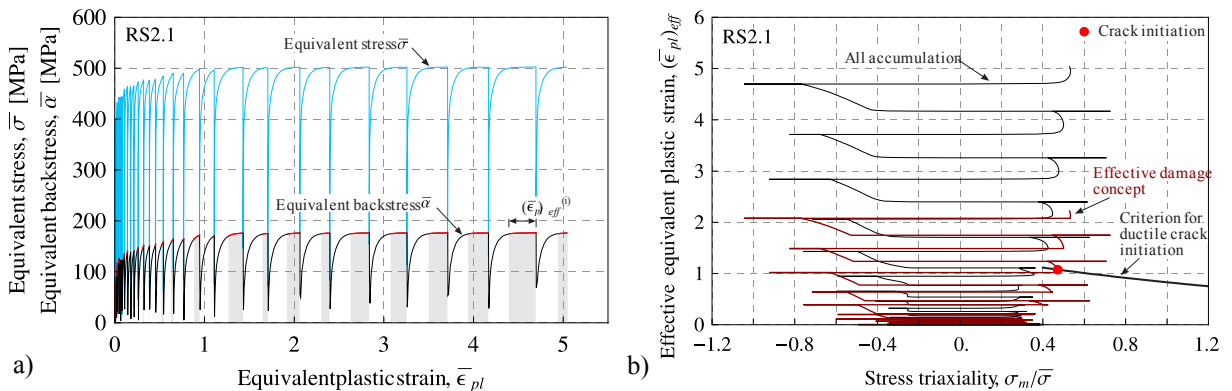


Fig. 189: Evaluation of ductile crack initiation based on the advanced 2-parameter criterion: a) evolution of equivalent backstress and estimation of effective damage strain, b) cumulative history of $(\bar{\epsilon}_{pl})_{eff}$ vs. $\sigma_m / \bar{\sigma}$
 Slika 189: Določitev nastopa duktilne razpoke na osnovi naprednega dvoparametričnega kriterija: a) potek ekvivalentnih napetosti z določitvijo efektivnih deformacij poškodb, b) prikaz zgodovine $(\bar{\epsilon}_{pl})_{eff} - \sigma_m / \bar{\sigma}$

Fig. 190 presents predicted location of local failure for specimen RS2.1 in terms of PEEQ plotted over deformed shape, at the instance of the ductile cracking criterion met, compared with the experimental result.

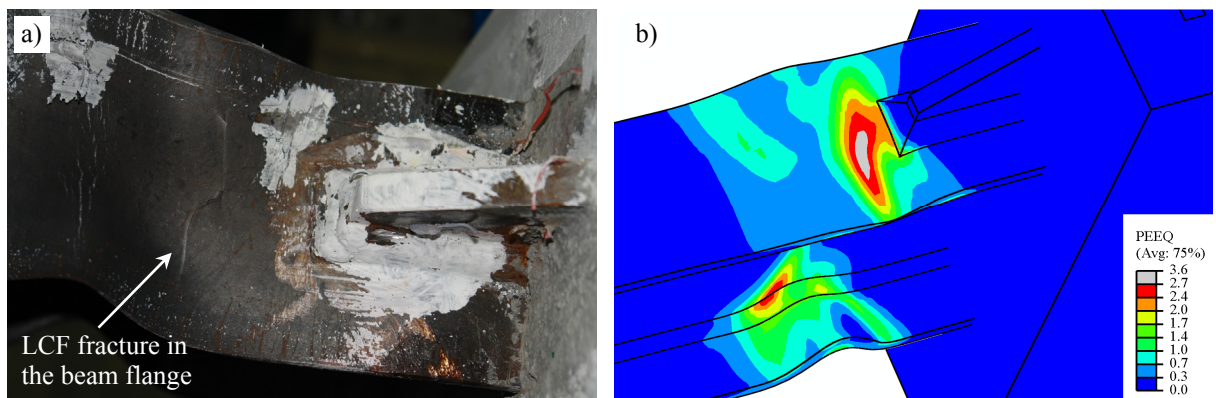


Fig. 190: Location of crack initiation for specimen RS2.1: a) experiment (deformation after the test), b) simulation (state with prediction of ductile cracking onset)
 Slika 190: Mesto nastopa duktilne razpoke za preizkušane RS2.1: a) eksperiment (deformacijsko stanje po končanem testu), b) simulacija (stanje napovedanega nastopa duktilne razpoke)

As can be observed, simulation shows close agreement with the experimentally obtained location of failure in the unstiffened beam region somewhat remote from the tip of the rib-stiffener. Also in case of the rest three RS specimens – RS1.1, RS2.1 and RS2.2 - simulation result was found consistent with the experimental response, with ductile cracking region located away from the end of the rib-stiffener in the most buckled region of the beam flange.

Similarly, high level of consistency between experimental and simulated response was noticed in all four CP specimens – CP1.1, CP1.2, CP2.1 and CP2.2. Although some local concentrations are present close to the end of the cover plate at the beam flange edges (also observed from the tests, see Figs 34 to 37, the highest concentration of plastic strain field moved from the end of the cover-plate into the buckled plastic hinge region of the unstiffened beam section, Fig. 191.

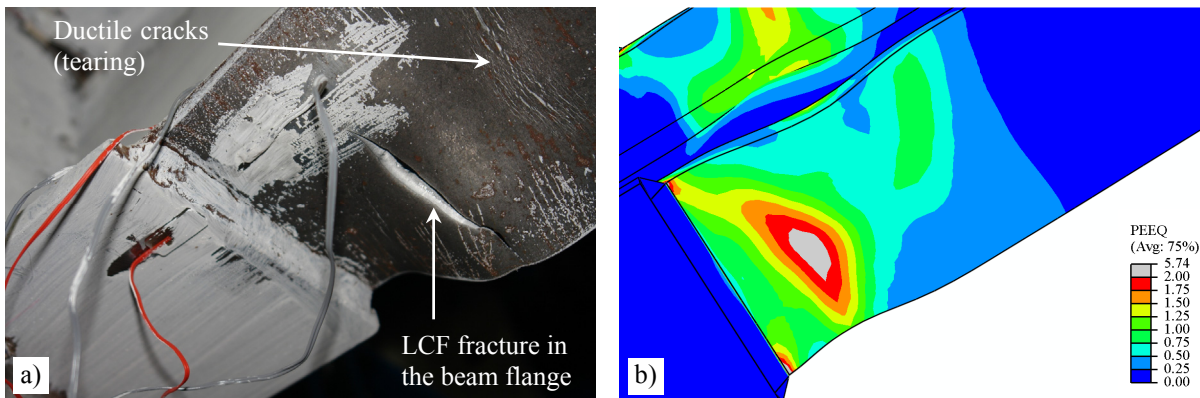


Fig. 191: Location of crack initiation for specimen CP1.2: a) experiment (deformation after the test), b) simulation (state with prediction of ductile cracking onset)

Slika 191: Mesto nastopa duktilne razpoke za preizkušane CP1.2: a) eksperiment (deformacijsko stanje po končanem testu), b) simulacija (stanje napovedanega nastopa duktilne razpoke)

Critical cycles with the onset of ductile cracking in the most buckled region on the beam flange in the plastic hinge zone as observed from the experiments and those predicted by FE simulations, applying the effective damage concept as proposed by Ohata and Toyoda (2004), is presented in Table 29. The last uncompleted cycle from the experiment with the ultimate failure of specimen, characterized by the fracture of the beam flange followed by the loss of load resistance, is reported as well.

Preglednica 29: Kritičen cikel za preizkušance testirane z naraščajočo amplitudo cikličnega obremenjevanja: eksperiment in napoved simulacije (concept efektivnih poškodb po Ohata in Toyoda (2004))

Table 29: Critical loading cycle for specimens tested with increasing cyclic loading amplitude: experiment vs. simulation prediction (effective damage concept by Ohata and Toyoda (2004))

RS specimen	simulation		experiment		CP specimen	simulation		experiment	
	$N_{crack}^{predicted}$	N_{crack}^{onset}	N_{crack}^{onset}	$N_{failure}$		$N_{crack}^{predicted}$	N_{crack}^{onset}	N_{crack}^{onset}	$N_{failure}$
RS1.1	12	10	10	14	CP1.1	14	11	11	16
RS1.2	11	10	10	15	CP1.2	13	11	11	16
RS2.1	15	13	13	18	CP2.1	16	13	13	18
RS2.2	15	13	13	18	CP2.2	15	13	13	17

As observed from Table 29, predictions for ductile cracking initiation based on the two-parameter critical condition are non-conservative for all the eight specimens subjected to variable cyclic loading. Compared to the cycle number with the first ductile cracking

observed from experiments, the applied approach results in 1 to 2 cycles more in case of RS specimens, and 2 to 3 cycles more for CP specimens.

However, in this case it is not the applied approach, but the type of the problem simulated, that is responsible for the reported mismatch. As a result of locally softened response, due to large plastic straining and consequently damage concentrations in the steel at inflection points, flange buckle amplitudes during the tests grows faster compared to the simulated response. Although local deformed beam member shows close agreement with the one from the experiment, no such prominent progress of the beam local buckling was obtained from the simulations, since no damage under LCF is accounted for in the applied cyclic material model. This is the reason for non-conservative results from the simulation.

Larger mismatch is observed in case of CP specimen, where cover-plate provides restraint to the beam flange over its complete width, causing more pronounced beam local buckling effects behind the stiffened region.

4.3.3.5.2 Prediction of crack initiation based LCF failure – proposed unified LCF approach

The main motivation for development of a new crack initiation criteria for steel components subjected to LCF loading is the limitation of already applied effective damage concept proposed by Ohata and Toyoda (2004). Namely, the effective damage concept is suitable only for components subjected to continually increasing stress/plastic strain demand, i.e. it is not appropriate for simulations with constant cyclic loading.

In case of beam-to-column joints subjected to variable stepwisely increasing cyclic loading amplitude, the effective damage approach provides acceptable results for buckled plastic hinge region, where localised continually increasing plastic strain demand is present. However, for other also critical locations with not so pronounced and continual increase of plastic strain demand, e.g. the end of the stiffened connection, it fails to provide appropriate result. Also in case of all the four specimens subjected to constant amplitude cyclic tests with small and even large amplitude, the effective damage approach failed to predict critical cycle with the LCF crack initiation.

The aim is to provide one uniform crack initiation based LCF failure criterion for structural steel components subjected to low-cycle fatigue loading with arbitrary loading amplitude history.

It is not the intention of this work to develop a comprehensive criterion for material failure mechanism based on observations of micro void formation, nucleation and their subsequent growth to final coalescence; i.e. crack initiation criterion was not defined as a specific instance in a cyclic loading at which a ductile crack of specific extent would be measured. The tough experimental clarification of a mechanism for cracking under LCF loading conditions is far beyond the scope of this study.

The onset of failure in the material was simply related to the observations of experimentally obtained strain history data, measured by uniaxial strain gauges oriented along the beam and placed in closed vicinity of location on specimen, where fracture growth on the beam flange took place during the experiments, Fig. 192a).

Measured strain-life data from particular strain gauge was analysed and divided into a part till the onset of crack and the following residual life part with crack propagation till the ultimate fracture of a structural component. Cycle with the estimated crack initiation, referred to as critical cycle, was defined as the last cycle conforming to the slope of the peak strain amplitudes characteristic for stabilised strain response.

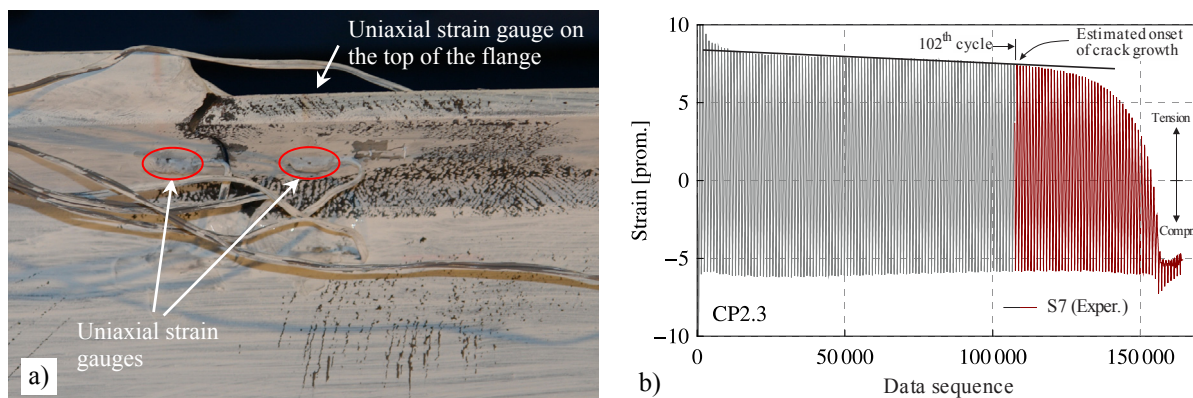


Fig. 192: Specimen CP2.3: a) strain gauges placed in the vicinity of the beam flange final fracture, b) experimentally obtained strain-life diagram with the determination of estimated onset of crack growth
 Slika 192: Preizkušane CP2.3: a) položaj merilnih lističev za deformacije v neposredni bližini končne razpoke na pasnici prečke, b) diagram poteka merjenih deformacij z določitvijo ocene začetka rasti razpoke

Information on the critical cycle number with the onset of particular observed failure instance for all the six specimens subjected to constant amplitude cycling is gathered in Table 18. The reader may also refer to the graphic representation presented in Figs 60 to 63.

The effect of eventually changed base steel material properties in HAZ of welds and other possible welding effects (residual stresses) at the end of the stiffened connection were not explicitly taken into account in the proposed criterion. However, all such effects are already implicitly taken into account by the strain measurements during the tests.

The complete procedure for the definition of derived damage curve as a criterion for LCF crack initiation is presented in the text below.

First, the mechanical conditions for LCF crack initiation were examined by finite element analyses of the four beam-to-column joints experimentally subjected to small constant amplitude cyclic loading, RS1.3, RS2.3, CP1.3 and CP2.3, and the two joints subjected to large constant amplitude cyclic loading, RS1.4 and RS2.4. In case of all the above six specimens ultimate failure occurred due to the fracture of the beam flange just behind the stiffened region in the HAZ of fillet weld.

In all the six tests taken into account the beam local buckling, if any, had limited extent. Furthermore, plastic straining was limited to narrow region across the beam flange width at the end of the stiffened region on the beam, with strain field all around bounded and not exceeding the strain limit 50 % of the applied type of strain gauges. This allowed the strain-life data to be measured at strategic positions to allow determination of critical cycle with the estimated LCF crack initiation.

In all the rest 12 specimens (all eight joints subjected to cyclic loading with stepwisely increasing cyclic amplitude and joints CP1.4 and CP2.4 subjected to cyclic loading with large constant amplitude) LCF failure occurred due to the progress of the beam local buckling in the middle of the plastic hinge zone. Due to the extremely high plastic straining in this buckled region, all strain gauges in experiments soon became overloaded and it was practically impossible to measure the actual strains.

The mechanical conditions under which the crack initiation mechanism would operate were defined for the stress and the strain field obtained by FE-analyses. The two-parameter criterion in which equivalent (accumulated) plastic strain $\bar{\epsilon}_{pl}$ and stress triaxiality $\sigma_m / \bar{\sigma}$ were adopted as mechanical parameters that control LCF cracking was applied. For the first group of six specimens (RS1.3, RS2.3, CP1.3, CP2.3 and RS1.4 and RS2.4) the equivalent

plastic strain at the crack initiation point as observed during experiments was related with the stress triaxiality for complete loading history till the critical loading cycle, which was already defined from the experimentally obtained strain life-data in the vicinity of crack propagation, Fig. 193.

The estimated stress and strain parameters from FE-analyses were adopted from locations corresponding to the crack initiation area observed in experiments: beam flange at the end of the stiffened region, at the flange edge and at the flange mid-width, for CP and RS joint specimens, respectively.

It should be noted that high level of consistency in terms of failure mechanism and critical location in the unstiffened beam region was found between experimental and simulated response for all the six specimens.

For the group of eight specimens subjected to cyclic loading with stepwisely increasing amplitude, the mechanical conditions for the LCF crack initiation mechanism were also defined from FE simulations. However, as already stated, information on the critical loading cycle from experiment could not be obtained for this group of specimens. Therefore, results from Table 29 defined by using effective damage concept according to Ohata and Toyoda (2004), in conjunction with damage curve for S355 J2 steel from the literature (Bleck et al., 2009. Feldmann et al., 2009), were adopted.

It is important to emphasize that the accuracy of mechanical conditions determined in the latter case remains unaffected by the non-conservative results presented in the Table 29, as it still remains exclusively dependent upon parameters defined by the authors of the proposed effective damage procedure.

Resulting points presenting the mechanical conditions for the LCF crack initiation mechanism, obtained following the described two approaches for both groups of specimens (14 beam-to-column joint specimens in total), are presented in Fig. 193.

Depicted curves for analysed first group of six specimens, RS1.3, RS2.3, CP1.3, CP2.3, RS1.4 and RS2.4, belong to the cyclic loading until the estimated onset of cracking defined from experimental strain data, and include points with the maximum value of the stress triaxiality reached per cycle.

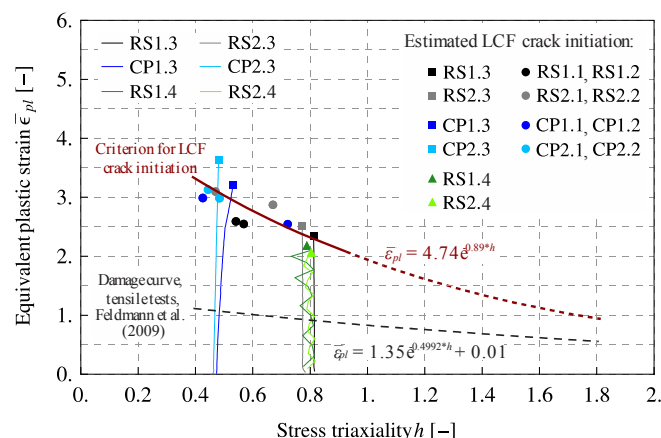


Fig. 193: Proposed damage curve for LCF crack initiation
Slika 193: Predlagana krivulja za nastanek nizkociklične razpoke

For the rest two specimens, CP1.4 and CP2.4, the corresponding critical points, to be included in the diagram in Fig. 193, were not defined, since the effective damage concept proposed by Ohata and Toyoda (2004) failed to provide the critical cycle with crack initiation within the

range of all the performed cycles in the tests, see Table 8. The two tests are used later as a part of verification of the proposed LCF damage curve, as described hereinafter.

As shown in Fig. 193, all of the obtained 14 critical points present reasonable and consistent result. Obtained critical local equivalent plastic strain required to initiate ductile cracking depends largely on the stress triaxiality. When the stress triaxiality is increased, critical equivalent plastic strain decreases.

Following observations of other authors from the literature (Ohata, Toyoda, 2004. Bleck et al., 2009. Feldmann et al., 2009), model of exponential decrease was used to define mathematical relation between the two mechanical parameters selected to describe LCF crack initiation. All 14 data points obtained on the basis of experimental tests and FE analyses were best fit to an exponential function of the form $a \cdot \text{Exp}(-b \cdot h)$, where h is the stress triaxiality. Parameters a and b were numerically defined to obtain the following equation:

$$\bar{\varepsilon}_{pl} = 4.74 \cdot \text{Exp}(-0.89 \cdot h). \quad (35)$$

It is necessary at this stage to note that the defined LCF damage curve only applies to the range of parameter h for which experimental results are available. Accordingly, dotted line is drawn outside the examined region in Fig. 193.

As already mentioned, the validity and consistency of the proposed LCF failure criterion was verified against CP1.4 and CP2.4 test results. As can be observed from Figs 194 and 195, in both cases simulation shows close agreement with experimental results in terms of deformed shape and location of critical region on the buckled beam flange in terms of accumulated plastic deformation.

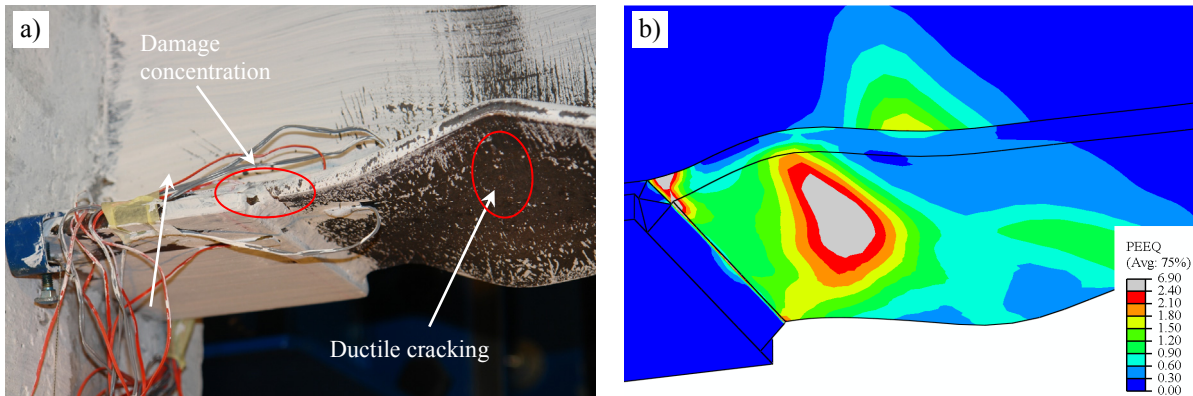


Fig. 194: Location of crack initiation for specimen CP1.4: a) experiment (24th cycle) and b) simulation (at the instance of LCF cracking criterion met in 19th cycle)

Slika 194: Območje nastopa razpok za preizkušane CP1.4: a) eksperiment (24. cikel) in b) simulacija (deformacijsko stanje ob izpolnjenem kriteriju za nastop nizkociklične razpoke v 19 ciklu)

On the basis of the proposed LCF cracking criterion, critical cycle from simulation was evaluated for CP1.4 and CP2.4 specimen. For that purpose, two critical regions on the beam flanges were taken into account, see Figs 194b and 195b: at the buckled flange in the centre of plastic hinge region, and at the beam flange edge just behind the fillet weld at the end of the cover-plate.

According to the proposed criterion, in case of CP1.4, onset of cracking due to the beam local buckling is present in 19th cycle, whereas cracking at the flange edge already in 17th cycle. Although somewhat larger plastic strain concentrations at the end of the stiffened region, critical plastic region in the buckled zone is significantly larger, which is consistent with experimental result, where final fracture occurred in the buckled beam flange region.

Simulated response in combination with the proposed cracking criterion proved to be fully consistent with observations from the experiment, where first ductile cracks on the buckled beam flange were observed in 22th cycle.

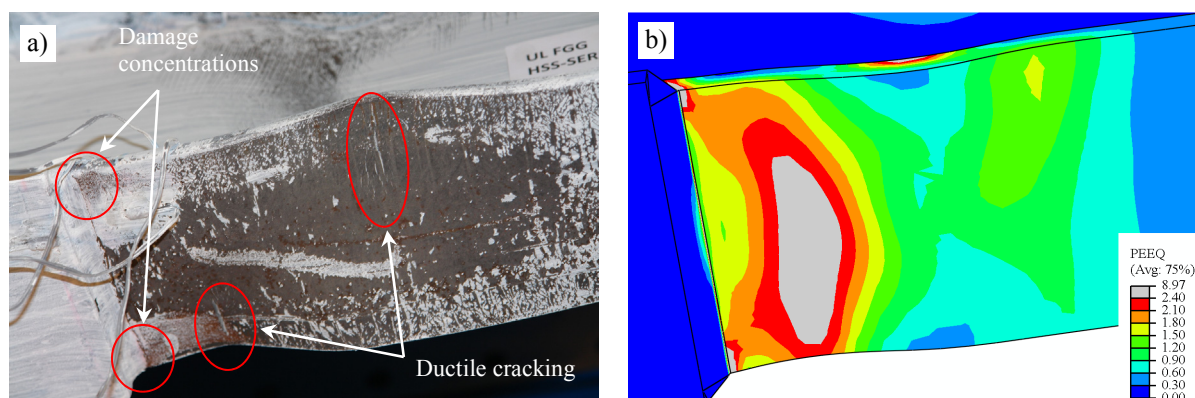


Fig. 195: Location of crack initiation for specimen CP2.4: a) experiment (55th cycle) and b) simulation (at the instance of LCF cracking criterion met in 33th cycle)

Slika 195: Območje nastopa razpok za preizkušane CP2.4: a) eksperiment (55. cikel) in b) simulacija (deformacijsko stanje ob izpolnjenem kriteriju za nastop nizkociklične razpoke v 33 ciklu)

Similarly, in case of CP2.4 specimen, according to the proposed criterion, the onset of cracking due to the beam local buckling and separately the instance of cracking at the flange edge just behind the fillet weld, are both present in 33th cycle. Again, in spite of somewhat intensive plastic strain concentrations at the end of the stiffened region, critical plastic region in the buckled zone is significantly larger. The result is consistent with the experimental response, where final fracture occurred, after the first ductile cracking of the beam flange was observed in 45th cycle.

In addition, consistency of the proposed LCF crack initiation criterion was checked against the experimental response of all eight joint specimens subjected to cyclic loading with stepwisely increasing amplitude. In this case, the analysis is not about the most critical region in the buckled zone of the beam, which was already used for the derivation of the proposed LCF cracking criterion.

In this case local region just behind the end of the stiffened region (fillet weld HAZ), where damage concentrations with minor cracking were also observed in the experiments, though not resulting to the final fracture, was taken under investigation.

Evolution of combined stress-strain damage index in terms of points with the maximum value of stress triaxiality reached per cycle, for the eight joint specimens subjected to cyclic loading with increasing amplitude, is depicted in Fig. 196.

The presented curves belong to the most critical finite element in the observed local region on the beam flange. Loading history till the predicted cycle with the onset of LCF cracking already defined for the buckled beam flange region of particular specimen is denoted with thicker curve.

The subsequent part of each curve belongs to the residual life of specimen, where cracks in the buckled flange of the plastic hinge region are already propagating to the ultimate fracture. Compared to the accumulated plastic strain demand in the residual part of the curves from simulations, in reality the demand is somewhat reduced due to larger flexural strength degradation present in the plastic hinge zone of the beam as a result of progressive material damage.

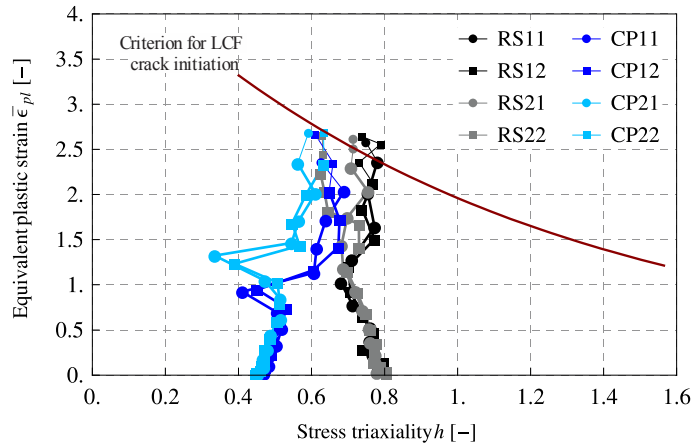


Fig. 196: Evolution of combined stress-strain damage index from the end of the stiffened region of the beam against the proposed LCF crack initiation criterion for complete loading history of all eight joint specimens subjected to cyclic loading with increasing amplitude

Slika 196: Razvoj kombiniranega indeksa poškodb napetost-deformacija za območje tik za ojačanim delom prečke v primerjavi s predlaganim kriterijem za nastop nizkociklične razpoke za celotno zgodovino cikličnega obremenjevanja spojev z naraščajočo amplitudo

As observed from the diagram, in case of all the eight beam-to-column joints, mechanical condition in the observed local region at the end of the stiffened beam section is very close or even reaches (in case of RS joint specimens) the proposed crack initiation based LCF failure criterion.

Also in this case all the FE results in combination with the proposed cracking criterion show close agreement with the experimental results. Namely, as already stated several times in the document, for this group of joints there also were locations on the beam flanges at the end of the stiffened region (fillet weld HAZ: flange mid-width and flange edge, for RS and CP specimens, respectively), where damage concentrations with moderate cracking were observed in the experiments, Fig. 197. In case of CP specimens, minor cracks only were observed at the end of the transverse fillet weld, whereas more prominent notch induced cracks were observed at the end of the rib-stiffener in case of all RS joints.

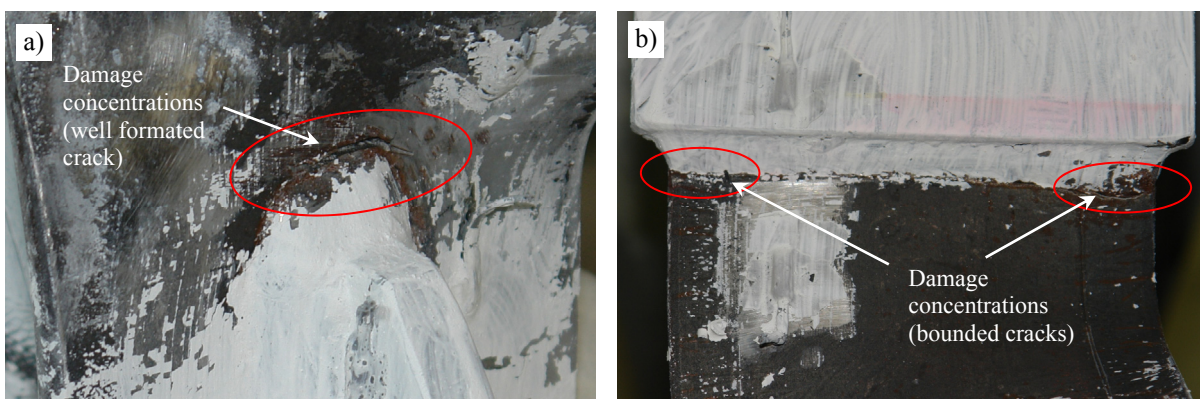


Fig. 197: Damage concentrations in the beam flange at the end of the stiffened region: a) RS1.1, b) CP2.2
 Slika 197: Koncentracije poškodb v pasnici prečke tik za ojačanim delom: a) RS1.1, b) CP2.2

4.4 Summary and conclusions

Complete finite element model development in Abaqus was presented, starting from finite element type selection and finite element discretisation mesh issues appropriate for modelling beam-to-column joints.

To this end, elastic mesh convergence study was conducted first on the subassembly of typical beam-to-column joint, simulating local behaviour of the beam-column connection. From the results of elastic convergence study it is clear that longitudinal stress distribution along the beam-to-column flange interface is sensitive to both type of finite element and mesh density applied. Therefore, these factors must be carefully considered when evaluating the large stress/strain concentration factors.

Solid-element models were utilised, rather than shell-element models as in preliminary analysis, in order to study realistic stress and strain distributions in the stiffened beam-to-column connections. As an agreement between computational efficiency on one side, and obtained accuracy on the other, the use of C3D8R or at the most C3D8I elements was suggested. In addition, mesh characterised by the largest element in-plane dimensions around $b_f/20$ mm should be used in the regions of the beam flange where high stress and strain concentrations are expected. Meshes comprising at least 2 solid elements through the thickness of webs and 4 elements through the thickness of flanges of I and H profiles as well should be used to obtain reasonable accuracy of results.

To reduce computational effort, number of variables in all the finite-element models of beam-to-column joints was reduced by using simple beam finite elements to model parts of the beam and the column that remain elastic throughout the entire analysis.

To account for a nonlinear material behaviour, nonlinear material stress-strain definitions were used for structural steel as well as for concrete material subjected to monotonic loading. In addition, much attention was paid to the calibration of a nonlinear isotropic/kinematic hardening cyclic constitutive model for the steel components of a joint subjected to arbitrary cyclic loading conditions.

In the first phase of the inelastic mesh convergence study, simulations of experimentally obtained response of cantilever I and H beam profiles were performed. The ultimate flexural behaviour of the beams, characterised by the occurrence of the beam local buckling in the beam plastic hinge zone, was found strongly dependent on the number of C3D8R finite elements used across the beam flange width: too little finite elements across the free-length of the beam flange, generally resulted in too stiff response. To overcome the problem, mesh with C3D8I elements for discretisation of the stiffened region including plastic hinge zone of the beam was used in all further models, with the same element in-plane dimensions and the number of elements through the flanges and the web of the beam section as defined in elastic convergence study. The other solid parts of a beam-to-column joint, comprising steel plates and concrete column encasement, which are subjected to minor extent of local bending, are modelled with computationally more efficient C3D8R elements.

The ultimate flexural resistance corresponding to the complete development of the beam local buckling was found highly dependent on value of the initial beam local imperfection applied in FE model. Based on the finite-element model calibration against the experimental monotonic response of the cantilever beams, local beam imperfection amplitude in terms of out-of-square deformation $k + k' = 0.8 \% b_f$ was chosen to be included in all the subsequent models comprising I and H beam profiles.

Simulated cyclic response of all the sixteen full-strength beam-to-column joints subjected to variable and constant amplitude cyclic loading showed close agreement with the experimental results for both global load deflection behaviour as well as local inelastic strain response. The developed finite-element model was able to capture all the key features of local inelastic beam response with satisfactory accuracy, e.g. the extent of plastic strain field in the plastic hinge zone on the beam and in the vicinity of the stiffened connection, beam local buckling shape as well as beam out of plane displacements.

The two main response parameters of the full-strength beam-to-column joint subjected to cyclic loading are flexural ultimate beam resistance and LCF degradation of the steel material. As observed from the experimental tests, material LCF degradation can be present with, in case of large amplitude cycling, or without the onset of beam local buckling, in case of small amplitude cyclic loading. While it is expected that design criteria should assure the full strength connection to allow for the full development of the beam plastic rotation capacity, it may happen, due to material defects or even insufficient geometric details of welded connection, that premature failure of a joint results from crack occurrence in the stiffened connection detail, e.g. due to stress/strain raisers at the end of the rib-stiffener like in case of specimens RS1.4 and RS2.4.

While the applied finite-element model consistently accounts for the beam local buckling in the plastic hinge zone, it does not allow for the material degradation due to the LCF effects. To overcome this limitation, phenomenological approach using stress/strain response indices was used to simulate LCF behaviour of beam-to-column joint up to the cracking initiation phase.

To this aim, material damage concept under reverse loading proposed by Ohata and Toyoda (2004), which correlates the material damage for micro void nucleation to macro-scale mechanical parameters, was applied for the prediction of the onset of ductile cracking for all eight joints subjected to cyclic loading with increasing amplitude.

The applied effective damage concept, along with the critical condition for ductile cracking adopted from literature, is applicable for the estimation of ductile cracking load of specimens of arbitrary geometry. However, the concept is appropriate only for specimens subjected to cyclic loading with increasing amplitude.

To overcome this limitation, new crack initiation based LCF failure criterion for structural steel components subjected to arbitrary cyclic loading conditions was proposed. In addition to the response parameters deduced from results on small-scale specimens as obtained from literature, the proposed LCF cracking criterion was derived also directly from the results of large scale beam-to-column joint cyclic tests.

Although the utilised methodology for derivation of the proposed damage curve does not base on observations of micro scale material failure mechanisms, estimated instance and location of the LCF crack initiation (according to the proposed criterion) were found highly consistent with the experimental response.

5 PARAMETRIC NUMERICAL STUDY

5.1 Introduction

The primary focus of the parametric numerical study is to explore any potentially adverse beam member size effects on the RS and CP full-strength joint response. Accordingly, additional cases comprising a set of different I and H beam profiles, typically used in the European design practice, within the range of practically applicable member sizes, were analysed in order to support and validate the proposed detailing rules as well as design procedure for both the stiffened beam-to-column connections.

It is important to derive plastic as well as seismic design rules for monotonic and cyclic loading conditions, and for the limit states characterised by different possible types of failure. In case of full-strength joints failure may occur due to the loss of strength and stiffness because of the beam local buckling in the plastic hinge zone, ductile low-cycle fatigue (LCF) fracture in the most buckled beam flange region, and finally ductile/non-ductile (the latter not desired) LCF fracture of a stiffened connection detail outside the intended plastic hinge region with or without the presence of the beam local buckling in the plastic hinge zone.

At the same time the research work brings forward valuable information on the ultimate behaviour of steel beams in combination with the two studied full-strength stiffened beam-to-column connections under monotonic as well as cyclic loading. According to the tendency of the recent research activities to better understand the overall performance of steel moment-resisting frames, importance was put on the main two response parameters that govern the ultimate behaviour of steel beams and consequently performance of full-strength beam-to-column joints, namely the rotation capacity and the beam flexural ultimate resistance.

As already noted in Chapter 3.3.1, beam-to-column joint member sizes used in the experimental cyclic tests were indirectly limited by composite column bearing capacity. It is well known fact within engineering community that extrapolation of joint behaviour prediction to connections of a substantially different size should be undertaken with care. Indeed, as it was clearly shown in Chapter 3.4 by the results of both variable and constant cyclic loading tests, the ability of beams to develop inelastic rotation may be somewhat diminished as beams become deeper and heavier.

All the basic modelling issues used in the complementary numerical study follow the outcomes of numerical simulations performed during calibration of the developed numerical model for beam-to-column joints presented in Chapter 4, including finite element mesh properties, finite element types, material nonlinearity along with methodology to account for geometric nonlinearity.

Remark should be made in relation to the above discussion that no actual material imperfections, geometric imperfections, residual stresses and strains (due to rolling and welding), and flaws or defects, which can be present in real structure, were included in FE models. In addition, this also implies the fact that the inherent restraints associated with joining thicker plates in case of heavier member profiles, are not accounted for in numerical models. The author is completely aware that these parameters may substantially affect performance of welded beam-to-column connections. However, complementary nonlinear FE analysis can provide considerable insight into the likely behaviour of complex welded stiffened connections.

This chapter consists of three subsections. The first one is dedicated to the additional exploration of the effect of high level of column axial compressive load on the beam-to-column welded interface, to support the experimental results with numerically obtained response indices. The remaining two chapters present the response of additional RS and CP full-strength beam-to-column joints subjected to monotonic and cyclic loading.

5.2 Influence of column axial compressive load

Except for minor cracks in the concrete encasement at the very local region around beam-to-column connection that had no detrimental effect on joint behaviour, the presence of column axial compressive load caused no apparent detrimental effect on the welded stiffened beam-column flange interface that would undermine the cyclic behaviour of the joints. From a detailed observations of the test results conclusion was made that the applied level of the column compressive axial force, being around 40 % of the actual composite column plastic resistance to compression $N_{pl,c}^{act}$, had no effect on the overall cyclic behaviour of the joints.

Our intention was to examine the stress state at the beam-column flange interface influenced by the presence of different levels of column compressive axial load. The load pattern is referred to the case of single-sided moment-resisting beam-to-column joint from a dual system structural frame, where the column is a part of bracing system and at the same time adjacent moment-resisting bay, see Fig. 22. During the strong earthquake horizontal actions, substantial axial compressive forces may reveal in columns of bracing systems.

For the numerical study three different levels of column axial compressive load were considered to observe its effect on welded stiffened beam-column flange interface stress state:

- zero level;
- the same level as the one used in the experimental cyclic tests: $\approx 40\% N_{pl,c}^{act}$ (≈ 3000 kN);
- $60\% N_{pl,c}^{act}$ (4870 and 4780 kN for the large and the small column, respectively. For description of both composite column cross-section characteristics see Chapter 3.3.1).

The last level of column compressive force was selected in order to explore possible negative effects in case where axial compressive force is higher than half the corresponding column plastic resistance to compression. Higher values of column axial compressive load were not tried to simulate. It is interesting to note at this stage that provisions from EN 1998-1 limit the maximum value of $N/N_{pl,c}$ ratio, accounting for member design resistance, to 0.30 for all types of composite columns.

FE analyses were performed on the same models as those used for the simulation of the experimental tests on specimens RS1, RS2, CP1 and CP2, presented in Chapter 4. The reader should bear in mind for possible effect of the column lateral plates, see Figs 17 and 18, on the distribution of stresses in particular column as presented in the figures hereinafter.

Analyses with both considered non-zero levels of column axial compressive load were computed with Abaqus/Standard solver, whereas simulation without column axial load was run in Abaqus/Explicit, since un-convergence issues had been encountered in Abaqus/Standard due to the softening response of concrete in tension parts of column in bending.

Compared to the case without the column axial force, no difference in global moment-rotation response of RS1, RS2, CP1 and CP2 joints was noticed for both the two non-zero levels (40 % and 60 % of $N_{pl,c}^{act}$) of column axial load.

Distribution of Mises stresses in beam-column web-centre plane around beam-to-column connection for the three different column compressive axial load levels in case of specimens RS1 and CP1 is presented in Figs 198 and 200. Steel parts of the composite columns are presented only. For each of the considered three column axial load levels two states are presented: stress state after the applied column axial load, and at the instance of the maximum joint flexural resistance under the subsequently applied transverse loading at the end of the cantilever beam.

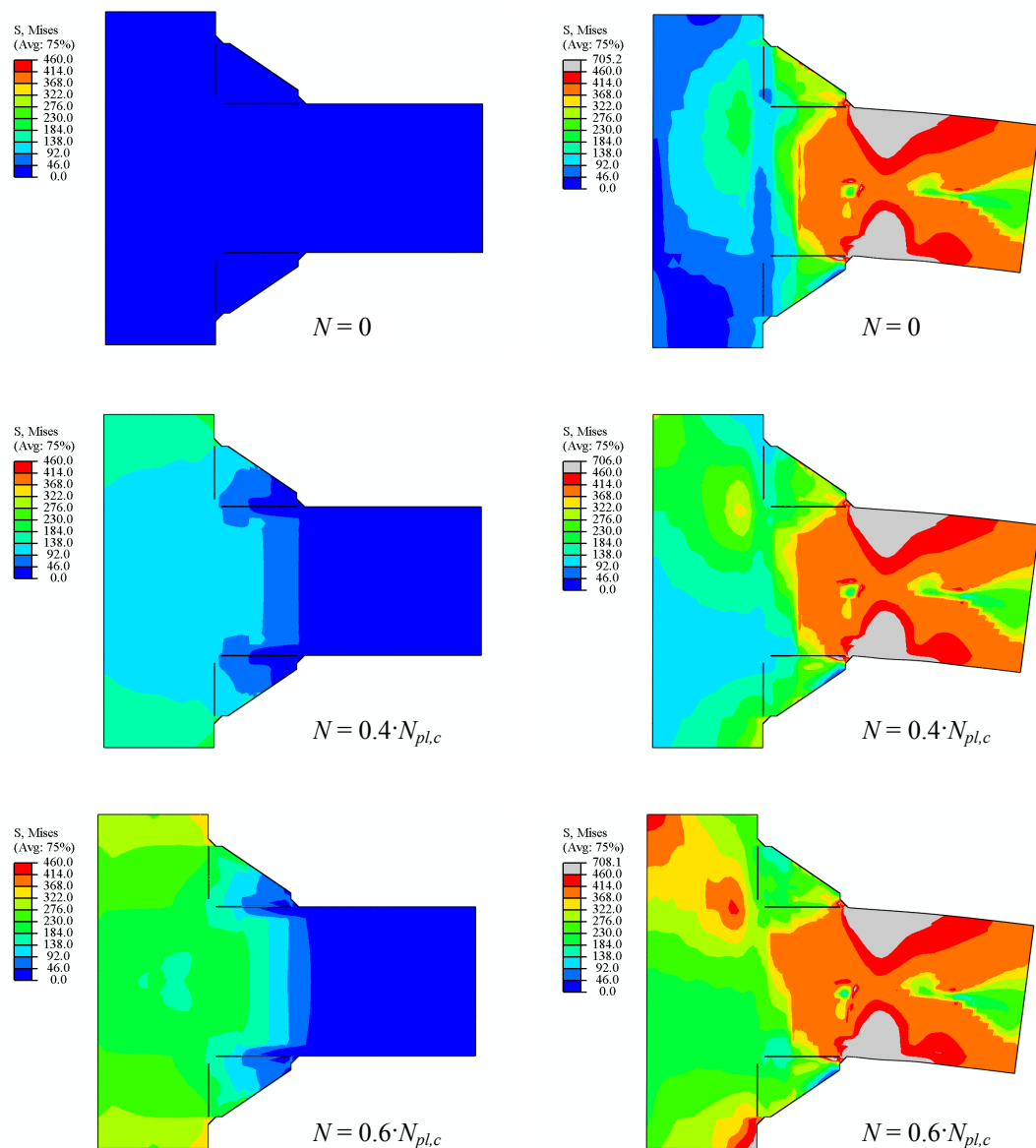


Fig. 198: Mises stress distribution in beam-column web-centre plane of joint RS1 for the considered three levels of column axial load: after the applied column axial load (left column), and at the maximum joint flexural resistance (right column)

Slika 198: Razporeditev Misesovih napetosti v ravnini stojine prečke in stebra za spoj RS1 za vse tri upoštevane nivoje tlačne osne sile v stebri: po vnosu osne sile v stebri (lev stolpec) in v trenutku dosežene mejne upogibne nosilnosti (desen stolpec)

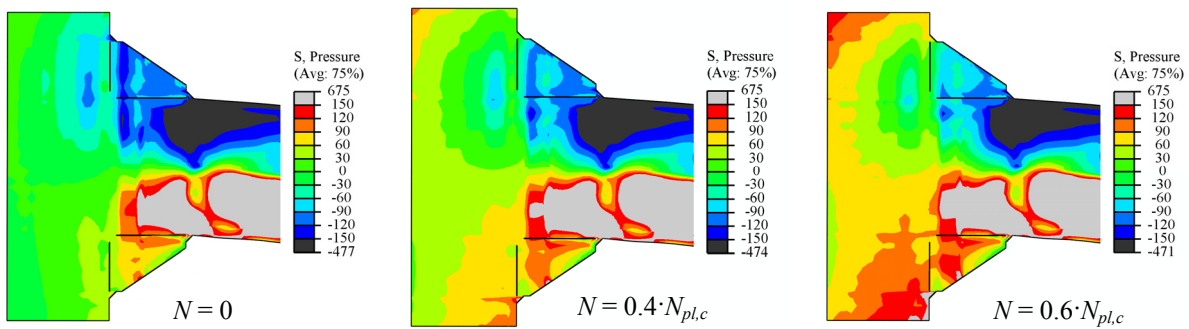


Fig. 199: Hydrostatic pressure distribution in beam-column web-centre plane of joint RS1 at its maximum flexural resistance for the considered three levels of column axial load

Slika 199: Razporeditev hidrostatskih pritiskov v ravnini stojine prečke in stebra v trenutku dosežene mejne upogibne nosilnosti spoja RS1 za vse tri upoštevane nivoje tlačne osne sile v stebra

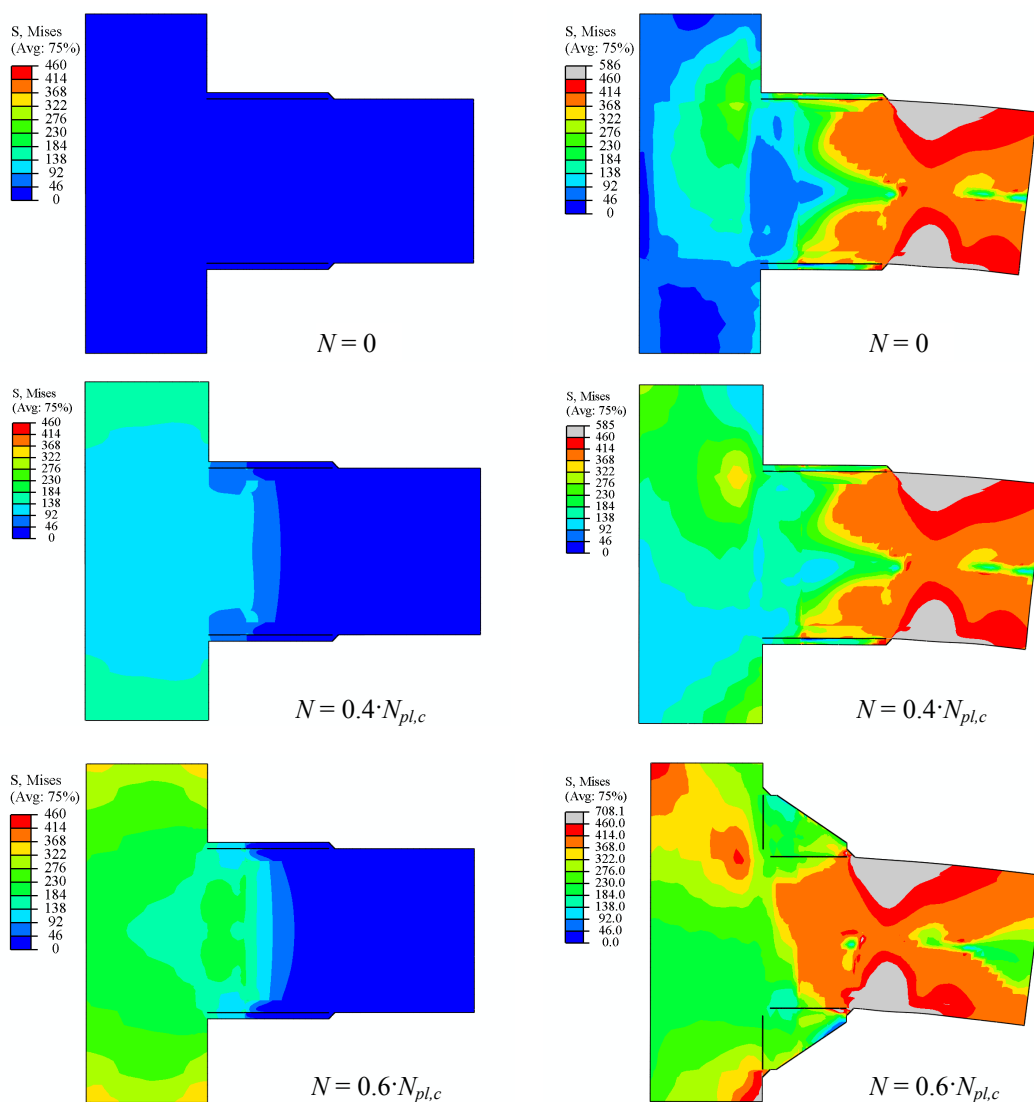


Fig. 200: Mises stress distribution in beam-column web-centre plane of joint CP1 for the considered three levels of column axial load: after the applied column axial load (left column), and at the maximum joint flexural resistance (right column)

Slika 200: Razporeditev Misesovih napetosti v ravnini stojine prečke in stebra za spoj CP1 za vse tri upoštevane nivoje tlačne osne sile v stebra: po vnosu osne sile v stebra (lev stolpec) in v trenutku dosežene mejne upogibne nosilnosti (desen stolpec)

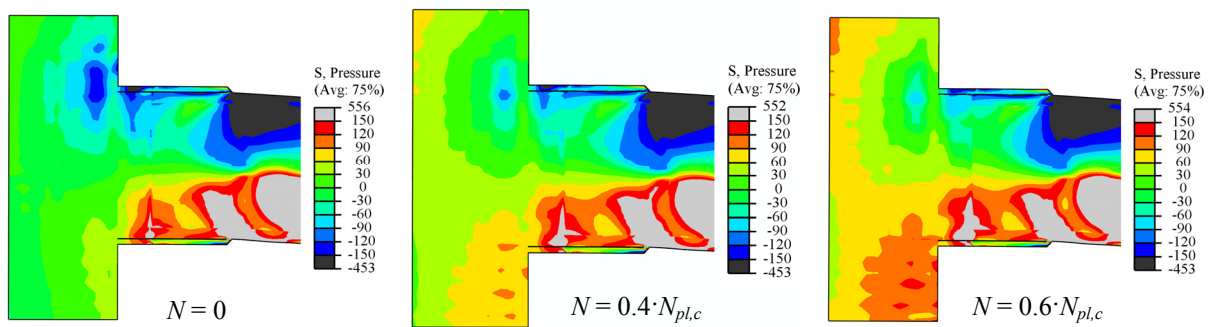


Fig. 201: Hydrostatic pressure distribution in beam-column web-centre plane of joint CP1 at its maximum flexural resistance for the considered three levels of column axial load

Slika 201: Razporeditev hidrostatskih pritiskov v ravnini stojine prečke in stebra v trenutku dosežene mejne upogibne nosilnosti spoja CP1 za vse tri upoštevane nivoje tlačne osne sile v stebri

From distribution of Mises stresses in the region around beam-to-column connection one can easily observe that increased level of column compressive axial load causes greater stress concentrations around beam flange-column flange interface in tensioned part of the beam for both RS and CP joint configurations.

Further evaluation of column axial compressive load effect on the local beam-to-column welded connection was performed by using stress response indices, namely pressure index PI , and triaxiality index TI .

The pressure index PI is defined as the hydrostatic stress (mean stress) σ_m divided by the yield stress σ_y and is a negative number for tensile hydrostatic stresses, Figs 199 and 201. A large tensile (negative) hydrostatic stress is often accompanied by large principal stresses and generally implies a greater potential for either brittle or ductile fracture.

The triaxiality index TI is defined as the hydrostatic stress σ_m divided by the Mises stress $\bar{\sigma}$. The stress triaxiality ratio is an important quantity when considering ductile rupture of metals, where high absolute value of triaxiality ($0.75 < |TI| < 1.5$) can cause large reduction in the rupture strain of metals. Very high triaxiality ($|TI| > 1.5$) can result in a brittle behaviour.

Distribution of both the selected fracture indices PI and TI across the beam flange in tension at the face of the column flange for RS1 and CP1 joints is presented in Fig. 202. The observed stress state corresponds to the state at maximum joint flexural resistance.

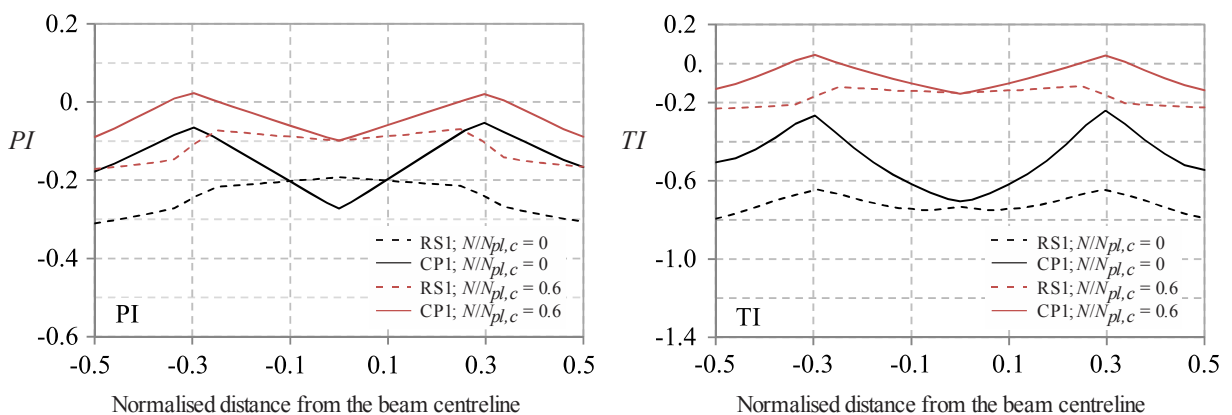


Fig. 202: Fracture indices for RS1 and CP1 beam flange in tension at the face of the column for the state at the maximum joint flexural resistance

Slika 202: Indeksa poškodovanosti za pasnico prečke v nategu ob pasnici stebra v trenutku dosežene mejne upogibne nosilnosti spojev RS1 in CP1

Compared to the case without column axial load, absolute values of both PI and TI indices are diminished in case of high level of column axial compressive force. In particular, in case of PI this means lower tensile (negative) hydrostatic stresses, i.e. decreased likelihood of fracture occurrence, while values TI moved closer to the positive region, where voids in material can grow under plastic straining. However, values of TI still remain small and mainly negative. The observations clearly show that column axial compressive load level up to 60 % of composite column plastic resistance to compression should not considerably increase the likelihood either of ductile or brittle fracture in the welded beam-to-column connection.

5.3 Behaviour of stiffened beam-to-column joints

5.3.1 Complementary set of stiffened joints

Basic parameter controlling the range and application of the complementary numerical analysis is a beam member cross-section type and size. Namely, according to the basic seismic design concept of full-strength welded stiffened beam-to-column moment-resisting connections applied in this study, it is the ultimate behaviour of the steel beam that deeply influences the overall performance of the joint.

In order to complement the set of beams that was already experimentally tested (IPE240, IPE270), additional eight different European hot rolled I and H beam profiles were selected to design sixteen beam-to-column RS and CP full-strength joints for the simulation of their response under monotonic and cyclic loading, Fig. 203. Summary information on all the RS and CP joints used for the complementary study, with the total number of simulations performed, is presented in Table 30.

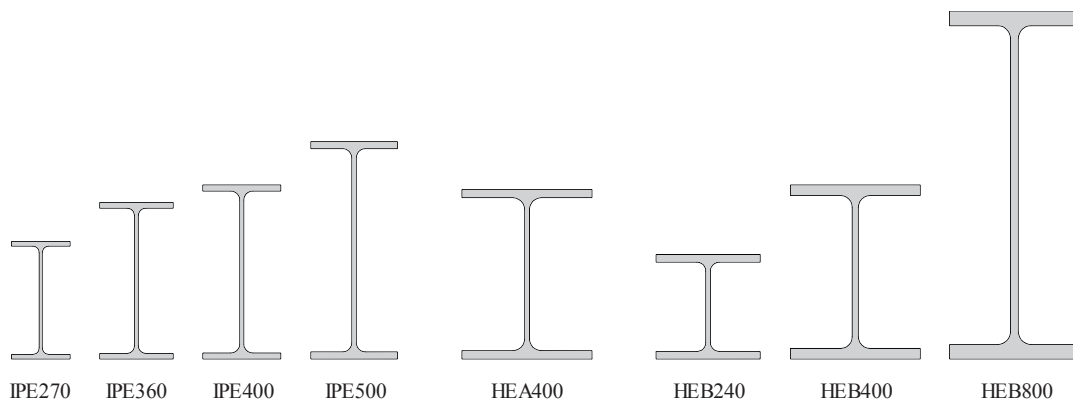


Fig. 203: I and H cross-sections used for the beams (actual relative geometric ratio preserved)
Slika 203: I in H prečni prerezi uporabljeni za prečke (dejansko relativno geometrijsko razmerje)

All the sixteen stiffened beam-to-column joints were designed according to the detailing and design guidelines already used to construct the test specimens, as presented in Chapters 3.2 and 3.3.1.

Strong column/weak beam requirement from EN 1998-1 was used to design all the stiffened joints. In order to satisfy the design provisions as well as to provide stiff column web panel response, additional contribution from transverse web stiffeners of thickness equal to the thickness of the beam flanges was taken into account for all the joints.

Behaviour of the stiffened joints, with the strong column/weak beam requirement applied, does not depend much on the column response, which is designed to remain elastic throughout the applied loading history. For the sake of using Abaqus/Standard solver type of analysis without un-convergence issues due to the nonlinear response of concrete, and more

economic job runtimes, all beam-to-column joints designed for this purpose comprise pure steel columns, rather than the concrete encased ones.

Preglednica 30: Spoji RS in CP uporabljeni v parametrični študiji
Table 30: RS and CP joints used for the complementary numerical study

Beam cross-section type	Column	Stiffened joint type	Loading	Tot No. of simulations
I	IPE270	RS and CP	monotonic and cyclic	32
	IPE360			
	IPE400			
	IPE500			
H	HEA400	RS and CP	monotonic and cyclic	32
	HEB240			
	HEB400			
	HEB800			

Single sided beam-to-column joints only were simulated, since the response of stiffened connection with the ultimate performance of the steel beam was put under investigation in this research. Further steps in the design of double-sided joint configuration is a matter of column design along with its web panel details, which is certainly beyond the scope of the work.

Complete FE model of a beam-to-column joint in Abaqus represents a typical subassembly from a steel frame in which points of contra-flexure of the beams and columns are located near the mid-lengths, see Fig. 204.

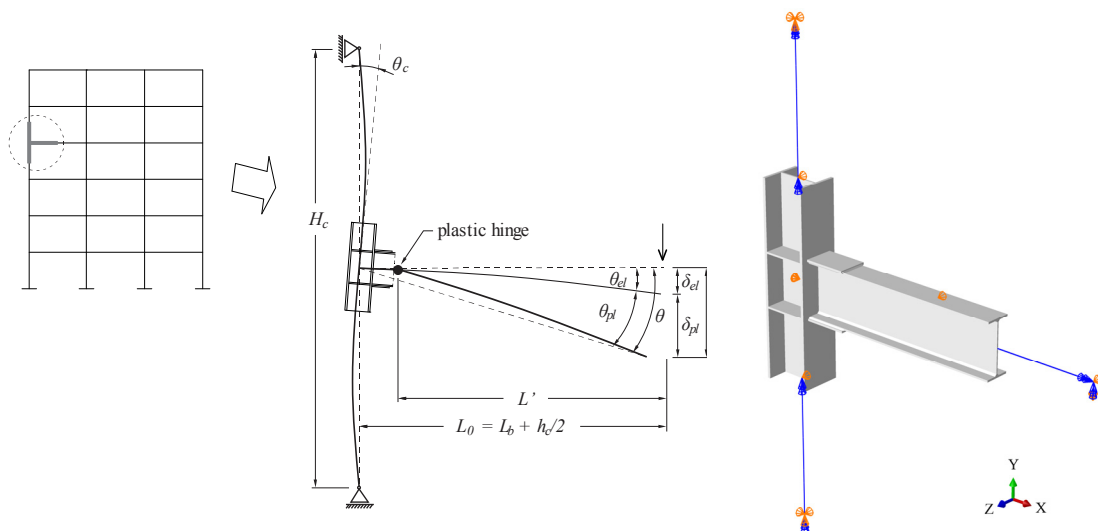


Fig. 204: Static model and geometry of single-sided beam-to-column joint FE model
Slika 204: Statični model in geometrija numeričnega modela enostransko vpetega spoja prečka-steber

To reduce the computational cost of FE models, a decision was made to use simple beam finite elements (a 2-node linear beam in space, element B31 from Abaqus element library) to model parts of the beam and the column that remain elastic throughout the entire analysis, Fig. 204. However, portions of the beam and the column near the beam-to-column connection were modelled with 3D solid elements (C3D8R and C3D8I). The same modelling issues as presented in Chapter 4.2.8 were applied for this purpose. Typical mesh refinement on the beam flange near the stiffened connection for RS and CP joints is presented in Fig. 205.

Monotonic and cyclic displacement control loading protocols were applied at the free end of the cantilever beam. No column axial force was considered in all the cases. All other basic modelling assumptions, including boundary conditions and local geometric imperfections on the beam, followed the outcomes of the numerical model calibration phase presented in Chapter 4. Note should be added regarding the application of butt rather than fillet welds joining the rib-stiffener plate to the beam and column flange in case of all the applied H beam profiles. This is due to considerably thicker rib-plates needed in case of H beam profiles compared to those used for I profiles, Fig. 206. The same cover-plate welding details were considered in case of all the CP joints.

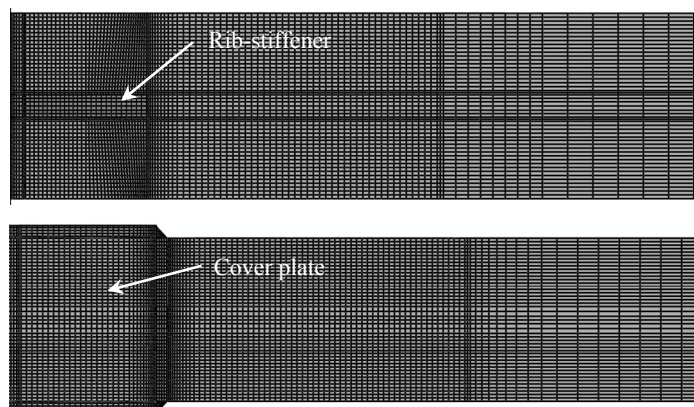


Fig. 205: Typical mesh refinement on the HEB400 beam flange for RS and CP joints
Slika 205: Tipična zgostitev mreže končnih elementov na pasnici prečke HEB400 za spoja RS in CP

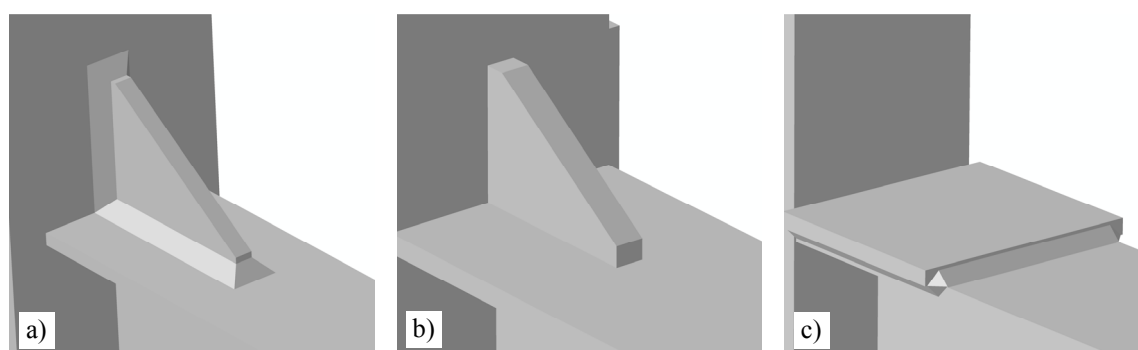


Fig. 206: Details of the stiffened beam-to-column connection models: a) RS joint in combination with beam IPE500, b) RS joint with beam HEB400, and c) CP joint in combination with beam HEB400
Slika 206: Detajli modelov ojačanih spojev prečka-steber: a) spoj RS v kombinaciji s prečko IPE500, b) spoj RS s prečko HEB400 in c) spoj CP v kombinaciji s prečko HEB400

It has been early underlined by the research activities (Kuhlmann, 1989. Mazzolani, Piluso, 1992. Gioncu, Mazzolani, 2000. Piluso, Rizzano, 2007. D'Aniello et al., 2012), that the ultimate behaviour of steel beams, i.e. rotation capacity and degree of developed overstrength due to material strain hardening, is governed by considerable number of parameters. In fact, it is influenced by the following issues: width-to-thickness ratios of the flanges and web of the beam, flange-web interaction, overall member slenderness, moment gradient, lateral restraints, and loading conditions (monotonic or cyclic).

As would be expected from the foregoing discussion, the degree of beam-to-column connection overstrength, needed to assure the full strength requirement, is directly related to the behavioural class of the beam section, i.e. ductile, compact, semi-compact and slender. In other words, decreasing the width-to-thickness ratio of the beam cross-sectional plates, the plastic deformation of the beam increases, but at the same time increased beam resistance may

lead to the exploitation of the connection overstrength and thus to excessive straining of non-ductile welded beam-column connection.

All the eight beam cross-sections selected for the complementary study meet the limits of the required cross-sectional Class 1 for dissipative members in bending according to EN 1998-1 and EN 1993-1-1. However, selected set of I and H beam profiles covers different local beam flange (in compression) and web (in bending) cross-sectional slenderness ratios, Figs 203, 207. Namely, profiles were selected in a way to integrate different joint responses, accounting for wide range within practically applicable beam cross-section sizes, in order to properly validate the proposed design as well as detailing rules for both the stiffened connection configurations.

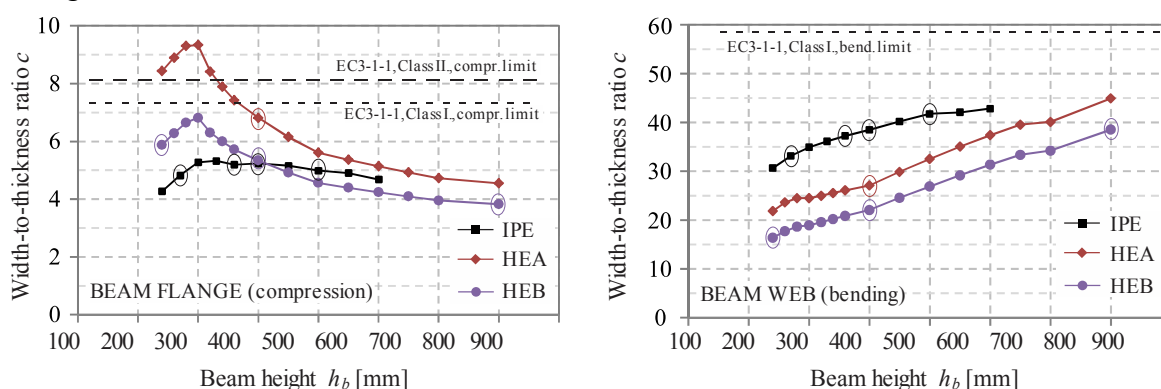


Fig. 207: Flange and web width-to-thickness ratios for I and H beam cross-sections in bending
Slika 207: Vrednosti razmerij dolžina-debelina za pasnico in stojino I in H prečnih prerezov prečk v upogibu

Taking into account fully laterally restraint beams, beside the beam geometric cross-sectional characteristics, there are two additional parameters governing the flexural ultimate beam response: the stress distribution across the beam section depth due to the moment gradient on the beam, and inherent steel material properties. Systematic characterisation of the two parameters is provided in the text below.

All the stiffened joints were consistently designed according to the procedure described below. The basic idea was to simulate as much as possible real design situation. To this end, two distinct design phases were used.

In the first phase, all the stiffened joints were designed considering structural system of a moment resisting bay (beam fixed on both its ends) in a typical residential building. Beam length of $20 \cdot h_b$ with seismic loading combination of 4.0 kN/m^2 of a permanent and 3.0 kN/m^2 of a live load was considered in the seismic design according to the provisions from EN 1998-1.

In the subsequent step, all the joints were redesigned according to the structural system of a cantilever beam loaded with transverse force at its free end, as the one to be used in the test simulations. For the start, cantilever beam length of half the beam span used in the first phase was applied. However, it was reduced later by a factor varying from 0.3 to 0.4, depending on particular case of beam member, in order to obtain certain level of a shear force in the supposed location of the plastic hinge in the beam. Namely, in the proposed design procedure it is assumed that the shear force is carried by the web of the beam, where the value of the shear force is less than half the beam plastic shear resistance, thus neglecting its effect on the moment resistance as well as rotation capacity of the beam.

According to the described approach, final determination of particular beam length was governed by the shear force-to-beam plastic shear resistance ratio being close to 0.5 in the

supposed centreline of the plastic hinge on the beam ($\frac{1}{4} h_b$ from the end of the stiffener for RS and CP joints).

It is interesting to note at this stage that final stiffened connection cross-section resistance check comparison between both design phases showed “phase two-phase one” utilisation ratio being between 0.99 and 1.02 for RS joints and between 0.99 and 1.13 for CP joints. Except for the thickness of the plates, the same geometric characteristics of rib-stiffeners and cover-plates were used in both phases.

The stress distribution across the beam section depth is directly influenced by the moment gradient on the beam. The influence of the longitudinal stress gradient on the ultimate stress depends on the ratio b_f / L' (Mazzolani, Piluso, 1992), where L' is the distance between the centre of the plastic hinge and the point of zero moment (shear length). For the selected set of joints, with the final length of the beam determined according to the above procedure, the b_f / L' ratio is between 0.082 and 0.102 for joints with IPE beams, and between 0.057 and 0.145 for joints with HEA and HEB beams.

For the simulation of all the stiffened beam-to-column joints response under monotonic and cyclic loading, the same material constitutive model definitions were used in Abaqus as described in Chapter 4.2.4, namely *classical metal plasticity* and *cyclic plasticity for metals* with the nonlinear isotropic/kinematic hardening model, for monotonic and cyclic loading, respectively.

To provide consistent comparison between the responses of all the stiffened joints, fixed material properties were used for all the joints, with the same material definition for particular group of steel components, i.e. for the beams, as dissipative members, and for the stiffening plates together with the columns acting as non-dissipative components. In this way, other potential geometric dependent effects on the flexural ultimate joint (beam) response, related to the beam cross-sectional characteristics, can be observed. Furthermore, such approach enables to perform consistent check of the proposed design procedure for all welded RS and CP beam-to-column joints.

As in the case of all the experimentally tested joint specimens, mild carbon steel grade S355 was considered for the beams as well as for the stiffening plates, whereas high strength steel grade S690 was used for the columns.

At this stage of the study, special consideration was dedicated to the steel material curves to be taken into account. As already explained, the basic aim is to provide consistent check of the proposed design procedure for both the stiffened connections. According to the proposed seismic design approach for the full-strength welded stiffened connections, see Chapter 3.2.1, overall overstrength factor $\gamma_{ov}' = s \cdot \gamma_{ov} = 1.5$ was used, taking into account random variability of the steel grade S355 material yield stress $\gamma_{ov} = 1.25$ and additional strain hardening $s = 1.2$ of the fully yielded and strain hardened steel in the dissipative zone of the beam, see Eq. (12).

In accordance with the deterministic approach of interpretation of Eq. (12), uniaxial stress-strain material response curves, to be applied in the FE model for the simulation of both monotonic and cyclic loading, were defined according to the following two assumptions:

- for dissipative beam member, material yield strength f_y was taken to be of the order $1.25 \cdot f_y^{nom}$, to provide $\gamma_{ov} = 1.25$, where f_y^{nom} for steel grade S355 is 355 MPa;
- for all non-dissipative joint components, including stiffening plates and the column, material yield strength f_y was assumed to be equal to f_y^{nom} , where f_y^{nom}

for steel grade S355 is 355 MPa for stiffening plates, and similarly, for steel grade S690 $f_y^{nom} = 690$ MPa for the column.

In order to generate realistic and representative material stress-strain response curves, for both monotonic and cyclic loading, the following procedure was used. First, calibrated uniaxial stress-strain material curves for monotonic and cyclic loading, used in the FE models for the simulation of the experimentally tested joint specimens, were adopted, hereinafter referred to as reference monotonic and reference cyclic material curves.

In the second step, the reference curves were scaled up or down to obtain material curves with the desired level of the yield strength f_y for dissipative and non-dissipative joint members in accordance with the foregoing idea.

Flexural ultimate beam resistance, considering different levels of the corresponding yield strength parameter f_y (up to the value of $1.25 \cdot f_y^{nom}$), was also investigated in the study. To provide consistent comparison between different cases, fixed value of the ultimate-to-yield stress ratio f_u/f_y , which may be related as the upper limit for additional flexural resistance s of the beam due to the strain hardening, was considered in all the cases.

According to the stated objective, the method used to derive material stress-strain curves for the beam requires careful consideration. Namely, simple scaling of a stress-strain curve along vertical stress axis results in modified shape of the curve, i.e. stress ratio of the two points on the curve is changed, resulting in modified post-yield hardening properties. However, as far as concerning the ultimate beam flexural behaviour, the steel post-yield hardening properties influence both the beam rotation capacity and the extent of the flexural ultimate resistance (D'Aniello et al., 2012). To this end, reference monotonic and cyclic curve shape characteristics (f_u/f_y ratio, relative increment between the consecutive two points on the curve along stress axis) were preserved in generated new material stress-strain curves for the beam.

Derivation of monotonic stress-strain material curve from the corresponding reference curve is presented in Fig. 208 for the case of dissipative and non-dissipative steel joint components.

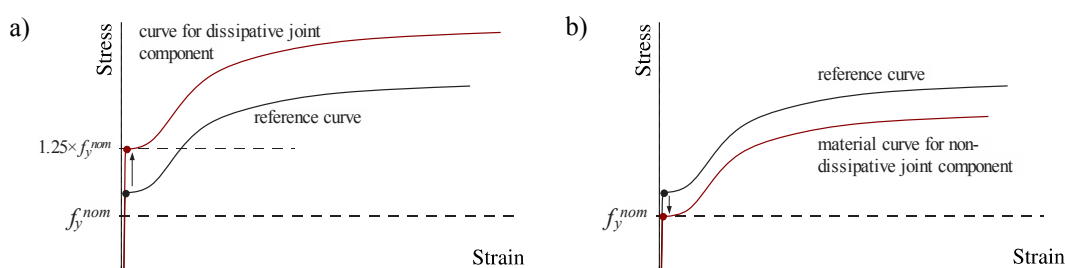


Fig. 208: The method used for derivation of the steel material stress-strain curves to be applied in the complementary numerical analysis: a) for dissipative, and b) for non-dissipative components

Slika 208: Metoda za določitev materialnih krivulj napetost-deformacija jekla uporabljenih v parametrični študiji: a) za dissipativne in b) nedissipativne komponente

Comparison of monotonic material stress-strain curve characteristics between the reference curve and the generated curves for the beam material ($f_y = 1.25 \cdot f_y^{nom}$) and material of the stiffening plates ($f_y = f_y^{nom}$) are presented in Preglednica 31: Karakteristike monotonega odziva napetost-deformacija jekla S355 za parametrično študijo

Table 31.

Preglednica 31: Karakteristike monotonega odziva napetost-deformacija jekla S355 za parametrično študijo
Table 31: S355 steel material monotonic stress-strain curve characteristics used in the parametric study

	f_u/f_y	$f_y/f_y^{nom} = \gamma_{ov}$	f_u/f_y^{nom}
Reference material curve		1.07	1.37
Stiffening plates material	1.28	1.00	1.28
Beam material		1.25	1.60

To conclude, in order to check the adequacy of the proposed design procedure for both the stiffened connections, unfavourable material quality combination was chosen for dissipative ($f_y = 1.25 \cdot f_y^{nom}$) and non-dissipative ($f_y = f_y^{nom}$) joint members from deterministic point of view. The generated material curves (monotonic and cyclic) applied to the dissipative beam member allow for the development of theoretically full-level of the beam overstrength $\gamma_{ov}' = \gamma_{ov} \cdot s$, with the resulting stress corresponding to the complete development of the beam local buckling of the order $1.60 \cdot f_y^{nom}$. On the other hand, material stress-strain curves comprising nominal value of material yield stress f_y^{nom} are accounted for all non-dissipative steel joint components, including stiffening plates and complete steel column member.

The generated material stress-strain curves for all the steel joint components in terms of nominal stress-strain relationship up to the point of the ultimate tensile strength are presented in Fig. 209.

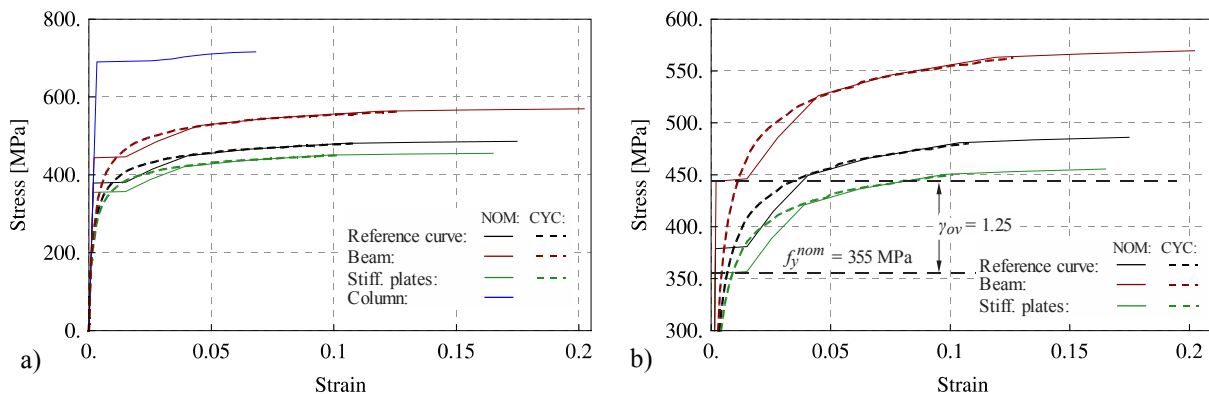


Fig. 209: a) Monotonic, and b) cyclic material curves for steel joint components used in the study

Slika 209: V analizi uporabljene a) monotone in b) ciklične materialne krivulje za jeklene komponente spojev

In order to provide complete consistency for response evaluation of all the joints, the stiffened connections were designed with the stiffened cross-section check utilisation factor close to 0.90. Information about the obtained rib-stiffener and cover-plate thicknesses according to the proposed design procedure for complete range of IPE, HEA and HEB beam profiles is depicted in Fig. 210. Normalised stiffening plate thicknesses according to the corresponding beam flange thicknesses are presented.

In general, it is preferred to use stiffening plates with reasonable thicknesses. Thicker plates require larger welds with correspondingly larger heat input during the welding process. The inherent restraint associated with joining thicker materials can substantially deteriorate stiffened connection LCF resistance.

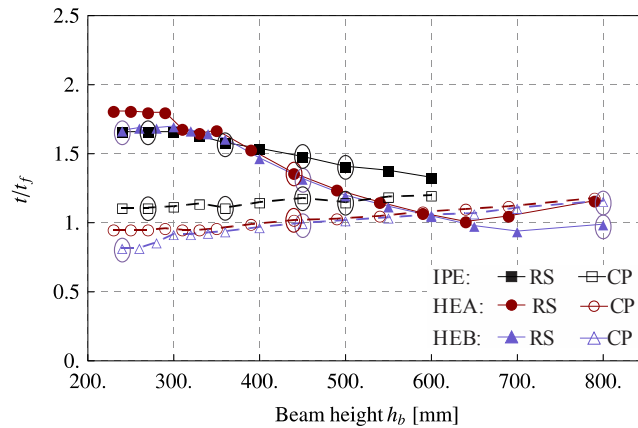


Fig. 210: Rib-stiffener and cover-plate thicknesses obtained for complete range of I and H beam profiles according to the proposed design procedure

Slika 210: Debeline reber in veznih pločevin dobljene z uporabo predlagane procedure dimenzioniranja v kombinaciji s celotnim naborom I in H profilov prečk

Normalised cover-plate thicknesses obtained by the proposed design procedure for the considered range of all the three beam section types, see Fig. 210, is close to 1.0 with gently sloped tendency growing with the beam section height, which seems to be rational. However, greater and negative bias with larger values (up to 1.8) for smaller beam sections can be observed for normalised rib-stiffener thicknesses in case of all beam section types.

5.3.2 Monotonic loading

For all the analysed stiffened joints in the complementary study, column was designed to provide strong column/weak beam requirement. Indeed, for all the joints subjected to monotonic loading column remained in elastic state. In all cases total column rotation (column elastic bending together with column panel zone deformation) was not more than 0.007 rad.

Comparison of monotonic response between all the analysed RS and CP beam-to-column joints is presented in Figs 211 and 212. Diagrams in terms of moment to the plastic hinge centreline M_h as a function of total beam rotation θ_b computed to the column centreline presented in Fig. 211 provide an overview of the difference between the analysed stiffened joint responses.

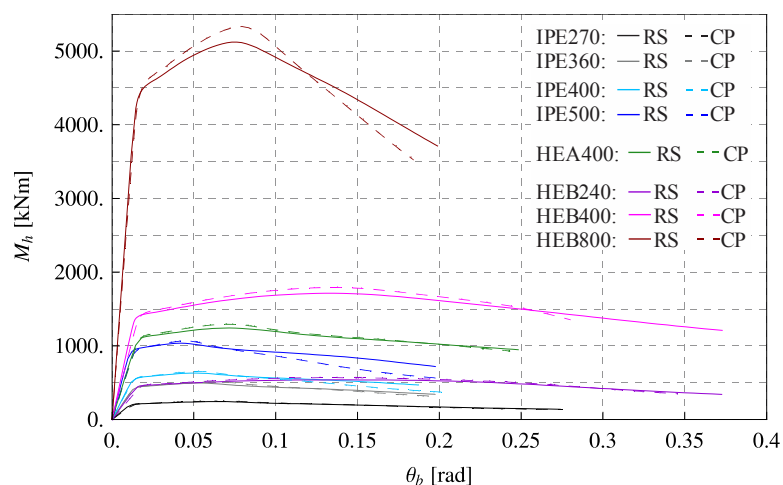


Fig. 211: M_h vs. θ_b diagrams for all 16 beam-to-column stiffened joints
Slika 211: Diagrami $M_h - \theta_b$ za vseh 16 ojačanih spojev prečka-steber

As already noted, in all the 16 cases complete joint response was governed by the inelastic beam flexural response, with the onset of the beam local buckling in the plastic hinge zone beyond the stiffened region of the beam, which can be observed as the descending part of the curves. It should be noted that the end of particular simulation was not governed by any damage issue, since no damage had been accounted for in the applied constitutive material model in Abaqus. Each FEM simulation was run until considerable ($> 20\%$) joint flexural strength degradation was observed.

From Fig. 211 one can also observe that all the 16 joints reach the yield point at more or less the same total beam rotation θ_b . Indeed, this can be even better seen from Fig. 212, where the same curves are presented in terms of moment to the plastic hinge centreline and normalised according to the nominal beam plastic moment $M_h/M_{pl,b}^{nom}$ as a function of the total beam rotation θ_b . From the subsequent processing of the response data it was found that yield rotation for all the joints varies between 0.0111 and 0.0180 rad in terms of total beam rotation θ_b , with the value increasing as the beam depth is growing, Table 32.

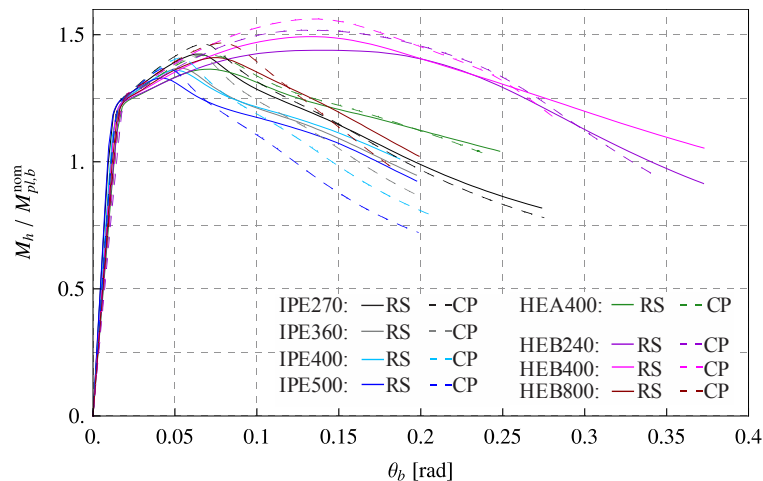


Fig. 212: Normalised M_h vs. θ_b diagrams for all 16 beam-to-column stiffened joints
 Slika 212: Normirani diagrami $M_h - \theta_b$ za vseh 16 ojačanih spojev prečka-steber

Preglednica 32: Razdalja med točko vnosa prečne sile in središčem plastičnega členka na prečki L' , z vrednostmi pripadajočega faktorja b_f/L' in plastične rotacije prečke $\theta_{b,y}$, za vse analizirane spoje RS in CP

Table 32: Distance between load insertion point and plastic hinge centreline on the beam L' with the corresponding b_f/L' ratio and beam yield rotation $\theta_{b,y}$ for all the analysed RS and CP joints

RS joint	L' [m]	b_f/L'	$\theta_{b,y}$ [rad]	CP joint	L' [m]	b_f/L'	$\theta_{b,y}$ [rad]
IPE270	1.30	0.10	0.0115	IPE270	1.22	0.11	0.0136
IPE360	1.79	0.10	0.0135	IPE360	1.64	0.10	0.0140
IPE400	1.94	0.09	0.0131	IPE400	1.64	0.10	0.0137
IPE500	2.43	0.08	0.0111	IPE500	2.29	0.09	0.0138
HEA400	2.60	0.12	0.0159	HEA400	2.52	0.12	0.0167
HEB240	1.65	0.15	0.0154	HEB240	1.75	0.14	0.0180
HEB400	2.63	0.11	0.0140	HEB400	2.54	0.12	0.0163
HEB800	5.26	0.06	0.0147	HEB800	5.08	0.06	0.0157

Comparison between monotonic responses of the joints as presented in Fig. 212 enables further examination in terms of strength and ductility response characteristics. In addition,

from the ultimate beam flexural response resulting strength demand on the stiffened connection can also be observed.

Summary on full-strength RS and CP joint responses in terms of the two basic parameters controlling their ultimate behaviour, i.e. plastic rotation capacity and flexural overstrength, is gathered in Table 33.

Failure occurrence of a beam-to-column joint under both monotonic and cyclic loading was not simulated. Therefore, instead of reporting a rotation capacity value at the instance of failure, two other characteristic states in joint response were chosen for that purpose.

Rotation capacity $R_{mon,1}$ is determined with the ultimate beam rotation taken as the deformation corresponding to the instance in which the flexural moment resistance drops below $M_{pl,b}$, see Fig. 4, while rotation capacity $R_{mon,2}$ is determined with the ultimate beam rotation taken as the deformation corresponding to 20 % drop of the maximum moment resistance (FEMA, 2011).

Reported values of both plastic joint rotation capacities were defined according to Eq. (2) in relation to the corresponding plastic beam rotations reported in Table 32. Flexural overstrength factor s was calculated by using Eq. (3).

Preglednica 33: Povzetek informacij za monotoni odziv spojev RS in CP
Table 33: Summary on RS and CP joint responses under monotonic loading

Stiffened joint type	Response parameters	Beam cross-section							
		IPE				HEA	HEB		
		270	360	400	500	400	240	400	800
RS	s	1.14	1.10	1.09	1.06	1.09	1.15	1.19	1.13
	γ_{ov}'	1.42	1.37	1.36	1.33	1.36	1.44	1.49	1.41
	$R_{mon,1}$	8.71	5.33	5.46	4.89	6.88	16.14	18.68	8.04
	$R_{mon,2}$	12.19	10.03	11.19	12.77	12.73	18.04	20.54	10.45
CP	s	1.17	1.14	1.13	1.10	1.14	1.21	1.25	1.17
	γ_{ov}'	1.46	1.42	1.41	1.37	1.42	1.51	1.56	1.47
	$R_{mon,1}$	7.75	6.00	5.12	3.88	7.06	14.08	15.27	7.15
	$R_{mon,2}$	9.53	8.25	7.47	6.40	10.58	14.53	15.28	8.10

$R_{mon,1}$ – determined with the ultimate beam rotation taken as the deformation corresponding to the instance in which the flexural moment resistance drops below $M_{pl,b}$.

$R_{mon,2}$ – determined with the ultimate beam rotation taken as the deformation corresponding to 20 % drop of the maximum moment resistance, (FEMA, 2011).

According to the proposed design procedure: $\gamma_{ov}' = \gamma_{ov} \cdot s$. In case of all the joints $\gamma_{ov} = 1.25$ applies.

The reported values of joint flexural overstrength s as well as values of joint rotation capacities $R_{mon,1}$ and $R_{mon,2}$ from Table 33 are graphically presented in Figs 213 and 214 as a function of the corresponding beam profile height.

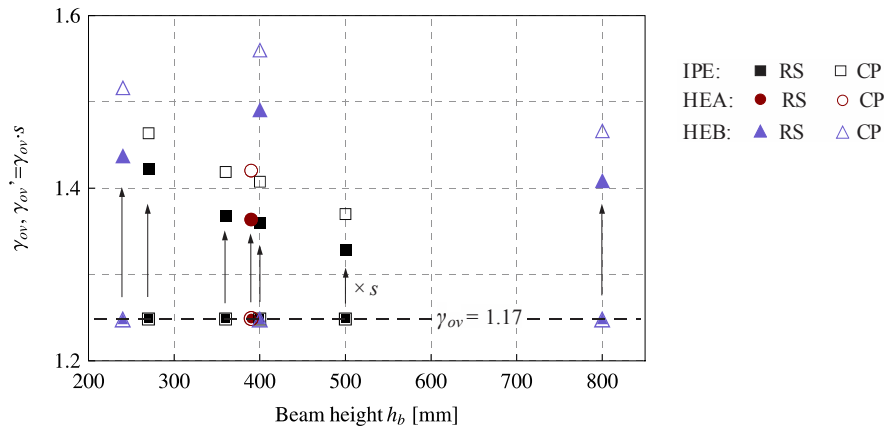


Fig. 213: Overall beam overstrength γ_{ov}' due to the considered γ_{ov} and s
 Slika 213: Celotna dodatna nosilnost γ_{ov}' z upoštevanjem faktorjev γ_{ov} in s

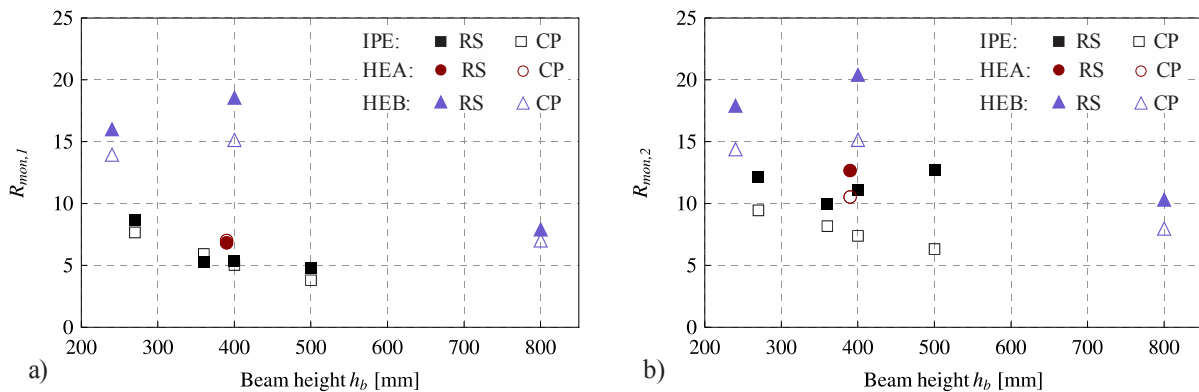


Fig. 214: Beam rotation capacity: a) $R_{mon,1}$ and b) $R_{mon,2}$
 Slika 214: Rotacijska kapaciteta prečke: a) $R_{mon,1}$ in b) $R_{mon,2}$

As can be observed from Table 33 and Figs 213 and 214, the degree of beam rotation capacity as well as the level of the beam-to-column joint overstrength depends on the beam cross-section geometric characteristics as well as on the stiffened joint configuration (RS and CP). It should be noted once again, that all the other parameters governing the ultimate joint response had been systematically chosen in order to provide fixed and unique conditions for all the analysed RS and CP joints: unique steel material definition, similar bending moment gradient on the beam, overall member slenderness effects prevented by providing fully laterally supported beams.

In case of all the joints with beam sections IPE, the obtained values of s range between 1.06 and 1.17, where the parameter value decreases with increasing beam section height. For both joints with beam profile HEA 400, value of s is 1.09 and 1.14, for RS and CP joints, respectively. In case of joints with beams HEB, values of s are much greater and range between 1.13 and 1.25. It is interesting to note at this stage, that the applied stress-strain curve for the beam material in case of all the joints inhere ultimate-to-yield stress ratio equal to $f_u/f_y = 1.28$, which can be interpret as a theoretical maximum value of s (Mazzolani, Piluso, 1993), see Table 31.

A steady decline tendency of the overstrength factor s with growing beam height can be observed from Fig. 213 in case of all the joints with beam sections IPE. However, in case of beams HEB, the maximum obtained value of the beam flexural overstrength was obtained with beam HEB400, rather than for the smallest beam section HEB240. In addition, values s obtained from all CP joints are greater than the corresponding values obtained from RS joints, with the corresponding ratio between 1.03 and 1.05.

In relation with the obtained values of the overall overstrength factor $\gamma_{ov}' = \gamma_{ov} \cdot s$, the maximum reported values for RS and CP joints, 1.49 and 1.56, respectively, are very close or even above the value 1.5, as proposed by the design procedure for both full-strength joint configurations. However, as can be observed from deformed meshes of the joints presented in Figs 215 to 224, the design procedure still provides enough robust stiffened beam-to-column connections in order to prevent excessive plastic straining in the close vicinity of the vulnerable beam-column welded connection at the column flange.

Concerning the obtained values of beam rotation capacities, values of both parameters $R_{mon,1}$ and $R_{mon,2}$ are proportional to the corresponding values of the beam overstrength factor s due to the material strain hardening for all the joints, except for value $R_{mon,2}$ for IPE400 and IPE500: the higher the s the larger the rotation capacities $R_{mon,1}$ and $R_{mon,2}$, see Figs 213 and 214. The latter observation fully corresponds to the observations of laboratory test results reported in the literature (D'Aniello et al., 2012).

Based on the above observations of the ultimate full-strength RS and CP joints responses, it is clear that flexural ultimate behaviour of a beam, characterised by rotation capacity and the corresponding flexural ultimate resistance, does not relate only to the width-to-thickness ratios of the plates constituting the cross-section, Fig. 207, but it certainly depends also on the aspect ratio of cross-sections. In particular it depends on cross-section flange characteristics (width, cross-section flange area) and flange-web interaction. This has been already underlined in the existing empirical formulations for parameters R and s that can be found in literature (Mazzolani, Piluso, 1992. 1993. Piluso, Rizzano, 2007. D'Aniello et al., 2012. Güneyisi et al., 2013).

Particularly of interest is demand on stiffened connection components (reinforcing plates, welds) and force transfer mechanism at the face of the column and at the end of the stiffener, which can be observed from Figs 215 to 222. Plastic equivalent strain PEEQ is plotted over the deformed mesh of particular joint.

Presented deformed meshes of all the joints correspond to the onset of maximum strength developed by the beam. Deformation scale factor 1.0 is used in all the figures. According to the purpose of the proposed design procedure, reinforcing plates of all the simulated stiffened joints remain basically in elastic state, although some plastic strain concentrations can also be observed in the stiffened region close to the column flange.

In case of the RS joints, plastified region on the beam flange tends to extend even beyond the end of the rib-stiffener, with the tip of the stiffener-plates already subjected to plastic flow.

During the research work it was found out, that it is not able to completely prevent plastic straining at the end of the rib-stiffener. To be more explicit, rib-stiffened configuration obviously succeeds in relocating plastic action from the vulnerable welded beam-column connection, but it still inherits critical detail at the end of the stiffened region due to unfavourable higher stress/strain concentrations, which may substantially deteriorate performance of the rib-stiffened connection.

For this reason RS joint configuration proved to be more critical under LCF effects compared to CP connection as already concluded from experimental test results in Chapter 3.4 as well as from evaluation of simulated cyclic response in the following Chapter 5.3.3.

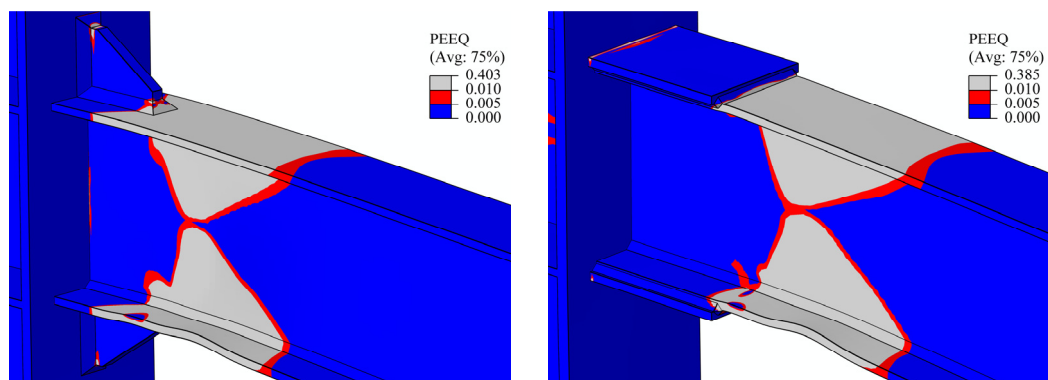


Fig. 215: RS and CP joints with IPE270 beam, instance of maximum flexural resistance, scale factor 1.0
 Slika 215: Spoja RS in CP s prečko IPE270 pri doseženi mejni upogibni nosilnosti, faktor povečave def. 1.0

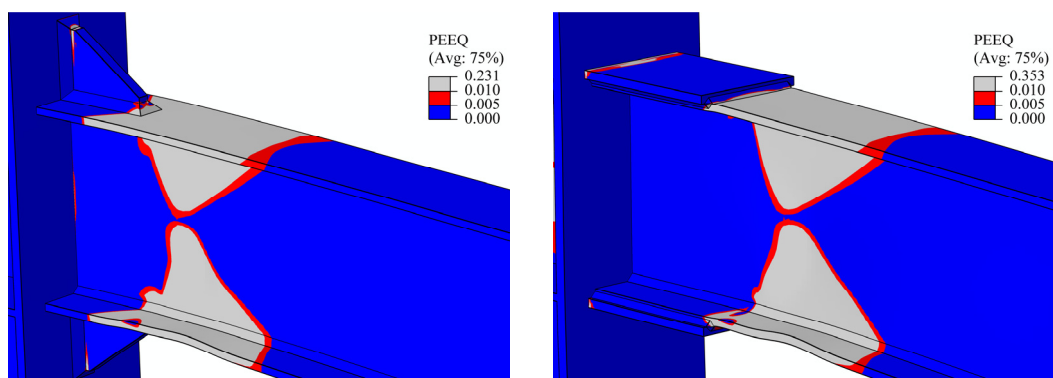


Fig. 216: RS and CP joint with IPE360 beam, instance of maximum strength, scale factor 1.0
 Slika 216: Spoja RS in CP s prečko IPE360 pri doseženi mejni upogibni nosilnosti, faktor povečave def. 1.0

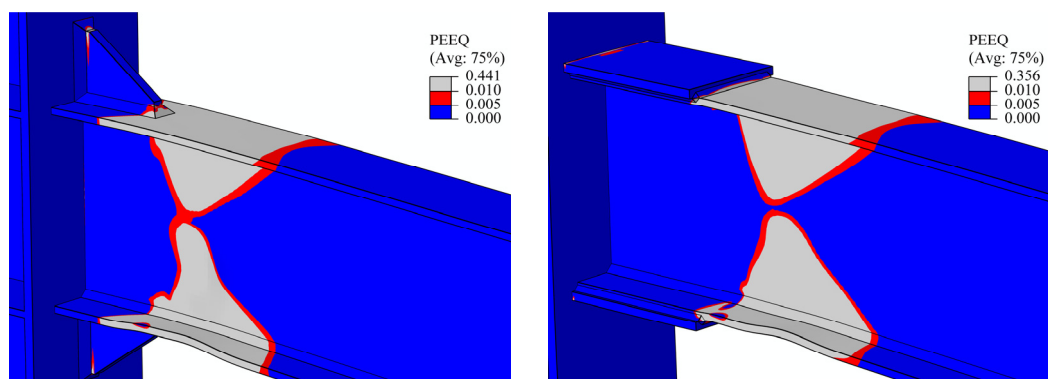


Fig. 217: RS and CP joint with IPE400 beam, instance of maximum strength, scale factor 1.0
 Slika 217: Spoja RS in CP s prečko IPE400 pri doseženi mejni upogibni nosilnosti, faktor povečave def. 1.0

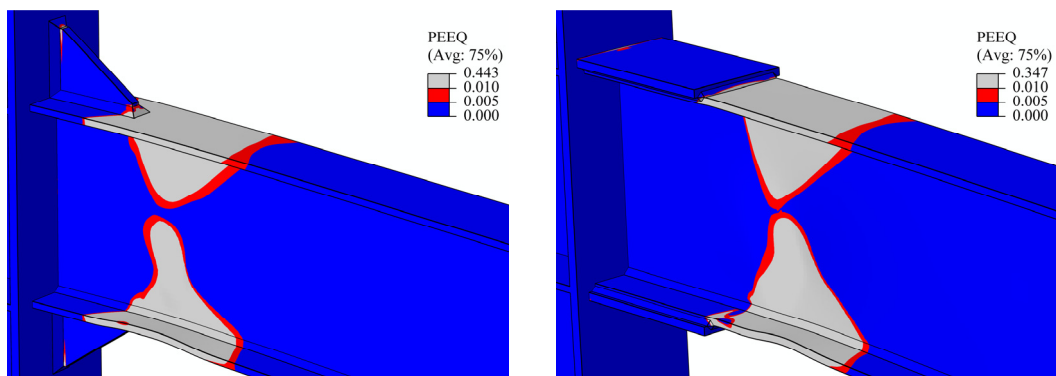


Fig. 218: RS and CP joint with IPE500 beam, instance of maximum strength, scale factor 1.0
 Slika 218: Spoja RS in CP s prečko IPE500 pri doseženi mejni upogibni nosilnosti, faktor povečave def. 1.0

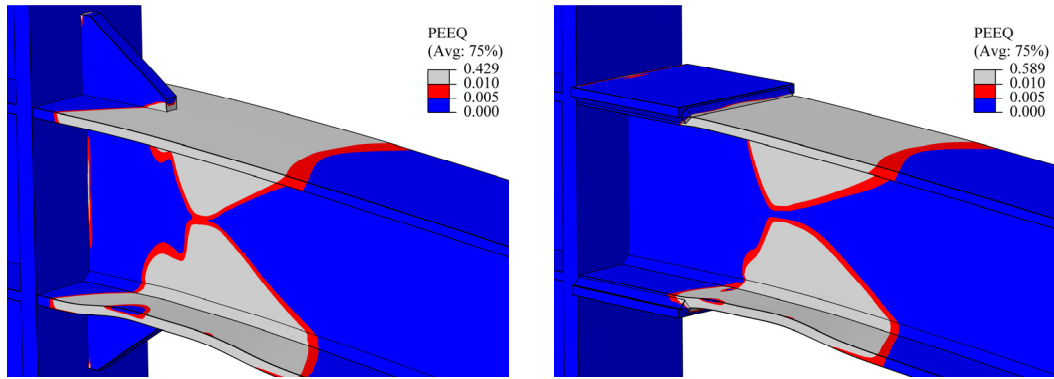


Fig. 219: RS and CP joint with HEA400 beam, instance of maximum strength, scale factor 1.0
Slika 219: Spoja RS in CP s prečko HEA400 pri doseženi mejni upogibni nosilnosti, faktor povečave def. 1.0

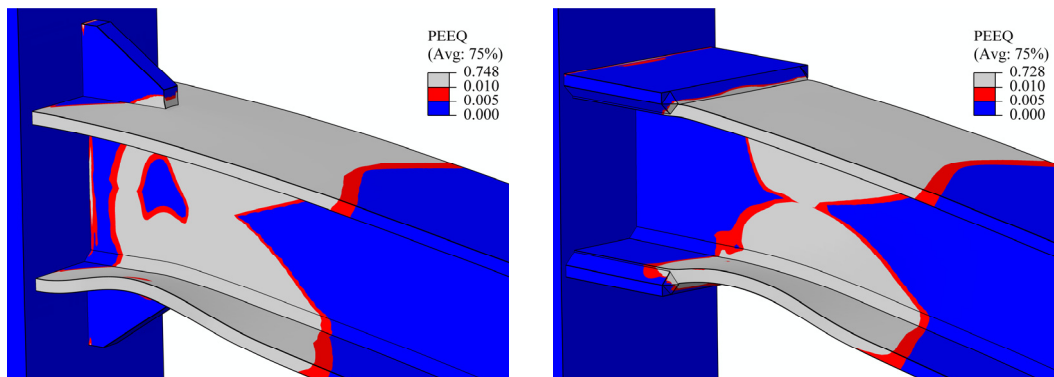


Fig. 220: RS and CP joint with HEB240 beam, instance of maximum strength, scale factor 1.0
Slika 220: Spoja RS in CP s prečko HEB240 pri doseženi mejni upogibni nosilnosti, faktor povečave def. 1.0

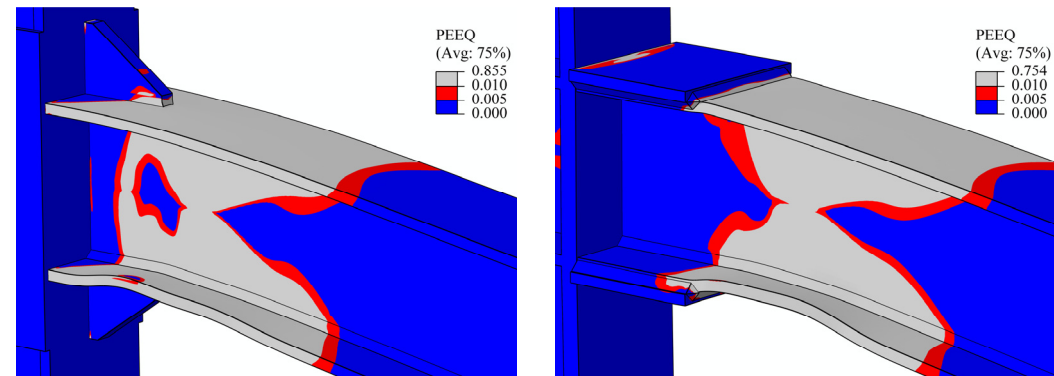


Fig. 221: RS and CP joint with HEB400 beam, instance of maximum strength, scale factor 1.0
Slika 221: Spoja RS in CP s prečko HEB400 pri doseženi mejni upogibni nosilnosti, faktor povečave def. 1.0

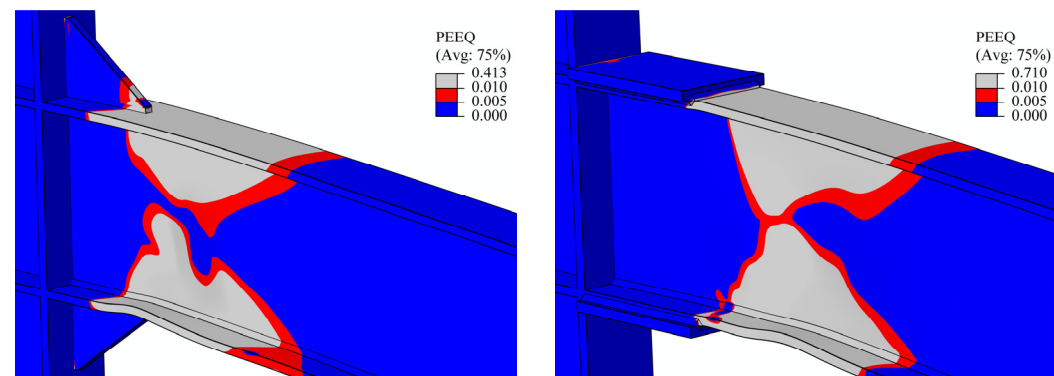


Fig. 222: RS and CP joint with HEB800 beam, instance of maximum strength, scale factor 1.0
Slika 222: Spoja RS in CP s prečko HEB800 pri doseženi mejni upogibni nosilnosti, faktor povečave def. 1.0

Deformed mesh corresponding to the state with 20 % drop of the maximum moment resistance for the selected three RS and CP joints comprising IPE400, HEA400 and HEB400 beams is presented in Figs 223 and 224. While cover plates remain still essentially elastic propagation of plastic straining on the rib-stiffener plates, at their end as well as on the beam flange beyond the end of the stiffener toward the column face, can be observed in case of all three RS joints. Compared to the joint with beam IPE400, more intensive plastic strain propagation on the beam flange toward the column face can be observed in case of both wide-flange beam profiles HEA and HEB.

Although CP joint proved to be superior than RS configuration, preventing more effectively plastic strain propagation toward the column face, its beneficial contribution may somewhat be reduced due to the presence of increased plastic strain concentrations in the region of the beam-column welded interface, Fig. 224c.

It is to be noted that direct comparison of local plastic strain demands between stiffened joint configurations comprising I and H beam profiles, as presented in Figs 215 to 224, can be misleading without considering actual global joint rotation that is reached at the reported state in case of particular joint. Namely, substantial differences in plastic joint rotations can be observed between the analysed joints for characteristic response instances, i.e. the onset of maximum strength, and the instance in which the flexural moment resistance drops below certain portion of maximum strength, see Fig. 212 and Table 33.

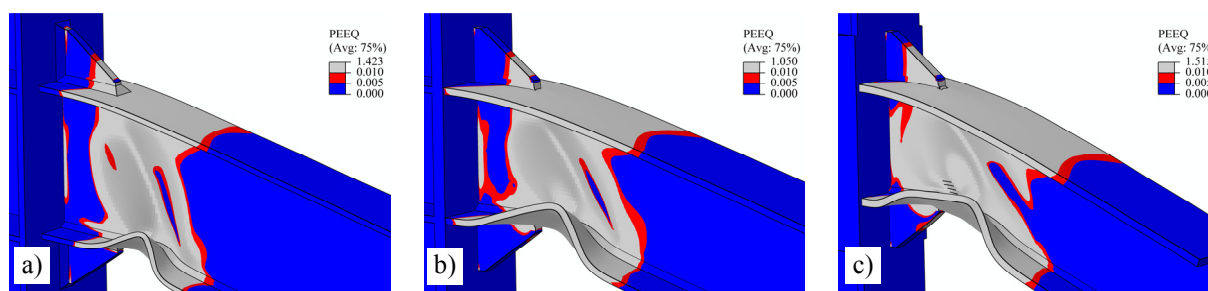


Fig. 223: Deformed shape of RS joints corresponding to 20 % fall of the maximum moment resistance: a) beam IPE400, b) beam HEA400, c) beam HEB400. Deformation scale factor 1.0

Slika 223: Deformacijska oblika spojev RS pri 20 % padcu največje momentne nosilnosti: a) prečka IPE400, b) prečka HEA400, c) prečka HEB400. Faktor povečave deformacij 1.0

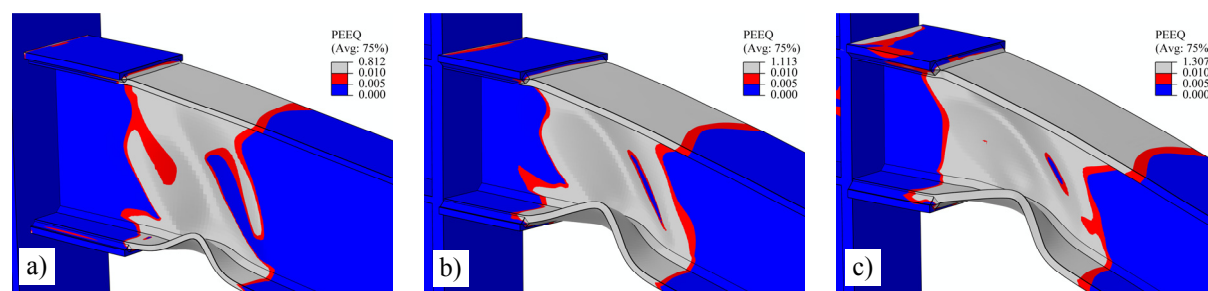


Fig. 224: Deformed shape of CP joints corresponding to 20 % fall of the maximum moment resistance: a) beam IPE400, b) beam HEA400, c) beam HEB400. Deformation scale factor 1.0

Slika 224: Deformacijska oblika spojev CP pri 20 % padcu največje momentne nosilnosti: a) prečka IPE400, b) prečka HEA400, c) prečka HEB400. Faktor povečave deformacij 1.0

From the comparison between the value of moment calculated to the supposed plastic hinge centre M_h and the corresponding value of the beam plastic moment, the centreline of the plastic hinge was estimated to form in the beam section at a distance of $\frac{1}{4} h_b$ from the end of the stiffened region in case of all the analysed RS and CP joints. Actually, this is the same as

observed in all the cyclic experimental tests. In this respect, it is interesting to note that also other researchers have come to the same conclusion, although in combination with different, i.e. American wide flange beams (Kim et al., 2000).

In addition, from the comparison of plastic mechanisms developed by the analysed joints, it was found that the greater the length of the plastic hinge the larger overstrength factor s and rotation capacity R is exhibited by the beam, see Table 33 and Figs 215 to 224.

In Figs 225 to 227 stress and plastic strain demands across the stiffened beam section near the column face is presented in terms of Mises stress and plastic equivalent strain PEEQ. For selected three beams, IPE400, HEA400 and HEB400, in combination with RS and CP stiffened joint typologies the stress/plastic strain distribution is presented for the state of the maximum beam flexural resistance. Upper part of the stiffened section is in tension.

As observed from the figures, not complete stiffened cross-section remains in perfectly elastic state for all observed RS and CP joints. Mises stresses close or even higher than the yield stress ($f_y = 444$ MPa) can be observed in the outer region of the rib-stiffener and in the beam web in case of RS joints. In case of CP joints, Mises stresses higher than the yield stress are observed in both beam flanges at their mid-width in the region of transition between the flange and the web.

In general, only localised plastic strain concentration zones with moderate PEEQ values up to 0.7 % are observed, except for joints RS IPE400, RS HEB400 and CP HEB400. In case of the first two joints, plastic strain concentrations larger than 1 % revealed at the outer part of both rib-stiffeners and on the edge of the beam flanges for RS IPE400 and RS HEB400 joints, respectively. In case of joint CP HEB400, plastic strain concentration zones with PEEQ values around 1 % appeared in top and bottom beam flange and cover-plate at their mid-width.

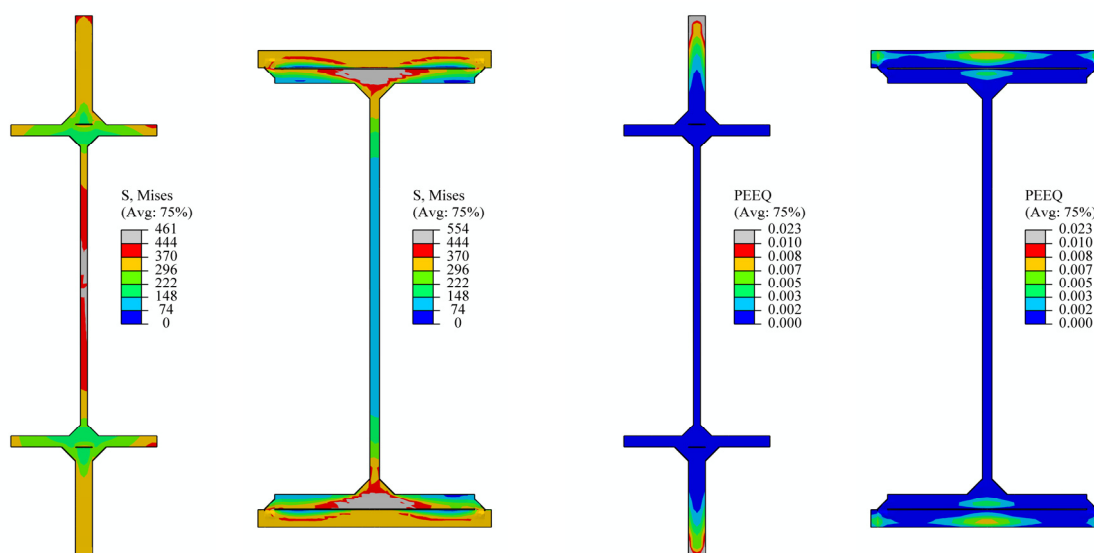


Fig. 225: RS and CP joints with beam IPE400: Mises stress and PEEQ strain state in the stiffened connection at the column flange at the instance of maximum joint flexural resistance

Slika 225: Spoja RS in CP s prečko IPE400: Misesove napetosti in deformacije PEEQ v ojačanem prerezu tik ob pasnici stebra v trenutku dosežene največje momentne nosilnosti spoja

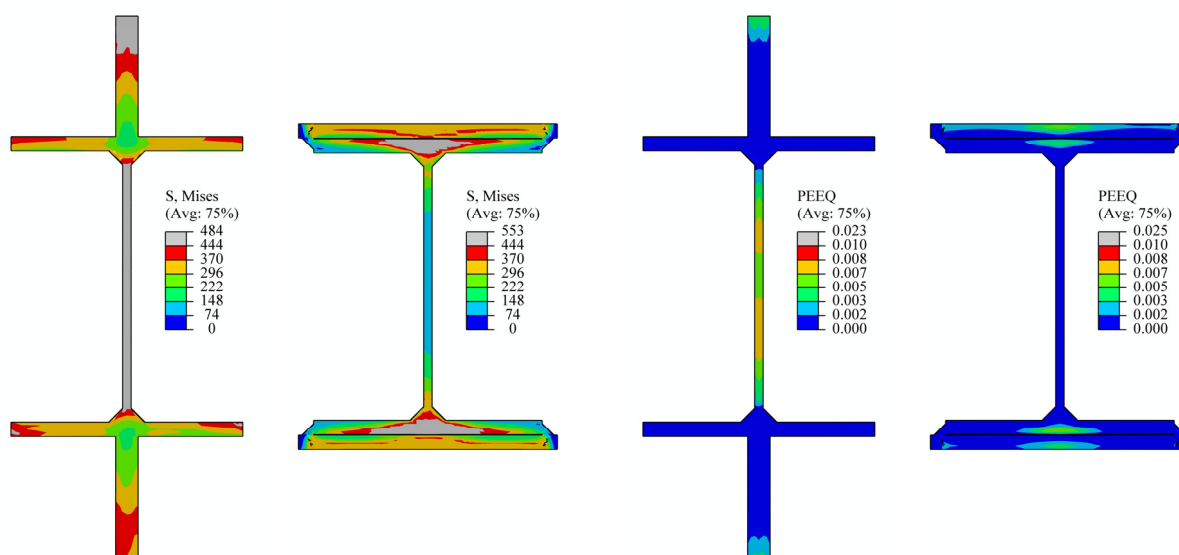


Fig. 226: RS and CP joints with beam HEA400: Mises stress and PEEQ strain state in stiffened connection at the column flange at the instance of maximum joint flexural resistance

Slika 226: Spoja RS in CP s prečko HEA400: Misesove napetosti in deformacije PEEQ v ojačanem prerezu tik ob pasnici stebra v trenutku dosežene največje momentne nosilnosti spoja

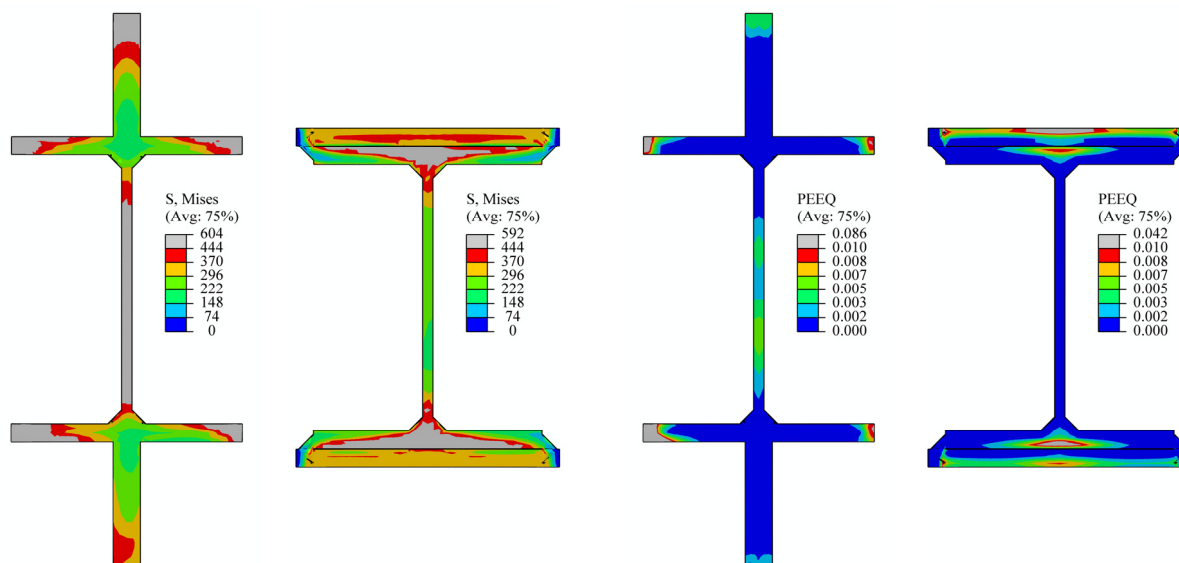


Fig. 227: RS and CP joints with beam HEB400: Mises stress and PEEQ strain state in stiffened connection at the column flange at the instance of maximum joint flexural resistance

Slika 227: Spoja RS in CP s prečko HEB400: Misesove napetosti in deformacije PEEQ v ojačanem prerezu tik ob pasnici stebra v trenutku dosežene največje momentne nosilnosti spoja

5.3.3 Cyclic loading

To facilitate consistency in comparison between the responses of all the sixteen stiffened beam-to-column joints, the same loading protocol according to ANSI/AISC-341-10 was used for the cyclic loading.

According to the selected cyclic loading history, cycles in the plastic range only were simulated, with the first cyclic loading amplitude 0.015 rad, Fig. 27. It has to be noted that the applied loading amplitude 0.015 rad for the first two cycles in the ANSI/AISC-341-10 loading protocol almost matches with the joint yield rotation θ_y , obtained for all the analysed RS and CP joints. Namely, for all the joints value θ_y ranges between 0.015 and 0.020 rad. A good

correlation was therefore found between the first inelastic deformation level of the selected loading protocol and the state with the onset of permanent plastic deformation, representing damage limitation, in case of all 16 beam-to-column joints.

Cyclic response of all the sixteen stiffened joints in terms of moment calculated to the plastic hinge centreline, and normalised with the nominal beam plastic moment $M_h/M_{pl,b}^{nom}$, as a function of the total beam rotation θ_b is presented in Figs 228 to 231. Response of each stiffened joint is presented for all the simulated cycles, which is different for particular joint, see Table 34.

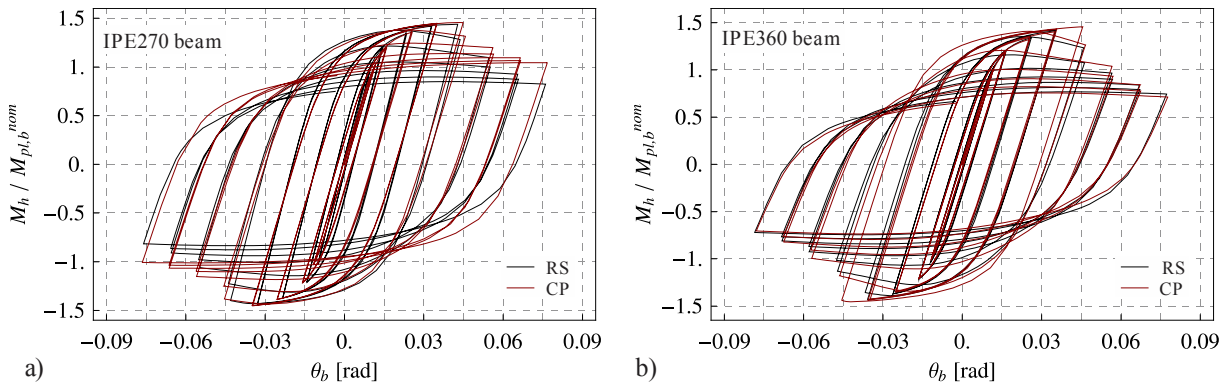


Fig. 228: Cyclic response of RS and CP joints: a) beam IPE270 (15 cycles), b) beam IPE360 (15 cycles)
Slika 228: Ciklični odziv spojev RS in CP: a) prečka IPE270 (15 ciklov), b) prečka IPE360 (15 ciklov)

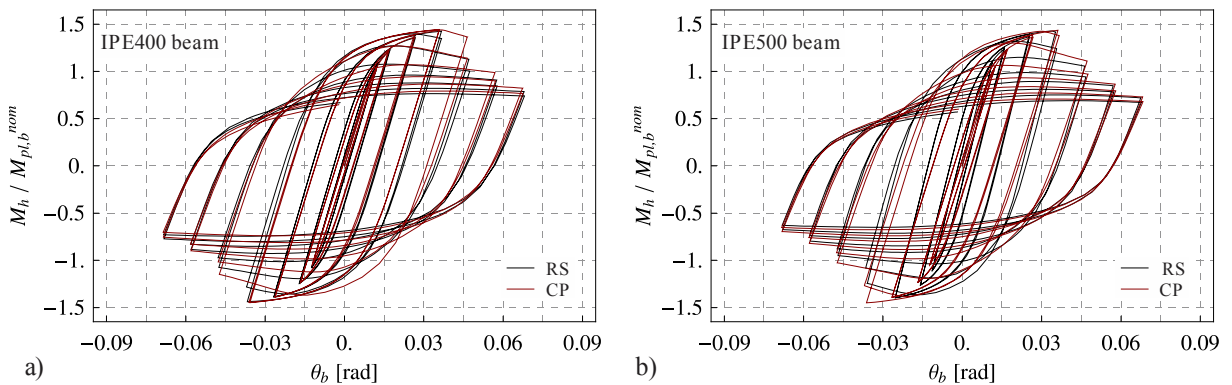


Fig. 229: Cyclic response of RS and CP joints: a) beam IPE400 (14 cycles), b) beam IPE500 (14 cycles)
Slika 229: Ciklični odziv spojev RS in CP: a) prečka IPE400 (14 ciklov), b) prečka IPE500 (14 ciklov)

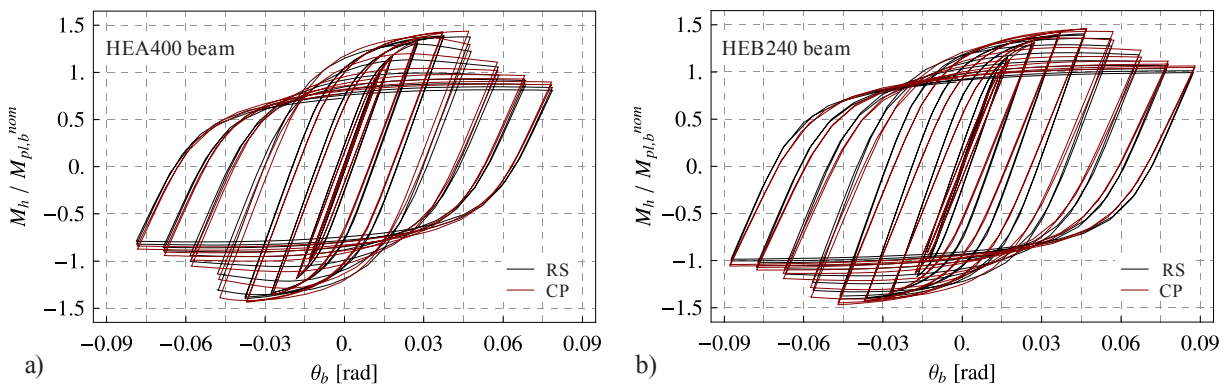


Fig. 230: Cyclic response of RS and CP joints: a) beam HEA400 (16 cycles), b) beam HEB240 (18 cycles)
Slika 230: Ciklični odziv spojev RS in CP: a) prečka HEA400 (16 ciklov), b) prečka HEB240 (18 ciklov)

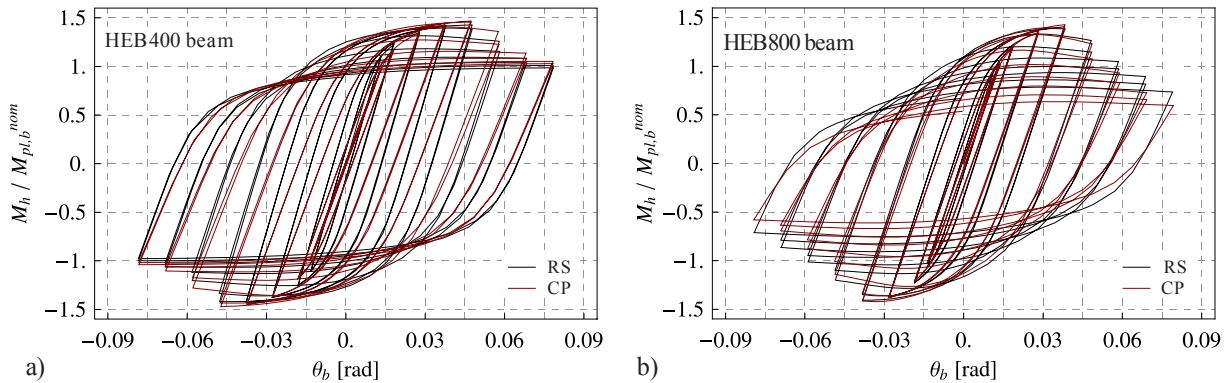


Fig. 231: Cyclic response of RS and CP joints: a) beam HEB400 (16 cycles), b) beam HEB800 (15 cycles)

Slika 231: Ciklični odziv spojev RS in CP: a) prečka HEB400 (16 ciklov), b) prečka HEB800 (15 ciklov)

Before further cyclic response evaluation of the joints, estimation of low-cycle fatigue (LCF) life in terms of identification of the LCF crack initiation was performed. The following residual life part with crack propagation phase till the ultimate fracture of a structural component was not tried to simulate. It was early observed from the experimental tests that the rate of crack propagation is the most important resistant characteristic for steel structures subjected to low-cycle fatigue and in particular for welded structures. In case of a welded beam-to-column connection, crack propagation rate may depend on its geometric details along with local stress/strain field during loading as well as inherent material characteristics of parent steel, welds, and steel in HAZ regions.

According to the above discussion, crack propagation rate may be different for all the eight selected beam profiles as well as different for both the stiffened joint configurations (RS and CP). This means different low-cycle fatigue life for all the 16 beam-to-column joints. As it was shown by the experimental cyclic tests, the ability to develop inelastic rotation may be somewhat diminished as beams become deeper and heavier. In addition, an important adverse beam scale effect that can affect welded stiffened beam-to-column connection performance is related to the inherent restraint associated with joining thicker plates. As a consequence, total number of cycles to complete failure would likely decrease as beams become larger.

Based on the response of all the 16 experimental cyclic tests on the RS and CP beam-to-column joints performed in the framework of this research work, see Chapter 3, conclusion can be made that complete stiffened joint failure in the unstiffened beam region is less likely to occur in completely brittle manner, without previously sustained certain number of cycles with well-developed large plastic strain concentrations. However, as reported from the past research activities (Engelhardt, Sabol, 1995. Whittaker, Gilani, 1996. Anderson, Duan, 1998), complete failure of the specimen may result abruptly in a non-ductile manner, due to the presence of unfavourable defects in steel material.

Even though the subsequent crack propagation to the final fracture of a steel joint component was not simulated, identification of critical cycle with crack occurrence and its location is useful for joint performance evaluation and is used also as a means of comparison of LCF response between the stiffened joints.

Beside the proposed crack initiation based LCF failure criterion, hereinafter referred to as *crit.^a*, effective damage concept for prediction of ductile cracking onset proposed by Ohata and Toyoda (2004), referred to as *crit.^b*, was used. The results in terms of consecutive critical cycle number with identified LCF crack initiation are gathered in Preglednica 34: Število simuliranih ciklov z identificiranim nastopom nizkociklične razpoke (kritičen cikel)

Table 34. Critical location with observed crack initiation in the stiffened beam-to-column joint is provided in the same table as well.

Preglednica 34: Število simuliranih ciklov z identificiranim nastopom nizkociklične razpoke (kritičen cikel)
Table 34: Complete number of simulated cycles with LCF crack initiation onset identification (critical cycle)

Beam	No. of simulated cycles		LCF crack initiation (critical cycle)			
			RS		CP	
	RS	CP	crit. ^a	crit. ^b	crit. ^a	crit. ^b
IPE270	15		13 ^{(2), I}	15 ^{(1), I}	14 ^{(2), I}	15 ^{(2), I}
IPE360	15		13 ^{(1), I}	14 ^{(2), I}	13 ^{(2), I}	14 ^{(2), I}
IPE400	14		12 ^{(2), I}	14 ^{(1), I}	13 ^{(1), I}	14 ^{(1), I}
IPE500	14		12 ^{(1), I}	14 ^{(1), I}	13 ^{(1), I}	14 ^{(1), I}
HEA400	16		9 ^{(1), II}	/	15 ^{(2), I}	/
HEB240	18		10 ^{(2), II}	/	18 ^{(2), I}	/
HEB400	16		8 ^{(2), II}	/	16 ^{(2), I}	/
HEB800	15		8 ^{(2), II}	/	14 ^{(2), I}	/

crit.^a: Proposed crack initiation based LCF failure criterion.

crit.^b: Effective damage concept according to Ohata and Toyoda (2004).

cycle No.^(1/2): crack initiation observed in the first, ⁽¹⁾, or the second half, ⁽²⁾, of the reported critical cycle.

Critical location on the beam flange: away from the end of the stiffener, ^I, at the end of the stiffener, ^{II}.

In case of all the stiffened full-strength beam-to-column joints, plastic hinge occurred in the unstiffened beam section beyond the end of the stiffened region. Accordingly, critical site with crack initiation appeared in the beam flange at either the end of the stiffener or away from it in the most buckled region of the beam flange. Based on the laboratory test results, the latter situation is the preferred one, due to the larger LCF resistance of the parent steel material in the unstiffened beam compared to the material in the weld HAZ at the end of the stiffener.

In relation to the estimation of LCF crack initiation in the joints, presented in Preglednica 34: Število simuliranih ciklov z identificiranim nastopom nizkociklične razpoke (kritičen cikel)

Table 34, both the applied criteria provide quite the same results for RS and CP joints in case of all the IPE beams as well as in case of the CP HEB800 joint. Somewhat non-conservative result can be observed in case of the effective damage concept proposed by Ohata and Toyoda (2004), *crit.^b*.

However, for all the other RS and CP joints, comprising beams HEA and HEB, *crit.^b* does not provide consistent results at all. In some cases the crack occurrence was not even met for the applied number of cycles. On the contrary, the proposed criterion *crit.^a* appears to provide fully consistent and logical results for all the 16 analysed RS and CP joints.

Based on the above discussion, results obtained on the basis of the proposed criterion *crit.^a* only are presented and discussed below.

Comparison of cyclic performance between RS and CP joint configurations in terms of deformed shape together with the corresponding PEEQ field for the critical step with

identified LCF crack occurrence, according to *crit.*^a, is depicted in Figs 232 to 234. Joints with beams IPE400, HEA400 and HEB400 are presented.

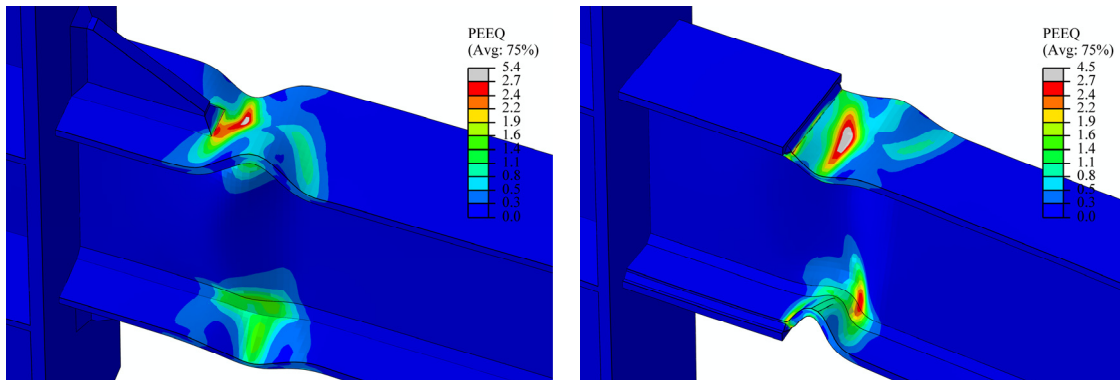


Fig. 232: Deformed shape of RS and CP joints with beam IPE400. Predicted instance of LCF crack initiation according to the proposed criteria *crit.*^a. Deformation scale factor 1.0

Slika 232: Deformirana oblika spojev RS in CP s prečko IPE400. Napoved nastopa nizkociklične razpoke v skladu s predlaganim kriterijem *crit.*^a. Faktor povečave deformacij 1.0

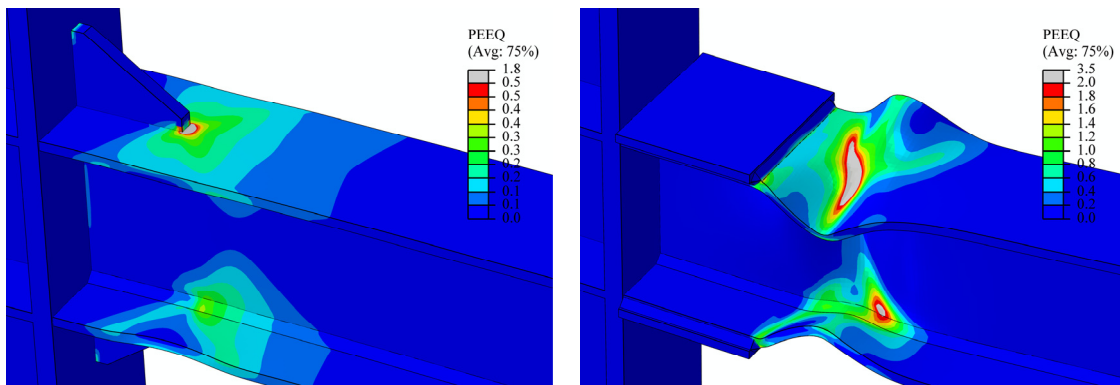


Fig. 233: Deformed shape of RS and CP joints with beam HEA400. Predicted instance of LCF crack initiation according to the proposed criteria *crit.*^a. Deformation scale factor 1.0

Slika 233: Deformirana oblika spojev RS in CP s prečko HEA400. Napoved nastopa nizkociklične razpoke v skladu s predlaganim kriterijem *crit.*^a. Faktor povečave deformacij 1.0

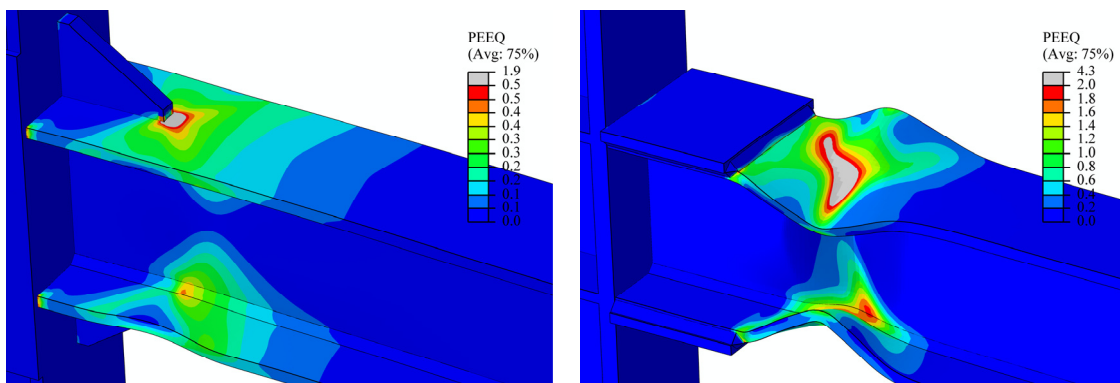


Fig. 234: Deformed shape of RS and CP joints with beam HEB400. Predicted instance of LCF crack initiation according to the proposed criteria *crit.*^a. Deformation scale factor 1.0

Slika 234: Deformirana oblika spojev RS in CP s prečko HEB400. Napoved nastopa nizkociklične razpoke v skladu s predlaganim kriterijem *crit.*^a. Faktor povečave deformacij 1.0

Observed differences in the number of cycles to LCF crack initiation between RS and CP joints comprising IPE beams from Table 34 are negligible and thus the performance of this group of joints appears to be fully comparable, see also Fig. 235.

However, in case of all the RS joints comprising H beam profile (HEA, HEB), the LCF crack initiation mechanism was triggered substantially earlier compared to all the CP joints, Table 34 and Fig. 235.

From comparison of deformed shapes presented in Figs 232 to 234 it is clear that the RS joint detail is critical in terms of large plastic strain concentrations in the much localised region on the beam flange at the end of the rib-stiffener. On the contrary, no such intense stress/plastic strain concentrations were observed in case of CP joints: in the latter case critical region is shifted away from the welded detail at the end of the cover-plate in the most buckled plastic hinge region of the beam flange.

The reason for quite early attained mechanical conditions under which the crack initiation mechanism would operate in case of RS HEA and HEB joints may be also due to the detail at the end of the rib-stiffener considered in the FE models. Namely, the fillet weld is present in the FE model of all the RS joints comprising IPE beams, while for the case of all RS joints with HEA and HEB beams it was not included in order to simulate actual geometry where butt weld is used to join the rib-plate to the beam and the column flange, see Fig. 206. In the latter case sharper end of the stiffened region certainly led to somewhat increased stress/strain concentrations in the nearby region of the beam.

According to the above discussion, the CP joint was found superior to the RS joint.

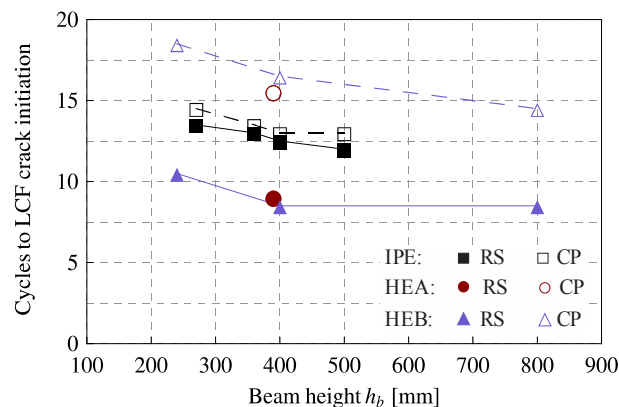


Fig. 235: Number of cycles to LCF crack initiation according to the proposed criterion $crit.^a$, see also Table 34
 Slika 235: Število ciklov do nastopa nizkociklične razpoke po predlaganem kriteriju $crit.^a$, glej preglednico 34

In order to establish comprehensive comparison of cyclic response between both stiffened connection types RS and CP as well as to explore the effects of the beam cross-section geometric characteristics on the ultimate flexural response of the joints, further evaluation of particular joint response is made in terms of three different failure criteria as presented in the text below.

Designation of the failure criteria is applied by the analogy with the three criteria used for evaluation of cyclic experimental joint response described in Chapter 3.4, although the two sets of criteria are not completely the same.

The first criterion ($N_1, \theta_{pl,1}, \Sigma\theta_{pl,1}$) accounts for joint flexural strength degradation of not more than the actual beam plastic moment $M_{pl,b}^{act}$, taken in the complementary analysis as $M_{pl,b}^{nom} \times 1.25$, see Fig. 209. The second criterion ($N_2, \theta_{pl,2}, \Sigma\theta_{pl,2}$) relates to 20 % fall of the maximum joint strength. The third one ($N_3, \theta_{pl,3}, \Sigma\theta_{pl,3}$) represents the state with the predicted LCF crack initiation according to the proposed crack initiation based LCF failure criterion $crit.^a$.

Additional data on the cyclic response of all the 16 analysed RS and CP beam-to-column joints in terms of number of cycles N_i , achieved plastic rotation $\theta_{pl,i}$, and the corresponding cumulative plastic rotation $\Sigma\theta_{pl,i}$, defined according to the three failure criteria are presented in Tables 35 to 37: Karakteristike nizkocikličnega odziva spojev CP

Table 37. Reported plastic joint rotations are evaluated with respect to the column centreline and represent the smaller absolute value obtained from positive and negative loading directions.

Preglednica 35: Celotno število polnih neelastičnih ciklov N_i v skladu z izbranimi mejnimi kriteriji
Table 35: Total number of completed inelastic cycles N_i according to the selected failure criteria

Beam	RS joint			CP joint		
	Failure criterion					
	N_1	N_2	N_3	N_1	N_2	N_3
IPE270	9	10	13	10	10	14
IPE360	8	8	13	9	10	13
IPE400	8	8	12	8	8	13
IPE500	6	7	12	8	8	13
HEA400	9	10	9	9	10	15
HEB240	11	13	10	12	13	18
HEB400	10	11	8	11	11	16
HEB800	8	9	8	8	9	14

Preglednica 36: Karakteristike nizkocikličnega odziva spojev RS
Table 36: LCF response characteristics for RS joints

RS joint	θ_{pl} (rad)			$\Sigma\theta_{pl}$ (rad)		
	Failure criterion					
	$\theta_{pl,1}$	$\theta_{pl,2}$	$\theta_{pl,3}$	$\Sigma\theta_{pl,1}$	$\Sigma\theta_{pl,2}$	$\Sigma\theta_{pl,3}$
IPE270	0.030	0.032	0.057	0.393	0.518	1.081
IPE360	0.020	0.020	0.058	0.288	0.288	1.134
IPE400	0.023	0.023	0.049	0.319	0.319	0.968
IPE500	0.013	0.023	0.050	0.155	0.248	1.015
HEA400	0.030	0.032	0.030	0.394	0.520	0.394
HEB240	0.040	0.052	0.029	0.644	1.003	0.488
HEB400	0.033	0.044	0.023	0.598	0.772	0.338
HEB800	0.022	0.033	0.022	0.312	0.444	0.312

Preglednica 37: Karakteristike nizkocikličnega odziva spojev CP
Table 37: Response characteristics for CP joints

CP joint	θ_{pl} (rad)			$\Sigma\theta_{pl}$ (rad)		
	Failure criterion			Failure criterion		
	$\theta_{pl,1}$	$\theta_{pl,2}$	$\theta_{pl,3}$	$\Sigma\theta_{pl,1}$	$\Sigma\theta_{pl,2}$	$\Sigma\theta_{pl,3}$
IPE270	0.031	0.031	0.055	0.505	0.505	1.269
IPE360	0.029	0.032	0.058	0.380	0.507	1.078
IPE400	0.020	0.020	0.058	0.280	0.280	1.130
IPE500	0.021	0.021	0.050	0.292	0.292	1.167
HEA400	0.028	0.030	0.066	0.348	0.467	1.474
HEB240	0.038	0.050	0.073	0.715	0.907	2.131
HEB400	0.039	0.039	0.065	0.619	0.619	1.685
HEB800	0.021	0.033	0.061	0.278	0.407	1.335

According to the reported number of cycles in terms of the three failure criteria presented in Table 35, the first criteria N_1 yields the critical, i.e. the minimum, number of cycles for all the analysed joints, except for the case of RS joints with all H beam profiles, where the third criteria with LCF crack occurrence results to be equally or even more stringent.

Further evaluation is concentrated on the beam profile type and its cross-sectional geometric characteristic effects on the cyclic response of the RS and CP joints. To this end, data on plastic rotations $\theta_{pl,i}$ and cumulative plastic rotations $\Sigma\theta_{pl,i}$, evaluated according to the three failure criteria, provided in Tables 36 and 37, are graphically presented in Figs 236 to 238.

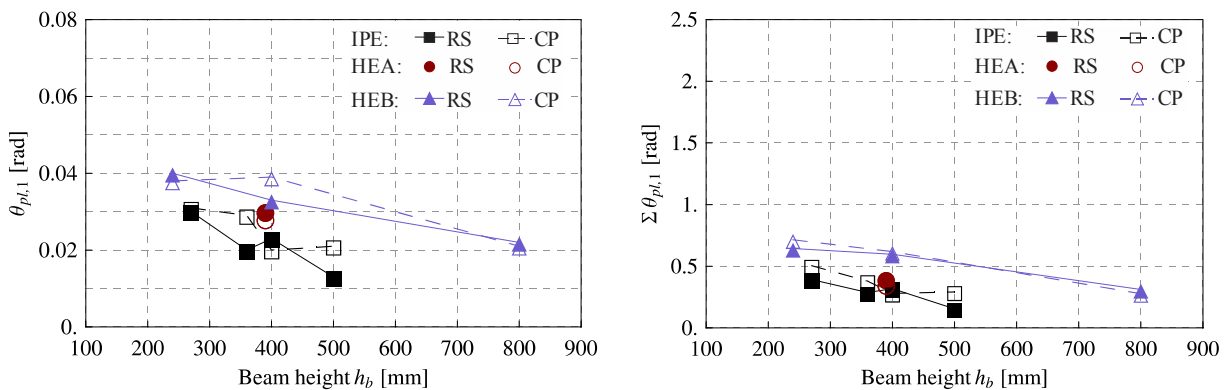


Fig. 236: Plastic rotation $\theta_{pl,1}$ and the corresponding cumulative plastic rotation $\Sigma\theta_{pl,1}$ as a function of beam profile type and its depth

Slika 236: Plastična rotacija $\theta_{pl,1}$ in pripadajoča akumulirana plastična rotacija $\Sigma\theta_{pl,1}$ v odvisnosti od tipa prečnega prereza prečke in njegove velikosti

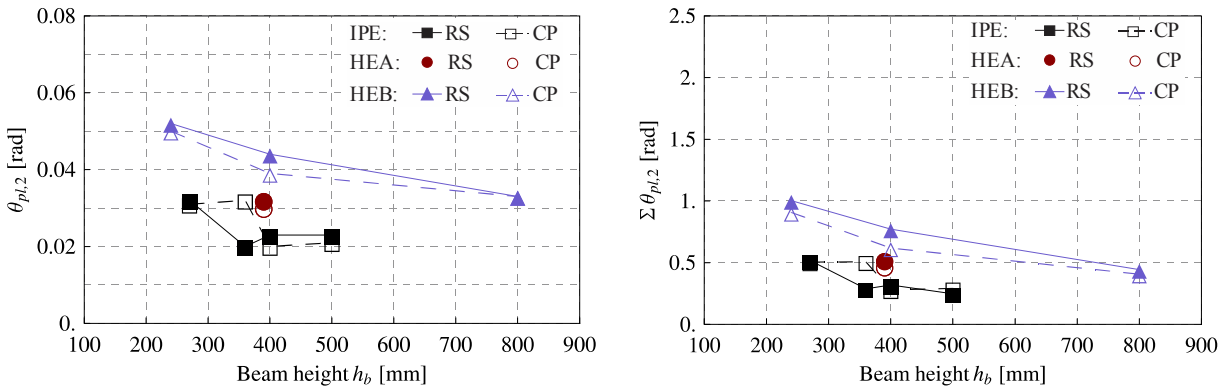


Fig. 237: Plastic rotation $\theta_{pl,2}$ and the corresponding cumulative plastic rotation $\Sigma\theta_{pl,2}$ as a function of beam profile type and its depth

Slika 237: Plastična rotacija $\theta_{pl,2}$ in pripadajoča akumulirana plastična rotacija $\Sigma\theta_{pl,2}$ v odvisnosti od tipa prečnega prereza prečke in njegove velikosti

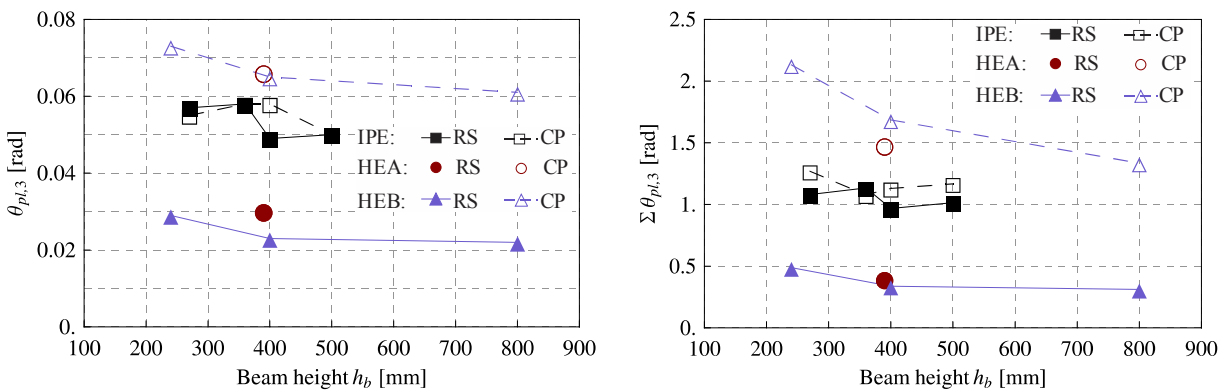


Fig. 238: Plastic rotation $\theta_{pl,3}$ and the corresponding cumulative plastic rotation $\Sigma\theta_{pl,3}$ as a function of beam profile type and its depth

Slika 238: Plastična rotacija $\theta_{pl,3}$ in pripadajoča akumulirana plastična rotacija $\Sigma\theta_{pl,3}$ v odvisnosti od tipa prečnega prereza prečke in njegove velikosti

Even though a clear tendency cannot be drawn from the relatively small number of stiffened beam-to-column joints taken into account, the most important conclusion on the basis of the above diagrams is that the geometric characteristics of a beam cross-section significantly affect the cyclic response of the RS and CP beam-to-column joints.

Not only the beam flange and the web width-to-thickness ratio, but also relative restraint between the flange and the web appears to have an important effect on the cyclic performance of the joints in terms of the beam buckling onset and its magnitude.

The second indirect effect of the beam profile cross-section geometric characteristics is related to the stiffened connection typology. While the mechanical conditions under which the crack initiation mechanism would operate in the beam flange at the end of the CP joints proved not to be much affected upon the beam cross-section type and its characteristics, RS joint configuration exhibited considerably poorer LCF performance for the selected set of H beam profiles, see Fig. 238.

Values of cyclic rotation capacity R_{cyc} with the corresponding beam flexural overstrength s_{cyc} for all the joints are presented in Tables 38 and 39. Similarly as in case of monotonic loading, two different definitions for rotation capacity were used, i.e. according to the first $R_{cyc,1}$ and the second $R_{cyc,2}$ failure criteria, respectively. In addition, normalised values of both the reported rotation capacity factors according to the corresponding values obtained from monotonic loading, already presented in Table 33, are provided in the same tables.

Preglednica 38: Ciklična rotacijska kapaciteta in dodatna upogibna nosilnost za spoje RS

Table 38: Cyclic rotation capacity and flexural overstrength for RS joints

RS joint	$R_{cyc,1}$	$R_{cyc,1} / R_{mon,1}$	$R_{cyc,2}$	$R_{cyc,2} / R_{mon,2}$	s_{cyc}	s_{cyc}/s_{mon}
IPE270	2.71	0.31	2.79	0.23	1.15	1.01
IPE360	1.61	0.30	1.61	0.16	1.14	1.04
IPE400	1.80	0.33	1.80	0.16	1.15	1.06
IPE500	1.28	0.26	2.17	0.17	1.14	1.07
HEA400	1.99	0.29	2.01	0.16	1.12	1.02
HEB240	2.66	0.17	3.34	0.19	1.12	0.98
HEB400	2.40	0.13	3.13	0.15	1.14	0.96
HEB800	1.58	0.20	2.27	0.22	1.13	1.00

Preglednica 39: Ciklična rotacijska kapaciteta in dodatna upogibna nosilnost za spoje CP

Table 39: Cyclic rotation capacity and flexural overstrength for CP joints

CP joint	$R_{cyc,1}$	$R_{cyc,1} / R_{mon,1}$	$R_{cyc,2}$	$R_{cyc,2} / R_{mon,2}$	s_{cyc}	s_{cyc}/s_{mon}
IPE270	2.35	0.30	2.35	0.25	1.16	0.99
IPE360	2.25	0.38	2.31	0.28	1.17	1.03
IPE400	1.61	0.32	1.61	0.22	1.16	1.03
IPE500	1.66	0.43	1.66	0.26	1.16	1.06
HEA400	1.82	0.26	1.85	0.17	1.15	1.01
HEB240	2.19	0.16	2.75	0.19	1.17	0.97
HEB400	2.53	0.17	2.53	0.17	1.17	0.94
HEB800	1.45	0.20	2.10	0.26	1.14	0.97

Data on the rotation capacities provided in Tables 38 and 39 are graphically presented in Figs 239 and 240.

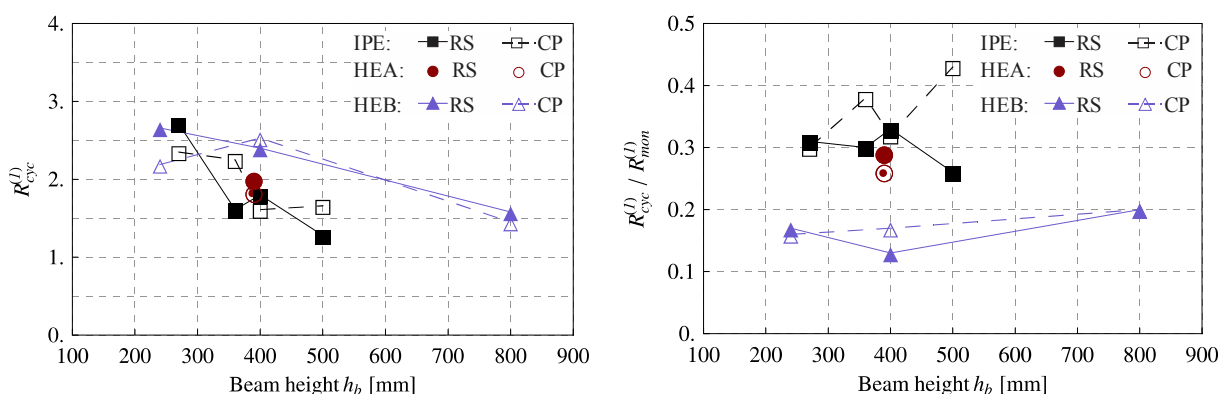


Fig. 239: Cyclic rotation capacity $R_{cyc,1}$ and the corresponding ratio $R_{cyc,1} / R_{mon,1}$ as a function of beam profile type and its depth for all the joints

Slika 239: Ciklična rotacijska kapaciteta $R_{cyc,1}$ in pripadajoč faktor $R_{cyc,1} / R_{mon,1}$ v odvisnosti od tipa prečnega prereza prečke in njegove velikosti

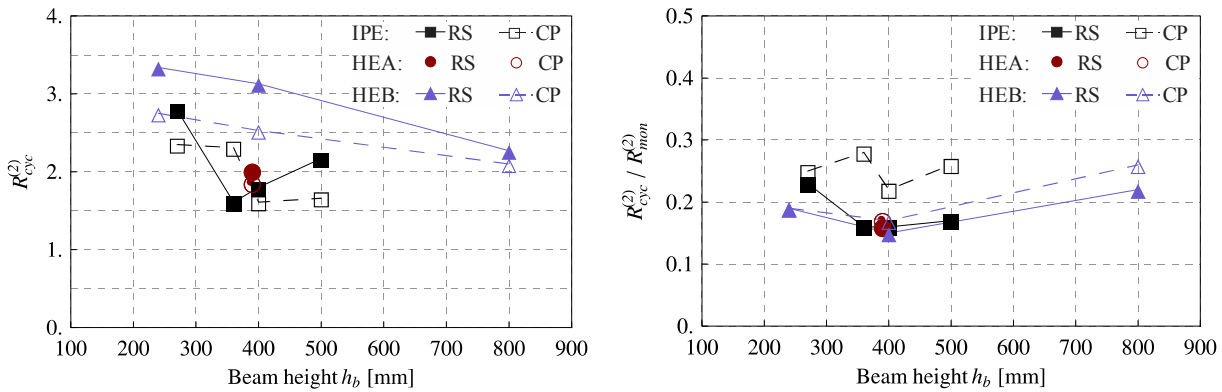


Fig. 240: Cyclic rotation capacity $R_{cyc,2}$ and the corresponding ratio $R_{cyc,2} / R_{mon,2}$ as a function of beam profile type and its depth for all the joints

Slika 240: Ciklična rotacijska kapaciteta $R_{cyc,2}$ in pripadajoč faktor $R_{cyc,2} / R_{mon,2}$ v odvisnosti od tipa prečnega prereza prečke in njegove velikosti

Although a general trend of cyclic rotation capacities $R_{cyc,1}$ and $R_{cyc,2}$ as well as the corresponding flexural overstrength due to material strain hardening s_{cyc} , cannot be clearly identified due to the relatively small number of results, the following conclusions can be drawn from Tables 38 and 39 as well as Figs 239 and 240:

- the flexural overstrength exhibited by all I and H beam profiles under cyclic loading conditions s_{cyc} is similar to that occurred under monotonic loading s_{mon} , without important difference between RS and CP joint configurations;
- as expected, all the joints subjected to cyclic loading conditions produced lower rotation capacity compared to that obtained from monotonic loading due to the pronounced effects of the beam local buckling and low-cycle fatigue in the plastic hinge region;
- ratio $R_{cyc,1} / R_{mon,1}$ ranges between 0.16 and 0.41, while somewhat smaller values of ratio $R_{cyc,2} / R_{mon,2}$ between 0.15 and 0.30 are observed;
- the obtained values for both rotation capacities $R_{cyc,1}$ and $R_{cyc,2}$ tend to decrease with increasing beam cross-section height.

In relation to the reported values of rotation capacity and beam flexural overstrength obtained from simulations of monotonic and cyclic responses of the stiffened joints, Tables 33, 38 and 39, it is interesting to provide comparison with the experimentally obtained data of the sort, as presented below.

The data obtained from the eight RS and CP beam-to-column joint specimens subjected to variable stepwisely increasing cyclic loading, performed in the experimental part of this research work, are presented in Table 40.

Preglednica 40: Rotacijska kapaciteta in dodatna upogibna nosilnost za osem preizkušancev RS in CP testiranih s spremenljivo ciklično amplitudo, rezultati laboratorijskih testov

Table 40: Rotation capacity and beam flexural overstrength for the eight RS and CP joint specimens subjected to variable cyclic loading, experimental test results

Beam profile	RS joint				CP joint			
	$R_{cyc,1}$	$R_{cyc,2}$	s_{cyc}	γ_{ov}'	$R_{cyc,1}$	$R_{cyc,2}$	s_{cyc}	γ_{ov}'
IPE240	4.97	3.82	1.24	1.36	5.88	3.65	1.24	1.37
	5.21	4.19	1.23	1.35	5.11	3.94	1.24	1.36
IPE270	5.80	3.84	1.17	1.25	5.94	4.66	1.22	1.27
	5.98	4.06	1.19	1.27	5.57	4.26	1.21	1.26

According to the design procedure: $\gamma_{ov}' = \gamma_{ov} \cdot s$, where γ_{ov} ranges between 1.04 and 1.10 (material tests)

In addition, experimentally obtained data on flexural performance of steel beams from research work performed by D'Aniello et al. (2012) are presented in Table 41. The results were obtained from monotonic and cyclic bending tests carried out on cantilever beams, see also Chapter 4.3.2.1 for a detailed description. Except for the beam profile HEB240, the other two profiles, IPE300 and HEA160, were not included in the set of beam profiles selected for the parametric numerical study. However, experimental results from D'Aniello et al. (2012) for all the three beam sections can be used as a means of general evaluation of the simulated joint responses.

Values of rotation capacity presented in Table 41, were determined according to the maximum beam rotation before the failure of particular test specimen, D'Aniello et al. (2012). To manage direct comparison with the reported values from the numerical simulations, corresponding values for $R_{mon,1}$, $R_{mon,2}$ as well as $R_{cyc,1}$, $R_{cyc,2}$ were derived from data in D'Aniello et al. (2012) and are gathered in Table 42.

Preglednica 41: Upogibni odziv jeklenih prečk, eksperimentalni testi iz D'Aniello in drugi (2012)

Table 41: Flexural performance of steel beams, experimental tests by D'Aniello et al. (2012)

Beam	R_{mon}	R_{cyc}	R_{cyc} / R_{mon}	s_{mon}	s_{cyc}	s_{cyc} / s_{mon}
IPE300	14.69	7.26	0.49	1.22	1.26	1.03
HEA160	14.44	4.64	0.32	1.30	1.31	1.01
HEB240	54.52	15.79	0.29	1.36	1.30	0.96

Preglednica 42: Rotacijski kapaciteti R_1 and R_2 , dobljeni iz rezultatov eksperimentalnih testov iz D'Aniello in drugi (2012)

Table 42: Rotation capacities R_1 and R_2 , derived from experimental test results in D'Aniello et al. (2012)

Beam	$R_{mon,1}$	$R_{cyc,1}$	$R_{cyc,1} / R_{mon,1}$	$R_{mon,2}$	$R_{cyc,2}$	$R_{cyc,2} / R_{mon,2}$
IPE300	11.71	5.10	0.44	13.08	5.04	0.39
HEA160	14.43	2.88	0.20	13.60	2.84	0.21
HEB240	49.30	12.57	0.25	44.19	12.57	0.28

From comparison of cyclic response of the beams IPE270 and IPE300 obtained from both cyclic experimental investigations, Tables 40 and 42, a good agreement in terms of both rotation capacity and flexural overstrength can be found.

However, compared to the experimentally obtained values, rotation capacity and beam flexural overstrength obtained from the simulations are found quite smaller. The reason for lower absolute values of both the rotation capacity R and the beam flexural overstrength s obtained from the numerical simulations can be justified by the use of larger value of overstrength factor (accounting for random variability of the steel yield stress) equal to $\gamma_{ov} = 1.25$, in order to provide consistent check of the proposed design procedure. Note that the overstrength factor obtained from material tests on IPE beams in case of our own experimental tests ranged between 1.04 and 1.10, see Table 40.

During the parametric numerical study of the flexural ultimate response of steel beams, yield stress value f_y was found to affect both the main flexural response parameters of a beam: increasing the value f_y result in decreased values of R and s . As an example, RS IPE270 joint response, accounting for different values γ_{ov} , is depicted in Fig. 241.

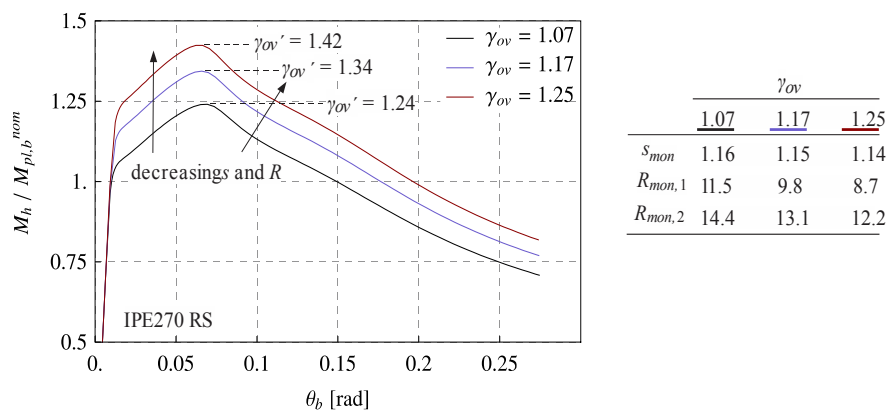


Fig. 241: Effect of parameter γ_{ov} on the beam flexural ultimate response
Slika 241: Vpliv parametra γ_{ov} na mejni upogibni odziv prečke

In spite of quite large differences between absolute values of rotation capacity and flexural overstrength obtained from the simulations and the presented experimental tests, close agreement can be observed between the corresponding ratios R_{cyc} / R_{mon} and s_{cyc} / s_{mon} , see Tables 38, 39, 41 and 42.

5.3.4 Conclusions and discussion

Additional simulations of rib-stiffened (RS) and cover-plate (CP) beam-to-column joint responses under bending and simultaneous column compressive axial load were performed. In combination with damage indices it was shown that column axial compressive load level up to 60 % of the corresponding composite column plastic resistance to compression should not considerably increase the likelihood either of ductile or brittle fracture in the welded beam-to-column connection.

The applied material stress-strain curves (for monotonic and cyclic responses) for beams were characterised by overstrength factor accounting for random variability of the steel yield stress equal to $\gamma_{ov} = 1.25$ and the ultimate-to-yield stress ratio $f_u/f_y = 1.28$. On the other hand, material stress-strain curves comprising nominal value of material yield stress f_y^{nom} were accounted for all non-dissipative steel joint components, including stiffening plates and complete column member.

As found from numerical analyses results, all the RS and CP beam-to-column joints, designed according to the proposed design procedure for full-strength joints, developed full plastic capacity of the connected beam under monotonic loading.

Both stiffened joint configurations behave very well in terms of relocating plastic straining from the beam-column welded interface into the unstiffened region of the beam beyond the stiffened connection, referred to as plastic hinge region. The centreline of the beam plastic hinge was located at a distance of $\frac{1}{4} h_b$ from the end of the stiffened region in case of all the simulated RS and CP joints, which is the same as observed in all the cyclic experimental tests.

Reinforcing plates of both RS and CP joints, subjected to monotonic loading, should remain essentially elastic if the proposed design procedure is used. It should be emphasised that the proposed design procedure will not prevent yielding of the rib-stiffeners or cover-plates but should limit the maximum strains to modest levels. Moderate yielding of the stiffening plates should not lead to premature fracture or undesired behaviour of the stiffened beam-to-column joints.

Although all the beams applied in the parametric study meet cross-sectional Class 1 requirements according to EN 1993-1-1, quite large differences, in terms of exhibited rotation capacity and the corresponding degree of beam flexural overstrength, were observed between the applied I and H beam profiles as well as their different sizes. In fact, joint overstrength needed for the development of the full plastic capacity of the connected beam is directly related to its ultimate behaviour.

Maximum values of the overall beam flexural overstrength factor $\gamma_{ov}' = \gamma_{ov} \cdot s$ obtained from the joints subjected to monotonic loading are very close or even above $\gamma_{ov}' = 1.5$ as considered in the proposed design procedure for both full-strength stiffened joint configurations, i.e. 1.49 and 1.56 for RS and CP joints, respectively. However, as observed from the deformed shapes of the joints, the design procedure still provides robust enough stiffened beam-to-column connections in order to prevent excessive plastic straining in the close vicinity of the vulnerable beam-column welded connection at the column flange.

All the stiffened joints subjected to cyclic loading with stepwisely increasing loading amplitude according to ANSI/AISC-341-10 possessed sufficient degree of overstrength to allow for the development of the full beam plastic rotation capacity. However, from the subsequent analysis of low-cycle fatigue (LCF) life, in terms of identification of the LCF crack initiation, important difference in fatigue behaviour between RS and CP joints was found, as described below.

In case of CP joints, mechanical conditions under which the crack initiation mechanism would operate were always met after the overall joint strength degradation, characterised by well-developed beam local buckling, in the most buckled region of the beam flange. The response of all the RS joints comprising IPE beams was found fully comparable to the aforementioned fatigue response of the CP joints.

On the other hand, in case of all the RS joints comprising H beam profiles (HEA, HEB), the LCF crack initiation mechanism was triggered substantially earlier compared to the corresponding CP joints, and in the state before the onset of strength degradation due to the local beam buckling. From the observations of damage indices on the deformed shapes of the joints, the RS joint detail was found critical in terms of large plastic strain concentrations in the much localised region on the beam flange at the end of the rib-stiffener. Consequently, the CP joint configuration was found to behave superior to the RS connection type.

In relation to the two applied criteria for the evaluation of crack initiation under low-cycle fatigue loading, the effective damage concept proposed by Ohata and Toyoda (2004) did not provide consistent results, particularly in case of the RS joints, where critical region was observed at the end of the stiffened connection. On the other hand, the new proposed criterion appears to provide fully consistent and logical results for all the 16 analysed RS and CP joints.

From comparison between the simulated monotonic and cyclic responses of the stiffened joints, the following conclusions can be drawn.

Flexural overstrength s exhibited by all I and H beam profiles under cyclic loading conditions is similar to that occurred under monotonic loading, without important difference between RS and CP joint configuration.

As expected, all the joints subjected to cyclic loading conditions produced lower rotation capacity compared to that obtained from monotonic loading, due to the pronounced effects of the beam local buckling and low-cycle fatigue in the plastic hinge region on the beam.

Monotonic and cyclic rotation capacities of all the joints tend to decrease with increasing beam cross-section height. Reported cyclic-to-monotonic rotation capacity ratio, determined with the ultimate beam rotation corresponding to the moment resistance drop below actual beam plastic moment, varies between 0.16 and 0.41. The same ratio corresponding to the 20 % fall of the maximum moment resistance is very similar and ranges between 0.15 and 0.30.

The outcomes of the numerical parametric study present an important contribution also in terms of flexural ultimate behaviour of steel beams and confirm the need for a twofold classification of steel members according to their ductility and overstrength as the most appropriate approach for seismic design applications (Mazzolani, Piluso, 1992. 1993. Gioncu, Mazzolani, 2000. Piluso, Rizzano, 2007. D'Aniello et al., 2012). Especially, clear distinction was made in the parametric study between overstrength due to random material variability γ_{ov} and overstrength due to strain-hardening s , which is still not clearly addressed in the current European seismic design code.

In particular, maximum value of complete overstrength factor $1.1 \times \gamma_{ov} = 1.1 \times 1.25 = 1.375$ as exists in the current code EN 1998-1, was proved to be too small to guarantee sufficient overstrength of a connection in order to assure the development of the full plastic capacity of the connected beam. This is mainly due to the insufficient overstrength level (factor 1.1), which should take into account additional flexural resistance of the connected beam due to the strain hardening until the complete development of local buckling. Proposed values for both $\gamma_{ov} = 1.25$ and $s = 1.2$ result in overall overstrength factor $\gamma_{ov}' = s \cdot \gamma_{ov} = 1.5$, which proved to be satisfactory.

6 DESIGN GUIDELINES FOR PREQUALIFIED FULL-STRENGTH WELDED STIFFENED BEAM-TO-COLUMN JOINTS

6.1 Introduction

This chapter provides requirements for prequalified rib-stiffened (RS) and cover-plate (CP) connections that, if followed, should guarantee adequate response of the joints under monotonic and seismic loading. Design guidelines for both studied stiffened joint configurations are presented. The connection prequalification data and the design guidelines are based on the results of this experimental and numerical study as well as findings from prior research activities on stiffened connections.

Beam-to-column joints presented below consist of one connection (single-sided joint configuration), but can be extended to joints with two connections (double-sided joint configuration).

6.2 Welded rib-stiffened (RS) beam-to-column joint

6.2.1 Detailing guidelines

The joint consists of a hot-rolled I or H cross-section beam framing into H cross-section column, Fig. 242. The column can be made in steel or it may be fully concrete encased column. The joint represents stiffened connection solution, in which a single tapered vertical rib plate is welded to both beam flanges.

Fillet welds are used to join all the components together, including complete beam-column connection. A full-strength peripheral fillet weld is provided all around the beam cross-section before attaching both rib plates. Throat thicknesses of fillet welds joining the rib to the beam and column flange are designed to develop at least the nominal yield strength of the rib plate. In case of H beam profiles, butt weld should be used to attach the rib plates to the beam and the column flanges, rather than fillet welds, due to larger thicknesses of the plates.

The geometry of the stiffened connection requires the beam to be rotated midway through the shop joining the ribs to the beam flanges using down hand fillet welding of a standard workmanship quality.

Column side plates in case of concrete fully-encased column (in order to facilitate casting) and transverse web stiffeners or supplementary web plates in case of steel column may be used to increase column web panel shear resistance, if needed.

The joint is designed as a full strength connection. Thus, plastic hinge is expected to occur in the beam section beyond the end of the stiffening plates.

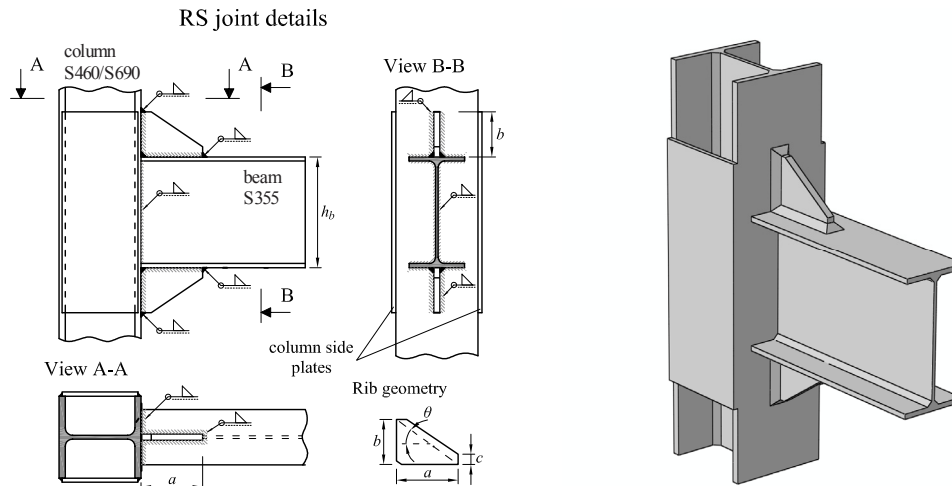


Fig. 242: Welded RS beam-to-column joint details (concrete column encasement not illustrated)
 Slika 242: Konstrukcijski detajli varjenega spoja prečka-steber RS (betonski del sovprežnega stebra ni prikazan)

The complete solution does not require additional preparations for beam flanges before welding.

Complete joint solution takes into account also details regarding fabrication of fully encased composite column with proposed solution for the placement of transverse reinforcement around the beam-to-column connection, Fig. 243.

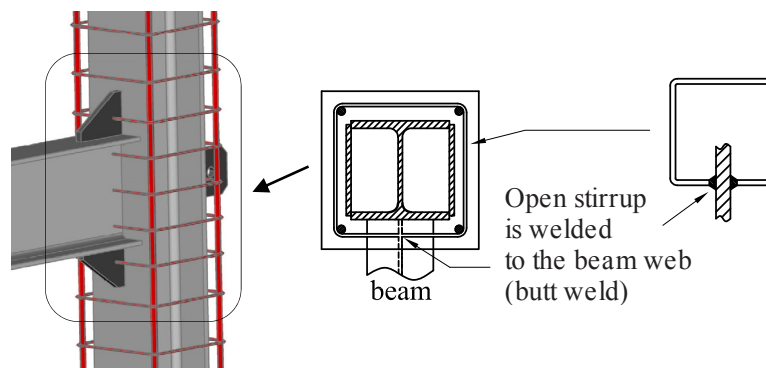


Fig. 243: Detail of composite column transverse reinforcement in the region of the beam-to-column connection
 Slika 243: Detajl prečne armature sovprežnega stebra v območju stikovanja prečke na steber

6.2.2 Design procedure

6.2.2.1 Introduction

The design objective for the RS connection, based on the capacity design concept, is to transfer inelastic action away from the face of the beam-to-column connection, thus reducing the possibility for the appearance of brittle failure conditions. Since full-strength connection with strong column/weak beam concept is applied, plastic hinge is expected to occur in the beam section just beyond the end of the reinforcing plates. Plastic hinge in the beam section is the preferred location for inelastic action in the frames, since flexural yielding of the beam is the preferred behavioural mode capable of exhibiting acceptable levels of inelastic rotations (FEMA, 2000b. Kim et al., 2000).

A hybrid-steel approach can be implemented, where high strength steel (HSS, grade S460 or S690) is used for the column, representing non-dissipative elastic member, and mild carbon steel (MCS, grade S355) for the beam, acting as dissipative member during earthquake,

resulting in two different MCS-HSS beam-column material combinations. Both column-beam HSS/MCS material combinations showed a good performance in all the tests with no damage of welds observed in the beam-column connection. However, the solution can also be applied using the same MCS grade for both the beam and the column.

The overall design criterion adopted is that the region of the connection at the face of the column should remain nominally elastic under the maximum bending moment and shear force developed by the fully yielded and strain hardened beam.

General design procedure used in seismic design situation for single-sided full strength beam-to-column joint (exterior column in multi-storey moment frame building or inner column in dual braced frame) is presented, Fig. 244.

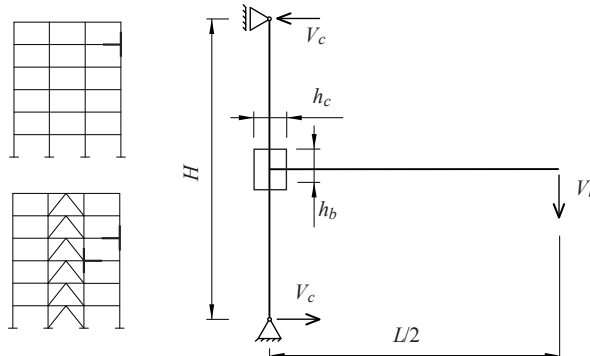


Fig. 244: Sample frames with single-sided beam-to-column joint configuration
Slika 244: Primer okvirjev z enostranskim spojem prečka-steber

The following subsections provide guidelines for the design of RS joint.

6.2.2.2 Local ductility requirements

For the design of the prequalified RS joint the following presumptions are taken into account. Alternatively, other material and joint component material combinations, appropriate for seismic design, may also be applied.

- Beam: hot rolled I or H cross-section, steel grade S355 (MCS), with toughness class at least J2 or N/M steel.
- Column: fully concrete encased H cross-section or steel H cross-section, steel grade S355, S460, S690 (MCS or HSS):
 - side plates welded to the steel profile in case of concrete encased column (to facilitate casting of concrete from the top of the column);
 - transverse web stiffeners or supplementary web plates in case of steel column solution.
- Rib-stiffener: plates from steel grade S355. The nominal yield stress of the reinforcing plate material should closely match that of the beam.

In order to achieve reliable inelastic deformation capacity attributed to the resistance to local buckling well into the inelastic range, the beam should meet the compactness limits for cross-sectional Class 1 or at least Class 2 according to EN 1993-1-1 provisions. In addition, according to EN 1998-1 (CEN, 2005c) §6.6 the beam should be verified to have sufficient resistance against lateral and lateral torsional buckling in accordance with EN 1993-1-1 (CEN, 2005a) §6.3.5, assuming the formation of plastic hinges at both ends of the beam.

6.2.2.3 Selection of the component size

According to the recommendations from the literature (FEMA, 2000b. Lee, 2002), and findings from our study the following trial values for preliminary rib sizing can be used: rib height $b = \frac{1}{3} h_b$; rib diagonal angle $\theta = 30^\circ - 40^\circ$; rib length $a = b/\tan(\theta)$, trimmed length $c = 25$ mm and rib thickness $t = 1.35 t_f$ with t_f being the thickness of the beam flange (for standard European I and H beam profiles), Fig. 242.

The final rib characteristics b , a and t are determined by applying the design criterion that stiffened connection at the column face remains nominally elastic under the maximum moment developed by the connected beam.

The column side plates should be provided throughout the effective width of the steel column web in tension and compression according to EN 1993-1-8 provisions §6.2.6.2.

6.2.2.4 Evaluation of plastic hinge location

Based on the test results and additional complementary numerical study on rib-stiffened stiffened joints, the centreline of the plastic hinge is assumed to be located at a distance of one-quarter of the beam depth ($\frac{1}{4}h_b$) from the end of the rib-stiffener.

6.2.2.5 Evaluation of nominal actions in the plastic hinge

Nominal value of moment $M_{pl,hinge}^{nom}$ and the corresponding shear force V_{hinge}^{nom} in the beam at the centreline of the assumed plastic hinge can be determined as:

$$M_{pl,hinge}^{nom} = M_{pl,b}^{nom}, \quad (36)$$

$$V_{hinge}^{nom} = V_{Ed,G} + V_{Ed,M}, \quad (37)$$

$$V_{Ed,G} = \frac{(p + \psi_{2,i} k \cdot q) \cdot L_{0,x} \cdot L_{0,y}}{2}, \quad (38)$$

$$V_{Ed,M} = \frac{2 \cdot M_{pl,hinge}^{nom}}{L'}, \quad (39)$$

where:

- $M_{pl,b}^{nom}$ is a plastic moment of unstiffened beam section considering the nominal value of yield stress;
- $V_{Ed,G}$ is the shear force from gravity forces in the seismic design situation;
- $V_{Ed,M}$ is the shear force corresponding to the application of the plastic moments in the beam;
- $L_{0,x}$ and $L_{0,y}$ represent beam span to the column centreline in both horizontal directions of considered frame;
- L_h is the distance between plastic hinges on the beam, Fig. 245;
- p is a permanent load;
- q is a live load.

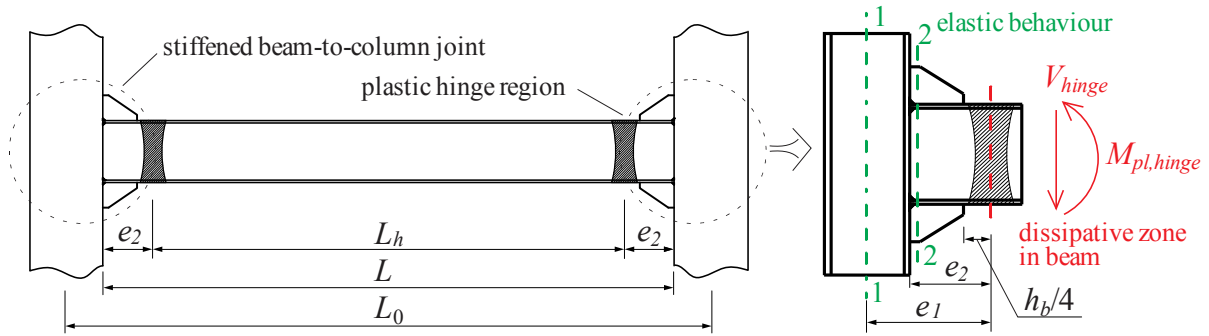


Fig. 245: Typical beam span with stiffened joint, plastic hinge location and cross-sections used for design check
Slika 245: Primer prečke v okvirju z ojačanima spojem, pozicija plastičnega členka na prečki z označenimi prerezi za računsko kontrolo

6.2.2.6 Global ductility condition

In order to check if a stiffened joint meets the strong column-weak beam requirement from EN 1998-1, the corresponding moment at the centreline of the column is determined assuming linear distribution of moment on the beam.

$$\sum M_{Rc} \geq 1.3 \sum M_{Rb}, \quad (40)$$

where:

- $\sum M_{Rc}$ is the sum of the nominal bending resistance of the columns framing the joint;
- $\sum M_{Rb}$ is the sum of the nominal bending resistance of the beams framing the joint.

M_{Rb} from particular beam, taking into account nominal material characteristics, is determined as:

$$M_{Rb} = M_{Ed}^{1-1,nom} = M_{pl,hinge}^{nom} + V_{hinge}^{nom} \cdot e_1, \quad (41)$$

where:

e_1 is the distance from the centreline of the assumed plastic hinge to the column centreline, Fig. 245.

6.2.2.7 Welded beam-to-column connection

Evaluation of actions

The size of the ribs is determined taking into account the moment at the face of the column $M_{Ed}^{2-2,ov}$ and using the elastic section modulus of the stiffened section for the moment resistance, treating the beam and the reinforcing plates as an integral section.

$$M_{Ed}^{2-2,ov} = \gamma_{ov}' \cdot M_{pl,hinge}^{nom} + V_{hinge}^{ov} \cdot e_2, \quad (42)$$

$$V_{Ed}^{2-2,ov} = V_{hinge}^{ov}, \quad (43)$$

$$V_{hinge}^{ov} = V_{Ed,G} + \gamma_{ov}' \cdot V_{Ed,M}, \quad (44)$$

where:

e_2 is the distance from the centreline of the assumed plastic hinge to the column face, Fig. 245.

Maximum assumed moment that could be generated by the unreinforced beam is of the order of $\gamma_{ov}' \cdot M_{pl,b}^{nom}$, where $\gamma_{ov}' = s \cdot \gamma_{ov}$, with γ_{ov} being overstrength factor accounting for the random

variability of the steel yield stress, while s covers the additional flexural beam strength due to the material strain hardening in the post yield region.

According to EN 1998-1, maximum value of the overall overstrength factor $\gamma_{ov}' = 1.1 \cdot \gamma_{ov} = 1.375$ ($\gamma_{ov} = 1.25$). Our proposal for the value of factor γ_{ov}' to be used in Eq. (42) and (44) is $\gamma_{ov}' = 1.5$, taking into account probable material overstrength $\gamma_{ov} = 1.25$ and strain hardening $s = 1.2$ of the steel material in dissipative zone of the beam.

Capacity evaluation

The capacity of the stiffened connection in terms of bending moment and shear force is:

$$M_{Rd}^{2-2} = \frac{W_{el}^{2-2} \cdot f_y}{\gamma_{M0}}, \quad (45)$$

$$V_{Rd}^{2-2} = \frac{A_v \cdot f_y}{\sqrt{3} \cdot \gamma_{M0}}, \quad (46)$$

where:

- W_{el}^{2-2} is the elastic section modulus of the stiffened connection taken in cross-section 2-2, taking the beam and the reinforcing plates as an integral section;
- A_v is the shear area of the beam.

Check of the strengthened connection

The resistance of the stiffened connection to bending and shear is checked using the following two inequalities:

$$\frac{M_{Ed}^{2-2,ov}}{M_{Rd}^{2-2}} \leq 1.0, \quad (47)$$

$$\frac{V_{Ed}^{2-2,ov}}{V_{Rd}^{2-2}} \leq 0.5. \quad (48)$$

For the shear force it is assumed that it is carried by the web of the beam, where the value of the shear force is less than half the plastic shear resistance, neglecting its effect on the moment resistance of the beam web and therefore overall rotation capacity of the beam.

Welds

The fillet welds joining the complete beam section to the column flange and the reinforcing plates to the beam and column flanges (T-joints) are designed to develop at least the nominal yield strength of the connected plate in tension.

Considering material of grade S355 for the beam and the rib plates, the maximal needed fillet weld throat thickness according to EN 1993-1-8 (CEN, 2005b) ($\beta_w = 0.9$), see Fig. 246, can be expressed as:

$$\begin{aligned} a_{max} &= 0.58 \cdot t \quad \dots \text{ for S355 J2 or N} \\ &= 0.60 \cdot t \quad \dots \text{ for S355 M,} \end{aligned} \quad (49)$$

where:

- t is the thickness of a particular connected plate of steel grade S355 (rib, beam flange and web).

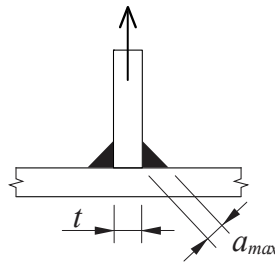


Fig. 246: Maximal throat thickness of fillet weld in T-joint
 Slika 246: Največja debelina kotnega zvara v T-spoju

Column side plates in case of concrete fully-encased column are welded to the column flanges using fillet welds with a maximal throat thickness $0.7 \cdot t_{sp}$ (lap joint).

It is to be noted that additional overstrength factor $1.1 \gamma_{ov}$ is prescribed in EC8-1 §6.5.4(3) for fillet welds of non-dissipative connections. The present design procedure includes the overstrength factor already in the evaluation of actions ($M_{Ed}^{2-2,ov}$, $V_{Ed}^{2-2,ov}$) to which the stiffened connection is designed from the start.

The throat thickness of the fillet welds joining the rib to the beam and column flanges can also be defined according to the design method based on equivalent strut model, presented in Chapter 6.2.2.10.

6.2.2.8 Column design

6.2.2.8.1 Column web panel

Evaluation of actions

The shear resistance check of the column panel is done according to EN 1998-1, where the design shear force in the web panel due to action effects ($V_{wp,Ed}$) should take into account the plastic resistance of the adjacent dissipative zones in the beams. Beam overstrength should be taken into account. The shear buckling resistance of the web panel should also be checked according to EN 1993-1-5 (CEN, 2007) §5. Since provisions from EN 1998-1 do not provide additional information on the relation, the shear force in the column panel zone is determined using the procedure from EN 1993-1-8 §5.3(3), Figs 244 and 247.

$$V_{wp} = \sum M_b / h_b - V_c, \quad (50)$$

where:

- $\sum M_b$ is the sum of bending moments in the beam at the column face;
- h_b is the beam height;
- V_c is the average shear force in the column.

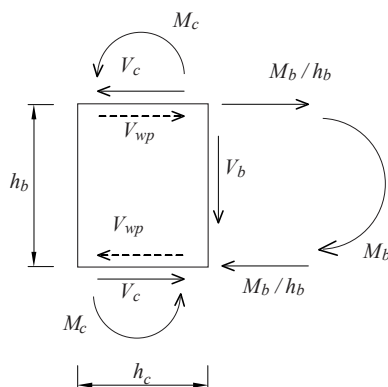


Fig. 247: Internal forces in the column panel zone for single-sided joint
 Slika 247: Notranje sile v območju panelu stebra za primer enostranskega spoja

In case of a single-sided joint configuration (assumption is true for external joints and approximately true for joints adjacent to concentrically braced bays, $\beta = 1.0$), the shear force in the column panel zone $V_{wp,Ed}$ is:

$$V_{wp,Ed} = M_{Ed}^{2-2,ov} / h_b - V_c, \quad (51)$$

with $M_{Ed}^{2-2,ov}$ already defined by Eq. (42).

Capacity evaluation

Design plastic shear resistance of unstiffened column web panel ($V_{wp,a,Rd}$) is computed according to EN 1993-1-8 §6.2.6.1(2):

$$V_{wp,a,Rd} = \frac{0.9 \cdot A_v \cdot f_y}{\sqrt{3} \cdot \gamma_{M0}}, \quad (52)$$

where:

- A_v is the shear area of the steel column profile.

In case of concrete encased steel column web the design shear resistance of the panel, determined in accordance with EN 1993-1-8, may be increased to allow for the encasement (if conditions from EN 1998-1 §7.5.4(7) are satisfied). The design shear resistance of concrete encasement to the column web panel ($V_{wp,c,Rd}$) according to EN 1994-1-1 (CEN, 2004) §8.4.4.1 is:

$$V_{wp,c,Rd} = 0.8 \cdot \nu \cdot A_c \cdot f_{cd} \cdot \sin \theta, \quad (53)$$

where:

$$A_c = 0.8 \cdot (b_c - t_w) \cdot (h - 2t_f) \cdot \cos \theta, \quad (54)$$

$$\theta = \arctan \left[(h - 2t_f) / z \right], \quad (55)$$

$$\nu = 0.55 \left(1 + 2 \left(N_{Ed} / N_{pl,Rd} \right) \right) \leq 1.1. \quad (56)$$

The panel zone resistance defined as the sum of contributions from the concrete and steel shear panel, according to EN 1998-1 §7.5.4(7), is then:

$$V_{wp,Rd} = \max \left(V_{wp,a,Rd}; 0.8 \cdot (V_{wp,a,Rd} + V_{wp,c,Rd}) \right). \quad (57)$$

The contribution of the column side plates throughout the effective width of the column web in case of composite column and transverse web stiffeners or supplementary web plates in case of steel column may also be taken into account, if needed.

Check of the column panel in shear

The check of the column panel zone shear resistance is performed using the following inequality:

$$\frac{V_{wp,Ed}}{V_{wp,Rd}} \leq 1.0 \quad (58)$$

6.2.2.8.2 Column web in transverse compression and tension

The design resistance of an unstiffened column web subject to transverse compression and tension ($F_{c,wc,Rd}$, $F_{t,wc,Rd}$) should be checked according to EN 1993-1-8 §6.2.6.2 and §6.2.6.3. In case of full strength joints, stiffeners are generally needed to increase the design resistance of the column web in both, compression and tension zone. Most commonly, transverse stiffeners aligned with the corresponding beam flange are used. However, in case of side plates welded on the steel column, their contribution may be taken by analogy to that of the column web.

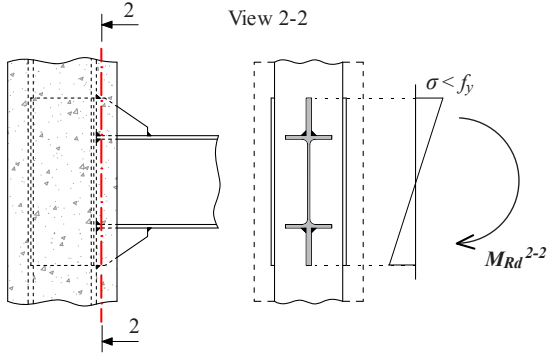
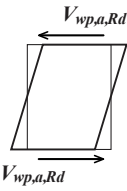
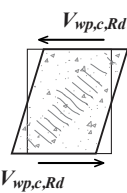
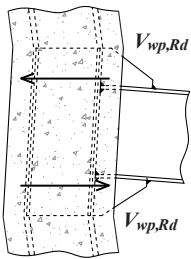
The design forces due to action effects ($F_{c,wc,Ed}$, $F_{t,wc,Ed}$) should take into account the plastic resistance of the adjacent dissipative zones in the beams. Beam overstrength should be taken into account.

Where the steel column web is encased in concrete the design resistance of the column web in compression, determined in accordance with EN 1993-1-8 §6.2.6.2 may be increased to allow for the encasement, EN 1994-1-1 §8.4.4.2.

6.2.2.9 Summary

The joint components and the corresponding design rules for RS joint are presented in Table 43.

Preglednica 43: Projektna nosilnost osnovnih component spoja RS
 Table 43: Design capacity of basic RS joint components

Joint component	Reference to code provisions, design rules
1. Stiffened connection	
Elastic check of stiffened beam cross-section (integral section)	
	<p>Code provision (EN 1993-1-1)</p> $M_{Rd}^{2-2} = \frac{W_{el}^{2-2} \cdot f_y}{\gamma_{M0}}, \quad V_{Rd}^{2-2} = \frac{A_v \cdot f_y}{\sqrt{3} \cdot \gamma_{M0}}$
2. Column panel in shear	
Unstiffened steel column web panel (+ contribution of stiffeners, if needed)	
	<p>Code provision (EN 1993-1-8)</p> $V_{wp,a,Rd} = \frac{0.9 \cdot A_v \cdot f_y}{\sqrt{3} \cdot \gamma_{M0}}$
Concrete encasement	
	<p>Code provision (EN 1994-1-1)</p> $V_{wp,c,Rd} = 0.85 \cdot \nu \cdot A_c \cdot f_{cd} \cdot \sin \theta$
Composite section	
	<p>Code provision (EN 1998-1)</p> $V_{wp,Rd} = \max \left(V_{wp,a,Rd}; 0.8 \cdot (V_{wp,a,Rd} + V_{wp,c,Rd}) \right)$

6.2.2.10 Design of rib-stiffened connection based on equivalent strut model

In addition to the classical beam theory principle, a practical component design procedure for welded rib-stiffened moment connection is presented below. The main idea follows the observation that force transfer mechanism in the ribs can be represented by a strut model. The approach of seismic design of rib-reinforced moment connections according to Lee (2002) was taken into account, reproducing much of the formulation from the literature.

In order to be in accordance with the proposed design procedure, the method for determination of resultant forces in the rib-stiffened section was reformulated in order to express actions directly with maximal plastic moment and related shear force from the plastic hinge centreline. Additionally, final relations were calibrated against experimental results as well as results from nonlinear FEA simulations.

The overall features of the component model are shown in Fig. 248. Evaluation of seismic actions in the plastic hinge zone in the beam should be done in accordance with the proposed procedure in 6.2.2. In the model, the rib is replaced by an equivalent strut element. The equivalent strut force corresponds to the resultant of N and Q at the beam-rib interface in the actual connection.

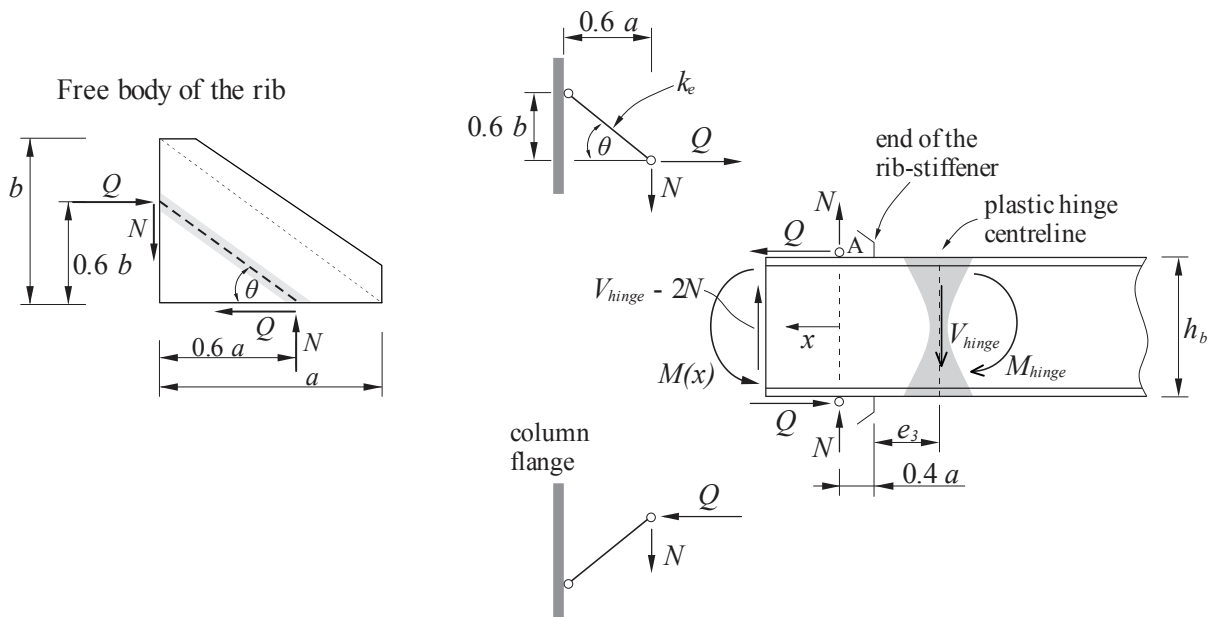


Fig. 248: Interaction model for deformation compatibility as defined in Lee (2002)

Slika 248: Interakcijski model z upoštevanjem deformacijske kompatibilnosti določen v Lee (2002)

The relations given by Eqs. (59) to (61) are derived from the adopted rib-stiffener geometry with supposed locations of rib resultant normal force N and total shear force Q at the beam/column-rib interface.

Equivalent strut area, A_e , is defined as

$$A_e = \eta \cdot h_e \cdot t, \quad (59)$$

where t is rib thickness, h_e is a span perpendicular to the strut line, see Fig. 249, and η is defined as equivalent strut area factor:

$$h_e = \frac{ab - c^2}{\sqrt{(a-c)^2 + (b-c)^2}}. \quad (60)$$

The value of equivalent strut area factor η is determined in a way to obtain the correct value of the strut force acting in the actual rib. It is defined throughout a calibration approach by means of nonlinear FEA analysis.

Normal force N can be computed with the following expression:

$$N = \left(\frac{b}{a} \right) \cdot Q. \quad (61)$$

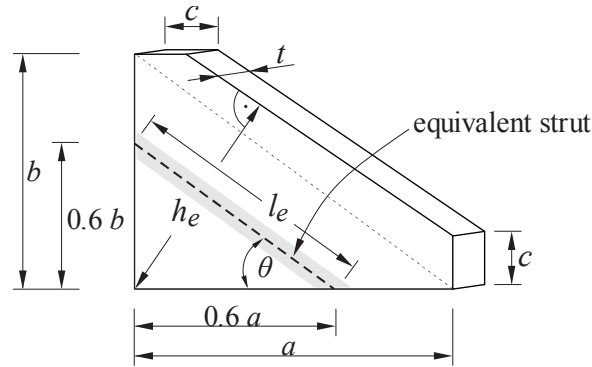


Fig. 249: Definition of rib geometry with equivalent strut as defined in Lee (2002)
 Slika 249: Definicija geometrije rebra z nadomestno vezjo, povzeto po Lee (2002)

The horizontal shear force Q remains the only unknown of the problem. The relationship between Q and η is derived from a deformation compatibility condition on the interface between the rib-stiffener and beam flange at point A, see Fig. 248, as provided below.

The horizontal displacement components of the equivalent strut at point A:

$$d_{x, strut} = \frac{Q}{k_e}, \quad (62)$$

where k_e is axial stiffness of the equivalent strut defined as

$$k_e = \frac{A_e \cdot E}{l_e}, \quad (63)$$

$$\text{with } l_e = 0.6 \sqrt{a^2 + b^2}. \quad (64)$$

The horizontal component of the beam flange deformation at point A is obtained by integrating the axial strain within the equivalent strut region:

$$d_{x, beam} = \int_0^{0.6a} \varepsilon(x)_{flange} dx, \quad (65)$$

with horizontal displacement component of beam flange at point A expressed as

$$\varepsilon(x)_{flange} = \frac{M(x)}{E I_b} \cdot \frac{h_b}{2}, \quad (66)$$

where $M(x)$ is a beam moment within the equivalent strut region:

$$M(x) = M_{pl, hinge} + V_{hinge} (e_3 + 0.4a + x) + 2N x - Q h_b. \quad (67)$$

In our case of seismic design situation, the moment and the shear force in Eq. (67) imply overstrength factor as defined in 6.2.2.7 by Eqs. (42) to (44).

The relationship between Q and η is finally obtained by equating Eqs. (62) and (66):

$$Q = \frac{M_{pl,hinge} + V_{hinge} (0.7 a + e_3)}{\frac{1}{\eta} \cdot \frac{10}{3} \cdot \frac{I_b L_e}{a h_b h_e t} + \frac{3}{5} b + hb} \quad (68)$$

To calibrate the equivalent strut area factor, a parametric study was performed within the range of practically applicable member sizes. The value 0.6 proved to give enough accurate results.

NOTE: Overstrength factor, in our case γ_{ov}' , should be accounted for in the expression for $M_{pl,hinge}$ and V_{hinge} .

Based on the von Mises yield criterion, the minimum rib thickness is computed as follows:

$$f_v = \frac{N}{bt}, f_n = \frac{Q}{bt} : \sqrt{f_n^2 + 3 \cdot f_v^2} \leq f_{y,rib} \rightarrow t \geq \frac{\sqrt{Q^2 + 3 \cdot N^2}}{b \cdot f_{y,rib}} \quad (69)$$

The rib is fillet welded to both the column and beam flanges. According to EC3-1-8 the throat thickness of two sided fillet weld between the rib and beam flange is defined as

$$\sqrt{\left(\frac{N}{2 \cdot a \cdot a_w}\right)^2 + 3 \left(\frac{Q}{2 \cdot a \cdot a_w}\right)^2} \leq \frac{f_u}{\beta_w \gamma_{M2}} \rightarrow a_w \geq \sqrt{N^2 + 3Q^2} \frac{\beta_w \gamma_{M2}}{2 a f_u} \quad (70)$$

and the throat thickness of two sided fillet weld between the rib and column flange as

$$\sqrt{\left(\frac{Q}{2 \cdot b \cdot a_w}\right)^2 + 3 \left(\frac{N}{2 \cdot b \cdot a_w}\right)^2} \leq \frac{f_u}{\beta_w \gamma_{M2}} \rightarrow a_w \geq \sqrt{Q^2 + 3N^2} \frac{\beta_w \gamma_{M2}}{2 b f_u} \quad (71)$$

6.3 Welded cover-plate (CP) beam-to-column joint

6.3.1 Detailing guidelines

The joint consists of a hot-rolled I or H cross-section beam framing into a fully concrete encased H cross-section column, Fig. 250. The joint presents stiffened connection solution, in which a flat rectangular cover plate is welded to both beam flanges.

Rectangular cover plates of a width greater than that of the beam flange are used to provide the required space for longitudinal fillet welds as well as to reduce the thickness of the plates. The thickness of the cover plate is taken to be nearly the same as that of beam flange. The length of cover plate is chosen to permit the placement of a sufficient length of fillet weld, joining the cover plate to the beam flange, to develop at least the yield strength of the cover plates. Final length of the reinforcing plates is chosen to be nearly three quarters of the beam height ($\frac{3}{4}h_b$).

Cover plates are first attached to the beam flanges using three-sided fillet welds of the same size (two longitudinal and one transverse). The fillet welds should be runoff onto backing so as to maintain the full throat thickness at the end of the plate. The backing is removed and the transition zone ground smoothly. After that, complete joint penetration single-bevel-butt weld is used to join combined thickness of a cover plate and beam flange to the column flange. Runoff should be used at both plate edges in order to provide complete joint penetration and good quality of the weld metal. The backing should be removed and the transition zone ground smoothly. Permanent backing bar is not used, since its presence may be undesirable under fatigue conditions (Engelhardt, Sabol, 1998). Butt weld is completed by depositing a sealing run on the back of the joint using fillet weld, which continues over the root radius of the beam section to the web connection, see Figs 250 and 251.

The butt weld at the beam-column interface is made without using a weld access hole, and is therefore not a prequalified weld in the area of the beam flanges above the root radius, where backing cannot be provided, Fig. 251. However, the complete solution, taking into account the robustness of elastic design, overcomes the lack of the detail.

The geometry of the stiffened connection with weld arrangements adopted required the beam to be rotated midway through the shop joining the subassemblies using down hand fillet and groove welding. In case of on-site welding, the cover plate on the top beam flange may be narrower than the beam flange in order to facilitate down hand fillet welding.

Column side plates in case of concrete fully-encased column (in order to facilitate casting) and transverse web stiffeners or supplementary web plates in case of steel column may be used to increase column web panel shear resistance, if needed.

The joint is designed as full strength connection. Thus, plastic hinge is expected to occur in the beam section beyond the end of the stiffening plates.

Beam flanges together with the cover plates have to be bevelled prior groove welded to the column flange.

Complete joint solution takes into account also details regarding fabrication of fully encased composite column with proposed solution for the placement of transverse reinforcement around beam-to-column connection, Fig. 243.

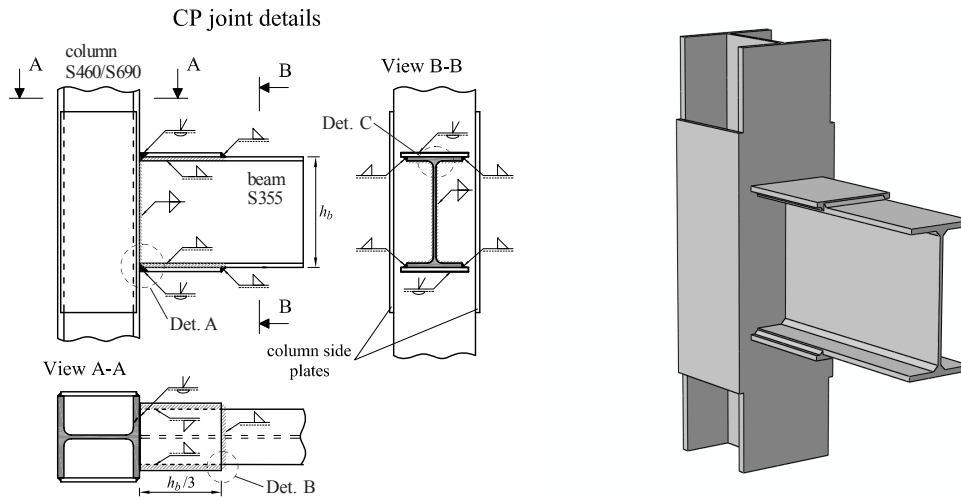


Fig. 250: Welded CP beam-to-column joint details (concrete column encasement not illustrated)
Slika 250: Konstrukcijski detajli varjenega spoja prečka-steber CP (betonski del sovprežnega stebra ni prikazan)

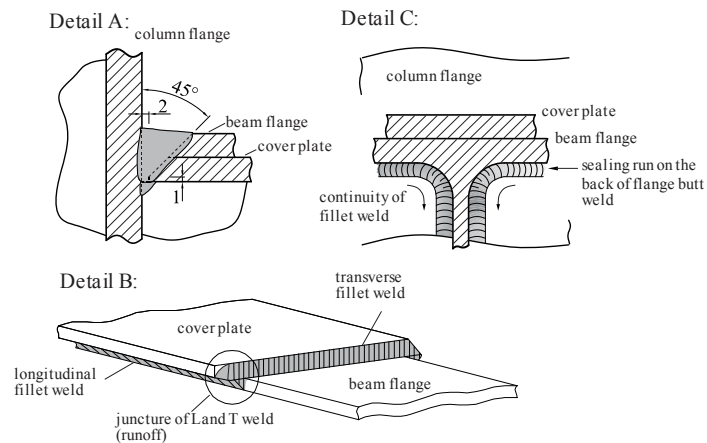


Fig. 251: Welding details of CP beam-to-column joint
Slika 251: Detajli varjenih stikov za spoj prečka-steber CP

6.3.2 Design procedure

6.3.2.1 Introduction

The design objective for the CP connection, based on the capacity design concept, is to transfer inelastic action away from the face of the beam-to-column connection, thus reducing the possibility for the appearance of brittle failure conditions. Since full-strength connection with strong column/weak beam concept is applied, plastic hinge is expected to occur in the beam section just beyond the end of the reinforcing plates.

A hybrid-steel approach can be implemented, where high strength steel (HSS, grade S460 or S690) is used for the column, representing non-dissipative elastic member, and mild carbon steel (MCS, grade S355) for the beam, acting as dissipative member during earthquake, resulting in two different MCS-HSS beam-column material combinations. Both column-beam HSS/MCS material combinations showed a good performance in all the tests with no damage of welds observed in the beam-column connection after the tests. However, the solution can also be applied using the same MCS grade for both the beam and the column.

The overall design criterion adopted is that the region of the connection at the face of the column should remain nominally elastic under maximum bending moment and shear force developed by the fully yielded and strain hardened beam.

Design recommendations for enhanced performance of the cover-plate connection were adopted from (FEMA, 2000c. 2000d. 2000b. Kim et al., 2002a).

General design procedure used in seismic design situation for single-sided full strength beam-to-column joint (exterior column in multi-storey moment frame building or inner column in dual braced frame) is presented, Fig. 138.

The following subsections provide guidelines for the design of CP joint.

6.3.2.2 Local ductility requirements

For the design of the prequalified CP joint the following presumptions are taken into account. Alternatively, other material and joint component material combinations, appropriate for seismic design, may also be applied.

- Beam: hot rolled I or H cross-section, steel grade S355 (MCS), with toughness class at least J2 or N/M steel.
- Column: fully concrete encased H cross-section or steel H cross-section, S355, S460, S690 steel grade (MCS or HSS):
 - side plates welded to the steel profile in case of concrete encased column (to facilitate casting of concrete from the top of the column);
 - transverse web stiffeners or supplementary web plates in case of steel column solution.
- Cover-plate: plates from steel grade S355. The nominal yield stress of the stiffening plate material should closely match that of the beam.

In order to achieve reliable inelastic deformation capacity attributed to the resistance to local buckling well into the inelastic range, the beam should meet the compactness limits for cross-sectional Class 1 or at least Class 2 according to EN 1993-1-1 provisions. In addition, according to EN 1998-1 §6.6, the beam should be verified to have sufficient resistance against lateral and lateral torsional buckling in accordance with EN 1993-1-1 §6.3.5, assuming the formation of plastic hinges at both ends of the beam.

6.3.2.3 Selection of the component size

According to the recommendations from the literature (Kim et al., 2000. 2002a. 2002b) as well as findings from our study the following trial values for preliminary cover-plate sizing can be used: rectangular plate with a thickness equal to that of the beam flange, $t_{cp} = t_f$, width equal to the beam flange width, increased at least by two times the plate width to provide space for longitudinal fillet welds placement, $b_{cp} = b_b + 2 \cdot t_{cp}$ and length $l_{cp} = \frac{3}{4} \cdot h_b$, Fig. 250. In case of on-site welding, the cover plate on the top beam flange may be narrower than the beam flange in order to facilitate down hand fillet welding.

The final cover-plate geometric characteristics b_{cp} and t_{cp} are determined by applying the design criterion that stiffened connection at the column face remains nominally elastic under maximum moment developed by the connected beam. The final length of the cover plate l_{cp} is chosen to permit the placement of sufficiently long longitudinal fillet welds to develop at least the yield strength of the cover plate.

The column side plates should be provided throughout the effective width of the steel column web in tension and compression according to EN 1993-1-8 provisions §6.2.6.2.

6.3.2.4 Evaluation of plastic hinge location

Based on the test results, the centreline of a plastic hinge is assumed to be located at a distance of one-quarter of the beam depth ($\frac{1}{4} h_b$) from the end of the cover-plate.

6.3.2.5 Evaluation of nominal actions in the plastic hinge

Nominal value of moment $M_{pl,hinge}^{nom}$ and the corresponding shear force V_{hinge}^{nom} in the beam at the centreline of the assumed plastic hinge can be determined according to equations already defined in Chapter 6.2.2.5.

6.3.2.6 Global ductility condition

In order to check if a stiffened joint meets the strong column/weak beam requirement from EN 1998-1, the corresponding moment at the centreline of the column is determined assuming linear distribution of moment on the beam.

All relations to be considered are already defined in Chapter 6.2.2.6.

6.3.2.7 Welded beam-to-column connection

Evaluation of actions

Relations already presented in Chapter 6.2.2.7 should be considered.

Capacity evaluation

Relations presented in Chapter 6.2.2.7 should be considered.

Check of the stiffened connection

Relations presented in Chapter 6.2.2.7 should be considered.

Welds

Complete joint penetration single-bevel butt weld is used to join the combined thickness of a cover plate and beam flange to the column flange. No permanent backing bar is used. Butt weld is completed by depositing a sealing run on the back of the joint using fillet weld, which continues over the root radius of a beam section to the web connection.

Fillet welds joining the beam web to the column flange as well as fillet welds used to connect cover plate to the beam flange are designed to develop at least the nominal yield strength of the connected plate.

Throat thickness of a fillet weld on the beam web (T-joint) is determined taking into account the yield strength of the beam web in tension, see Eq. (49).

Three-sided (2 longitudinal and 1 transverse) fillet welds joining the cover plate to the beam flange, Fig. 252, are designed to develop at least the nominal yield strength of the cover plate. Fillet welds of one size only should be used.

Assuming the full throat thickness for both longitudinal and transverse welds at the end of the plate (use of runoff tabs), the minimal needed throat thickness of fillet welds according to EN 1993-1-1 can be defined as:

$$a \geq \frac{(t_{cp} \cdot b_{cp}) \cdot f_y / \gamma_{M0}}{\frac{f_u / \sqrt{3}}{\beta_w \cdot \gamma_{M2}} \cdot (2 \cdot l_{cp} + b_b)} \quad (72)$$

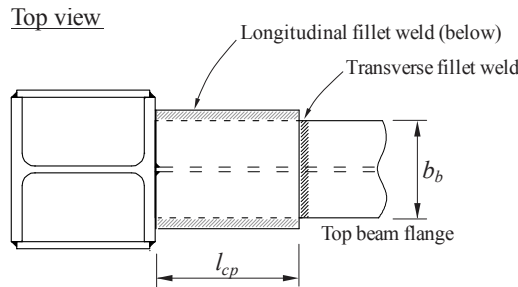


Fig. 252: Three-sided fillet weld joining the cover-plate to the beam flange
 Slika 252: Tristranski kotni zvar med vezno pločevino in pasnico prečke

Column side plates in case of concrete fully-encased column are welded to the column flanges using fillet welds with a maximal throat thickness $0.7 \cdot t_{sp}$ (lap joint).

It is to be noted that additional overstrength factor $1.1 \cdot \gamma_{ov}$ is prescribed in EN 1998-1 §6.5.4(3) for fillet welds of non-dissipative connections. The present design procedure includes the overstrength factor already in the evaluation of actions ($M_{Ed}^{2-2,ov}$, $V_{Ed}^{2-2,ov}$) to which the stiffened connection is designed from the start.

6.3.2.8 Column design

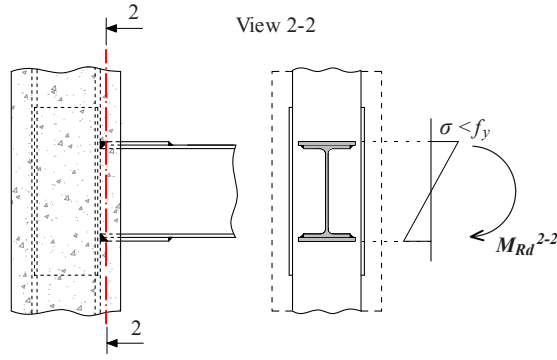
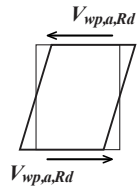
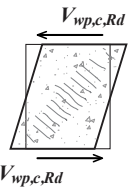
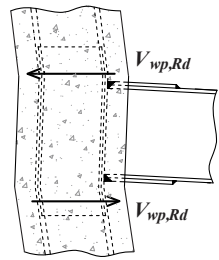
All considerations already presented in Chapter 6.2.2.8 should be applied.

6.3.2.9 Summary

The joint components and the corresponding design rules for CP joint are presented in Table 44.

Preglednica 44: Projektna nosilnost osnovnih component spoja CP

Table 44: Design capacity of basic CP joint components

Joint component	Reference to code provisions, design rules
1. Stiffened connection	
Elastic check of stiffened beam cross-section (integral section)	
	<p>Code provision (EN 1993-1-1)</p> $M_{Rd}^{2-2} = \frac{W_{el}^{2-2} \cdot f_y}{\gamma_{M0}}, \quad V_{Rd}^{2-2} = \frac{A_v \cdot f_y}{\sqrt{3} \cdot \gamma_{M0}}$
2. Column panel in shear	
Unstiffened steel column web panel (+ contribution of stiffeners, if needed)	
	<p>Code provision (EN 1993-1-8)</p> $V_{wp,a,Rd} = \frac{0.9 \cdot A_v \cdot f_y}{\sqrt{3} \cdot \gamma_{M0}}$
Concrete encasement	
	<p>Code provision (EN 1994-1-1)</p> $V_{wp,c,Rd} = 0.85 \cdot \nu \cdot A_c \cdot f_{cd} \cdot \sin \theta$
Composite section	
	<p>Code provision (EN 1998-1)</p> $V_{wp,Rd} = \max \left(V_{wp,a,Rd}; 0.8 \cdot (V_{wp,a,Rd} + V_{wp,c,Rd}) \right)$

7 CONCLUSIONS AND OUTCOMES

7.1 Summary and conclusions

The primary aim of the research work was to provide seismic design guidelines for full-strength welded rib-stiffened (RS) and cover-plate (CP) moment-resistant beam-to-column joints applied to hybrid-steel moment-resisting frames.

To this end, experimental prequalification cyclic tests on both the stiffened joint types were performed. Test specimens were designed taking into account the existing design recommendations for their enhanced performance. In addition, joint design was supported by preliminary numerical simulations. Based on an accurate FE numerical model, developed throughout the study, additional complementary numerical analysis was done on both stiffened connection configurations subjected to monotonic and cyclic loading. The primary objective was to support the proposed joint design guidelines against possibly adverse beam member type and size effects. For this purpose, a set of beams within the range of practically applicable I and H profiles typically used in the European practice was applied.

Summary of the research work with the principal conclusions is presented in the text below, starting with the main idea of the proposed design procedure for full-strength welded stiffened beam-to-column joints.

The proposed design criterion for full-strength welded stiffened joint is that the region of the welded connection at the column face remains nominally elastic under maximum bending moment of the order $\gamma_{ov}' M_{pl,b}$ and the corresponding shear force, developed by the fully yielded and strain hardened beam. In addition, overall overstrength factor $\gamma_{ov}' = 1.5$ was proposed, taking into account random variability of the material yield stress $\gamma_{ov} = 1.25$ and additional strain hardening factor $s = 1.2$ for steel in the dissipative zone of the beam.

Sixteen large-scale cyclic tests on full-strength welded RS and CP beam-to-column joints were carried out to study their seismic performance. A hybrid-steel approach was implemented with high strength steel used for the columns as non-dissipative elastic members and mild carbon steel for the beams acting as dissipative members. Additional parameter of the study was axial force of high level compression in the column. A total of 16 cyclic tests were carried out: eight tests using variable loading with stepwisely increasing amplitude and additional eight tests at two different inelastic constant displacement levels.

Detailed description of experimental test results is presented. Systematically addressed results provide valuable database on the behaviour of the stiffened beam-to-column joints and thus fill the gap of knowledge in the field, especially in combination with the type of steel profiles commonly used in the European design practice.

All 16 welded rib-stiffened and cover-plate beam-to-column joints subjected to variable and constant cyclic loading amplitude fulfilled the objective of the applied design concept: the whole inelastic action was transferred away from the face of the beam-to-column connection into the beam section behind the stiffened region, referred to as plastic hinge.

Unlike the events from the past major earthquakes, where premature brittle failures without prior signs of plastic deformation were observed at the unstiffened beam-column welded connections of moment-resisting frames, complete stiffened beam-to-column connection remained undamaged in all the 16 joint specimens; i.e. no damage of welds, either in beam-

column connection or around reinforcing plates, was observed from macro examination after the tests. In this aspect both designed RS and CP beam-to-column connections would behave substantially better under seismic loading than the unstiffened ones.

Since cyclic response was governed solely by the behaviour of unstiffened beams, possessing reliable inelastic deformation capacity as compact sections, all the joints experimentally tested with stepwisely increasing amplitude met the pre-qualification requirements according to the EN 1998-1 and ANSI/AISC 341-10 seismic provisions. Maximum plastic rotations of eight specimens subjected to variable amplitude loading, at 20 % degradation of maximum strength and initial stiffness, were between 0.030 and 0.044 rad with the corresponding cumulative plastic rotations between 0.480 and 0.921 rad.

The total number of completed cycles to failure obtained from constant amplitude cyclic tests varied between 76 and 155 for small ($\theta = 0.019$ rad) and from 29 to 62 for large ($\theta = 0.033$ rad) amplitude tests, with the corresponding total cumulative plastic rotations between 1.728 and 3.960 rad.

During large constant amplitude loading, beam local buckling occurred. This led to the reduction of strength and stiffness, and finally to LCF failure in the buckled zone of the beam in case of both CP joints. However, both RS joints subjected to large constant amplitude cycling failed due to the beam flange fracture in the HAZ of the fillet weld at the end of the rib-stiffener. Accordingly, both RS joints sustained considerably fewer cycles to failure compared to the corresponding CP beam-to-column joints.

Beam local buckling was not observed under small amplitude loading and the degradation of joint resistance took place only during the last few cycles when LCF fracture of the flange just behind the stiffened region led to complete joint failure. Also in this case, the CP joint displayed better fatigue performance, attributed to the increased level of unfavourable strain concentrations, larger weld residual stress and HAZ at the end of the rib-stiffener in the RS joint.

Both experimentally tested column-beam HSS/MCS material combinations evidenced good performance without any noticeable effect of the applied level of column compressive axial force, being around 40 % of the actual composite column plastic resistance to compression, on the cyclic response of the specimens.

Tests clearly evidenced that the proposed concept of both full-strength beam-to-column joints provides a good solution in all aspects. Beside excellent performance, an important advantage is simple design and fabrication of these connections. During seismic action the vulnerable welded connection at the face of the column remains nominally elastic under maximal forces from the connected beam, reducing the possibility for the appearance of brittle failure conditions at the beam-column interface, and thus no additional requirements for welds are needed, while a compact beam section can easily provide adequate ductility. The application of full-strength stiffened connections, especially rib-stiffened solution, can be extended to the end plate moment resisting connections.

It is to be noted that beam-to-column member sizes used in the test specimens were limited by composite column bearing capacity, designed in such way that relatively high level of compressive axial load-to-plastic resistance ratio was achieved with laboratory equipment capacities. Extrapolation of joint behaviour prediction to connections of a substantially different type and size should be undertaken with care. Namely, the observed trend from the experimental test results clearly shows that as beams become deeper and heavier, their ability to develop inelastic rotation may be somewhat diminished.

In order to provide reliable and comprehensive design guidelines for both the stiffened beam-to-column connection types in combination with hot rolled I and H steel beam profiles commonly used in the European design practice, additional parametric numerical study was performed. For this purpose, developed advanced numerical FE model in Abaqus for the simulation of monotonic and cyclic behaviour of beam-to-column joints, was applied.

First of all, simulations of rib-stiffened (RS) and cover-plate (CP) beam-to-column joint responses under bending and simultaneous column compressive axial load were performed. In combination with damage indices it was shown that column axial compressive load level up to 60 % of the corresponding composite column plastic resistance to compression should not substantially increase the likelihood either of ductile or brittle fracture in the local welded beam-to-column connection. In this aspect the numerical study fully confirmed the outcomes of the experimental tests.

The applied material stress-strain curves (for monotonic and cyclic responses) for beams were characterised by overstrength factor accounting for random variability of the steel yield stress equal to $\gamma_{ov} = 1.25$ and the ultimate-to-yield stress ratio $f_u/f_y = 1.28$. On the other hand, material stress-strain curves comprising nominal value of material yield stress f_y^{nom} were accounted for all non-dissipative steel joint components, including stiffening plates and complete column member.

All the sixteen RS and CP beam-to-column joints designed for the parametric numerical study according to the proposed design procedure for full-strength joints developed full plastic capacity of the connected beam under monotonic loading.

Both stiffened joint configurations behave very well in terms of relocating plastic straining from the beam-column welded interface into the unstiffened region of the beam beyond the stiffened connection. The centreline of the beam plastic hinge was located at a distance of $\frac{1}{4} h_b$ from the end of the stiffened region in case of all the simulated RS and CP joints, which is the same as observed in all the cyclic experimental tests.

According to the simulation results, reinforcing plates of both RS and CP joints subjected to monotonic loading should remain essentially elastic if the proposed design procedure is used. It should be emphasised that the proposed design procedure will not prevent yielding of the rib-stiffeners or cover-plates but should limit the maximum strains to modest levels. Moderate yielding of the stiffening plates should not lead to premature fracture or undesired behaviour of the stiffened beam-to-column joints.

Although all the beams applied in the parametric study meet cross-sectional Class 1 requirements according to EN 1993-1-1, quite large differences, in terms of exhibited rotation capacity and the corresponding degree of the beam flexural overstrength, were observed between the applied I and H beam profiles as well as their different sizes. In fact, joint overstrength, needed for the development of the full plastic capacity of the connected beam, is directly related to its ultimate behaviour.

Maximum values of the overall beam flexural overstrength factor $\gamma_{ov}' = \gamma_{ov} \cdot s$ obtained from the joints subjected to monotonic loading are very close or even above $\gamma_{ov}' = 1.5$ as considered in the proposed design procedure for both full-strength stiffened joint configurations, i.e. 1.49 and 1.56 for RS and CP joints, respectively. However, as observed from the deformed shapes of the joints, the design procedure still provides robust enough stiffened beam-to-column connections in order to prevent excessive plastic straining in the close vicinity of the vulnerable beam-column welded connection at the column flange.

All the stiffened joints subjected to cyclic loading simulations with stepwisely increasing loading amplitude according to the ANSI/AISC 341-10 possessed sufficient degree of

overstrength to allow for the development of the full beam plastic rotation capacity. However, from the subsequent analysis of low-cycle fatigue (LCF) life, in terms of identification of the LCF crack initiation, important difference in fatigue behaviour between RS and CP joints was found, as described below.

In case of CP joints, mechanical conditions under which the crack initiation mechanism would operate were always met after the overall joint flexural strength degradation, characterised by well-developed beam local buckling, in the most buckled region of the beam flange. The response of all the RS joints comprising IPE beams was found fully comparable to the aforementioned fatigue response of the CP joints.

On the other hand, in case of all the RS joints comprising H beam profiles (HEA, HEB), the LCF crack initiation mechanism was triggered substantially earlier compared to the corresponding CP joints, and in the state before the onset of the overall joint flexural strength degradation due to the local beam buckling. From the observations of damage indices on the deformed shape of the joints, the RS joint detail was found critical in terms of large plastic strain concentrations in the much localised region on the beam flange at the end of the rib-stiffener. Consequently, the CP joint configuration was found to behave superior to the RS connection.

In relation to the two applied criteria for the evaluation of crack initiation under low-cycle fatigue loading, the effective damage concept proposed by Ohata and Toyoda (2004) did not provide consistent results, particularly in case of the RS joints, where critical region was observed at the end of the stiffened connection. On the other hand, the new proposed criterion appears to provide fully consistent and logical results for all the 16 analysed RS and CP joints.

From comparison between the simulated monotonic and cyclic responses of the stiffened joints, the following conclusions can be drawn.

Flexural overstrength s exhibited by all I and H beam profiles under cyclic loading conditions is similar to that occurred under monotonic loading, without important difference between RS and CP joint configuration.

As expected, all the joints subjected to cyclic loading conditions produced lower rotation capacity compared to that obtained from monotonic loading, due to the pronounced effects of the beam local buckling and low-cycle fatigue in the plastic hinge region.

Monotonic and cyclic rotation capacities of all the joints included in the parametric analysis tend to decrease with increasing beam cross-section height. Reported cyclic-to-monotonic rotation capacity ratio, determined with the ultimate beam rotation corresponding to the moment resistance drop below actual beam plastic moment, varies between 0.16 and 0.41. The same ratio corresponding to the 20 % fall of the maximum moment resistance is very similar and ranges between 0.15 and 0.30.

The outcomes of the parametric numerical study present an important contribution also in terms of flexural ultimate behaviour of steel beams and confirm the need for a twofold classification of steel members according to their ductility and overstrength as the most appropriate approach for seismic design applications (Mazzolani, Piluso, 1992. 1993. Gioncu, Mazzolani, 2000. Piluso, Rizzano, 2007. D'Aniello et al., 2012). Especially, clear distinction was made in the study between overstrength due to random material variability γ_{ov} and overstrength due to strain-hardening s , which is still not clearly addressed in the current European seismic design code.

In particular, maximum value of complete overstrength factor $1.1 \times \gamma_{ov} = 1.1 \times 1.25 = 1.375$ as exists in the current code EN 1998-1, was proved to be too small to guarantee sufficient overstrength of a connection in order to assure the development of the full plastic capacity of the connected beam. This is mainly due to the insufficient overstrength level (factor 1.1), which should take into account additional flexural resistance of the connected beam due to the strain hardening until the complete development of local buckling. Proposed values for both $\gamma_{ov} = 1.25$ and $s = 1.2$ result in overall overstrength factor $\gamma_{ov}' = s \cdot \gamma_{ov} = 1.5$, which proved to be satisfactory.

7.2 Original contributions

In contrast to extensive research and detailed guidelines on enhanced connection performance in seismic design of moment-resisting frames in the US and Japan, lack of research activities directly addressing the seismic behaviour of welded stiffened moment-resisting beam-to-column joints can still be found in Europe.

In the light of this, the present research work contributes to the improved knowledge of monotonic and low-cycle fatigue behaviour of full-strength welded stiffened beam-to-column joints that is currently not thoroughly addressed in the present standards for seismic design.

Original contributions of the research work can be summarised as follows:

- eight experimental prequalification cyclic tests on large-scale welded rib-stiffened and cover-plate moment-resisting beam-to-column joints subjected to variable stepwisely increasing loading amplitude (ANSI/AISC 341-10 loading protocol);
- eight experimental cyclic tests on large-scale welded rib-stiffened and cover-plate moment-resisting beam-to-column joints subjected to constant amplitude cyclic loadings. Two different inelastic constant rotation levels were applied;
- cyclic qualification of hybrid-steel (dual-steel concept) full-strength stiffened beam-to-column joints by experimental tests;
- first comparative study on welded rib-stiffened and cover-plate joints with systematically chosen test parameters, taking into account variable and two different constant amplitude cyclic loadings in combination with two different I beam profiles;
- experimental results of two distinct types of low-cycle fatigue response (failure mechanism) for both stiffened joint configurations: with the presence of the beam local buckling in the plastic hinge region and without it.
- systematically addressed experimental and numerical results with direct comparison of cyclic responses of the two studied stiffened joint types;
- developed advanced nonlinear FE model capable of simulating beam-to-column joint response under monotonic and cyclic loading conditions.
- proposed crack initiation based low-cycle fatigue failure criterion for structural steel components subjected to cyclic loading;
- systematic parametric numerical study on monotonic and cyclic responses of the two studied stiffened joint configurations in combination with different hot rolled I and H European beam profile types and their sizes;

- seismic design guidelines for full-strength welded rib-stiffened and cover-plate beam-to-column joints.

7.3 Suggestions for further work

Critical detail in welded stiffened beam-to-column joints still remains related to the welding details; not at the beam-column interface, as in case of unstiffened connections, but at the end of the stiffened region. Improvement of the FE model to account for the low-cycle fatigue damage is needed for more accurate analysis of cyclic behaviour of the joints.

Deterministic approach was applied in the study to account for the reliability of the proposed design procedure for full-strength stiffened joints. In addition, a probabilistic approach should be considered with reference to overstrength due to random material variability.

Finally, the obtained results from local analyses on beam-to-column joints can be tied to the global frame behaviour, and vice versa, to obtain the actual demands, which the stiffened joints should be capable to resist.

I UVOD

Jekleni pomični in zavetrovani okviri so danes pogosto uporabljeni konstrukcijski sistemi. Uporabljajo se za nosilne sisteme poslovnih, stanovanjskih in industrijskih objektov. Njihova statična zasnova je sestavljena iz stebrov in prečk, medseboj povezanih z vijačenimi ali varjenimi spoji, in povezij v primeru zavetrovanih okvirov. Jekleni okviri zaradi svoje duktilnosti predstavljajo eno izmed najpogosteje uporabljenih zasnov nosilnega sistema na potresnih območjih. Njihova duktilnost izhaja iz materialnih karakteristik konstrukcijskega jekla in iz ustrezne statične zasnove okvira.

Glede na vpliv horizontalne obtežbe predstavljajo pomični okviri manj togo zasnovo v primerjavi z nosilnimi sistemi, ki uporabljajo povezja. Zaradi tega jekleni pomični okviri težje izpolnijo kriterij omejitve poškodb v primerjavi s povezji in se zato uporabljajo predvsem v nizkih in srednje visokih konstrukcijah. Njihovo obnašanje med potresno obtežbo je odvisno predvsem od rotacijske kapacitete in nizkocikličnega utrujanja spojev. V zavetrovanih okvirih med potresom igrajo bistveno vlogo povezja, kjer se v stebrih pojavljajo visoke vrednosti osnih sil, ki lahko vplivajo na obnašanje spojev. Poleg tega momentni spoji zagotavljajo višjo disipacijsko kapaciteto pod histereznimi krivuljami (cikli dinamične obremenitve), ki so poleg tega stabilnejše in večje kot so histerezne krivulje dobljene iz povezij (Gioncu in Mazzolani, 2000).

Do potresa v Kaliforniji (Northridge, 17. januar 1994) in leto kasneje potresa na Japonskem (Kobe, 17. januar 1995) je veljalo, da se jekleni momentni okviri v splošnem dobro obnašajo v primeru potresne obtežbe in imajo dovolj veliko odpornost. Vendar se je v obeh primerih potresov izkazalo, da so jekleni varjeni momentni spoji prečke na steber v konstrukcijah v bližini epicentra potresa utrpeli relativno veliko poškodb. Po obeh dogodkih je bilo v ZDA in na Japonskem narejenih veliko raziskav, ki so potrdile, da potresno obnašanje okvirov v veliki meri zavisi od pristopa k njihovi začetni zasnovi. Z določitvijo mesta plastifikacije, ki je potrebna za disipiranje energije, z ustrezno izbiro materiala in geometrijskih detajlov posameznih komponent spoja, je mogoče dimenzionirati momentne spoje, ki se dobro obnašajo tudi pod vplivom dinamične obremenitve.

Ideja potresno odpornega projektiranja danes temelji na principu načrtovane nosilnosti konstrukcij. Konstrukcije, izpostavljene potresni obtežbi, želimo projektirati tako, da se obnašajo skladno z načrtovanim odzivom. Dobro poznavanje obnašanja spojev je pri tem bistvenega pomena. Na osnovi velikega števila eksperimentov se je izkazalo, da je samo na osnovi analitičnih formulacij in numeričnih izračunov težko zadovoljivo opisati kompleksen odziv varjenih momentnih spojev. Eksperimentalni del raziskav je pri tem nepogrešljiv.

Glavni parameter obnašanja momentnih spojev torej v pomičnih okvirih predstavlja rotacijska kapaciteta s pojavom nizkocikličnega utrujanja. Kot je bilo ugotovljeno v dosedanjih študijah, sta oba pojava v veliki meri povezana predvsem s stopnjo lokalne duktilnosti. Ustrezno obnašanje momentnih okvirjev med potresno obtežbo namreč temelji na zadostni deformacijski kapaciteti ter ustrezni disipaciji energije.

Zaradi privzetega načrtovanega obnašanja spojev v momentnih okvirih, ki dopušča pojav plastičnih deformacij le v prečki, je mejno obnašanje spojev tesno povezano z mejnim obnašanjem jeklene prečke. V ta namen je v raziskovalnem delu velik pomen posvečen študiju obnašanja prečke, od katere je odvisen nivo obremenitve, ki ga prevzema ojačan spoj.

V delu privzet princip načrtovane nosilnosti je izpolnjen, če odziv ojačanega dela prečke ob stebru ostane elastičen tekom celotne zgodovine obremenjevanja. V tem primeru so vse plastične deformacije skoncentrirane v osnovnem neojačanem prerezu prečke (plastični členek) tik za ojačanim delom, neduktilni varjeni spoj prečke na pasnico stebra pa ostane v elastičnem območju, torej obvarovan pred velikimi (plastičnimi) deformacijami.

Veliko število raziskovalnih del, opravljenih na področju potresnega obnašanja jeklenih varjenih spojev prečka-steber, priča o aktualnosti obravnavanega problema. Z razvojem naprednih računskih metod, ki uspešno dopolnjujejo rezultate pridobljene na osnovi laboratorijskih testov, predvsem v smislu nizko cikličnega utrujanja materiala, so se v zadnjih letih odprle nove možnosti za obravnavo problema in izboljšavo smernic za detajliranje in dimenzioniranje tovrstnih spojev.

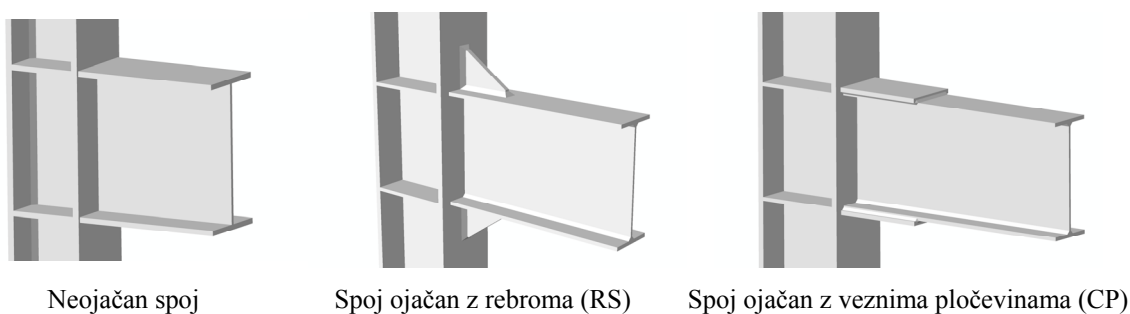
Doktorsko delo temelji na eksperimentalnih raziskavah, ki služijo kot osnova za predkvalifikacijo predlaganih dveh konfiguracij ojačanih varjenih spojev prečka-steber. Eksperimentalni rezultati so bili poleg tega uporabljeni za razvoj in kalibracijo naprednega računskega modela, s pomočjo katerega je bila preverjena ustreznost predlagane metode za detajliranje in dimenzioniranje obravnavanih ojačanih spojev.

Glavni cilji doktorske disertacije so povzeti v sledečih točkah:

- Izvedba laboratorijskih testov dveh konfiguracij jeklenih momentnih ojačanih spojev v hibridnih momentnih okvirih, katerih uporaba predstavlja inovativno alternativo na področju protipotresnega projektiranja konstrukcij v Evropskem prostoru. Obstoječi standard Evrokod EN 1993-1-8 namreč ne obravnava hibridnega koncepta zasnove konstrukcij.
- Obširna in detajlna obravnava dobljenih eksperimentalnih rezultatov, ki omogoča neposredno primerjavo odziva obeh obravnavanih konfiguracij jeklenih momentnih ojačanih spojev. Določena bo njihova rotacijska kapaciteta in odpornost na nizkociklično utrujanje v primeru ciklične obremenitve. Vrednotenje ustreznosti odziva testiranih konfiguracij spojev glede na kvalifikacijske kriterije iz ustreznih standardov v smislu njihove standardizacije.
- Izdelava in kalibracija naprednega računskega modela z uporabo programa na osnovi metode končnih elementov.
- Izvedba komplementarne numerične parametrične študije na dodatnem naboru jeklenih profilov različnih velikosti, ki se uporabljajo v evropski inženirski praksi. Glavni namen je potrditev ustreznosti predlagane metode dimenzioniranja momentnih ojačanih spojev.
- Na podlagi zaključkov analize eksperimentalnih in numeričnih rezultatov bodo podana priporočila za protipotresno projektiranje, konstruiranje in izvedbo obeh obravnavanih tipov spojev.
- Kljub velikemu obsegu že opravljenih raziskav na tem področju, ostaja vpliv osne sile v stebru na obnašanje varjenih momentnih spojev slabo raziskan. V študiji je vpliv osne sile vključen tako v eksperimentalnem delu, kot tudi v dodatnih numeričnih simulacijah.

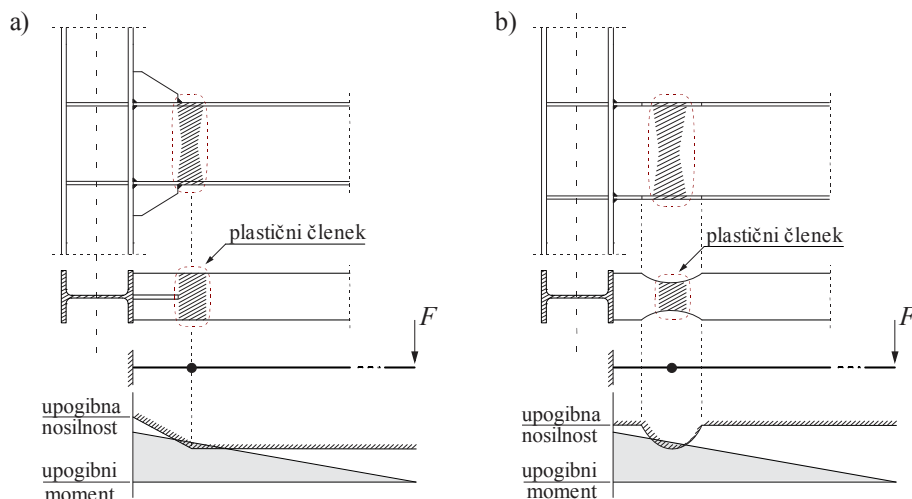
II EKSPERIMENTALNI TESTI

V obsegu raziskovalnega dela sta bili obravnavani dve različni konfiguraciji varjenih momentnih ojačanih spojev prečka-steber. Varjeni spoj ojačan z navpično privarjenim trikotnim rebrom na zgornji in spodnji pasnici prečke (spoj RS), in spoj z dodatno vezno pločevino privarjeno na zunanjo stran vsake od pasnic profila prečke (spoj CP). Primerjava geometrije obeh uporabljenih konfiguracij ojačanega spoja z neojačanim spojem je prikazana na sliki 1.



Slika 1: Konfiguracije varjenih spojev prečka-steber

Glavna ideja momentnega ojačanega spoja, v skladu z idejo načrtovane nosilnosti, je odmik plastične cone stran od pasnice stebra v osnovni profil prečke, slika 2a. S tem se izognemo potencialno neduktilnemu obnašanju spoja, do katerega lahko pride že pri manjših plastičnih deformacijah zaradi neduktilne krhke porušitve varjenega stika med prečko in pasnico stebra.



Slika 2: Osnovni koncept izboljšane zasnove momentnega spoja prečka-steber: a) obravnavan koncept ojačanega spoja, b) alternativna rešitev z oslabilnim prerezom prečke (RBS)

Z namenom ocene potresnega odziva obeh tipov ojačanih spojev je bilo opravljenih šestnajst cikličnih testov na preizkušancih naravne velikosti. V skladu s konceptom hibridnih momentnih okvirov sta bili v vsakem od spojev uporabljeni dve različni kvaliteti konstrukcijskega jekla. Za stebre, katerih predvideno obnašanje ostane elastično, je bilo uporabljeno visokovredno jeklo (HSS), medtem ko je bilo v primeru dissipativne prečke uporabljeno mehko konstrukcijsko jeklo (MCS). V vseh šestnajstih preizkušancih so bili uporabljeni sovprežni polno obbetonirani stebri, ki se v praksi običajno uporabljajo za večjo požarno odpornost stebrov ter za povečanje njihove nosilnosti in togosti. Poleg dveh konfiguracij ojačanega spoja prečka-steber in dveh različnih kombinacij kvalitet jekla za

prečko (S355) in jekleni profil stebra (S460/S690), študija vključuje še sledeče parametre: dva različna protokola cikličnega obremenjevanja (konstantna in spremenljiva amplituda) in visok nivo tlačne osne sile v stebri, do katerega lahko pride zlasti v primeru stebrov v zavetrovanih okvirih. Glavni parametri študije, skupaj s celotnim številom preizkušancev, so predstavljeni v preglednici 1.

Preglednica 1: Parametri eksperimentalne študije s številom preizkušancev

PARAMETER	SPREMENLJIVKA	Št. VARIANT	Št. PREIZKUŠ.
Tip ojačanega spoja	z rebroma (RS) & z veznima plošč. (CP)	2	
Kombinacija HSS/MCS	S460 (RS1, CP1) & S690 (RS2, CP2)	2	
Amplituda cikličnega obremenjevanja	spremenljiva (.1, .2) & konstantna (.3, .4)	2	16
Nivo osne sile v stebri	nizek (.1) & visok (.2, .3, .4)	2	

Glavni cilj zgoraj opisanega obsega eksperimentalnih testov je ugotovitev ustreznosti obnašanja obeh zasnovanih tipov varjenega ojačanega spoja. Rezultati testov so bili kasneje uporabljeni za potrditev ustreznosti predlagane metode dimenzioniranja, kot tudi osnova za podana priporočila protipotresnega projektiranja, konstruiranja in izvedbe obeh obravnavanih tipov spojev.

DIMENZIONIRANJE IN DETAJLIRANJE OJAČANIH SPOJEV

Pred samo izvedbo preizkušancev je bila študija osredotočena na ustrezno projektiranje in izbiro ustreznih detajlov geometrije in varjenja obeh tipov ojačanih spojev prečka-steber. Osnova za vse nadaljne rešitve so bila priporočila dobljena iz literature, kot so navedena v primeru posameznega spoja v nadaljevanju tega poglavja. Nepogrešljivi pa so bili pri tem tudi izsledki preliminarne numerične analize spojev, opravljene s pomočjo metode končnih elementov v programu Abaqus.

Glavni kriterij uporabljen pri dimenzioniranju polnonosilnih varjenih ojačanih spojev je, da območje spoja tik ob varjenem stiku prečke na pasnico jeklenega stebra ostane v elastičnem območju odziva tudi pod vplivom največje obremenitve, ki prihaja iz priključene polno plastificirane jeklene prečke, pri čemer je pomembno upoštevati tudi utrditev materiala po doseženi plastifikaciji. Pri tem je upoštevana vrednost upogibnega momenta plastičnega členka v osnovnem neojačanem prerezu prečke $\gamma_{ov}' \cdot M_{pl,b}$ in pripadajoča prečna sila. Skladno s pristopom je bila privzeta vrednost celotnega faktorja dodatne nosilnosti $\gamma_{ov}' = 1.5$, pri čemer je bil upoštevan faktor naključne spremenljivosti napetosti tečenja jekla v prečki $\gamma_{ov} = 1.25$ in dodaten faktor za materialno plastično utrjevanje $s = 1.2$ (Piluso, Rizzano, 2007. D'Aniello et al., 2012. Güneyisi et al., 2013).

$$M_j \geq s \cdot \gamma_{ov} \cdot M_{pl,b} = \gamma_{ov}' \cdot M_{pl,b},$$

kjer je:

$$\left. \begin{array}{l} s = 1.2 \\ \gamma_{ov} = 1.25 \end{array} \right\} \rightarrow \gamma_{ov}' = 1.5.$$

Pripadajoč moment v geometrijski osi stebra M_c , kakor tudi moment v ojačanem delu prereza prečke tik ob pasnici stebra M_{cf} sta bila določena z upoštevanjem statičnega modela enostranskega momentnega spoja prečke na steber. Z upoštevanjem linearnega poteka upogibnega momenta vzdolž prečke, sta omenjena momenta določena kot sledi:

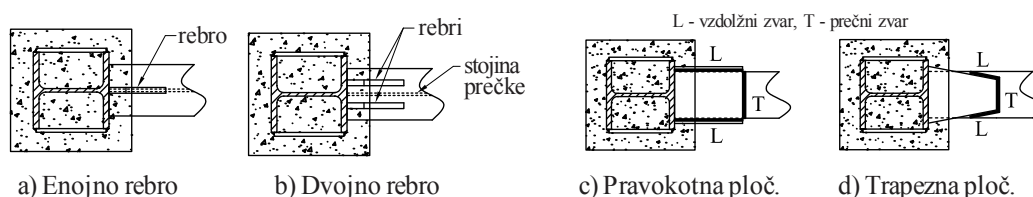
$$M_c \geq M_{pl,b} \cdot \left(\frac{L}{L - d_h} \right), \quad M_{cf} \geq M_{pl,b} \cdot \left(\frac{L - h_c / 2}{L - d_h} \right),$$

kjer je:

- L razdalja od centra stebra do točke vnosa prečne sile na prostem koncu prečke,
- d_h razdalja od centra stebra do privzeteka središča plastičnega členka na prečki,
- h_c višina jeklenega profila stebra.

M_{cf} torej predstavlja vrednost momenta pri kateri mora ojačan prerez prečke ob pasnici stebra ostati v elastičnem območju odziva. V skladu z omenjenim principom se geometrija ojačilnih pločevin, t.j. rebri in veznih pločevin, določi z upoštevanjem vrednosti momenta M_{cf} in elastičnega odpornostnega momenta ojačanega prereza prečke tik ob pasnici stebra.

V sklopu preliminarne analize sta bili obravnavani dve različni konfiguraciji spoja ojačanega z rebri: z enim in s po dvema rebroma privarjenima na vsako pasnico prečke, slika 3a,b. Iz rezultatov numerične analize ni bilo zaznati bistvene razlike v globalnem odzivu med obravnavanima spojema. Analiza lokalnega obnašanja je pokazala, da je v primeru uporabe dveh rebri lažje omejiti širjenje plastifikacije in lokalnega gubanja po pasnici prečke v predel za koncem rebri. Vendar pa rebri v tem primeru nista tako dobro izkoriščeni, kot v primeru uporabe enojnega rebra, kjer je le-to postavljeno v ravnino stojin prečke in stebra, in je s tem omogočen neposreden prenos prečnih sil med prečko in stebrom, slika 3a.



Slika 3: Obravnavane zasnove ojačanega spoja z rebri in veznima pločevinama

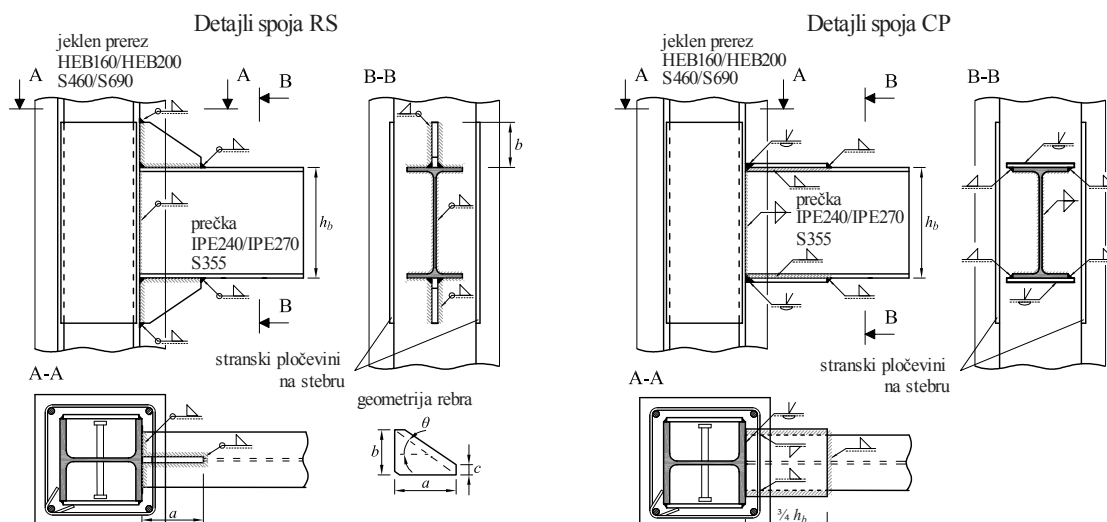
Ker uporaba dveh rebri ne daje bistvenega doprinosa k izboljššanemu lokalnemu obnašanju spoja, in ob dodatnem dejstvu, da je izdelava ojačanega spoja z enojnim rebrom bistveno enostavnejša za izdelavo, je bila na koncu izbrana konfiguracija s po enim rebrom privarjenim na posamezno pasnico prečke.

Za določitev izhodiščne geometrije rebra, je bil uporabljen pristop za protipotresno dimenzioniranje momentnih z rebri ojačanih spojev v skladu z Lee (2000). Pri tem so bili upoštevani sledeči geometrijski parametri, glej sliko 4: višina rebra $b \approx h_b/3$; naklon diagonal rebra $\theta \approx 35^\circ$; dolžina rebra $a = b/\tan(\theta)$, $c = 25$ mm.

Kot je bilo že omenjeno, je debelina rebra določena iz projektega pogoja, da ojačan prerez prečke ob pasnici stebra, izpostavljen največji momentni obremenitvi iz plastificiranega dela prečke, ostane v linearnem območju odziva.

Za stikovanje posameznih component spoja so predvideni polnonosilni kotni zvari, tudi za celoten stik prečnega prereza prečke na pasnico stebra. Pri tem se najprej izvede priključitev prečke na steber in zatem se zavarita še obe rebri na pasnici prečke in pasnico stebra.

V primeru spoja ojačanega z veznima pločevinama sta bila glavna dva parametra preliminarne študije oblika vezne pločevine in razpored kotnih zvarov med pločevino in pasnico prečke, slika 3b,c. Glede na zaključke raziskav, podanih v Kim et al. (Kim et al., 2000. 2002a. 2002b), sta bili obravnavani pravokotna in trapezna oblika vezne pločevine v kombinaciji z uporabo samo vzdolžnih in obeh vzdolžnih ter prečnega kotnega zvara na koncu vezne pločevine, slika 3.



Slika 4: Konstrukcijski detajli spojev RS in CP (betonski ovoj sovprežnih stebrov ni prikazan)

Primerjava iz numeričnih izračunov dobljenega lokalnega odziva je pokazala daleč najprimernejšo uporabo pravokotne vezne pločevine z uporabo vzdolžnih in prečnega kotnega zvara na koncu pločevine, slika 3b,c. Uporaba kotnih zvarov po vseh treh stranicah pločevine namreč uspešno preprečuje širjenje plastifikacije in gubanja po pasnici prečke preko konca vezne pločevine v smeri proti stebru. Prav tako je razpored normalnih napetosti po širini prečnega prereza pločevine veliko bolj enakomeren kot v primeru uporabe le vzdolžnih zvarov ob prostem robu pasnice prečke. Ob uporabi zvarov po vseh treh stranicah, vezna pločevina pravokotne oblike zagotavlja večjo dolžino kotnih zvarov, slika 3b,c, kar omogoča ugodno zmanjšanje debeline kotnih zvarov. Na podlagi zgoraj omenjenih razlogov, je bila za nadaljnjo študijo izbrana pravokotna vezna pločevina v kombinaciji z razporeditvijo kotnih zvarov po vseh treh stranicah pločevine, slika 4.

Priporočila za dimenzioniranje izboljšane obnašanja spoja ojačanega z veznima pločevinama so bila povzeta iz literature (FEMA, 2000c. 2000d. 2000b. Kim et al. 2002a). Uporabljene so bile vezne pločevine, katerih širina je večja od širine pasnice prečke. S tem se je njihova debelina ustrezno zmanjšala, kar je ugodno predvsem pri izvedbi polnonosilnega čelnega zvara med pločevino in pasnico stebra. Izbrana debelina vezne pločevine je bila enaka debelini pasnice prečke.

Dolžina vezne pločevine je pogojena z zadostno dolžino vzdolžnih kotnih zvarov med pločevino in pasnico prečke, katerih strižna nosilnost mora znašati vsaj toliko kot plastična osna nosilnost prečnega prereza vezne pločevine. Izbrana končna dolžina pločevin enaka trem četrtinam višine profila prečke $\frac{3}{4} \cdot h_b$ zadosti prej omenjenemu pogoju.

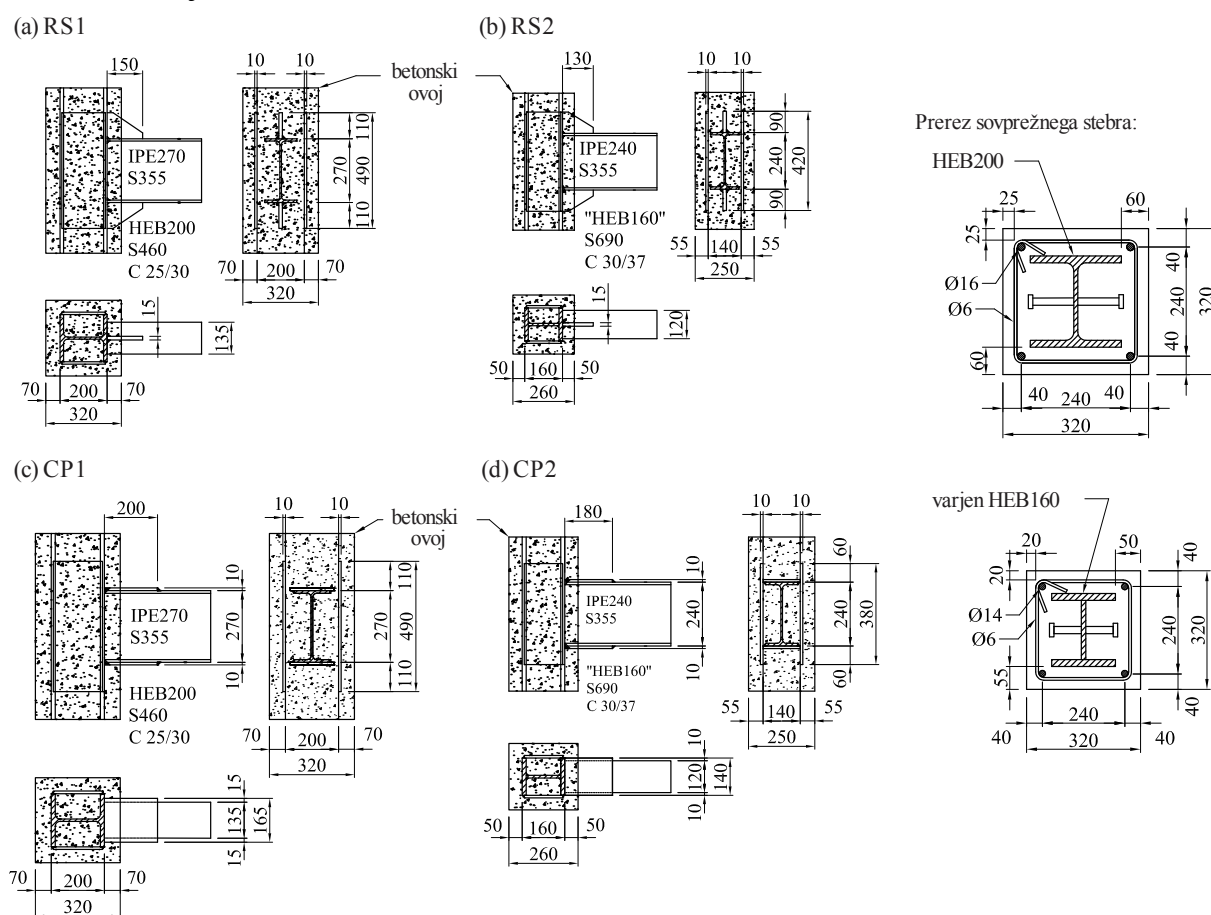
Za stikovanje skupne debeline pasnice prečke in vezne pločevine na pasnico stebra je predviden polnopenetriran v-čelni zvar, slika 4. Pri tem se zahteva, da se po opravljenem čelnem zvaru varilni trak uporabljen pod korenem zvara odstrani in naknadno povari s kotnim zvarom. Prisotnost varilnega traku se je namreč v preteklosti izkazala kot vir razpok pri nizko cikličnem utrujanju detajla (Engelhardt, Sabol, 1998).

OPIS PREIZKUŠANCEV

Za študijo dveh različnih kombinacij kvalitet konstrukcijskega jekla uporabljenih za prečko in steber, namreč prečka izvedena iz S355 v kombinaciji z jeklenim delom stebra iz materiala S460/S690, sta bila za vsako konfiguracijo ojačanega spoja prečka-steber zgrajena dva preizkušanca. Skupno so bili torej izdelani štirje različni momentni varjeni ojačani spoji, slika 5. Kot je razvidno iz slike, na jekleni prečki ni bilo predvidene betonske plošče. Vsi spoji so

bili projektirani kot polnonosilni, z izpolnjenim pogojem močan steber/šibka prečka kot je zahtevano v EN 1998-1, in s predvideno pozicijo plastičnega členka v osnovnem prerezu prečke tik za ojačanim delom spoja.

Spoja z oznako RS1 in CP1 vključujeta prečko s profilom IPE270 v materialu S355 in jekleni profil stebra HEB200 izveden iz materiala S460, v nadaljevanju imenovan velik steber. Spoja z oznako RS2 in CP2 vključujeta prečko s profilom IPE240 v materialu S355 in jekleni profil stebra HEB160 izveden iz materiala S690, v nadaljevanju imenovan mali steber. Obe uporabljeni prečki izpolnjujeta kriterije prvega razreda kompaktnosti iz standarda EN 1993-1-1 in določil za protipotresno projektiranje ANSI/AISC 341-10. Pri dimenzioniranu sovprežnih stebrov so bila upoštevana določila iz EN 1994-1-1 in EN 1998-1. Uporabljena sta bila betona običajnih trdnostnih razredov C25/30 in C30/37, za velik in mali steber. Zaradi lažje vgradnje svežega betona, so bili v mešanici uporabljeni dodatki, kar je pripomoglo k doseženim večjim vrednostim dejanskih tlačnih trdnosti betona, ki so znašale med 51 in 66 MPa.



Slika 5: Konstruktivni detajli zasovanih štirih različnih ojačanih spojev

Pri tem je potrebno poudariti, da je bil izbor velikosti jeklenih prerezov stebrov, in s tem posledično tudi izbor velikosti profilov prečk, pogojen z omejeno nosilnostjo sovprežnih stebrov. Z namenom analize vpliva osne sile v stebri, smo namreč v študiji hoteli, glede na kapaciteto razpoložljive laboratorijske opreme (3000 kN), doseči čim višji nivo tlačne osne sile glede na polnplastično osno nosilnost sovprežnega stebra. Odtod izhajata relativno nizka profila obeh uporabljenih prečk. Končni v testih dosežen nivo tlačne osne sile v stebri, z upoštevanjem dejanskih materialnih karakteristik jekla in betona, je znašal med 37 in 41% polnplastične tlačne nosilnosti za oba sovprežnega stebra. Z upoštevanjem projektne nosilnosti sovprežna stebra pa med 41 in 48%.

Poudariti je potrebno, da so bili vsi jekleni deli spojev (profili, pločevine) med seboj zvarjeni z uporabo standardne kvalitete, ki se uporablja v evropski praksi. Povprečne vrednosti izmerjenih mehanskih lastnosti za posamezne jeklene komponente spojev, dobljenih iz standardnih enoosnih nateznih preizkusov, so zbrane v preglednici 2.

Ker je v študiji obravnavan nizkociklični odziv jeklene konstrukcije, predstavlja informacija o lomni žilavosti pomemben podatek za vnaprejšnjo presojo odziva spojev izpostavljenih ciklični obtežbi. Lomna žilavost v skladu s standardnim Charpy V-testom je bila opravljena za vse jeklene komponente spojev. Dobljene vrednosti absorbirane energije za jeklo kvalitete S355 znašajo med 108 in 226 J, za jeklo S460 med 151 in 185 J ter za jeklo S690 med 91 in 185 J, kar je sprejemljivo.

Preglednica 2: Mehanske karakteristike jeklenih komponent spojev

vzorec	jeklo	napetost tečenja f_y (N/mm ²)	natezna trdnost f_u (N/mm ²)	f_u/f_y	deformacija ob pretrgu A (%)
IPE 240, web	S355	435	516	1.19	32
IPE 240, flange	S355	385	486	1.26	31
IPE 270, web	S355	444	514	1.16	33
IPE 270, flange	S355	385	498	1.29	32
“HEB 160” web	S690	808	864	1.07	18
“HEB 160” flange	S690	783	818	1.04	18
HEB 200	S460	468	576	1.23	28
Rib stiffener	S355	450	491	1.09	33
Cover plate	S355	424	501	1.18	34

PROTOKOL OBREMENJEVANJA

Za vseh šestnajst cikličnih testov je bilo uporabljeno kvazi statično obremenjevanje. V primeru elastičnih ciklov je bil protokol obremenjevanja voden s silo, pri vseh ostalih večjih amplitudah v plastičnem območju pa pomik. Največja med testi merjena hitrost deformacij je znašala 0,0009/s. Celoten pregled obremenjevanja za vseh 16 testov je prikazan v preglednici 3.

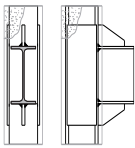
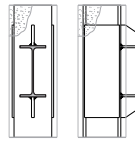
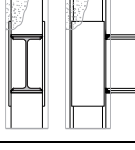
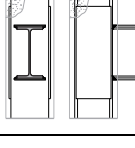
V primeru prvih dveh izvedenih testov, RS1.1 in RS1.2, je bil uporabljen obtežni protokol iz priporočil ECCS N°45, vendar modificiran kot v primeru Calado (2000). V skladu s predhodno izvedenimi numeričnimi simulacijami je bilo namreč ugotovljeno, da originalen protokol obremenjevanja po ECCS N°45 vsebuje prevelike priraste pomikov v plastičnem območju: iz napovedi dobljenih na podlagi predhodnih numeričnih simulacij bi preizkušane do porušitve vzdržal največ štiri različne amplitude plastičnih pomikov, kar je premalo za ustrezno vrednotenje nizkocikličnega obnašanja spoja.

V skladu z omenjenim modificiranim protokolom, predlaganim po Calado (2000), je bilo uporabljeno naslednje zaporedje amplitud cikličnega obremenjevanja: (1) trije cikli v elastičnem območju odziva spoja s pomiki v amplitudah enakimi $\frac{1}{4}$, $\frac{1}{2}$, $\frac{3}{4}$, $1 \times \delta_y$, kjer δ_y predstavlja pomik na meji tečenja za posamezen spoj, določen iz predhodne numerične analize spoja; (2) po trije cikli pri določeni amplitudi $i \times \delta_y$, kjer je $i = 2, 3, 4, \dots$, do porušitve preizkušanca.

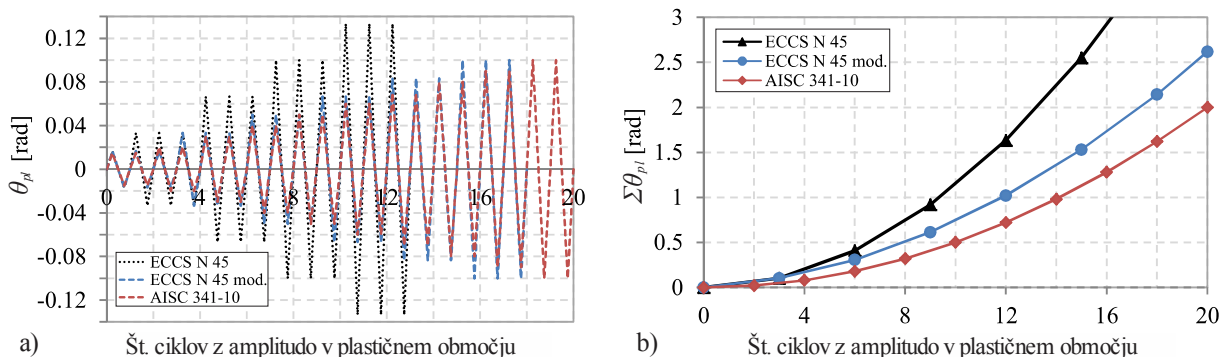
Na osnovi analize rezultatov iz prvih dveh testov je bilo ugotovljeno, da je prirast med posameznimi plastičnimi amplitudami še vedno prevelik, zato je bil za ostalih šest testov s sprejemljivo postopno naraščajočo amplitudo cikličnega obremenjevanja izbran protokol v

skladu z dokumentom ANSI/AISC 341-10 (ANSI/AISC, 2010b). Primerjava med vsemi tremi omenjenimi obtežnimi protokoli je prikazana na sliki 6. V ta namen izbrani pomik na meji elastičnosti znaša 0.017 rad.

Preglednica 3: Pregled po vseh 16 laboratorijskih testih

Spoj	karakteristike steber/prečka		amplituda cikl. obremenjevanja	tlačna osna sila v stebru
	jeklen prerez	materialna kombinac.		
RS1.1	IPE270/HEB200	S355/S460	spremenljiva	0
RS1.2			spremenljiva	3000 kN
RS1.3			konst., majhna	3000 kN
RS1.4			konst., velika	3000 kN
RS2.1	IPE240/HEB160	S355/S690	spremenljiva	0
RS2.2			spremenljiva	3000 kN
RS2.3			konst., majhna	3000 kN
RS2.4			konst., velika	3000 kN
CP1.1	IPE270/HEB200	S355/S460	spremenljiva	0
CP1.2			spremenljiva	3000 kN
CP1.3			konst., majhna	3000 kN
CP1.4			konst., velika	3000 kN
CP2.1	IPE240/HEB160	S355/S690	spremenljiva	0
CP2.2			spremenljiva	3000 kN
CP2.3			konst., majhna	3000 kN
CP2.4			konst., velika	3000 kN

Protokol s spremenljivo postopno naraščajočo otežbo je bil uporabljen na prvih osmih preizkušancih. Vsak izmed štirih različnih spojev (RS1, RS2, CP1 in CP2) je bil obremenjen z in brez osne sile v stebru, kar je v nadaljnjem besedilu označeno z dodatno oznako 1 in 2 k imenu vsakega od štirih različnih preizkušancev: RS1.1 in RS1.2, RS2.1 in RS2.2, CP1.1 in CP1.2, CP2.1 in CP2.2, glej preglednici 1 in 3.



Slika 6: Primerjava med protokolom obremenjevanja ECCS N°45, modificiranim ECCS N°45 in protokolom AISC 341-10: a) amplitude pomikov in b) akumulirana plastična deformacija. Prikazani so le cikli z amplitudami v plastičnem območju.

Ker v raziskovalnem delu želimo ovrednotiti nizkociklično utrujanje ojačanih spojev v primeru splošne ciklične obremenitve, smo poleg običajno uporabljene spremenljive

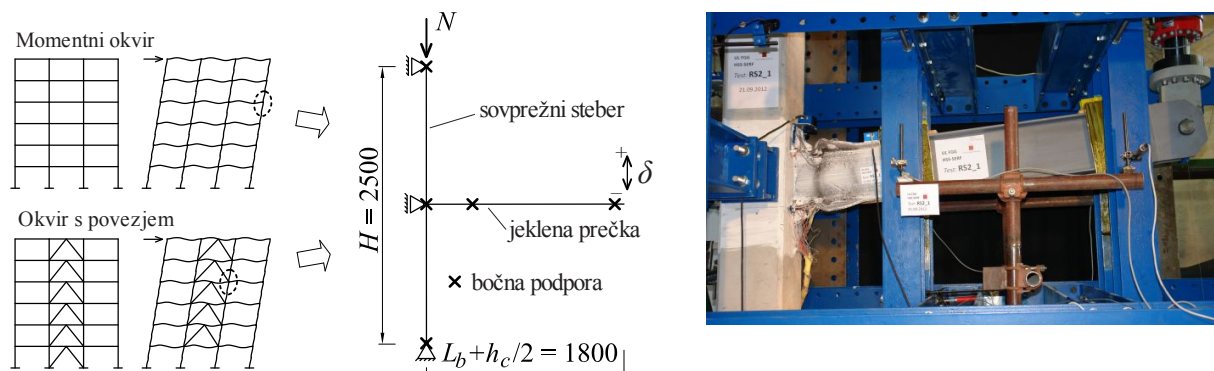
zgodovine obremenjevanja za namene predkvalifikacije spojev, uporabili dodatna dva obremenitvena protokola s konstantno amplitudo obremenjevanja. Na podlagi analize lokalnega inelastičnega odziva že testiranih spojev, sta bili izbrani dve različni amplitudi: 35 mm (0,019 rad) in 60 mm (0,033 rad), v nadaljnjem besedilu imenovani mala in velika konstantna amplituda. Obe amplitudi sta bili vnaprej skrbno izbrani z namenom, da se v primeru vsakega od štirih različnih spojev dosežeta dva različna nizkociklična odziva: z in brez nastopa lokalnega izbočenja prečke v območju plastičnega členka, za veliko in malo konstantno amplitudo.

Oba protokola s konstantno amplitude cikličnega obremenjevanja sta bila uporabljena na vsakem od štirih različnih spojev RS1, RS2, CP1 in CP2, v nadaljnjem besedilu označenih z dodatno oznako 3 in 4, glej preglednici 1 in 3. Poleg tega je bila v vseh osmih testih prisotna polna osna sila v stebri.

Vsak test je trajal do nastopa porušitve preizkušanca zaznamovane s pretrgom pasnice, čemur je sledil očiten padec nosilnosti in togosti spoja.

IZVEDBA TESTOV

Celoten test je bil zasnovan kot simulacija enostranskega zunanjskega spoja v jeklenem momentnem okviru ali notranjega spoja v zavetrovanem okviru izpostavljenem horizontalni seizmični obtežbi, slika 7. Celoten preizkušavec je podprt v smeri izven ravnine na treh mestih na stebri. Dodaten sistem bočnih podpor je nameščen na prečki; v bližini plastičnega členka in na prostem koncu prečke.

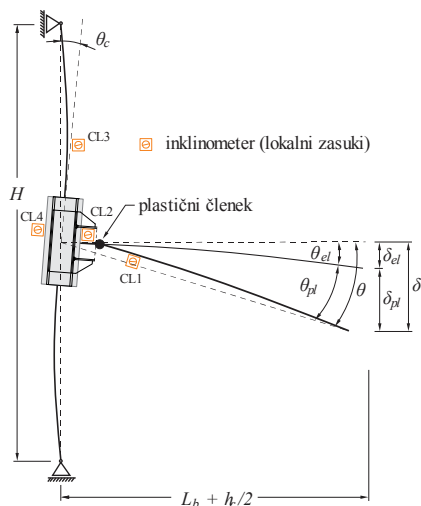


Slika 7: Statični model preizkušanca s postavitvijo eksperimenta v laboratoriju

REZULTATI TESTOV

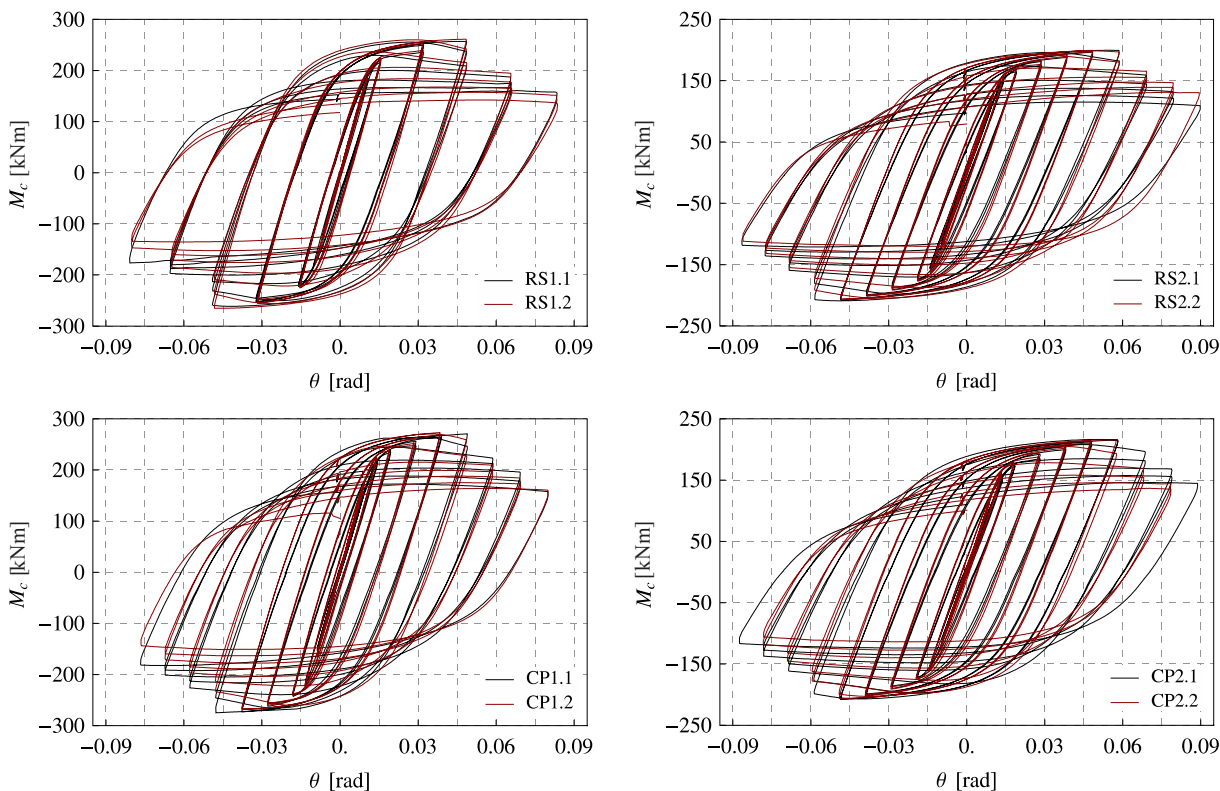
Celoten opis rezultatov šestnajstih laboratorijskih cikličnih testov na štirih zasnovanih momentnih polnonosilnih varjenih spojih prečka-steber je predstavljen tako, da omogoča neposredno primerjavo nizkocikličnega odziva obeh konfiguracij ojačanih spojev. V nadaljevanju je najprej predstavljen koncept beleženja in določitve komponent rotacije spoja, uporabljen kot osnovni parameter v analizi odziva spojev. Podani so rezultati prvih osmih testov s spremenljivo, korakoma naraščajočo, amplitudo obremenjevanja, nato pa še odziv preostalih osem obremenjenih s konstantno amplitudo. Predstavljena je primerjava rezultatov vseh testov v smislu analize duktilnosti in nizkocikličnega utrujanja spojev.

Za natančen opis odziva posameznega spoja, obremenjenega s prečno obtežbo na prostem koncu prečke, so bile določene posamezne elastične in plastične komponente rotacije. Celotna rotacija spoja θ je določena s kvocientom med celotnim vnešenim pomikom na koncu prečke in razdaljo med točko vnosa pomika in središčno osjo stebra (1800 mm), slika 8.



Slika 8: Kinematika spoja prečka-steber

Plastični del rotacije spoja θ_{pl} je dobljen z odštetjem elastičnih upogibnih in strižnih deformacij prečke, kot tudi celotnega prispevka stebra zaradi elastičnega upogiba in deformacije strižnega panela. Čeprav se deformacija strižnega panela stebra ponavadi upošteva kot plastična, v tej študiji ni bila prišteta k plastičnim deformacijam spoja θ_{pl} . Zaradi uporabljenega koncepta močan steber/šibka prečka in dodatnega doprinosa k nosilnosti in togosti, zaradi prisotnosti betona ter dodatnih stranskih pločevin privarjenih na jeklen profil, sliki 4 in 5, je bila v testih izmerjena deformacija panela stebra zelo majhna (največja celotna rotacija stebra v vseh šestnajstih testih je bila manjša od 0,005 rad). V skladu z zgoraj opisanim postopkom plastična rotacija spoja θ_{pl} torej predstavlja plastično rotacijo prečke $\theta_{pl,b}$, slika 8.



Slika 9: Primerjava odziva vseh štirih različnih spojev z in brez prisotnosti tlačne osne sile v stebru

Kot je razvidno iz slike 9, je vseh osem RS in CP spojev preizkušanih s spremenljivo postopno naraščajočo amplitudo rotacije izkazalo stabilen histerezni odziv z doseženo veliko

plastično rotacijo pred nastopom porušitve posameznega preizkušanca, slika 9. V nobenem izmed osmih spojev ni prišlo do predčasne neduktilne porušitve.

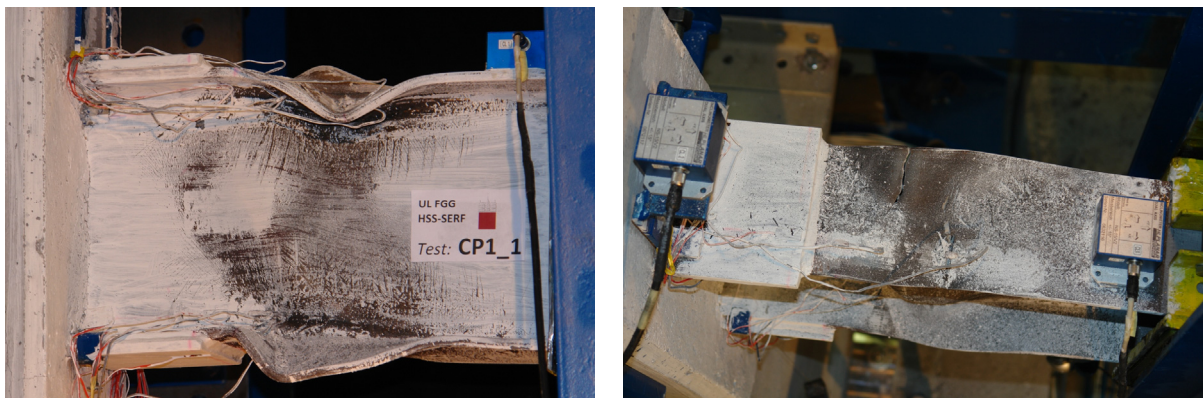
Vsak od štirih različnih spojev v skupini preizkušancev testiranih brez tlačne osne sile v stebri, RS1.1, RS2.1, CP1.1 in CP2.1, je izkazal zelo podoben odziv v primerjavi z istim spojem testiranim ob prisotnosti tlačne osne sile v stebri, RS1.2, RS2.2, CP1.2 in CP2.2, slika 9. Tudi po opravljeni analizi poškodovanosti zvarov med ojačanim delom prečke in pasnico stebra, med omenjenima skupinama ni bilo opaziti pomembnih razlik. Na podlagi primerjave lokalnega in globalnega odziva med omenjenima skupinama preizkušancev testiranih z in brez prisotnosti tlačne osne sile v stebri, lahko zaključimo sledeče:

- uporabljen nivo tlačne osne sile v stebri (cca. 40 % dejanske plastične tlačne nosilnosti sovprežnega stebra) ni povzročil opaznih dodatnih poškodb v profilu zvara med ojačanim prerezom prečke in pasnico stebra, ki bi lahko poslabšale ciklični odziv celotnega spoja;
- rezultati dobljeni na vseh štirih različnih spojih, RS1, RS2, CP1 in CP2, so ponovljivi.

Tipični odziv ojačanega spoja po končanem testu je predstavljen na sliki 10, za preizkušanec RS1.1 in na sliki 11 za preizkušanec CP1.1. Iz obeh slik je lepo razvidno mesto plastifikacije z lokalnim uklonom obeh pasnic in stojine prečke tik za ojačanim delom spoja. Dobljeni eksperimentalni rezultati na vseh osmih RS in CP spojih so potrdili ustreznost uporabljene metode dimenzioniranja ojačanih polonosilnih spojev: v vseh primerih je plastični členek nastal v neojačanem delu prečke, medtem ko je ojačan del spoja ostal praktično v elastičnem območju in nepoškodovan.



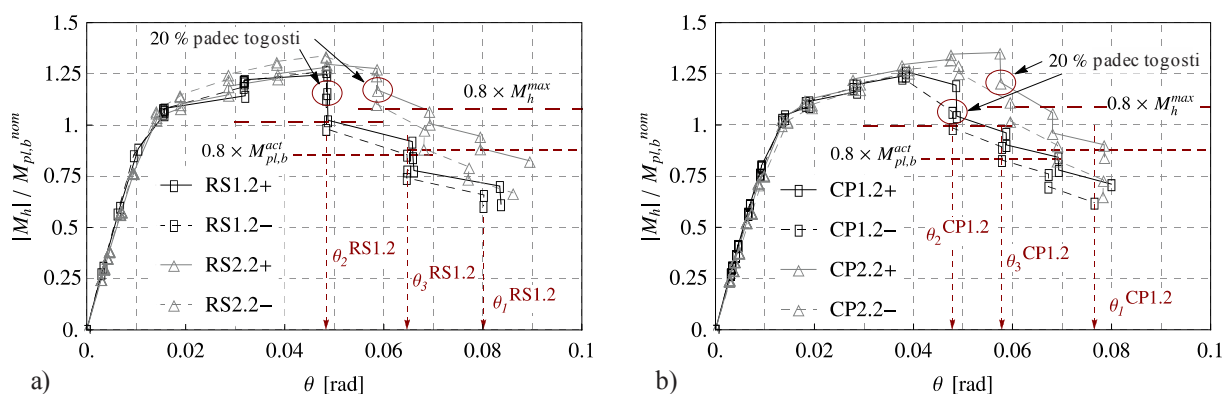
Slika 10: Preizkušanec RS1.1 po končanem testu



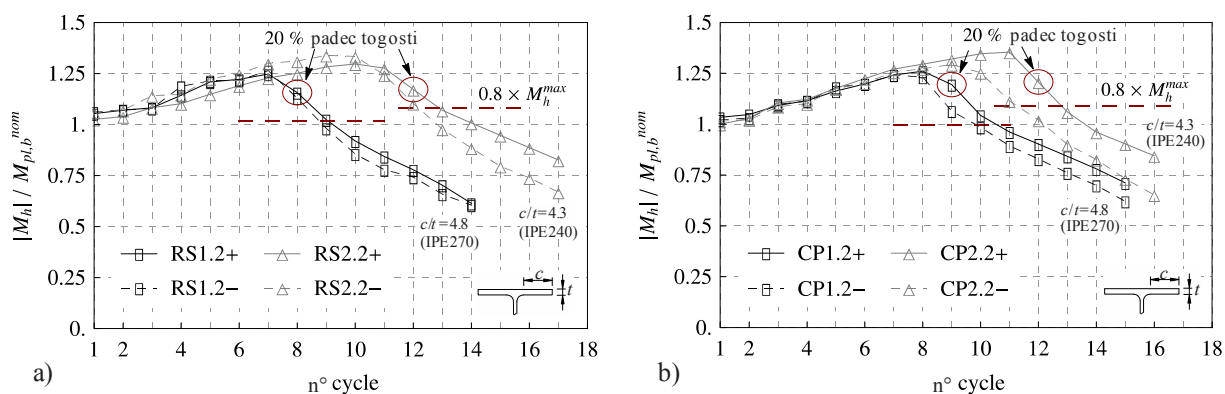
Slika 11: Preizkušanec CP1.1 po končanem testu

Po končanih testih ni bilo opaziti poškodb v zvarih ojačanega dela spoja ob pasnici stebra, kot tudi ne v zvarih okrog reber in veznih pločevin. Pri tem je potrebno poudariti, da so se v primeru vseh RS spojev prve razpoke med testom pokazale v območju tik za koncem rebra v toplotno vplivni coni (HAZ) kotnega zvara, vendar v nobenem od primerov niso vplivale na končno obnašanje spoja, saj se je cona največje koncentracije plastičnih deformacij, z naraščajočo amplitudo rotacije spoja, in posledično pod vplivom hkratnega povečevanja lokalnega izbočenja pasnic, preselila v območje plastičnega členka nekoliko proč od konca ojačanega dela prečke.

Ciklično obnašanje RS in CP spojev je bilo v nadaljevanju obravnavano prek analize nosilnosti in togosti glede na doseženo celotno oziroma plastično rotacijo spojev. Pomembni parametri, ki jih pri tem obravnavamo so nosilnost (dodatna nosilnost), togost in plastična rotacija (rotacijska kapaciteta) spojev. V ta namen so na slikah 12 in 13 za preizkušance RS1.2, RS2.2, CP1.2 in CP2.2 predstavljene krivulje odziva v doseženih amplitudah rotacije z momentom M_h določenim v centru plastičnega členka, in normiranim z nominalno vrednostjo plastičnega momenta prečke $M_{pl,b}^{nom}$, v odvisnosti od celotne rotacije stebra θ oziroma števila ciklov plastičnega odziva. Za posamezen preizkušanec so predstavljene vrednosti momentov za pozitivno in negativno smer obremenjevanja. Privzeto mesto plastičnega členka za obe konfiguraciji ojačanega spoja, RS in CP, je četrtnina višine prečke stran od konca ojačanega dela spoja. Prav tako sta označeni vrednosti momenta pri 20% padcu največje dosežene nosilnosti spoja M_h^{max} in 20% padcu dejanske plastične nosilnosti prečke $M_{pl,b}^{act}$. Dodatno je za vsak preizkušanec označena točka, ki pripada ciklu, ki še ustreza mejnemu kriteriju z manj kot 20% padcem začetne togosti spoja.



Slika 12: Normiran moment M_h v zaporednih amplitudah rotacije: a) RS1.2 in RS2.2, b) CP1.2 in CP2.2



Slika 13: Normiran moment M_h v zaporednih amplitudah rotacije v odvisnosti od števila ciklov: a) RS1.2 in RS2.2, b) CP1.2 in CP2.2

Iz obeh zgornjih slik je za oba tipa ojačanega spoja dobro razviden kasnejši nastop padca nosilnosti in togosti v primeru male, bolj kompaktne, prečke IPE240 v primerjavi z večjo

prečko IPE270. Temu ustrezno je bilo, ne glede na konfiguracijo ojačanega spoja, za malo prečko potrebno tudi večje končno število ciklov do nastopa porušitve preizkušanca, slika 13, preglednica 4.

Vrednosti beležene dodatne upogibne nosilnosti $M_h^{max}/M_{pl,b}^{nom}$ testiranih ojačanih spojev prečka-steber so podane v preglednicah 5 in 6. Poročane vrednosti dodatne nosilnosti v primeru osmih preizkušancev testiranih z uporabo spremenljive korakoma naraščajoče amplitude cikličnega obremenjevanja izkazujejo visoko konsistentnost. Vrednosti, dobljene za veliko prečko IPE270, znašajo med 1.25 in 1.27, za malo prečko IPE240 pa med 1.35 in 1.37, neodvisno od konfiguracije ojačanega spoja, kar kaže na pravilnost določitve pozicije plastičnega členka na prečki za oba tipa ojačanega spoja. Opazne so večje vrednosti dosežene dodatne upogibne nosilnosti male, bolj kompaktne prečke, v primerjavi z vrednostmi za veliko prečko.

Za nadaljno oceno in primerjavo cikličnega odziva preizkušanih spojev so bili uporabljeni trije mejni kriteriji, ki so grafično predstavljeni na sliki 12. Prvi kriterij (N_1, θ_1) predstavlja stanje nastopa popolne porušitve spoja. Pri tem je upoštevan zadnji še polni cikelj v odzivu preizkušanca. Drugi kriterij (N_2, θ_1) se nanaša na stanje preizkušanca z ne več kot 20% padcem največje nosilnosti oziroma začete togosti, in ustreza kriteriju podanem v EN 1998-1. Tretji mejni kriterij (N_3, θ_3) pa se nanaša na stanje z ne več kot 20% padcem dejanskega plastičnega momenta prečke $M_{pl,b}^{act}$.

Število polnih ciklov N_i v povezavi s tremi uporabljenimi mejnimi kriteriji je prikazano v preglednici 4 za vseh šestnajst testiranih spojev.

Preglednica 4: Število doseženih ciklov N_i glede na tri izbrane mejne kriterije

spoj	amplituda	N_1	N_2	N_3	spoj	N_1	N_2	N_3
RS1.1	spremen.	13 ^{LB}	9 ^{a,b}	10	CP1.1	15 ^{LB}	11 ^a , 10 ^b	13
RS1.2	spremen.	14 ^{LB}	8 ^{a,b}	10	CP1.2	15 ^{LB}	9 ^{a,b}	12
RS1.3	konst. majhna	76 ^{FR}	73 ^a , 76 ^b	73	CP1.3	126 ^{FR}	124 ^a , 125 ^b	125
RS1.4	konst. velika	29 ^{FR}	13 ^a , 23 ^b	26	CP1.4	40 ^{LB}	12 ^a , 38 ^b	36
RS2.1	spremen.	17 ^{LB}	12 ^{a,b}	14	CP2.1	17 ^{LB}	12 ^{a,b}	15
RS2.2	spremen.	17 ^{LB}	12 ^{a,b}	14	CP2.2	16 ^{LB}	11 ^a , 12 ^b	15
RS2.3	konst. majhna	138 ^{FR}	133 ^a , 138 ^b	134	CP2.3	155 ^{FR}	153 ^a , 154 ^b	153
RS2.4	konst. velika	32 ^{FR}	31 ^{a,b}	31	CP2.4	62 ^{LB}	41 ^a , 61 ^b	61

Porušni mehanizem: LB – lokalni plastični uklon prečke, FR – duktilni pretrg pasnice prečke.

Drugi mejni kriterij (N_2): ^a 20 % padec nosilnosti, ^b 20 % padec togosti.

Kot je razvidno iz preglednice 4 in slik 12 in 13, 20 % padec nosilnosti in togosti, ki je vključen v drugi mejni kriterij, za vse spoje obremenjene s spremenljivo amplitudo rotacije nastopi v istem ciklu. Izjema sta le preizkušanca CP1.1 in CP2.2, kjer sta oba pogoja izpolnjena v sledečih si ciklih. Na podlagi tega lahko zaključimo, da oba kriterija, glede na nosilnost in togost, za omenjeno skupino preizkušancev predstavljata enakovreden kriterij.

V preglednicah 5 in 6 so zbrani preostali merjeni parametri odziva vseh šestnajstih testiranih RS in CP spojev. Poleg že omenjenih vrednosti v zvezi z dodatno upogibno nosilnostjo $M_h^{max}/M_{pl,b}^{nom}$, tabeli vsebujeta vrednosti največje dosežene plastične rotacije prečke θ_{pl} ($\theta_{pl,1}$, $\theta_{pl,2}$, $\theta_{pl,3}$) in ustrezne akumulirane plastične rotacije $\Sigma\theta_{pl}$ ($\Sigma\theta_{pl,1}$, $\Sigma\theta_{pl,2}$, $\Sigma\theta_{pl,3}$), izvrednotene za vse tri izbrane mejne kriterije.

Preglednica 5: Eksperimentalni rezultati za skupino preizkušancev RS

skupina spojev: RS1&RS2	M_h^{max} (kNm)	$M_h^{max}/M_{pl,b}^{nom}$	parameter odziva					
			θ_{pl} (rad)			$\Sigma\theta_{pl}$ (rad)		
			$\theta_{pl,1}$	$\theta_{pl,2}$	$\theta_{pl,3}$	$\Sigma\theta_{pl,1}$	$\Sigma\theta_{pl,2}$	$\Sigma\theta_{pl,3}$
RS1.1	215.2	1.25	0.071	0.036	0.054	1.505	0.626	0.829
RS1.2	218.3	1.27	0.074	0.036	0.055	1.832	0.531	0.877
RS1.3	192.8	1.12		0.006		1.728	1.640	1.640
RS1.4	210.2	1.22		0.021		2.167	0.930	1.930
RS2.1	177.7	1.36	0.076	0.041	0.055	2.044	0.852	1.264
RS2.2	175.7	1.35	0.078	0.044	0.056	2.138	0.921	1.344
RS2.3	149.5	1.15		0.006		2.305	2.191	2.212
RS2.4	165.1	1.27		0.017		2.018	1.942	1.942

Poročane vrednosti plastičnih rotacij spojev so določene glede na središčno os stebra in predstavljajo manjšo vrednost dobljeno za pozitivno in negativno smer obremenjevanja.

Preglednica 6: Eksperimentalni rezultati za skupino preizkušancev CP

skupina spojev: CP1&CP2	M_h^{max} (kNm)	$M_h^{max}/M_{pl,b}^{nom}$	parameter odziva					
			θ_{pl} (rad)			$\Sigma\theta_{pl}$ (rad)		
			$\theta_{pl,1}$	$\theta_{pl,2}$	$\theta_{pl,3}$	$\Sigma\theta_{pl,1}$	$\Sigma\theta_{pl,2}$	$\Sigma\theta_{pl,3}$
CP1.1	218.8	1.27	0.062	0.030	0.051	1.547	0.546	1.088
CP1.2	217.3	1.26	0.071	0.037	0.061	1.658	0.480	0.967
CP1.3	198.2	1.15		0.005		2.316	2.272	2.293
CP1.4	220.5	1.28		0.021		2.920	0.809	2.609
CP2.1	177.9	1.37	0.076	0.039	0.064	1.981	0.815	1.458
CP2.2	177.2	1.36	0.068	0.040	0.054	1.815	0.726	1.103
CP2.3	148.7	1.14		0.004		2.302	2.260	2.260
CP2.4	166.8	1.28		0.019		3.960	2.526	3.887

Za vseh osem RS in CP spojev testiranih s spremenljivo korakoma naraščajočo amplitudo cikličnega obremenjevanja plastična rotacija $\theta_{pl,1}$ znaša med 0.062 in 0.078 rad, brez večjih razlik med obema tipoma ojačanega spoja. Za RS spoj so opazne konsistentnejše vrednosti kot v primeru CP spoja. Vse vrednosti $\theta_{pl,1}$ dobljene za bolj kompaktno manjšo prečko IPE240 so večje od tistih dobljenih za prečko IPE270. Vrednosti $\theta_{pl,2}$ variirajo med 48 in 59% ustrezne plastične rotacije ob nastupu porušitve $\theta_{pl,1}$. Pri tem so za RS kot tudi za CP spoj vrednosti dobljene za večjo prečko 10% manjše od tistih dobljenih za manjšo prečko. Vrednosti kvocienta $\theta_{pl,3}/\theta_{pl,1}$ znašajo med 0.72 in 0.86, pri čemer so vrednosti za CP spoje približno 12% večje od vrednosti dobljenih v primeru RS spojev, ne glede na velikost prečke.

Vrednosti akumulirane plastične rotacije $\Sigma\theta_{pl,1}$ se za manjšo prečko gibljejo med 1.815 in 2.138 rad in so precej večje od vrednosti dobljenih za večjo prečko, katere se gibljejo med 1.505 in 1.832 za vseh osem RS in CP spojev testiranih s spremenljivo amplitude rotacije. Zopet je razlog za omenjeno razliko med akumulirano plastično deformacijo spojev z malo in veliko prečko mogoče pojasniti z večjo odpornostjo na nizkociklično utrujanje manjše in bolj kompaktne prečke, pri kateri se lokalno izbočenje prečke v plastičnem členku pojavi kasneje

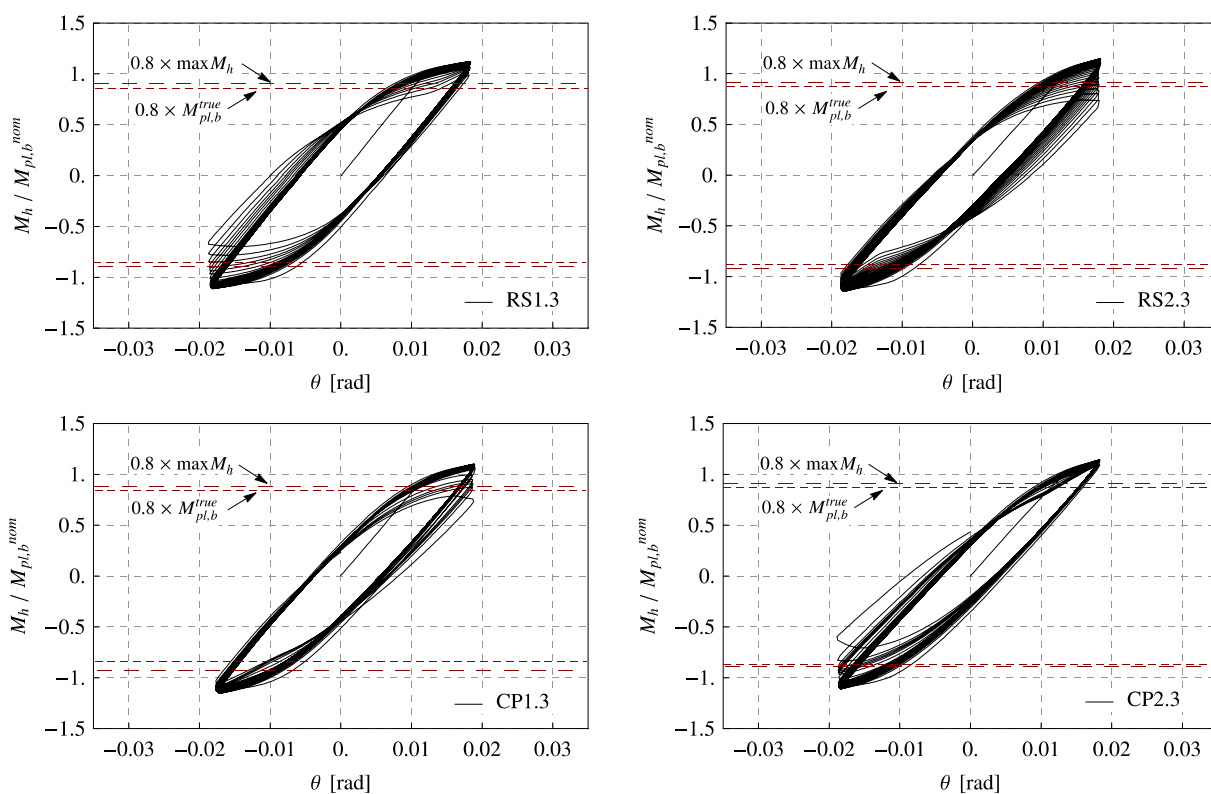
kot v primeru večje prečke. Vpliv lokalnega izbočenja prečke za oba tipa ojačanega spoja ter za obe prečki je razviden iz precej manjših vrednosti $\Sigma\theta_{pl,2}$ and $\Sigma\theta_{pl,3}$.

Odziv ostalih osem RS in CP spojev testiranih s konstantno amplitudo cikličnega obremenjevanja, v prisotnosti konstantne tlačne osne sile v stebru, je prikazan na sliki 14 za malo amplitudo 0,019 rad (35 mm) in na sliki 15 za veliko amplitude 0,033 rad (60 mm). Vseh osem preizkušancev izpostavljenih cikličnemu obremenjevanju s konstantno amplitudo je izkazalo dober in stabilen odziv.

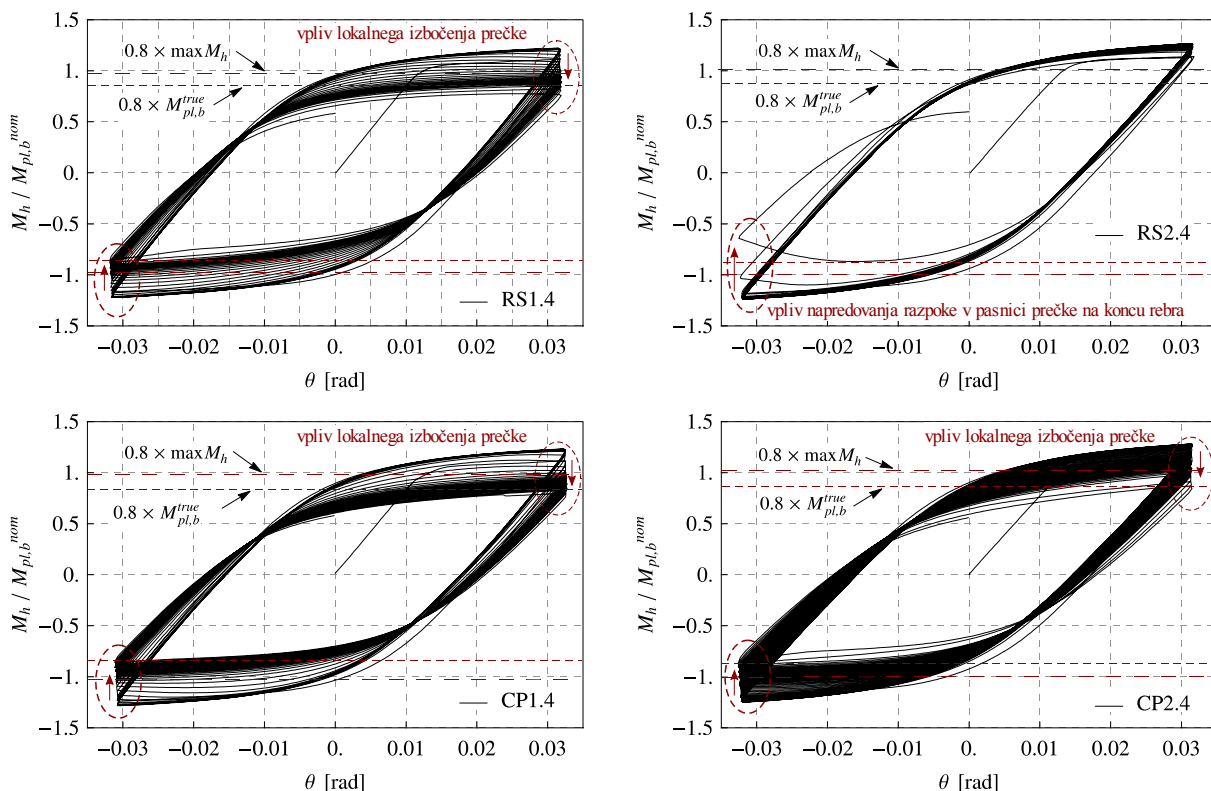
Z ustrezno načrtovano izbiro parametrov študije, pri čemer sta bili uporabljeni dve amplitudi konstantne ciklične obremenitve (mala in velika) v kombinaciji z dvema različnima profiloma prečk (IPE240 in IPE270) in za dva različna ojačana tipa spojev (RS in CP), sta bila dobljena dva različna odziva nizkocikličnega utrujanja spojev, ki sta natančneje opisana v nadaljevanju.

Kot je bilo željeno, ni v nobenem izmed štirih preizkušancev testiranih z malo konstantno amplitudo, RS1.3, RS2.3, CP1.3, CP2.3, prišlo do lokalnega izbočenja prečke v območju plastičnega členka vse do končne porušitve posameznega ojačanega spoja. Za vse štiri preizkušance je značilen praktično konstanten potek amplitude momenta skozi celoten test. Do izrazitejšega padca nosilnosti je prišlo šele v zadnjih nekaj ciklih, ko je razpoka tik za zvarom na koncu ojačanega dela napredovala v popoln pretrg pasnice in s tem do dokončne porušitve preizkušanca, slike 16 do 20.

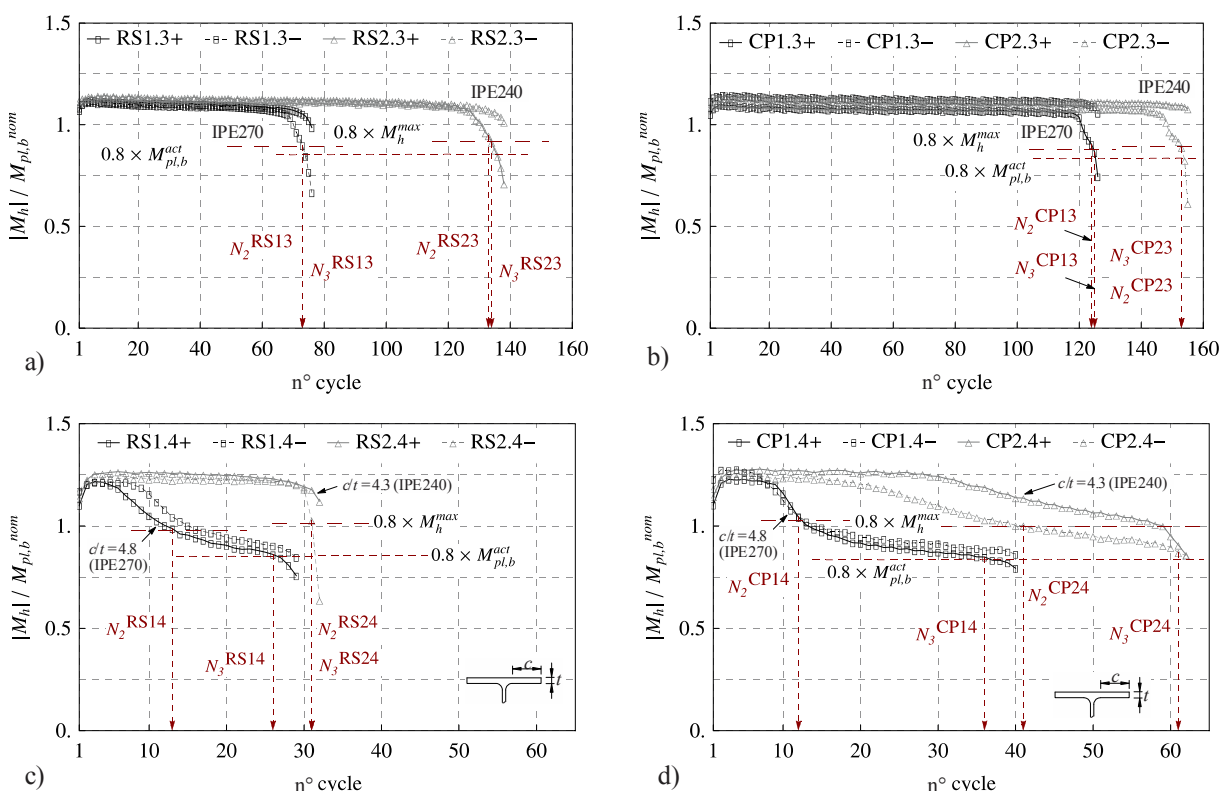
Glavni vzrok porušitve v omenjenih štirih RS in CP spojih je bila razpoka v pasnici prečke na koncu ojačanega dela prečke, ki je nastala zaradi stabilnega napredovanja duktilnih razpok v tem delu. V primeru obeh RS spojev, je bil opažen začetek razpok na sredini pasnice prečke, v toplotno vplivni coni (HAZ) kotnega zvara rebra, slika 17, medtem ko so se v primeru obeh CP spojev razpoke širile v območju HAZ prečnega kotnega zvara na koncu vezne pločevine od prostega robu pasnice prečke v notranjost, slika 18.



Slika 14: Odziv preizkušancev testiranih z malo konstantno amplitudo



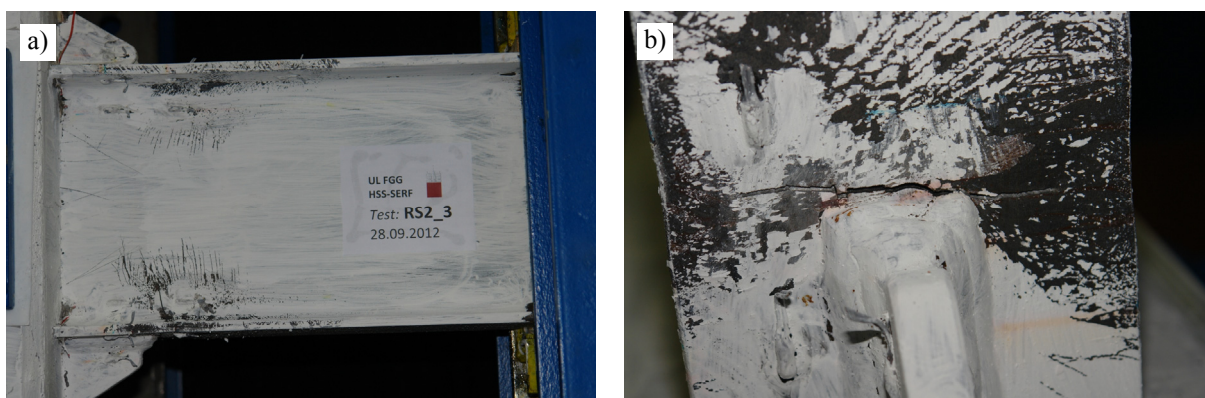
Slika 15: Odziv preizkušancev testiranih z veliko konstantno amplitudo



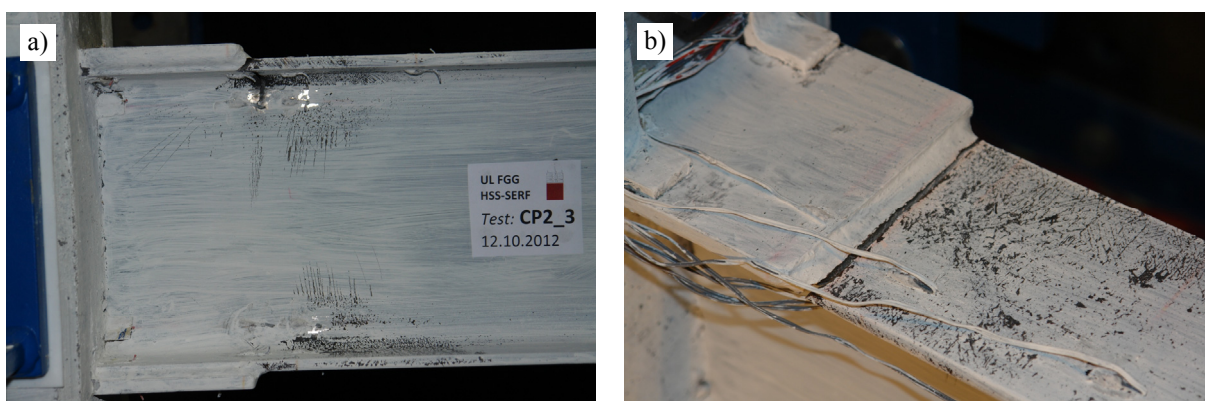
Slika 16: Normiran moment M_h v zaporednih amplitudah rotacije v odvisnosti od števila ciklov: a) RS1.3 in RS2.3, b) CP1.3 in CP2.3, c) RS1.4 in RS2.4, d) CP1.4 in CP2.4

V vseh štirih preizkušancih je ojačan del prečke ostal v elastičnem območju in nepoškodovan. Prav tako ni bilo zaslediti nobenih poškodb v zvarih ob pasnici stebra in okrog ojačilnih pločevin.

Kratek pregled deformirane oblike spojev RS2.3 in CP2.3, z detajlom mesta razpoke na pasnici prečke tik za ojačanim delom spoja, je prikazan na slikah 17 in 18.



Slika 17: Preizkušavec RS2.3 po končanem testu: a) lokalno plastificirana prečka takoj za koncem ojačanega dela b) frakcija zgornje pasnice



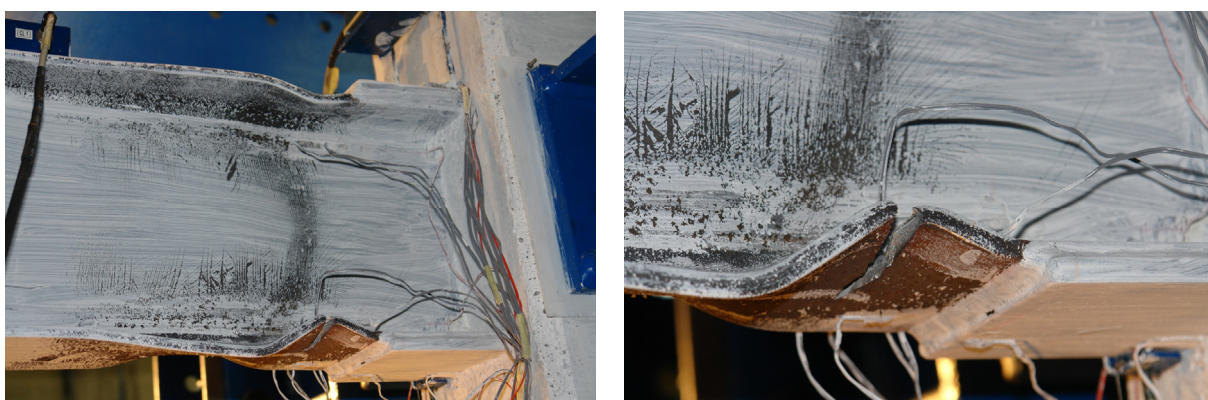
Slika 18: Preizkušavec CP2.3 po končanem testu: a) lokalno plastificirana prečka takoj za koncem ojačanega dela b) frakcija zgornje pasnice

Ciklični odziv preostalih štirih preizkušancev testiranih z veliko konstantno amplitudo, RS1.4, RS2.4, CP1.4 and CP2.4, je bil zaznamovan s pojavom lokalnega izbočenja prečke v območju plastičnega členka tik za ojačanim delom, sliki 19 in 20.

Porušitev obeh CP spojev je bila podobna tisti pri preizkušancih testiranih s spremenljivo postopoma naraščajočo amplitude rotacije: redukcija nosilnosti zaradi lokalnega izbočenja pasnic ter naknadnega izbočenja stojine prečke, ki mu je sledil pojav duktilne razpoke v najbolj zgubanem delu pasnice prečke, slika 20. V nasprotju s tem pa je v primeru obeh RS spojev, začetek duktilnih razpok v HAZ kotnega zvara na koncu rebra vodil v popoln pretrg pasnice prečke, podobno kot v primeru obeh RS spojev testiranih z malo konstantno amplitudo.



Slika 19: Preizkušavec RS2.4 po končanem testu: a) lokalno plastificirana prečka takoj za koncem ojačanega dela b) frakcija zgornje pasnice



Slika 20: Preizkušavec CP2.4 po končanem testu: a) lokalno plastificirana prečka takoj za koncem ojačanega dela b) frakcija spodnje pasnice

V obeh primerih RS spojev je prišlo pred končno porušitvijo preizkušanca do omejenega pojava lokalnega izbočenja prečke v območju plastičnega členka.

V skladu z zgoraj opisanim obnašanjem spojev v primeru cikličnega obremenjevanja z veliko konstantno amplitudo, je odziv obeh RS spojev izkazal slabše obnašanje v primerjavi z odzivom obeh CP spojev, saj do končne porušitve ni prišlo v najbolj zgubnem delu prečke sredi plastičnega členka, temveč v toplotno vplivni coni zvara na koncu rebra, kar je vplivalo na bistveno manjšo odpornost spoja na nizkociklično utrujanje, slika 16, preglednice 4 do 6.

V nasprotju s preizkušanci testiranimi s spremenljivo postopno naraščajočo amplitudo, se je pri spojih obremenjenih s konstantno amplitudo kot kritičen izkazal kriterij nosilnosti, preglednica 4.

Presoja odziva vseh osmih RS in CP preizkušancev testiranih s spremenljivo postopno naraščajočo amplitudo ciklične obremenitve je bila izvedena tudi v skladu s kvalifikacijskimi kriteriji iz ustreznih standardov.

Standard EN 1998-1 zahteva, da je rotacijska kapaciteta plastičnega členka na prečki 0,035 rad za konstrukcije razreda duktilnosti DCH in 0,025 rad za konstrukcije duktilnostnega razreda DCM. V obeh primerih mora rotacijska kapaciteta biti zagotovljena pri cikličnem obremenjevanju, pri čemer padec največje nosilnosti oziroma začetne togosti ne sme presežati 20%. Za momentne spoje prečka-steber standard ANSI/AISC 341-10 zahteva, da znaša najmanjša celotna rotacija stebra 0,04 rad za najbolj duktilne okvirje (SMF) oziroma 0,02 za srednje duktilne okvirje (IMF). Pri tem najmanjša sprejemljiva nosilnost spoja znaša vsaj

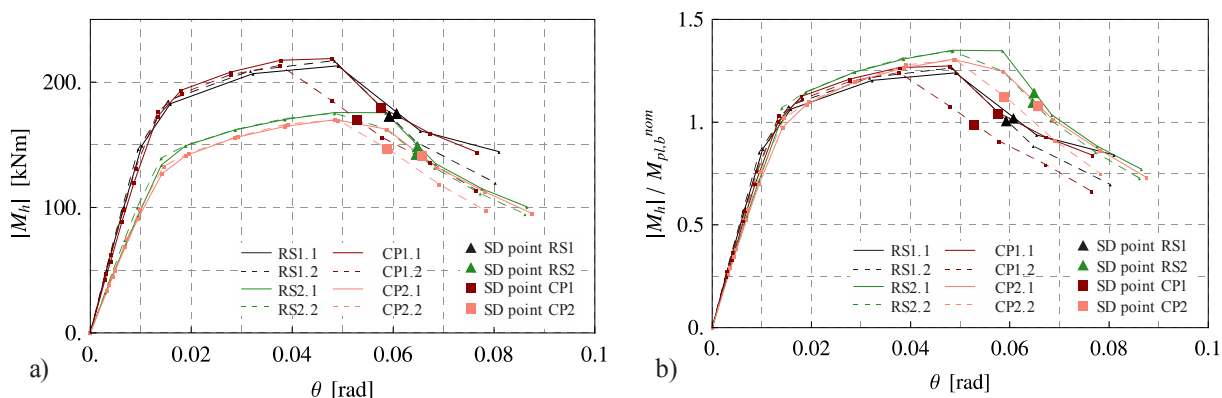
80 % M_{pl} , kjer je M_{pl} nominalni plastični moment prečke. Iz preglednice 7 je razvidno, da oba tipa spojev, RS in CP, v vseh osmih primerih izpolnjujeta najstrožja kriterija iz obeh standardov.

Preglednica 7: Celoten zasuk prečke in spoja

Spoj	θ_b (rad)	θ (rad)	Spoj	θ_b (rad)	θ (rad)
RS1.1	0.043	0.065	CP1.1	0.037	0.067
RS1.2	0.045	0.065	CP1.2	0.044	0.058
RS2.1	0.050	0.068	CP2.1	0.048	0.078
RS2.2	0.054	0.068	CP2.2	0.050	0.068
mejni zasuk	$> 0.035^a$	$> 0.04^b$		$> 0.035^a$	$> 0.04^b$

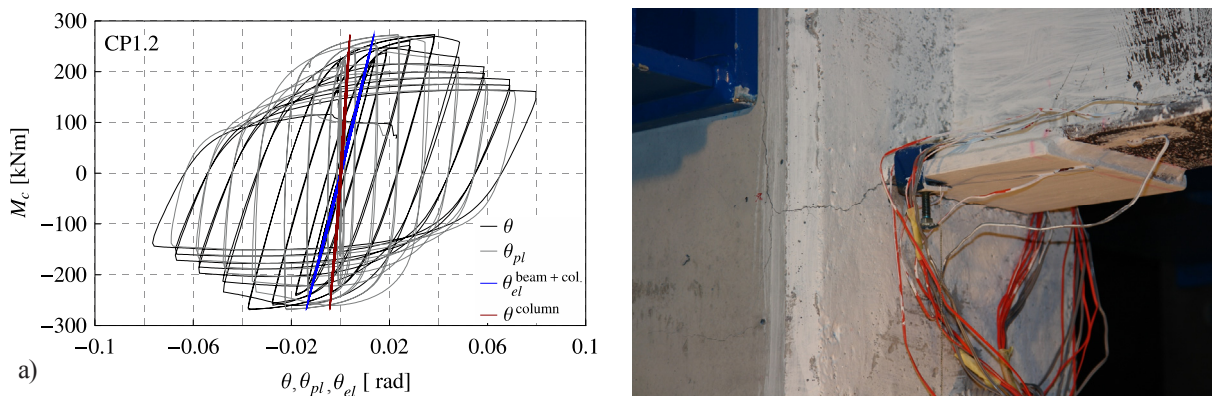
Zahtevana rotacijska kapaciteta: ^a EN 1998-1, ^b AISC 341-10

Dodatno so bili rezultati osmih testov s spremenljivo amplitudo cikličnega obremenjevanja ovrednoteni s pomočjo privzetih nivojev odziva. V ta namen so bile izrisane ovojnice odziva, slika 21, iz katerih je razvidno, da so vsi štirje zasnovani RS in CP spoji razvili stabilen ciklični odziv, s kriterijem rotacije v opazovanem stanju znatnih poškodb spoja $SD = 0.04$ rad izpolnjenem v vseh osmih primerih.



Slika 21: Ovojnice za vseh osem RS in CP spojev testiranih s spremenljivo amplitude cikličnega oremenjevanja: a) moment v središču plastičnega členka v odvisnosti od celotnega zasuka spoja, b) normiran moment v centru plastičnega členka v odvisnosti od celotnega zasuka spoja

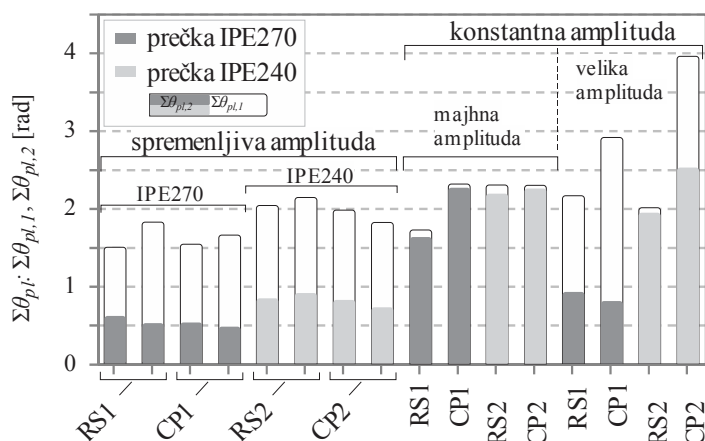
Kot je bilo že omenjeno, uporabljen nivo tlačne osne sile v stebri, ki je znašal približno 40% dejanske polnoplastične tlačne nosilnosti sovprežnega stebra, ni vplival na nizkociklično obnašanje ojačanih spojev. Prispevek stebra k celotni rotaciji spoja je znašal med 5.8 in 9.3% v primeru večjega in med 5.4 in 8.1% v primeru manjšega stebra, slika 22.



Slika 22: Delež rotacije celotnega spoja po posameznih komponentah in odziv stebra po končanem testu

Kot pričakovano, je sovprežen steber v vseh šestnajstih testih ostal v elastičnem območju odziva, pri tem pa je betonski ovoj, razen manjših razpok v lokalnem območju spoja prečka-steber, ostal popolnoma nepoškodovan, slika 22.

Končen pregled rezultatov iz vseh izvedenih testov, s poudarkom na primerjavi nizkocikličnega odziva med obema obravnavanima konfiguracijama, RS in CP, ojačanega spoja je predstavljena na sliki 23. Na histogramu so predstavljene vrednosti kumulativne plastične deformacije $\Sigma\theta_{pl}$, poročane v preglednicah 5 in 6. Natančneje, za vsak preizkušanec je izrisana primerjava med doseženima vrednostma $\Sigma\theta_{pl,1}$ and $\Sigma\theta_{pl,2}$.



Slika 23: Primerjava kumulativnih plastičnih rotacij iz vseh 16 testov

V primeru vseh osmih preizkušancev testiranih s spremenljivo amplitudo rotacije je opazna precejšnja redukcija vrednosti $\Sigma\theta_{pl,2}$, z vrednostjo kvocienta $\Sigma\theta_{pl,2}/\Sigma\theta_{pl,1}$ med 0.28 in 0.41. Pri tem je lahko opaziti večje vrednosti obeh kumulativnih plastičnih deformacij v primeru manjše prečke.

Vrednosti kumulativnih plastičnih deformacij sta precej večji v primeru preostalih osmih testov s konstantno amplitudo, predvsem zaradi večjega števila ciklov do porušitve, razen v primeru spojev z večjim profilom prečke IPE270, v kombinaciji z veliko konstantno amplitudo, kjer je prišlo do lokalnega izbočenja prečke v plastičnem členku.

Iz primerjave vrednosti kumulativnih plastičnih deformacij, predvsem $\Sigma\theta_{pl,2}$, dobljenih iz testov s konstantno amplitudo, je mogoče med RS in CP preizkušanci z enakima profiloma prečke in stebra opaziti precejšnjo razliko. Vrednosti akumuliranih plastičnih rotacij RS spojev so namreč precej manjše od tistih dobljenih s CP spoji. Tako očitna razlika med obema konfiguracijama spojev iz preostalih osem testov s spremenljivo amplitudo ni razvidna.

Iz zgornjih opažanj lahko povzamemo sledeči ugotovitvi:

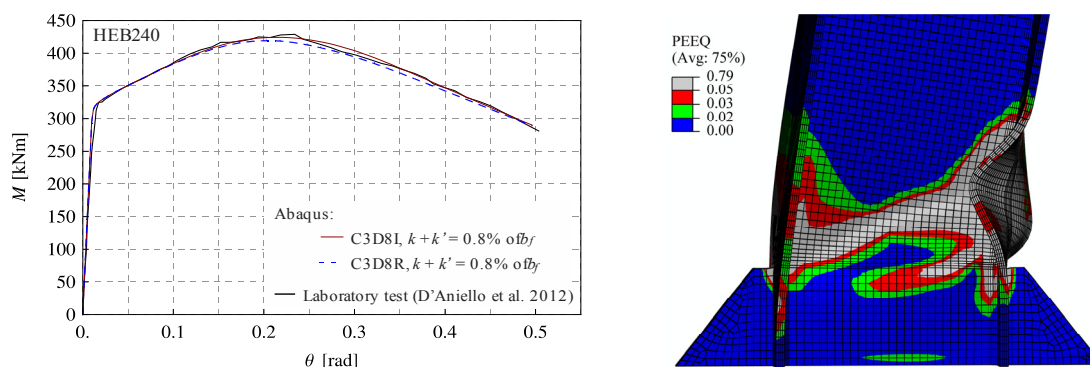
- med cikličnim obremenjevanjem z veliko amplitudo je prišlo v vseh primerih do lokalnega izbočenja prečke v območju plastičnega členka, kar je vodilo v nastanek razpoke zaradi nizkocikličnega utrujanja v pasnici prečke sredi plastičnega členka, ne glede na tip ojačanega spoja. To velja tako za obremenjevanje s spremenljivo postopno naraščajočo amplitudo kot tudi za veliko konstantno amplitudo;
- v nasprotju s prej omenjenim obnašanjem spojev obremenjenih z veliko amplitudo, je pri mali amplitudi šlo za nizkociklično utrujanje materiala brez prisotnosti lokalnega izbočenja prečke. V tem primeru je RS spoj izkazal slabši odziv v primerjavi s CP spojem, k čemur je prispevala predvsem visoka koncentracija napetosti/deformacij skupaj z veliko koncentracijo zaostalih napetosti v HAZ območju kotnega zvara na koncu rebra.

III NUMERIČNI MODEL

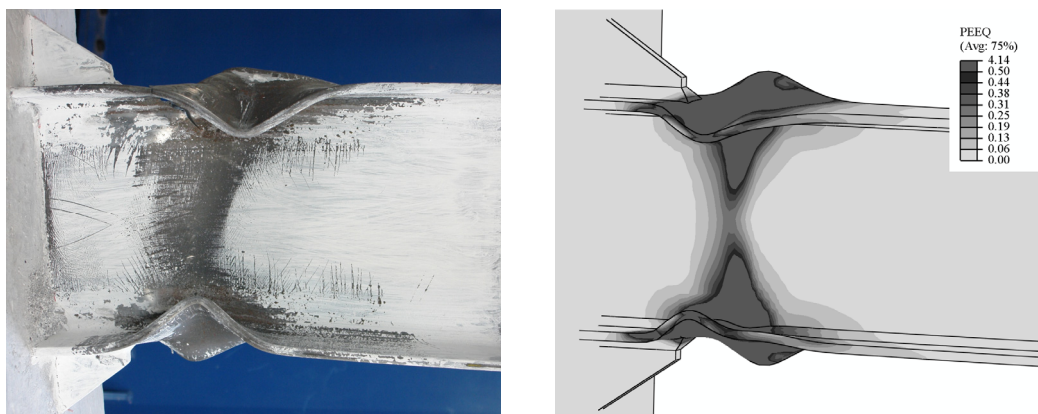
V obsegu študije je bil za potrebe nadaljne natančne obravnave obnašanja RS in CP ojačanih spojev razvit napreden računski model na osnovi metode končnih elementov. V ta namen je bil uporabljen program Abaqus v 6.12-2 (SIMULIA, 2012). Razvit numerični model omogoča simulacije odziva spojev prečka-steber različnih geometrij ojačitev za monotone in ciklične obremenitve.

V prvi fazi razvoja numeričnega modela je bila izvedena obširna konvergenčna študija elastičnega in plastičnega odziva, na podlagi katere so bili izbrani ustrezni končni elementi, opravljena kalibracija konstitutivnih materialnih modelov, izbrana metoda za vnos geometrijskih nepopolnosti na modelu ter določitev ustreznih parametrov procedure računa v program Abaqus. V drugi fazi je sledila kalibracija razvitega numeričnega modela na podlagi simulacije odziva laboratorijskih testov na spojih prečka-steber. Na podlagi monotoničnih simulacij je bila najprej določena velikost amplitude lokalnih deformacij na prečki v območju plastičnega členka, ki je zelo pomembna za natančno simulacijo monotonega in cikličnega odziva prečke in posledično tudi obnašanja celotnega spoja prečka-steber. Ker v obsegu študije ni bilo izvedenih monotoničnih eksperimentalnih testov, so bili v ta namen uporabljeni podatki iz literature.

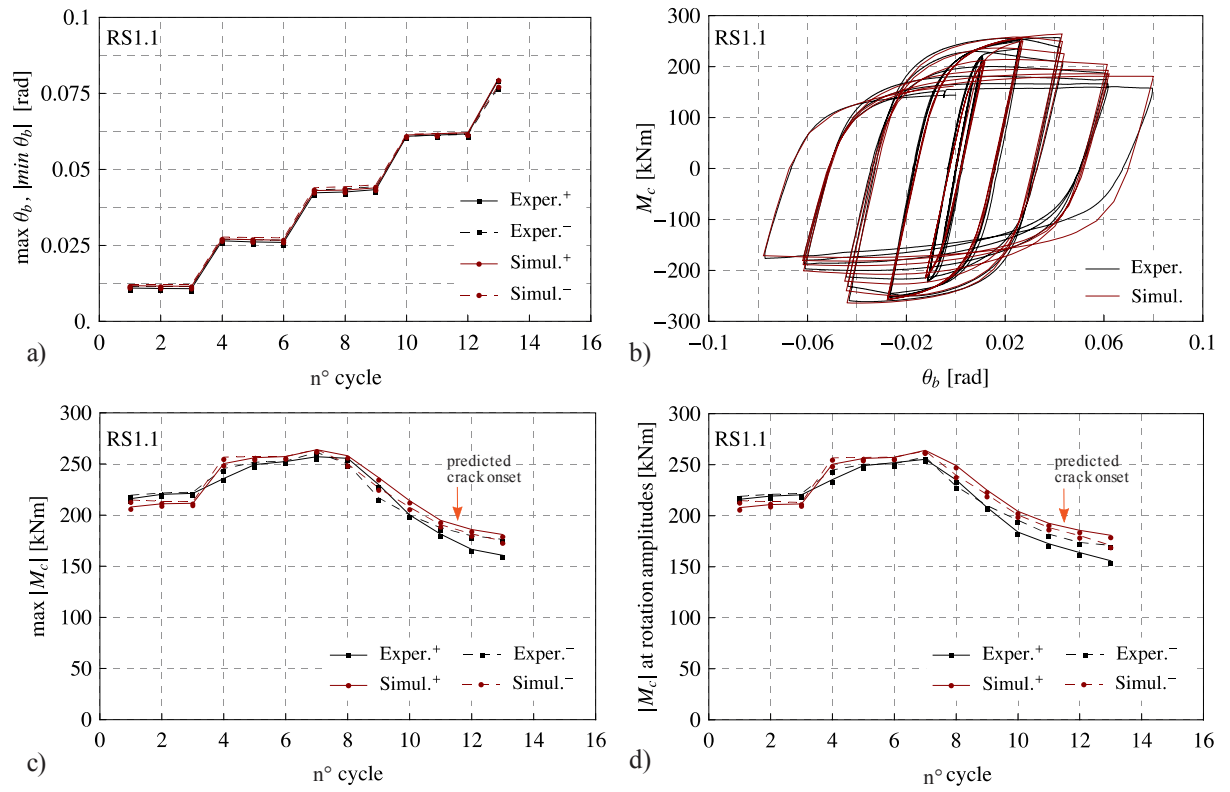
Razvit napreden numerični model daje zelo konsistentne rezultate v primerjavi z eksperimentalnim monotonim in cikličnim odzivom, slike 24 do 26.



Slika 24: Simulacija monotonega testa na prečki IPE300



Slika 25: Deformirana oblika preizkušanca RS1.1: eksperiment in simulacija



Slika 26: Odziv preizkušanca RS1.1: eksperiment in simulacija

IV PARAMETRIČNA ŠTUDIJA

Glavni namen numerične parametrične študije je preveriti ustreznost predlagane procedure protipotresnega dimenzioniranja, detajlov konstruiranja in izvedbe momentnih varjenih ojačanih spojev prečka-steber v kombinacijami z različnimi tipi vročevaljanih prerezov prečk, ki se najpogosteje uporabljajo v evropski inženirski praksi. Zaradi kompleksnega obnašanja momentnih varjenih ojačanih spojev, izpostavljenih monotonemu in še posebej cikličnemu obremenjevanju, je ob uporabi različnih prečk praktično nemogoče vnaprej napovedati nizkociklično obnašanje teh spojev. Predvsem so v dosedanjih študijah ugotovili, da ima pri tem velik vpliv geometrija prečnega prereza prečke. Predvsem z naraščajočo višino profila prečke se njena sposobnost duktilnega obnašanja manjša.

V ta namen je bilo opravljenih 32 simulacij odziva ojačanih spojev, kot to prikazuje preglednica 8.

Preglednica 8: Karakteristike spojev RS in CP v parametrični študiji

Prečni prerez prečke	Steber	Ojačan spoj	Obremenitev	Celotno št. simulacij
I	IPE270	HEB240	RS in CP	Monotona in ciklična
	IPE360	HEB300		
	IPE400	HEB340		
	IPE500	HEB400		
H	HEA400	HEM340	RS in CP	32
	HEB240	HEM280		
	HEB400	HEM450		
	HEB800	HEM1000		

Na podlagi simuliranih monotonih in cikličnih odzivov so bili podani sledeči zaključki:

- vpliv osne sile v stebru, do 60% ponoplastične tlačne nosilnosti stebra, nima večjega negativnega vpliva na lokalno razporeditev napetosti oziroma deformacij v območju varjenega stika prečka-steber ob pasnici stebra;
- vseh šestnajst ojačanih spojev izpostavljenih monotonim in cikličnim obremenitvam je razvilo dober odziv, s pojavom plastičnega členka v osnovnem prerezu prečke, medtem ko je ojačan prerez prečke ob pasnici stebra ostal praktično v elastičnem območju;
- predlagana procedura za dimenzioniranje RS in CP ojačanih spojev se je izkazala ustrezna za celoten nabor analiziranih spojev. Predlagan faktor za dodatno nosilnost ojačanega spoja 1.5 je povsem ustrezen;
- uporaba predlagane procedure dimenzioniranja s konceptom detajliranja obeh konfiguracij ojačanih spojev daje primerne, t.j. nepredebele, debeline pločevin, kar je zelo pomembno za izvedbo in ne prevelik vpliv toplotne obdelave materiala zaradi varjenja;
- ciklični odziv RS spojev je izkazal bistveno slabši odziv v primerjavi s CP spoji v smislu pojava nizkociklične razpoke.

IV ZAKLJUČEK

Na podlagi eksperimentalnih testov in numeričnih simulacij, s katerimi smo študirali obnašanje momentnih varjenih ojačanih spojev v primeru monotonega in cikličnega obremenjevanja, lahko zaključke raziskovalnega dela strnemo v sledečih točkah:

- Vseh šestnajst izvedenih eksperimentov na ojačanih spojih z rebri in veznimi pločevinami je pokazalo zelo dobro obnašanje preizkušencev z doseženimi velikimi plastičnimi deformacijami in dobro odpornostjo na nizkociklično utrujanje.
- Laboratorijski testi so potrdili ustreznost metode dimenzioniranja s konceptom detajliranja obeh obravnavanih konfiguracij ojačanih spojev: plastični členek se je pojavil v osnovnem prerezu prečke, medtem ko je ojačan del spoja, vključno s stebrom, ostal v elastičnem odzivu in nepoškodovan.
- Obe testirani konfiguraciji spojev vključno z upoštevanjo kombinacijo različnih kvalitet konstrukcijskega jekla v stebri in prečki ustrezata kvalifikacijskim kriterijem tako iz evropskega standarda EN 1998-1, kot tudi ameriškega standarda ANSI/AISC 341-10.
- Vpliv visokega nivoja (do 60% polnoplastične tlačne osne nosilnosti stebra) tlačne osne sile v stebri na obnašanje spoja je zanemarljivo.
- Razvit je bil napreden numerični model za simulacijo obnašanja spojev prečka-steber, s katerim je omogočena zelo natančna simulacija odziva spojev izpostavljenim tako monotoni in ciklični obremenitvi.
- Na podlagi parametrične študije z uporabo razvitega naprednega računskega modela za simulacijo spojev, je bila potrjena ustreznost predlagane metode dimenzioniranja za oba tipa momentnega varjenega ojačanega spoja.
- Na podlagi zaključkov analize eksperimentalnih in numeričnih rezultatov so bila podana priporočila za protipotresno projektiranje, konstruiranje in izvedbo obeh obravnavanih tipov spojev.

REFERENCES

- Anderson, J. C., Duan, X. 1998. Repair/upgrade procedures for welded beam-to-column connections. PEER 98/03, In: Richmond, CA, Pacific Earthquake Engineering Research Center (PEER).
- ANSI/AISC. 1997. Seismic provisions for structural steel buildings. I. American Institute of Steel Construction, (ed.), Chicago.
- ANSI/AISC. 2010a. Prequalified Connections for Special and Intermediate Steel Moment Frames for Seismic Applications. American Institute of Steel Construction, Chicago, Illinois.
- ANSI/AISC. 2010b. Seismic provisions for structural steel buildings. American Institute of Steel Construction, Chicago, Illinois.
- ANSI/AISC. 2010c. Specification for structural steel buildings. American Institute of Steel Construction, Chicago, Illinois.
- ASCE. 1971. Plastic design in steel: a guide and commentary. Manual and report on engineering practice, no.41. W. R. C. a. ASCE, (ed.).
- ATC. 1992. Guidelines for cyclic testing of components of steel structures. In: Report No. ATC-24. Redwood City, Calif., Applied Technology Council.
- Barsom, J. M., Rolfe, S. T. 1999. Fracture and fatigue control in structures: Applications of fracture mechanics, West Conshohocken, PA.: Woburn: Butterworth-Heinemann: 516 p.
- Becker, R. C., Smelser, R. E., Richmond, O., Appleby, E. J. 1989. The effect of void growth and ductility in axisymmetric tension tests. *Metalurgical transactions A*, 20A, 5: 853-861.
- Begum, M., Driver, R. G., Elwi, A. E. 2007. Numerical simulations of the behaviour of partially encased composite column. In: Structural Engineering Report No. 269. Alberta, Canada, Department of Civil and Environmental Engineering, University of Alberta.
- Bernuzzi, C., Castiglioni, C. A., Vajna de Pava, S. 1999. Behaviour of beam-to-column joints in moment-resisting steel frames. In. 6th International Colloquium on Stability and Ductility of Steel Structures. Timisoara.
- Bjorhovde, R., Goland, L. J., Benac, D. J. 1999. Tests of full-scale beam-to-column connections., The Bjorhovde Group, Tuscon, Ariz.
- Bleck, W., Dahl, W., Nonn, A., Amlung, L., Feldmann, M., Schafer, D., Eichler, B. 2009. Numerical and experimental analyses of damage behaviour of steel moment connection. *Engineering Fracture Mechanics*, 76, 10: 1531-1547.
- Bokan Bosiljkov, V., Duh, D., Bosiljkov, V., Žarnić, R. 2010. Time evolution of properties of SCC mixtures produced using crushed limestone aggregate and high content of limestone filler. SCC2010, Design, production and placement of self-consolidating concrete, K. H. Khayat, D. Feys, (eds.). Montreal, Canada, 317-327.
- Calado, L. 2000. Influence of column size. In: F. M. Mazzolani, (ed.). Moment resistant connections of steel frames in seismic areas, Design and reliability. London, E & FN Spon. p. 267-290.

Carreira, D. J., Chu, K. H. 1985. Stress-Strain Relationship for Plain Concrete in Compression. *Journal of the American Concrete Institute*, 82, 6: 797-804.

CEN. 1993. Structural steel I and H sections. Tolerances on shape and dimensions. European Committee for Standardisation (Technical committee ECISS/TC 103 - Structural steels other than reinforcements), Brussels.

CEN. 2004. Eurocode 4: Design of composite steel and concrete structures - Part 1-1: General rules and rules for buildings. European Committee for Standardisation, Brussels.

CEN. 2005a. Eurocode 3: Design of steel structures - Part 1-1: General rules and rules for buildings, EN 1993-1-1. European Committee for Standardisation, Brussels.

CEN. 2005b. Eurocode 3: Design of steel structures - Part 1-8: Design of joints. European Committee for Standardisation, Brussels.

CEN. 2005c. Eurocode 8: Design of structures for earthquake resistance - Part 1: General rules, seismic actions and rules for buildings. European Committee for Standardisation, Brussels.

CEN. 2007. Eurocode 3: Design of steel structures - Part 1-5: Plated structural elements, EN 1993-1-5. European Committee for Standardisation, Brussels.

Chen, C. C., Chen, S. W., Chung, M. D., Lin, M. C. 2005. Cyclic behaviour of unreinforced and rib-reinforced moment connections. *Journal of Constructional Steel research*, 61, 1: 1-21.

Čermelj, B., Beg, D. 2011. Numerical analysis of stiffened and cover-plate beam-to-column joints with fully-encased composite columns. Eurosteel, L. D. e. al., (ed.), ECCS European Convention for Constructional Steelwork, Budapest, Hungary, 363-368.

Čermelj, B., Beg, D. 2012. Numerical study on welded beam-to-column joints in hybrid-steel building frames. Stessa, M. F. M. H. R., (ed.), CRC Press/Balkema, Santiago, Chile, 173-178.

Čermelj, B., Beg, D. 2014. Cyclic behaviour of welded stiffened beam-to-column joints - Experimental tests. *Steel Construction*, 7, 4: 221-229.

Čermelj, B., Može, P., Beg, D. 2014. Experimental and numerical analysis on welded stiffened beam-to-column joints. In: F. M. M. Raffaele Landolfo, (ed.). Abstract book of the 7th European Conference on Steel and Composite Structures (Eurosteel). Naples, Italy, September 10 - 12, Brussels, Belgium, ECCS European Convention for Constructional Steelwork: 261-262.

D'Aniello, M., Landolfo, R., Piluso, P., Rizzano, G. 2012. Ultimate behavior of steel beams under non-uniform bending. *Journal of Constructional Steel research*, 78: 144-158.

Driscoll, G. C. 1957. Rotation capacity requirements for single-span frames. 268.5, In, Lehigh University, Fritz Engineering Laboratory.

Dubina, D., Stratan, A., Muntean, N., Dinu, F. 2008. Experimental program for evaluation of moment beam-to-column joints of high strength steel components. In: R. Bjorhovde, F. S. K. Bijlaard, L. F. Geschwindner, (eds.). Sixth International Workshop "Connections in steel structures VI". Chicago, USA, June 22-25: 355-366.

Dubina, D., Vulcu, C., Stratan, A., Ciutina, A., Grecea, D., Loan, A., Tremeeea, A., Braconi, A., Fulop, L., Jaspert, J., Demonceau, J. F., Hoang, V. L., Comelieau, L., Kuhlmann, U., Kleiner, A., Rasche, K., Landolfo, R., D'Aniello, M., Portioli, F., Beg, D., Čermelj, B., Može, P., da Silva, L. S., Rebelo, C., Tenchini, A., Kesti, J., Salvatore, W., Caprili, S., Ferrini, M. 2014. High Strength Steel in Seismic

Resistant Building Frames (HSS-SERF). Final Technical Report. In: RFCS, Steel RTD, RFSR-CT-2009-00024.

Duh, D. 2008. Self-compacting and vibrated concretes with limestone powder. Ljubljana, Slovenia, University of Ljubljana: 241 p.

ECCS. 1976. Manual on stability of steel structures. In: N 22/1976, European Convention for Constructional Steelwork (ECCS), Technical Committee 8: Stability.

ECCS. 1986. Recommended testing procedures for accessing the behaviour of structural elements under cyclic loads. European Convention for Structural Steelwork, Technical Committee 1 - Structural Safety and Loadings, Technical Working Group 1.3 - Seismic Design.

ECCS. 1994. ECCS Manual on Design of Steel Structures in Seismic Zones. In: N 76/1994, European Convention for Constructional Steelwork (ECCS), Technical Committee 13: Seismic design.

ECCS. 2013. Assessment of EC8 provisions for seismic design of steel structures. In: N 131/2013. Multicomp Lda, Mem Martins, Portugal, European Convention for Constructional Steelwork (ECCS), Technical Committee 13: Seismic design.

El-Tawil, S., Mikesell, T., Vidarsson, E., Kunnath, S. K. 1998. Strength and ductility of FR welded-bolted connections. SAC/BD-98/01, In: Background document (SAC Joint Venture). Sacramento, California, Department of Civil and Environmental Engineering, University of Central Florida.

Engelhardt, M. D., Sabol, T. A. 1995. Testing of welded steel moment connections in response to the Northridge earthquake in Northridge steel update I. Available from AISC:312-670-2400., In, American Institute of Steel Construction.

Engelhardt, M. D., Sabol, T. A. 1998. Reinforcing of steel moment connections with cover plates: benefits and limitations. *Engineering Structures*, 20, 4-6: 510-520.

Engelhardt, M. D., Sabol, T. A., Aboutaha, R. S., Frank, K. H. 1995. Testing connections. *Modern Steel Construction*, AISC, 35(5): 36 - 44.

Feldmann, M., Schafer, D., Eichler, B., Vayas, I., Carlos, V., Spiliopoulos, A. 2009. An upper shelf criterion for the choice of steel based on damage mechanics. 33rd IABSE Symposium Sustainable Infrastructure - Environment Friendly Safe and Ressource Efficient, Bangkok, Thailand.

FEMA. 1995a. Interim guidelines: advisory No. 1, supplement to FEMA-267. SAC-99-01, In: FEMA-267A. Sacramento, California, prepared by the SAC Joint Venture for the Federal Emergency Management Agency.

FEMA. 1995b. Interim guidelines: Evaluation, repair, modification and design of welded steel moment frame structures. SAC-95-02, In: FEMA-267. Sacramento, California, prepared by the SAC Joint Venture for the Federal Emergency Management Agency.

FEMA. 1999. Interim guidelines advisory No. 2 supplement to FEMA-267 interim guidelines. SAC-99-01, In: FEMA-267B. Sacramento, California, prepared by the SAC Joint Venture for the Federal Emergency Management Agency.

FEMA. 2000a. Prestandard and commentary for the seismic rehabilitation of buildings. In: FEMA 356. Wshington, D. C., For Federal Emergency Management agency (FEMA) prepared by ASCE.

FEMA. 2000b. Recommended seismic design criteria for new steel moment-frame buildings. In: FEMA 350, For Federal Emergency Management agency (FEMA) prepared by SAC Joint Venture.

FEMA. 2000c. Recommended Seismic Evaluation and Upgrade Criteria for Existing Welded Steel Moment-Frame Buildings. In: FEMA-351. Sacramento, California, For the Federal Emergency Management Agency prepared by the SAC Joint Venture.

FEMA. 2000d. State of the art report connection performance. In: FEMA-355D. Washington (DC), For the Federal Emergency Management Agency prepared by the SAC Joint Venture.

FEMA. 2009. NEHRP Recommended Seismic Provisions for New Buildings and Other Structures. For Federal Emergency Management agency (FEMA) prepared by Building Seismic Safety Council (BSSC), Washington, D.C.

FEMA. 2011. Quantification of Building Seismic Performance Factors: Component Equivalency Methodology. In: FEMA P-795. Washington (DC), Prepared by Applied Technology Council (NEHRP), Redwood City, California.

Gioncu, V., Mazzolani, F. M. 2000. Ductility of seismic resistant steel structures, London (New York), Spon Pressp.

Güneyisi, E. M., D'Aniello, M., Landolfo, R., Mermerdas, K. 2013. A novel formulation of the flexural overstrength factor for steel beams. *Journal of Constructional Steel research*, 90: 60-71.

Hasan, S. W., Hancock, G. J. 1989. Plastic bending tests of cold-formed rectangular hollow sections. *Steel Construction*, 23, 4: 2 - 19.

Huang, P. 1994. Finite element analysis of structural steel beams and bridge girders. Ithaca, NY, Cornell University.

Iwankiw, N. R., Carter, C. J. 1996. The dogbone: a new idea to chew on. *Modern Steel Construction*, 36, 4: 18-23.

Jesus, A. M. P., Matos, R., Fontoura, B. F. C., Rebelo, C., da Silva, L. S., Veljkovic, M. 2012. A comparison of the fatigue behavior between S355 and S690 steel grades. *Journal of Constructional Steel research*, 79, 12: 140-150.

Kanvinde, A. M., Deierlein, G. G. 2004. Micromechanical simulation of earthquake-induced fracture in steel structures. In: 145. Stanford, The John A. Blume Earthquake Center, Department of Civil and Environmental Engineering, Stanford University.

Kato, B., Akiyama, H. 1968. The ultimate strength of the steel beam-to-column (part 4). *Journal of Structural and Construction Engineering (Transactions of AIJ)*, 151: 15-20.

Kim, T., Whittaker, A. S., Gilani, A. S. J., Bertero, V. V., Takhirov, S. M. 2000. Cover-plate and flange-plate reinforced steel moment-resisting connections. Report to sponsor SAC Joint Venture, In. Berkeley, Pacific Earthquake Engineering Research Center (PEER), College of Engineering, University of California.

Kim, T., Whittaker, A. S., Gilani, A. S. J., Bertero, V. V., Takhirov, S. M. 2002a. Cover-plate and flange-plate steel moment-resisting connections. *Journal of Structural Engineering-Asce*, 128, 4: 474-482.

Kim, T., Whittaker, A. S., Gilani, A. S. J., Bertero, V. V., Takhirov, S. M. 2002b. Experimental evaluation of plate-reinforced steel moment-resisting connections. *Journal of Structural Engineering-Asce*, 128, 4: 483-491.

Krawinkler, H. 1998. SAC testing program and loading histories. Report to the SAC Joint Venture. Report to sponsor SAC Joint Venture, In. Sacramento, California, SAC Joint Venture.

Krawinkler, H., Zohrei, M. 1983. Cumulative damage model in steel structures subjected to earthquake ground motion. *Computers & Structures*, 16, 1-4: 531-541.

Kuhlmann, U. 1989. Definition of Flange Slenderness Limits on the Basis of Rotation Capacity Values. *Journal of Constructional Steel research*, 14, 1: 21-40.

Lee, C. H. 2002. Seismic design of rib-reinforced steel moment connections based on equivalent strut model. *Journal of Structural Engineering-Asce*, 128, 9: 1121-1129.

Lemaitre, J. 1992. *A course of damage mechanics*, Berlin, New York, Springerp.

Lemaitre, J., Chaboche, J. L. 1990. *Mechanics of Solid Materials*, Cambridge University Pressp.

Li, Q. B., Ansari, F. 2000. High-strength concrete in uniaxial tension. *Aci Materials Journal*, 97, 1: 49-57.

Maranian, P. 2010. *Reducing Brittle and Fatigue Failures in Steel Structures*, American Society of Civil Engineering - ASCEp.

Mazzolani, F. M. 2000. *Moment resistant connections of steel frames in seismic areas. design and reliability*, London, E & FN Spoonp.

Mazzolani, F. M., Piluso, P. 1992. Evaluation of the rotation capacity of steel beams and beam-columns. COST C1, Proc. of First State of the Art Workshop, Strasbourg.

Mazzolani, F. M., Piluso, P. 1993. Member behavioural classes of steel beams and beam-columns. XIV CTA Congress, Viareggio, 405-416.

Mazzolani, F. M., Piluso, P. 1996. *Theory and design of seismic resistant steel frames*, London, E & FN Spon an imprint of Chapman & Hallp.

McClintock, F. A. 1968. A criterion for ductile fracture by the growth of holes. *J. Appl. Mech.*, 35: 363-371.

McClintock, F. A. 1996. Ductile fracture by hole growth in shear bands. *Int. J. Fract. Mech.*, 2, 4: 614-627.

Mikesell, T. D. 1997. *Strength and ductility of welded-bolted steel connections*. Orlando FL, University of central Floridap.

Miller, D. K. 1998. Lessons learned from the Northridge earthquake. *Engineering Structures*, 20, 4-6: 249-260.

Nakashima, M., Inoue, K., Tada, M. 1998a. Classification of damage to steel buildings observed in the 1995 Hyogoken-Nanbu earthquake. *Engineering Structures*, 20, 4-6: 271-281.

Nakashima, M., Suita, K., Morisako, K., Maruoka, Y. 1998b. Tests on welded beam-to-column subassemblies. I: Global behaviour. *Journal of structural engineering*, 124, 11: 1236-1244.

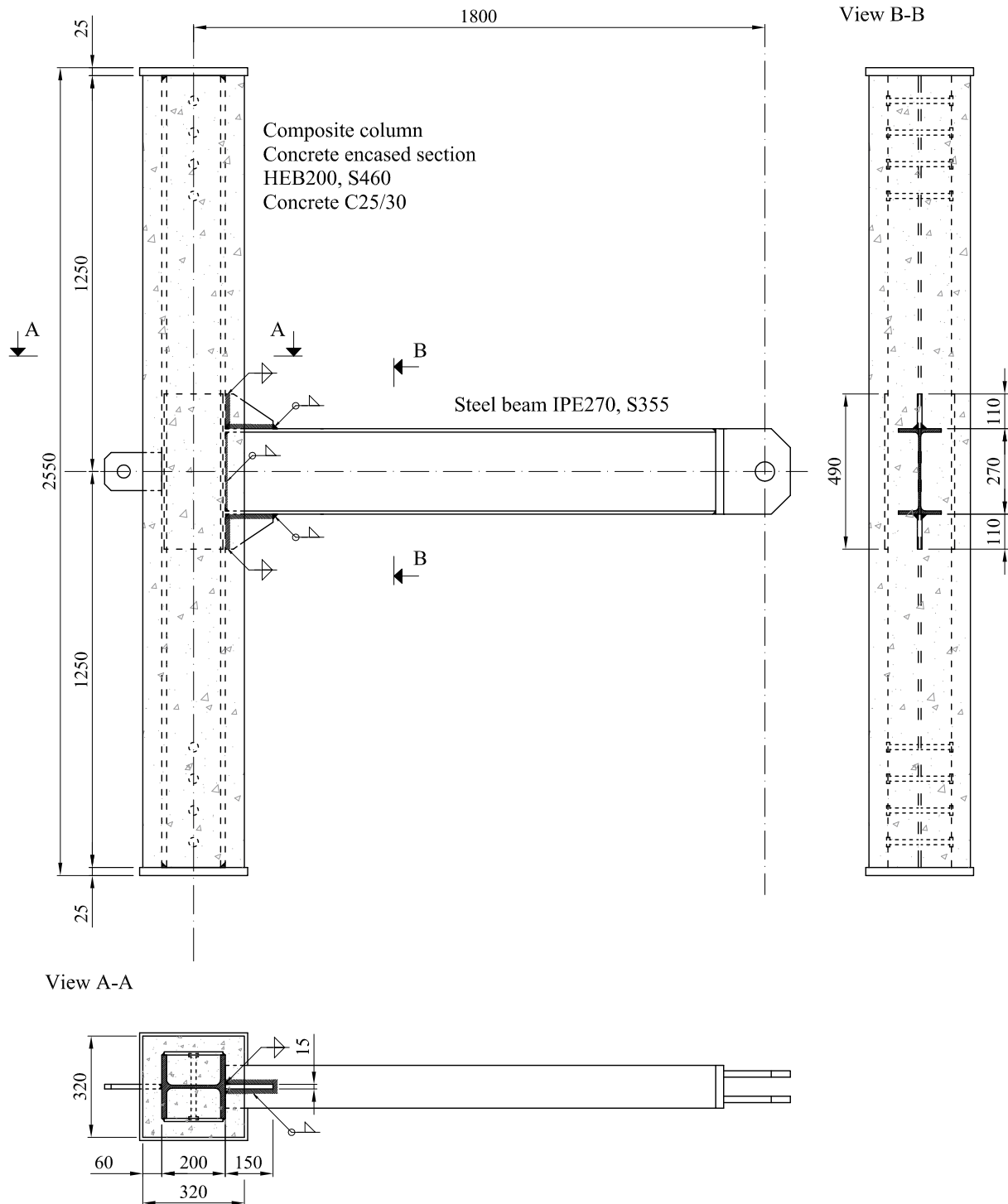
Nip, K. H., Gardner, L., Davies, C. M., Elghazouli, A. Y. 2010. Extremely low cycle fatigue tests on structural carbon steel and stainless steel. *Journal of Constructional Steel research*, 66, 1: 96-110.

Ohata, M., Toyoda, M. 2004. Damage concept for evaluating ductile cracking of steel structure subjected to large-scale cyclic loading. *Science and Technology of Advanced Materials*, 5, 1-2: 241-249.

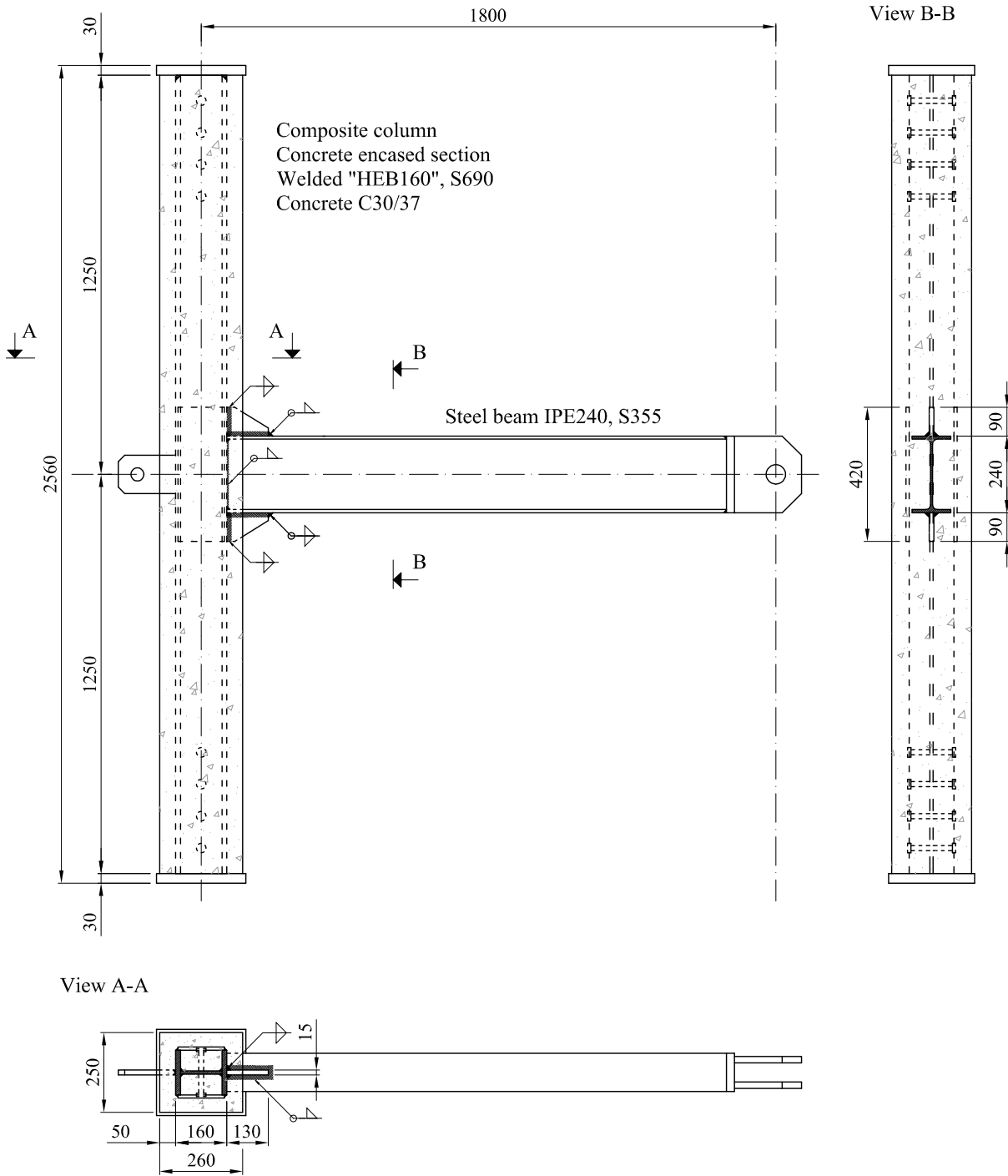
- Piluso, V., Rizzano, G. 2007. Random material variability effects on full-strength end-plate beam-to-column joints. *Journal of Constructional Steel research*, 63, 5: 658-666.
- Plumier, A. 1997. The dogbone: Back to the future. *Engineering Journal-American Institute of Steel Construction Inc*, 34, 2: 61-67.
- Popov, E. P., Blondet, M., Stepanov, L. 1996. Application of "dog bones" for improvement of seismic behaviour of stel connections. In. Berkeley, Calif., Earthquake Engineering Research Center, University of California at Berkeley.
- Popovics, S. 1973. A numerical approach to the complete stress-strain curve of concrete. *Cement and Concrete Research*, 3, 4: 583-599.
- Radomski, M., White, D. J. 1968. Some theoretical considerations relating to strain concentrations in elastic-plastic bending of beams. *Journal of Strain Analysis*, 3, 4: 304-312.
- Rice, J. R., Tracey, D. M. 1969. On the ductile enlargement of voids in triaxial stress fields. *J. Mech. Phys. Solids*, 17: 201-217.
- Roeder, C. W. 2002. General issues influencing connection performance. *Journal of Structural Engineering-Asce*, 128, 4: 420-428.
- Rondal, J., Boeraeve, P. H., Sedlacek, G., Stranghöner, N., Langenberg, P. 1995. Rotation capacity of hollow beam sections. In, CIDECT.
- Schafer, D., Eichler, B., Amlung, L. 2005 - 2008. PLASTOTOUGH: Modern plastic design of steel structures. In. RFSR-CT-2005-00039.
- SIMULIA. 2012. Abaqus Online Documentation: Version 6.12-2. Dessault Systèmes.
- Skuber, P. 2003. Analiza nizkocikličnega utrujanja jeklenih konstrukcij na osnovi mehanskih poškodb. Univerza v Ljubljani: 132 p.
- Suita, K., Nakashima, M., Morisako, K. 1998. Tests on welded beam-to-column subassemblies. II: Detailed behavior. *Journal of structural engineering*, 124, 11: 1245-1252.
- Thomason, P. F. 1968. A theory for ductile fracture by internal necking of cavities. *J. Inst. Met.*, 96: 360-365.
- White, D. J., Radomski, M. 1968. Strain concentrations in beams under cyclic plastic straining. *Journal of Strain Analysis*, 3, 4: 313-324.
- Whittaker, A. S., Bertero, V. V., Gilani, A. S. 1996. Experimental investigations of beam-column subassemblages. In. SAC-96-01, part 1. Sacramento, Calif.
- Whittaker, A. S., Gilani, A. S. 1996. Cycling testing of steel beam-column connections. In. EERC-STI 1996/04. Berkeley, Calif., Earthquake Engineering Research Center, University of California at Berkeley.
- Wolfram Research, I. 2012. Mathematica. Wolfram Research, Inc., Champaign, Illinois.
- Zekioglu, A., Mozaffarian, H., Chang, K. L., Uang, C. M., Noel, S. 1997. Designing after Northridge. *Modern Steel Construction*, 37(3): 36 - 42.

APPENDIX A Geometric data of the test specimens

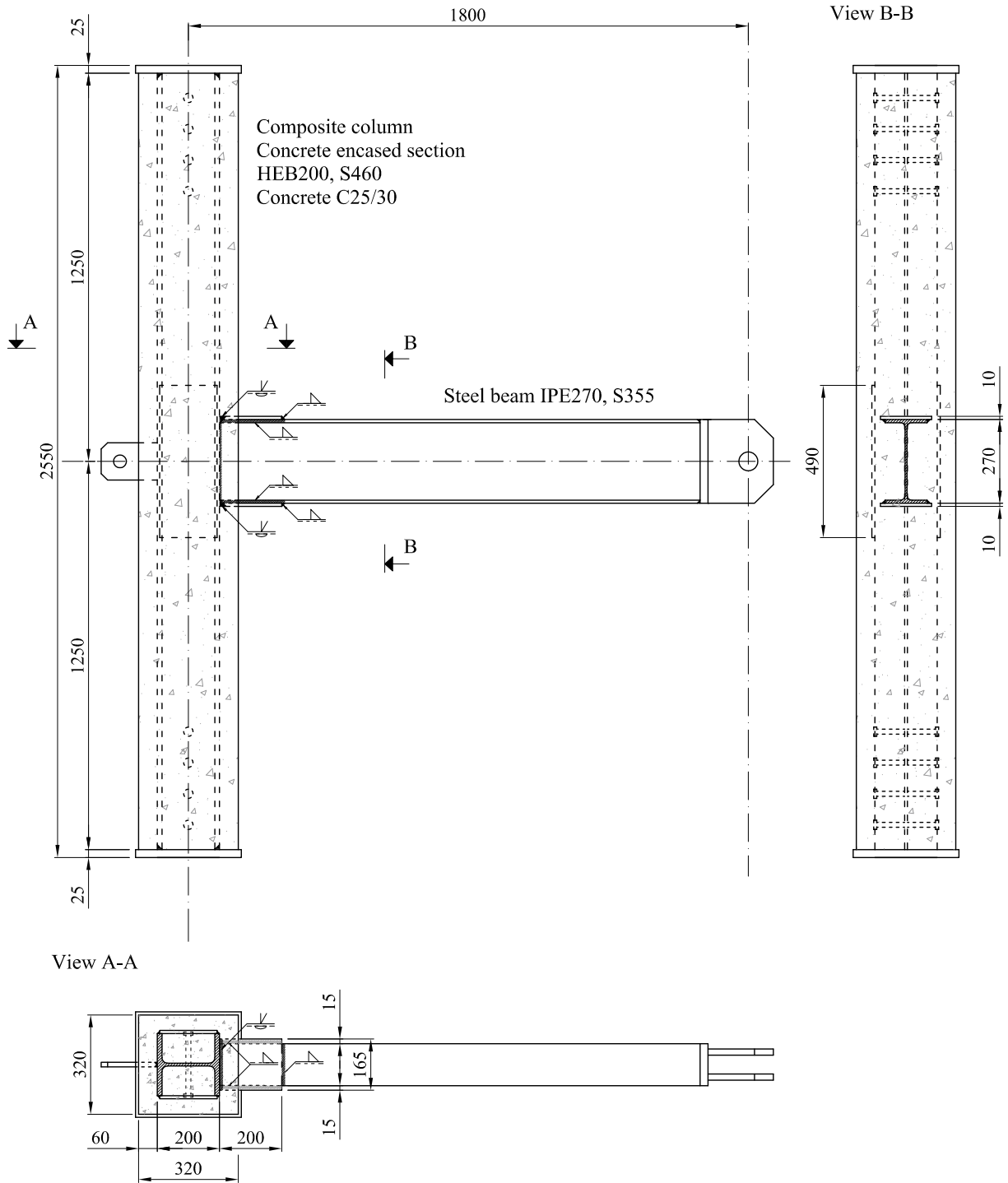
Specimen RS1



Specimen RS2



Specimen CP1



Specimen CP2

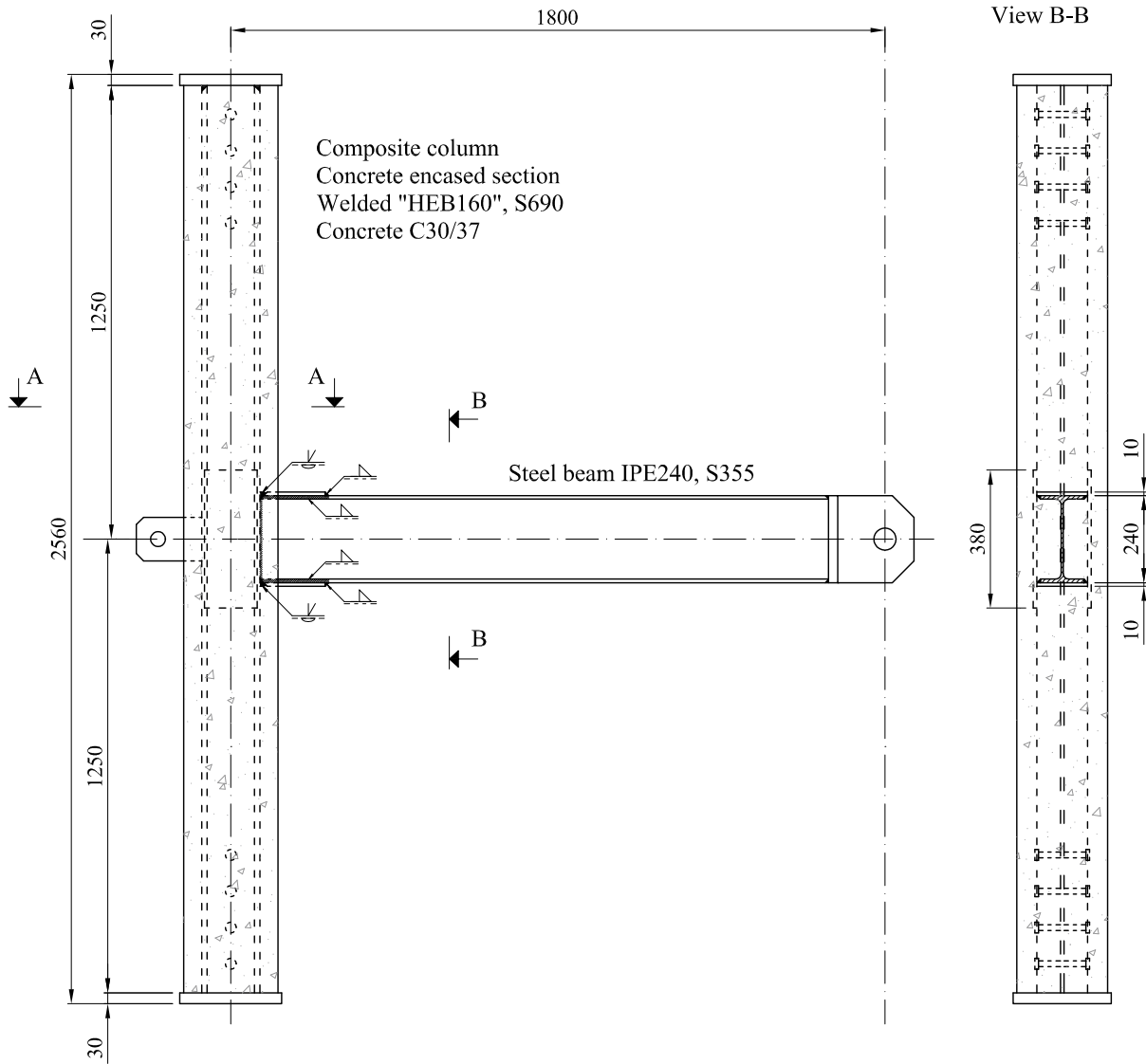


Table below presents measured geometric characteristics of all eight rib-stiffened (RS) beam-to-column joints.

Specimen	Element type	Measured values [mm]							
		h	b_f	t_f	t_w	r	a	b	t
RS1.1	Beam IPE 270	268	135	9.8	6.5	15			
	Column HEB 200	200	199	14.1	9.0	18			
	Rib stiffener						150	110	15.7
	Side plate						490	185	10.7
RS1.2	Beam IPE 270	269	135	9.8	6.5	15			
	Column HEB 200	200	200	14.4	9.0	18			
	Rib stiffener						148	110	15.6
	Side plate						490	185	10.5
RS1.3	Beam IPE 270	269	135	9.8	6.5	15			
	Column HEB 200	198	200	14.4	9.0	18			
	Rib stiffener						150	110	15.6
	Side plate						490	185	10.8
RS1.4	Beam IPE 270	267	135	9.7	6.5	15			
	Column HEB 200	199	199	14.3	9.0	18			
	Rib stiffener						142	110	15.6
	Side plate						490	185	10.5
RS2.1	Beam IPE 240	242	121	9.4	6.5	15			
	Col "HEB 160"	159	140	15.4	10.1	a			
	Rib stiffener						130	90	15.5
	Side plate						420	145	10.4
RS2.2	Beam IPE 240	240	121	9.5	6.3	15			
	Col "HEB 160"	160	141	15.2	10.1	a			
	Rib stiffener						130	90	15.6
	Side plate						420	145	10.4
RS2.3	Beam IPE 240	239	121	9.3	6.2	15			
	Col "HEB 160"	159	139	15.4	10.2	a			
	Rib stiffener						130	90	15.6
	Side plate						420	145	10.4
RS2.4	Beam IPE 240	240	120	9.3	6.3	15			
	Col "HEB 160"	159	140	15.3	10.2	a			
	Rib stiffener						130	90	15.4
	Side plate						420	145	10.4

NOTE: All measured values were rounded to a whole number, except for values of plate thicknesses

Table below presents measured geometric characteristics of all eight cover-plate (CP) beam-to-column joints.

Specimen	Element type	Measured values [mm]							
		h	b_f	t_f	t_w	r	l	b	t
CP1.1	Beam IPE 270	268	136	10.1	6.3	15			
	Column HEB 200	200	200	14.1	8.4	18			
	Cover plate						199	164	10.7
	Side plate						490	185	10.2
CP1.2	Beam IPE 270	270	135	10.3	6.3	15			
	Column HEB 200	199	200	14.4	8.6	18			
	Cover plate						198	163	10.6
	Side plate						490	185	10.3
CP1.3	Beam IPE 270	168	135	10.1	6.2	15			
	Column HEB 200	200	199	14.5	8.8	18			
	Cover plate						200	164	10.8
	Side plate						490	185	10.3
CP1.4	Beam IPE 270	169	134	10.2	6.4	15			
	Column HEB 200	200	199	14.5	8.7	18			
	Cover plate						200	164	10.6
	Side plate						490	185	10.1
CP2.1	Beam IPE 240	239	239	9.5	6.2	15			
	Col "HEB 160"	158	120	15.2	10.1	a			
	Cover plate						179		10.6
	Side plate						490	185	10.2
CP2.2	Beam IPE 240	241	121	9.4	6.3	15			
	Col "HEB 160"	159	120	15.3	10.2	a			
	Cover plate						180		10.7
	Side plate						490	185	10.3
CP2.3	Beam IPE 240	240	120	9.4	6.2	15			
	Col "HEB 160"	160	121	15.4	10.1	a			
	Cover plate						180		10.8
	Side plate						490	185	10.2
CP2.4	Beam IPE 240	239	120	9.2	6.3	15			
	Col "HEB 160"	159	120	15.3	10.1	a			
	Cover plate						180		10.6
	Side plate						490	185	10.2

NOTE: All measured values were rounded to a whole number, except for values of plate thicknesses

Geometric as well as material characteristics of the composite columns are gathered in the following table.

Specimen	Composite column characteristics		
	Cross section dimensions; b/h [mm]	Compressive strength of concrete [MPa]	Modulus of elasticity [†] [GPa]
RS1.1	320/324	64.6	
RS1.2	319/325	51.0	40
RS1.3	319/321	59.0	
RS1.4	318/324	54.6	
RS2.1	250/261	50.3	
RS2.2	248/264	49.4	40
RS2.3	247/264	47.5	
RS2.4	247/263	56.5	
CP1.1	321/322	58.3	
CP1.2	319/322	62.0	40
CP1.3	320/323	52.9	
CP1.4	322/321	54.8	
CP2.1	250/262	67.9	
CP2.2	248/263	62.1	40
CP2.3	249/261	66.7	
CP2.4	248/263	65.1	

NOTE: [†] Modulus of elasticity was not measured from the test on concrete samples, but was supposed on the basis of data provided from literature (Bokan Bosiljkov et al., 2010).

In the following table information on the distance between the centres of lateral beam supports (d_1), and distance from the edge of the stiffener (rib or cover plate) to the centre of the first support (d_2) is provided for all four different beam-to-column joints designed for the tests.

Specimen group	d_1, d_2 [mm]	Specimen group	d_1, d_2 [mm]
RS1	770, 465 (1.72 h_b)	CP1	770, 420 (1.56 h_b)
RS2	870, 405 (1.69 h_b)	CP2	770, 460 (1.92 h_b)

h_b is a height of the beam profile.

NOTE: Dimensions were taken from measurements on site and they completely suite to design sketches.

Position of inclinometer CL1 on the beam in terms of distance from the edge of the stiffener (rib or cover plate) to the inclinometer centre is given in the table below.

Specimen	d_{CL1} [mm]	Specimen	d_{CL1} [mm]
RS1.1	330	CP1.1	310
RS1.2	330	CP1.2	320
RS1.3	310	CP1.3	310
RS1.4	310	CP1.4	310
RS2.1	310	CP2.1	305
RS2.2	310	CP2.2	310
RS2.3	305	CP2.3	310
RS2.4	310	CP2.4	300